EXPERIMENTAL CHARACTERIZATION OF TURBULENCE IN STEEP ROUGH STREAMS

by

Cristina Fernandez Lopez

Supervised by

Prof. Dr. Allen Bateman Pinzon

Prof. Dr. Vicente Medina Iglesias

SEDIMENT TRANSPORT RESEARCH GROUP

UNIVERSITAT POLITÈCNICA DE CATALUNYA

Ph.D. PROGRAM: CIVIL ENGINEERING

ESCOLA TÈCNICA SUPERIOR D'ENGINYERS DE CAMINS, CANALS I PORTS DE BARCELONA

Funded by:

Generalitat de Catalunya

AGAUR

Barcelona,
September 2018

UNIVERSITAT POLITÈCNICA DE CATALUNYA BARCELONATECH

Experimental characterization of turbulence in steep rough streams

by

Cristina Fernandez Lopez

UNIVERSITAT POLITÈCNICA DE CATALUNYA
BARCELONATECH
Escola de Doctorat

Acta de calificación de tesis doctoral

Curso académico:

Nombre y apellidos

Programa de doctorado

Unidad estructural responsable del programa

Resolución del Tribunal

Reunido el Tribunal designado a tal efecto, el doctorando / la doctoranda expone el tema de su tesis doctoral titulada_____

_____.

Acabada la lectura y después de dar respuesta a las cuestiones formuladas por los miembros titulares del tribunal, éste otorga la calificación:

☐ NO APTO ☐ APROBADO ☐ NOTABLE ☐ SOBRESALIENTE

(Nombre, apellidos y firma) Presidente/a	(Nombre, apellidos y firma) Secretario/a

(Nombre, apellidos y firma) Vocal	(Nombre, apellidos y firma) Vocal	(Nombre, apellidos y firma) Vocal

_____, _____ de _____ de _____

El resultado del escrutinio de los votos emitidos por los miembros titulares del tribunal, efectuado por la Comisión Permanente de la Escuela de Doctorado, otorga la MENCIÓ CUM LAUDE:

☐ SÍ ☐ NO

(Nombre, apellidos y firma) Presidente/a de la Comisión Permanente de la Escuela de Doctorado	(Nombre, apellidos y firma) Secretario/a de la Comisión Permanente de la Escuela de Doctorado

Barcelona, _____ de _____ de _____

Mención Internacional en el título de doctor o doctora

- Como secretario/a del tribunal hago constar que parte de la tesis doctoral, como mínimo el resumen y las conclusiones, se ha redactado y presentado en una de las lenguas habituales para la comunicación científica en su campo de conocimiento y diferente de las que son oficiales en España. Esta norma no se aplica si la estancia, los informes y los expertos provienen de un país de habla hispana.

(Nombre, apellidos y firma) Secretario/a del Tribunal

Abstract

Torrential flows have so far been studied less than have river flows, due to the difficulty of faithfully reproducing them in the laboratory, and the few field measurements available. For this reason, this present research tries to shed some light on the turbulent description of this type of flows, evaluating the effects posed by the energy slope and the roughness of the bed. With this study we have made a significant contribution to the knowledge of how turbulent properties develop along the profile of the depth of the flow and thus improve all the engineering aspects that affect the high mountain flows (<<D50/d), from the valuation of the energy losses produced in the rough layer until the beginning of movement of the particles.

For this purpose, different flows have been characterized by the description of classic turbulent parameters (turbulent intensity, turbulent kinetic energy, Reynolds shear stress, dissipation, length scales, etc.). In addition, a detailed analysis of quadrants has been carried out due to the implications of bursting turbulence at the beginning of particle movement. Some of the results obtained from the analysis of quadrants have shown that the turbulence does not happen randomly, showing certain temporal and spatial patterns that can be of great help in the development of generation models of synthetic velocity series. The analysis of quadrants has been complemented with an analysis of the pulses, promoted for the temporary coherence observed in the quadrant sequences. One pulse is defined as the uninterrupted time that an event $u'w'$ remains in the same quadrant. This analysis yields very interesting results since they show a certain proportionality in both quantity and duration of turbulent pulses, as if it were a condition to be fulfilled by all flows.

Many authors have shown that the impulse applied (force x time application) is responsible for the initial movement of the particles rather than only the magnitude of the applied force. This idea has been the point of departure for the realization of a conceptual model to assess the rate of transport of sediment of a flow. This model is based on the consideration that Reynolds shear stress has the most important role in the beginning of the bed material's movement. Therefore, the time in which the bed shear stress applies in the same direction defines the intensity of the impulses applied to a surface. This last hypothesis together with the concept of pulses and pulse sequence are the bases for a methodology for assessing the transport rate of a flow and a specific sediment. The conceptual model has been evaluated by comparison with the transport rates measured in the laboratory.

To carry out this study, different laboratory experiments were performed in the Laboratory of Fluvial Morphodynamics II "*The Cube*" of the GITS-UPC research group. The experiments are divided into two groups; the first encompasses the RG tests (Rounded Gravel) and second group the CG tests (Crushed Gravel). The first group consists of a total of 10 experiments, all with the same bed roughness, formed with rounded gravel (D_{50}=55-mm y σ=16-mm), but with 10 different discharges, which allows the evaluation of the effects of the flow rate over turbulent variables. In the second group of experiments (CG), crushed gravel (not rounded) is used to form the test bed. Up to three different diameters are used (D_{50}= 17.8-mm, D_{50}= 30.0-mm, and D_{50}= 51.1-mm) that give rise to three different experiments. In addition, each of these materials is tested twice, the first testing the material simply poured and the second smoothing the surface as much as possible to reduce relative roughness, which

makes a total of 6 experiments. In this second group the data collection is made once the start of the movement of the particles has been reached.

The instantaneous velocity at each point of the profile was measured using an Acoustic Doppler Velocimeter (ADV) to obtain time series of instantaneous velocity in three dimensions (X, Y, Z). The measurements obtained by ADV in highly turbulent flows are linked to certain uncertainties such as the presence of spikes, low SNR signal and low correlation data. The low correlation favors a high percentage of data filtered through the most common filtering limits (COR <70), obtaining up to 50% of erroneous data in some areas near the bed.

The replacement of the low correlation data subtracts turbulent energy to the series of velocity with the consequent modification of the turbulent parameters, distancing it from its natural turbulent behavior. In addition, the elimination of data of low correlation does not avoid the need to apply other filters to eliminate the spikes produced by aliasing. For this reason, an in-depth study has been carried out on the quality of the data, using analysis of quadrants and pulses in addition to other turbulent parameters, finding that low correlation data have a behavior similar to high correlation data. On the other hand, the need for a broader knowledge of the effects produced by the ADV configuration on the characterization of the turbulence studied throughout the thesis motivated an additional study. These analyses related to the reliability of the data have been included as an appendix since they involve all the concepts analyzed during the execution of the thesis together. Since the checks have been made recursively throughout the study, to include these works within the body of the thesis would lead to confusion. The reader will be indicated at certain points of the thesis to consult these appendices.

Resumen

Los flujos torrenciales están actualmente menos estudiados que los de tipo fluvial, debido a la dificultad de reproducirlos fielmente en laboratorio y a las pocas medidas de campo de las que se dispone. Es por este motivo que la presente investigación intenta arrojar algo de luz sobre la descripción turbulenta de este tipo de flujos, evaluando los efectos que la pendiente motriz y la rugosidad del lecho tienen sobre ésta. Con este estudio se ha contribuido al conocimiento de cómo se desarrollan las propiedades turbulentas a lo largo del perfil de profundidad y así mejorar todos los aspectos ingenieriles que afectan a los flujos de alta montaña ($<<D_{50}/d$), desde la valoración de la pérdidas de energía producidas en la capa rugosa hasta el inicio de movimiento de las partículas.

Para ello, se han caracterizado diferentes flujos mediante la descripción de los parámetros turbulentos clásicos (intensidad turbulenta, energía cinética turbulenta, tensión de Reynolds, disipación, longitudes de escala etc.). Además, se ha realizado el análisis detallado de cuadrantes debido a las implicaciones que tienen los eventos turbulentos (bursting turbulence) en el inicio del movimiento de las partículas. Algunos de los resultados obtenidos del análisis de cuadrantes han puesto de manifiesto que la turbulencia no sucede de manera aleatoria, mostrando ciertos patrones temporales y espaciales que pueden ser de gran ayuda en el desarrollo de modelos de generación de series de velocidad sintéticas. Se ha complementado el análisis de cuadrantes con un análisis de pulsos, promovido por la coherencia temporal observada en las secuencias de cuadrantes. Un pulso se define como el tiempo ininterrumpido que un evento u'w' permanece en el mismo cuadrante. Este análisis arroja resultados muy interesantes ya que muestran una cierta proporcionalidad tanto en cantidad como en duración de pulsos turbulentos, como si se tratase de una condición a cumplir por todos los flujos.

Son muchos los autores que han demostrado que el impulso aplicado (fuerza x tiempo aplicación) es el responsable de la puesta en movimiento de las partículas en lugar de sólo la magnitud de la fuerza aplicada. Se ha partido de esta idea para la realización de un modelo conceptual que valore la tasa de transporte de sedimentos de un flujo. Este modelo está basado en la consideración de que la tensión de Reynolds tiene el papel más importante en el inicio de movimiento del material del lecho. Por lo tanto, el tiempo en el que la tensión de fondo se aplica en una misma dirección define intensidad de los impulsos aplicados a una superficie. Ésta última hipótesis junto con el concepto de pulsos y secuencia de pulsos son las bases para una metodología de valoración de la tasa de transporte de un flujo y un sedimento en concreto. El modelo conceptual ha sido evaluado mediante la comparación con las tasas de transporte medidas en laboratorio.

Para llevar a cabo este estudio se han realizado diferentes experimentos en el laboratorio de morfodinámica fluvial II "El cubo" del grupo de investigación GITS-UPC. Los experimentos están divididos en dos grupos, el primero engloba los tests RG (Rounded Gravel) y el segundo los tests CG (Crushed Gravel). El primer grupo está compuesto por un total de 10 experimentos, todos con la misma rugosidad de lecho, conformado con grava redondeada (D_{50}=55-mm y σ=16-mm), pero con 10 caudales diferentes, lo que permite la evaluación de los efectos del caudal del flujo sobre las variables turbulentas. En el segundo grupo de experimentos (CG) se utiliza grava partida (no redondeada) para conformar el lecho de ensayo. Se utilizan hasta tres diámetros diferentes (D_{50}= 17.8-mm, D_{50}= 30.0-mm, and D_{50}= 51.1-mm) que dan lugar a tres experimentos diferentes. Además, cada una de estos

materiales se ensaya dos veces, la primera ensayando el material simplemente vertido y la segunda alisando la superficie todo lo posible para reducir la rugosidad relativa, lo que hace un total de 6 experimentos. En este segundo grupo la toma de datos se realiza una vez el inicio del movimiento de las partículas ha sido alcanzado.

La velocidad instantánea en cada punto del perfil se ha medido usando un velocímetro de efecto doppler (ADV), que permite obtener series temporales de velocidad instantánea en las tres dimensiones (X, Y, Z). Las medidas obtenidas mediante ADV en flujos altamente turbulentos están ligadas a ciertas incertidumbres tales como presencia de spikes, baja señal SNR y datos de baja correlación. La baja correlación propicia un alto porcentaje de datos filtrados mediante los límites más comunes de filtrado (COR<70) obteniéndose hasta un 50% de datos erróneos en algunas zonas cercanas al lecho.

El reemplazo de los datos de baja correlación sustrae energía turbulenta a la serie de velocidad con la consiguiente modificación de los parámetros turbulentos, alejándola de su comportamiento turbulento natural. Además, la eliminación de datos de baja correlación no evita la necesidad de aplicación de otros filtros para eliminar los spikes producidos por aliasing. Por este motivo se ha realizado un estudio en profundidad sobre la calidad de los datos, aplicando el análisis de cuadrantes y de pulsos además de otras parámetros turbulentos, obteniéndose que los datos de baja correlación tienen un comportamiento similar a los datos de alta correlación. Por otro lado, la necesidad de un conocimiento más amplio de los efectos que produce la configuración del ADV sobre la caracterización de la turbulencia estudiada a lo largo de la tesis motivó un estudio adicional. Estos análisis relacionados con la fiabilidad de los datos han sido incluidos en formato de apéndice ya que involucran de manera conjunta todos los conceptos analizados durante la ejecución de la tesis. Las comprobaciones se han ido realizando de manera recursiva durante todo el estudio, por lo tanto, incluir estos trabajos dentro del cuerpo de tesis daría lugar a confusión. El lector será indicado en ciertos puntos de la tesis a consultar estos apéndices.

Preface

This work has been possible thanks to a scholarship granted by the Generalitat of Catalonia (Help destined for universities and research centers for the hiring of new personnel, FI-DGR 2015), which I have enjoyed for a period of three years within the GITS-UPC research group. During this time, I carried out the experimental campaign, developed the conceptual model and performed the analysis of the results.

Previously, I had the opportunity to be involved in a project within the GITS-UPC group for two years (SCOURTECH), where my main functions were designing and managing the construction of the hydraulic channel "the cube", as well as the organization and execution of experiments of bridge pier protections with partially grouted riprap. This period gave me a background in terms of resolving unforeseen events during the execution of experiments and a broad knowledge of the operation of the hydraulic flume "the cube", in which I would later perform the experiments for the development of my thesis. During this time arose the concern of a deeper knowledge of high mountain rivers, with large flow rates and steep slopes, and thanks to the FI-DGR scholarship it was possible to investigate this topic.

This thesis gathers a whole compendium of thoughts directed towards the application of turbulence of high mountain rivers at the incipient motion of the bed particles, for its future application to the design of linings and protections with riprap of small dimensions.

The results have been of great interest, obtaining the evidence that the turbulence is not chaotic at all but that it occurs in a certain specific way. Therefore, the results obtained in this thesis can be very useful when it comes to improving the generation models of synthetic velocity series, giving the fluctuations not only an adequate value but also a temporal coherence.

Experimental data series have been obtained using an Acoustic Doppler Velocimeter (ADV), despite some of the limitations that these devices can show when measuring highly turbulent flows. In the appendices of the present thesis, an analysis of the quality obtained by the data can be found, since these showed very low correlation values. The remove of the “bad” data caused large information gaps that broke the history of the velocity signal, which was a handicap for the study of the sequences of events. In addition, when the "bad” data were replaced through some interpolation method, the new values showed a very different trend compared to the data considered "correct" (with high correlation), removing the velocity series from its turbulent behavior. In addition, a study has been made of how the configuration of the apparatus affects the different turbulent properties analyzed throughout the thesis. These comparisons related to the quality and sensitivity of the data have been included in the appendices, firstly so as not to unnecessarily lengthen the thesis, and secondly, because many of the verifications made come from arguments developed throughout the thesis. Therefore, to include them at the beginning of the thesis could lead to confusion, since many of those concepts are developed later in their corresponding section. This shows that the work developed in these appendices is done recursively during the development of the thesis. As an issue related to the turbulence was analyzed, we wondered what involvement had the configuration of the device in the matter.

To carry out the thesis, two campaigns of experiments were conducted, the first in the channel "the cube" of the GITS-UPC, related to the experiments analyzed throughout the thesis. However, a campaign of experiments is also performed in the "FRITZ" Laboratory of the University of Lehigh, during a three-month stay under the supervision of Professor Panos Diplas. These experiments were carried out a posteriori, during the phase of results analysis, so they only attend the assessment of how the configuration of the apparatus affects the properties analyzed in the first group of experiments since the ADV used in the first set of experiments did not allow varying the configuration of the apparatus.

The partial results of the thesis have been presented in different congresses (which are detailed below), and are the subject of a paper currently under review, referring to the low correlation of results in highly turbulent flows. It is also expected to write at least one more article in which all the results referring to the analysis of quadrants and statistics of turbulent events will be included.

- Fernández C., Bateman A. & Medina .V. (2015), 'Estudio experimental de protección con escollera parcialmente cementada contra la erosión en cauces'. 1er congreso iberoamericano sobre sedimentos y ecología. Querétaro, Méjico.
- Fernández C., Bateman A. & Medina .V. (2017), 'Quadrant analysis of high-turbulent flows.' RCEM, Trento, Italy.
- Fernández C., Bateman A. & Medina .V. (2017), 'Spatial and temporal pattern of coherent structures over a hydraulically rough bed'. International workshop on complex turbulent flows. Tanger, Morocco.
- Fernández C., Bateman A. & Medina .V. (2018), 'Efectos de la turbulencia en el inicio de movimiento de las protecciones de fondo en ríos de alta montaña.' XXVIII Congreso latinoamericano de hidráulica, Buenos Aires, Argentina.
- Fernández C., Bateman A. & Medina .V. 'ADV Data quality in highly turbulent flows'. *Experiment in fluids*. Under revision.

Acknowledgments

There are many people to thank for their support since there are many different ways of helping that one needs along this journey.

First, I want to express my sincere gratitude to my thesis tutors, Allen Bateman and Vicente Medina. I have learned many things from them, both technically and personally. I have learned to have an enthusiasm for research, to enjoy hard laboratory work and above all to never stop asking questions. I am very grateful to have been part of the GITS research group and to have learned so many things, such as from Allen his enormous scientific intuition, the fruit of many years of hard work, and from Vicente his wide knowledge for any subject that may come up. Thank you very much to both of you.

I would also like to thank Professor Panos Diplas for his dedication during the three-month stay I enjoyed at the University of Lehigh, making available to me all the resources of the FRITZ laboratory and permitting me to carry out the necessary experiments for the validation of my thesis results.

To all the comrades who have passed through GITS and who at some point have helped me, either to load stones as unblock MATLAB situations, or simply moral support. Thanks to Francesco, Alberto, Andres, Anna, Khaled, Blanca, Raul etc. Thanks to Stefania for her help and friendship in this last stage. Thanks also to those who do not belong to GITS but who are fight partners and whom I spent a long time with: Anais, Sergi, Edu, Agus etc. Happiness is greater and pain is less painful when shared.

I would also like to thank my committee members, Professor Dr. Albert Falques Serra – *Polytechnic University of Catalonia* (Physics department), Professor Dr. Michele La Rocca – *University of Rome "Roma Tre"* (Department of Engineering), Professor Dr. Guillermo Palau Salvador – *Polytechnic University of Valencia* (UPV), Albert Herrero Casas – *Institut Català de Recerca de l'Aigua* (ICRA) and Albert Falquès i Serra– *Polytechnic University of Catalonia* (Physics department) for serving as my committee members.

A special thanks for Professor Dr. Fabian A. Bombardelli from *University of California* (UCDAVIS) for all the efforts done to revise my thesis and for their comments and observations about my work that help me to improve this dissertation.

Thanks to my life partner Santiago, who always knows how to encourage me to pull forward and get rid of the negativity to bring out the positivity and practicality that is sometimes so difficult to find. Especial thanks for enduring the days of discouragement with multiple forms of appearance.

I also have to thank TYPSA for the facilities they have given me to travel to Saudi Arabia to be with Santiago and spend long periods there, where I found the peace necessary to write this thesis.

A special thanks to my family for the sincere support they have offered me every time I have needed it and to have taught me to fight to get what I want.

Thanks a lot to all my friends, those who knew me in kindergarten and those who have stayed by my side have always trusted me, sometimes even when I did not.

At the end, a great thanks to the Generalitat of Catalonia, AGAUR, for financially supporting this work through a governmental scholarship (FI-DGR 2015).

Table of Contents

List of Tables

List of Figures

List of Symbols

ε	Dissipation rate (m^2/s^3).
C	Chezy coefficient
C	Universal constant of Kolmogorov (C=0.49)
C^*	Dimensionless Chezy coefficient
C_{21}, C_{12}, C_w	Third order moment ratios
c_f	Friction coefficient
d	Hydraulic Depth (m)
D	Shift distance of the velocity profile (m)
D_{50}	Mean diameter of the bed particle (m)
d_c	Critical depth (m)
D_{min}, D_{max}	Minimum and maximum diameter of the bed particle (m)
d_n	Normal depth (m)
E	Energy rate
E_n	Energy Noise rate
f	Frequency (Hz)
F	Dimensionless frequency
Fr	Froude Number
f_c	Cutoff Frequency (Hz)
h	Control Volume height (mm)
H	Hole size
h_r	CV height set by the flow (m)
I	Impulse (N·s)
I_{cr}	Critical Impulse (N·s)
k	Roughness height (m)
K	Von Karman Constant
k_s	Relative Roughness (m)
k_w	Wavenumber (m^{-1})
L_i	Integral length scale (m)
L_p	Pulse length, measured in steps (δ)
M_{12}	Diffusion factor of $\overline{w'w'}$
M_{21}	Diffusion factor of $\overline{u'u'}$
Motion I.	Motion Index
Motion R.	Motion Rate
n	Manning coefficient

N_D	Number of displaced particles
N_E	Number of exposed particle
N_T	Number of total particles
p	Momentum (N·s)
Q	Flow Rate (m^3/s)
R	Hydraulic Radius (m)
r	Inertial length scale (m)
R/D_{50}	Relative Submergence (m/m)
Re	Reynolds number of the channel
$Re*$	Particle Reynolds number
Re_ρ	Roughness Reynolds number
R_{uw}	Correlation coefficient
R_{xx}	Autocorrelation function
S	Skewness factor
S_f	Energy slope (m/m)
S_u	Skewness of u'
S_w	Skewness of w'
S_{xx}	Streamwise velocity power spectra (m^2/s^{-1})
T_p	Pulse duration, measured in time intervals (Δt)
U	Mean Flow velocity (m/s)
$u*$	Shear Velocity (m/s)
u, v, w	Streamwise, Transversal and Vertical velocity (m/s)
u', v', w'	Streamwise, Transversal and Vertical velocity fluctuation (m/s)
$\bar{u}_p$	Mean local streamwise velocity on the particles (m/s)
$\bar{u}$	Mean local streamwise velocity (m/s)
U_0	Mean interstitial flow velocity (m/s)
U_c	Convective velocity (m/s)
u_{cr}	Critical shear velocity (m/s)
W	Power rate of the flow (w/kg)
z	Height in the depth profile (m)
z/d	Dimensionless height (m/m)
z'	Distance of the CV to the bed (m)
z_0	Origin of the velocity profile (m)
z_w	Water elevation (m)
α	Texture factor (Shape and packing of the bed particles)

ΔE	Energy expenses (J)
Δu, Δw	Streamwise and vertical velocity increment (m/s)
η	Kolmogorov length scale (m)
λ	Taylor Length scale (m)
ν	Kinematic viscosity (m^2/s)
ρ_s	Density of sediment (N/m^3)
$-\rho u'w'$	Reynold Shear stress (N/m^2)
ρ_w	Density of water (N/m^3)
σ	Standard Deviation
τ^*	Dimensionless Shields Stress
τ_0	Bed Shear Stress (N/m^2)
τ_{cr}	Critical Shear Stress (N/m^2)

List of Abbreviations

ADV	Acoustic Doppler Velocimeter
CFS	Coherent Flow Structures
CG	Crushed Gravel
CV	Control Volume
COR	Correlation
COR_{CR}	Critical Correlation
FDC	Frequency of Data Acquisition
GC	Gram-Charlier
GITS	Research Group of Sediment Transport
GVF	Gradually Varied Flow
JPDF	Joint Probability Density Function
LDV	Laser Doppler Velocimetry
OS	Original Series
PDF	Probability Density Function
PDH	Pulse Duration Histogram
PIV	Particle Image Velocimetry
PLH	Pulse Length Histogram
PSD	Power Spectral Density
QTF	Quadrant Time Fraction
QP	Poincaré quadrant
RG	Rounded Gravel
RMS	Root Mean Square
SCS	Small Coherent Structure
SD	Standard Deviation
SNR	Signal Noise Ratio
SNR_{CR}	Critical SNR
TF	Time Fraction
TI	Turbulence Intensity
TKE	Turbulent Kinetic Energy
VDD	Velocity-Duration-Density Map
VFD	Variable Frequency Drive

xxx

Chapter 1: Introduction

1.1 Motivation

"When I meet God, I am going to ask him two questions: Why relativity? and why turbulence? I really believe he will have an answer for the first."

Werner Heisenberg

The study of turbulence is of great interest in a large number of scientific and technological disciplines. It can be stated, without any exaggeration, that there is almost no branch of fluid mechanics in which the flows of practical relevance are not turbulent. Meteorological flows, movements of seas and oceans, sediment scour, dam outlets, gases inside an engine, and even respiration in humans, among others, are all affected by turbulence.

More than 120 years have passed since the first observations allowed Osborne Reynolds in 1895 to divide the fluid variables into a mean and a fluctuating field, by means of the decomposition of the instantaneous velocity (u) and pressure components from the Navier-Stokes equations into their mean ($\bar{u}$) and fluctuating parts (u'), i.e. $u = \bar{u} + u'$ (Figure 1.1). This decomposition is applied to the hydrodynamic equations and is the first step to account for the fluctuation of the variables due to turbulence. The time-averaged Reynolds stresses ($-\rho\overline{u'w'}$) is the term accounting for the mechanism of momentum exchange with structures generated at the near-bed region of the mean flow.

The Reynolds number (Re) establishes a relationship between the inertial and the viscosity forces of the flow. Below a certain number of Reynolds, the flow is considered laminar, and analytical and numerical solutions are available by means of a mathematical formulation like that of the Navier-Stokes equations. From a critical Reynolds number the flow becomes unstable and, as it grows, it gives rise to a turbulent flow.

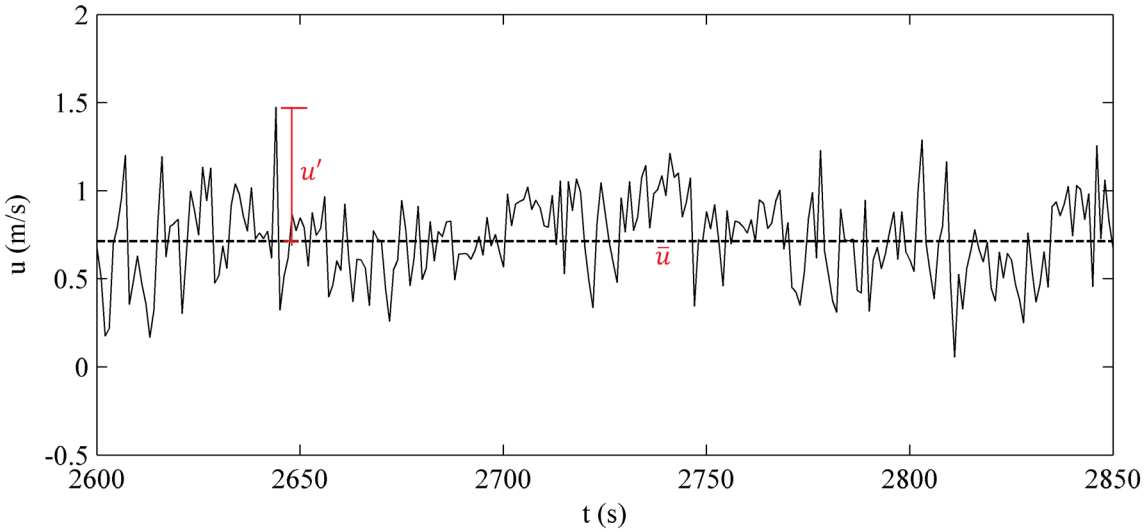

Figure 1.1- Turbulent velocity signal and illustration of the application of Reynolds decomposition.

Despite being a commonly used term, of which one may have an intuitive idea, it is difficult to define the turbulence. Some of its characteristics are defined below:

- Fluid motion is unsteady (even if the mean flow is stable). The distribution of the turbulent variables is very irregular in space and time.
- It is essentially three-dimensional (even if the mean flow is only two-dimensional).
- It has a high dissipative capacity, needing an input of external energy to maintain itself over time.
- The turbulent motion has a wide spectrum of eddy sizes, with large and small eddies coexisting in the same volume of fluid. Larger eddies are associated with low-frequency fluctuations and are responsible for most of the momentum transport. The smallest eddies are associated with high-frequency fluctuations and are determined by viscous forces.
- It is a chaotic process so that, in order to be able to predict the evolution of the systems, it would be necessary to have an accuracy in the initial conditions impossible to obtain experimentally or numerically.
- This great sensitivity to the initial conditions and irregularity make these flows almost random and their direct simulation with the Navier-Stokes equations is extremely expensive.

Turbulence is responsible for the physical processes in rivers, such as the transport and mixing of diluted (or not) substances, the transfer of temperature, as well as the movement and suspension of the sediment. The large eddies are responsible for the conversion of the total flow energy, from the average velocity to turbulent energy. The large eddies decompose into smaller eddies, which become smaller and smaller until they are consumed by viscosity, where the energy of the flow is finally lost as waste heat, making turbulence the main sink of the total energy of the flow.

Turbulence in rivers remains a challenge for researchers and engineers working in hydraulics and fluid mechanics. Among the most interesting applications of turbulence to fluvial dynamics is the flow resistance originated by the bed-roughness, the formation of coherent flow structures in the roughness layer and its growth, the processes that trigger the sediment motion among many others.

Regardless of quick development in the technical literature during the lasts decades, the hydraulics of Mountain Rivers is still not fully understood compared to that of lower gradient alluvial rivers. This makes sense since the latter is the most common typology in the transport processes and in final stretches of large rivers, and also have more relevance for agriculture and other human needs. However, Mountain Rivers have very different characteristics. In general, these are courses of steep slope flowing on macro-roughness beds, subject to heavy seasonal floods, which tend to flow in a critical or supercritical flow regime. The conditions of these flows and the roughness of the bed generate high turbulent fluctuations, which give them a great erosive capacity. Therefore, the consideration of turbulence is fundamental for fluvial environmental applications and requires a correct description.

This thesis aims to shed some light on the development of turbulence in highly turbulent flows, on the one hand by analyzing the effects that the effective roughness has on the typical variables that describe the turbulence and the evolution of these variables throughout the water column. On the other hand, this thesis explores the development of microturbulence through the bursting cycles that turbulent events follow in the Quadrant Map and their statistical description. In this way, this thesis aims to

develop a methodology that allows the coherent flow structures and the effects that these have on the onset in motion of the bed particles to be analyzed.

For the purposes of the thesis, experiments have been conducted in the hydraulic channel "The Cube" of the Morphodynamics Laboratory II of the Research Group Sediment Transport (GITS). The data acquisition of 3D instantaneous velocities has been carried out using an Acoustic Doppler Velocimeter (ADV). However, the device has shown some difficulties in taking measurements under certain flow conditions such as highly turbulent flows. For this reason, the effectiveness of the device to obtain the turbulent measurements and its sensitivity under different scenarios is also analyzed throughout the present work.

Below, there is a brief summary of the topics addressed in the thesis, developed in more detail throughout the dissertation.

1.2 Flow measurements

ADVs have been widely used for the measurement of 3D instantaneous velocities of flows, in both river field and experimental laboratory tests, over the last two decades. The device works on the Doppler shift principle; an acoustic ultrasound signal is sent by the emitter (10 MHz) and reflected by the suspended particles inside the control volume in the water.

Nevertheless, the capability of the device to solve flow turbulence accurately is still uncertain (Barkdoll, 2002). Some problems tend to appear when measuring at distances below 3 cm from the bed (Finelli et al. 1999), or in aerated flows in highly turbulent flows (Martin et al. 2002), becoming more significant as the roughness of the bed surface increases. As a result, spurious spikes, low Signal-Noise-Ratio (SNR) and Correlation values (COR) are obtained from the signal. Because these spikes may contribute considerably to the total turbulent kinetic energy (TKE) in highly turbulent flows, a filtering process is necessary to estimate the correct turbulence parameters (Cea et al. 2007). However, for the experiments carried out in the present work, when using the conventional filters (based on correlation values) more than 50% of the time series velocities are eliminated, and this percentage is even higher at the near-bed region, resulting in high filtering effects, which are analyzed in the present thesis.

On the other hand, low correlation values do not necessarily mean that data is wrong (e.g. Martin et al. 2002), Cea et al. 2007)). Due to this fact, the reliability of the measurements taken in these conditions, high roughness and low relative submergence, have been analyzed through the statistic behavior of the low-quality data.

The configuration of the device plays an important role in data collection since one of the main sources of error normally encountered when analyzing ADV velocity time series apart from the Doppler noise is signal aliasing. These problems have been intensely studied by some users since ADV appeared (Garcia et al. 2005; Goring and Nikora 2002; Nikora and Goring 1998; Wahl 2000). Due to this fact, an additional study was motivated by the necessity of further understanding about the effects of the ADV configuration on the turbulent properties of the flow.

1.3 Turbulence in open channel flows

Flow in Mountain Rivers is typically shallow, with the ratio of mean depth to effective roughness height (relative submergence), often being less than ten in flood conditions and less than five during low-flow conditions (e.g. Bathurst 1985, Lee & Ferguson 2002). Besides, the bed of almost all mountain rivers contains grains of sand, gravel, and boulders, which constitute the roughness surface (microtopography) and could have more complicated bed configurations (dunes, pools etc.) defined as macro-roughness. In the present thesis, only the effects that the first kind has on the turbulent flow characteristics have been studied.

Turbulence is characterized by statistical parameters due to its chaotic nature, with the aim of looking for organized behavior. Experimental investigations have shed light on the structure of statistical description of turbulent characteristics in open channel flows (e.g. Nakagawa & Nezu 1977; Hurther & Lemmin 2000; Nikora & Goring 2000) and especially in the boundary layer or near-bed region (Raupach 1981; Antonia & Krogstad 2001; Jimenez 2004). However, roughness effects on the main turbulent characteristic remain still not well understood.

ADV has been widely used in many experimental works (Hurther & Lemmin 2000; Nikora & Goring 2000), but its suitability to obtain distributions of time-averaged turbulence quantities has not been unraveled yet.

The thesis tries to characterize the turbulent properties of highly turbulent open-channel flow over rough beds using ADV measurements. Effects of different flow rates; bed particles (roughness) and bed-packing density, on the main turbulent characteristics, are also assessed.

1.4 Coherent flow structures

Richardson (1922) stated that the fully developed turbulence consists of a hierarchy of eddies, ‘‘*Big whorls have little whorls, which feed on their velocity; and little whorls have lesser whorls, and so on to viscosity…*’’.

The structure of turbulence is chaotic, containing a large variety of vortices sizes and length scales. The aim of studying the internal structure of turbulence is to understand how the boundary layer is produced from the mean velocity, thus from coherent motions. Nevertheless, this issue becomes more complicated in highly turbulent flows where the range of turbulence length scales is larger. The flow structure in a highly turbulent flow remains not deeply yet comprehended due to the complexity and stochastic nature of the phenomena.

A coherent motion, or coherent flow structure (CFS), can be thought as a three-dimensional region of the flow where at least one fundamental flow variable shows substantial correlation with itself or with another variable over a range of space and/or time that is considerably greater than the lowest local scales of the flow (Robinson 1991). Adrian (2007) demonstrated that it is possible to decompose complex, multiscaled, quasi-random flow fields into more elementary organized structures that show both spatial and temporal coherence, which have been termed either eddy (Townsend 1976) or CFS (Cantwell 1981).

The presence of these organized motions is supported by the TKE production in the near-bed region and is responsible for the turbulent dissipation. This turbulent production in the near-bed region occurs during intermittent, quasi-cyclic sequence of burst events, thus low-speed fluid is ejected away from the bed and inrushes of high-speed fluid towards the bed.

The interest in burst events (bursting turbulence) dates back to early experiments of Kline et al. (1967), who assured that flow motion at the near-wall region is "far from being completely chaotic in nature", but reveals a definite "sequence of ordered motions" (Clifford et al. 1991; Grass et al. 1991). Since then, great interest has developed in CFS in the turbulent boundary layer and its applicability in the entrainment phenomenon.

Burst events are divided into four quadrants: 1st Quadrant (Q1) also called "outward interactions" (u'>0, w'>0), 2nd Quadrant (Q2) or "ejections" (u'<0, w'>0), 3rd Quadrant (Q3) or "inward interactions" (u'<0, w'<0) and 4th Quadrant (Q4) or "sweeps" (u'>0, w'<0), defining each pair of value in the data series as a burst event.

The burst events constitute a near-bed CFS in open-channel flows, closely related to the generation of turbulent energy Reynolds stresses in the near-bed region and the entrainment process. The development of bursting motions can yield longer coherent structures, such as kolk-boil processes, that move from the boundary to the surface as a result of horseshoe vortex development (Nezu and Nakagawa 1993). A better understanding of these coherent motions (burst events) and their vertical distribution along the depth profile would be an essential key to understand how CFSs are generated in the boundary layer and grow towards the water surface.

Several studies (Nakagawa and Nezu 1977; Wu and Yang 2004) have suggested that the Gram-Charlier probability density function (GC PDF) describes correctly the distribution of near-bed bursting events. Wu and Jiang (2007) incorporated a Gram-Charlier third-order distribution $g_3(U, W)$, which adjusts the 2D joint probability of $u'w'$ in the near-bed region. A deeper comprehension of the statistical behavior of coherent motions would be helpful to aid predictive models of turbulence characteristics and to improve probability density functions of instantaneous velocity.

1.5 Role of turbulence on the threshold of motion

The threshold of motion is a term used to determine the critical condition that defines the set in motion of a sediment particle that is initially at rest. The correct prediction of threshold conditions and incipient motion is essential for the study of sediment transport. In addition, it has a multitude of practical applications, such as designing riprap protections in riverbeds.

The initiation of movement has traditionally been treated in a deterministic manner that is, assuming that there is a univocal relationship between a threshold condition (critical) and an incipient movement (Shields 1936). The deterministic view emphasizes the time-averaged boundary shear stress and, therefore, cannot account for the fluctuating forces encountered in turbulent flows. These fluctuating forces become more important for hydraulically rough beds, due to high instantaneous variations in both the local flow velocity and instantaneous Reynolds stress. Besides, different roughness geometries may produce the same effect on the mean velocity profile, but the turbulent characteristics (e.g., Reynold stress, the microstructure of turbulence) may differ significantly (Krogstad et al. 1992).

As a consequence, time-averaged characteristics of the flow may be inadequate to describe the effects of roughness on flow characteristics, demonstrating that incipient motion criteria based solely on time-averaged bed shear stress may unknot correctly predict sediment transport.

From this need arose the stochastic methods, which are based on the intermittent nature of near-bed turbulence. These methods consider the interaction fluctuation of grain induced by CFS (with spatial and temporal coherence (Adrian 2007) as responsible for the initial dislodgement of sediment. Identifying the flow structures that generate such peak forces has been an active area of research during the last 25 years.

Bursting turbulence (or burst events) constitutes a near-bed CFS in open-channel flows (Nezu and Nakagawa 1993) and is closely related to the generation of turbulent energy and the transport of momentum in the near-bed region, hence to entrainment process (Grass 1983; Williams et al 1989). Burst events in the 2nd and 4th quadrant have been considered conventionally responsible for sediment transport, because of their positive contribution to the Reynolds shear stress ($-\rho\overline{w'u'}$)due to their definition, Q2 (u'<0, w'>0) and Q4 (u'>0, w'<0). Specifically, some researchers identified sweeps (Q4) as the cause of the initiation of bed motion and ejections (Q2) are mostly responsible for particle suspension (Grass 1983; Niño & Garcia 1996; Celik et al. 2014).

However, the latest findings have provided enough evidence that in addition to the magnitude, the duration of energetic near-bed turbulent flow events is equally important in predicting grain removal from the bed surface, e.g. Diplas et al. 2008; Valyriakis et al. 2013; Celik et al. 2014. They proposed that the product of a force and its duration, or impulse of the force, is a more appropriate criterion for identifying suitable conditions for particle dislodgement. Therefore, understanding the statistical characteristics of impulse imparted by turbulent flow over several grain-size beds is essential for describing the effect of the bed in the sediment entrainment process.

1.6 Objectives of the Thesis

The main objective of the thesis is to shed light on the turbulence description of highly turbulent flows and to assess the effects of the power-flow and bed-roughness on its structure. This has been achieved by means of experimental data collected with an Acoustic Doppler Velocimeter (ADV). From the observations of this first part of the investigation are derived many other issues, such as the ability of the ADV to solve highly turbulent flows in an accurate way, or the application of the results for its implementation to the improvement of numerical models to predict turbulent fluctuations.

The second aim pursued in this thesis is the development of a methodology to assess the initiation of movement of the bed particles by means of the examination of the role that Reynolds shear stress has on the commencement of sediment motion. Specifically, the main emphasis is placed on the coupling of the impulse applied by the Reynolds shear stress with the rate of the entrained sediment. The final outcome of this methodology is the development of an incipient motion model that accounts for the role of turbulence. The applicability of the methodology obtained will be validated through the estimation of the sediment transport rate by visualizing the experiments and counting the displaced particles so that effects of different bed conditions can be assessed.

1.7 Organization of the Thesis

The thesis consists of eight chapters and three appendices, bound in two volumes, the first of which contains the eight chapters and the second the three appendices.

In the first chapter '*Introduction*', the main objectives of the thesis are established, as well as a short introduction.

In the second chapter '*Experimental Setup*', the experimental device that supports the experiments is defined, as well as the experimental campaign, the methodology of execution and materials used in each trial. This chapter also includes the hydraulic calculation prior to the experiments for its correct execution and handling of the hydraulic channel, along with some calibration work carried out prior to the experimental campaign.

The third chapter '*ADV Measurements*' encompasses a set of checks carried out on the data series with the aim of verifying their quality and correct execution, which are widely described by means of the appendices. The filtering effects on the data series have been analyzed (Appendix A) that together with an analysis of the low-quality data (Appendix B) determine the filtering process on the data series in this thesis. In addition, it is included an evaluation of how the device configuration affects the main turbulent parameters analyzed in this thesis (Appendix C). This chapter contains only a summary of the mentioned works, which are widely developed in the appendices of the thesis.

The fourth chapter '*Turbulent Characterization of the Experiments*' describes and characterizes the experiments by means of some basic turbulence terms, such as log-law velocity profiles, turbulent intensity (TI), turbulent kinetic energy (TKE), Reynolds tensions (τ_{xz}), power spectral density (PSD), dissipation (ε) and the cascade of energy among others. The calculations are made along the depth profile. Besides, the flow resistance coefficient obtained from the experimental data is also evaluated against some typical formulations for high mountain flows.

The fifth chapter '*Coherent Structures and Quadrant Analysis*' is a complete analysis of quadrants trying to relate their statistics with coherent flow structures. It also exposes new aspects of analysis that lead to the next chapter.

The sixth chapter '*Pulse Analysis*' exposes a new methodology of analysis linked to the study of quadrants by means of which it is intended to relate coherent structures with other aspects of the quadrant map. The concept developed in this chapter is the central axis of the chapter below.

The seventh chapter '*Threshold of motion*' evaluates by means of a simple conceptual model the initiation of sediment movement of the tests conducted, on the one hand, using the real results obtained from the observation of the tests, and on the other one by the turbulence description of the ADV data series.

The eighth chapter '*Concluding remarks and future research lines*", as its name suggests, includes a summary of the conclusions obtained from each part that comprise the thesis. It also includes some lines of research acquired from the research results.

The appendix A '*Filtering Effects*' analyzes the variation underwent by the turbulent variables, the basic ones and the ones defined through the thesis, after filtering, as well as the percentage of data filtered by each considered filtering method.

The appendix B '*Low-Quality Data Evaluation*' focuses on the analysis of the data considered incorrect by the filtering methods (low-quality data or 'bad' data) and their turbulent characteristics. In the same way as the previous appendix, new turbulent concepts developed during the thesis have been included in order to assess the behavior of the low-quality data. At the end of this appendix, in this respect, an article, currently under review, in which the results are shown in a more summarized form, is included.

The appendix C '*ADV Configuration Analysis*' analyzes the variations produced by the device configuration. This appendix includes a new set of experiments performed in another hydraulic channel and using another ADV, which allowed the variation of the configuration. However, a theoretical analysis of the main experiments of the thesis was made in order to evaluate somehow the effect of the ADV configuration on the main experiments. It is true that this study was performed once the main experiments had been carried out, with the configuration that had initially been determined. However, the sensitivity of the turbulent calculations to the use of filters, thus to the variations of the velocity signal, motivated a deeper analysis of the configuration of the apparatus, using some of the concepts developed throughout the thesis. As in the previous appendix, an article (not released) is included that gathers the results obtained by device configuration.

It is crucial to mention that, during the completion of the thesis, in each step forward in the definition of the methodology of analysis and turbulent variables, filtering, data quality and configuration of the device verification have been done, almost recursively. That is why the appendices contain certain analysis related to concepts that are exposed more extensively in the thesis. For this reason, it is convenient to read these appendices once the thesis is finished, in order to understand all the concepts. However, chapter three makes reference to part of these appendices, including some of the conclusions obtained from them to verify the veracity of the data, necessary previously to a deeper analysis of the results.

Finally, Appendix D shows the results from the analysis of sediment transport rate of each experiment. On the one hand, the statistics of the impulse series to evaluate this transport, and on the other hand, the real transport rate observed in the experiments.

Chapter 2: Experimental Setup

2.1 Laboratory facilities

The experiments were carried out in the hydraulic channel "The Cube" of the Morphodynamics Laboratory II of the group GITS, Research Group Sediment Transport, located in the Technology Park of the UPC, Agropolis, BarcelonaTech. The flume dimensions are a 14 m long, 1.2 m wide, and 1 m deep straight rectangular concrete channel, Figure 2.1. Equally spaced piezometers along the channel are installed as a purpose to measure the pressure of the flow. The recirculation system consists of two tanks connected to one another by a pumping system. The upstream tank (spillway tank), receives the water propelled by the pumps which it discharges into the channel through a triangular weir. The discharge is calculated using a piezometer installed in the upstream tank. The discharge curve was adjusted experimentally with the aid of a magnetic flow meter. The channel flushes the water into the reception tank and a grid downstream of the channel avoids the sediment going into the tank. Two centrifugal pumps are installed at the reception tank, with 22 hp of power and a nominal flow of 180 l/s each, and drive the water throughout two pipes toward the upstream tank. The discharge was controlled by a Variable Frequency Drive, VFD, installed in one of the pumps, achieving a flow rate (Q) in the system ranging from 30 l/s to 180 l/s. The most important components that make up the hydraulic system are defined below.

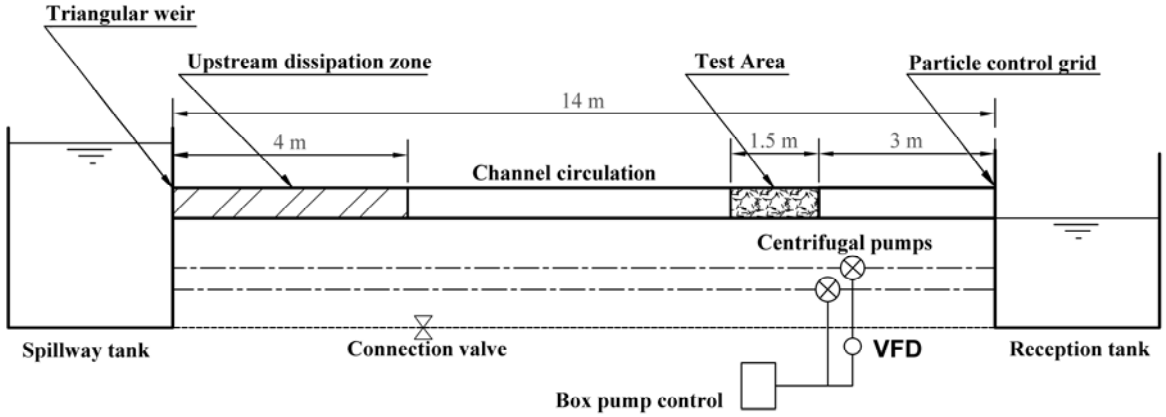

Figure 2.1- Longitudinal profile of the experimental device scheme.

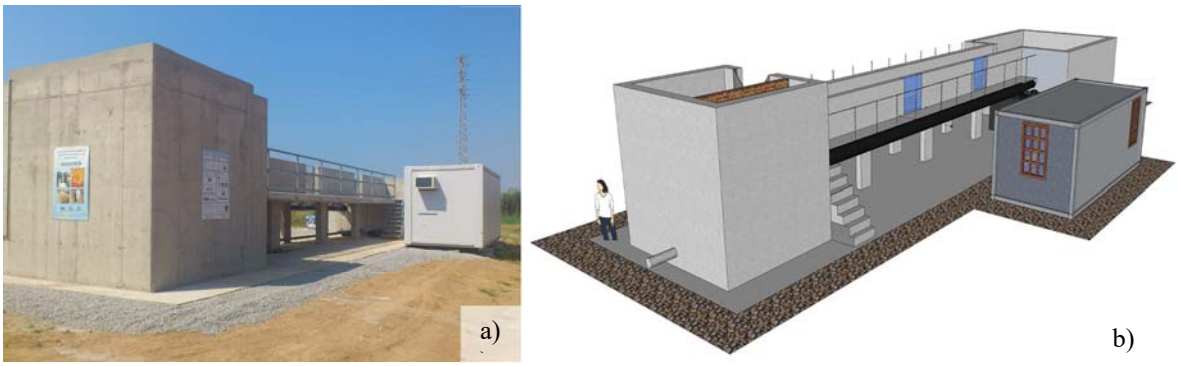

Figure 2.2- Experimental device (a) picture and (b) scheme.

2.1.1 Pumping system

The pumping system consists of two pumps with same characteristics placed in parallel as shown in Figure 2.3 which propels the water from the reception tank, downstream the channel, to the Spillway tank, upstream the channel, through two pipes of 350 mm (one for each pump).

The operating point is defined at a flow rate of 179.3 l/s, with a column water of 5.7 m. At this point, the pump performance is 67.4 %, and the power supplied to the pump shafts is P=22 hp.

The flow regulation is carried out by means of a Variable Frequency Drive, VFD installed in one of them, which allows varying the velocity of the blades depending on the electric frequency supplied. That is, we vary the frequency, decreasing it below the 50 Hz supplied through the electricity network, up to a minimum of 20 Hz, achieving a range from 35.9 l/s to 179.3 l/s. The other pump works with direct starting, thus it provides the maximum flow (depending on the working point).

For a precise functioning of the pump with optimum performance and a correct cooling of the pump, the circulating flow must not be less than 20% of the operating flow; therefore, the flow must be at a minimum of 35.9 l/s.

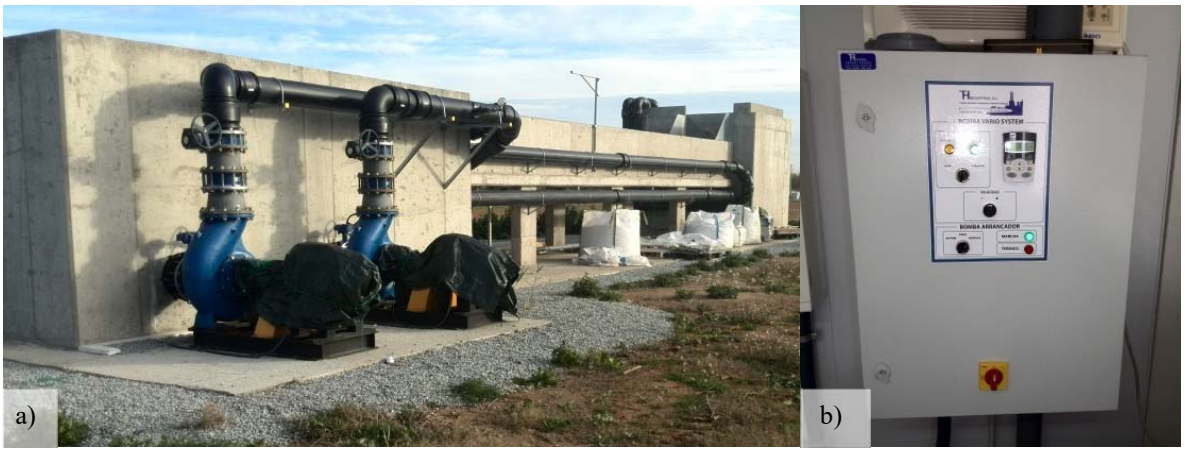

Figure 2.3- Pumping system (a) picture and (b) VFD.

2.1.2 Flow-rate measurement

The flow-rate has been measured by means of a triangular weir installed in the spillway tank placed upstream the channel. Due to a magnetic flow meter, which works by applying a magnetic field to a pipe and measuring its voltage from end to end of the pipe, it was possible to calibrate the weir in just one day.

Thanks to the piezometer installed in the spillway tank, each flow-rate was referenced, measured by the flow-meter in the impulsion pipes, with a water height, thus obtaining the performance curve (Figure 2.4) of the triangular weir. This calibration was necessary since given the characteristics of the system, spillway tank instead of a hydraulic channel upstream the weir, thus with an inferior length to the required by the different authors, it is not possible the direct use of the existent formulas.

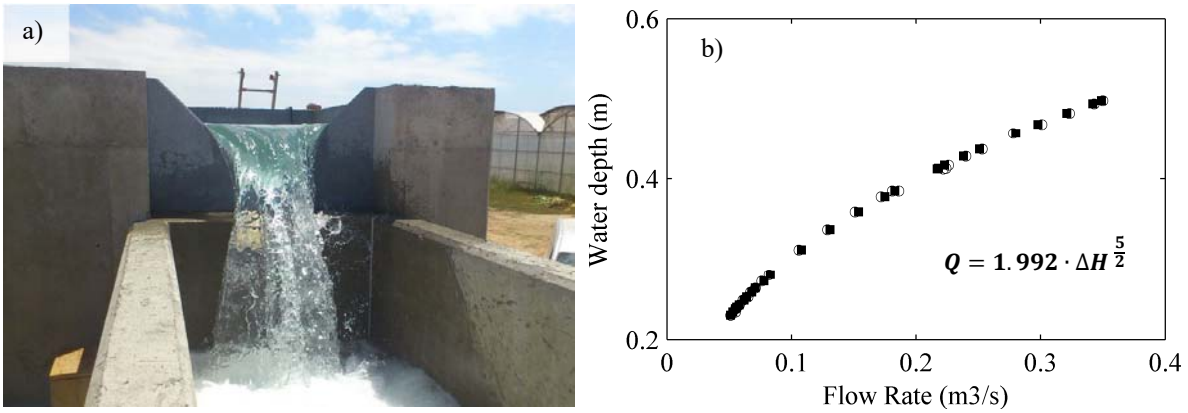

Figure 2.4- Triangular weir (a) picture and (b) performance curve. *Legend,* ■ *experimental data and* ○ *adjustment.*

2.1.3 Water depth measurement

The water depth (*d*) has been measured in two ways: one from the use of a water level gauge at specific points installed on a metal platform that can be moved along the channel through a guidance system installed on the walls of the channel, Figure 2.5-a. The second way is by means of two piezometers (pressure measurement) placed upstream and downstream the experiment placement, under the consideration of uniform flow and therefore hydrostatic pressures along the channel, Figure 2.5-b.

As said before, there are different piezometers installed along the channel. These measurements will be used to determine the energy slope and the average water depth of the experiments so that the characterization of the hydraulic variables of each scenario can be assessed. The tubes installed are glass and have a diameter of 1cm with a distance between each other in the channel of 1 m. The tubes start at the bottom channel and protrude on one side of the channel as shown in Figure 2.5-b. Besides, another piezometer, with a diameter of 2 cm is installed in the spillway tank, Figure 2.5-c, so that the column water in the triangular weir can be accurately obtained.

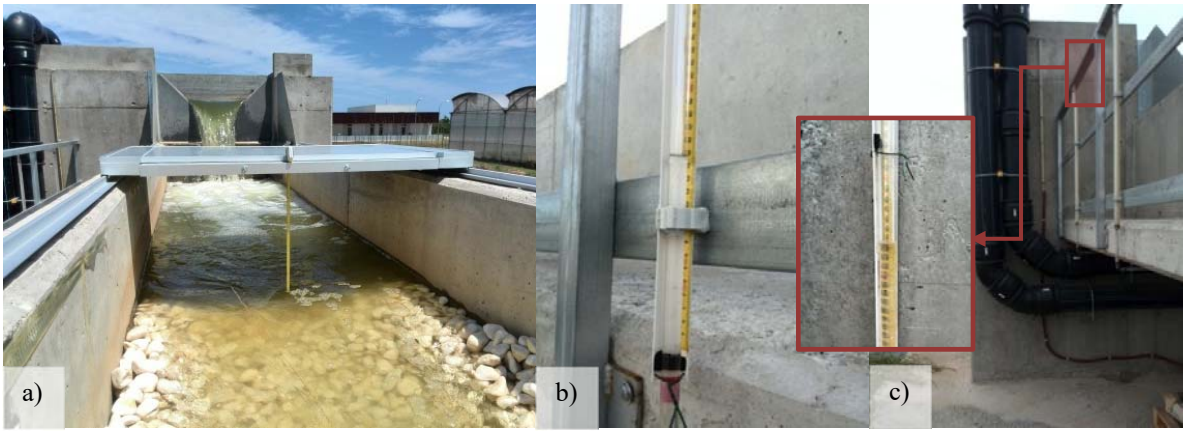

Figure 2.5- Water depth measurements (a) water level gauge, (b) channel piezometer and (c) spillway tank piezometer.

2.1.4 Sediment control

Downstream the channel there is a plate installed which avoid the sediment to go in the reception tank, besides it is used as a support to the material slope, Figure 2.6.

Figure 2.6- Plate control sediment

2.1.5 Acoustic Doppler Velocimeter (ADV)

Velocity measurements were taken using a 3D SONTEK 10 MHz ADV with a cable mount probe and side looking physical arrangement. The probe is the part responsible for the emission of the pulse and the reception of the corresponding echoes. It is an emitter of 10 MHz surrounded by three legs, each of 2.9 cm arranged in the same plane forming 120º between them, at the end of which the ultrasonic receivers are placed, see Figure 2.7-a. More information about the ADV function and the configuration of the device can be found in chapter 4, section 4.2.

The traditional way of placing the ADV is to introduce the device through the water surface of the flow until reaching the target zone of measurement. However, the stem of the ADV (the head is placed at its end) could introduce bubbles around the receivers and contaminate the data measurements when the depth (*d*) is low. In order to this effect, the ADV was introduced in the flow differently to the usual way, the device was introduced through the bottom-channel into the flow as shown in Figure 2.7-b. The final example of surface placement is shown in Figure 2.8.

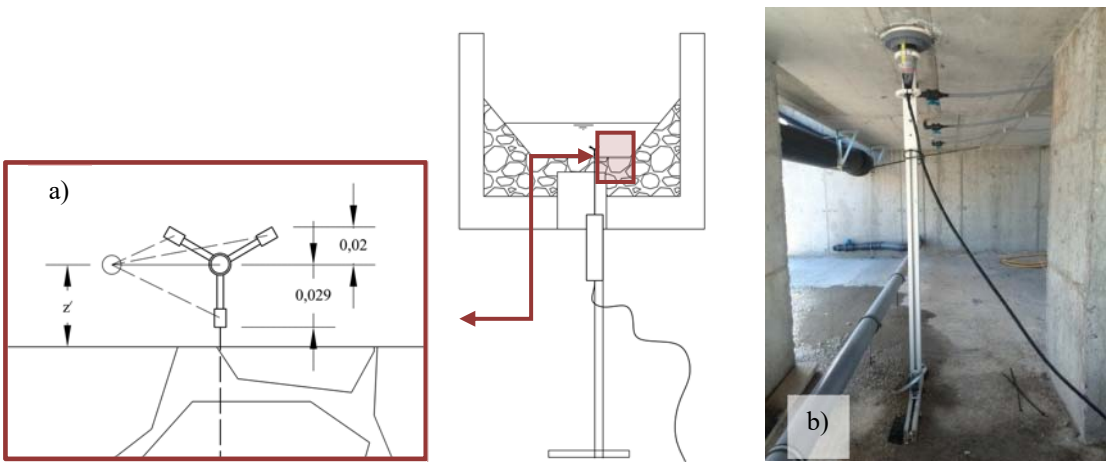

Figure 2.7- ADV placement (a) scheme, (b) picture.

Figure 2.8- ADV placement on the bed surface.

2.2 Characteristics of the materials

The main characteristics of the four materials used in the experiments are shown below, as well as the methodology used to obtain these characteristics. First, the rounded gravel is defined (Figure 2.9-a). This is the material that will be used to perform the test slope, besides it is the tested material in the group 1 of experiments (RG tests).

The second group of experiments (CG tests) is performed with broken gravel, Figure 2.9, where three different particle diameters are defined. A more detailed definition of the experiments and the experimental methodology can be found in section 2.4.

Figure 2.9-Photograph of the Crushed Gravel (a) CG-D1, (b) CG-D2, and (c) CG-D3.

2.2.1 Density and void ratio

The void ratio and the density were obtained by immersion and weighing (see Figure 2.10). First, the material is confined in a container, with a known volume, and then weighed. Later, the volume of voids is filled by water and weighed again. The difference between the two weights, along with the conversion of the water weight to volume of water, the void ratio is obtained. This procedure is repeated also to obtain the void ratio for a higher packing density when the surface of the material is level. The results obtained for the three size particles are shown in Table 2.1.

Figure 2.10- Experimental device scheme

Table 2.1 Results of void rates and density

	CG-D1		CG-D2		CG-D3	
	loose	**packed**	**loose**	**packed**	**loose**	**packed**
Sample volume (dm3)	0,7	0,7	0,7	0,7	0,7	0,7
Weight (kg)	1,1	1,2	1,1	1,22	1,17	1,2
Water volume (dm3)	0,37	0,29	0,34	0,31	0,36	0,33
Void rate	0,53	0,41	0,49	0,44	0,51	0,48
density (kg/dm3)	1,57	1,71	1,57	1,74	1,67	1,71

2.2.2 Sieve analysis

The granulometry was determined by a graphical method using MATLAB. By means of photographs, Figure 2.11, of a representative sample of material, the minimum and maximum diameters of an ellipse circumscribed in the particle are determined. The radius (*a*) and radius (*b*) define this ellipse. The third dimension of the particle (*c*), which is the smallest, cannot be represented in the photographs, however, the dimension that defines the sieve size through which it passes is the radius (*b*), see Figure 2.12.

Along with this methodology, the determination of the Feret diameters (minimum diameter of the sieve through which the stone would pass) was also studied. Nevertheless, differences between the ellipses obtained by the two methods are around $\mp$2-3 %. For this reason, the first method is validated and used since the second method implies high computational costs.

The methodology consists in taking photos of a representative sample of particles (200 units) achieving the correct discretization of the particles by improving the contrast by a binary image. Then the RGB thresholds are evaluated obtaining the circumscribed ellipses using a MATLAB script. Once the diameter of each particle is obtained, the statistical distribution of the sizes can be represented, Figure 2.13-a. The granulometric curve of each material is defined by the weight fraction that passes through a sieve size, Figure 2.13-b. The weight (w) of the particles are approximated by using the expression, $w = 4/3 \cdot \pi \cdot a \cdot b \cdot c \cdot \rho$, with the assumption of radius (c), parameterized it as $c = 0.7b$. The results obtained from the sieve analysis for each material are shown in Table 2.2, where cu is the coefficient

of uniformity $c_u = D_{60} / D_{10}$ (c_u <3 uniform soil) and c_c is the coefficient of curvature, $c_c = D_{30}^2 / D_{10} \cdot D_{60}$ (c_c <1 poorly graduated soils). Therefore, all materials cases have a uniform granulometry.

The amount of stones analyzed in the statistical study is 2-kg for the case of the CG-D1 material and a minimum of 100 stones for the rest (RG, CG-D2, and CG-D3).

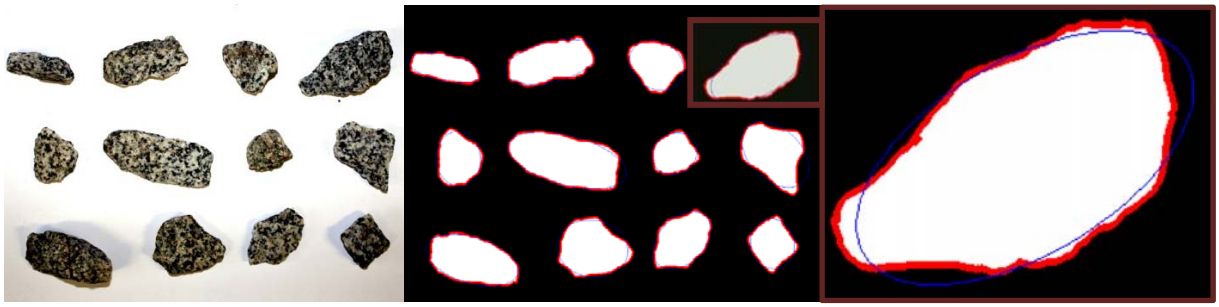

Figure 2.11- Example of images for sieve analysis (CG-D2).

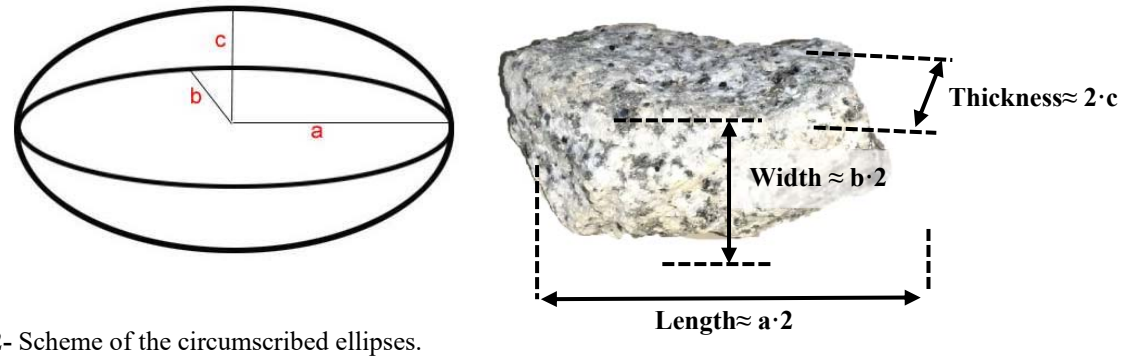

Figure 2.12- Scheme of the circumscribed ellipses.

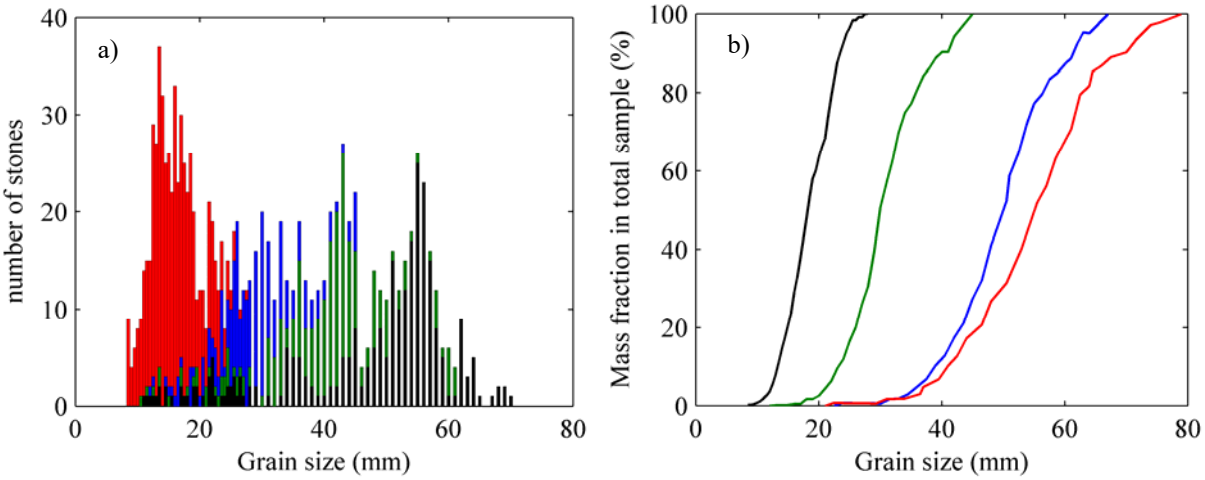

Figure 2.13- Sieve analysis. Figure (a) distribution of the sample, and (b) Graphs of cumulative percent passing. *Legend, —RG, —CG-D3, —CG-D2, and —CG-D1.*

Table 2.2 Size characteristics of the materials

	D_{30}	D_{50}	D_{90}	D_{max}	D_{min}	σ	c_u	c_c
RG	49,45	55,25	68,15	69,03	26,34	15,92	1,41	1,03
CG-D1	14,72	17,82	23,01	27,32	7,51	3,84	1,46	1,07
CG-D2	27,81	30,02	39,78	44,61	12,96	6,18	1,37	1,06
CG-D3	45,48	51,08	60,51	62,04	20,16	10,31	1,43	0,98

2.3 Experimental design

For a correct characterization of the system, the length of the channel has been divided into three sections, as shown in Figure 2.14, and the test area is located in section 3, with the center 4 meters upstream of the end of the slope.

All the experiments analyzed in this thesis have certain characteristics in common, such as the tilt of the experimental slope, the material of which the slope is made, and the area where the experiment is placed. As already mentioned above, the material that is available to perform the slope of the tests is the rounded gravel (RG). This material has a mean diameter of D_{50}=0.055 m, with a standard deviation of σ = 16 mm (Table 2.2).

The RG material has been used to make the slope of the channel because it reproduces the characteristics of a torrential flow, besides; its large size allows testing materials of inferior size without concern about its set in motion. The gravel ramp is placed with a 0.03 m/m slope along the 10 m of test slope (section 3, Figure 2.14) of the 14 m that the channel measures, leaving upstream of this slope a 4 m long zone of energy dissipation (section 1, Figure 2.14) in order to achieve calm water conditions at the entrance of the slope test.

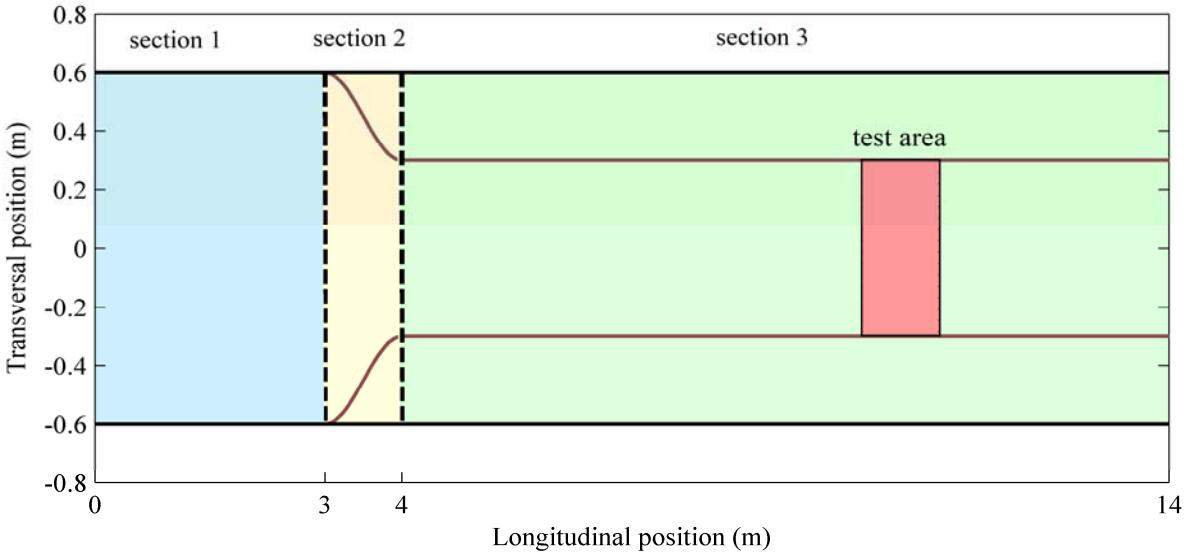

Figure 2.14- General plant of the channel

The particular setting studied was a trapezoidal cross-section. This allows increasing the specific flow rate and the shear stresses in the bed surface, thus it is possible to model more extreme scenarios. In addition, it represents more faithfully the reality of torrential rivers with fast floods. The integration of the embankments is done gradually along the section 2 (Figure 2.14), i.e. before the 0.03 m/m slope starts. The internal friction angle of the bed material (angle of repose) is 46°, obtained by trial and error. Finally, the embankments are arranged at an angle of 38-40º, as shown in Figure 2.15. Along the section 2, where the embankments are integrated increasingly until section 3, the maximum height of the slope is achieved gradually.

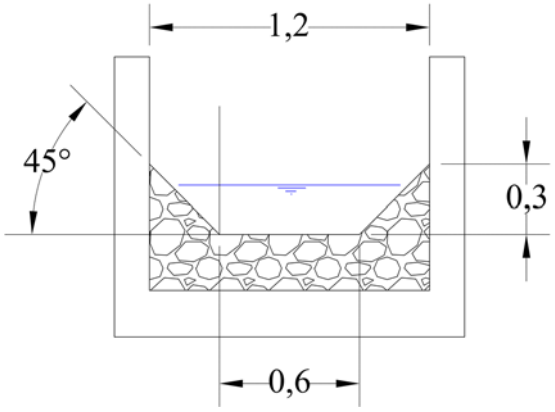

Figure 2.15- Channel section configuration

2.3.1 Hydraulic calculations

In this section, the hydraulic calculation procedure is described, in a simplified manner, to assess the design of the experiments and define the characteristics necessary for its correct development prior to its execution. The regulation of the flow rate is fundamental to determine the operating efficiencies in open channels. It consists in the determination of the circulating discharge and/or the water levels to be regulated within the system, according to the spatial and temporal variation during the operation. In addition to the selection of a correct pumping system and the approximate water levels, it is necessary to know the volume of water needed by the system.

Three flow rates have been studied a priori in order to organize the hydraulic operation of the channel. The three selected flow rates are Q_1=0.36 m^3/s (maximum available by the pumping system), Q_2=0.20 m^3/s, and Q_3=0.04 m^3/s (minimum to achieve the needed submergence of the pumps).

2.3.1.1 Section 1_ Dissipation zone

This section is characterized by the waterfall from the triangular weir upstream, and by the entrance on section 2 downstream. The section 2, as said before, is where the embankments and slope are progressively created, however, in this part of the hydraulic calculation, section 2 is ignored, and integrated into the section 1, Figure 2.16. In this way, it can be assumed that the entrance to section 3 works as a wide-edged weir where the water level upstream is determined by the minimum energy (E_{min}) that the channel needs to circulate. This energy corresponds to the energy that the critical flow needs to run (E_c), and it is obtained from Eq. (2-1. The upper elevation of the slope is 0.3 m (0.03 m/m·10 m) for the three studied flow rates.

If the channel flows in supercritical regime, the boundary condition of the tests slope (section 3) is conditioned by the depth upstream (*d*), which coincides with the critical depth ($d=d_c$). Nevertheless, in the case of having a subcritical regime, the depth (*d*) at the entrance of section 3 will be $d_c < d < d_n$.

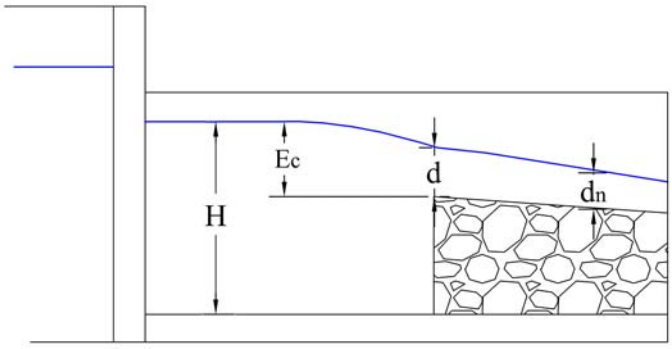

Figure 2.16- Schematic longitudinal profile of section 1.

The hydraulic calculation of the test slope is performed as a steady flow using the Manning equation (Eq. (2-2) for the three analyzed flow, the hydraulic characteristics are summarized in Table 2.3. An approximation of the Manning coefficient is made by means of the Strickler equation (Eq. (2-3) obtaining a value of n=0.025 for the RG.

$$E_c = H + {U_1}^2/2g = 3/2 \cdot d_c \quad (2\text{-}1)$$

$$Q = 1/n \cdot A \cdot R^{2/3} \cdot {S_0}^{1/2} \quad (2\text{-}2)$$

$$n = (D_{90})^{1/6}/26 \quad (2\text{-}3)$$

Table 2.3 Hydraulic results for the section 1

Q (m³/s)	***d_n***	***d_c***	***E_{min}***	***U (m/s)***	***F***
0,36	0,274	0,289	0,433	2,17	1,12
0,2	0,198	0,203	0,304	1,68	1,06
0,04	0,077	0,074	0,111	0,086	0,92

2.3.1.2 Section 2_ Transition zone

The transversal section contraction (embankments) is performed along the section 2 (1 m) in a smooth sinusoidal manner (see Figure 2.17-a). The transition of the slope in this section must also occur progressively since otherwise turbulences would affect the entire test slope. To avoid this, the slope upgrowth (Figure 2.17-b), which reaches the maximum elevation of the tests slope in section 2, has been designed imposing a sinusoidal transition of the Froude number (*Fr)* along section 2, Figure 2.18. That is to say, it is necessary to impose a value *Fr* upstream and downstream the section 2. The upstream value of *Fr* must be known from section 1 since the depth in section 1 (*H*) is known ($H=E_{min}+z_{max}$, Figure 2.16).

The transition of the slope in section 2 is only obtained for the maximum flow rate (0.36 m^3/s) since it runs in supercritical flow. The Subcritical flow condition it is not necessary since the test slope boundary condition would be located downstream of section 3. Therefore, considering a supercritical

regime, the value of *Fr* downstream of section 2 corresponds to *Fr* = 1, since as we saw in the previous section the depth (d) at this point coincides with the critical depth ($d=d_c$).

Once the *Fr* value has been defined, the depth (*d*) at each point of section 2 can be found (Eq. (2-4). Thus, with the known depth and combining Eq. (2-5 and Eq. (2-2, the bed elevation along the section 2 that satisfies the imposed *Fr* values transition (Figure 2.18) can be found.

$$d = \sqrt[3]{q^2/g(Fr^2)} \tag{2-4}$$

$$z_1 + d_1 + {U_1}^2/2g = z_2 + d_2 + {U_2}^2/2g + \Delta H \tag{2-5}$$

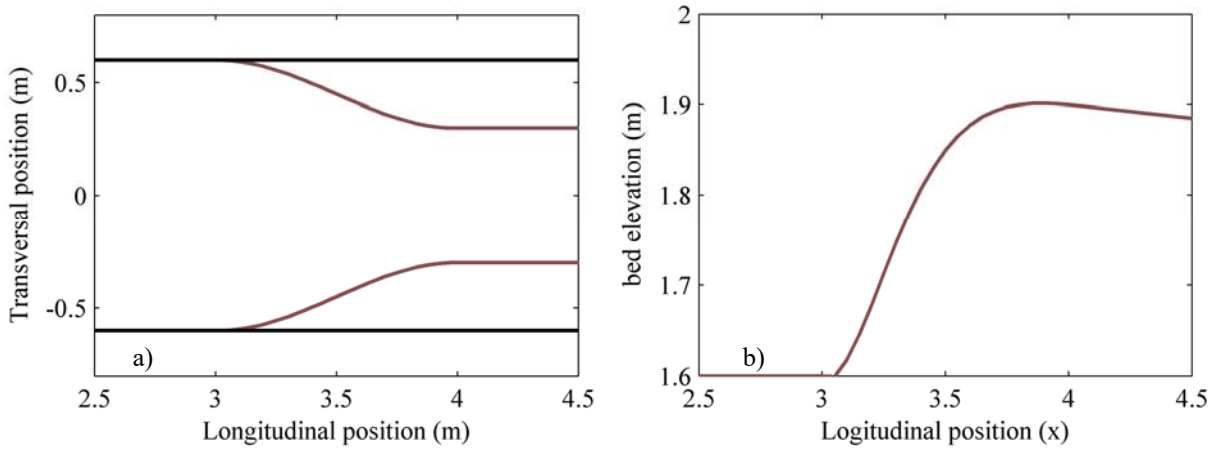

Figure 2.17- (a) Longitudinal bottom elevation and (b) constriction plant along the section 2.

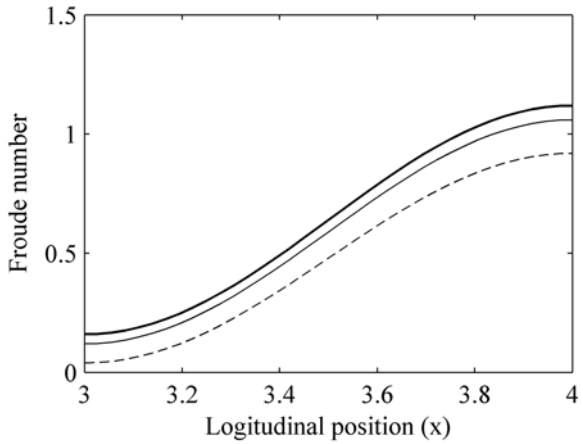

Figure 2.18- Longitudinal Froude number distribution along section 2. *Legend, ▬ Q_1=0.36 m^3/s, ▬ Q_2=0.20 m^3/s, – – Q_3=0.04 m^3/s.*

2.3.1.3 Section 3_ Test slope

The water in the test slope runs in gradually varied flow (GVF), and therefore backwater curves can appear, upstream for supercritical flow, and downstream for a subcritical. The calculation of the flow through GVF equation is necessary to make sure that the test area is sufficiently far from these curves.

The upstream boundary conditions are set as critical depth (d_c) for supercritical flow and the depth obtained at the end of section 2 for subcritical flow. The downstream boundary conditions are set as

normal depth (d_n) for supercritical flow and critical depth (d_c) for subcritical flow since it is expected that the spill in the reception tank is free so that hydraulic jumps are avoided. The energy slope (S_f) is obtained at each point by the Manning Eq.(2-2, and the energy losses between transversal sections with the Eq.(2-6 that is derived from the Momentum equations of Saint-Venant in 1D.

$$\partial d/\partial x = (So - Sf)/(1 - Fr^2) \tag{2-6}$$

2.3.1.4 Water surface elevation

Finally, the unification of the hydraulic calculations for the three sections gives the definition of the water elevation along the channel, for the three studied flow rates, Figure 2.19.

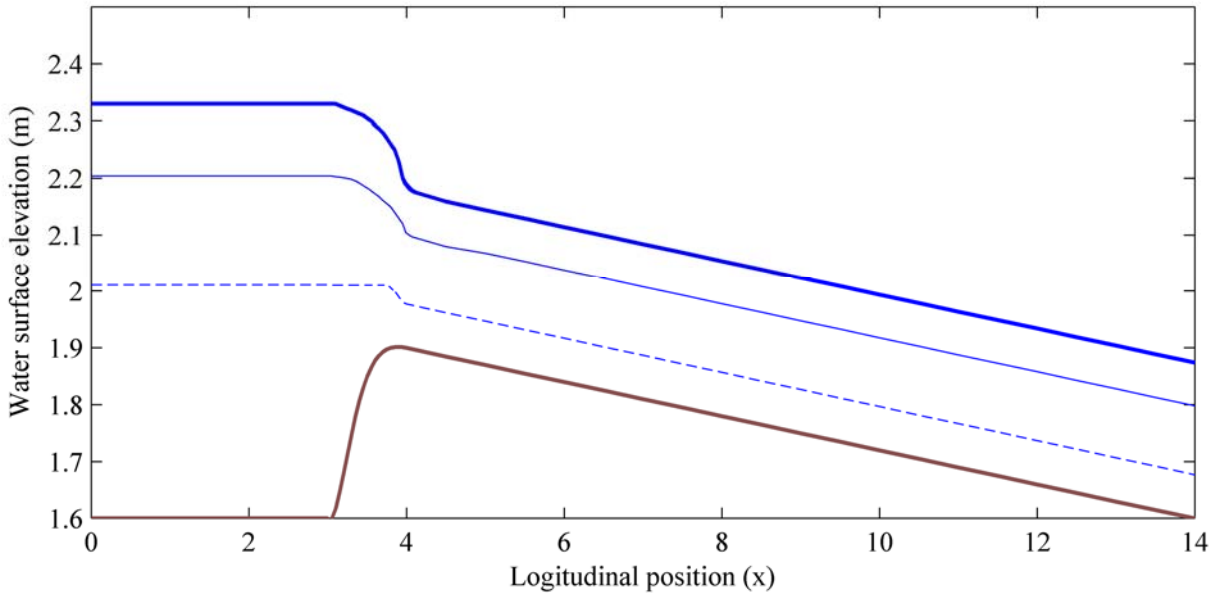

Figure 2.19- Water surface profile. *Legend,* Q_1=0.36m³/s, Q_2=0.20m³/s, Q_3=0.04m³/s.

2.3.2 Volume of water

For the proper operation of the channel, it is also necessary to calculate the volume of water in the system (channel and tanks) for the different flow rates. This volume is defined by the water levels in the different parts of the system.

The maximum water elevation in reception tank is set in 1.6 m so that the test slope is not affected by the downstream water height and a hydraulic jump cannot occur. Moreover, this water height in the reception tank allows the minimum submersion required by the pumps. The water elevation in the spillway tank is conditioned by the flow rate that controls the water elevation in the triangular weir. Finally, the volume of water needed by the system is obtained through the integration of water levels in the different spaces of the channel system Table 2.4.

To fill the channel system, the water elevation at rest (z_w) has been defined for each of the studied flows, thus, it is known the level to reach at any point of the system during the channel filling, see Table 2.4.

Table 2.4 Volume of water in the system results

Q (m^3/s)	Volume of water (m^3)	Water surface WS at rest (m)	WS elevation (m) Spillway tank	WS elevation (m) Reception tank
0,36	78,5	2,4	2,9	1,62
0,2	74,5	2,28	3,11	1,63
0,05	68,8	2,12	3,23	1,62

2.3.2.1 Operation of water volume

In the most extreme tests, the flow rate will go from 68.8 m^3 (0.04 m^3/s) to 78.55 m^3 (0.36 m^3/s), thus with 10 m^3 of difference. Therefore, assuming that the time to arrive from the minimum flow rate (0.04 m^3/s) to the maximum (0.36 m^3/s) is 3 hours, a constant water supply of at least 0.93 l/s will be required. A hose with large diameter (19 mm), which is connected to the aquifer under the hydraulic laboratory "The Cube", and is able to supply up to 1.15 l/s is available for the channel operation (filling). Therefore, assuming a starting point at 40 l/s, with an initial volume of water of 68.8 m^3, each time the flow rate is increased by 10 l/s it is needed to introduce 312.5 liters in the channel system, which is achieved in about 5 minutes.

2.4 Experimental procedure

2.4.1 Description of the experiments

In the present thesis, two different groups of experiments have been conducted. The first group is the Rounded Gravel tests and the second is the Crushed gravel test, from now on RG and CG tests respectively.

2.4.1.1 RG experiments

The experiments of the first kind have the aim of studying the material used to perform the test slope (Figure 2.20) and calibrate the ADV system, but also give us information about the turbulent variables that are studied in this work. The material is called white Rounded Gravel with a mean grain diameter of D_{50}=55 mm, D_{90}=69 mm, and σ=16 mm (see Table 2.2)

This diameter size allows performing highly turbulent flows without movement of the bed sediment. In fact, it was selected as slope material because it permits taking smaller particles until incipient motion conditions and achieving the immobility of the rounded gravel. Although the slope was formed manually, it is reasonable to consider the material as a loose (L, "bed leveling" in Table 2.5), that is to say, the surface has not been leveled and therefore is highly rough.

Figure 2.20- Test slope

A total of 10 tests with different flow rates were carried out to study the influence of the high roughness over the turbulence. The hydrodynamic data variables were collected both, manually and with the aid of the ADV to take the velocity profiles. The ADV device was placed in the center of the tests area, and the control volume (target of the measurement) was located at a distance (*z'*) of 1 cm from the bed surface, see Figure 2.7-a and Figure 2.24 for *z'* reference.

The bed in all RG experiments was placed by dumping, only the leveled of the surface to achieve the slope was made, but the crests of the particles were not flattened, designated with a D (Dropped) in the column "bed leveling" from Table 2.5.

Flow depth was in the range from about 0.078 m to about 0.208 m, and the flow rate from about 43 l/s to 308 l/s. Flow conditions corresponded to values of the Reynolds number, $Re = U4R/v$, in the range from about $5.56 \cdot 10^4$ to $2.7 \cdot 10^5$. All velocity data series were sampled at a rate of 25 Hz for 5 min, resulting in 7,500 velocity measurements per time series. In all, 340-time series were recorded. The main characteristics of these experiments are shown in Table 2.5.

Table 2.5 Summary of hydraulic and physical conditions of the RG experiments

Nº TEST	D_{50} m	Flow R. l/s	s m/m	Bed Leveling	d m	R m	S_f m/m	R/D_{50}	U m/s	Fr	Re
RG1	0,055	42,75	0,03	D	0,078	0,07	0,038	1,4	0,959	1,10	2,69E+05
RG2	0,055	48,79	0,03	D	0,083	0,074	0,037	1,47	1,006	1,11	2,98E+05
RG3	0,055	54,68	0,03	D	0,089	0,078	0,037	1,56	1,051	1,12	3,28E+05
RG4	0,055	73,24	0,03	D	0,1	0,086	0,037	1,73	1,139	1,15	3,92E+05
RG5	0,055	97,49	0,03	D	0,116	0,098	0,038	1,96	1,202	1,13	4,71E+05
RG6	0,055	120,01	0,03	D	0,129	0,107	0,036	2,14	1,419	1,26	6,07E+05
RG7	0,055	162,92	0,03	D	0,15	0,121	0,036	2,42	1,434	1,18	6,94E+05
RG8	0,055	204,41	0,03	D	0,171	0,135	0,037	2,7	1,582	1,22	8,54E+05
RG9	0,055	238,46	0,03	D	0,183	0,142	0,038	2,85	1,603	1,20	9,11E+05
RG10	0,055	307,65	0,03	D	0,208	0,158	0,039	3,16	1,784	1,25	1,13E+06

2.4.1.2 CG experiments

In the case of the second group, the crushed gravel tests (CG tests) three different particles sizes were evaluated during the experiments and the density of the bed packing was also a variable in the experiments in order to see the effects on the turbulent parameters. The tests were done under incipient motion conditions; the flow rate was progressively increased until the beginning of the movement of the particles tested in each experiment CG-D1, CG-D2, and CG-D3 with diameters of D_{50}=17,82 D_{50}=30,02 D_{50}=51.08 respectively (see Table 2.2). The methodology to detect incipient motion conditions is based on the visualization of the bed that has been possible through the painting of the bed surface (see section 2.4.2.2.2).

As mentioned, in contrast to the first kind of experiments, it has been distinguished between loose/dropped beds (D, Dropped, not leveled beds) and shaped/well-packed beds (P, Packed, leveled beds), as can be checked in the column "bed leveling" from Table 2.6. Figure 2.21 shows two pictures of these two types of colocation (more pictures of the experiments can be found in chapter 8, "Sediment transport".

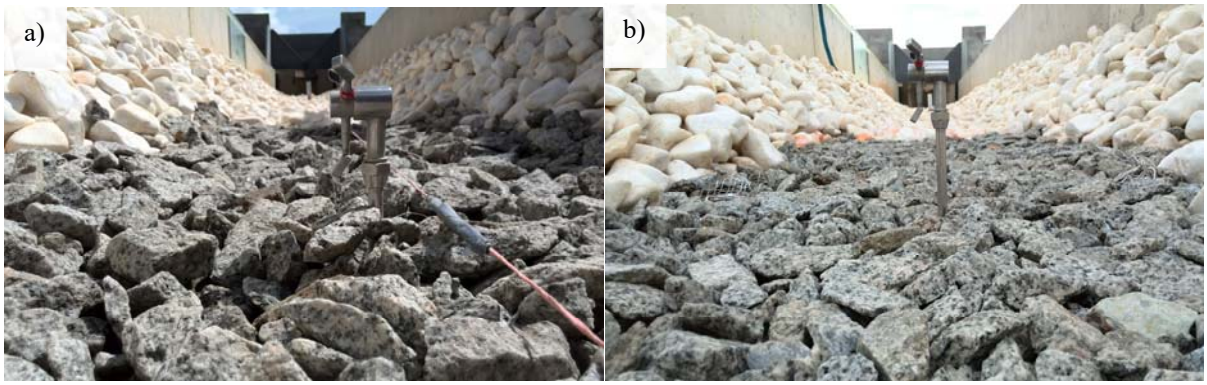

Figure 2.21- (a) Loose bed and (b) well-packed bed.

A total of 6 experiments, 2 with each size particle (CG-D1, CG-D2 CG-D3), the first with loose bed (L), i.e. dropped colocation of the material, and the second with well-packed bed, that is, shaped colocation of the material or leveled. The flow rate in each experiment corresponds to the incipient motion discharge evaluated in the experiments, with the aim of seeing effects on the turbulent parameters. Both hydrodynamic variables and velocity profiles were assessed in the experiments. The main characteristics of these experiments are shown in Table 2.6. The ADV device was placed in the center of the tests area, as in the other experiments. However, in this case, the control volume was located at a distance (z') of 2 mm from the bed surface, Figure 2.7-a or Figure 2.24.

Flow depth was in the range from about 0.082 m to about 0.202 m, and the flow rate from about 62 l/s to 260 l/s. Flow conditions corresponded to values of the Reynolds number, $Re = U4R/v$, in the range from about $5.56 \cdot 10^4$ to $2.7 \cdot 10^5$. All velocity data series were sampled at a rate of 25 Hz for 5 min, resulting in 7,500 velocity measurements per time series. In all, 210-time series were recorded.

Table 2.6 Summary of hydraulic and physical conditions of the CG experiments

Nº TEST	D_{50} m	Flow R. l/s	s m/m	Bed Leveling	d m	R m	S_f m/m	R/D_{50}	U m/s	Fr	Re
CG1	0,0177	61,6	0,031	D	0,082	0,073	0,027	4,12	0,929	1,04	2,71E+05
CG2	0,0177	65,24	0,029	P	0,086	0,076	0,025	4,29	0,976	1,06	2,97E+05
CG3	0,0292	137,4	0,031	D	0,13	0,102	0,03	3,49	1,262	1,08	5,15E+05
CG4	0,0292	157,84	0,03	P	0,138	0,108	0,031	3,69	1,268	1,12	5,48E+05
CG5	0,052	231,41	0,03	D	0,181	0,141	0,03	2,72	1,566	1,18	8,83E+05
CG6	0,052	260,38	0,03	P	0,202	0,154	0,029	2,97	1,641	1,17	1,01E+06

2.4.2 Experimental procedure

2.4.2.1 Assembly of the channel configuration

Both, the embankments and the test slope were carried out manually, with the help of a traction pulley to raise the material into the channel and a calibrated rope to achieve the inclination of 0.3 m/m. Once the slope has been formed, the testing material is placed in the test area, in the case of the RG experiments is not necessary since is the material of the slope the one which is tested. However, in the tests CG, the material has to be replaced for each diameter to be tested. It is important to make sure that the slope in the study area is the same as for the slope (Figure 2.22).

Figure 2.22- Level of the test area.

When the material of each experiment has been placed in the test area, the ADV is positioned. This is a delicate process since the unusual placement of ADV, inverted position (Figure 2.7), makes the ADV positioning process to be arranged for each experiment. A hole in the testing material is opened, where the tube that protects the ADV rod is located. Once the ADV is assembled in the lower structure and introduced into the tube, it is isolated by a balloon. The lip of the balloon has had to be previously stuck to the rod with silicone. In this way, the body of the ADV is isolated from the water. It may not be a very sophisticated system, but after different trial and error attempts, apart from being the most economical solution, it was also the most effective, Figure 2.23.

Figure 2.23- Fastening system and isolation of the ADV with a balloon.

Placed the ADV at the required from the bed surface, the protection pipe of the ADV is covered with the testing material. The first ADV measurements should be as close to the bed as possible since it is the turbulence values measured in the roughness layer that will give us information about what is happening around the particles. For this reason, a small hole is made around the ADV legs (transmitters), in order to get as close as possible to the bed. This hole does not affect the measurements since it is known that the turbulent characteristics are transmitted along the flow direction at an angle of 13°, therefore, the little hole of the ADV placement does not affect the results, Figure 2.24. An example of the real placement of the ADV on the bed is sown in Figure 2.25.

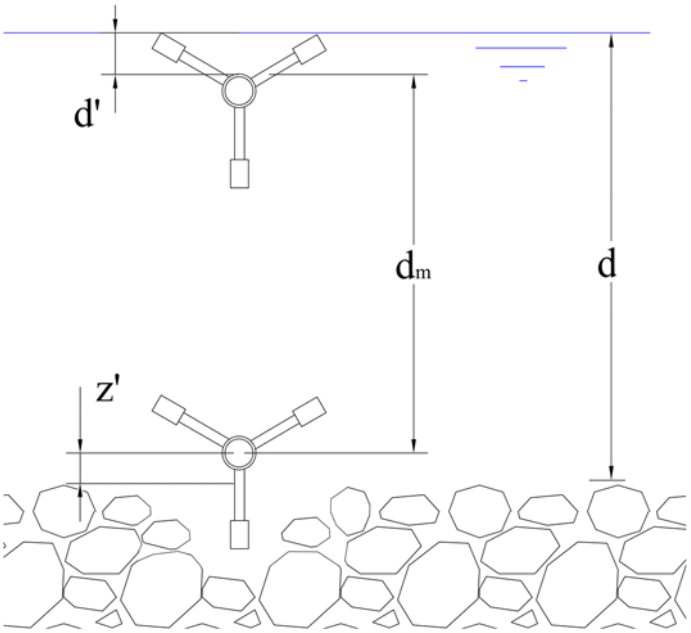

Figure 2.24- ADV positioning scheme.

Figure 2.25- ADV placed on the bed surface

2.4.2.2 Experiment execution methodology

2.4.2.2.1 Common procedure for both test types

Once the sensor device is correctly positioned, the VFD pump is switched on and the minimum flow rate is set. This point is very important because we must ensure that this discharge does not arrive suddenly because, even being the minimum, it can set the particles in motion due to the wavefront. The latter is avoided by turning on and off the pump a few times so that the spillway tank start to discharge a lower flow rate than the minimum of 33 l/s.

At the time the minimum flow rate is running on the test slope without any movement of the bed material, the experiment begins. The flow rate is gradually increased, by means of the VFD, until reaching the desired discharge. It has to be taken into account that for every 10 l/s the flow is increased, the volume of water within the system must be increased by 312.5 liters, which means a time of 5 minutes between each flow rate increase. In order to avoid flow wavefronts, the flow is increased every minute by approximately 2 l/ s. These two minutes is the time available to take measurements of depth for each experiment and check if there has been a movement of the testing particles.

As mentioned before in section 2.1.1, just one pump has a VFD (to modify the flow rate); consequently, this has to be the first one to put into operation. Once this reaches its maximum discharge (180 l/s), it is stopped and the other is put into operation, which provides this maximum flow rate. If the flow rate is needed to be increased, the VFD pump is restarted again so that both of them are working at the same time; however, there is an unavoidable sudden rise of 30 l/s (minimum discharge of the pump).

Once the test flow is reached, the ADV data collection begins. As can be seen in Figure 2.24 from the previous section (2.4.2.1), the effective depth of measurement (d_m) does not correspond to the hydraulic depth (d) of the experiment, since both the positioning in the bed, and the legs of the transmitters when it gets close to the water surface restrict the measurable depth (see Figure 2.24).

All experiments were performed under uniform flow conditions. That is, once the target flow is reached, it circulates for a minimum of 10 minutes until uniform flow conditions are achieved, before starting ADV measurements. Each point has been measured for 5 minutes, enough to achieve stability by the evaluation

with a running average of the most important statistical parameters. The points have been taken equidistantly, depending on the hydraulic depth of each test.

As shown in Figure 2.24 of the previous section, three measurement equidistances are defined, from z=[z'-3 cm] the equidistance is 2 mm, from that point until z=5 cm the equidistance is increased until 4 mm, and the third equidistance is 6 mm or 10 mm subject to the water depth (d) of the experiment. Table 2.7 and Table 2.8 show the values referred to in Figure 2.24 for each experiment, as well as the measurement duration time of the tests.

The measurement times to consider here have been, the ADV placement time (T_1, placement in the structure, gluing of the balloon, placement in the tube etc.), the time necessary to reach the test flow rate (T_2), and the collection time of the velocity profile by the ADV (T_3). In addition, in the case of CG tests, the preparation time of each scenario (T_0) must be considered, since the particle in the test area has to be changed. The preparation of the scenario test depends on whether new particles have to be placed in the test area (CG1, CG3, and CG5) or if only those moved in the previous test have to be recovered and the bed shaped (CG2, CG4, and CG6). This process lasts approximately 4 hours in the first case and one hour in the second. For a better continuity of the experiments, the test scenario was prepared the day before its performance. Table 2.7 and Table 2.8 shows these times associated with each experiment.

In the case of the RG experiments, it is not necessary to evaluate the movement of the test particles during the execution of the experiment, since they only start to move at very high flow rates above 300 l/s, which is not exceeded in any case for the RG experiments (Table 2.5). Nevertheless, it is necessary to check that there is no particle obstructing the ADV operation. However, in CG tests, it is required a constant observation of the test area, in order to write the movements down and detect the incipient motion of the test particles. The criterion to detect the incipient motion is standardized in the next section (2.4.2.2.2).

Table 2.7 Summary of ADV conditions and timings of the RG experiments

Nº TEST	Flow R. l/s	d (m)	d_m (m)	z' (m)	D (m)	Time series	T_0 (h)	T_1 (h)	T_2 (h)	T_3 (h)	Total (h)
RG1	42,75	0,078	0,048	0,011	0,02	24	0	2	0,02	2,9	4,9
RG2	48,79	0,083	0,053	0,011	0,02	26	0	2	0,07	3,2	5,2
RG3	54,68	0,089	0,059	0,012	0,02	28	0	2	0,12	3,2	5,3
RG4	73,24	0,1	0,07	0,0115	0,02	28	0	2	0,28	3,3	5,5
RG5	97,49	0,116	0,086	0,013	0,02	31	0	2	0,48	3,5	6,0
RG6	120,01	0,129	0,099	0,0135	0,02	30	0	2	0,67	3,4	6,1
RG7	162,92	0,15	0,12	0,014	0,02	32	0	2	1,02	3,6	6,6
RG8	204,41	0,171	0,141	0,014	0,02	30	0	2	1,37	3,7	7,1
RG9	238,46	0,183	0,153	0,016	0,02	30	0	2	1,65	3,9	7,5
RG10	307,65	0,208	0,178	0,017	0,02	34	0	2	2,23	4,0	8,2

Table 2.8 Summary of ADV conditions and timings of the CG experiments

Nº TEST	Flow R. l/s	d (m)	d_m (m)	z' (m)	D (m)	Time series	T0 (h)	T1 (h)	T2 (h)	T3 (h)	Total (h)
CG1	61,6	0,082	0,06	0,003	0,02	26	4	2	0,18	3	9,1
CG2	65,24	0,086	0,064	0,0035	0,02	24	1	2	0,21	2,8	6,1
CG3	137,4	0,13	0,108	0,003	0,02	29	4	2	0,98	3,4	10,3
CG4	157,84	0,138	0,116	0,002	0,02	29	1	2	0,81	3,4	7,2
CG5	231,41	0,181	0,159	0,002	0,02	30	4	2	1,60	3,5	11,1
CG6	260,38	0,202	0,18	0,002	0,02	31	1	2	1,84	3,6	8,5

2.4.2.2.2 Incipient motion conditions CG

As previously mentioned, in the case of the RG experiments, the incipient motion discharge associated to each experiment was determined by observation of the bed particles, the velocity profile (ADV) and hydrodynamic data were collected under this flow rate. The approach to detect this incipient motion point can be very subject, for this reason, a methodology to be followed has been defined, so that all experiments are evaluated with the same criterion. After carrying out some tests, it is concluded that it is important to determine the fraction of particles (%) that move out for each flow rate, so it is decided to discretize the test area by painting the surface of the stones (Figure 2.26), and placing a particle trap downstream of the test area, so that the particles do not enter in the reception tank.

The flow increase procedure is carried out gradually as described above (section 2.4.2.2.1). Each time the flow is increased, the number of displaced particles is noted down in order to have a movement statistics based on the circulating discharge. The painting of the stones and the visualization through the "periscope" (see Figure 2.27) facilitate this task.

Figure 2.26- Preparation of the test, painting of the particles

Figure 2.27- Displacement particle visualization with the "periscope"

The criterion established to start taking the velocity is based on considering the incipient motion discharge as the one that sets in motion at least a 2% of the particles placed in the test area during the 10 minutes of application. The mobilization of more particles would correspond to a generalized movement that is not the target of the CG experiments. Once this discharge is established, velocity profiles and hydraulic data is taken. Since the data collection of the profile lasts about 2-4 hours (depending on the depth), the total number of displaced particles is counted during this time.

When the velocity profile is finished, the flow rate is reduced progressively (reducing the frequency of the CFD) until shut the pump down. When there is no water in the channel, the particles mobilized during the taking of the velocity profile are counted. Some pictures of the final scene of the CG tests are shown below in Figure 2.28.

Figure 2.28- Final result of the RG tests.

2.5 Calibration of the experimental setup

2.5.1 Interstitial flow

From the visual inspection of the first experiments throughout the glass window installed in the hydraulic channel, it was noticed that some flow run below the test zone, thus the direct flow rates obtained from the triangular weir could not be used until the quantification of this subsurface flow.

The weir discharge and the actual flow rate that flows on the bed surface has been calibrated by measuring the interstitial flow rate in ten different discharges (from *Q1* to *Q10*). The discharge from calibration tests is not exactly the same that the obtained from the RG experiments since different conditioning factors such as the volume of water in the tanks control the discharge. Therefore, two different weir flow rates can be found even for the same frequency (Hz) at the pump. However, the differences between the flow rates from the RG tests and calibration tests (Q) are always less than 5%.

The calibration methodology consisted in the injection of ink (tracer) and later small plastic particles (avoiding the molecular dispersion and diffusion of ink) at different heights into the flow. As can be seen in Figure 2.29, two layers of sediment were tested, the rounded-gravel (white stones) which perform the channel slope, and the crushed-gravel D-1. The result showed that the velocity of the interstitial flow was similar in the two layers. The plastic particles and the ink stain were tracked and recorded (30 frames per second), through the glass window of the channel. The subsequent display of the video allows to obtain the interstitial velocity and thus the subsurface flow rate as a function of the flow depth (d) of each experiment. The velocity results from the video visualization of the calibration tests are shown in Table 2.9.

Figure 2.29- Example of the interstitial flow calibration

From the interstitial velocities and its integration over the cross section that occupies the gravel is possible to obtain the interstitial flow below the test zone and subtracting this flow rate to the weir flow rate, the surface flow is obtained. That is to say, the flow rate to consider to the experiment area it is different from the obtained from the weir adjustment. Figure 2.30 shows the weir flow rate as a function of the interstitial flow rate and the mean interstitial velocity (U_0), in addition to the linear adjustment of both quantities. This expression will be used to calibrate the weir flow rate from each experiment conducted in “the Cube” channel, as long as the physic characteristic of the slope, inclination, and sediment of the ramp (RG), are maintained. The percentage of interstitial flow (or seepage flow) is not proportional to the weir discharge, decreasing for more powerful-flows since the interstitial velocity does not show a wide range of variation, Table 2.10.

Table 2.9 Results from recorded videos (30 frames per second)

Weir flow rate (m3/s)		below-bed area				within banks area			
		number of frames in 50 cm		time elapsed (sec)	U_0 (m/s)	number of frames in 50 cm		time elapsed (seg)	U_0 (m/s)
Q-1	0,051	679	854	5,833	0,086	1322	1479	5,233	0,096
Q-2	0,060	569	726	5,233	0,096	1075	1195	4,000	0,125
Q-3	0,068	455	624	5,633	0,089	1105	1249	4,800	0,104
Q-4	0,082	398	566	5,600	0,089	1200	1328	4,267	0,117
Q-5	0,112	584	748	5,467	0,091	1133	1243	3,667	0,136
Q-6	0,132	707	876	5,633	0,089	1479	1593	3,800	0,132
Q-7	0,181	308	456	4,933	0,101	780	877	3,233	0,155
Q-8	0,219	500	635	4,500	0,111	914	1015	3,367	0,149
Q-9	0,261	476	612	4,533	0,110	923	1015	3,067	0,163
Q-10	0,323	332	466	4,467	0,112	1226	1334	3,600	0,139

Table 2.10 Comparison between discharges from the Weir-adjustment, Surface flow (without interstitial flow)

Weir flow rate (m3/s)		Average velocity (m/s)	Water depth(m)	section area (m2)	interstitial flow rate (m3/s)	Surface flow (m3/s)	(%) seepage flow
Q-1	0,051	0,091	0,078	0,093	0,008	0,043	16,4%
Q-2	0,060	0,110	0,089	0,094	0,010	0,050	15,9%
Q-3	0,068	0,105	0,098	0,094	0,010	0,058	12,9%
Q-4	0,082	0,103	0,100	0,094	0,010	0,072	11,9%
Q-5	0,112	0,114	0,129	0,097	0,011	0,101	8,5%
Q-6	0,132	0,110	0,150	0,098	0,011	0,121	6,3%
Q-7	0,181	0,128	0,155	0,099	0,013	0,168	7,0%
Q-8	0,219	0,130	0,171	0,101	0,013	0,205	5,9%
Q-9	0,261	0,137	0,198	0,104	0,014	0,247	4,7%
Q-10	0,323	0,125	0,206	0,105	0,013	0,310	3,8%

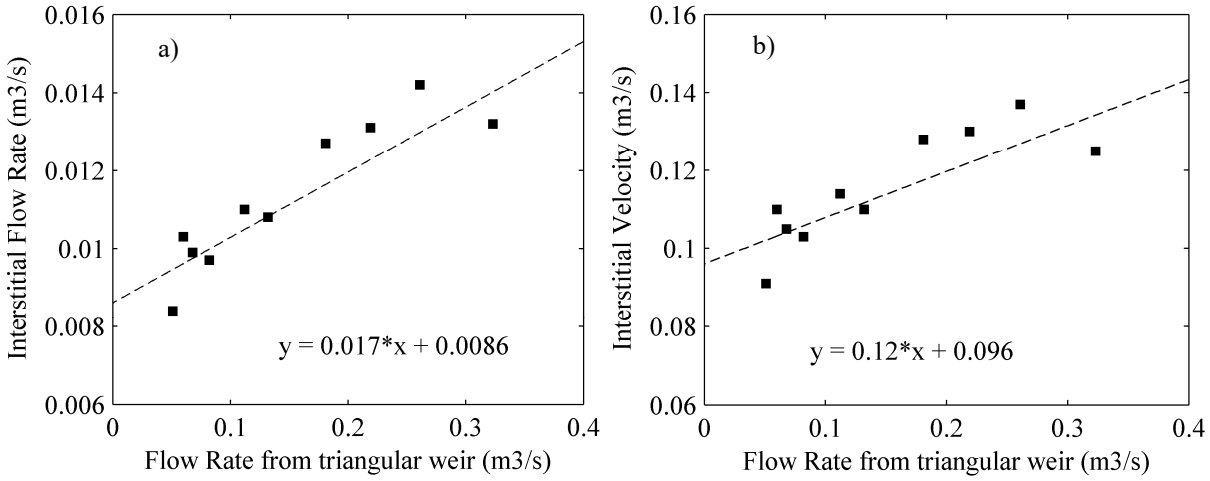

Figure 2.30- Flow rate from triangular weir as a function of (a) the interstitial flow rate and (b) the interstitial velocity. *Legend,* ■ *experimental data and --- linear adjustment.*

2.5.2 Average velocities in the transverse axis

The local mean velocity measured by the ADV gives us information about the instantaneous velocity at the center of the channel, where the device is located; therefore, the velocity profile obtained corresponds to the velocity distribution along a vertical at this point. However, velocity in Channel Rivers, with a trapezoidal cross-section and high rough bed, is not constant along the transversal area, just as it is not along the vertical, with a maximum velocity located at the center of the channel.

Therefore, the integration of the velocity profile (ADV) over the flow cross-section will give us a flow rate greater than the actual flow, since we are overestimating the average velocity of the flow. In order to assess this overestimation and the transverse velocity distribution of the experiments, the same 10 discharges have been testes and the velocity in the transverse axis was measured by means of a micro-pinwheel (see Figure 2.31), which obtains the local average velocity at each point. The pinwheel was placed into the flow and located at a distance of 5 cm on the bottom bed. The transverse distribution of the velocities for each flow rate are graphed in Figure 2.32.

Figure 2.31- Measurement of interstitial flow with pinwheel

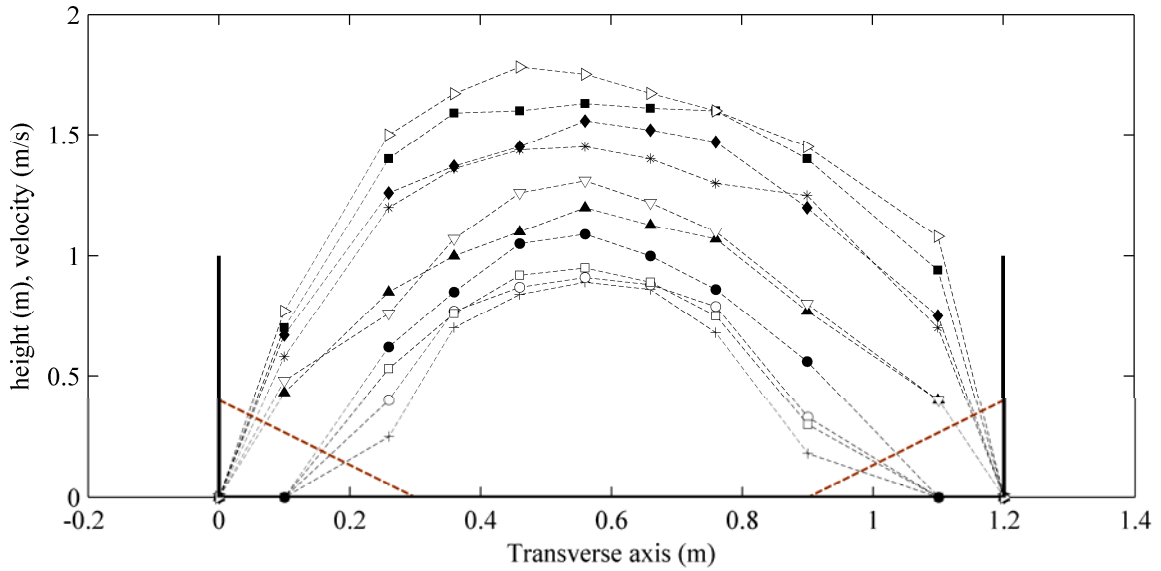

Figure 2.32- Distribution of average velocities in the transverse axis. *Legend, + Q-1, ○ Q-2, □ Q-3, ● Q-4, ▲ Q-5, ▽ Q-6, ∗ Q-7, ♦ Q-8, ■ Q-9, ▷ Q-10.*

The interstitial flow velocity was also evaluated using the pinwheel (Figure 2.31-b) for a flow rate of 42.4 l/s, obtaining a velocity of 0.05 m/s, which is lower than that obtained by the injection of ink and particles. However, the validity of the measurement is not reliable for values below 0.2 m/s, therefore, the values from the previous section are considered.

2.5.3 Calibration check

The purpose of this section is not the evaluation of the velocity profiles, however, it was a premise to ensure that the device was working correctly. For this, the calculation of the flow rate was made, based on the velocity profiles obtained from the RG experiments, and compared with the surface flow rate.

The flow that runs on the surface has been calibrated by subtracting the interstitial flow, using the expression in Figure 2.30-a, which relates the flow discharged by the triangular weir and the flow that runs on the surface. The results obtained show that the flow rate of the velocity profile is between 1-9% higher than the flow that runs on the surface, Table 2.11. The difference being greater for smaller flows.

However, it has been seen that the velocity is not homogeneous in the transversal axis, therefore, when placing the ADV in the center of the channel, the measured velocity t corresponds to the maximum in the cross-section, so that it makes sense that the calculated flow rate is a little higher than the actual flow. In the same Table 2.11, the comparison between the maximum velocity (located in the center of the channel) and the mean velocity obtained by using the pinwheel is shown. From the comparison it is obtained that the maximum velocity (in the center of the channel) differs from the mean velocity between 15 and 3% approximately, decreasing with increasing flow. Therefore, the overestimation of the flow rate of the ADV profiles is due to the transversal non-homogeneity of the velocity and the profile data obtained by the ADV can be considered good, and the calibration of the ADV set up is concluded.

It should be mentioned again that the interstitial flow experiments do not correspond exactly to the RG, although the flow rates are very similar and the scenario (slope and channel bed) are the same. Therefore, the calculations can be compared without errors.

Table 2.11 Comparison between discharges from the Surface flow (without interstitial flow) and from the integration of the velocity profile, and local and average velocities obtained from the micro-pinwheel.

VEL-Profile (ADV)					Micro-Pinwheel				
	Surface flow (m3/s)	Flow rate (m3/s)	Average velocity (m/s)	Flow rate error (%)		Surface flow (m3/s)	Velocity center channel (m/s)	Average velocity (m/s)	Velocity Over-estimation
RG1	0,043	0,048	0,959	10,90%	**Q1**	0,043	1,074	0,953	12,60%
RG2	0,049	0,056	1,006	12,90%	**Q2**	0,05	1,100	0,979	13,00%
RG3	0,055	0,063	1,051	13,20%	**Q3**	0,058	1,147	1,013	13,20%
RG4	0,073	0,079	1,139	7,30%	**Q4**	0,072	1,234	1,098	12,10%
RG5	0,097	0,112	1,202	13,00%	**Q5**	0,101	1,274	1,102	15,30%
RG6	0,12	0,135	1,419	11,10%	**Q6**	0,121	1,505	1,400	7,50%
RG7	0,163	0,178	1,434	8,50%	**Q7**	0,168	1,485	1,381	7,40%
RG8	0,204	0,221	1,582	7,50%	**Q8**	0,205	1,658	1,604	3,20%
RG9	0,238	0,256	1,603	6,90%	**Q9**	0,247	1,652	1,509	9,80%
RG10	0,308	0,321	1,784	4,20%	**Q10**	0,31	1,860	1,735	7,10%

Chapter 3: ADV Measurements

3.1 Introduction

The Acoustic Doppler Velocimeter (ADV) has been widely used for the measurement of 3D instantaneous velocities, in both river field and experimental laboratory tests, over the last two decades. ADVs are capable of measuring accurate mean values of flow velocity in the three directions (X, Y, Z), even at low energy flows, Voulgaris & Trowbridge (1998). Nevertheless, the capability of the device to solve flow turbulence accurately is still uncertain (Barkdoll 2002).

Despite being widely used due to their effectiveness and affordability, ADVs have shown some difficulties taking measurements in certain flow conditions such as highly turbulent flows. Some of these problems tend to appear measuring at distances below 3 cm from the bed (Finelli et al. 1999), or in aerated flows in high turbulent flows (e.g. Martin et al. 2002; Cea et al. 2007). For instance, ADV signal correlation values obtained in turbulent flows near the bed sometimes are below the minimum recommended by the manufacturer to accept data as reliable. Although these problems could appear even over smooth boundaries, they become more significant as the roughness and porosity increase.

The latter could be explained by different phenomena that might contaminate the received signal, such as bubbles in the control volume (CV), disturbance of the water surface, interferences of the CV with the boundary, acoustic signal interferences between the sample volume and the boundary reflection, etc. As a result, spurious spikes, low Signal-Noise-Ratio (SNR) and signal correlation values (COR) are obtained from the signal. These spikes may contribute considerably to the total turbulent kinetic energy (TKE) in highly turbulent flows, owing to these uncertainties, a filtering process is necessary to estimate the correct turbulent parameters.

The filtering effects on the RG (Rounded gravel), experiments from test RG1 to RG10 (described in chapter 2), have been evaluated. The flow rate in these tests is increased in each experiment, therefore, the effects of increasing the turbulence can be elucidated.

For the experiments carried out in the present thesis, when using the conventional filter analysis for ADV measurements of Wahl (2000), may eliminate more than 50% of the time series velocities, and this percentage is even higher at the near-bed region. However, low correlation values do not necessarily mean that data is corrupt (Martin et al. 2002). Due to this fact, the reliability of the measurements taken in these conditions, high roughness and low relative submergence ($<<R/D_{50}$), and the capability of the filtering methods to conserve the primary turbulent characteristics are analyzed in this chapter.

3.2 Acoustic Doppler Velocimeter

3.2.1 Principle of operation

The device used for the experiments was a 3D SONTEK 10 MHz ADV with a cable mount probe and side looking physical arrangement, Figure 3.1. The probe head of the device is composed of three acoustic receivers and an acoustic emitter mounted on a 0.008 m diameter, 0.40 m long stem that is

attached by a 0.8 m flexible cable to the signal-conditioning module. This module contains analog electronics, which detect and amplify acoustic signals.

The device works on the Doppler shift principle; an acoustic ultrasound signal is sent by the emitter (10 MHz), considered approximately unidirectional due to the high frequency. The signal travels through the water and is reflected by the suspended particles inside the CV in the water. These particles are thought to be at the same velocity as the flow, and the echo is received and captured by the receivers. This acoustic echo is a superposition of several reflections from coherent groups of particles passing through the remote sampling volume located 10 cm from the tip of the transmitter.

The data processing module measures the phase change between the transmitted and the received signal. The phase is modified because of the relative velocity of the particles, owing to the Doppler Effect. The Doppler Effect is the apparent change in the signal frequency produced by the relative movement of the source with respect to its observer. Therefore, measuring the frequency alteration in each receiver is possible to obtain the 3D velocities of the particles respect to the emitter-receiver system, i.e., in the axes defined by the three receivers. With the application of the rotation matrix to the velocity vectors, the velocities transform into the reference axes X, Y, and Z. More information about ADV principles of operations is available in SonTek (2001).

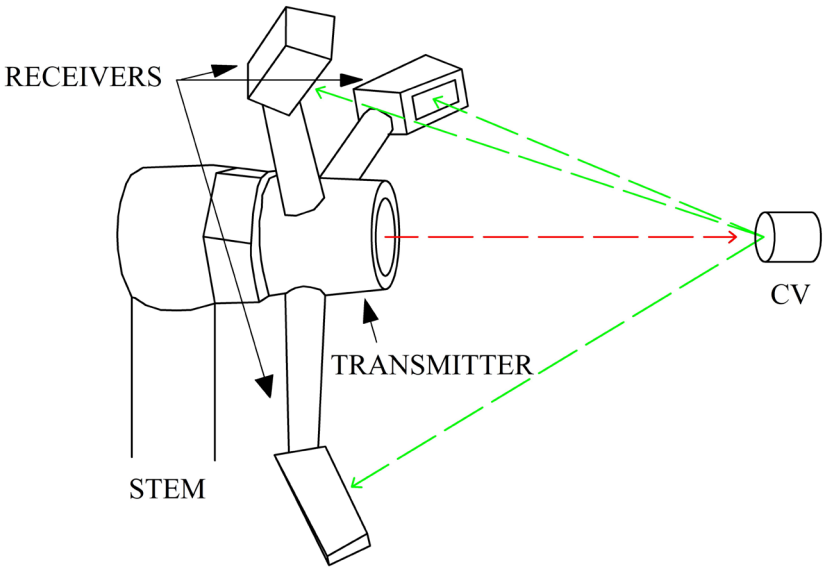

Figure 3.1- Side-looking head equipped with three receivers, inverted position.

3.2.2 Placement of the ADV

The traditional way of placing the ADV is to introduce the device through the water surface of the flow until reaching the target zone of measurement. However, the stem of the ADV (the head is placed at its end) could introduce bubbles around the receivers and contaminate the data measurements when the depth (d) is low. In order to avoid this effect, the ADV was introduced in the flow differently to the usual way, through the bottom-channel into the flow, (inverted position, as explained in chapter 2). The goal was achieved since the values of Signal-Noise-Ratio were high in all the measurements.

3.2.3 Configuration of the device

In order to perform the calculations correctly, the device requires, in general, five different input variables before starting using it; i) the temperature of the water; ii) the salinity of the fluid; iii) the control volume (CV) size; iv) the nominal velocity range and v) the frequency of data collection (FDC). Among all the configuration parameters, the last three values are more subjective and depend on the user's criteria.

The FDC determines the amount of data acquired per second. The maximum FDC that can be set by the user is 200, which is the maximum data storage capacity of the sensor; therefore, if the FDC is less than this the device averages the data. Due to the Nyquist criteria, the FDC has to be twice the frequency with the resolution wanted. Therefore, according to the assumption that Doppler noise appears in the signal around 10 Hz (Lohrmann 94), measuring at frequencies over 20 Hz the signal has a significant amount of Doppler noise. Besides this, the manufacturer no longer ensures errors less than 1%. For all these reasons, the velocity data series were sampled at a rate of 25 Hz.

The CV, or sampling volume, is a cylinder of water with a diameter of 6 mm and height set by the user. The CV height (h) refers to the length of the cylinder, which defines the region of the reflected echoes. Typically, the device allows different volumes from h=2.5 mm until h=9 mm. When the h is too small, the received echoes are low, thus increase measurement error. For this reason, the cylindrical sampling volume was established with a length of 9 mm; the midpoint is located at a distance of 10 cm from the acoustic transmitter.

The last parameter is the nominal velocity range. Five nominal velocity ranges [3, 10, 30, 100 and 250 cm/s] can be set by the user. The maximum velocity determines the maximum Doppler Effect seen in the signal; consequently, if the flow velocity is higher than the maximum, the device considers that the phase difference is 180 degrees, and it changes the velocity sign. This effect is called Aliasing and occurs when the phase change between two consecutive signals are $>\pm\pi$ or caused by the reflections of previous signals (Nikora & Goring 1998). With the aim of avoiding Aliasing caused by the high turbulence of the flow, the nominal velocity range was established at 2.5 m/s. This configuration of the device guarantees a low level of spikes and the presence of the big flow structures in the velocity signal.

A running average for each statistical parameter was performed until the computed values do not change, so that validate the sampling time. According to this, the velocity data series were sampled at a rate of 25 Hz during 5 min, resulting in 7,500 velocity measurements per time series. In the case of the RG experiments, which will be analyzed in this chapter, 340-time series were recorded.

3.3 Data quality of the Experiments

3.3.1 COR and SNR parameters

Among all the indicators of data quality offered by the device, the correlation value (COR) and Signal-Noise-Ratio (SNR), are considered the most important to evaluate the reliability of the measurements. Due to this fact, some filtering methods have defined the specific requirements for the signal quality based on these two parameters, such as Wahl (2000).

The SNR is given in dB (decibels) and represents the relative amplitude of the returned signal compared with the electronic noise of the instrument. The COR is a measure of the similarity between two consecutive echoes. A value of 100% of correlation would be obtained if the echoes from two consecutive signals were identical and only the phase had changed. The ADV operates with a constant frequency of 10 MHz, the maximum Frequency of Data Collection (FDC) is 200 Hz, although the frequency set at the experiments was 25 Hz. Therefore, as the FDC set at the configuration is less than 200 Hz, the collected data by the device is the result from several averaged velocities (8) and the COR value indicates the similarity of these averaged readings between them to obtain the one provided by the device (Nortek 2004).

In order to evaluate data quality from the RG experiments, the mean value and the standard deviation (σ) of the COR and SNR parameters were evaluated along the profile for all the RG experiments (RG1 to RG10) as can be seen from Figure 3.2 to Figure 3.4.

In all the experiments the average value of SNR, Figure 3.2-a, is somewhat steady over the water depth and, considering the minimum suggested by Wahl (2000) (SNR>15), large enough to consider all the RG experiments as good. Moreover, its standard deviation (σ_{COR}), Figure 3.2-b, is in all cases lower than 2, except in the highest turbulent experiments and only at some points near the water surface, which was probably caused by disturbance of the water surface by the ADV. However, the values are always under 4.5, demonstrating the robustness of the value. As the flow rate rises for each experiment, the reflected signal received by the ADV becomes stronger and the mean SNR value increases, conversely, the standard deviation maintains (σ_{SNR}), in value stable.

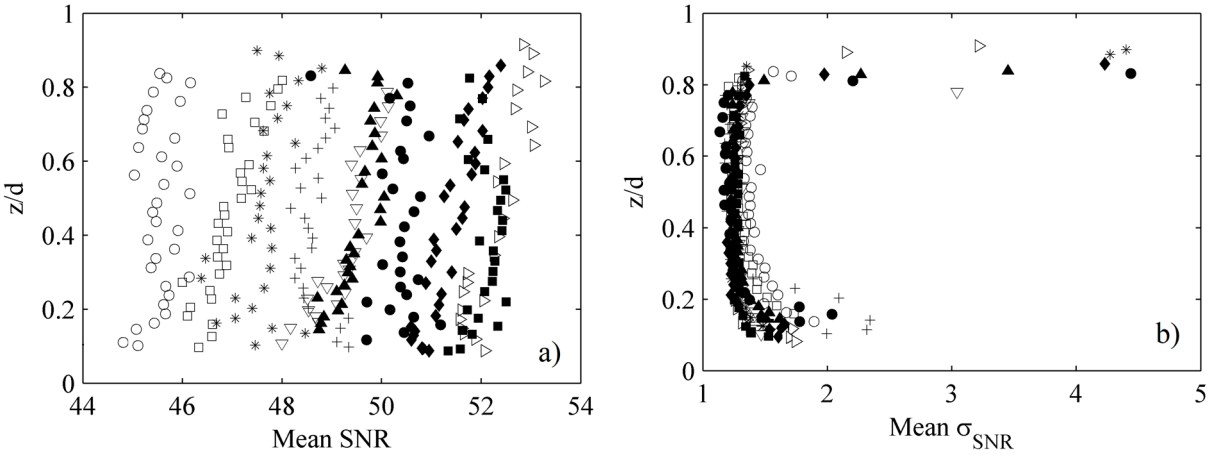

Figure 3.2- Vertical distribution of the mean value of (a) SNR and (b) σ_{SNR} as a function of *z/d*. (tests RG1 to RG10). *Legend, + RG1, ○ RG2, □ RG3, ● RG4, ▲ RG5, ▽ RG6, ∗ RG7, ♦ RG8, ■ RG9, ▷ RG10.*

On the other hand, the mean COR values are not steady along the profiles and increase with the distance to the bed, with a similar pattern in all the experiments as can be seen in Figure 3.3-a, showing a higher quality further away from the bed. Moreover, the average COR values decrease with the flow rate, in most cases, although not as proportionally as the average SNR decreases. A layer over the boundary is appreciable (z<3.5 cm) where the mean COR remains rather constant, albeit showing a trend of increase with the distance to the bed. It seems that the thickness is around 3.5-4 cm, although disappearing in some cases (RG8 and RG10), Figure 3.4, where the evolution of the COR value is depicted along the depth profile. On the other hand, the σ_{COR} depicts the variability of the COR over

the profundity, Figure 3.3-b, and it shows that even though the mean COR is low in the near-bed region, the σ_{COR} tends to be lower in this zone, which means that correlation is robust. In all cases the mean COR values do not achieve the minimum value suggested by Wahl (2000) (COR>70) therefore, almost all the data can be expected to be removed from this consideration. However, as mentioned above, for highly turbulent flows this does not necessarily mean that data is wrong. For this reason, a deeper insight into the data quality of the experiments will be developed along the present chapter.

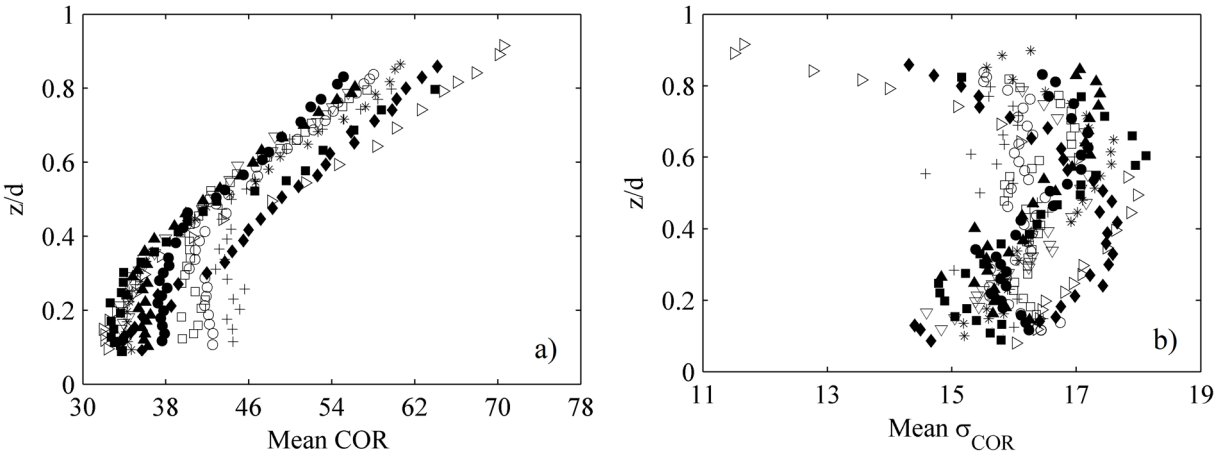

Figure 3.3- Vertical distribution of the mean value of (a) COR and (b) σ_{COR} as a function of *z/d*. (tests RG1 to RG10). *Legend, + RG1, ○ RG2, □ RG3, ● RG4, ▲ RG5, ▽ RG6, ∗ RG7, ♦ RG8, ■ RG9, ▷ RG10.*

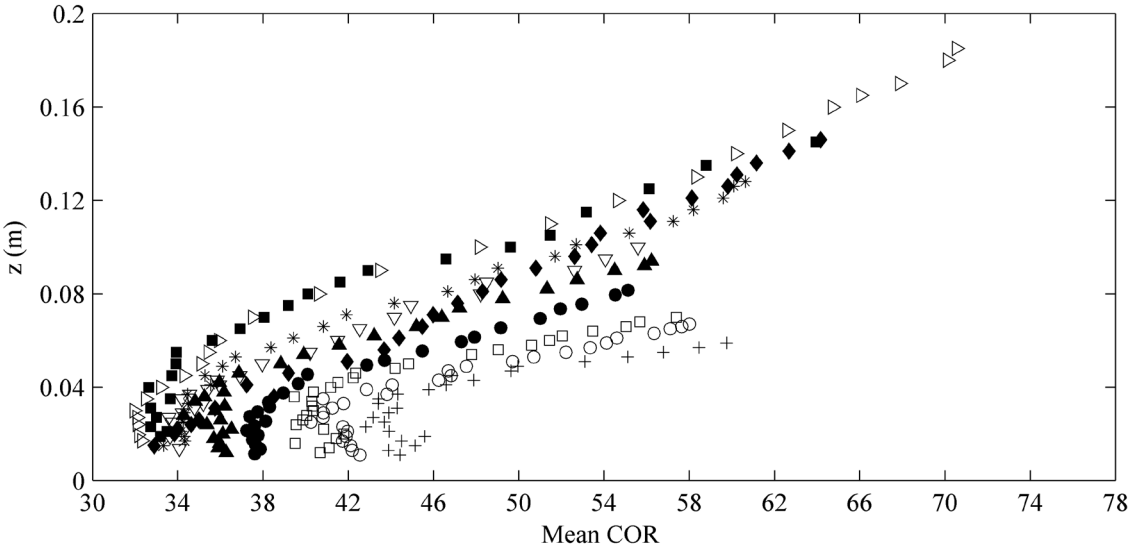

Figure 3.4- Vertical distribution of the mean COR value (RG1 to RG10). *Legend, + RG1, ○ RG2, □ RG3, ● RG4, ▲ RG5, ▽ RG6, ∗ RG7, ♦ RG8, ■ RG9, ▷ RG10.*

Experiment RG3 serves as an example to study in more detail the data quality over the profile. Figure 3.5-a plots the three average COR axes and their standard deviation for the mentioned experiment, showing a pattern of increase from the bed to the water surface. In this case, the three values of (COR_X, COR_Y, COR_Z) are around 38-43% in the near-bed region, starting to grow progressively as of the point 0.4 of the dimensionless depth profile (*z/d*). Despite the increase in the mean COR value, its σ_{COR} remains stable between values of [15.8-17.4], Figure 3.5-b, even in the near-bed region, with the lowest values of COR. Regarding the mean SNR, Figure 3.6-a shows a good SNR value at each point and a robust value of standard deviation for the three axes, Figure 3.6-b.

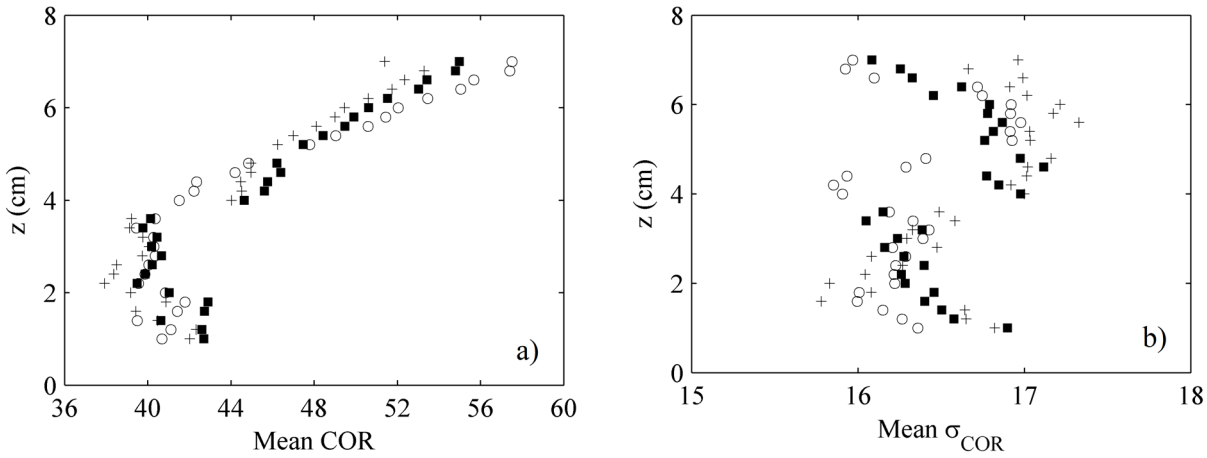

Figure 3.5- Vertical distribution of the mean values of (a), COR and (b), σ_{COR}. Test RG3. *Legend,* ○ *X-axis,* ■ *Y-axis,* ＋*Z-axis.*

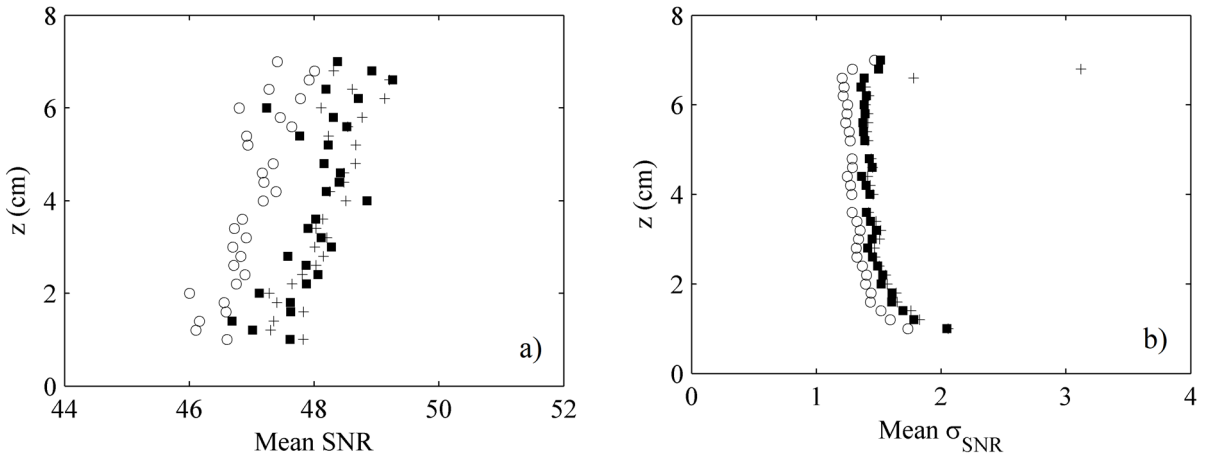

Figure 3.6- Vertical distribution of the mean values of (a), SNR and (b), σ_{SNR}. Test RG3. *Legend,* ○ *X-axis,* ■ *Y-axis,* ＋*Z-axis.*

Finally, Figure 3.7 depicts the COR histograms of some of the calculated points, (a) z/d=0.16, (b) z/d=0.35 and (c) z/d=0.7. The histograms revealed that normality is achieved in the near-bed region (a and b) whilst a negative skewness appears further away from the bed, out of the roughness layer. Although mean COR value increases with depth, low values of COR are still appearing.

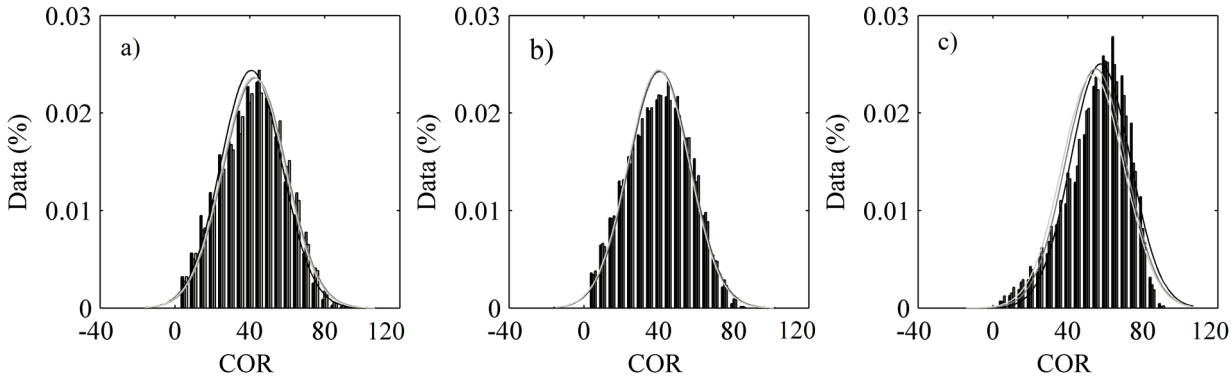

Figure 3.7- Correlation histograms of the points (a) z/d=0.16, (b) z/d=0.35, (c) z/d=0.7. Test RG3. *Legend,* ▬ COR_x, ▬ COR_y, ▬ COR_z.

3.3.2 Signal Noise

Data quality of ADV measurements is closely affected by signal noise, which is considered an inherent part of Doppler backscatter systems when measuring turbulence. Some sources of noise are due to *i*) high turbulent flows, the particles in the CV do not maintain their relative position thus Doppler noise is added and the correlation decay, Voulgaris & Trowbridge (1998). Moreover; *ii*) if the turbulent structures are smaller than the CV the correlation will decay even more, and the noise is increased, Nikora & Goring (1998). Other reasons for these low-COR values are *iii*) air bubbles in the flow; *iv*) low SNR values (Liu et al. 2002); *v*) Acoustic signal interferences from the boundary reflection (Finelli et al. 1999; Goring & Nikora 2002; Martin et al. 2002); *vi*) Overlapping of the CV with the boundary (Lane et al. 1998; Voulgaris & Trowbridge 1998; Hurther & Lemmin 2001); *vii*) large particles such as saltating grains inside the CV, Martin et al. (2002); *viii*) large velocity gradients within the control volume, (Lhermitte & Lemmin 1994), *ix*) Velocity aliasing (Rusello 2009), and *x*) lack of particles in the water.

To avoid the low correlation problem that involves the bubbles, the ADV was placed through a hole in the bottom of the channel as shown in chapter 3 (section 3.2.5). Hence, it can be reliably assured that there were no contaminating bubbles in the CV. The results exposed in Figure 3.2-a and Figure 3.2-b, showed a high SNR ratio and low σ_{SNR}, demonstrating the success of the particular placement of the ADV. As a consequence, some of the possible sources of noise *(iii, iv*) are discarded.

On the other hand, no interferences with the boundary are expected (*v*) from the type side-looking of the device Moreover, the device was set over the bed roughness, avoiding the superposition with the CV (*vi*), and considering that it could have been overlapping, this would not extend beyond the near-bed region. Furthermore, as the experiments were kept under no-motion conditions, hypothesis (*vii*) can be rejected. Concerning hypothesis (*viii*), the noise due to shear velocity can be ignored above elevations of z/d=0.1 (Voulgaris & Trowbridge, 1998; Martin et al. 2002). The velocity range was established at 2.5 m/s, and aliasing was avoided, hence hypothesis (*ix*) can be discarded. Finally, there was particle seeding (~10 μm) during the tests to reduce the noise of the received signal so hypothesis (*x*) can be also rejected.

In conclusion, the considered sources of error in the experiments are i, and ii, both related to the high level of turbulence of the flow. This high turbulence resulted in low correlation values in the near-bed region. Therefore, although the collected data in the near-bed region may not have the highest quality, it does not mean that they cannot be interpreted.

3.3.2.1 Doppler Noise

The primary source of acoustic Doppler velocimeter's noise is the Doppler Noise (SonTek 1997), even when COR and SNR values are within the established ranges. As a consequence of that, when Doppler noise dominates, the combined noise could be supposed as white noise. Therefore, it can be approximated by a Gaussian probability distribution, then the noise effect on the mean values, Reynolds Stresses and mean velocity, could be neglected (Lohrmann et al. 1994; Voulgaris & Trowbridge 1998).

Doppler noise has a flat power spectrum, in other words, have the same energy for all frequencies, which makes impossible to remove it from the velocity signal using filters. If a flat plateau is detected

in the power spectrum at high frequencies, close to the Nyquist frequency [11.5–12.5]Hz with an FDC of 25 Hz), indicates the presence of uncorrelated noise. Consequently, the autocorrelation function reduces its value to zero faster than in signals without noise, diminishing temporal scales, while the Turbulent Kinetic Energy (TKE) is increased.

The white noise energy level can be deducted from the power spectrum, and by its integration, the corrected variances for each direction are obtained and consequently the corrected TKE. Furthermore, the corrected autocorrelation function can be obtained from the inverse fast Fourier transform of the modified power spectrum thus the associated timescales; this is called "spectral analysis" (Voulgaris & Trowbridge 1998).

However, for high-energy flows, the plateau cannot be found in the spectrum, although the noise is present. In these cases, a potential noise energy level can be calculated by using the energy value at the Nyquist frequency, with the assumption that the flat plateau is present beyond that frequency. Garcia et al. (2005) assure that the noise energy is less than 10% of the real total energy for highly turbulent flows; while Nikora & Goring (1998), confirmed that energy inserted by the Doppler noise in these cases could be considered negligible.

Garcia et al. (2005) evaluated the energy noise rate (*E)* as the noise energy E_n divided by the real turbulent flow energy E_r, which is obtained from the power spectra integrated up to the Nyquist frequency. The E_n can be obtained as the product of the Nyquist frequency and the noise energy level (E_{11n}), considered within the range [10^{-7} m^2/s<E_{11n}<10^{-5} m^2/s], based on the results from Nikora & Goring (1998), typical for ADV measurements. Therefore, *E* evaluates the significance of noise in highly turbulent flows. Figure 3.8 depicts the energy noise ratio *E*, considering a noise energy level of 10^{-5} m^2/s is depicted for the RG experiments (RG1 to RG10), used to validate data in the present chapter. The ratio *E* decreases as the distance to the bed increases, thus as the length scale decreases. However, in all cases, the percentage of the ratio *E* remains under a 1%, as predicted by Garcia et al. (2005) that stated that the Doppler noise contribution to the total measured energy is lower than 10%.

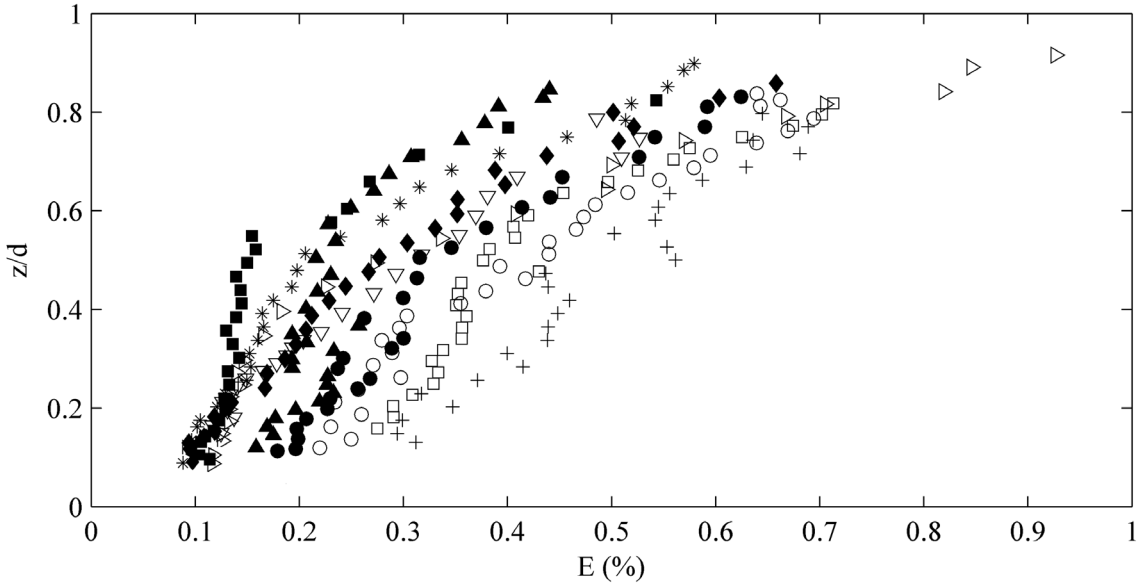

Figure 3.8- Vertical distribution of the *E* (Test RG1 to RG10). *Legend,* + *RG1,* ○ *RG2,* □ *RG3,* ● *RG4,* ▲ *RG5,* ▽ *RG6,* ∗ *RG7,* ♦ *RG8,* ■ *RG9,* ▷ *RG10.*

Further evaluation was done by calculating the Energy level from the power spectrum of the signal after the filtration with a high-pass filter, which permits evaluating the associated energy at the highest frequencies presents in the sample series. Figure 3.9 shows the noise energy levels obtained from three experiments (RG1, RG5, and RG11) in three different points of the profile (z=10 mm, z=20 mm, and z=40 mm) as a function of the cutoff frequency (f_c). The graphics show that the energy level decays when the f_c increases, showing a typical trend of a power spectrum diagram. The energy levels for each frequency do not show an increase or flat plateau for high frequencies, and therefore, the noise energy level has no significance in the data series. As predicted by Garcia et al. (2005) the levels of noise energy are not crucial in highly turbulent flows. Therefore, the spectral analysis method cannot be used to subtract noise from the computed turbulent parameters because the white noise plateau is not observed in the power spectrum.

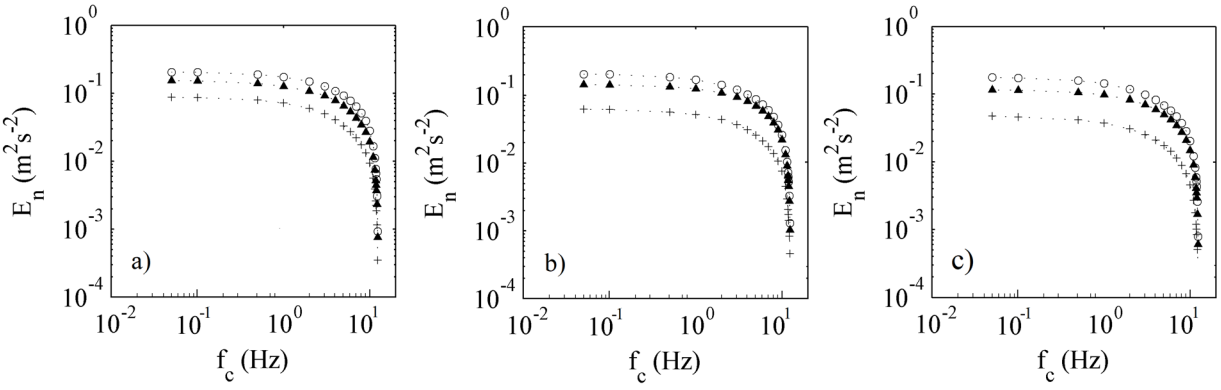

Figure 3.9- Accumulated energy of the signal as the f_c increases of the points (a) z=10 mm, (b) z=20 mm, (c) z=40 mm. *Legend: Test RG1 (+), Test RG5 (▲) and Test RG10 (○).*

3.3.3 Steadiness in the signal

The velocity signals obtained with ADV could present time scales much larger than the representative scales of turbulence caused by the existence of steadiness in the signal. The presence of this pseudoturbulence, as referred in the literature, Garcia et al. (2004), has low frequencies and are not random fluctuations. It has to be removed from the data before the calculation of the turbulent parameters since the turbulent energy, and the time and length scales in the flow could be overestimated.

In order to detect if there is a high energy level associated with a low frequency, it was used a low pass filter (Butterworth 6th order) to divide the signals obtained from the experiments to lower frequencies. As the sampling time was set at 5 min, enough to achieve stability of the running average of the most important turbulent parameters, the minimum frequency that can be performed is f=0.0033 Hz (1/300-s). The energy values are computed by integrating the power spectrum of the signals obtained after the application of low pass filter. The next figure shows a comparison between an original series (OS) (raw data) and the low-frequency signals obtained from the application of a low-pass filter.

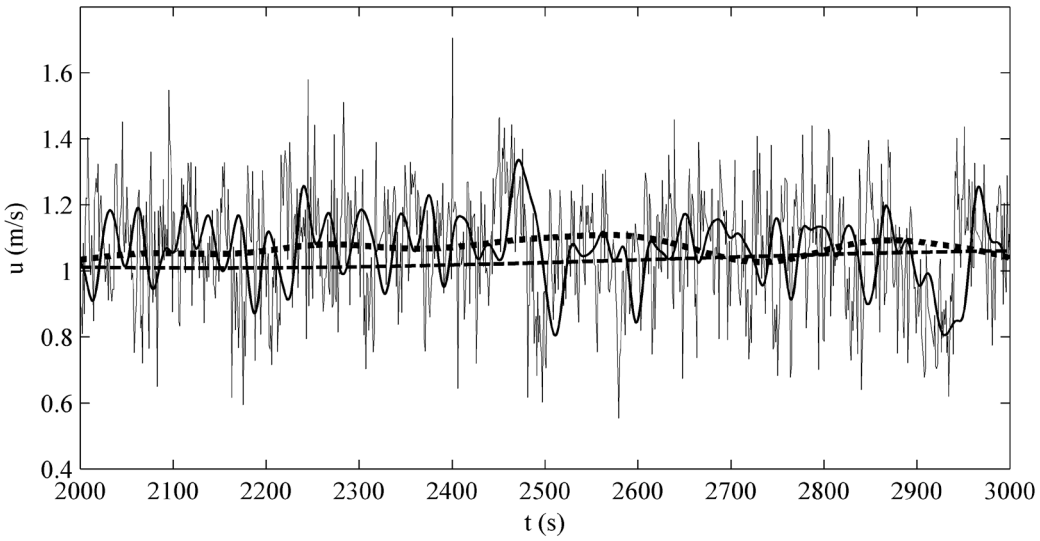

Figure 3.10- Velocity signals from the low-frequency component. *Legend, — OS, – – f_c= 0.02 Hz, ▪▪▪▪ f_c =0.1 Hz, —— f_c= 1 Hz.*

Figure 3.11 shows the energy levels obtained from three experiments (RG1, RG5, and RG11) in three different points of the profile (z=10 mm, z=20 mm, and z=40 mm) as a function of the f_c. The turbulent process has the same trend, do not show any different behavior for low frequencies, and there is no injection of energy at any low frequency. Moreover, the signal has energy values almost zero at frequencies under 0.02 Hz. Therefore, it is concluded that there is no steadiness behavior in the recorded signals.

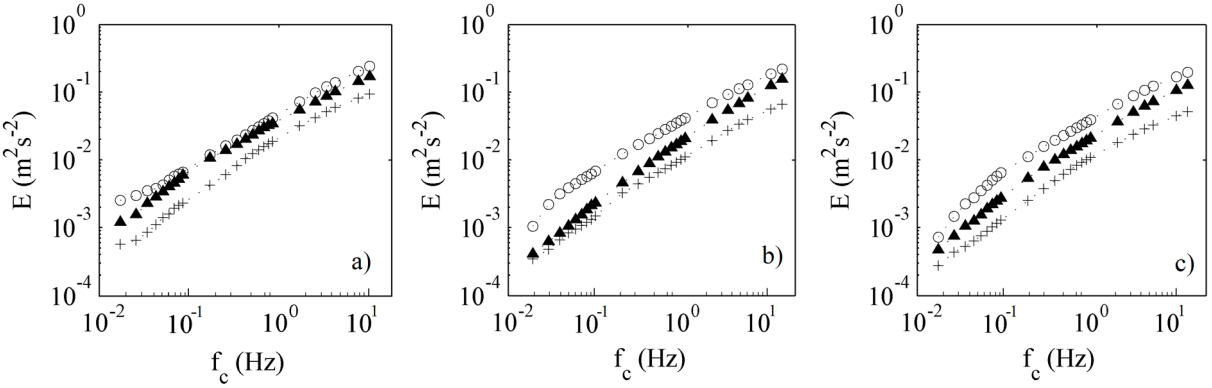

Figure 3.11- Accumulated energy of the signal as the f_c increases of the points, (a) z=5 mm, (b) z=20 mm, (c) z=40 mm. *Legend: Test RG1 (+), Test RG5 (▲) and Test RG10 (○).*

3.4 Filtering ADV measurements

Filtering the ADV data is necessary to remove the undesired spikes, i.e., low-quality measurements and the aliased points. Traditionally, in the conventional quadrant analysis, filtering methods based on a threshold condition are adopted, so that removes minor turbulence events from the signal. For instance, the most common technique is the threshold 'hole size' (H) (Lu & Willmarth 1973). This method establishes the imposition of a condition (set by the user), termed hole size, which permits excluding small-scale deviations from the mean in the analysis of turbulence structure. This method considers only bursting events from a particularly large instantaneous Reynolds Stresses ($-\rho u'w'$), excluding fluctuations that fail to exceed this. The hole size H is defined by $|u'w'|\geq H$ ($\sigma_u\sigma_w$) with σ_u

and σ_w the root-mean-square intensity of u' and w', respectively with typical values of H ranges from 0 to 8. However, the assumption of threshold value filter is considered here rather arbitrary; besides, it breaks down the time history of the signal velocity, making it no suitable for the present study.

3.4.1 Filtering methods

The filtering techniques considered in this work have been; i) the phase-space threshold filter "Despiking" of Goring & Nikora (2002) and ii) filter based on COR_{CR} and SNR_{CR}, Wahl (2000), henceforth referred to as COR-SNR filter.

3.4.1.1 The phase-space threshold filter

The phase-space threshold filter (Despiking) of Goring & Nikora (2002) is based on the fact that the high-frequency moments could be improved by the derivation of the signal. The method consists in plotting the fluctuating components of the velocity ($u' = u - \bar{u}$), its first (Eq. 3-1) and second (Eq. 3-2) time derivatives, ($\Delta u'/\Delta t$) and ($\Delta^2 u'/(\Delta t)^2$) respectively, in a 3D phase-space map, based on the Poincare maps. They estimate $\Delta u'$ and $\Delta^2 u'$ by central differencing as follow in order to avoid that the ellipsoids attains large aspect ratios.

$$\Delta u_i' = \Delta t \frac{du\prime}{dt} = \frac{u\prime_{i+1} - u\prime_{i-1}}{2} \tag{3-1}$$

$$\Delta^2 u' = (\Delta t)^2 \frac{d^2 u\prime}{dt^2} = \frac{\Delta u\prime_{i+1} - \Delta u\prime_{i-1}}{2} \tag{3-2}$$

The reliable data gather inside an ellipsoid in the phase-space, while the data outside this ellipsoid are considered as spikes. The ellipsoid is projected into *u'-Δu', u'-Δ²u'*, and *Δ u'-Δ²u'* planes and the boundaries are obtained using the expected absolute maximum of the time series u_m, Δu_m and $\Delta^2 u_m$. Assuming that the instantaneous velocity fluctuations in a turbulent flow follow a normal distribution they define the Eq. 3-3. Where *n* is the number of the data points and σ_u is the standard deviations of the velocity series. The axes of the thresholding ellipsoid decrease as the spikes are removed in every iteration. The iterative approach finishes when no spikes are detected in the sample.

$$u_m = \sigma_u \sqrt{2\, ln\, n} \tag{3-3}$$

Some authors have modified on several occasions the despiking filter of Goring & Nikora (2002). Wahl (2003) modified the method by means of a real ellipsoid instead of its projections and using robust statistics to avoid the need for iterations. Parsheh et al. (2010) applied preconditioned robust statistics to compute the ellipsoid. The method also requires iterations. Recently, Islam & Zhu (2013) developed an algorithm that used a bivariate kernel-density estimator to generate a density plot in the *u-Δu* and *w-Δw* space. The cutoff threshold is determined from the data and spike morphology.

The number of spikes detected by the different methods is similar. Besides this, the spikes are the same if the threshold cutoff of the phase-state map is similar. Therefore, it is not the aim of this work to evaluate the effectiveness of the despiking methods since all of them work similarly in the experiments and no aliasing or well-differentiated spikes appear in the signals.

The filter selected to detect the spikes has been the Goring & Nikora (2002) method since the spikes detected are more extreme than Wahl (2003) and Parsheh et al. (2010). As for the method of Islam

(2013), despite working very well with very contaminated series, the cutoff threshold (bandwidths) is somewhat arbitrary, and it requires the visual inspection of all the data series. Figure 3.12 show in the Phase state map an example of the ellipsoid of the despiking methods.

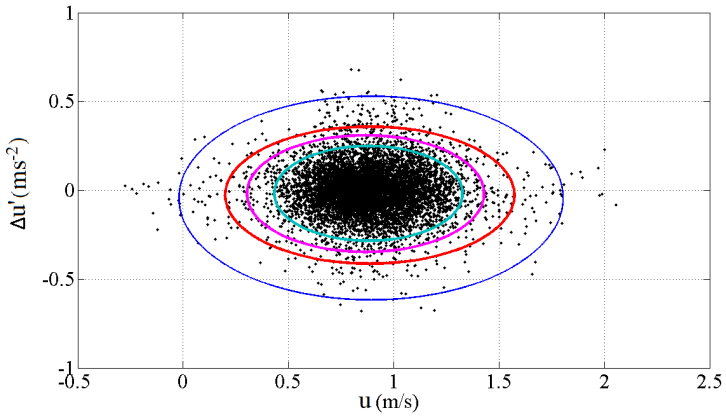

Figure 3.12- Phase-state-Map. Test RG3, point *z/d*=0.16. *Legend,* *Goring & Nikora 2002,* *Wahl 2003,* *Islam 2013 (hx=hy=0.05),* *Islam 2013 (hx=hy=0.02)*

3.4.1.2 COR-SNR filter

COR-SNR filter entails removing the measured points which COR or SNR values are below than some critical values set by the user. Generally, a minimum COR value of 70% and an SNR higher than 15-dB, for the three beams or directions, are indicative of a good turbulent representation of the flow, Wahl (2000).

However, these values can be somewhat subjective due to the value of the COR parameter being strongly affected by the high-frequency turbulent fluctuations, (Martin et al. 2002; Cea et al. 2007). Therefore, a COR value of less than 70 could be a consequence of sampling a highly turbulent flow and might not necessarily be indicative of low-quality point as will be explained below.

3.4.1.3 Replacement of Low-Quality Data

While the replacement of the spikes is not necessary for the computation of mean values and statistical moments of turbulence, it is indispensable for the computation of turbulent variables from the autocorrelation function. Moreover, the study of the time history of the velocity signal is one of the main targets of the present thesis; therefore, it is important to refill the gaps of the spikes to maintain the time interval between data.

The replacement method initially used was linear interpolation since Cea et al. (2007) stated that it might be a good option for highly turbulent flows, as long as the time integral scale is of the same order as the sampling time step.

3.4.2 Filtering Effects

Strom & Papanicolau (2007) stated that filtering methods based on COR and SNR alone are not sufficient to remove the spikes in the signal at the region near the bed (z<3 cm) due to aliasing; therefore, both filters, Despiking (Goring & Nikora 2002) and COR-SNR filter (Wahl 2000), should be applied together. On the other hand, for both groups of "bad" data, spikes and low-COR data Cea et al. (2007) recommended being replaced by linear interpolation.

However, it was observed that filtering ADV data with standard filter criteria (Wahl 2000) might yield highly reliable data, but removing significant data (>50%) above all in the near-bed region. For this reason, an exhaustive evaluation of the effects that filters have on the main turbulent characteristics was carried out. Appendix A is dedicated to analyzing the data quality and to describing the effects that the despiking filter and COR-SNR filters have on the turbulent characterization. The analysis has been carried out by comparing the turbulent parameters obtained from the series after filtering, by the described methods, with the original series (OS) (raw data), only for the test RG3 for simplicity.

The first part of the filter evaluation (Appendix A) is focused on the main turbulent parameters typically used to characterize the flow. However, Appendix A is a compilation of various analysis completed during the research. That is to say, in each step forward of the methodology developed in this thesis, the effects of the filters were recursively evaluated. As the methodology became more specific, more attention to data and to the effects of different agents involved was paid, with the aim of validating the suitability of the data to the methodology developed throughout the thesis. Because of that, a more profound evaluation of the effects of filtering on the quadrant analysis, i.e., "bursting turbulence" and pulse analysis developed in this thesis, has been assessed in the second part of the filter analysis. For the sake of simplicity, the analysis has been separated in appendix A.

The major findings of the analysis are described below. Generally, mean values such as velocity are not affected by the use of filters, however, the effects on turbulent properties are numerous. Reynolds Stresses, turbulent intensities, TKE, and energy dissipation rate, are intensely decreased by the use of filters. Thus, the high energy is erased and biased toward the mean value. Autocorrelation and therefore the Integral length scale, and both the Taylor and Kolmogorov scales are increased. It should be pointed out that in the appendix A only the evaluation of the changes produced by the data treatment is commented since the analysis of the characterization of the flow under different flow conditions it is examined in chapter 4. Moreover, quadrant analysis and pulse analysis, developed in chapter 5 and 6 respectively, are deeply affected by the application of filters. All filters produce changes of the time fraction occupied by each quadrant, these being more remarkable the COR_{CR} value increases. The Despiking filter changes less the values than the other filters, which makes sense due to the low amount of removed data.

3.4.3 Low-Quality Data Evaluation

After the evaluation of the filters and their effects on the turbulent parameters, it turned up one important question, which maybe should have appeared before. Are the "bad" data really wrong? The latter suggested a broader examination of the nature of the spikes and the low-COR values thru the most significant aspects studied throughout this thesis and it is included in Appendix B.

Moreover, the replacement of that bad data by linear interpolation has demonstrated to eliminate essential peak velocities introducing significant effects over the signal. Besides, the vast amount of removed data breaks the temporal continuity of the series and modifies the turbulent properties. For this reason, it was carried out an evaluation of how the replacement of the bad data affects the turbulent parameters and the history of the velocity data, also included in Appendix B.

From the evaluation of the detected as "bad" data by the filters, it turned out that spikes are not related to the low-COR values since the former have a well-sorted distribution of COR values. Therefore,

discarding data with a low correlation removes a significant amount of useful data while retaining a portion of spikes and does not eliminate the necessity of applying the Despiking filter, as stated by Strom & Papanicolau (2007).

Moreover, the low-COR values and spikes showed a more similar distribution of the longitudinal velocity increments (Δu) than those obtained from the different methods of replacement (evaluated for experiment RG3), which changed the pattern, increasing the density of the histogram in Δu~zero. All results show that the low-COR data has a normal behavior in comparison with "good" data and better follows the trend of the data series than after the replacement. The replacement of a large amount of low-COR data (>50%) can distort other results related to the history of the velocity signal breaking the natural trend of highly turbulent events and making them look like velocities with a high COR value, removing the series from its real nature. Consequently, the COR-SNR filter is not convenient in highly turbulent flows.

On the other hand, spikes have shown a particular behavior in comparison with good data and low-COR data in experiment RG3, however, spikes do not always show the aspect of aliasing data (as the case of experiment RG3), having characteristics referred to data that falls outside an arbitrary ellipse in the phase-state map.

Due to the arbitrary operation of filtering methods and the effects that they have on the results show that the filter should not be applied without prior study of suitability. It is noteworthy that, in some cases, any filtering method has to be considered if the configuration of the device it is not enough to avoid aliasing; there is an excess of turbulence introducing spurious spikes; there are boundary interferences with any of the sources of noises defined here. Hence, a prior visual inspection of the data series is recommendable before discarding the filter. In any case, the replacement method is always quite arbitrary and has to be evaluated to reproduce the correct behavior of the series.

In our experiments, aliasing has appeared in some points when the level of turbulence of the experiments in high, in particular in experiments from RG6 to RG10 and (CG4 to CG6), and may also appear in low levels of turbulence close to the water surface due to the disturbance produced by the ADV. Figure 3.13-a and Figure 3.13-b show an example of the aliasing produced, where the appearance of the biased data is the same as the spikes defined by Goring & Nikora (2002), Appendix B. In the figures it is also appreciated the different behaviours of velocities in the near-bed region, Figure 3.13-b, where fluctuations are very extreme and close to the water surface (Figure 3.13-a) where velocities remain more stable (without consideration of the spikes). The turbulent maps of these same points have been represented for the OS and after the filtering by despiking in Figure 3.14-a and Figure 3.14-b respectively, where it is clearly observed that aliasing occurs.

Thanks to the visual inspection point by point for each experiment, it has also been noticed a certain effect that is not detected by any of the filters. It is observed that in certain occasions when approaching the ADV close to the water surface, there is a large section (stretch) where the velocity variation of u and w is linear with a constant velocity increment (Δu and Δw), see Figure 3.15-a. It seems as if the device would interpolate the velocity between two velocities very separated in the time (> 0.48-s).

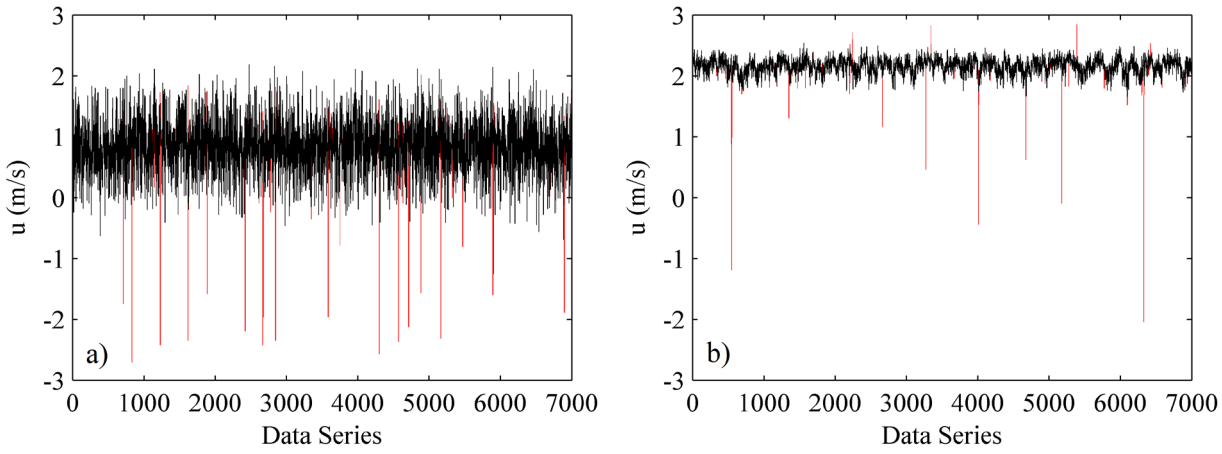

Figure 3.13- Velocity data series of the Original series (black) highlighting the spikes (red) of a point at height of (a) *z/d*=0.1 and (b) *z/d*=0.80. Experiment RG10.

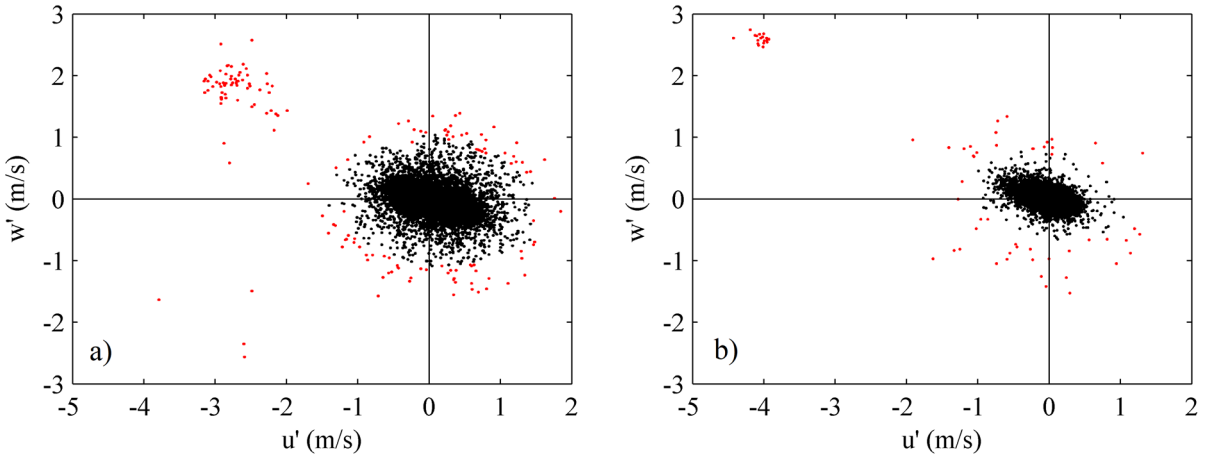

Figure 3.14- Turbulent map of the Original series (black) highlighting the spikes (red) of a point at height of (a) *z/d*=0.1 and (b) *z/d*=0.80. Experiment RG10.

This "interpolating" effect translates into a straight line of events on the turbulent map (Figure 3.15-b). However, none of the filters considered here, despiking (Figure 3.16-a) and SNR-COR (Figure 3.16-b) manage to detect these values as wrong. Although if they would be detected, an effective interpolation would not be possible since there are many velocities consecutive in time. This effect must be due to the disturbance of the water surface by the ADV.

Table 3.1 and Table 3.2 indicate the point heights of each of the experiments, RG and CG respectively, were the Despiking filter of Goring & Nikora (2002) it is necessary after the visual inspection of the velocity series in search of aliasing data (X). In the same tables, it has been also included points where the disturbance of the water surface made an "interpolating" effect on the velocity signals (I).

From the evaluation of the replacement methods, it has been concluded that although the application of the Despiking filter is not necessary for all experiments and points, it will be applied in all data series to avoid incongruities. In all cases, the data considered as spikes be replaced using interpolation by a third-order polynomial using two points at each side of the spike.

However, it has to be mentioned that the application of Despiking does not solve the "interpolating" effect in some of the points near the surface of the water. This highlights the necessity for a filtering method which takes into account not only the velocity increments (*Δu, Δw)* but also their distribution time-wise. That is to say, it has to be considered also how they occur in a sequence of events since same values of *Δu* and *Δw* are not expected to occur in a chain. Short streamwise velocity increments (*Δu*) fall in the center of their distribution, where there is more density (see Appendix B), for this reason, the history of occurrence of these *Δu* has to be also considered.

Finally, it is emphasized the fact that the results near the surface of the water, the last 2-3 measure points, do not obtain reliable results in the analysis carried out in the following chapters.

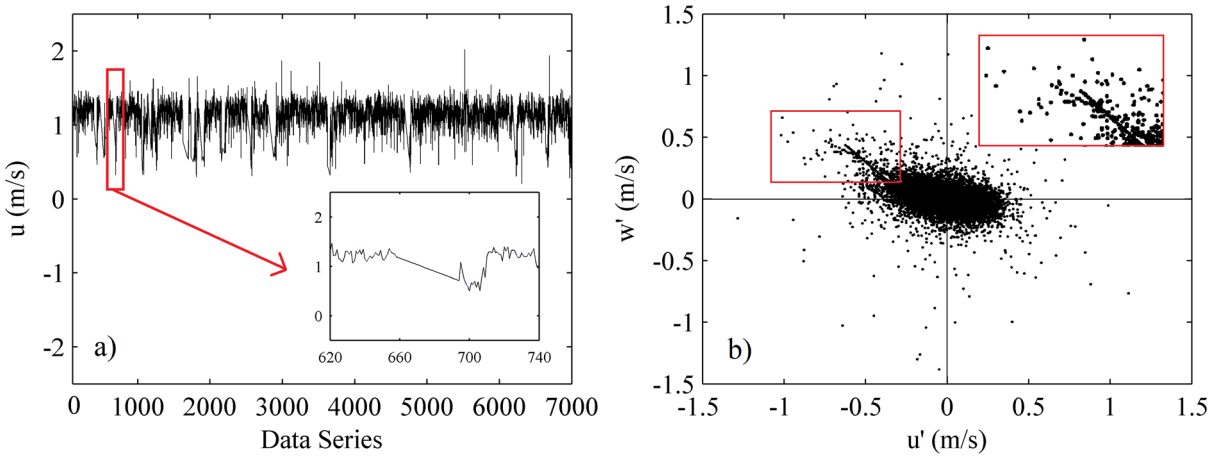

Figure 3.15- Representation of the Original velocity series of a point at height of *z/d*=0.78 from experiment RG1, (a) as a function of time steps (*Δt*) and (b) on the Turbulent map.

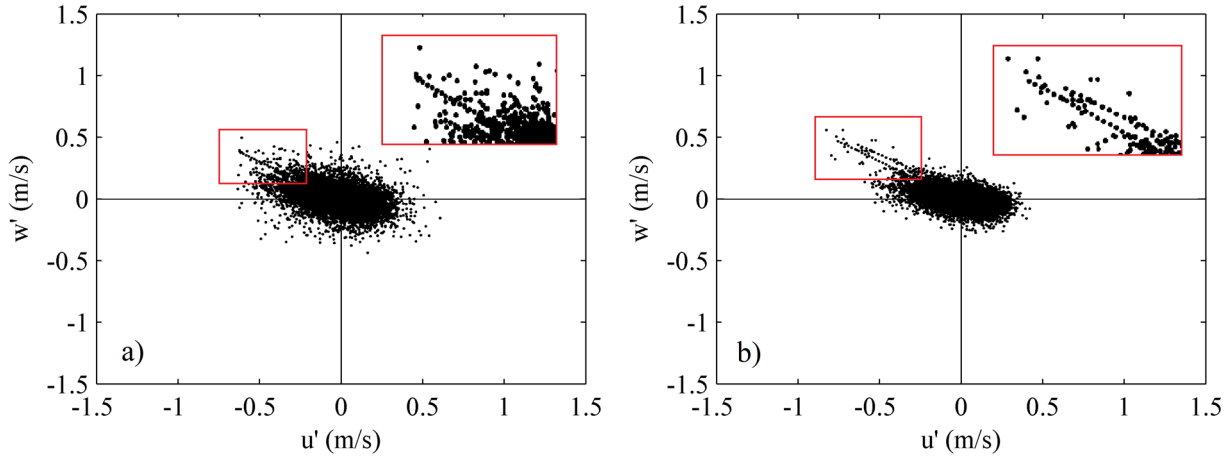

Figure 3.16- Velocity data series after (a) despiking and (b) COR-SNR filter with COR_{CR}=40, on the turbulent map. Experiment RG10, *z/d*=0.78.

Table 3.1- Points where the Despiking filter has been applied in the RG experiments

RG1		RG2		RG3		RG4		RG5		RG6		RG7		RG8		RG9		RG10	
z	*D*	*z*	*D*	*z*	*D*	*z*	*D*	*z*	*D*	*z*	*D*	*z*	*D*	*z*	*D*	*z*	*D*	*z*	*D*
0,011	-	0,011	-	0,012	-	0,0115	-	0,013	X	0,0135	X	0,014	X	0,014	X	0,016	X	0,017	X
0,013	-	0,013	-	0,014	-	0,0135	-	0,015	X	0,0155	X	0,016	X	0,016	X	0,018	X	0,019	X
0,015	-	0,015	-	0,016	-	0,0155	-	0,017	-	0,0175	X	0,018	X	0,018	X	0,02	X	0,021	X
0,017	-	0,017	-	0,018	-	0,0175	-	0,019	-	0,0195	X	0,02	X	0,02	X	0,022	X	0,023	X
0,019	-	0,019	-	0,02	-	0,0195	-	0,021	-	0,0215	X	0,022	X	0,022	X	0,024	X	0,025	X
0,021	-	0,021	-	0,022	-	0,0215	-	0,023	-	0,0235	X	0,024	X	0,024	X	0,026	X	0,027	X
0,023	-	0,023	-	0,024	-	0,0235	-	0,025	-	0,0255	X	0,026	X	0,026	X	0,028	X	0,029	X
0,025	-	0,025	-	0,026	-	0,0255	-	0,027	-	0,0275	-	0,03	X	0,028	X	0,03	X	0,031	X
0,027	-	0,027	-	0,028	-	0,0275	-	0,029	-	0,0295	-	0,034	X	0,03	X	0,032	X	0,036	X
0,029	-	0,029	-	0,03	-	0,0295	-	0,031	-	0,0315	-	0,038	-	0,034	X	0,036	X	0,041	X
0,031	-	0,031	-	0,032	-	0,0315	-	0,033	-	0,0335	-	0,042	-	0,04	X	0,04	X	0,046	X
0,033	-	0,033	-	0,034	-	0,0335	-	0,035	-	0,0355	-	0,046	-	0,046	-	0,045	X	0,051	X
0,035	-	0,035	-	0,036	-	0,035	-	0,037	-	0,0375	-	0,05	-	0,051	-	0,05	X	0,056	X
0,037	-	0,037	-	0,038	-	0,0375	-	0,039	-	0,0395	-	0,054	-	0,056	-	0,055	X	0,061	X
0,039	-	0,039	-	0,04	-	0,0395	-	0,041	-	0,0435	-	0,058	-	0,061	-	0,06	X	0,066	X
0,041	-	0,041	-	0,042	-	0,0415	-	0,045	-	0,0475	-	0,062	-	0,066	-	0,065	X	0,071	X
0,045	-	0,045	-	0,046	-	0,0495	-	0,053	-	0,0555	-	0,071	-	0,076	-	0,075	X	0,091	X
0,047	-	0,047	-	0,048	-	0,0515	-	0,057	-	0,0595	-	0,076	-	0,081	-	0,08	X	0,096	X
0,049	-	0,049	-	0,05	-	0,0555	-	0,061	-	0,0635	-	0,081	-	0,086	-	0,085	X	0,101	X
0,051	-	0,051	-	0,052	-	0,0595	-	0,065	-	0,0675	-	0,086	-	0,091	-	0,09	X	0,106	X
0,053	-	0,053	-	0,056	-	0,0615	-	0,069	-	0,0715	-	0,091	-	0,096	-	0,095	X	0,111	X
0,055	I	0,055	-	0,058	-	0,0655	-	0,073	-	0,0755	-	0,096	-	0,101	-	0,1	X	0,116	X
0,057	I	0,057	I	0,06	-	0,0695	-	0,077	-	0,0795	-	0,101	-	0,106	-	0,105	X	0,121	X
0,059	I	0,061	I	0,064	-	0,0735	-	0,081	-	0,0835	-	0,106	-	0,111	-	0,11	X	0,126	X
-		0,065	I	0,068	-	0,0755	-	0,085	X	0,0875	-	0,111	-	0,116	-	0,0105	X	0,131	X
-		0,067	I	0,072	I	0,0795	I	0,089	X	0,0915	-	0,116	-	0,121	-	0,12	X	0,136	X
-		-		-		0,0815	I	0,093	X	0,0955	-	0,121	-	0,126	-	0,125	X	0,141	X
-		-		-		-		0,095	I/X	0,0995	-	0,126	X	0,131	-	0,13	X	0,146	X
-		-		-		-		0,097	I/X	0,101	I	0,131	I	0,136	-	0,135	X	0,151	X
-		-		-		-		-		-		0,133	I	0,141	-	0,14	X	0,156	X
-		-		-		-		-		-		-		0,146	-	0,145	X	0,166	X
-		-		-		-		-		-		-		-		0,15	I	0,176	I
-		-		-		-		-		-		-		-		-	-	0,186	I

Table 3.2- Points where the Despiking filter has been applied in the CG experiments

CG1		CG2		CG3		CG4		CG5		CG6	
z	*D*	*z*	*D*	*z*	*D*	*z*	*D*	*z*	*D*	*z*	*D*
0,003	-	0,0035	-	0,003	X	0,002	X	0,002	-	0,002	X
0,005	-	0,0055	-	0,005	X	0,004	X	0,004	X	0,004	X
0,007	-	0,0075	-	0,007	X	0,006	-	0,006	-	0,006	X
0,009	-	0,0095	-	0,009	X	0,008	-	0,008	-	0,008	X
0,011	-	0,0115	-	0,011	X	0,01	-	0,01	-	0,01	-
0,013	-	0,0135	-	0,013	-	0,012	X	0,012	-	0,012	-
0,015	-	0,0155	-	0,015	-	0,014	X	0,014	X	0,014	X
0,017	-	0,0175	-	0,017	-	0,016	X	0,016	-	0,016	-
0,019	-	0,0195	-	0,019	-	0,018	X	0,018	-	0,018	-
0,021	-	0,0215	-	0,021	-	0,02	-	0,02	-	0,02	X
0,023	-	0,0235	-	0,023	-	0,022	-	0,022	-	0,022	-
0,027	-	0,0275	-	0,027	-	0,026	-	0,026	X	0,026	-
0,029	-	0,0295	-	0,031	-	0,03	-	0,028	-	0,028	-
0,033	-	0,0315	-	0,035	-	0,038	-	0,03	-	0,032	X
0,037	-	0,0355	-	0,041	-	0,044	-	0,034	-	0,036	-
0,041	-	0,0395	-	0,047	-	0,05	-	0,038	-	0,04	-
0,045	-	0,0435	-	0,053	-	0,056	-	0,042	X	0,044	-
0,049	-	0,0475	-	0,059	-	0,062	-	0,046	-	0,048	X
0,053	-	0,0515	-	0,065	-	0,068	-	0,05	-	0,052	X
0,057	-	0,0595	-	0,077	-	0,08	-	0,07	-	0,071	X
0,059	-	0,0635	-	0,085	-	0,088	-	0,08	-	0,082	-
0,061	-	0,0655	-	0,091	-	0,094	-	0,09	-	0,092	-
0,063	-	0,0675	I	0,095	-	0,1	-	0,1	-	0,102	-
0,065	I	0,0675	I	0,097	-	0,106	-	0,11	-	0,112	-
0,068	I	0,0705	I	0,099	I	0,112	I	0,12	-	0,122	-
-	-	-	-	0,101	I/X	0,118	I	0,13	-	0,132	-
-	-	-	-	0,103	I/X	0,124	I	0,14	X	0,142	-
-	-	-	-	0,106	I/X	-	-	0,15	X	0,152	-
-	-	-	-	-	-	-	-	0,16	X/I	0,162	X/I
-	-	-	-	-	-	-	-	-	-	0,172	I
-	-	-	-	-	-	-	-	-	-	0,181	I

3.5 ADV Configuration analysis

The configuration of the device plays an important role in data collection since one of the main sources of error normally encountered when analyzing ADV velocity time series is signal aliasing, as commented in section 3.2.3. These problems have been intensely studied by some users since ADV appeared (Garcia et al. 2005; Goring and Nikora 2002; Nikora and Goring 1998; Wahl 2000).

Although the configuration of the ADV is, in principle, able to correctly represent the turbulent phenomena from the main experiments (section 3.2.3), a study of how the configuration of the different parameters of the device affect the turbulent properties analyzed throughout this thesis was carried out. Therefore, this evaluation was motivated by the necessity of further understanding about the effects of the ADV configuration on the turbulent properties of the flow. However, the device used for the primary experiments, the experiments from "the Cube" channel (see chapter 2), was unable to change the configuration parameters. For this reason, some other experiments were carried out on the FRITZ channel (Lehigh University) using another ADV. The frequency of Data Collection (FDC), the size of the CV (h) and the velocity range, were the target parameters of the device configuration of this study.

As an explanatory note, in this section (as well as in Appendix C), reference is made to the experiments carried out in the FRITZ channel of the University of Lehigh as FRITZ experiments, while the experiments carried out in "the Cube" channel (RG and CG test) are called CUBE experiments.

The analysis of the configuration of the apparatus (Appendix C) was conducted after carrying out the main experiments (CUBE), once the analysis methodology of this thesis had been developed almost in its entirety, as discussed in the introductory chapter. This allowed the verification of how the configuration of the device affected the turbulent distributions of quadrants, pulses, pulse-sequences etc., however, in this section of the thesis these kind of results are not discussed here since the concepts have not been largely developed yet.

In appendix C there is an extensive comparison of the different results of the turbulent parameters (distributed along the depth profile) between the different data series (from the FRITZ channel), taken with different ADV configurations. Besides this, the configuration effects are analyzed also by means of the performance curves, which plot different turbulent properties against the FDC or the CV height (h) that represents each data series.

The performance curves of the experiments represent the value of the turbulent parameter as a function of the FDC or the CV height (h), for a particular point in the depth profile. The difference of these curves with the analysis of the experiments taken with different ADV configurations is that with the performance curves defined in Appendix C it is possible to analyze the effects of the configuration (FDC and CV size) by means of averaging window methods. Therefore, different series, representing a changed configuration can be obtained from an original data series. This allows the analysis of configuration effects without the need to take several series of data modifying the configuration of the device. Therefore, it is possible to analyze also the effects that the FDC and the CV have on the CUBE experiments (RG and CG tests). It should be mentioned that only configurations of less resolution could be reproduced in the case of the CUBE experiments.

The outcomes from the study (Appendix C) are very interesting and the results from it will be recalled througout the thesis, so readers will be advised to consult it. However, its consultation can be confusing

at this stage of the thesis, since as mentioned before, both the evaluation of the data quality and the filtering effects, as well as the analysis of the ADV configuration have been made during the development of the thesis. That is, each step forward in the methodology, the quality, and the configuration analysis have been applied recursively. That is why in this section only some of the most important conclusions are mentioned for the correct reading of the thesis, without advancing events.

While the COR and SNR parameters are not strongly affected by the configuration of the device, the attenuation of the peak velocity due to the decrease of the FDC or the increase of the CV height (h) reduces the intensity of some turbulent variables such as Reynold stresses, TKE or the dissipation rate. The length scales, on the other hand, are augmented. The variations are more pronounced the higher the level of turbulence analyzed in each scenario. Of all the conclusions presented in Appendix C (section C.10, Discussion), the ability of the device configuration to favor the representation of small or large flow structures, which are present in the flow, in the measured data series is highlighted.

For the specific flow conditions from the FRITZ experiments, the boundary layer starts in the bed and ends at a height around $z/d \approx 0.3$. In that region, called here near-bed, steep velocity gradients and small turbulence structures (Finelli et al. 1999) yields elevated turbulence intensities and a significant amount of spikes, above all when a small CV is set in the device. Then, it could be thought that a small h and a high FDC has to be used within the near-bed region and then increase the h progressively with the height in the depth profile, but this yields an experimental problem and uncertainty about how and where. On the other hand, the size of the coherent structures near the bed is strongly related to the size of the bed sediment. Therefore, the configuration of the device should be studied in the first instance for each scenario and level of turbulence, and determine whether the accuracy of big or small flow structures has to be prioritized. For example, in sediment transport of big stones, could be useful to detect big since Valyryakis et al. (2013) stated that full grain entrainment is due to flow structures as large as at least twice the grain size, and so removing high-frequency signals is necessary to bring out the most impactful coherent structures. Therefore, oversampling the flow velocity might compromise the analysis by introducing non-essential high-frequency velocity fluctuations.

Moreover, due to the Nyquist criteria, as commented in section 3.2.3 of the present chapter, the FDC has to be twice the frequency with the resolution wanted. Therefore, according to the assumption that Doppler noise appears in the signal around 10 Hz (Lohrmann 94), measuring at frequencies over 20 Hz the signal has a significant portion of Doppler noise, and the manufacturer no longer ensures errors less than 1%.

For all the mentioned reasons, the configuration of the CUBE experiments guarantees a low level of spikes and the representation of big structures in the velocity signal, which is considered optimal for the present thesis. However, it has to be taken into account how the turbulent parameters are affected by the ADV configuration.

Chapter 4: Turbulent Characterization of the Experiments

4.1 Introduction

Mountain Rivers flows are typically shallow, with a relative submergence (R/D_{50}) often being less than 10–20 in flood conditions and less than five during low-flow conditions (e.g. Bathurst 1985; Lee & Ferguson 2002). Besides, the bed of almost all Mountain rivers contains grains of sand, gravel, and boulders, which constitute the roughness surface (microtopography) and could have even more complicated bed configurations (dunes, pools etc.) defined as macro-roughness. In this chapter, only the effects that the first kind has on the turbulent flow characteristics have been assessed.

Numerous experimental studies have shed light on the structure of statistical description of turbulent characteristics in open channel flows (e.g. Nakagawa & Nezu 1977; Niño & Garcia 1996; Hurther & Lemmin 2000; Nikora & Goring 2000) and especially in the near-bed region (Raupach 1981; Antonia & Krogstad 2001; Jimenez 2004). Some of them have used ADV for experimental data collection (Hurther & Lemmin 2000; Nikora & Goring 2000), but much remains to be explored about its suitability to obtain time-averaged distributions of turbulence properties in highly turbulent flows. The comparison of the results yielded in this work and the aforementioned studies is difficult to discuss since the experimental conditions for the available data are not exactly the same, usually coming from less powerful flows.

This chapter presents the experimental results from the tests with the purpose of characterizing the average and turbulent properties of highly turbulent open-channel flow over rough beds using ADV. Effects of different flow rates, bed particles (roughness) and bed-packing density, on the main turbulent characteristics are also assessed.

4.1.1 Velocity distribution in fluvial channels

Velocity in rivers is not homogeneously distributed; it reaches its maximum at the water-surface and a value of zero at the boundary due to the flow-soil interaction. The boundary layer is the area where the fluid velocity distribution is disturbed by the presence of the surface in contact. The law of the wall theory was introduced by Prandtl (1926) and states that all friction losses occur in this layer and it establishes two hypothesis, first, the proportionality of the mixing length with the distance to the boundary, and second, constant shear stresses.

The law of the wall governs the boundary region; the region in which the characteristic scales of length and velocity are the shear velocity (u^*) kinematic viscosity (ν/u^*), which are used to define the inner variables. In the wall region ($z/d < 0.3$), the distribution of the mixing-length can be assumed to be linear (Raupach et al. 1991; Nezu & Nakagawa 1993). The turbulence characteristics of flow in the near-bed region are important in the analysis of transport phenomena. Accurate velocities in river flows are necessary in order to characterize the conditions of the incipient motion of bed particles and the evaluation of the bed-load transport rates and erosion depths. The main depth and velocity formulas in rivers have been verified under controlled conditions and rely on knowledge of local slope, which is difficult to measure accurately (Smart 1999).

4.1.1.1 Subdivision of flow into specific layers

Nikora et al. (2001) proposed that flow over a hydraulically rough bed is divided into four specific regions. The first is the outer layer (*i*), comprising the near-surface and intermediate regions, in the sense of Nezu & Nakagawa (1993), similar to the outer layer for smooth beds and its distribution may be described by the velocity defect law. The second is the logarithmic layer (*ii*) which is similar to the logarithmic layer for flows with hydraulically smooth beds, where the distribution of the streamwise velocity (*u)* in this layer follow the logarithmic formula. The third is the roughness-induced sublayer (*iii*), which occupies the region just above the roughness crests. In this sublayer appear form-induced stress due to flow separation from the roughness elements. As Raupach et al. (1991) states, the thickness of the roughness-induced sublayer may be up to five times the bed roughness height. If the bed surface is permeable, there is also an additional sublayer below the roughness layer, the interfacial sublayer (*iv*), which occupies the flow region between roughness crests and troughs. The flow in this layer occupies pores between granular particles and is driven by the gravity force and momentum fluxes from the above layers. The flow in the experiments has a low relative submergence (R/D_{50}), thus containing all the mentioned sublayers (Nikora 2001).

The sublayers (*iii*) and (*iv*) form the roughness layer where the flow may be influenced by individual roughness elements; typically is two to five times bed roughness height (Raupach et al. 1991). The flow region of roughness layer and logarithmic layer corresponds to the wall or inner layer in hydraulically smooth beds. Thus, the role of the roughness layer can be considered the same as the viscous and buffer sublayers for smooth beds. The interfacial sublayer corresponds to the viscous sublayer while the roughness-induced sublayer is analogous to the buffer sublayer. However, in gravel riverbeds, which are hydraulically rough, the thickness of a viscous sublayer is assumed to be insignificant. Above this roughness layer, i.e. layer (*i*) and (*ii*), the viscous effects and roughness-induced momentum fluxes are negligible.

4.1.1.2 Logarithmic Velocity profile

The relationship between the local mean velocity ($\bar{u}$) and the shear velocity (u^*) in a turbulent flow was developed by Ludwig Prandtl (1926) by considering the transfer of fluid momentum in a turbulent boundary layer can be approximated by the Eq. (4-1 (Prandtl/Karman's law of velocity distribution in the neighborhood of a solid wall). Where K is the Von Karman constant (0.4) and B is a function of the roughness Reynolds number (Re_ρ), Eq. (4-2. The variable k_s is the height of the relative (sand height) roughness defined by Nikuradse (1933) which consider effects of placement, packing density etc., in contrast to the roughness height (k) that does not.

$$(\bar{u}/u_*) = (1/K) \cdot ln(z/k_s) + B(u_* k_s/\nu) \tag{4-1}$$

$$Re_\rho = u^* \cdot k_s/\nu \tag{4-2}$$

Nikuradse studied the behavior of different sizes of sand in pipeline revetment and was extended by Keulegean (1938) for channels. Keulegan obtained that when the viscous sublayer is interrupted by the roughness ($\mathrm{Re}^* = u_* k_s/\nu > 100$, Nezu & Nakagawa 1993) the expression of the last term $B(u_* k_s/\nu)$ is 8.5. The Keulegean expression is only applicable above a near-bed roughness region in

which the time-averaged velocity is influenced by individual roughness elements and below an ‘‘outer’’ region in which the profile deviates from its logarithmic form and the wake function is necessary to apply. Song et al. (1994) found that the mean velocity profile could be expressed by the log-law in open channels even with a moving gravel bed.

The difficulty of the application of the Eq. (4-1 resides in obtaining k_s since the relative submergence (R/D_{50}) plays an important role. However, some authors claim that it is possible to express k_s based on the characteristic bed material, $k_s=\alpha \cdot D_{50}$. Therefore, α (texture factor) includes the effects of shape and packing of the particles and R/D_{50} and it is usually in the range of [2-5], being for gravel rivers around [3.5-5]. While Keulegean (1938) assumed a value of α=1, some other authors found from empirical works other values for α in gravel rivers (e.g., ***3.3*** Strickler 1923; ***8.5*** Limerinos 1970; ***6.8*** Bray 1982; ***5.9*** Millar 1999; ***7.1*** Lopez & Barragan 2003 among others).

For a smooth boundary and fully turbulent flow, the origin of the velocity profile (Z_0) is taken on the boundary. Nevertheless, it exists a potential problem in locating the theoretical wall level in a rough boundary. The latter gets more difficult when the bed becomes mobile and entrained in the flow. The position of the reference bed Z_0 it is unknown, however, it is considered located where the local mean velocity of the flow ($\bar{u}$) is zero see Figure 4.1.

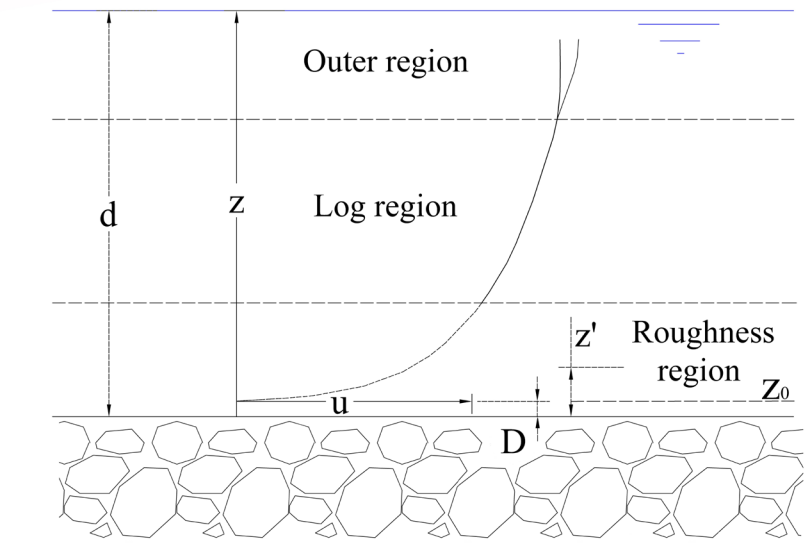

Figure 4.1- Schematic illustration of Velocity profile into bed.

There is no standard definition for finding the location of the velocity origin. However, it is common to set the origin of the experimental profile (Z), where the data measurements start, and shift a distance (D) below Z, after the first logarithmic approximation profile, to find the theoretical origin of velocities ($D=Z_0$). This distance D is related to the relative roughness (k_s). Keulegan (1938) developed the logarithmic velocity profile for hydraulically rough flows under the assumption that for $d>>k_s$ the height of the relative is $k_s=33Z_0$, then $D=Z_0=0.03\ k_s$. However other authors describe the range of D/k_s is between 0.10-0.3 depending on the different studies; for instance, Einstein & El-Samni (1949) found that $D = 0.2k_s$, Grass (1971) found that $D= 0.18k_s$ and Nakagawa *et al*. (1975) reported that $D = 0.25k_s$.

4.1.2 Flow resistance coefficient

The difficult prediction of the flow resistance coefficients has implications in hydraulic engineering since it is commonly used to predict level floods based. The flow resistance coefficient evaluates the forces exerted by the boundaries and other elements in contact with the flow that compensate for the gravity action (driving force) by producing energy losses. Shape resistance refers to irregularities in the surface such as grain diameter and shape, channel shape, obstructions and sediment transport, Roberson & Crowe (1993).

Because of the "law of the wall" the bed shear stress, produce energy losses by viscous dissipation known as skin friction, Tritton (1988). This friction coefficient (C_f), Eq. (4-5, is obtained from the ratio between the bed shear stress (τ_0), Eq. (4-3, and momentum of the flow, thus, from the squared-division of the shear velocity (u^*), Eq. (4-4, and mean flow velocity (U), which can be obtained from the integration of the Keulegan expression.

$$\tau_0 = \gamma \cdot R \cdot S_f \tag{4-3}$$

$$u^* = \sqrt{\tau_0/\rho} \tag{4-4}$$

$$C_f = (\tau_0/\rho \cdot U^2) = (u^*/U)^2 \tag{4-5}$$

All these forms of energy dissipation can be summarized within a single coefficient of energy loss. Some of the most commonly used in rivers are the flow resistance coefficient of Manning (n), Darcy-Weisbach (f), Chezy (C), and the dimensionless Chezy coefficient (C*), being the Manning coefficient (n) the most used in river characterization. All the coefficients are related to n as shown in Eq. (4-6.

Keulegan (1938) developed flow resistance equations for hydraulically rough channels, based on the integration of Prandtl 'law of the wall' over a channel cross-section to derive an expression for the average velocity for the section. In this manner, he obtained an expression for flow resistance coefficient (C*), Eq. (4-7.

$$n = (1/C)R^{1/6} = \sqrt{C_f/g}\, R^{1/6} = \sqrt{f/(8 \cdot g)} \cdot R^{\frac{1}{6}} = (1/C^*\sqrt{g}) \cdot R^{\frac{1}{6}} = (u^*/U\sqrt{g})R^{\frac{1}{6}} \tag{4-6}$$

$$C^* = U/u_* = 1/K\ ln(11d/k_S) \tag{4-7}$$

4.2 Velocity profiles adjustment

With the appropriate shift (D) of the experimental velocity profile origin (Z), where the ADV measurements start (control volume location), the theoretical origin (Z_0) is obtained, and the flow can be described by a logarithmic profile (Figure 4.1). The distance of the ADV control volume to the bed (z') was indicated in chapter 2 for each experiment.

The adjustment using the logarithmic description of Eq. (4-2 with $B(u_*k_s/\nu) = 8{,}5$ represents hydraulically rough flows. The involved variables are $\bar{u}$, u^*, k_s and ν. However, only the u^*, k_s can be adjusted by the log-profile, while $\bar{u}$ is the mean location velocity obtained from the measurements and ν is the Kinematic viscosity of water ($1 \cdot 10^{-6}$ m^2/s).

In the first place, the value of k_s was considered constant for experiments with the same bed diameter (all RG experiments, CG1 and CG2, CG3 and CG4, CG5 and CG6), since as seen in section 4.1.1.2 $k_s=\alpha \cdot D_{50}$. That is, the roughness layer and the flow resistance coefficient depends on the mean grain diameter and the shape and packing of the particles (α). The measured velocity profiles from all experiments and the fitted log-velocity profiles under this assumption, for the RG and CG experiments, are shown in Figure 4.2 and Figure 4.3 respectively.

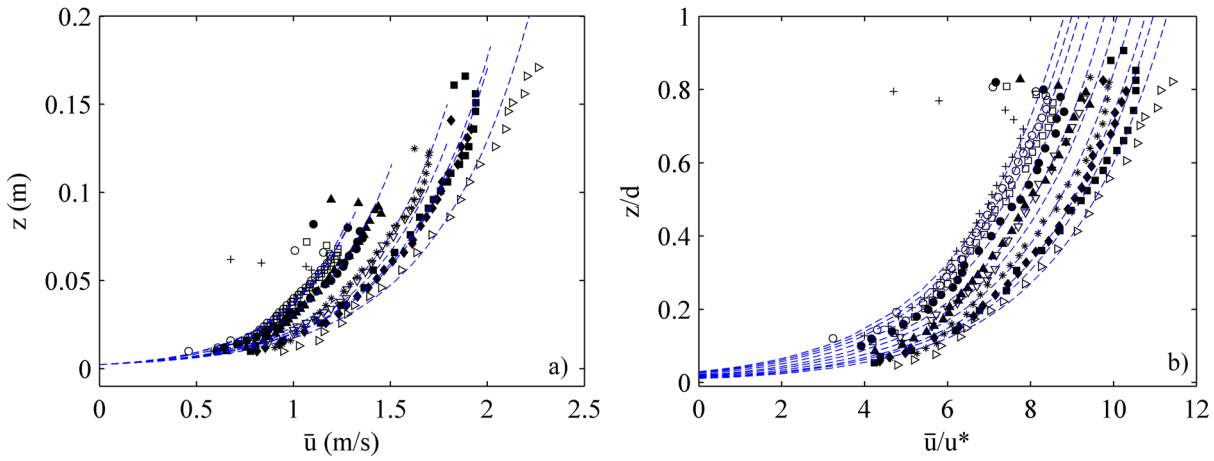

Figure 4.2- Mean vel-profiles and log-profile (with constant k_s) of the RG experiments. *Legend, + RG1, ○ RG2, □ RG3, ● RG4, ▲ RG5, ▽ RG6, ∗ RG7, ♦ RG8, ■ RG9, ▷ RG10 and, - - - log-fitted velocity (blue).*

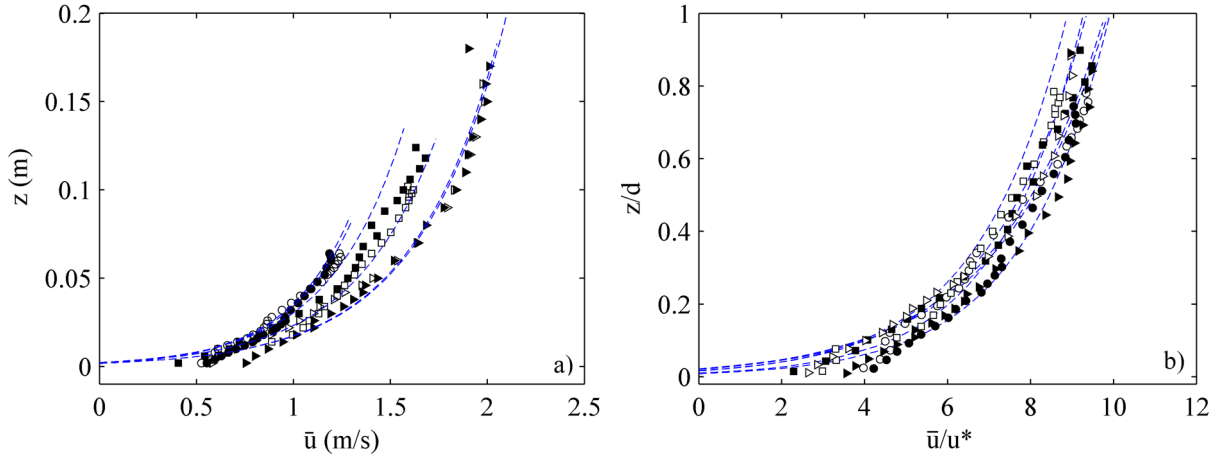

Figure 4.3- Mean vel- profiles and log-profile (with constant k_s) of the CG experiments. *Legend, ○ CG1, ● CG2, □ CG3, ■ CG4, ▷ CG5, ► CG6 and, - - - log-fitted velocity (blue).*

The velocities fit well to the logarithmic profile between the range [0.15-0.7]-*z/d*. However, as the flow rate is increased from RG1 to RG10, the velocities differ a little in the area close to the water surface in comparison with the log-profile, due to the defect-law. Inside the roughness layer, the mean velocity profile has a linear behavior, which is in concordance with Nikora et al. (2004), with a softer decrease in velocity than the logarithmic description. Thus, the logarithmic zone is reduced below inasmuch as the rough layer increases in size.

It has to be mentioned that in the RG experiments (Figure 4.2) it was not possible to approach more the control volume to the crest heights, as explained in chapter 2, and so the near-bed description is incomplete.

Regarding the CG experiments, Figure 4.3, the region of z/d<0.15 do not fit well with the logarithmic profile, showing a linear decrease behavior (Nikora et al. 2004). The effect is more notable than in the RG experiments, partly because in this type the experiments the measurements are taken closer to the bed. The effects of flattening the bed surface (from CG1 to CG2, CG3 to CG4 and CG5 to CG6), are imperceptible along the entire profile for the cases CG1 and CG2 (small bed diameter and low depth). However, as the flow rate and the bed diameter increase, the fact of compacting the bed shows some differences in the near-bed region, increasing the streamwise velocity in comparison to the loose bed (loose packing density). This effect is accentuated in the tests CG5 and CG6, loose and densely packed respectively, where both log-velocity profiles are very similar, but in the zone z/d<0.15 the velocity on the compacted surface (CG6) has greater value.

A second adjustment was made; in this case, considering k_s unique for each experiment instead, i.e. the value can change from one experiment to another even with the same bed diameter, in order to assess how the value of k_s can be related to the relative submergence.

All the RG experiments have the same mean bed-diameter (D_{50}) and the same bed slope, and only the flow rate was increased in each test, hence also R/D_{50}. The adjustment of these experiments, each with its respective k_s, will allow seeing the effects that the R/D_{50} has on the k_s. In the case of the CG experiments, can also be adjusted and compared with the results obtained by a constant k_s. Moreover, the effects of packing the bed surface on u^* and k_s can be investigated since CG experiments with the same diameter have also a similar R/D_{50}. It has to be taken into account that the range of experiments with the same diameter is smaller (only two). Below, the measured velocity profiles from all experiments and the fitted log-velocity profile, with a changeable value of k_s for the RG and CG experiments, are shown in Figure 4.4 and Figure 4.5 respectively.

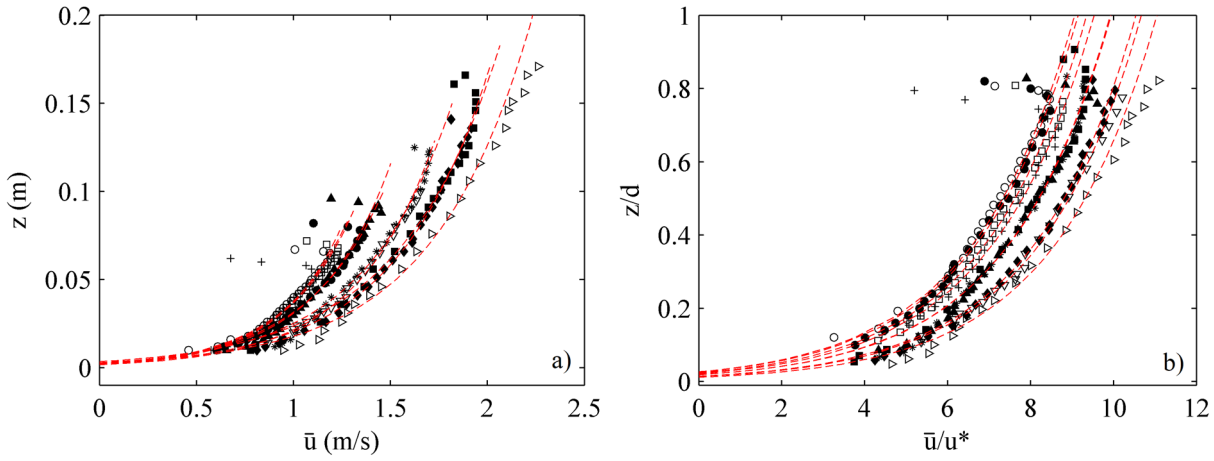

Figure 4.4- Mean vel-profiles and log-profile (with variable k_s) of the RG experiments. *Legend, + RG1, ○ RG2, □ RG3, ● RG4, ▲ RG5, ▽ RG6, ∗ RG7, ♦ RG8, ■ RG9, ▷ RG10 and, - - - log-fitted velocity (blue).*

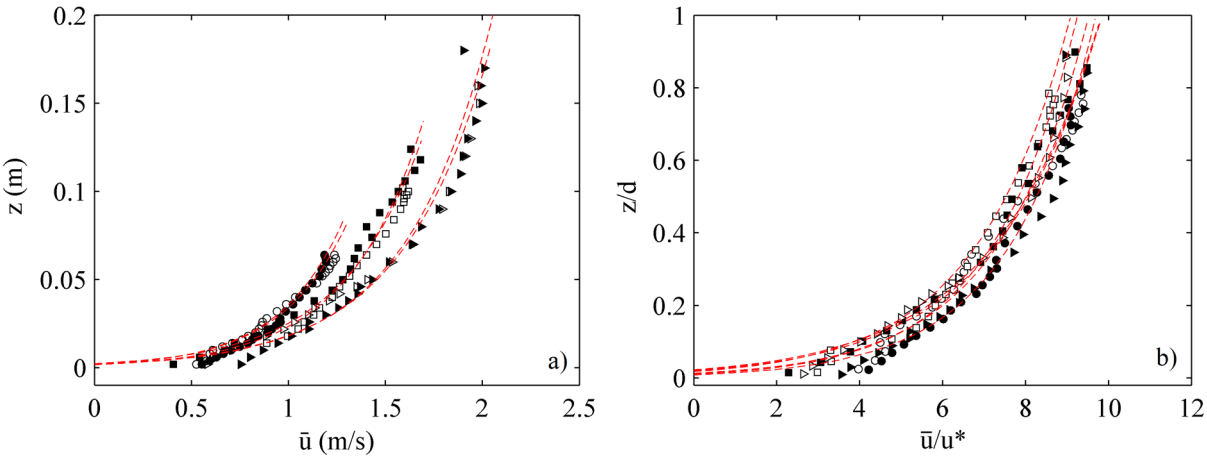

Figure 4.5- Mean vel- profiles and log-profile (with variable k_s) of the CG experiments. *Legend,* ○ *CG1,* ● *CG2,* □ *CG3,* ■ *CG4,* ▷ *CG5,* ▶ *CG6 and, - - - log-fitted velocity (blue).*

In principle, no large differences are observed between the adjustments made with a variable or constant value of the k_s, observing the same characteristics since a variation of k_s is counteracted by u^*. The different values of these two variables are discussed in more detail below.

Table 4.1 shows the main measured hydraulic characteristics from all the experiments. The depth-averaged velocity (U) is obtained by integrating the experimental velocity profile over the flow depth, and the depth (d) is measured using the piezometers installed upward and backwards the experimental zone, thus the experimental energy slope (S_f) may be determined.

Table 4.1- Hydraulic characteristics of the experiments.

Nº TEST	**Flow R.**	**D_{50}**	**Bed**	***s***	***d***	***R***	***U***	***S_f* m/m**	***R/D_{50}***	***Fr***	***Re***
	l/s	**m**	**Lev.**	**m/m**	**m**	**m**	**m/s**				
RG1	42,75	0,055	D	0,03	0,078	0,07	0,959	0,038	1,4	1,1	2,69E+05
RG2	48,79	0,055	D	0,03	0,083	0,074	1,006	0,037	1,47	1,11	2,98E+05
RG3	54,68	0,055	D	0,03	0,089	0,078	1,051	0,037	1,56	1,12	3,28E+05
RG4	73,24	0,055	D	0,03	0,1	0,086	1,139	0,037	1,73	1,15	3,92E+05
RG5	97,49	0,055	D	0,03	0,116	0,098	1,202	0,038	1,96	1,13	4,71E+05
RG6	120,01	0,055	D	0,03	0,129	0,107	1,419	0,036	2,14	1,26	6,07E+05
RG7	162,92	0,055	D	0,03	0,15	0,121	1,434	0,036	2,42	1,18	6,94E+05
RG8	204,41	0,055	D	0,03	0,171	0,135	1,582	0,037	2,7	1,22	8,54E+05
RG9	238,46	0,055	D	0,03	0,183	0,142	1,603	0,038	2,85	1,2	9,11E+05
RG10	307,65	0,055	D	0,03	0,208	0,158	1,784	0,039	3,16	1,25	1,13E+06
CG1	61,6	0,0177	D	0,031	0,082	0,073	0,929	0,027	4,12	1,04	2,71E+05
CG2	65,24	0,0177	P	0,029	0,086	0,076	0,976	0,025	4,29	1,06	2,97E+05
CG3	137,4	0,0292	D	0,031	0,13	0,102	1,262	0,03	3,49	1,08	5,15E+05
CG4	157,84	0,0292	P	0,03	0,138	0,108	1,268	0,031	3,69	1,12	5,48E+05
CG5	231,41	0,052	D	0,03	0,181	0,141	1,566	0,03	2,72	1,18	8,83E+05
CG6	260,38	0,052	P	0,03	0,202	0,154	1,641	0,029	2,97	1,17	1,01E+06

The typical coefficients of flow resistance in rivers n and C^* (see section 4.1.2) are calculated from the hydraulic values of Table 4.1. The Manning coefficient (n) is defined by Eq. (4-8 (Manning equation), by means of the experimental hydraulic characteristics. Besides, the Manning coefficient (n) can be obtained as well from the log-velocity profile with the C^* (obtained by Eq. (4-7 for each fitted profile) by using Eq. (4-9.

$$n = ({S_f}^{1/2} R^{4/2})/U \tag{4-8}$$

$$n = (1/C^* \sqrt{g}) \cdot R^{1/6} \tag{4-9}$$

Table 4.2 shows the parameters that involve flow resistance obtained from the hydraulic measures (Table 4.1). The bed shear stresses were calculated from Eq. (4-3, the shear stress velocity (u^*) is obtained by Eq. (4-4, the C^* by Eq. (4-7, and finally n from Eq. (4-9.

Table 4.2- Hydraulic characteristics of the experiments.

Nº TEST	Hydraulic variables						
	Flow R. l/s	τ_0 N/m²	S_f m/m	U m/s	u^* m/s	**Chezy** C^*	**Manning** n
RG1	42,75	26,07	0,038	0,959	0,161	5,940	0,035
RG2	48,79	26,83	0,037	1,006	0,164	6,141	0,034
RG3	54,68	28,28	0,037	1,051	0,168	6,249	0,033
RG4	73,24	31,18	0,037	1,139	0,177	6,450	0,033
RG5	97,49	36,50	0,038	1,202	0,191	6,292	0,034
RG6	120,01	37,75	0,036	1,419	0,194	7,303	0,030
RG7	162,92	42,69	0,036	1,434	0,207	6,941	0,032
RG8	204,41	48,95	0,037	1,582	0,221	7,150	0,032
RG9	238,46	52,88	0,038	1,603	0,230	6,971	0,033
RG10	307,65	60,39	0,039	1,784	0,246	7,260	0,032
CG1	61,6	19,32	0,027	0,929	0,139	6,683	0,031
CG2	65,24	18,62	0,025	0,976	0,136	7,176	0,029
CG3	137,4	29,99	0,03	1,262	0,173	7,295	0,028
CG4	157,84	32,81	0,031	1,268	0,181	7,006	0,030
CG5	231,41	41,45	0,03	1,566	0,204	7,676	0,030
CG6	260,38	43,77	0,029	1,641	0,209	7,852	0,030

From the calculated log-velocity profiles are obtained the variables related with the friction losses in the roughness layer (u^*, C^*, k_s and α), and the displacement of the velocity profile origin (D). Those variables include any effect of the bed roughness, being a composite parameters resulting from the logarithmic distributions found to describe a portion of bed-gravel velocity profiles. The variables obtained from the two considered log-profile adjustments, on the one hand, considering k_s as a constant (method A) value for the same bed-particle sizes, and on the other, considering k_s dependent on the relative submergence of the flow (method B), are presented in Table 4.3 and Table 4.4 respectively.

Table 4.3-Results from the logarithmic adjustment with k_s as a constant value (method A)

	Logarithmic adjustment (k_s as a constant for experiments with the same D_{50})								
Nº TEST	***R***	***U***	***u****	**Chezy**	**Manning**	***k_s***	***α***	***D***	***Sf***
	(m)	**m/s**	**m/s**	***C****	***n***	**(m)**		***m***	***(m/m)***
RG1	0,07	1,065	0,169	6,304	0,033	0,105	1,91	0,0020	0,042
RG2	0,074	1,082	0,17	6,365	0,033	0,105	1,91	0,0020	0,040
RG3	0,078	1,111	0,168	6,612	0,032	0,105	1,91	0,0020	0,037
RG4	0,086	1,205	0,181	6,658	0,032	0,105	1,91	0,0020	0,039
RG5	0,098	1,237	0,185	7,070	0,031	0,105	1,91	0,0020	0,032
RG6	0,107	1,536	0,204	7,530	0,029	0,105	1,91	0,0020	0,040
RG7	0,121	1,468	0,193	7,608	0,030	0,105	1,91	0,0020	0,031
RG8	0,135	1,545	0,207	7,461	0,031	0,105	1,91	0,0020	0,032
RG9	0,142	1,657	0,192	8,631	0,027	0,105	1,91	0,0020	0,026
RG10	0,158	1,827	0,218	8,382	0,028	0,105	1,91	0,0020	0,031
CG1	0,073	1,001	0,132	7,556	0,0271	0,054	3,05	0,002	0,0245
CG2	0,076	1,039	0,131	7,916	0,026	0,054	3,05	0,002	0,0231
CG3	0,102	1,317	0,186	7,088	0,0268	0,067	2,29	0,0025	0,0345
CG4	0,108	1,286	0,177	7,254	0,0285	0,067	2,29	0,0025	0,0297
CG5	0,141	1,587	0,200	7,937	0,0288	0,091	1,75	0,002	0,0289
CG6	0,154	1,662	0,220	7,556	0,0296	0,091	1,75	0,002	0,0320

Table 4.4-Results from the logarithmic adjustment with k_s as a variable value (method B)

	Logarithmic adjustment (Ks as a variable value)								
Nº TEST	***R***	***U***	***u****	**Chezy**	**Manning**	***k_s***	***α***	***D***	***Sf***
	(m)	**m/s**	**m/s**	***C****	***n***	**(m)**		***m***	***(m/m)***
RG1	0,07	1,003	0,155	6,471	0,032	0,072	1,31	0,0020	0,035
RG2	0,074	1,086	0,159	6,831	0,030	0,074	1,35	0,0025	0,035
RG3	0,078	1,110	0,165	6,726	0,031	0,085	1,55	0,0025	0,036
RG4	0,086	1,189	0,17	6,993	0,030	0,075	1,36	0,0030	0,034
RG5	0,098	1,210	0,188	6,435	0,034	0,102	1,85	0,0025	0,037
RG6	0,107	1,430	0,193	7,408	0,030	0,089	1,62	0,0020	0,035
RG7	0,121	1,469	0,198	7,419	0,030	0,114	2,07	0,0030	0,033
RG8	0,135	1,545	0,227	6,806	0,034	0,137	2,49	0,0030	0,039
RG9	0,142	1,654	0,214	7,728	0,030	0,143	2,60	0,0035	0,033
RG10	0,158	1,835	0,243	7,552	0,031	0,148	2,69	0,0025	0,038
CG1	0,073	1,004	0,137	7,346	0,028	0,055	3,11	0,002	0,0261
CG2	0,076	1,067	0,147	7,260	0,029	0,053	2,99	0,0015	0,0290
CG3	0,102	1,357	0,165	8,244	0,026	0,07	2,40	0,003	0,0271
CG4	0,108	1,312	0,173	7,583	0,029	0,063	2,16	0,004	0,0282
CG5	0,141	1,598	0,210	7,611	0,030	0,098	1,88	0,005	0,0319
CG6	0,154	1,695	0,215	7,886	0,030	0,084	1,62	0,003	0,0306

The results from the analyses show that both adjustments obtain similar fitted shear velocities (u^*) in comparison with the obtained through hydraulic variables, Figure 4.6, where it can be seen a good correlation between the three u^*. However, u^* from the adjustment with k_s considered as a variable (red) show closer values to the ones from hydraulic measurements (black), while the adjustment with k_s as a constant (blue) seem to overestimate u^* for low $<<R/D_{50}$ and underestimate for $>>R/D_{50}$.

From the above tables, it can be seen that method A (constant k_s) obtains a value of k_s =0.105 m for all experiments, while the k_s obtained by method B (variable k_s) the value of k_s increases with R. In this way, to adjust to the mean local velocities ($\bar{u}$), when the profile is adjusted to a lower k_s (than the obtained from method A), it is also obtained a lower u^* is (than that of method A), they counteract each other to adjust the profile.

The effects produced by the packing of the surface (CG experiments) on u^* are not very visible, although in general higher values are observed (between 2-6%) after the packing of the bed surface. However, it should be noted that velocities in the near-bed region did not adjust very well.

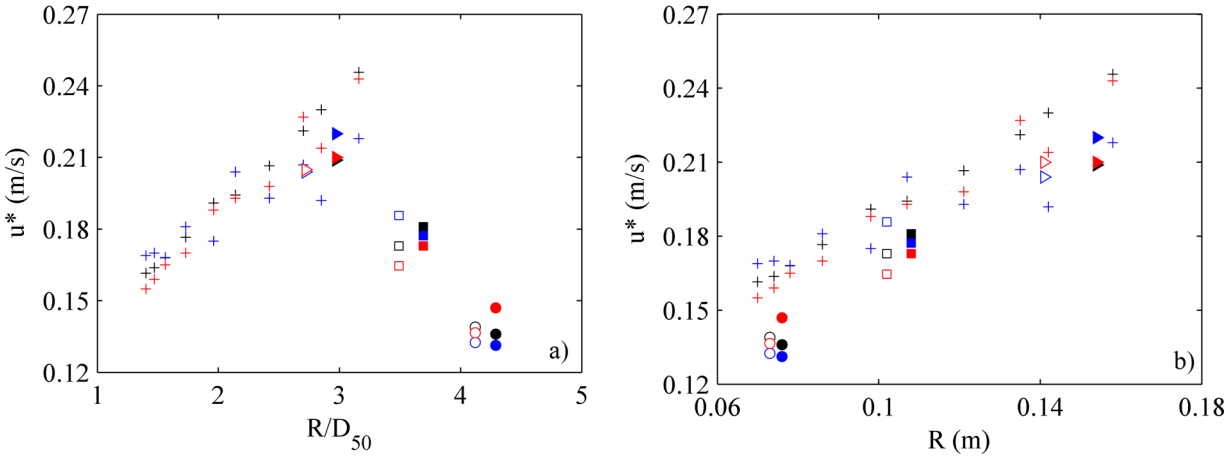

Figure 4.6- Shear velocity u* of all experiments as a function of (a) Relative submergence (R/D_{50}) and (b) hydraulic Radius (R). *Legend Markers, + RG experiments, ○ CG1, ● CG2, □ CG3, ■ CG4, ▷ CG5, ▶ and CG6. Legend colors, ● from hydraulic variables and from fitted log-profile, ● method A, ● method B.*

The value of k_s is determined by α and D_{50}, and the results show that for high values of relative submergence the value of α is between a range of [1.5-3] agreeing with values used by different authors (Strickler). The value of α is 2.1 for the RG experiments by method A, Table 4.3, significantly lower than the observed by several authors (e.g., *3.3* Strickler 1923; *8.5* Limerinos 1970; *6.8* Bray 1982; *5.9* Millar 1999; and *7.1* Lopez & Barragan 2003 among others). On the other hand, the value of α varies from 1.31 to 2.69 if k_s is considered to change with the relative submergence (Method B) despite having the same bed diameter, Table 4.4.

Figure 4.7 graphically represents the evolution of the relative roughness height (k_s) in terms of the shear velocity (u^*) (Figure 4.7-a) and relative submergence (R/D_{50}) (Figure 4.7-b). For the RG experiments (+), the k_s show a trend of proportionality and good correlation with both variables u^* and R/D_{50}. Evidently, under the assumption that k_s is defined as a function of the D_{50} (Method A), the same value is found in all RG experiment, thus a horizontal trend is shown in both figures.

Chamberlain (1983) showed that atmospheric k_s is proportional to $u^{*2}/2g$, with sand and snow forming the boundary roughness. In the experiments, this assumption is verified since it appears that the experiments follow the relationship $50u^{*2}/2g$ represented as a dashed line in Figure 4.7-a. As the experiments were always under uniform flow conditions, u^* is equivalent to the boundary shear velocity which implies that k_s varies also proportionally with the bed shear stress (τ_0).

In the case of the CG experiments, the value of k_s increases proportionally to the mentioned $50u^{*2}/2g$. However, it shows a trend of decrease as the R/D_{50} increases. It has to be taken into account that the experiments have not the same D_{50}. Moreover, two different scenarios could have same R/D_{50} but different u^* since the latter also implies the energy slope S_f. The k_s seem to be more related to the turbulence levels in the near-bed region than only to the R/D_{50}. Regarding the packing of the bed, the obtained k_s (and α) for well-packed beds (CG2, CG4, and CG6) are slightly lower than for loose beds (CG1, CG3, and CG5).

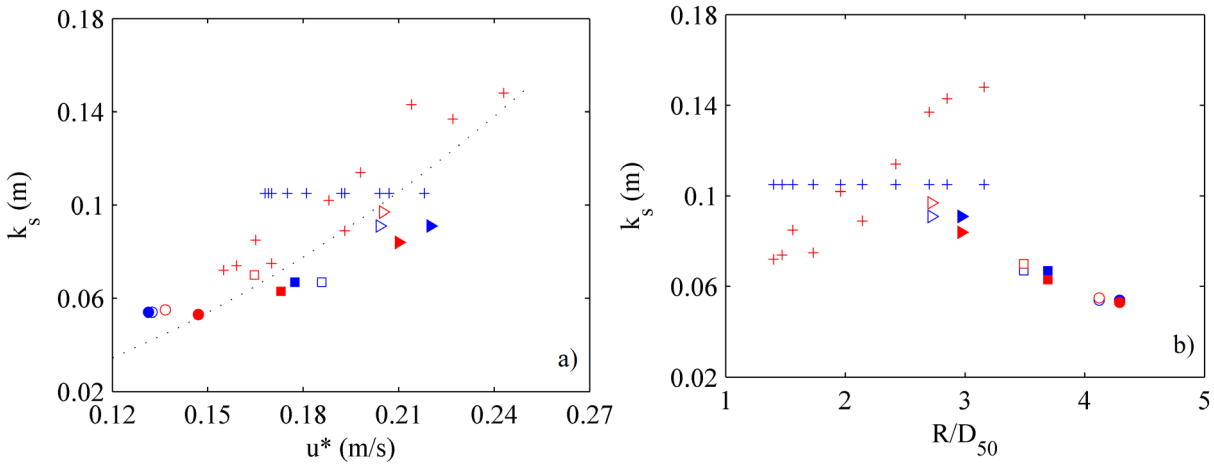

Figure 4.7- Relative roughness height as a function of (a) the shear velocity (u*) and (b) the relative submergence (R/D_{50}). *Legend Markers, + RG experiments, ○ CG1, ● CG2, □ CG3, ■ CG4, ▷ CG5, ▶ and CG6. Legend colors, from fitted log-profile, ● method A, ● method B.*

Regarding the displacement of the profile origin (downward origin shift D), the results do not show a clear trend of the D with any of the variables, since the displacement D is very low in all experiments.

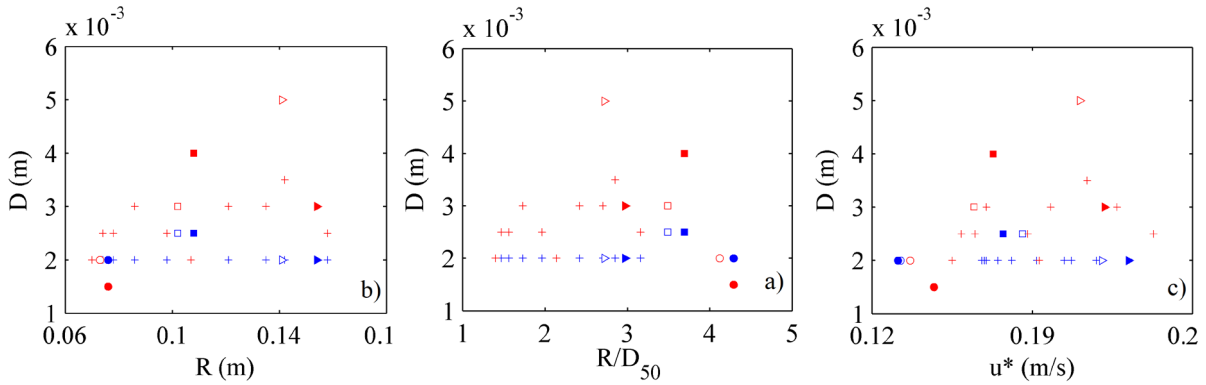

Figure 4.8- Downward origin shift of Z_0 (D) as a function of (a) Relative submergence, (b) Relative sand-roughness ks and (c) shear velocity. *Legend as for Figure 4.7.*

4.3 Flow resistance coefficients

Figure 4.9 depicts the evolution of the dimensionless Chezy coefficient (C^*) obtained from hydraulic variables and from both methods (A and B) of logarithmic adjustment as a function of the relative submergence (R/D_{50}) (Figure 4.9-a) and as a function of the Hydraulic radius R (Figure 4.9-b). The results show an increase correlation of C^* with R/D_{50}, in all cases. On the other hand, it is noticeable that C* from hydraulic measurements (black) is closer to the values obtained from the log-profile with k_s variable value (method B) (red).

The same conclusions can be obtained from Figure 4.10 where the Manning coefficient from the hydraulic variables and both logarithmic adjustments are depicted as a function of the relative submergence (R/D_{50}) and Hydraulic radius (R). The Manning coefficient n tends to decrease when R/D_{50} increases and values from the log-profile with variable k_s (red) are closer to n obtained from hydraulic variables (black).

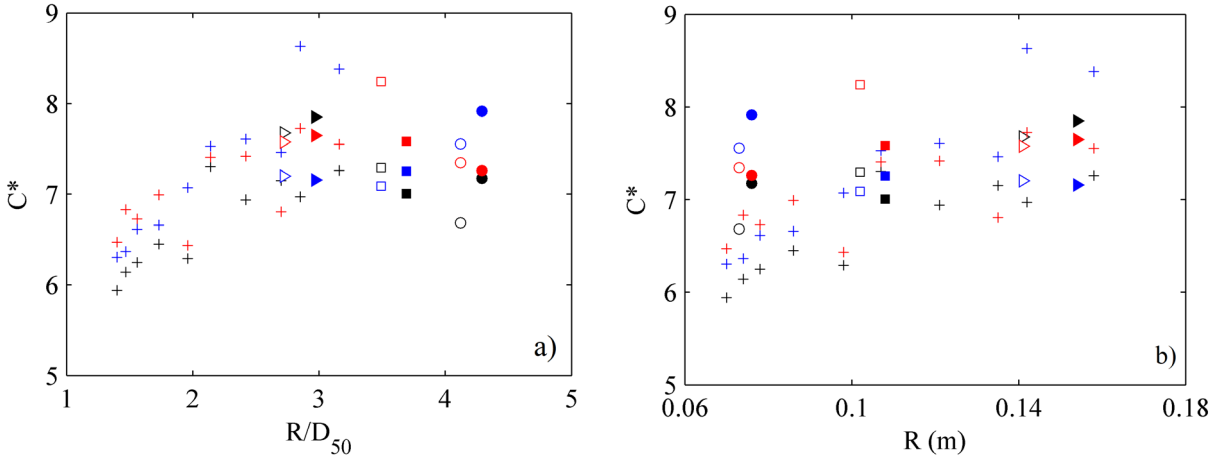

Figure 4.9- Dimensionless Chezy coefficient (C*) of all experiments as a function of (a) Relative submergence (R/D50) and (b) hydraulic Radius (R). *Legend Markers, +RG experiments, ○ CG1, ● CG2, □ CG3, ■ CG4, ▷ CG5, ► and CG6. Legend colors, ● from hydraulic variables and from fitted log-profile, ● method A and, ● method B.*

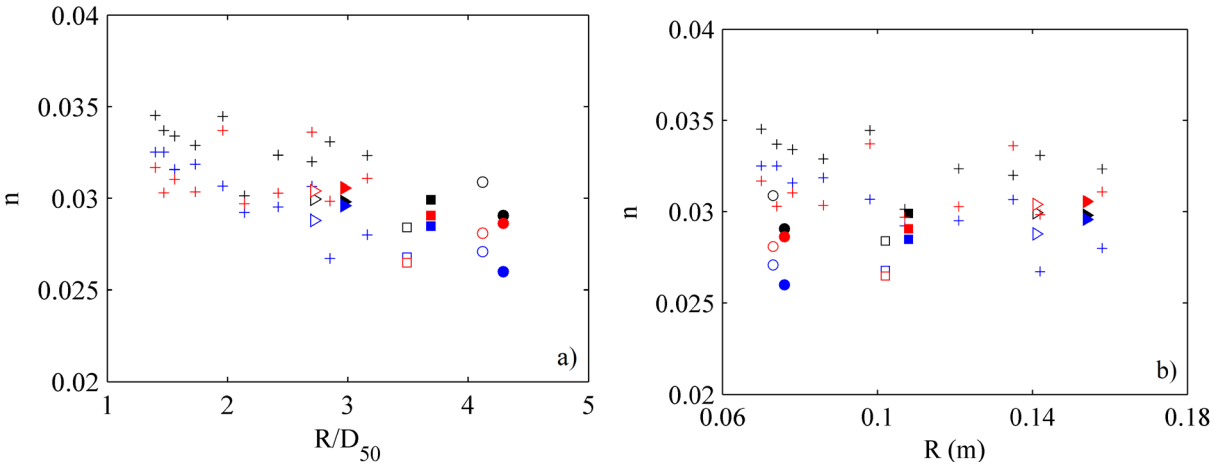

Figure 4.10- Manning coefficient of all experiments as a function of (a) Relative submergence (R/D_{50}) and (b) hydraulic Radius (R). *Legend as for Figure 4.9*

Flow resistance has found to be a little lower in cases with well-packed bed compared to loose bed with the same size of particles; nevertheless, more experiments would be necessary to assure it.

Some of the most common formulas used in predicting flow resistance in mountain rivers are presented in Table 4.5, and other commonly used are even more simple such as Strickler (Eq. (4-10), just based on the mean bed-diameter.

$$n = {D_{50}}^{1/6}/21 \tag{4-10}$$

The flow resistance coefficients (C^* and n) were evaluated in the previous section by means of the hydraulic variables and from the logarithmic adjustment and now they are assessed using the existing log-based formulas for hydraulic resistance in rough-bed flows over homogeneous sand-roughness and nonhomogeneous gravel-roughness. These formulas are based on Keulegean expression using semianalytic and purely empirical formulations for flow resistance in highly turbulent flows, in terms of the hydraulic characteristics of the flow and bed material in addition to the relative submergence (R/D_{50}). The authors considered in this study and their range of application are gathered in Table 4.5.

Table 4.5- Compilation of flow resistance formulas

Ref.	Equation	S_0 (%)	R/D	F	D (m)
Limerinos (1970)	$C^* = \sqrt{8/f} = 5.74 \cdot log\left[{R_h}/{D_{84}}\right] + 3.28$	0.068-2.4	0.9-68.5	-	0.019-0.75
Hey (1979)	$C^* = \sqrt{8/f} = 5.62 \cdot log\left[{d}/{D_{84}}\right] + 2.82$	0.049-3.1	0.7-22	0.14-0.8	0.046-0.25
Bathurst (1985)	$C^* = \sqrt{8/f} = 5.62 \cdot log\left[{d}/{D_{84}}\right] + 4$	0.4-4	0.4-11.4	0.15-1.17	0.113-0.5
Cao (1985)	1_ $C^* = \sqrt{8/f} = 5.91 \cdot log\left[{R}/{D_{50}}\right] + 3.75$	0.27-9	0.9-53	0.43-2.21	0.0044-0.0443
	2_ $C^* = \sqrt{8/f} = 6.08 \cdot log\left[{R}/{D_{50}}\right] + 3.9$	0.5-9	0.9-10	-	0.0115-0.0443
	3_ $C^* = \sqrt{8/f} = 6.17 \cdot log\left[{R}/{D_{50}}\right] + 3.41$	0.27-9	1.1-53	-	0.0044-0.0443
Ugarte & Mendez (1994)	$C^* = \sqrt{8/f} = 4.63 \cdot log\left[{R}/{D_{50}}\right] + 2.50$	0.2-4	0.5-17	0.22-1.17	1.0-4
Garcia (1996)	1_ $C^* = \sqrt{8/f} = 5.76 \cdot log\left[{d}/{D_{84}}\right] + 3.70$	2-9	8.1-29.5	1.18-3.84	0.00367
	2_ $C^* = \sqrt{8/f} = 5.76 \cdot log\left[{d}/{D_{84}}\right] + 2.28$	0.4-2.74	0.38-1.7	0.3-1	0.0811
Papanicolau & Maxwell (2000)	$C^* = \sqrt{8/f} = 5.68 \cdot log\left[{R}/{D_{84}}\right] + 5.68$	3-7	0.5-1.25	0.5-1.20	0.0508-0.1524
Aberle & Smart (2003)	$C^* = \sqrt{8/f} = 8.15 \cdot log\left[{d}/{D_{84}}\right] + 4.41$	2-10	0.25-3	-	-
Lopez & Barragan (2003)	$C^* = \sqrt{8/f} = 6 \cdot log\left[{R}/{D_{84}}\right] + 3.42$	0.95-5.20	0.17-7.1	0.1-1.26	0.05-0.91

The accurate estimation of the variables involved in the resistance coefficient has proved difficult to obtain in high turbulent flows such as Mountain Rivers characterized by the presence of large particles that generate vortices around them (R/D_{50}<10) (Bathurst 1985; Maynord 1991). This effect implies the existence of a shape resistance (due to the drag force generated by the roughness elements of the bed). For this reason, the error in the dimensionless Chezy coefficient calculated from the proposed formulations may differ from cases where (R/D_{50}<10) by 15-25%.

For comparative purposes, the criteria proposed by Bathurst et al. (1981) for the relative submergence are shown in Table 4.6, where equivalences of $D_{84} \approx 1.3 \cdot D_{50}$ y $D_{90} \approx 1.1 \cdot D_{84}$ have considered. Table 4.7 shows the different values proposed by the authors to characterize the flow. From it, it can be assumed that RG experiments from RG1 to RG7 can be considered as low relative submergence and the rest (RG8 to RG10, and CG1 to CG6) are in transitional relative submergence.

Table 4.6- Criteria for relative submergence. Bathurst et al. (1981)

Low relative submergence	$d/D_{84} < 2.4$	$d/D_{90} < 2.15$	$d/D_{50} < 2.8$
Transitional relative submergence	$2.4 \leq d/D_{84} \leq 7.6$	$2.15 \leq d/D_{90} \leq 6.9$	$2.8 \leq d/D_{50} \leq 9$
High relative submergence	$d/D_{84} > 7.6$	$d/D_{90} > 6.9$	$d/D_{50} > 9$

Table 4.7- Relative submergence of the experiments

Nº TEST	D_{50} m	D_{90} m	D_{84} m	R m	d m	Sf (m/m)	F	R/D_{50} (m/m)	R/D_{84} (m/m)	d/D_{50} (m/m)	d/D_{90} (m/m)	d/D_{84} (m/m)
RG1	0,055	0,068	0,062	0,07	0,078	0,038	1,1	1,27	1,13	1,42	1,03	1,26
RG2	0,055	0,068	0,062	0,074	0,083	0,037	1,11	1,35	1,20	1,51	1,09	1,34
RG3	0,055	0,068	0,062	0,078	0,089	0,037	1,12	1,42	1,26	1,62	1,15	1,44
RG4	0,055	0,068	0,062	0,086	0,1	0,037	1,15	1,56	1,39	1,82	1,26	1,62
RG5	0,055	0,068	0,062	0,098	0,116	0,038	1,13	1,78	1,59	2,11	1,44	1,88
RG6	0,055	0,068	0,062	0,107	0,129	0,036	1,26	1,95	1,73	2,35	1,57	2,09
RG7	0,055	0,068	0,062	0,121	0,15	0,036	1,18	2,20	1,96	2,73	1,78	2,43
RG8	0,055	0,068	0,062	0,135	0,171	0,037	1,22	2,45	2,18	3,11	1,99	2,77
RG9	0,055	0,068	0,062	0,142	0,183	0,038	1,2	2,58	2,30	3,33	2,09	2,96
RG10	0,055	0,068	0,062	0,158	0,208	0,039	1,25	2,87	2,56	3,78	2,32	3,36
CG1	0,0177	0,023	0,021	0,073	0,082	0,027	1,04	4,12	3,49	4,63	3,17	3,92
CG2	0,0177	0,023	0,021	0,076	0,086	0,025	1,06	4,29	3,63	4,86	3,30	4,11
CG3	0,0292	0,04	0,036	0,112	0,139	0,03	1,08	3,84	3,08	4,76	2,80	3,82
CG4	0,0292	0,04	0,036	0,108	0,131	0,031	1,12	3,70	2,97	4,49	2,70	3,60
CG5	0,052	0,06	0,055	0,141	0,181	0,03	1,18	2,71	2,59	3,48	2,35	3,32
CG6	0,052	0,06	0,055	0,154	0,202	0,029	1,17	2,96	2,82	3,88	2,57	3,70

Figure 4.11-a describes the Chezy coefficient C^* in terms of the relative submergence R/D_{50}. The figure overlaps the C^* values for all experiments (with no differentiation between experiments) obtained from the different methods. The figure includes the C^* obtained from the hydraulic variables (Table 4.2), the adjusted with U/u^* (Eq. (4-7) by means of the log-velocity profile adjustment with a constant k_s (method A) for experiments with the same D_{50} (Table 4.3) and the obtained from the adjustment by considering the k_s as a variable value (method B) (Table 4.4). In addition, the values obtained from the different authors log-equations (Table 4.5) are overlapped also in Figure 4.11-a. On the other hand, Figure 4.11-b shows the Manning coefficient (n) obtained by all mentioned approaches.

In all cases, the fitted values (blue and red) are similar to the hydrodynamic (black), while the closest value obtained from the log-equations is the obtained from Papanicolau & Maxwell (2000), above all in cases where $R/D_{84}<2$. The reason is probably that the experiments were inside the range of application of this formula (S_0=[0.03-0.07], R/D_{84}=[0.5-1.25] and F=[0.5-1.2]). From $R/D_{50}>3$, the values differ from Papanicolau & Maxwell (2000) and start to be closer to Bathurst (1985), due to the range of relative submergence d/D_{84} (defined by Bathurst) reaches a higher range [0.4-11.4].

It is noteworthy that the distribution of the values from the hydraulic values (black) and from both logarithmic adjustments (blue and red) along the relative submergence remain more stable than those defined by the authors, which show a clear decrease of the flow resistance as the R/D_{50} increase. However, these formulations were obtained from a large range of relative submergence in actual rivers and consider a constant value of k_s with diameter, determined as $k_s = \alpha \cdot D_{50}$.

All the results seem to be in accordance that the characteristic length to calculate flow resistance is not associated with particle diameter rather is proportional to the roughness height k_s which turned out to be dependent on the relative submergence and u^*.

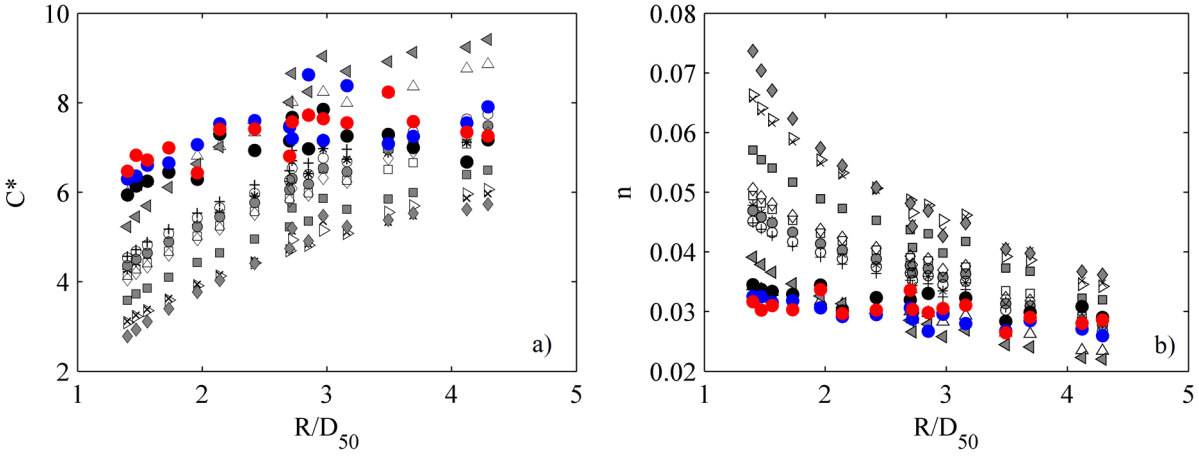

Figure 4.11- Figure (a) Manning coefficient n and figure (b) Dimensionless Chezy coefficient C^* as a function of the relative submergence (R/D_{50}). *Legend,* ● *from hydraulic variables and from fitted log-profile,* ● *with* k_s *as a constant and,* ● *with* k_s *as a variable value,* ■ *Limerinos (1970),* × *Hey (1979),* + *Bathurst (1985),* ● *Cao*$_1$ *(1985),* ○ *Cao*$_2$ *(1985),* ◇ *Cao*$_3$ *(1985),* ▷ *Ugarte & Mendez (1994),* ✳ *Garcia*$_1$ *(1996),* ◆ *Garcia*$_2$ *(1996),* △ *Papanicolau & Maxwell (2000),* ◁ *Aberle & Smart (2003) and* □ *Lopez & Barragan (2003).*

4.4 Turbulence Intensities

Turbulence intensities (TI) were evaluated using the root mean square value (RMS) of each fluctuation component (*u', v', w'*) at each point in the profile, and normalized by the local mean velocity of each axis ($\bar{u}, \bar{v}, \bar{w}$), Eq. (4-11.

$$TI_X = \sqrt{\langle u'^2 \rangle}/\bar{u} \qquad TI_Y = \sqrt{\langle v'^2 \rangle}/\bar{v} \qquad TI_Z = \sqrt{\langle w'^2 \rangle}/\bar{w} \tag{4-11}$$

Figure 4.12-a and Figure 4.12-b show the results obtained from the three components of the TI (TI_X, TI_Y, TI_Z), for the RG and CG experiments. In addition, Figure 4.13 and Figure 4.14 show a zoom of the roughness region (z/d<0.3) of the TI profiles.

The results from all the experiments showed a decrease of the three components of TI with the distance to the bed, revealing regions of highly turbulent flow in the near-bed region above all for the TI_Z, where the greatest turbulence intensities occur within the near-bed region (<0.3-*z/d*) for all experiments. In the case of the RG, the three components are well differentiated along the whole profile. By increasing the flow rate from RG1 to RG10, the intensities in the three axes rise due to the increase in the near-bed velocity and the amplification of the velocity fluctuations (*u', v', w'*), especially TI_Z. From the results of the CG experiments, it can be observed that cases with not leveled beds (CG1, CG3, and CG4) in comparison with the leveled ones (CG2, CG4, and CG6) obtain higher turbulent intensity in the vertical axis (TI_Z) near the bed region, while a little lower streamwise TI (TI_x).

In all cases, there is an intense continuous band of high turbulence intensity forming over the bed, originating in roughness layer. By the height of *z/d*≈0.3, the turbulence intensity is comparable for packed and loose surfaces. In all cases, the levels of turbulence near the bed increase with the flow rate, thus with $u*$ and τ_0.

It seems logical that if the roughness disturbs the flow, flow streaks are ejected from the bed surface, thus increasing the TI_Z, and maintaining a rather constant value in the near-bed region, unlike the densely packed cases where this value decreases slightly in the zone closest to the bed. In this regard, it is important to recall the results of the analysis that the configuration of the device has on the main turbulent quantities (Appendix C). In this appendix, we saw that variations in both the CV and the FDC modified the main turbulent parameters in a similar way. In section C.4 of the mentioned appendix, it is observed that, by means of the decrease of the FDC and the increase of the CV the turbulent intensities were altered, for the same experiment (same hydraulic conditions). Specifically, the TI_X was reduced up to 20% (on average in the depth profile) when the FDC was reduced from 100 Hz to 25 Hz, in the same way, it was reduced by 13% by increasing the CV from 2.5 mm to 7 mm. The TI_Y and TI_Z were diminished 30% and 50% respectively in the region near the bed, however, the average quantities along the depth profile were more similar. Therefore, it is expected that the turbulent intensities, especially in the region near the bed, would be if the FDC had been 100 Hz instead of 25 Hz.

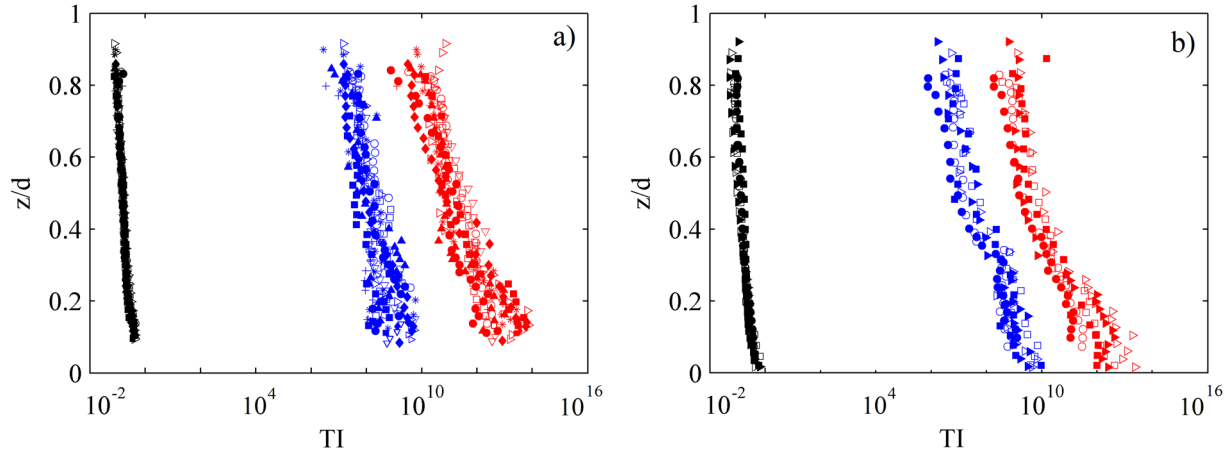

Figure 4.12- Vertical distribution of the Turbulence intensities of (a) the RG and (b) CG experiments. *Legend Markers (a), + RG1, ○ RG2, □ RG3, ● RG4, ▲ RG5, ▽ RG6, ∗ RG7, ♦ RG8, ■ RG9 and ▷ RG10. Legend Markers (b), ○ CG1, ● CG2, □ CG3, ■ CG4, ▷ CG5 and ▶ CG6. Legend Colors, ● (TI_X), ● (TI_Y) and ● (TI_Z).*

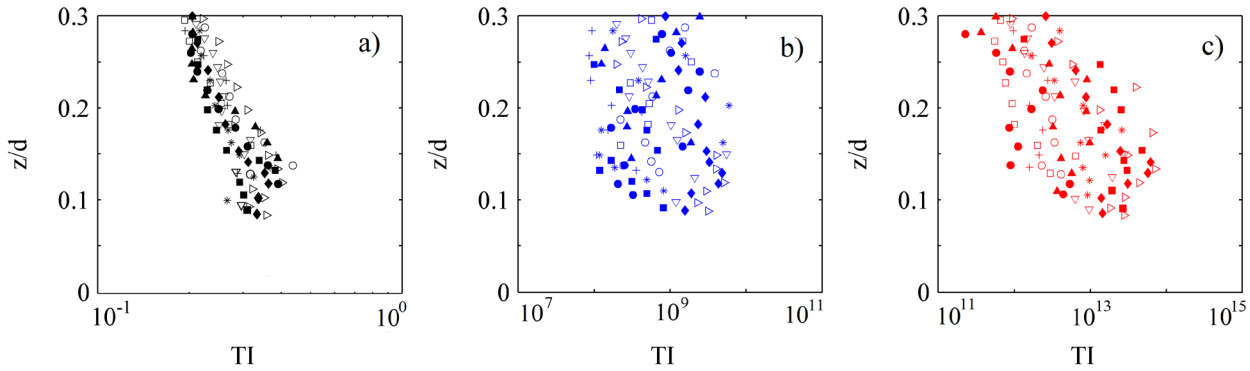

Figure 4.13- Zoom of the roughness region (z/d<0.3) of the TIs of the RG experiments. *Legend as for Figure 4.12.*

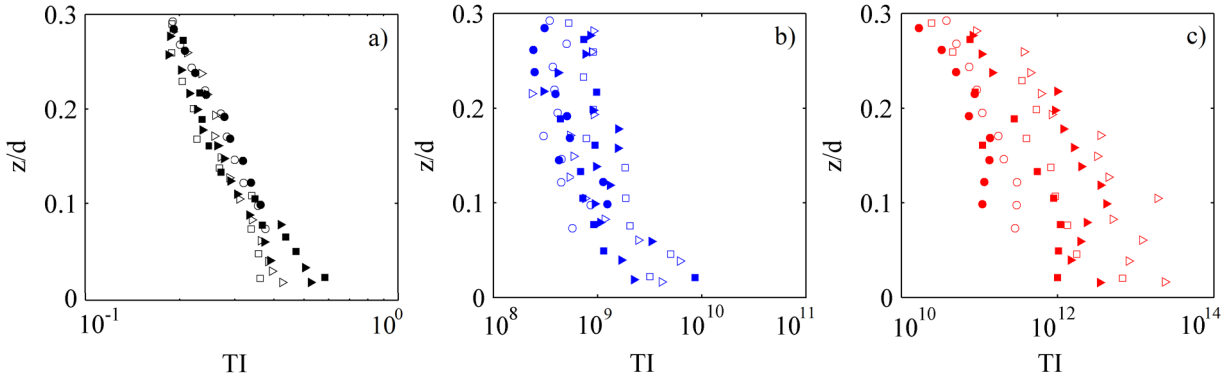

Figure 4.14- Zoom of the roughness region (z/d<0.3) of the TIs of the CG experiments. *Legend as for Figure 4.12.*

On the other hand, the streamwise component TI_X has been normalized by u^* instead of $\overline{u}$, thus (u'_{rms}/u^*), with the purpose of comparing with the exponential decay function of Nezu and Nakagawa (1993) for two-dimensional open channel flow, Eq. (4-12. The results are presented in Figure 4.15-a and Figure 4.15-b for the two groups of experiments.

$$u'_{rms}/u^* = 2.3\ exp(-z/d) \tag{4-12}$$

Despite all the profiles showed deviations from Nezu and Nakagawa's profile (dashed line), the trend of evolution agrees. Very close to the bed, the TI_X decreases a little, opposing to the prediction of the exponential profile, which is probably due to the low FDC used to the data acquisition. The profiles present a maximum at z/d <0.3, which is at higher elevation in comparison to the prediction of Nezu and Nakagawa's equation. The results are in agreement with Papanicolau et al. (2012), that found that over z/d=0.3 the profiles agreed with the exponential expression.

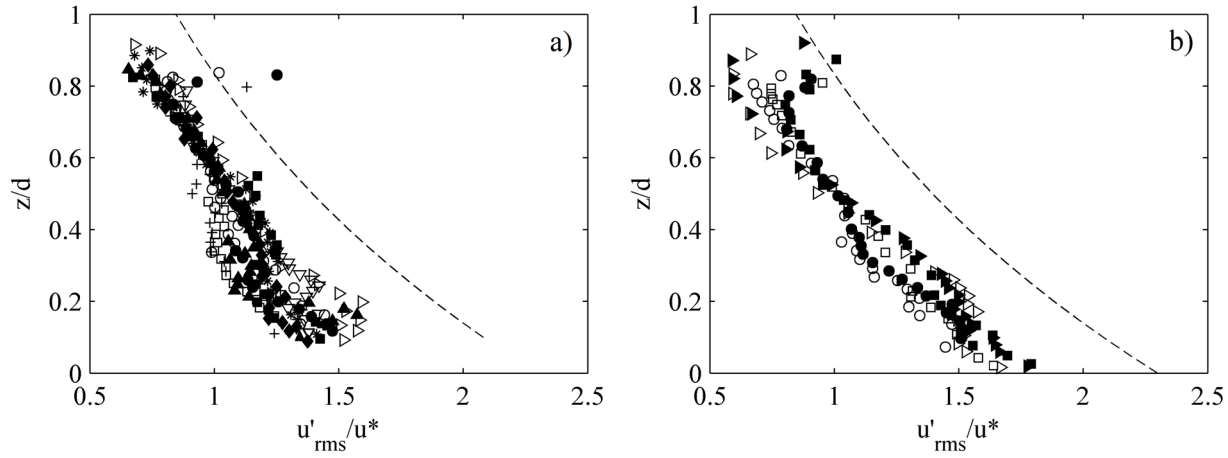

Figure 4.15- Vertical distribution of the TI_X (defined as u'_{rms}/u^*) for (a) RG experiments and (b) CG experiments. *Legend (a) as for Figure 4.12-a (Markers). Legend (b) as for Figure 4.12-b (Markers). The dashed lines (----) correspond to the Nezu and Nakagawa exponential function.*

4.5 Turbulent Kinetic Energy

Most studies of turbulent kinetic energy (TKE) in open channel flow concern both hydraulically smooth and transitionally rough flows, Nezu & Nakagawa (1993), Song et al. (1994); Balachandar & Bhuiyan (2007). The vertical distribution of the TKE, especially within the roughness of gravel-type bed, is an essential tool for understanding turbulent processes throughout the depth profile, having various applications on hydraulic engineering such as sediment transport or diffusion of contaminants.

In open-channel flows with hydraulically rough beds, conversion of mean kinetic energy into turbulent kinetic energy (TKE) corresponds to shear production. If the relative submergence is sufficiently high, the local equilibrium between TKE production and dissipation is expected to hold sufficiently far above the roughness elements of the channel bed, Ferreira et al. (2010).

The turbulent kinetic energy (TKE) per unit mass is obtained from the product of the absolute intensity of velocity fluctuations (*u', v', w'*) from the mean velocity, i.e. the variances of the flow within an XYZ coordinate system, and is defined by Eq. (4-13.

$$TKE = (1/2)\,(u'^2 + v'^2 + w'^2) \tag{4-13}$$

Figure 4.16-a and Figure 4.16-b show the vertical distribution of the TKE for the RG and CG experiments respectively. It is noticeable how in all the experiments the TKE gradually increases

vertically toward the water surface with increasing flow rates, being the increase greater in the near-bed region, in accordance with what was observed in the turbulent intensities. There is a region near the bed (z/d<0.2) where the values of TKE slightly decrease or maintain the value until the channel bed. Therefore, the peak value of the TKE is located around z/d=0.2 for all experiments, being that height decreased as the flow rate is increased, as can be seen in the TKE distribution of the RG experiments, Figure 4.16-a. Therefore, the TKE layer seems to decrease with the flow rate, placing its maximum value at a lower height. For example, the experiment RG1 has this maximum placed at a height of z/d=0.25, while in the test RG10 it is placed at a height z/d=0.15. However, the actual height in the depth profile of z/d=0.25 for the test RG1 is equivalent to a height of approximately 2 cm in the depth, whereas for z/d=0.15 (RG10) the height is equivalent to 2.7 cm. Thus, the high TKE band actually increases with the flow rate

In the case of the CG experiments, it is noticeable how the fact of leveling the bottom bed increase the TKE, probably due to the increase of TI_Z seen above. The surface packing has a similar effect on the TKE that on the vertical turbulent intensities (TI_Z), since the value increases towards the bed surface but remains constant in the near-bed region. From a height $z/d \approx 0.3$, the profiles of the experiments of equal bed diameter and depth (well-packed or not) collapse obtaining very similar values.

The same statement done in the previous section (turbulent intensities) can be said for the TKE in reference to the configuration of the device. That is, as noted in Appendix C, TKEs can be expected up to 50-60% higher in the case of having configured the ADV with a higher FDC or a lower CV. This effect is also noticeable through the performance curves defined in Appendix C (section C.9).

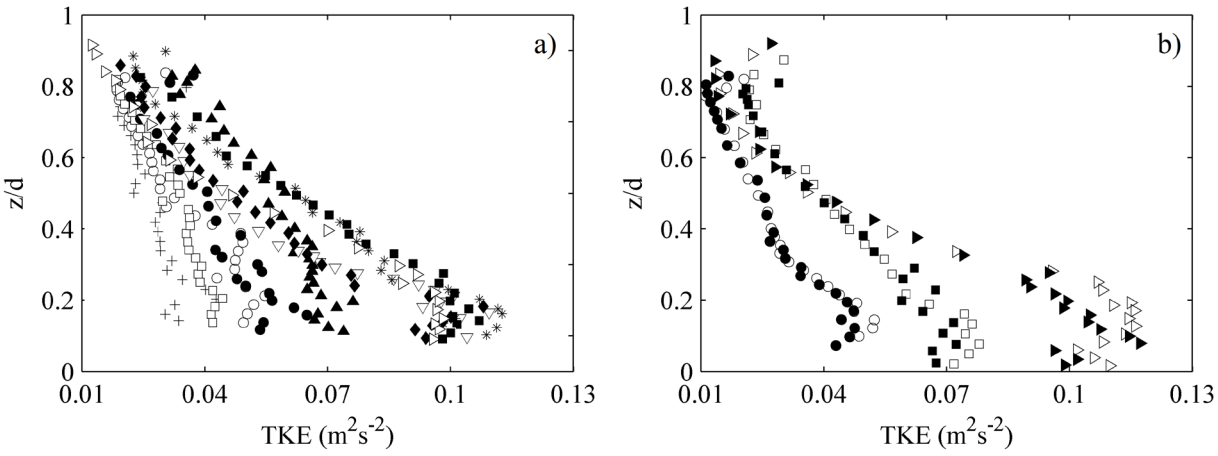

Figure 4.16- Vertical distribution of the TKE of the (a) RG and (b) CG tests. *Legend (a), + RG1, ○ RG2, □ RG3, ● RG4, ▲ RG5, ▽ RG6, ∗ RG7, ♦ RG8, ■ RG9 and ▷ RG10. Legend (b), ○ CG1, ● CG2, □ CG3, ■ CG4, ▷ CG5 and ► CG6.*

4.6 Reynolds shear stress

In 1895, Osborne Reynolds decomposed the instantaneous velocity and pressure components from the Navier-Stokes equations into their mean and fluctuating parts. The Reynold stresses, the term ($\partial \overline{u'_i u'_j}/\partial x_j$, spatial gradient) in the well-known Reynolds-averaged Navier-Stokes equation (RANS), appears after the decomposition and averaging. The time-averaged Reynolds shear stresses ($-\rho\overline{u'w'}$) is the mechanism of momentum exchange of the structures generated in the near-bed region to the mean flow.

Bigillon et al. (2006) observed that in hydraulically rough beds the Reynolds shear stress ($-\rho\overline{u'w'}$) reaches a maximum in the wall region and decreases towards the bed, due to the existence of a roughness layer where additional mechanisms for momentum extraction emerge.

The total shear stress across a shear plane in the flow is the sum of the turbulent shear stress (Reynold shear stress), caused by macroscopic diffusion of fluid momentum, and the viscous shear stress ($\tau_\mu = \nu/\rho \cdot \partial u/\partial z$), caused in part by molecular diffusion of fluid momentum and in part by attractive forces between molecules at the shear plane.

Figure 4.17-a and Figure 4.17-b depict the Reynold stress obtained from the experimental measures, from the RG and CG experiments respectively. A phenomenon similar to TKE and TI_Z is observed in the magnitude of the Reynolds shear stress ($-\rho\overline{u'w'}$). The value increases with the flow rate, increasing from the water surface to the bed, but maintaining a constant value in the region near the bed.

Besides, Reynold shear stresses were normalized by $\rho \cdot u^{*2}$ with the aim of comparing experiments between each other and overlap the theoretical trend of the shear stress (Eq. (4-3). Figure 4.18-a and Figure 4.18-b show the trend of the dimensionless shear stress as a function of the dimensionless depth, for the RG and CG experiments respectively.

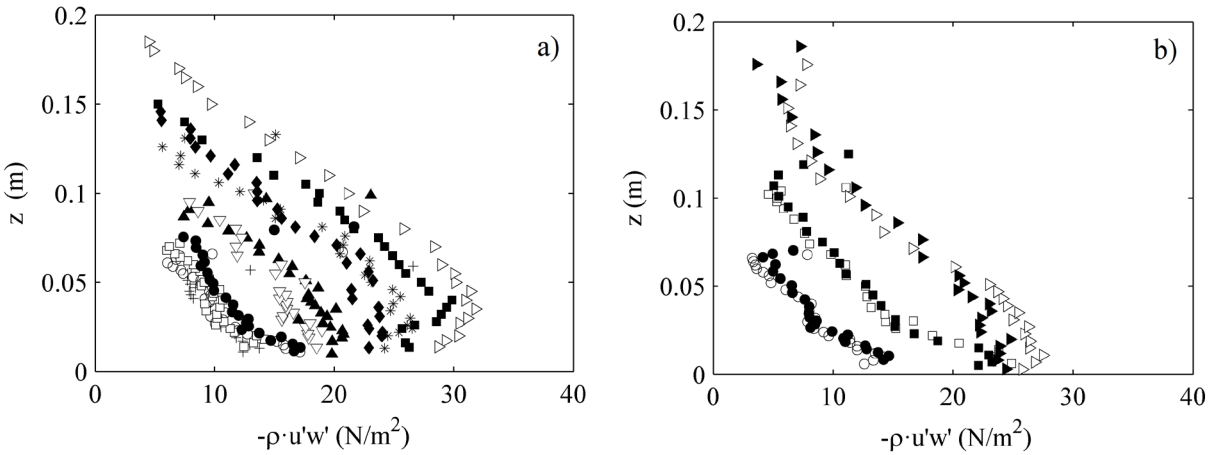

Figure 4.17- Vertical distribution of the Reynold shear stresses for (a) RG tests and (b) CG tests. *Legend (a), + RG1, ○ RG2, □ RG3, ● RG4, ▲ RG5, ▽ RG6, ✳ RG7, ♦ RG8, ■ RG9 and ▷ RG10. Legend (b), ○ CG1, ● CG2, □ CG3, ■ CG4, ▷ CG5 and ▶ CG6*

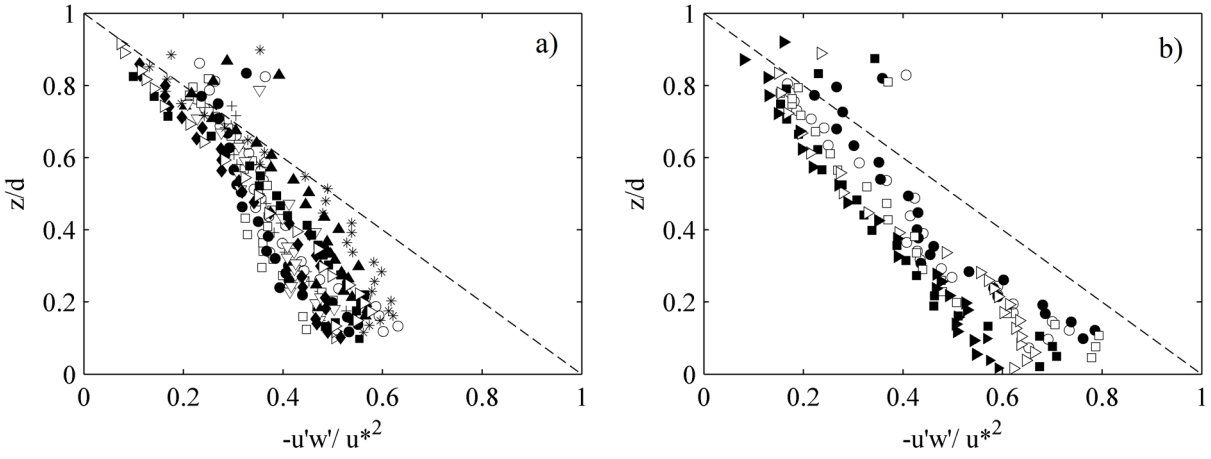

Figure 4.18- Vertical distribution of the dimensionless Reynolds stresses from (a) RG and (b) CG tests. *Legend (a), + RG1, ○ RG2, □ RG3, ● RG4, ▲ RG5, ▽ RG6, ∗ RG7, ♦ RG8, ■ RG9 and ▷ RG10. Legend (b), ○ CG1, ● CG2, □ CG3, ■ CG4, ▷ CG5 and ► CG6.*

It seems that the Reynolds shear stress for all of the experiments reaches a maximum value inside the roughness region at around $z/d \approx 0.2$, decreasing its value towards the bed surface. The results are similar to turbulence intensities; the greatest Reynolds shear stresses occur within the near-bed region and demonstrate the influence of the bed topography on near-bed flow. This is due to the existence of a continuous band of high turbulent stresses across the region of $z/d<0.3$. This band becomes wider (z) as the flow rate is increased, although the relative thickness decreases, Figure 4.18-a. In this figure is noticeable that the higher the flow rate, and higher k_s values, lead to higher values of the Reynolds shear stress, and decreases the relative height (z/d) where the maximum is located.

In order to discuss the roughness effects on the bed shear stress, the CG experiments are evaluated in Figure 4.18-b. It is noticeable that by flattening the bed, from the experiments CG1 to CG2, CG3 to CG4 and CG5 to CG6, the band of high-intensity Reynolds stresses becomes thinner and located lower in the flow. The roughness effect is no longer important far from the bed ($z/d>0.5$), where the loosed and packed rough bed profiles tends to overlap with each other.

Figure 4.19-a and Figure 4.19-b show the viscous stress along the depth profile (z) for both types of experiments, RG and CG respectively. The figures show the increase of these stresses as approaching the surface bed, however, the value of viscous stresses do not explain the lack of stress in the near-bed region. The relative contributions of Reynolds shear stress and viscous shear stress should change drastically near the boundary. That is to say, when the Reynolds stresses decrease very close to the bed, the viscous shear stress should increase reaching similar values than bed turbulent stress. Despite the increase of the viscous effect in the near-bed region, the mentioned effect has not been seen since the viscous stress remains rather inferior to the turbulent stresses.

Again, it should be mentioned that by varying the configuration of the ADV (reduction of the FDC from 100 Hz to 25 Hz) the term $\rho\overline{u'w'}$ was reduced by 40-30 % in the region near the bed. Therefore, Reynolds shear stresses of up to double can be expected in this area, being closer to the theoretical description.

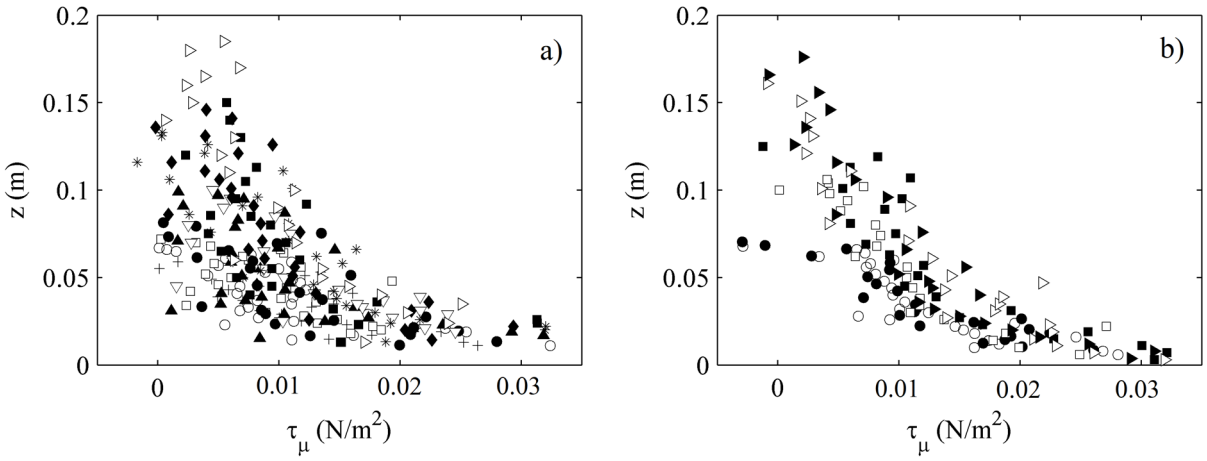

Figure 4.19- Vertical distribution of the viscous shear stresses profile for (a) RG tests and (b) CG tests. *Legend (a), + RG1, ○ RG2, □ RG3, ● RG4, ▲ RG5, ▽ RG6, ∗ RG7, ♦ RG8, ■ RG9 and ▷ RG10. Legend (b), ○ CG1, ● CG2, □ CG3, ■ CG4, ▷ CG5 and ► CG6.*

4.7 Autocorrelation

Turbulence is characterized by statistical parameters due to its chaotic nature, with the aim of looking for organized behavior. In this sense, the correlation is a useful tool, which is based on finding correlated behaviors between two data series. Therefore, autocorrelation (R_{ii}) tries to find the correlation of a series with itself. Autocorrelation function (Eq. (4-14) studies how a velocity series related to itself evolves after a certain time or a certain distance, spatial correlations or temporal correlations respectively. Since each series of experimental velocity belongs to a single point, it is possible to obtain the correlation of these series on themselves with a certain delay (t).

$$R_{ii}(t) = \overline{u_\iota(t_0)\, u_\iota(t_0 + t)}/{u_i}'^2 \tag{4-14}$$

Below in Figure 4.20-a and Figure 4.20-b, there is an example of the function R_{xx} of $u(t)$, in time scale and length scale respectively, obtained from all points in the profile of the experiment RG3.

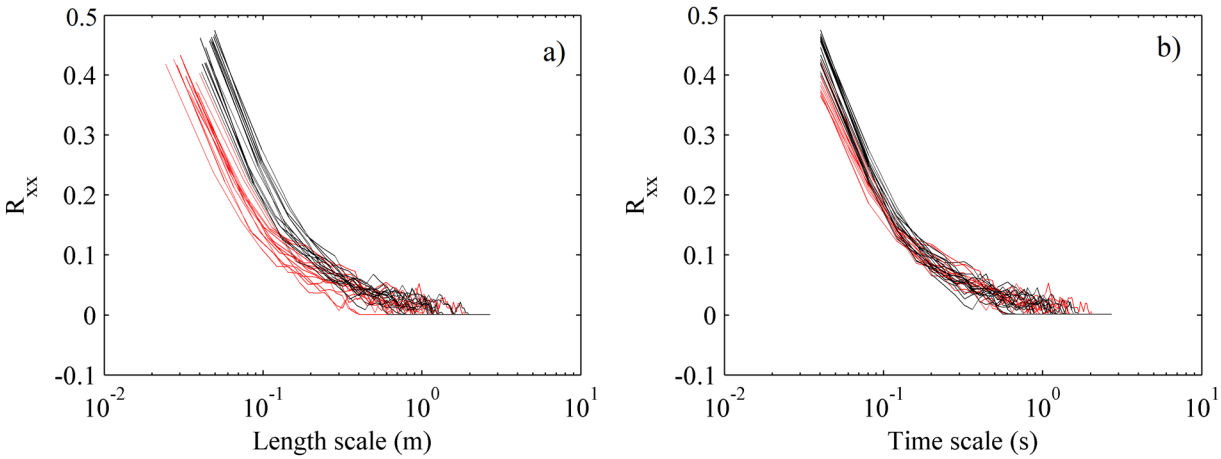

Figure 4.20- Autocorrelation function as function of (a) Length and (b) Time. *Legend, ● points with elevation z/d<0.5, and ● points with elevation z/d>0.5.*

From the figures above it is noticeable how the autocorrelation function changes depending on the point in the depth profile. Specifically, points closer to the roughness region, at a height of z/d<0.5 (red lines), show a lower autocorrelation between two points spaced in time and space than points at a height of z/d>0.5, showing that the characteristic length and characteristic time of the structures in this area are lower, due to a higher level of turbulence.

4.8 Power spectral density

The autocorrelation of a real, stationary signal $u(t)$ can be defined in terms of their spectrum, according to the definition of the Fourier transform, Eq. (4-15, thus the spectrum can be defined by Eq. (4-16, where k_w is the wavenumber and $S_{ii}(k_w)$ is the normalized power spectral density (PSD). Using Taylor's frozen turbulence hypothesis the spectrum $S_{ii}(k_w)$ can be transferred from the wave number domain (k_w) to the frequency domain (f), Eq. (4-17. The streamwise velocity power spectra $S_{xx}(f)$ explains how the turbulent energy of the streamwise velocity series $u(t)$ is decomposed in the different frequencies, thus how is distributed across the different eddy sizes.

$$R_{ii} = \int_0^\infty S_{ii}(k_w)\, cos(k_w \times t)\, dk_w \tag{4-15}$$

$$S_{ii}(k_w) = \frac{2}{\pi}\int_0^\infty R_{ii}\, cos(k_w \times t)\, dt \tag{4-16}$$

$$k_w = 2\pi\, f/\bar{u} \tag{4-17}$$

Some examples of the resulting PSD are shown below in Figure 4.21 from six different RG experiments at the same height z/d=0.2, inside the roughness layer. As mentioned in chapter 3 and the appendices, most of the obtained velocity power spectrums do not match with the theoretical Kolmogorov's universal slope of -5/3, or better said, they just follow the slope in a narrow range [1-3] Hz.

In order to evaluate the vertical distribution of the velocity power spectra slope (m), the slopes of each measured point, are overlapped in Figure 4.22 and Figure 4.23, for the RG and CG experiments respectively. Two slopes are obtained from the data series, the first slope (m_1) covers the range frequencies below 1 Hz (black markers) and the second (m_2) the frequencies above 1 Hz (red markers), being the second where usually starts to appear the universal Kolmogorov slope (inertial range).

A gradual decrease (negative slope) towards the -5/3 of Kolmogorov is obtained as getting far from the bed; moreover, the value becomes more stable. Conversely, the adjusted slope from the near-bed region is higher and have a more changeable value, showing that in this area the small frequencies have more energy than expected.

From Figure 4.22-a and Figure 4.22-b, all the experiments show similar distribution along the water depth (z), while more differences are observed if they are defined as a function of the dimensionless depth (z/d), Figure 4.23-a and Figure 4.23-b, due to the large differences in depth.

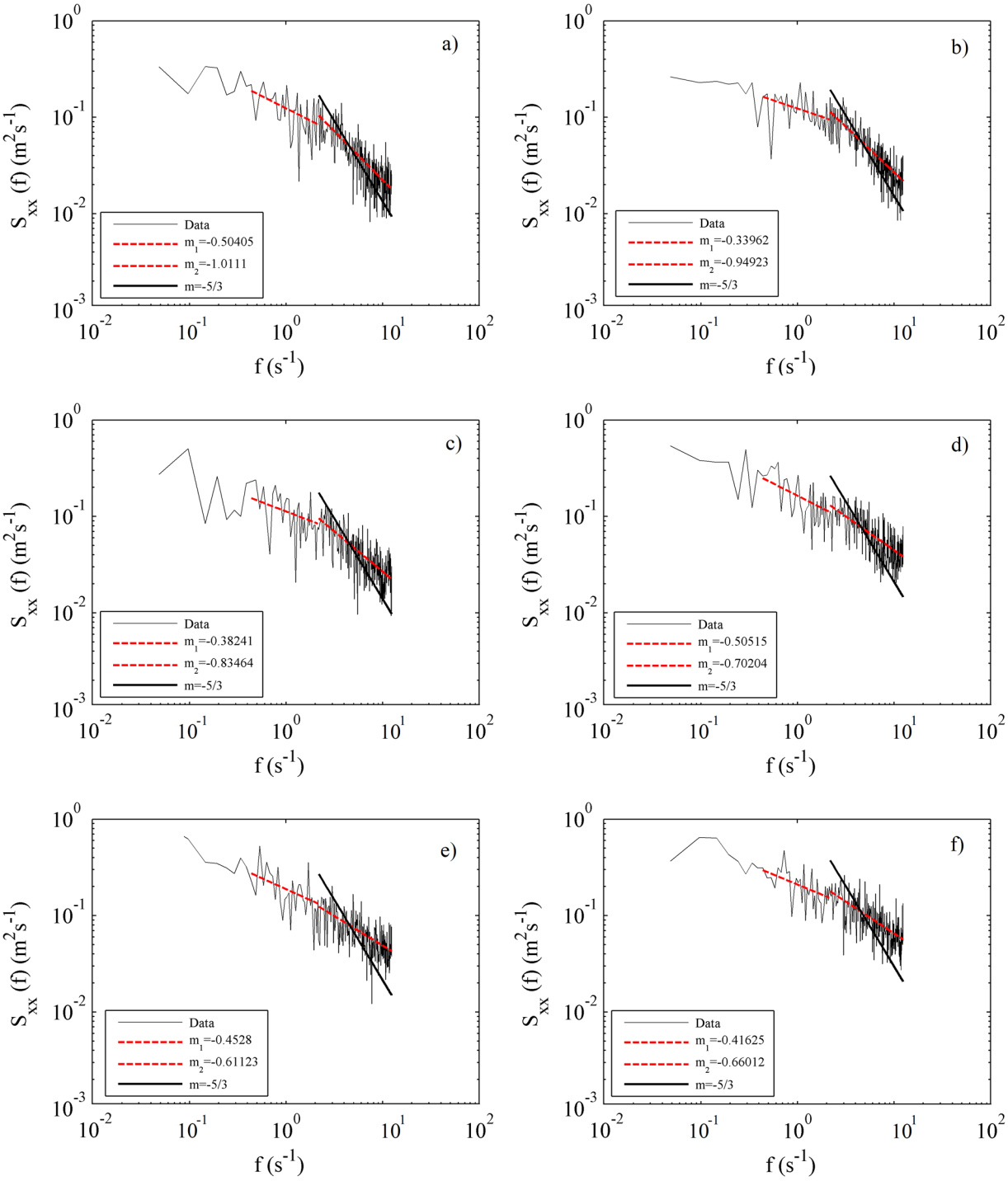

Figure 4.21- PSD of the streamwise velocity component at height of *z/d*=0.2 for the experiments (a) RG1, (b) RG3, (c) RG5, (d) RG7, (e) RG9 and (f) RG10.

The slope value of the PSD depends on the distance to the bed (*z*), rather than on the *z/d*, this will be later corroborated in section 4.10.2 by Taylor length (inertial scale). Turbulence scales increase their size with the *z*, the vortices become larger, although as we have seen it is in the area near-bed where there is more TKE, where the smaller structures are, therefore, they are also very energetic. This means that both large and small structures become less energetic, fluctuate less, with the height (*z*) in the profile. Near the water surface, the larger is the depth (*d*), the closer the second slope (*f*> 1 Hz, inertial range) approaches to the -5/3 of Kolmogorov.

As seen in chapter 3 and associated appendices, the fact that the data does not adjust well to the theoretical slope is possibly due to the high level of turbulence and the configuration of the ADV. Near the bed, there is a lot of energy that is not well represented due to a lack of accuracy in the data (due to the low frequency of data collection FDC). As a result, part of the energy from the not represented vortices is allocated to the represented ones, causing the energy in the PSD fluctuates and therefore does not follow the universal slope of Kolmogorov. In all cases, it can be observed how the trend of decrease in Figure 4.22 and Figure 4.23 is the same in all the tests.

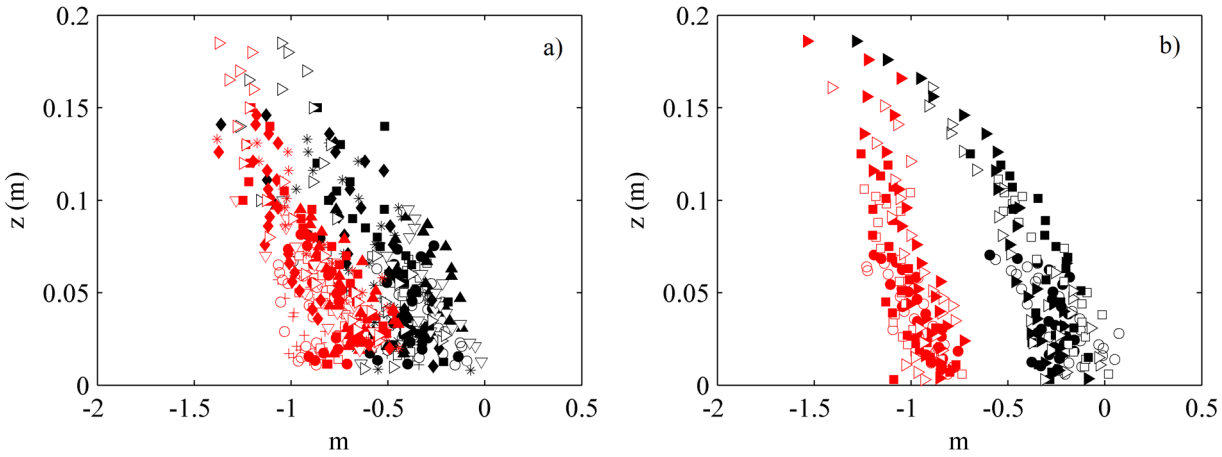

Figure 4.22- Vertical profiles of the PSD slope of the (a) RG and (b) CG experiments as a function of the depth (z). *Legend Markers (a), + RG1, ○ RG2, □ RG3, ● RG4, ▲ RG5, ▽ RG6, ✳ RG7, ♦ RG8, ■ RG9 and ▷ RG10. Legend Markers (b), ○ CG1, ● CG2, □ CG3, ■ CG4, ▷ CG5 and ► CG6. Legend colors, ● for f<1 Hz (m_1) and ● for f>1 Hz (m_2).*

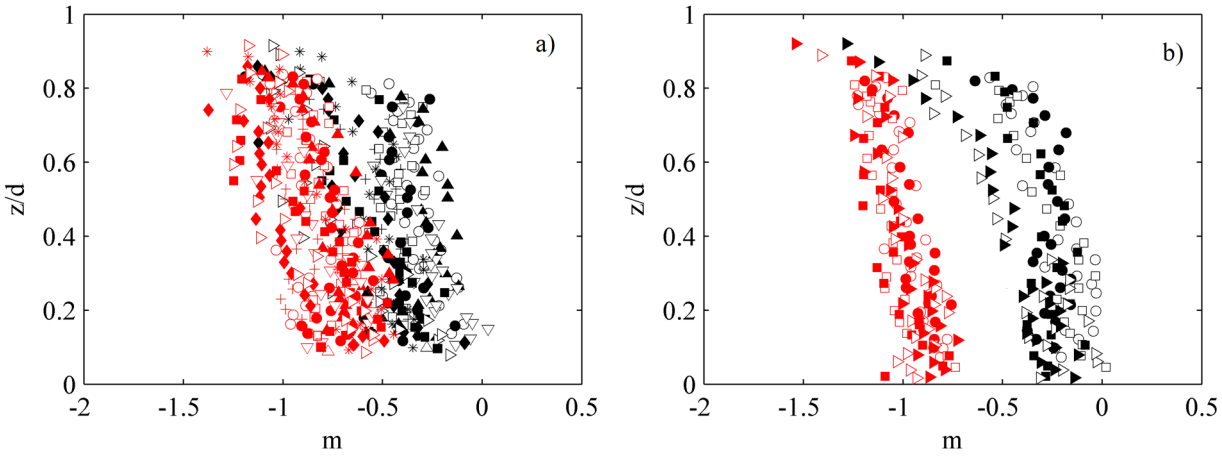

Figure 4.23- Vertical profile of the PSD slopes (m_1 and m_2) of the (a) RG and (b) CG experiments as a function of the dimensionless depth (z/d). *Legend as for Figure 4.22*

4.9 Dissipation

The flow in the experiments can be considered steady and uniform, therefore, the kinetic energy in all the sections of the same experiment is equal, but the potential energy depends on the elevation. As consequence of that, between two consecutive sections, the kinetic energy is the same, but the potential

energy has decreased. This loss of energy is due to the transport process. The mechanism of the dissipation of turbulent kinetic energy is probably one of the most fundamental aspects of turbulence.

The dissipated power for each experiment is measured as potential energy loss per unit area (watts/m^2) and can be evaluated as the power channel (W), Eq. (4-18, where (q) is the relative flow (q=Q/B), and B the width of the channel. Therefore, considering the water mass per unit area as (d · ρ), the weight is obtained in kg per meter squared (kg/m^2). Finally, the energy dissipated by the channel between the two sections can be obtained by Eq. (4-19, with units of power per unit mass (w/kg) and therefore dissipation units (m^2/s^3). The results of the power channel (W) obtained for each experiment are shown below in the first column of Table 4.8.

$$W = q \cdot S_f \cdot \gamma \tag{4-18}$$

$$\varepsilon = (q \cdot S_f \cdot \gamma) \,/\, (d \cdot \rho) \tag{4-19}$$

The energy dissipation rate was calculated in the **first** place using the Taylor (1935) expression for isotropic turbulence, Eq. (4-20. The results of the dissipation rate obtained from that expression in each point of the profile are depicted in Figure 4.24 and the mean value in the profile are shown in the second column of Table 4.8. The results do not converge with those obtained from the calculation of the energy dissipated by the channel (W), thus considering the origin of the energy that dissipates the flow, which is much higher than the obtained from Taylor's expression. For this reason, the energy dissipation rate was evaluated using other three approaches.

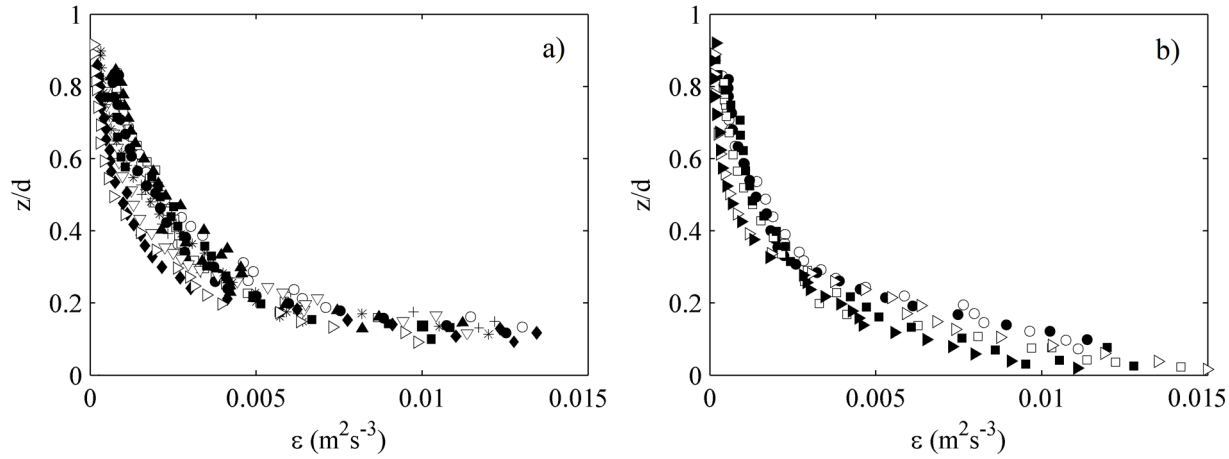

Figure 4.24- Vertical distribution of the dissipation rate obtained from Taylor's expression, for the experiments (a) RG and (b) CG. *Legend (a), + RG1, ○ RG2, □ RG3, ● RG4, ▲ RG5, ▽ RG6, ∗ RG7, ♦ RG8, ■ RG9 and ▷ RG10. Legend (b), ○ CG1, ● CG2, □ CG3, ■ CG4, ▷ CG5 and ► CG6.*

The **second** methodology used in the investigation to calculate the dissipation rate of TKE ε is based on the dimensional analysis, Garcia et al. (2004), Eq. (4-21. Where q' is the characteristic turbulent velocity that can be estimated by means of the Eq. (4-22, as a function of the TKE, Wernersson et al. (2000).

$$\varepsilon = 15\nu\,\overline{(\partial u/\partial x)^2} \tag{4-20}$$

$$\varepsilon = Aq'^3/L \tag{4-21}$$

$$q' = \sqrt{TKE} \tag{4-22}$$

The proportionality factor A will depend on the choice of the characteristic length L. Two approaches have been suggested for the estimation of L, Garcia et al. (2004). The first using the geometry of the experimental setup, and the second using the local integral scale L_i, from the autocorrelation function. The first approach implies that the energy contained in the eddies is independent of the local flow (Wernersson et al. 2000), being A subject to the experimental setup. The value of A used is 0.85, proposed by Wu et al. (1989) when using the characteristic length L. Nonetheless, Kresta & Wood (1993) suggested that using the L_i is the most stable method for the estimation of ε. Results of dissipation obtained from all experiments by this method are shown in Figure 4.25.

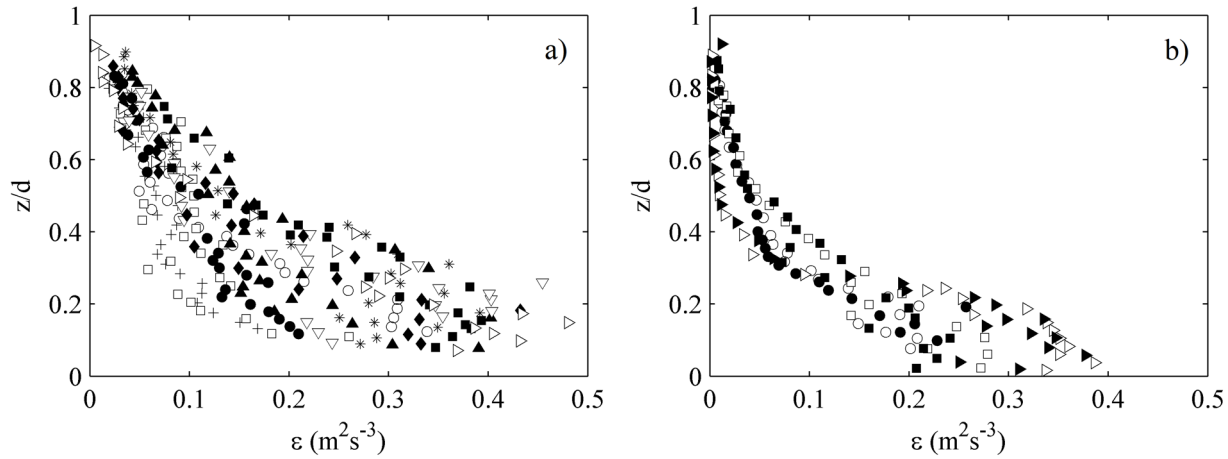

Figure 4.25- Vertical distribution of the dissipation rate obtained from the dimensional analysis for the experiments (a) RG and (b) CG. *Legend (a), + RG1, ○ RG2, □ RG3, ● RG4, ▲ RG5, ▽ RG6, ∗ RG7, ♦ RG8, ■ RG9 and ▷ RG10. Legend (b), ○ CG1, ● CG2, □ CG3, ■ CG4, ▷ CG5 and ▶ CG6.*

One of the hypotheses developed by Kolmogorov (1941) in his theory was that for a highly turbulent flow (with a high Reynolds number), the scale statistics in the inertial subrange ($\eta << r << L$) are universally and exclusively determined by the scale (r) and the energy dissipation rate (ε). For homogeneous turbulence, the characterization of the energy cascade is done through the velocity power spectrum function S_{ii}, as it was seen before. If S_{ii} is defined as a function of k_w, by dimensional analysis, the only possible form for the S_{ii} function according to the Kolmogorov's hypothesis is the shown by Eq. (4-23; which is the well-known 2/3 law of Kolmogorov, where **C** = 0.49 (universal constant) Pope, (2000).

The **third** methodology used in this work computes ε from -5/3 slope fitting of the power spectrum in the inertial range using the one-dimensional power spectrum in the spatial domain, Eq. (4-23. The value of ε is obtained by a non-linear fit in the inertial subrange. The limits of the range were the fitting is performed are defined based on visual inspection of the power spectrum in order to use only the range where -5/3 slope is visualized, usually has said beyond the 1 Hz, with the proper transformation to wave number. The vertical distributions of ε obtained from the third method of all experiments are depicted in Figure 4.26.

$$E_{ii}(k_w) = C\varepsilon^{2/3} k_i^{-5/3} \tag{4-23}$$

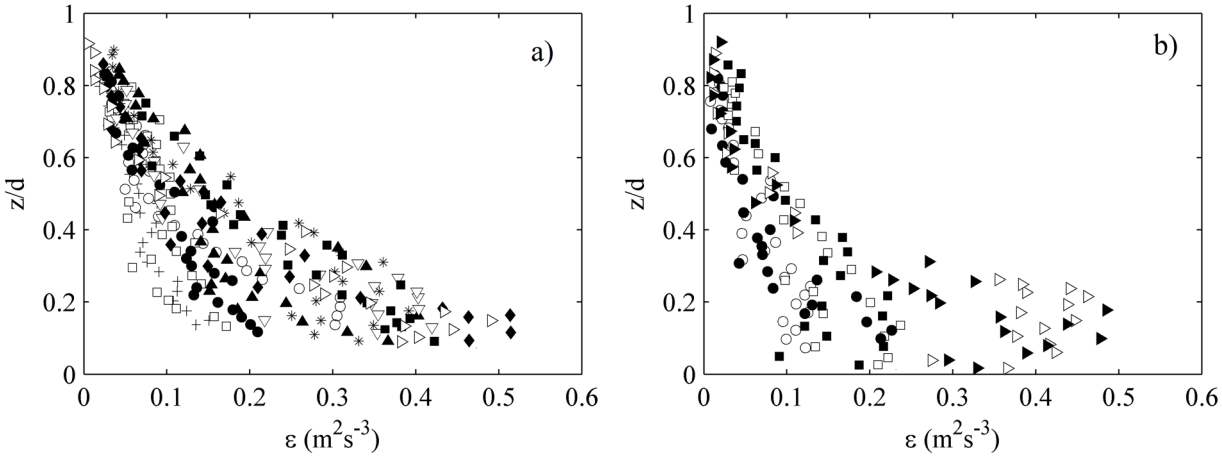

Figure 4.26- Vertical distribution of the dissipation rate obtained from spectral analysis, for the experiments (a) RG and (b) CG. *Legend (a), + RG1, ○ RG2, □ RG3, ● RG4, ▲ RG5, ▽ RG6, ∗ RG7, ♦ RG8, ■ RG9 and ▷ RG10. Legend (b), ○ CG1, ● CG2, □ CG3, ■ CG4, ▷ CG5 and ▶ CG6.*

Kolmogorov assumed that the turbulence along all scales was statistically self-similar. Therefore, the statistics are invariant of the inertial scale. The velocity increments are defined by Eq. (4-24. Therefore, the variation of velocity between two points distanced by a vector (r) depends exclusively on the modulus of r. Because of the statistical scale invariance, when r is scaled by a factor (λ) as $\Delta u(\lambda r)$, and the velocity increments are scaled with a single exponent (n), $\lambda^n \Delta u(r)$, with (n) independent of the scale (r), the statistical distribution of both expressions are the same. As a consequence of that, Kolmogorov's (1941) theory deduces that the statistical moments of the velocity increments (structure functions) must be scaled (Eq. (4-25) where the brackets denote the statistical average, and the β_p would be universal constants. Therefore, by isolating ε from the expression, a **fourth** method to calculate de dissipation rate is obtained.

$$[\Delta u(r)] = [u(x+r) - u(x)] \tag{4-24}$$

$$\langle [\Delta u(r)]^p \rangle = \beta_p (\varepsilon r)^{p/3} \tag{4-25}$$

$$\langle [\Delta u(r)]^4 \rangle / \langle [\Delta u(r)]^2 \rangle \tag{4-26}$$

In Figure 4.27-a, it is shown an example, at height z/d=0.1 of the experiment RG3, of the evolution of the dissipation rate (ε) computed by the structure functions. The three first structure functions (moments of the velocity increment) are depicted in the figure in terms of the vector (r) (distance in which is measured the velocity increment).

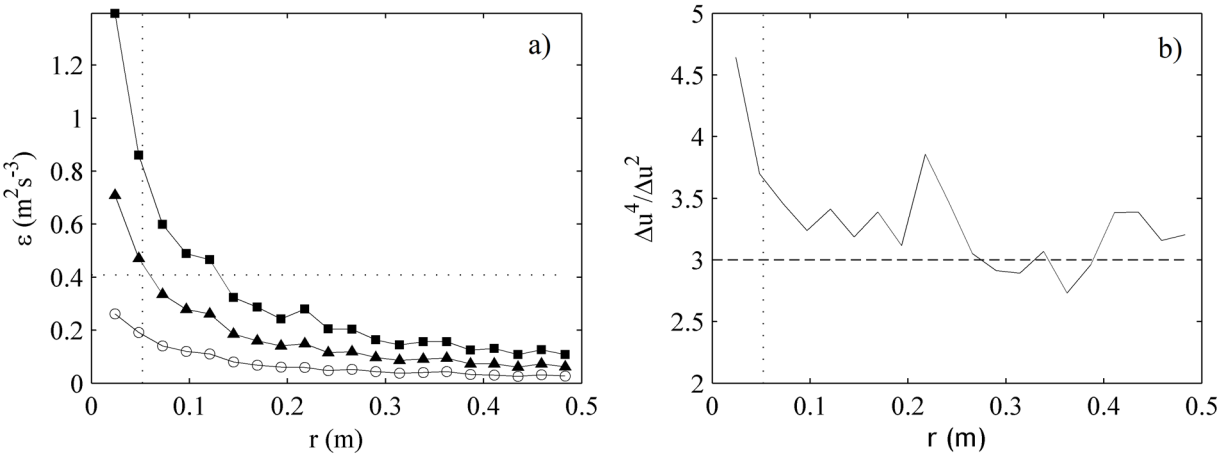

Figure 4.27- (a) Dissipation rate, obtained from the structure functions (SF) of order 2, 3 and 4, as a function of the vector (r). (b) Kurtosis factor as a function of the vector (r). Experiment RG3 at height of z/d=0.2. *Legend (a), ○ SF second-order, ▲ SF third-order and ■ SF fourth-order.*

In the figure are drawn two dashed lines, the vertical indicating the maximum r ($r<L$), the minimum is characterized by the Frequency of acquisition data FDC and the mean velocity $\bar{u}$ ($r=\bar{u}/FDC$). On the other hand, the horizontal dashed line represent the mean value of ε computing all the vector r ($r<L$) and the dissipation from the first and second order structure functions, since results from the fourth-order are not a good approximation (Davidson 2004).

Besides, in Figure 4.27-b, it is depicted the kurtosis factor (Eq. (4-26) as a function of the vector (r), in the same point as Figure 4.27-a. A kurtosis value of three denotes a Gaussian distribution of the increments. However, as it can be shown this value is reached only for large values of $r>L$, indicating that remote points are statistically independent (Davidson 2004).

As a result of the average of the ε obtained from the second and third order structure functions at each point, the vertical distribution are shown in Figure 4.28-a and Figure 4.28-b for the RG and CG experiments respectively.

The vertical distribution of the dissipation rate ε obtained for each calculation method have been overlapped in Figure 4.29. Moreover, the average ε of each experiment obtained from each calculation method has been gathered in Table 4.8, and the mean error % of each method in relation to the Channel power (W). From the results, it is obtained that all the calculation methods show the same trend of decrease as approaching to the water surface, with a maximum close to the near-bed region. In the CG experiments, it is appreciable that the value of ε maintain a constant value in the roughness layer, since in this group of experiments it was possible to be more near to the bed surface.

The closest value of ε (dissipation rate) to W (power channel), obtained at the beginning of the section, is the obtained from the last method of the structure functions.

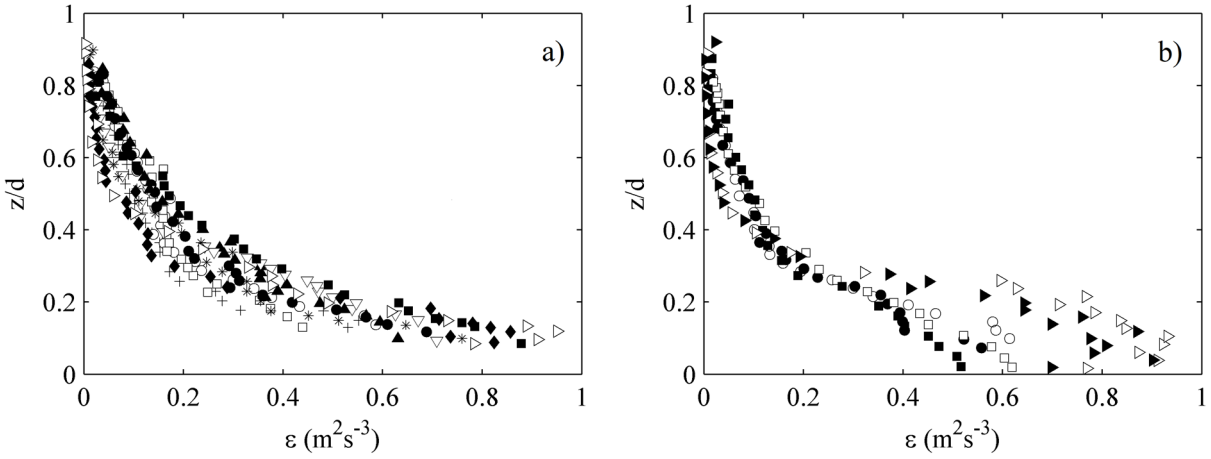

Figure 4.28- Vertical distribution of the dissipation rate obtained from the structure functions, for the experiments (a) RG and (b) CG. *Legend (a), + RG1, ○ RG2, □ RG3, ● RG4, ▲ RG5, ▽ RG6, ∗ RG7, ♦ RG8, ■ RG9 and ▷ RG10. Legend (b), ○ CG1, ● CG2, □ CG3, ■ CG4, ▷ CG5 and ► CG6.*

Table 4.8- Mean dissipation rate obtained from the different methods.

	Channel Power (W)	**Taylor**	**Dimensional Analysis**	**Power spectrum**	**Structure functions**
RG1	0,172	0,003	0,055	0,073	0,136
RG2	0,187	0,003	0,113	0,12	0,175
RG3	0,183	0,003	0,062	0,087	0,161
RG4	0,22	0,004	0,084	0,113	0,238
RG5	0,235	0,004	0,141	0,167	0,259
RG6	0,278	0,003	0,151	0,216	0,282
RG7	0,33	0,003	0,051	0,187	0,185
RG8	0,365	0,003	0,085	0,196	0,22
RG9	0,385	0,003	0,128	0,23	0,333
RG10	0,429	0,002	0,093	0,289	0,357
	error %	98,7%	62,8%	40,8%	16,7%
CG1	0,235	0,003	0,074	0,066	0,157
CG2	0,278	0,4%	8,4%	8,8%	23,0%
	error %	98,6%	69,1%	70,1%	25,2%
CG3	0,33	0,005	0,123	0,202	0,458
CG4	0,365	0,5%	7,9%	16,8%	38,8%
	error %	98,6%	70,5%	46,4%	22,5%
CG5	0,385	0,005	0,171	0,286	0,458
CG6	0,429	0,003	0,157	0,229	0,398
	error %	99,0%	59,5%	36,2%	13,1%

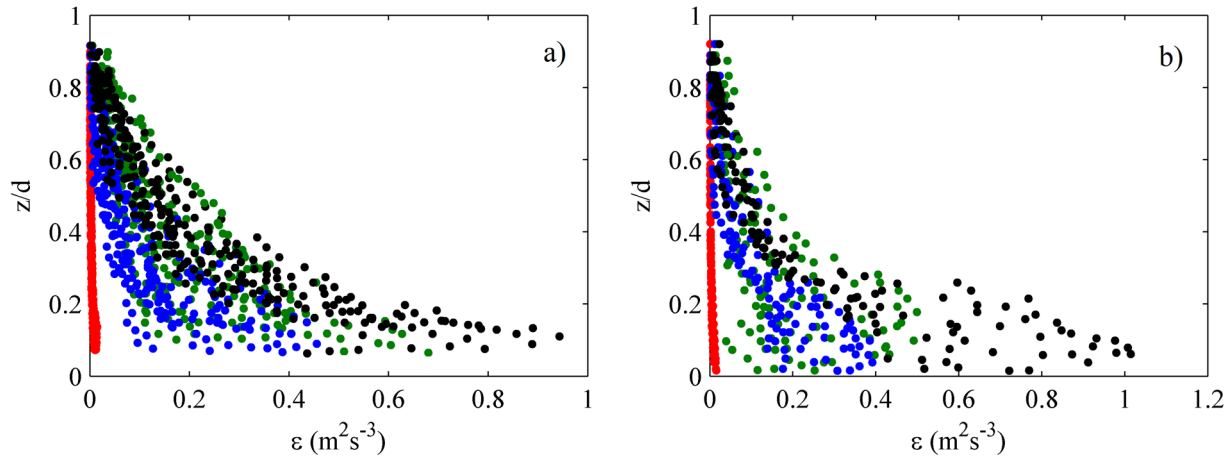

Figure 4.29- Superposition of the vertical distribution of the dissipation rate for the experiments (a) RG and (b) CG, calculated by different methods. *Legend colors,* ● *Taylor's expression,* ● *dimensional analysis,* ● *from the PSD and* ● *structure functions.*

From the exposure in this section, it is deduced that the fourth method (structure functions) is the best adjustment of the ε, in comparison with the power of the channel calculation (W). This is the method used in the calculations made in other sections of the thesis, where ε it appears, such as the ADV configuration analysis (Appendix C). In this appendix, it was shown that, by this method, an FDC of 25 Hz managed to represent well the value of ε, in comparison with W, the former being a little superior to the latter. However, in the experiments carried out in "The Cube" channel (RG and CG), it seems that ε is still smaller than W. However, it has to be taken into account, that these experiments are considerably more turbulent than those on which the configuration analysis was carried out (FRITZ experiments). Consequently, it is possible that certain sizes of eddies are not well represented, thus the dissipation obtained from the velocity series is a little lower. The velocity acquisition with a higher frequency would have yielded higher values of dissipation, as shown in the performance curves of Appendix C.

4.10 Energy cascade

Turbulent flow needs a constant supply from a source of energy for its development since it dissipates rapidly due to viscous shear stress actions transforming kinetic energy into internal energy. Different vortex sizes can be found in a turbulent flow, with the largest ones generating the most turbulent kinetic energy.

The decay of the energy cascade of Kolmogorov (an idea originally introduced by Richardson) explains how this energy passes from the large eddies to the small ones following an inertial mechanism. The instability of the large vortices causes them to break and new smaller ones arise and the kinetic energy of the first one is divided into the second ones, so on, until the energy can be dissipated by viscous dissipation (Kolmogorov microscale). This range of vortices can be described in terms of the velocity power spectra, which measures the energy of the velocity fluctuations for each eddy size.

4.10.1 Integral length scales

The energy that feeds this length scale vortex comes from the mean velocity of the flow and from the vortex themselves. That is to say, they produce and contain the most energy. Defining a characteristic length (L_i) or period (T_i) of the biggest scales in a turbulent flow is necessary in order to understand the process of energy production and dissipation in the flow. The integral scale can be defined as the measure of the longest connection or correlation distance between two points in the flow that are separated either by distance or time, time scale (T_i) and length scale (L_i) respectively. From the autocorrelation functions obtained as explained above, the integral time scale can be found by integrating the autocorrelation function, Eq. (4-27.

The velocity series *u(t)* may be converted into a simultaneous profile *u(x)* by setting $x = t \cdot \bar{u}$, assuming that the turbulence changes only little during the course of the measurement. This assumption of frozen turbulence is called Taylor's hypothesis, and allows to obtain the length scale by Eq. (4-28. The integral length scale L_i gives us an idea about the dimension of the biggest periodic elements in the data series. This is very important since it defines the scale of the biggest coherent structures.

$$T_i = \int_0^\infty R_{ii}(t) \tag{4-27}$$

$$L_i = \int_0^\infty R_{ii}\, \bar{u}(t) \tag{4-28}$$

Figure 4.30 and Figure 4.31 show the vertical distribution of the integral length scales (L_x) for the RG and CG experiments respectively. In all experiments, smaller structures are concentrated near the bed where the main dissipation takes place. Larger structures are found as we approach the water surface. These big structures, originated near the bottom, increase its size as they move upwards.

In the RG experiments, Figure 4.30 the integral scale enlarges all along the depth as the flow rate is increased; due to the high streamwise velocity elongates the structures. However, in the near-bed region, all experiments show similar length structure, because the roughness is the same, although the most powerful tests show a little increase due to the increase of the velocity near the bed and high Reynold stresses (high momentum exchange). The integral length scale is proportional to the Energy production of the big eddies, which is in accordance with the increase of the TKE and dissipation profiles.

In Figure 4.30-b, where the integral scale is defined in terms of *z*, it is observed that along the 5-6 cm near the bed the length scale is proportional to the height from the bed (*z*). The grey dashed line represents the Von Karman mixture length obtained as $L=K \cdot z$ (where ***K*** is the Von Karman constant 0.4). The slope of the length scale seems to be smaller and to adjust well, in those centimeters near the bed, to a constant value of $K'>1.2$, represented as a black dashed line in Figure 4.30-b. Figure 4.32 shows a zoom of the near-bed region for both groups of experiments to see better this effect. Therefore, it is possible that when the experiments are very turbulent, the length of the mixture is much higher; therefore, the exchange of momentum is much greater between separated flow layers, also causing the vortices to enlarge more along the profile.

The same can be perceived from the CG experiments, Figure 4.31. In the same way, the higher intensity experiments are separated from the Von Karman behavior (***K***) towards a *K'* around a height of $z/d=0.4$

or approximately 6 cm from the bed. In the case of the less turbulent tests (from CG1 to CG4), the proportionality is maintained throughout the depth. Moreover, cases where the bed is well packed (CG2, CG4, and CG6), show a slightly lower L_X close to the bed because the turbulent production is smaller, in comparison with the loose packing beds (CG1, CG3, and CG5). Consequently, the roughness is also affecting the integral scales although with a very limited effect. The fact that the diameters protrude more from the bed, there are more protuberances, implies that more turbulent structures can be generated thus producing more turbulent energy. In addition, if these protuberances are very large, although this is not the case, they can distort these structures by lengthening them due to the momentum convergence of the flow.

Regarding the effects of the configuration of the device, as shown in appendix C, it was obtained that the integral length scale was affected by the variation in the frequency of data acquisition, being decreased 20- 30% when the FDC was increased up to 100 Hz.

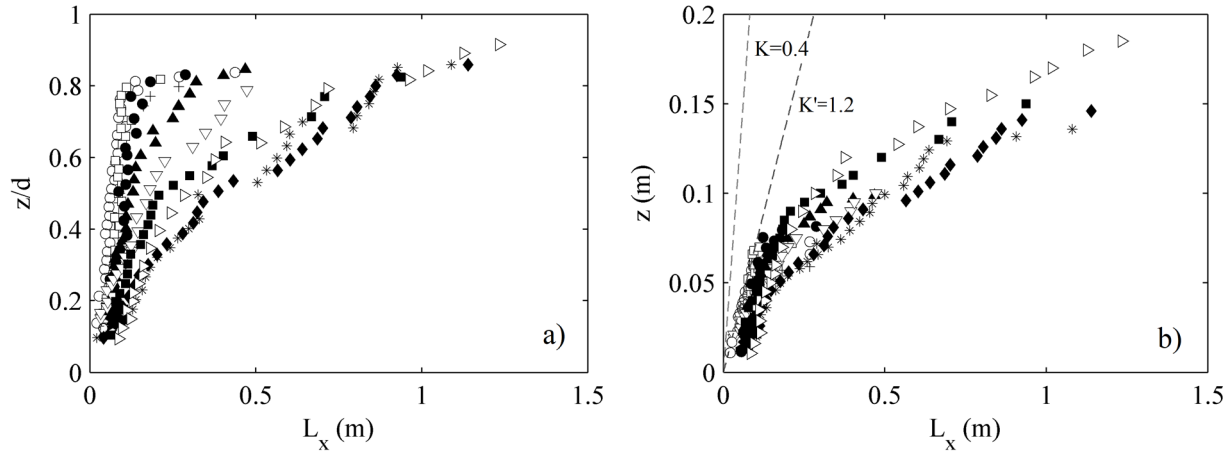

Figure 4.30- Vertical distribution of the L_X (RG experiments), as a function of the (a) *z/d* and the *z. Legend,* + *RG1,* ○ *RG2,* □ *RG3,* ● *RG4,* ▲ *RG5,* ▽ *RG6,* ∗ *RG7,* ♦ *RG8,* ■ *RG9 and* ▷ *RG10.*

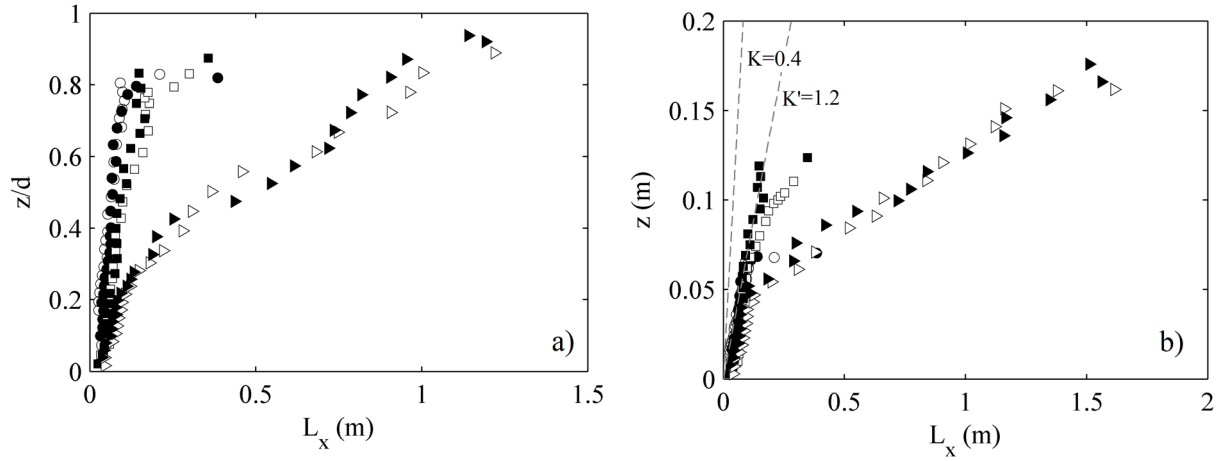

Figure 4.31- Vertical distribution of the L_X (CG experiments), as a function of the (a) *z/d* and the *z. Legend,* ○ *CG1,* ● *CG2,* □ *CG3,* ■ *CG4,* ▷ *CG5 and* ► *CG6.*

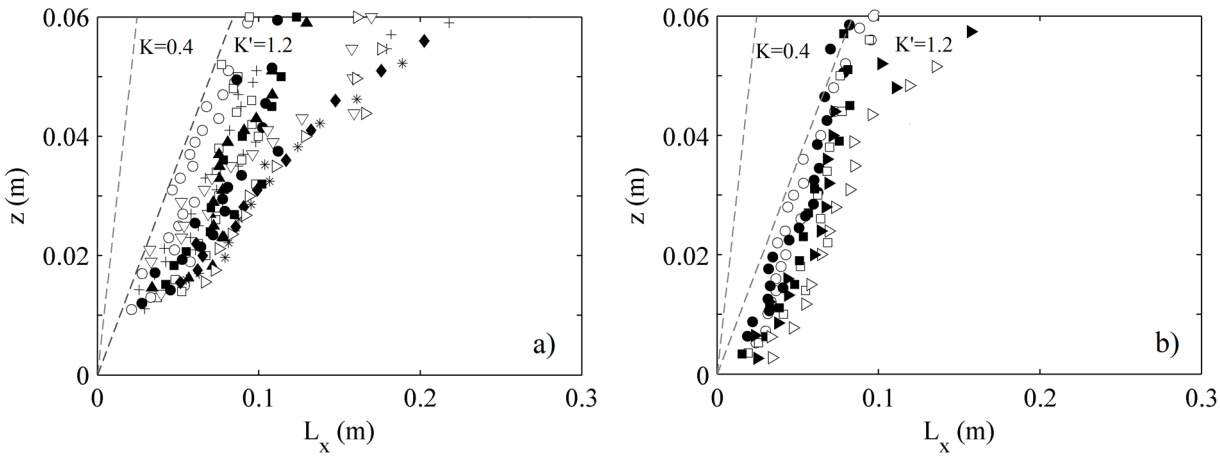

Figure 4.32- Zoom of the L_X vertical distribution of the (a) RG and (b) CG experiments, as a function of the depth. *Legend (a),* + *RG1,* ○ *RG2,* □ *RG3,* ● *RG4,* ▲ *RG5,* ▽ *RG6,* ∗ *RG7,* ♦ *RG8,* ■ *RG9 and* ▷ *RG10. Legend (b),* ○ *CG1,* ● *CG2,* □ *CG3,* ■ *CG4,* ▷ *CG5 and* ▶ *CG6.*

4.10.2 Taylor microscales

In the middle of the integral scale and the micro-scale of Kolmogorov, there is the intermediate scale or Taylor microscale, which form the inertial range. In the inertial range, the energy is transmitted from the large scales to the small ones without there being dissipation. Within this range, inertial effects are still much larger than viscous effects, and it is possible to assume that viscosity does not play a role in their internal dynamics. These microscales are important because of their fundamental role in the transfer of energy and momentum in the space of wave numbers. The characteristic length scale of Taylor (λ) can be computed by Eq. (4-29 and (4-30, Pope (2000).

$$\lambda = (10 \cdot \nu \cdot TKE/\mathcal{E})^{1/2} \tag{4-29}$$

$$\lambda = (15 \cdot \nu \cdot u^2/\mathcal{E})^{1/2} \tag{4-30}$$

In the next figures (Figure 4.33 and Figure 4.34), the Taylor microscale distribution along the depth (z) and dimensionless depth (*z/d*) are shown for the two groups of experiments, RG and CG.

All the experiments show the same trend of Taylor length scale, increasing towards the water surface, as it was seen for the integral scale. Near the bed, all the profiles show a very similar size, with fewer differences than in the case of the integral scale, showing that this scale is less susceptible to the streamwise velocity. In the same way, it is observed that the differences in the profile are much lower. That is, Taylor's inertial scale, despite also depending on the momentum flux, is a more robust value than the integral scale. The values of all the lower flow rate experiments collapse better in a line along the dimensionless depth, being thus closely linked to that value.

As in the case of the integral length scale, the Taylor scale can be affected by the FDC of the device up to 20-40%.

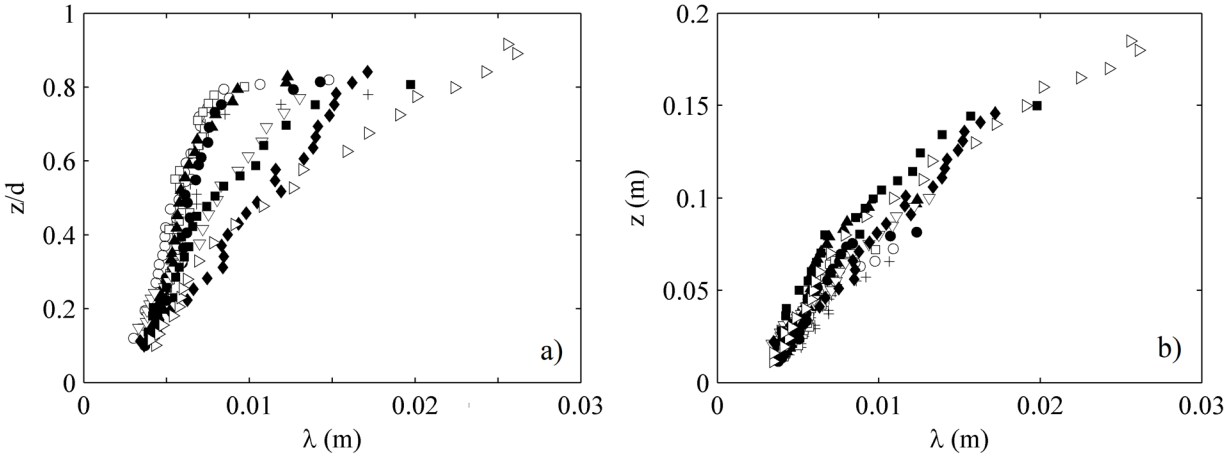

Figure 4.33- Vertical distribution of Taylor's scale of the RG experiments, as a function of the dimensionless depth (a) and the depth (b). *Legend, + RG1, ○ RG2, □ RG3, ● RG4, ▲ RG5, ▽ RG6, ∗ RG7, ♦ RG8, ■ RG9 and ▷ RG10.*

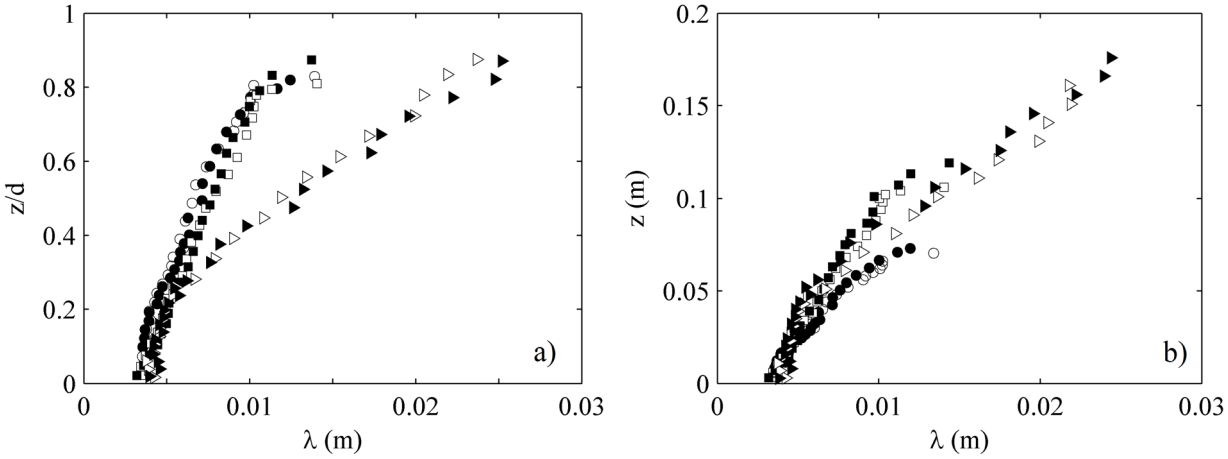

Figure 4.34- Vertical distribution of Taylor's scale of the CG experiments, as a function of the dimensionless depth (a) and the depth (b). *Legend, ○ CG1, ● CG2, □ CG3, ■ CG4, ▷ CG5 and ► CG6.*

4.10.3 Kolmogorov length scales

The Kolmogorov microscale (η) is the smallest scale in the range, occupying what is called viscous sub-layer range, where the viscous dissipation of energy and the energy obtained from bigger scales are in balance. The small scales have high frequency, causing turbulence to be locally isotropic and homogeneous. The Reynold's number of this scale is the unity. The Kolmogorov micro scales are the scales at which the smallest turbulent motion exists before they are dissipated by viscous effects. Observing that these small-scale motions have very small time scales, it can be assumed that these motions are statistically independent of the large-scale turbulence, which has a long turnover time.

Kolmogorov (1941) assumed that at sufficiently high Reynolds numbers the flow is locally homogeneous and isotropic and to be statistically in equilibrium in this range of high wave numbers. Kolmogorov stated that the small scales should only be dependent on the energy supplied from the large scales and the viscosity, but the supplied energy must equal the dissipated energy and therefore the small scales are a function of dissipation and viscosity. Kolmogorov stated that for very high Reynolds numbers, the statistics of small scales are determined by the kinematic viscosity v and the

energy dissipation rate ε. By means of dimensional analysis, a characteristic length scale η for the viscous eddies can then be defined by Eq. (4-31, Pope (2000).

$$\eta = (\nu^3/\mathcal{E})^{1/4} \tag{4-31}$$

Figure 4.35 and Figure 4.36 depict the vertical distribution of the Kolmogorov's length scale η (calculated with ε obtained by the structure functions method) from the RG and CG experiments respectively. Besides, it is depicted (dashed line) the theoretical value found by considering that the dissipation rate is equal to the power of the channel, that is to say, $\varepsilon=W$. This value is represented as a constant in the depth profile since W is a constant value for each experiment.

It is noticeable how the distribution of $(\eta(\varepsilon))$ reaches similar values than $(\eta(W))$, being both values almost coincident at a height of z/d=0.35. The Kolmogorov scale shows a small change of pattern with respect to the two previous ones; in this case, it is the experiments with a higher flow rate (and therefore greater depth, higher velocity, and bed shear stress) those which present smaller scales. This makes sense since near the bed there is more energy production, therefore the dissipation must also be high. Since it is the smaller vortices of the Kolmogorov scale that are responsible for dissipating this energy by viscosity, they decrease in size for high streamwise velocities.

However, this scale increases as well with the height (z) in the profile, thus higher hydraulic depth (d) manage to achieve higher η along the depth profile. Therefore, this scale is also related to the depth and the distance to the bed. On the other hand, the influence of the packing density is almost imperceptible, although the scale lengths very close to the bed z<2 cm shows values around 7% higher in the case of the leveled beds.

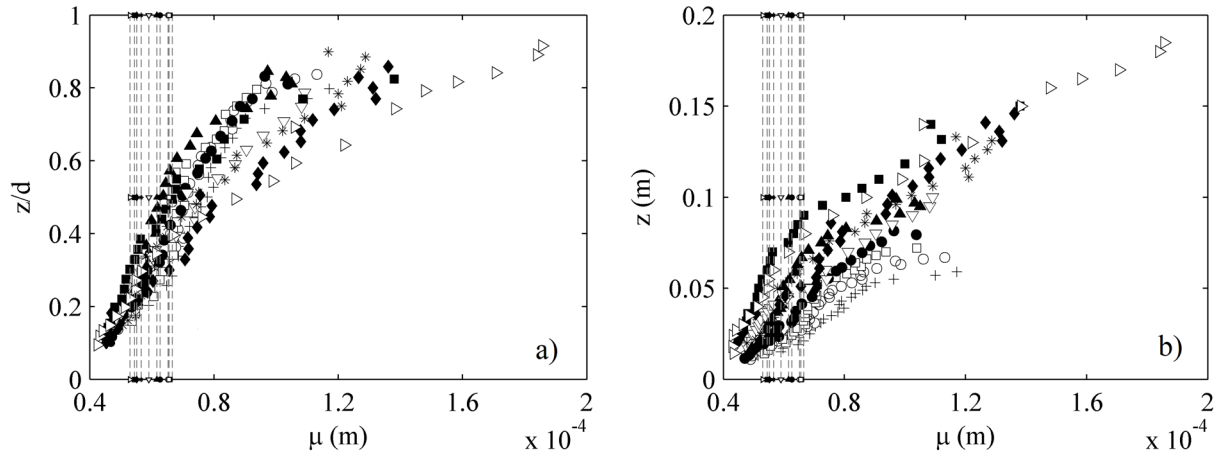

Figure 4.35- Vertical distribution of the Kolmogorov's scale of the RG experiments, as a function of the dimensionless depth (a) and the depth (b). *Legend, + RG1, ○ RG2, □ RG3, ● RG4, ▲ RG5, ▽ RG6, ∗ RG7, ♦ RG8, ■ RG9 and ▷ RG10.*

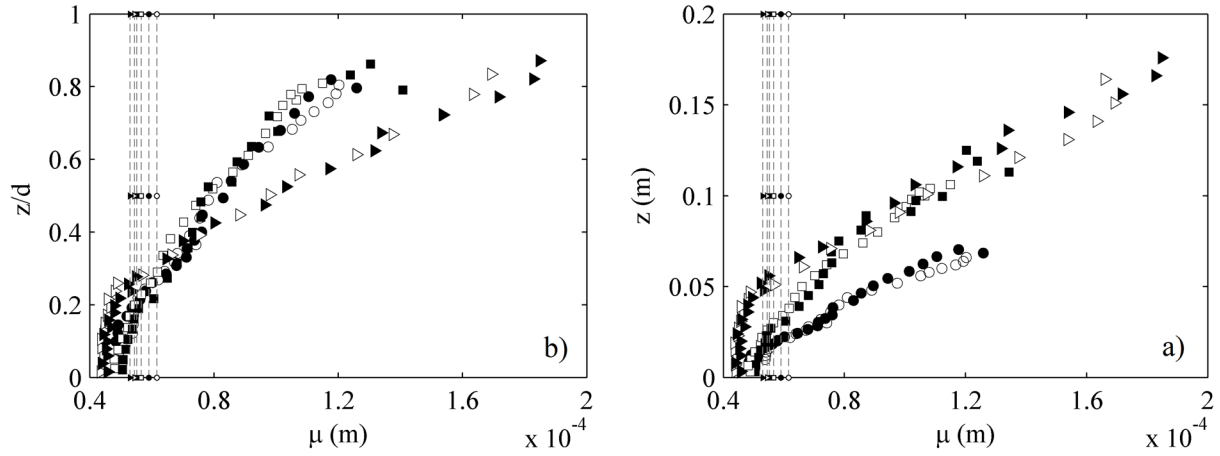

Figure 4.36- Vertical distribution of the Kolmogorov's scale of the CG experiments, as a function of the dimensionless depth (a) and the depth (b). *Legend, ○ CG1, ● CG2, □ CG3, ■ CG4, ▷ CG5 and ► CG6.*

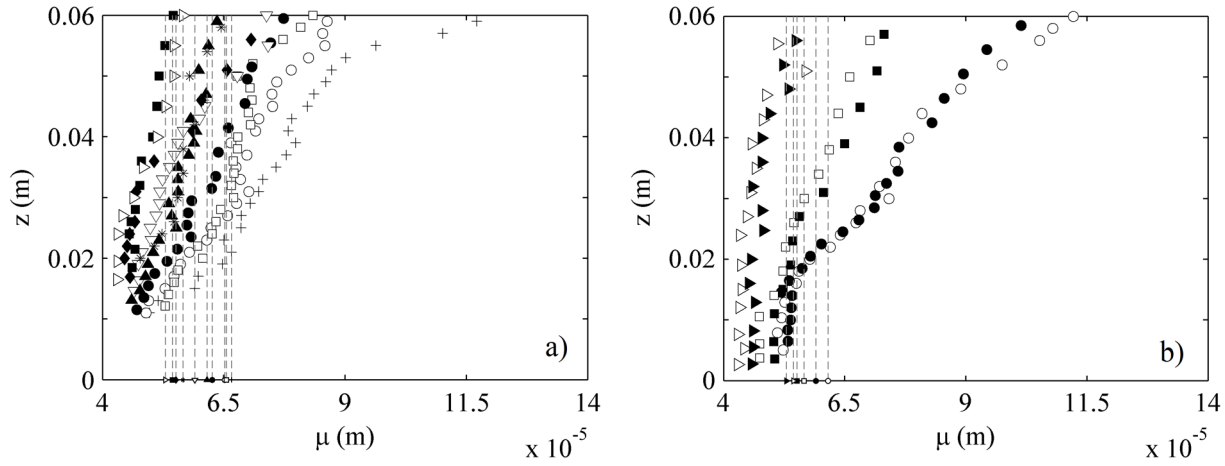

Figure 4.37- Zoom of the η vertical distribution of the (a) RG and (b) CG experiments, as a function of the depth. *Legend (a), + RG1, ○ RG2, □ RG3, ● RG4, ▲ RG5, ▽ RG6, ∗ RG7, ♦ RG8, ■ RG9 and ▷ RG10. Legend (b), ○ CG1, ● CG2, □ CG3, ■ CG4, ▷ CG5 and ► CG6.*

As in the two previous scales, the Kolmogorov length scale is affected by the configuration of the ADV, increasing its value (η) by reducing the extreme peaks of velocity, by reducing the FDC, and increasing the CV. However, the elongation of the η occurs more notably than in the previous cases, because it is the scales of smaller size which are more affected, that are better or worse represented in the data series depending on the configuration of the device (Appendix C).

Chapter 5: Coherent Structures and Quadrant Analysis

5.1 Introduction

5.1.1 Coherent Structures

In open channel flows, turbulence structure is chaotic, consisting of a large range of different vortex sizes and length scales. The goal of studying the internal structure of turbulence is to understand how the boundary layer is produced from the mean velocity, thus from coherent motions, and its dissipation. However, this issue for highly turbulent flows in rough beds becomes more complicated, where the range of turbulence length scales is larger. The flow structure in a highly turbulent flow remains not deeply yet comprehended due to the complexity and stochastic nature of the phenomena.

Richardson (1922) stated that the fully developed turbulence consists of a hierarchy of eddies, ''*Big whirls have little whirls, which feed on their velocity; and little whirls have lesser whirls, and so on to viscosity…*''. A coherent motion, or coherent structure, can be thought as a three-dimensional region of the flow where at least one fundamental flow variable shows substantial correlation with itself or with another variable over a range of space and/or time that is considerably greater than the lowest local scales of the flow (e.g. Robinson 1991; Adrian 2007).

Experimental measurements demonstrate that is possible to decompose complex, multiscaled, quasi-random flow fields into elementary organized structures that show both spatial and temporal coherence that has been termed either eddy (Adrian 2007), coherent flow structure (Cantwell 1981) or turbulent burst (Mujal-Colilles et al. 2016). This organization becomes apparent even for averaged properties such as Reynold stress ($-\rho u'w'$), that as seen earlier is the most important closure term in the RANS equation (chapter 4, section 4.7), which would have a zero value if the turbulent motions in the boundary layer behaved randomly without correlation between velocity components. The existence of these organized motions it is supported by the TKE production in the near-bed region (turbulent bursts have higher values of TKE at the leading edge of the turbulent burst (Mujal-Colilles et al. 2016), and are responsible for the turbulent dissipation. This turbulent production in the near-bed region occurs during intermittent, quasi-cyclic sequence of bursting cycles of ejections and sweeps, thus low-speed fluid ejected away from the bed and inrushes of high-speed fluid towards the bed.

In highly turbulent flows with high effective roughness, i.e. height crests, field and experimental velocity measurements evidence that the micrography of the bed has a significant influence on the cycle of coherent structures (generation, evolution, and dissipation) (e.g. Wiberg & Smith 1991; Kirkbride 1993; Roy et al. 2004; Hardy et al. 2007 and 2009; Mujal-Colilles et al. 2016). This implies that the bed roughness is tied closely to the initiation and transport of sediment, Hardy (2005). The studies where visualization was done, in addition to quantitative measurements, demonstrate that the size development of these structures is proportional to the flow depth (Roy et al. 2004), Reynolds number (Shvidchenko & Pender 2001; Hardy et al. 2009), and bed roughness (Shvidchenko & Pender 2001; Buffin-Bélanger & Roy 1998; Mujal-Colilles et al. 2016).

A better understanding of these motions would be an essential key to aid predictive models of turbulent characteristics and to improve probability density functions of instantaneous velocity.

5.1.2 Quadrant Analysis

With the aim of defining the coherent structures in a different way, and from the interest of knowing the mechanism of generation of the Reynolds stress, appears the analysis of quadrants, becoming a fundamental tool to characterize and predict the effects of turbulence.

The idea of quadrant analysis arises from Kline et al. (1967). In their study, small bubbles of hydrogen, used as markers, showed that the flow near-wall was organized in narrow streaks of high and low-moment fluid elongated in the streamwise direction. Streaks of low-momentum emerged intermittently away from the wall, where the bubbles accumulated, in a semi-chaotic process. As a conclusion, they found that the coherent structures of turbulent flows are quasi-periodic structures known as quadrant events and comprises four different events, according to the quadrant turbulent map (four quadrants). They assumed that these events, thus coherent structures of turbulent flow, are responsible for the momentum transfer into the turbulent boundary layer.

Corino & Brodkey (1969) observed that these events were not random. The decelerated flow was erupted away from the wall region (ejections), and was followed by large-scale motions towards the wall, called sweeps. The whole cycle is termed bursting turbulence by Kim et al. (1971), that found that almost all TKE near the wall occurred during these burst intervals. These bursting processes seemed to produce much of the vertical transport of momentum thus generating Reynolds stress and TKE in this layer. Kim et al. (1971) discovered that the turbulent energy and Reynolds stress were generated by bursting motions, especially ejections and sweeps. More precisely, they found that the ejections accounted for approximately 70% of the Reynolds shear stress despite representing a time fraction of 18%.

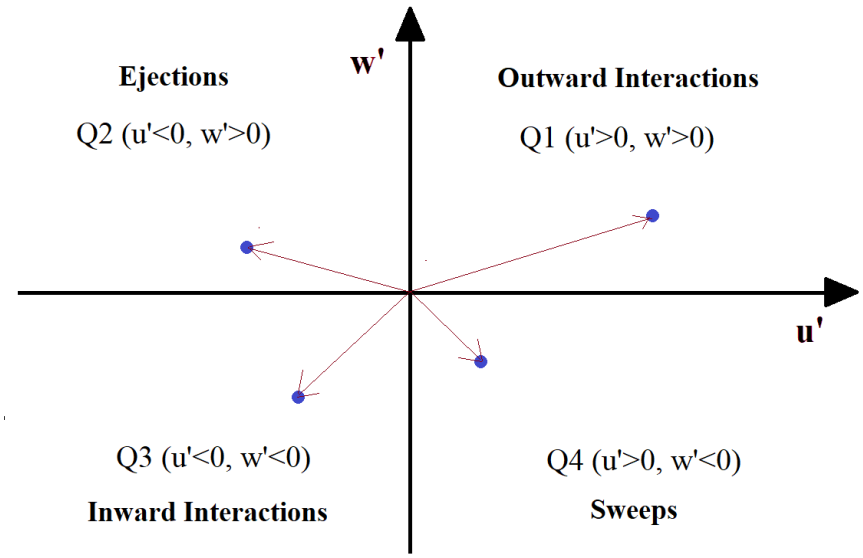

Figure 5.1- Quadrant Map, or turbulent map, defined by Wallace et al. (1972).

Wallace et al. (1972) ideated the first quadrant analysis of the Reynolds shear stress in order to evaluate the observations from Corino & Brodkey (1969). They divided the burst events (pairs of instantaneous velocities u'w') into four quadrants, 1st quadrant 'Q1' ($u'>0$, $w'>0$) named outward interactions, 2nd quadrant 'Q2' ($u'<0$, $w'>0$) called ejections, 3rd quadrant 'Q3' ($u'<0$, $w'<0$) named inward interactions and the 4th quadrant 'Q4' ($u'>0$, $w'<0$) named as sweeps, Figure 5.1. They observed, from the results

of Corino & Brodkey (1969), that the Q2 and Q4 motions were clearly related to the ejection and sweep events. They named the Q1 and Q3 motions outward and inward interactions, for the sake of simplicity. The representation of the *u'w'* pair in quadrants is also called turbulent velocity maps or turbulent maps.

5.2 Turbulent maps

Figure 5.2 shows an example of the turbulent maps obtained from the experiment RG1 at different heights in the profile. It is noticeable that the major axis of the turbulent map is inclined in the direction of Q2 and Q4 (red line), thus there is a correlation between *u'* and *w'* in all points. That correlation can be obtained from $cor(u'w') = cov(u'w')/(\sigma_u \sigma_w)$ and the covariance as $cov(u'w') = \sum u'_i w'_i/N$. Notice that then the Reynold stress can be obtained from the covariance of u'w' as $\tau_{RE} = -\rho\, cov(u'w') = -\sum u'_i w'_i/N$. As a result, that correlation is related to the Reynold stress. There is a relation between the regression line of the turbulent velocity maps and the covariance value (Reynold stress), thus the slope of the line ($m = cov(u'w')/\sigma_u{}^2$) tell us about the Reynold stress.

The results are in accordance with the Reynold stress profile obtained in chapter 4 (section 4.7). The slope of the line (covariance) becomes steeper in the region near the bed with a maximum at height of *z/d*=0.3. From that point to the water surface the value starts to decrease progressively. For the sake of brevity, no more information about turbulent maps is provided here since it results redundant.

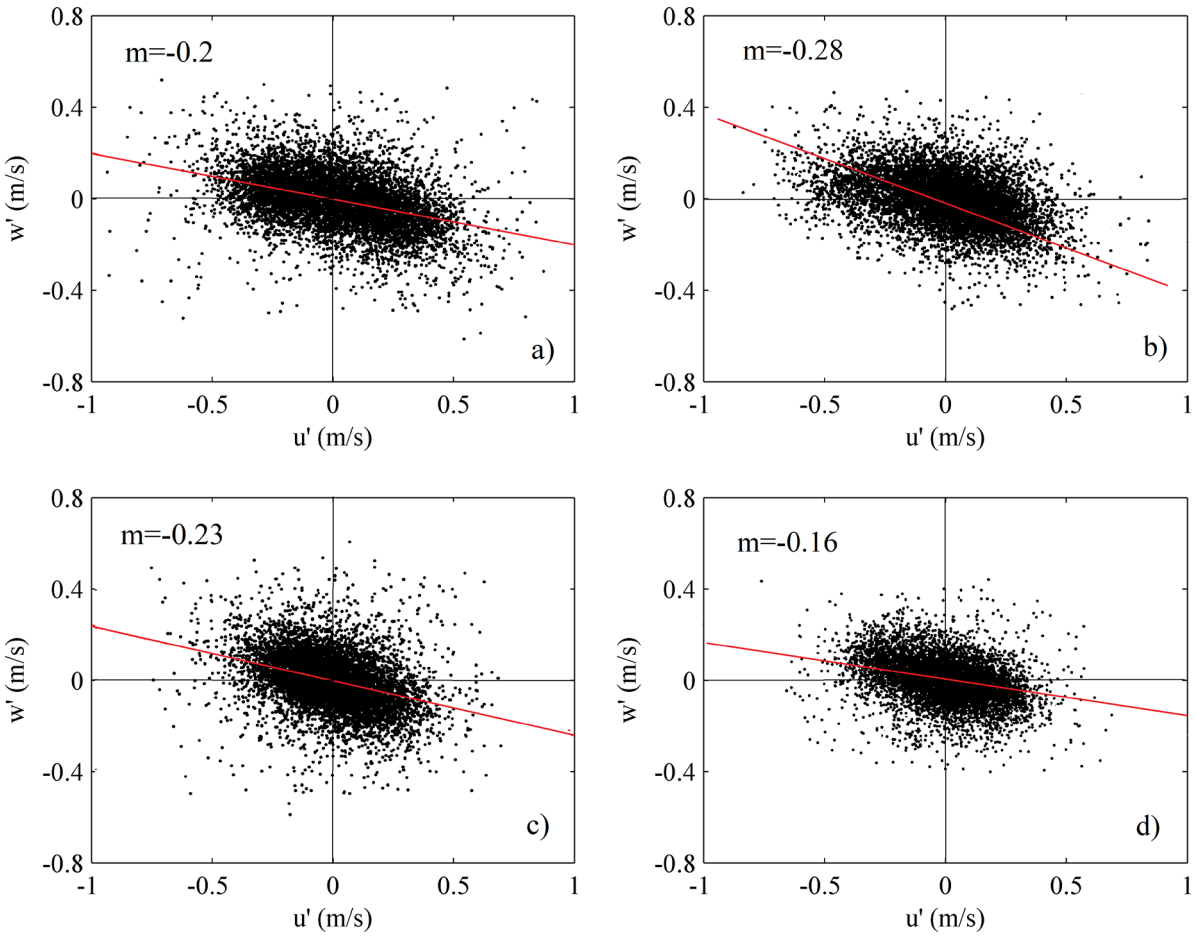

Figure 5.2- Turbulent maps from tests RG1 for points (a) z/d=0.12, (b) z/d=0.18, (c) z/d=0.3 and (d) z/d=0.57.

5.2.1 Trajectories of the events on the turbulent velocity maps

The succession of events (or trajectory) on the turbulent map has been investigated by observing its evolution in time. With this purpose, time intervals of 0.48 seconds ($12\Delta t$ with Δt=1/FDC=0.04 sec) have been represented on the map (u', w'). Figure 5.3 shows an example of these trajectories from a point located at z=0.5 mm (test RG1), the trajectories are divided into periods of $12\Delta t$. It is noticeable that the movements between quadrants seemed to follow a clockwise pattern through the conventional quadrants, also obtained by Ferguson et al. (1996). The trajectories of the quadrant events are deeper studied throughout the present chapter.

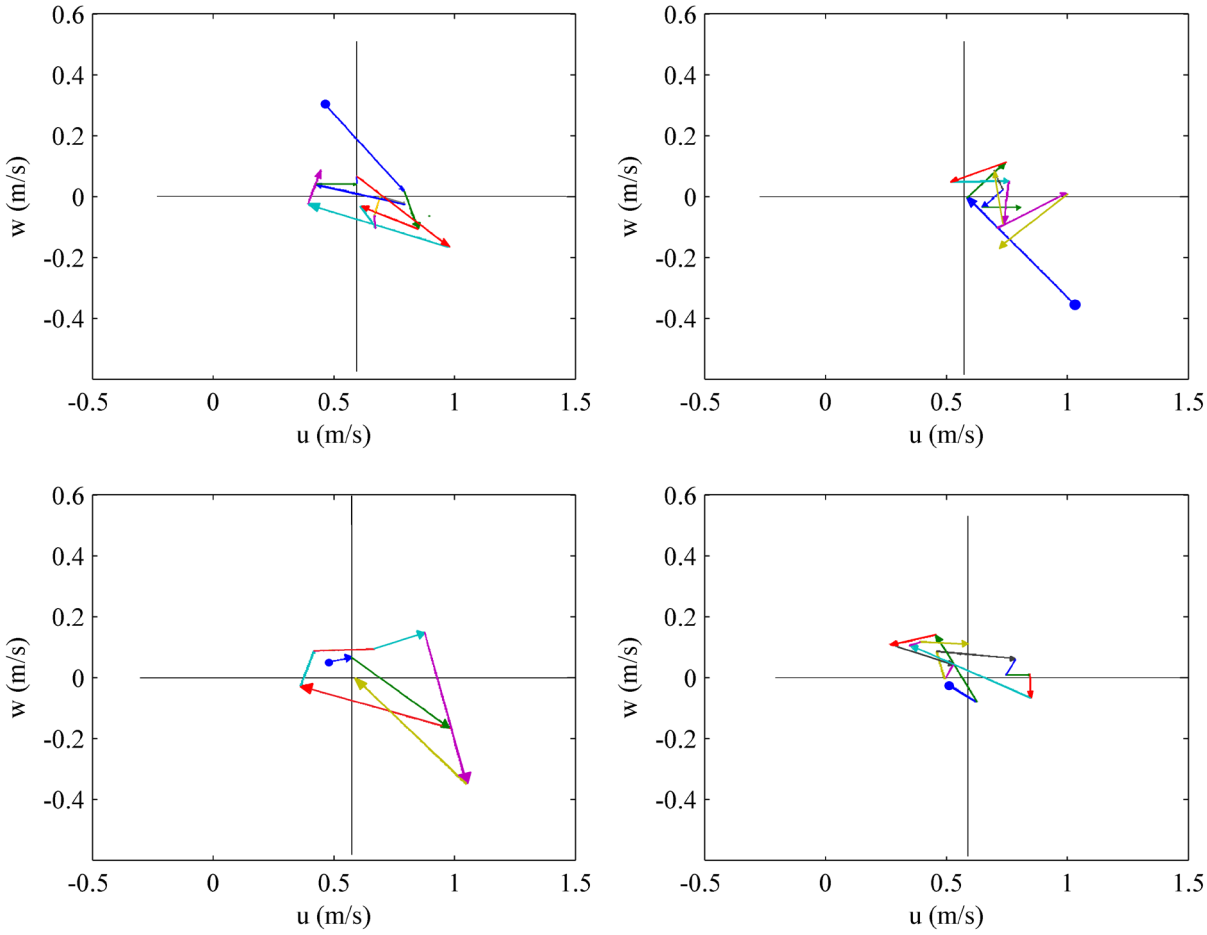

Figure 5.3- Turbulent maps (u, w) by frames of 0.48 seconds RG1 at z=0.5 mm.

5.3 Quadrant time fraction

Cycles of "sweeps" and "ejections" are quite stable regardless the bed surface, that is the fraction of events in smooth and rough surfaces are quite similar (Clifford et al. 1991, Grass et al. 1991). However, the mechanisms that generate these events are very different, in the case of smooth bed cycles "sweeps" are conditioned laminar retarding and organizes the sublayer, while in the rough case is the roughness who generates these cycles.

The vertical distribution of the time fraction (TF) of each quadrant, or quadrant time fraction (QTF) (decimal fraction) from all tests are depicted in Figure 5.4 and Figure 5.5 for the RG and CG experiments respectively, represented as a function of the (a) z and (b) z/d. Notice that in these figures,

there is no distinction between experiments, but the different QTFs have been differentiated by colors, Q1-TF (blue), Q2-TF (green), Q3-TF (red), and Q4-TF (black).

Quadrants Q1 and Q3, that is to say, outward and inward interactions, are the least likely quadrant-event in the depth profile, and both show a similar evolution along the column water (d). Moreover, both quadrants show a minimum value of their time fraction close to the bed, and from that point increase its presence in the data series by increasing the distance to the bed (z), reaching a maximum within the roughness layer. This maximum value, for the Outward (Q1-TF), is given approximately at the height of z/d=0.2, while for the inward interactions (Q3-TF) it seems to be a little higher around z/d=0.25. From this inflection point up, both events reduce their presence in the sample until reaching a minimum value in the depth profile, another inflection point, located in this case approximately at height of z/d=0.35. From this point, the Q1 events increase their TF in the data series again reaching a maximum value, with similar value to that which occurred in near the bed, very close to the water surface, denoting the effect of the water surface on turbulence. In the case of the Q3-TF (inward interactions), from that minimum value of inflection to the height z/d=0.35, the value remains rather constant in the upper half of the profile towards the surface. The last points, closer to the water surface, again have a decrease in the TF; however, as mentioned before, these drastic variations in the data are due, the most of the cases, to the disturbance of the control volume by the water surface or bubbles and therefore cannot be considered to have important veracity.

In the case of events Q2 and Q4, ejections and sweeps respectively, evolve in a manner contrary to the other two within the roughness layer. The sweep TF (Q4-TF) is a little lower than the ejections (Q2-TF) only close to the bed surface, but then it shows a maximum value around height z/d=0.15, within the roughness layer. From this height up, the TF decreases in the flow to reach a minimum at a height of z/d=0.3, from which it increases again its presence in the flow to dominate the events up to the water surface. In the case of the ejections, the Q2-TF profile shows a maximum value near the roughness surface and its value decreases until it reaches a minimum at height of approximately z/d=0.2. From this point and up to a height of z/d=0.4, the Q4-TF (sweeps) and Q2-TF (ejections) are very similar, however, above that point, the Q2-TF begin to decrease until obtaining its minimum value near the water surface.

The fact that Q2-TF is greater near the bed is due to the roughness ejecting streaks of low-momentum, as the distance to the bed (z) is increased the effect of the surface decreases, and the $\overline{u}$ increases that produces a pushing of the vertical velocities downwards, generating an increase of Q4-TF.

In the figures below, a behavior change in the QTF can be observed between the range $0.2<z/d<0.4$., where quadrant tendencies are reversed, Q2-TF>Q4-TF and Q3-T>Q1-TF in $z/d<0.2$ and Q2-TF<Q4-TF and Q3-T<Q1-TF in $z/d>0.4$. From z/d=0.4 all QTFs tend to 0.25, except the Q4-TF that despite decreasing in the last zone $z/d>0.7$ fails to reach 0.25. Therefore, far from the bed, it seems that the quadrants tend to equalize, which reflects the lack of correlation in the quadrant map and consequent decrease of the Reynolds stress. This decrease in correlation can also be interpreted as vortices, in addition to increasing in size with increasing z, also become more rounded, thus losing its ability to transport kinetic energy, but maintaining its dissipative capacity. It has to be pointed out that the log-velocity profile theory predicts that from z/d = 0.4 the profile stops behaving logarithmically.

According to Hardy et al. (2009), turbulent flows moving over a gravel bed develop large-scale, macroturbulent flow structures that are initiated at the bed, and grow and dissipate as they move upward through the flow depth. These large-scale flow structures change their form and magnitude at higher Reynolds numbers, becoming more distinct, with a clearer velocity.

It can be deduced from the trends of the quadrant patterns, that the near-bed turbulence is characterized by $u'<0$ since Q2-TF>Q4-TF and Q3-TF>Q1-TF (Figure 5.4 and Figure 5.5). On the other hand, along with the length scales analyzed in chapter 4, it suggests that the smallest length scales are also related to this quadrant distribution. This is in agreement with the observed in Appendix C, section C.6, where it was obtained that for ADV configurations allowing more accuracy and thus more representation to the SCS, such as high FDC and/or small CV, the Q4-TF is decreased at expenses of the Q1-TF and Q3-TF inside and outside the roughness region respectively.

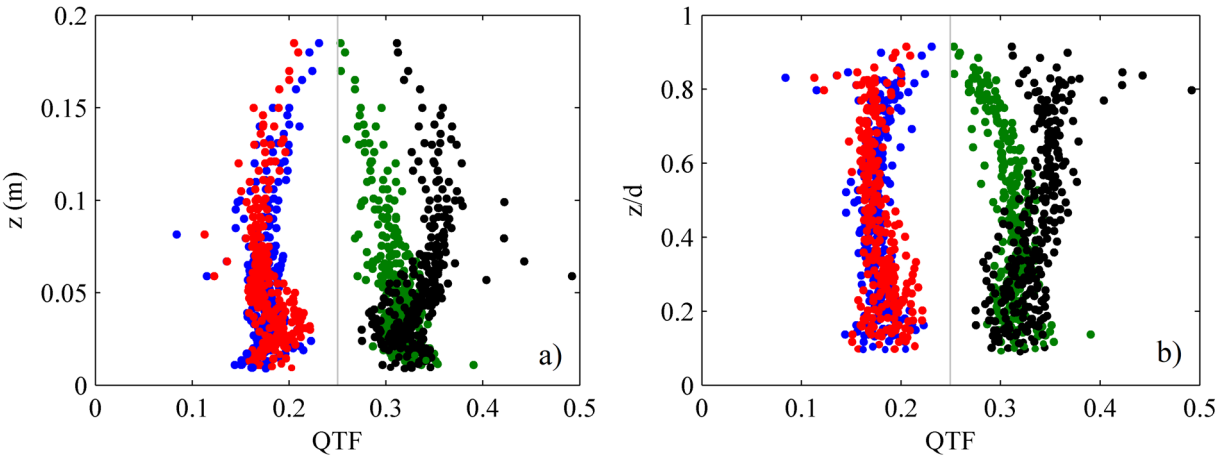

Figure 5.4- QTF vertical distribution of (RG tests) as a function of (a) the z (m) and (b) the z/d. *Legend,* ● *Q1-TF,* ● *Q2-TF,* ● *Q3-TF, and* ● *Q4-TF.*

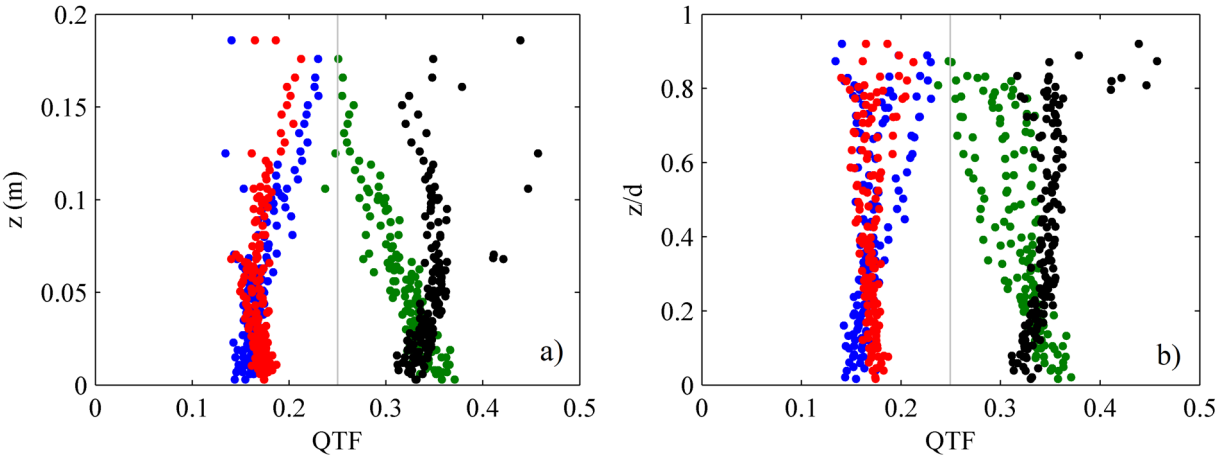

Figure 5.5- QTF vertical distribution of (CG tests) as a function of (a) the z (m) and (b) the z/d. *Legend,* ● *Q1-TF,* ● *Q2-TF,* ● *Q3-TF, and* ● *Q4-TF.*

It has become clear that the most frequent events along the profile are the sweeps (Q4), which increase their presence at the expense of the others, especially in the upper half of the profile. Within the roughness region, however, sweeps and ejections are directly proportional to the outward and inward interactions. Therefore, it seems that the turbulent energy production is linked to events Q4 and Q2

since these predominate in the bed. Other studies have also revealed that Q2 and Q4 events are the dominant ones in rough bed channels (Nasiri *et al.* 2011, Nezu *et al.* 1994, Thorne *et al.* 1989).

The mean (QTF) of each experiment is shown in Table 5.1. Besides, in Figure 5.6, the depth-averaged value of each experiment is represented as a function of the total water depth (d) of each test. That is to say, the figure is not a vertical distribution but the mean QTF of each experiment as a function of d. As a result, it is noticeable that the depth-averaged QTF remains very constant regardless the d of the experiment, with a slight increase of the Q1-TF and Q3-TF as the water depth increase, at expenses of the decrease of the other two. This makes sense since if d is bigger, the vortices have more travel distance and manage to round themselves more than for a low d.

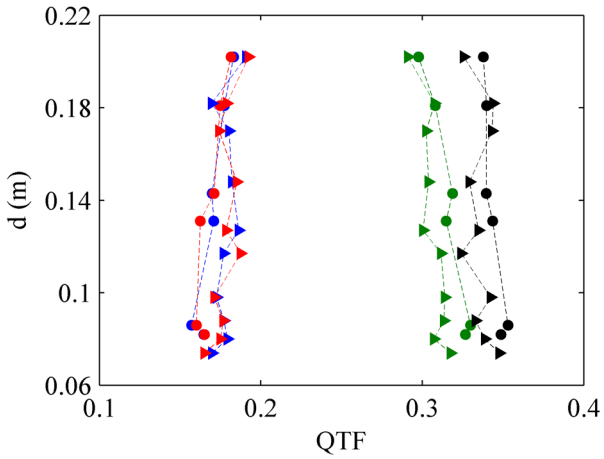

Figure 5.6- Depth-averaged QTFs of the RG and CG experiments as a function of the *d*. *Legend Markers, ○ RG, and ▷ CG. Legend Colors,* ● *Q1-TF,* ● *Q2-TF,* ● *Q3-TF, and* ● *Q4-TF.*

Table 5.1 Depth-averaged QTFs

TEST	Q1	Q2	Q3	Q4
RG1	0,170	0,317	0,165	0,348
RG2	0,179	0,307	0,175	0,339
RG3	0,177	0,313	0,177	0,333
RG4	0,173	0,314	0,171	0,342
RG5	0,177	0,311	0,188	0,324
RG6	0,186	0,300	0,179	0,335
RG7	0,182	0,304	0,185	0,329
RG8	0,180	0,303	0,174	0,343
RG9	0,170	0,308	0,179	0,344
RG10	0,191	0,291	0,192	0,326
MEAN	0,178	0,307	0,178	0,336
CG1	0,165	0,327	0,165	0,344
CG2	0,157	0,330	0,160	0,353
CG3	0,178	0,305	0,163	0,353
CG4	0,169	0,324	0,178	0,330
CG5	0,177	0,308	0,175	0,340
CG6	0,183	0,298	0,181	0,338
MEAN	0,172	0,315	0,170	0,343

On the other hand, QTFs of each experiment are illustrated in Figure 5.7 and Figure 5.8, RG and CG experiments respectively, where each quadrant is isolated in a different figure so that trends between experiments in the same quadrant could be interpreted.

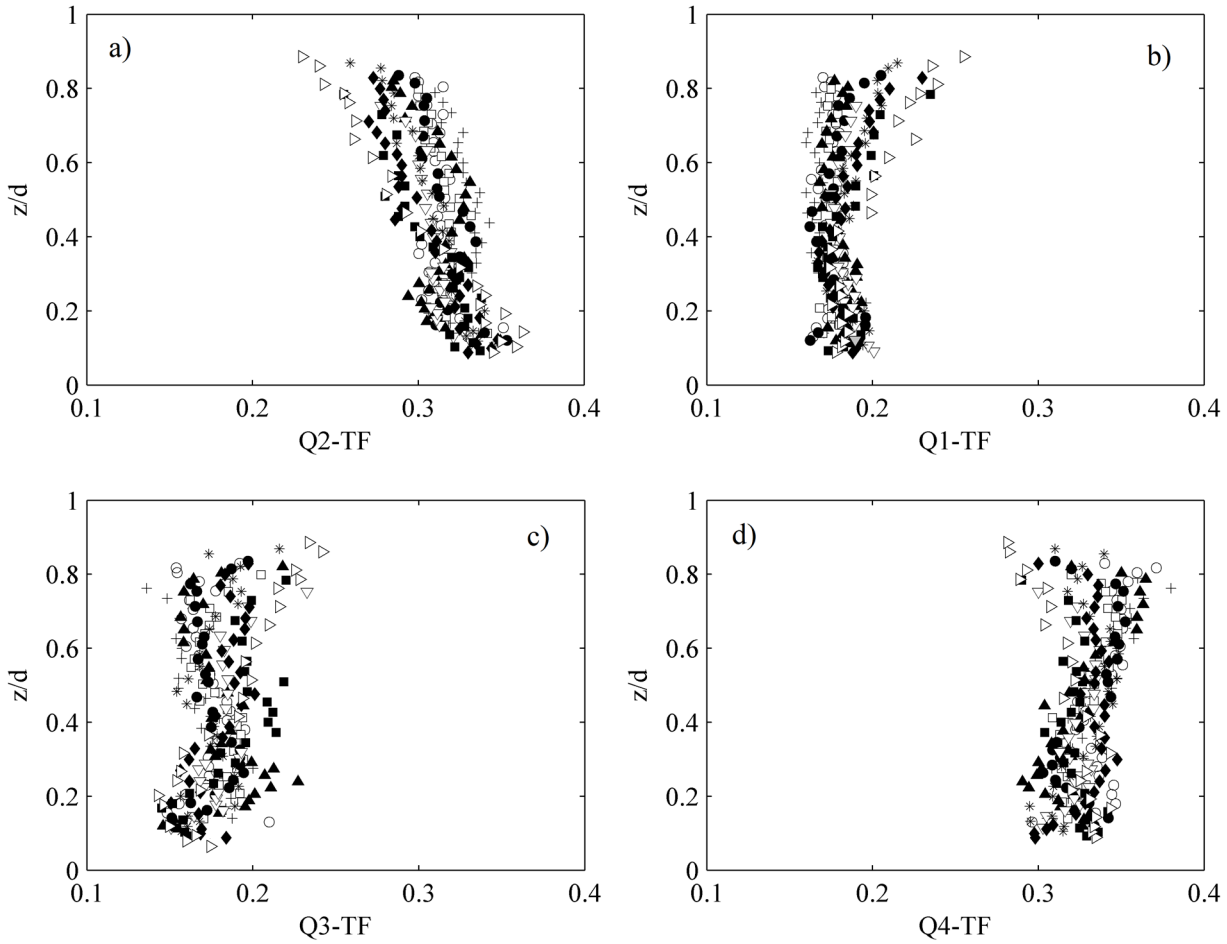

Figure 5.7- Vertical distibution of (a) Q2-TF, (b) Q1-TF, (c) Q3-TF and (d) Q4-TF (RG tests) as a function of *z/d. Legend, + RG1, ○ RG2, □ RG3, ● RG4, ▲ RG5, ▽ RG6, ✳ RG7, ♦ RG8, ■ RG9 and ▷ RG10.*

The variations of the QTFs due to the increase in the flow rate is a little increase of the Q2-TF and Q4-TF, although maintaining a similar pattern in all the experiments in the whole profile. The "natural" decrease of Q2 events and an increase of Q1 and Q3 in the upper half of the depth profile, near the water surface, it is more pronounced for cases with a higher hydraulic depth.

The roughness effect was firstly verified by Raupach (1981) who created rough surfaces that were constructed by placing cylindrical roughness elements in either square or diamond arrays on a smooth wall in boundary layer flows. He stated exists a sweep-dominated (Q4) region (roughness layer) with a thickness of up to several heights of the roughness element; its turbulence characteristics depended explicitly on wall roughness. Therefore, the distribution of quadrant events should change by varying the surface roughness, thus suggesting that the effective roughness dominates the nature of the flow field. The bursting motions associated with ejections and sweeps are closely connected to the turbulent energy budget in the form of the turbulent diffusion.

Some other authors have studied the variation of the QTF under different circumstances, for example, Sambrook Smith & Nicholas (2005) demonstrated that by decreasing the effective bed roughness, and

therefore the local friction of the particles, the bed shear stress along with the TKE decrease, which is consistent with the outcomes from the previous chapter. In addition, the mean streamwise velocity increase and the presence of quadrants Q2 (ejections of low downstream momentum fluid away from the near-bed region) and Q4 (inrushes of high downstream momentum fluid toward from the near-bed region) decline. Bigillon et al. (2006) and Hardy et al. (2010) corroborated the latter. Our experiments are in agreement with this effect, both quadrants Q4 and Q2 increase their TF near the bed region, and sweeps events (Q4) become stronger than ejections (Q2) events when the height of the roughness was increased.

Ferreira et al. (2009) assured that these two events, sweeps (Q4) and ejections (Q2), were also affected by sediment transport, reducing its presence. A general trend of increase of relative importance of sweep events towards the bed was registered. However, because the CG experiments were taken under incipient motion conditions, which cannot be considered as sediment transport conditions.

In the CG experiments (Figure 5.8), however, it is difficult to ensure if a considerable variation occurs by reducing the bed roughness (from CG1 to CG2, CG3 to CG4 and CG5 to CG6) since the differences near the bed are minimal. However, in the case of the CG5 (loose bed) and CG6 (leveled bed) the behavior follow the seen by the mentioned authors, with a higher TF of both Q2 and Q4 in the first (loose bed), with a decrease of Q1-TF very close to the bed z/d<0.2.

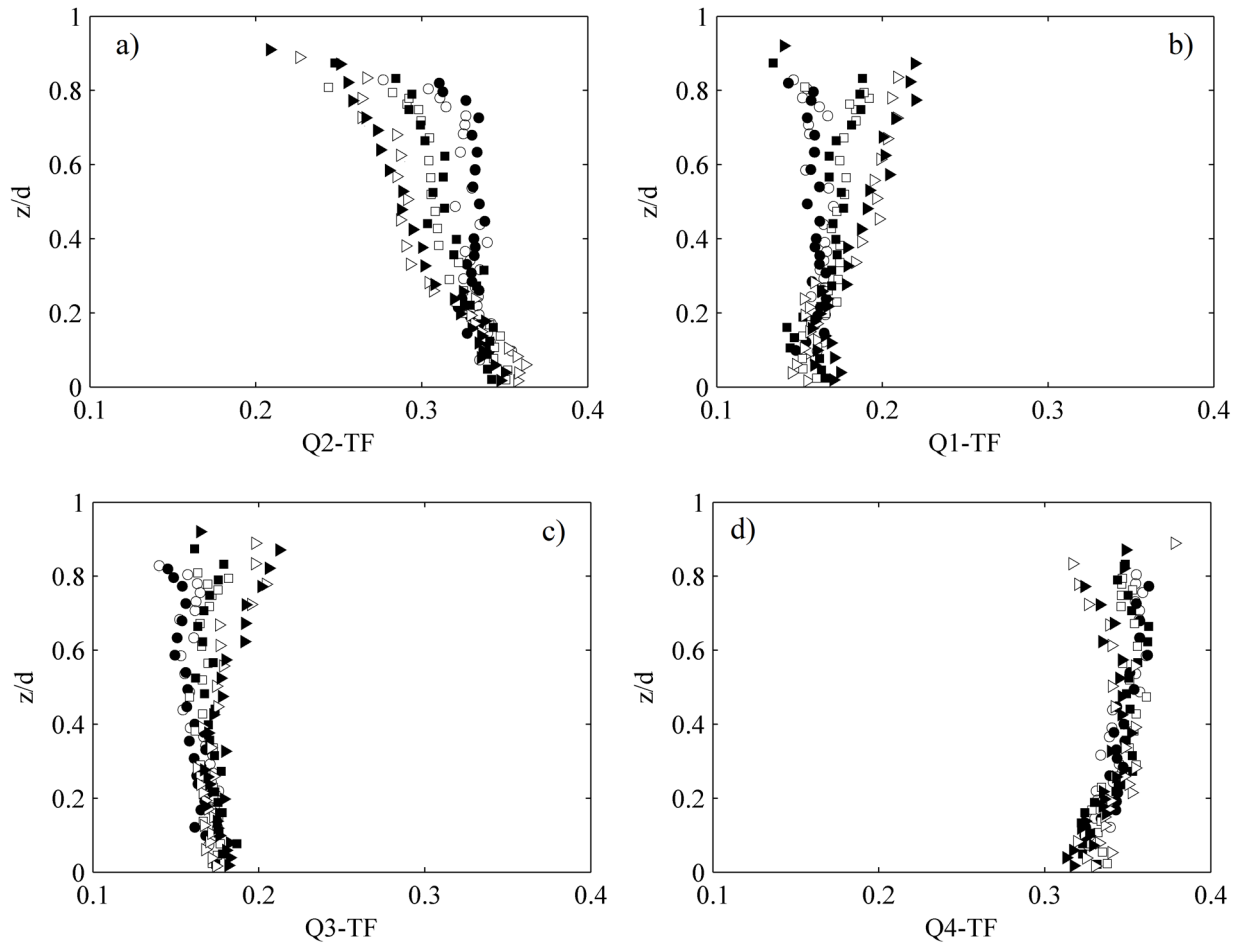

Figure 5.8- Vertical distribution of (a) Q2-TF, (b) Q1-TF, (c) Q3-TF and (d) Q4-TF (CG tests) as a function of *z/d*. *Legend,* ○ *CG1,* ● *CG2,* □ *CG3,* ■ *CG4,* ▷ *CG5 and* ► *CG6.*

These results are also consistent with what was observed in Appendix C, where it was seen that Q2-TF and Q4-TF decreased when SCS was given more representation, by a low CV or a high FDC, where a decay of all turbulent scales was also seen.

It is worth mentioning that throughout the analysis of quadrants the robustness of the method has been analyzed by including different methods of the quadrant detection. For example, it was verified by means of a 5º axis rotation that the values of the sequences were not modified, showing the same trends, and patterns of quadrant the time fractions.

5.4 Quadrant contribution to Reynolds stresses

There is a valuable information in considering the sign of the velocity fluctuations. The quadrants tell us about the local flow direction of the burst motions, away or toward the wall, and whether the flow is moving with an excess or deficit of momentum in comparison with the local mean velocity.

The quadrants Q2 and Q4, ejections and sweeps respectively, are discharges of vertical momentum fluxes upwards whether they have less streamwise momentum than the local mean streamwise momentum (Q2) and downwards whether it has more (Q4). Q2 and Q4 slow the flow above and accelerating it below respectively, thus increasing (positively) the bed shear stress τ_0 in the flow direction. In contrast, Q1 and Q3, which contribute negatively to the bed stress, the low-momentum flux is ejected upwards while the high-momentum flux downwards, accelerating the flow above and slowing it below.

Identifying coherent structures within the flow is possible by isolating the contributors to the Reynolds shear stresses. Those coherent structures are responsible for the production of turbulent kinetic energy; they also play an important role in the mechanism of sediment entrainment.

Instantaneous Reynolds shear stress ($-\rho w'u'$) becomes positive for sweeps (Q4, $u'<0$ $w'>0$), and ejections (Q2, $u'<0$ $w'>0$), while it is negative for outward (Q1, $u'>0$ $w'>0$), and inward interactions (Q3, $u'<0$ $w'<0$). Therefore, it can be assessed the contribution of each quadrant to the Reynold stress $(\sum(-u'w')_{Qj}/\sum(-u'w')_i$, where $(-u'w')_{Qj}$ is the set of stresses from a certain quadrant and $\sum(-u'w')_i$ is the sum of the stresses from all quadrants. Of course, the contribution of the Q2 and Q4 will be positive while the contributions from Q1 and Q3 will be negative, and the sum of the four contributions is the unity.

In the literature, there is a typical analysis of the Reynold shear stresses by focusing only on the extreme values of *u'w',* consisting in filtering the signal as explained in Chapter 3, section 3.4. The method was introduced by Willmarth & Lu (1972) and establishes the imposition of a condition set by the user, termed "hole size" (H), which permits excluding small-scale deviations from the mean in the analysis of turbulence structure. Thus, only bursting events from particularly large instantaneous Reynolds shear stresses are considered, excluding fluctuations that fail to exceed this. The hole size (H) is defined by the expression $|u'w'|\geq$H $(\sigma_u\sigma_w)$ with σ_u and σ_w the root-mean-square intensity of *u'* and *w'* respectively, with typical values of H ranges from 0 to 8.

Willmarth & Lu (1972) found that in the boundary layer almost the 50% of the total Reynolds shear stress come from Q2 motions that lie outside of a certain H, and these motions occur less than 10% of the sampling time. Only a small fraction results came from Q4 motions outside of the hole and none

from Q1 and Q3 motions. However, the assumption of a threshold value is considered rather arbitrary, besides, it breaks down the time history of the signal velocity, therefore is not considered suitable for the present study. As consequence the contribution to the Reynold shear stress in this work a hole size of H=0 has been considered, thus all burst events are admitted.

In Figure 5.9 and Figure 5.10 (RG and CG respectively) the four quadrant contributions to the Reynold shear stress, with no distinction between experiments, have been evaluated along the (a) *z* and (b) *z/d*. The analysis of the results allows concluding that ejections (Q2) and sweeps (Q4) events have higher contributions to the Reynolds stresses and that both events have similar contributions values on average. In the near-bed region, the contributions to the Reynolds shear stress of the sweeps (Q4) are higher than those from the ejections (Q2). However, with the increase of *z* (distance to the bed) it is possible to observe that the contributions of the ejections increase and dominate over the sweeps. Therefore, although the Q2 events become less present in the sample as increasing *z*, as we saw in the previous section, they become more intense. The events of outward (Q1) and inward (Q3) interactions have the shortest TF and the smallest contributions to Reynolds shear stress, indicating that the momentum transfer between the flow and the roughness region is mostly carried by ejections and sweep events.

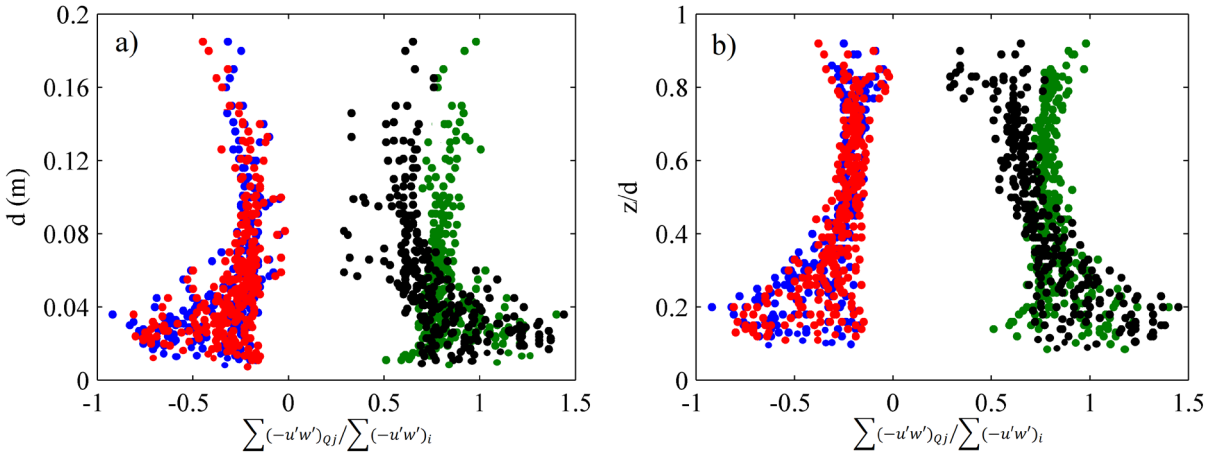

Figure 5.9- Vertical distribution of the Quadrant contribution to Reynold shear stress (RG tests) as a function of (a) *z* and (b) *z/d*. *Legend,* ● *Q1,* ● *Q2,* ● *Q3, and* ● *Q4.*

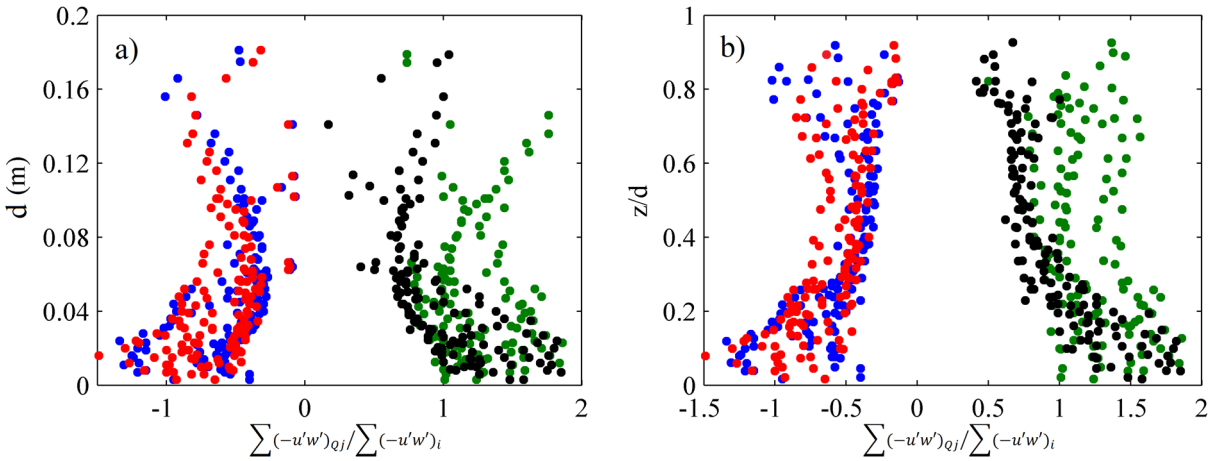

Figure 5.10- Vertical distribution of the Quadrant contribution to Reynold shear stress (CG tests) as a function of (a) *z* and (b) *z/d*. *Legend,* ● *Q1,* ● *Q2,* ● *Q3, and* ● *Q4.*

The next figures, Figure 5.11 and Figure 5.12 depict the contribution to the Reynolds shear stress separated by quadrants again for the RG and CG experiments respectively, where the trends of each quadrant are more clearly identified. The maximum contribution of the four quadrants occurs in all experiments around $0.1<z/d<0.2$, coinciding with the height where the maximum Reynold shear stress value occurs (see chapter 4, section 4.7). Although Q2 and Q4 events have a high QTF very close to the bed, the magnitude of the pair $u'w'$ is a little higher in the roughness region z/d=0.2, resulting in a greater contribution to the shear stress.

In general, the contributions of the four quadrants increase in the near-bed region with the flow rate, since the turbulent intensities in the three axes increase. Nevertheless, from a height of z/d=0.4 the contribution values of Q1 and Q3 events collapse in a slightly decreasing line towards the water surface, while the contributions of Q2 and Q4 depend more on the flow rate, increasing the Q2 contribution and decreasing the Q4 with the increase of the flow rate, separating both tendencies.

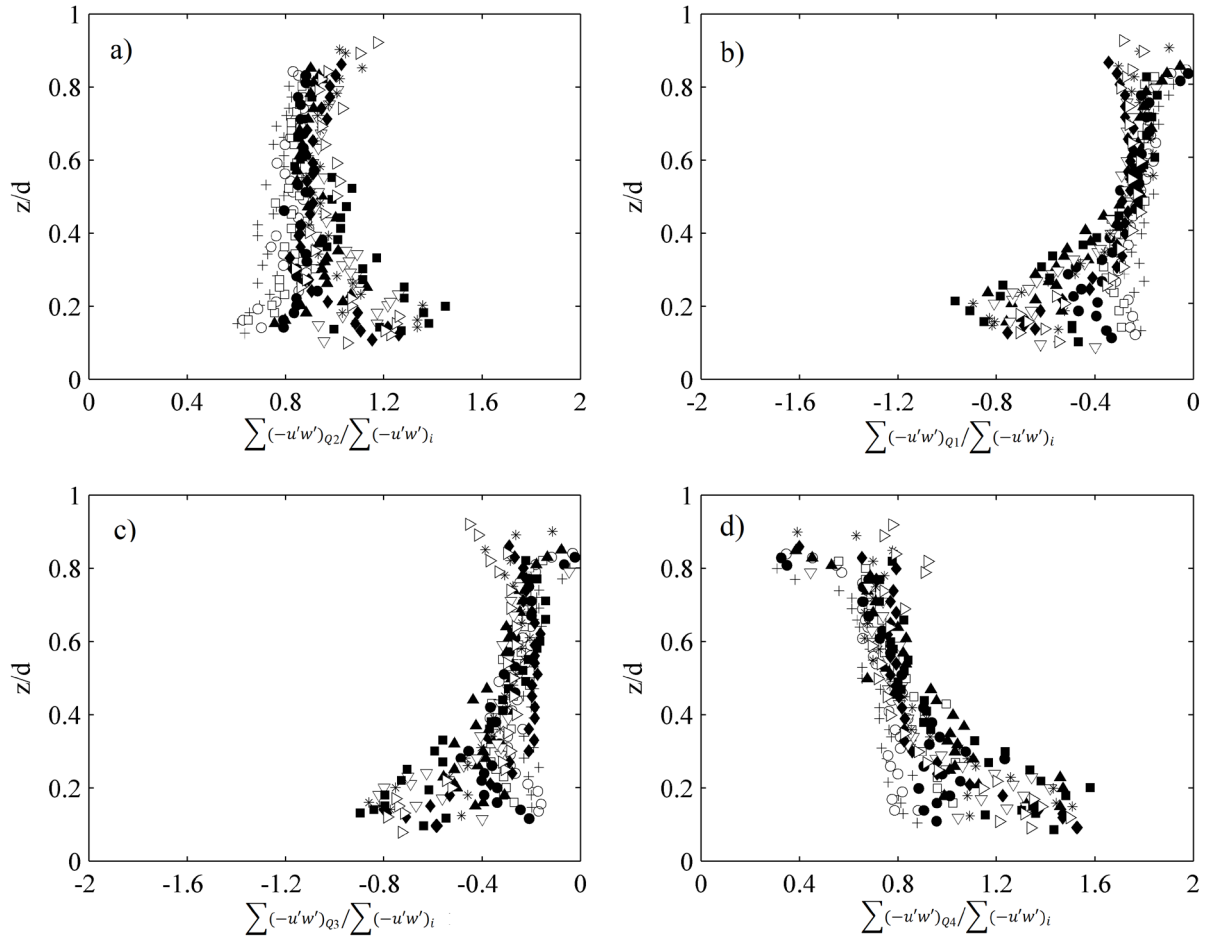

Figure 5.11- Vertical distribution of the contribution to Reynold stress of (a) Q2, (b) Q1, (c) Q3 and (d) Q4 (RG tests) as a function of z/d. *Legend,* + *RG1,* ○ *RG2,* □ *RG3,* ● *RG4,* ▲ *RG5,* ▽ *RG6,* ✶ *RG7,* ♦ *RG8,* ■ *RG9 and* ▷ *RG10.*

Regarding the CG experiments (Figure 5.12), in some of them the bed has been leveled, especially for the CG6 case in comparison to the CG5 since the leveling is more noticeable, a small decrease in the contributions of the quadrants Q2 and Q4 is observed in the area near the bed when flattening the bed. Therefore, there is greater momentum transport due to the increase of the bed roughness.

The plot in Figure 5.13 illustrates the vertical distribution of the ratio $(u'w')_{Q2}/(u'w')_{Q4}$, for the (a) RG and (b) CG experiments, revealing the dominating contributions of the sweeps over the ejections in the near-bed region ($(u'w')_{Q2}/(u'w')_{Q4}<1$), up to the height of z/d=0.4. From that height, the value exceeds the unit, and therefore denoting the preponderance of the contribution of the ejections over the sweeps. The predominant QTF in the upper part of the profile ($z/d>0.4$) was demonstrated to be the Q4, however, it is noteworthy that regarding contributions to the Reynolds stress the Q2 events exceed those of Q4. That is to say, the magnitude of $u'w'$ in Q4 ($u'>0$, $w'<0$) decreases in the profile towards the surface, while those of Q2 ($u'<0$, $w'> 0$) does not do so sharply, causing more contribution from the second ones. This can be due to what was shown in chapter 4, where it was observed that the vertical velocity increments tend to become negative near the bed, therefore, they also take more extreme values.

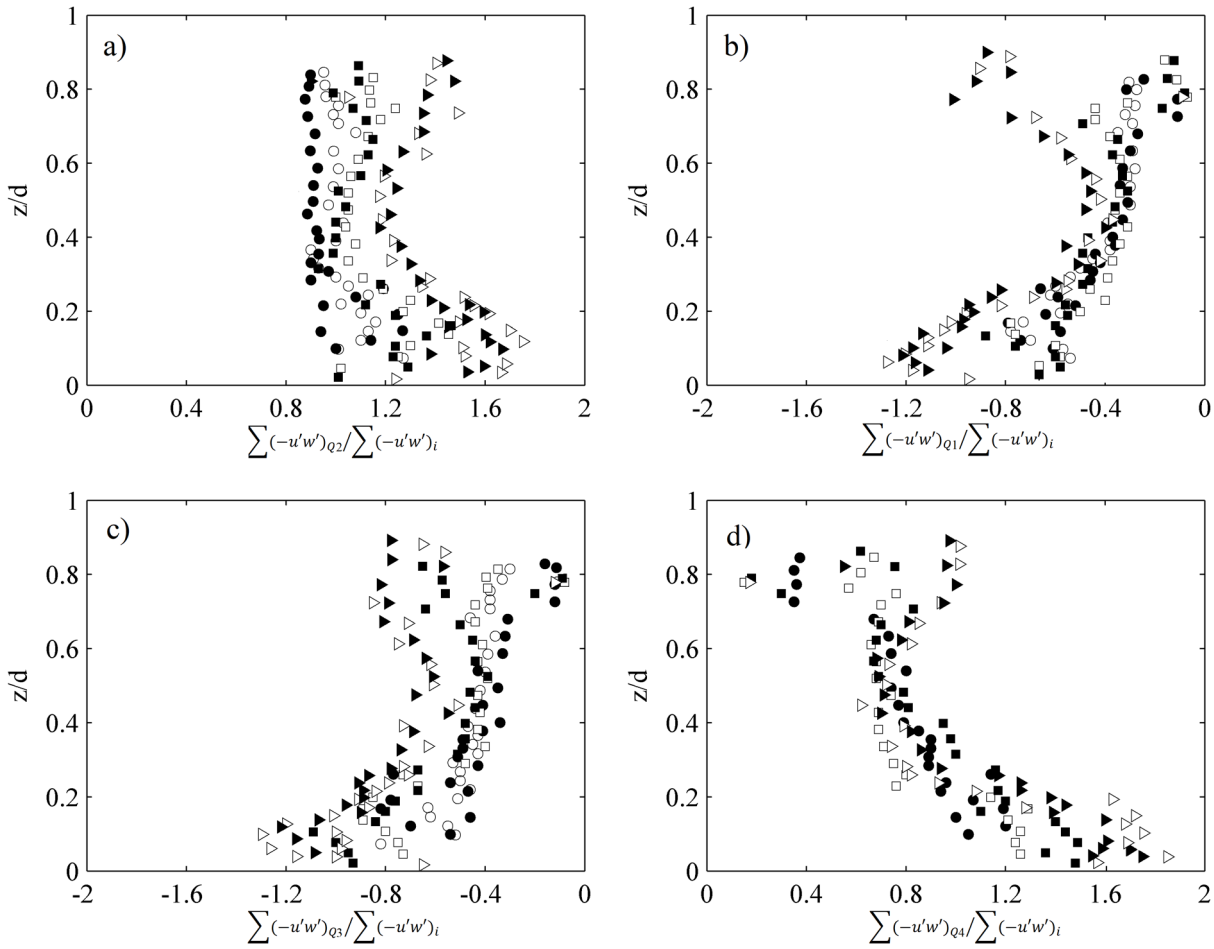

Figure 5.12- Vertical distribution of the contribution to Reynold stress of (a) Q2, (b) Q1, (c) Q3 and (d) Q4 (RG tests) as a function of *z/d*. *Legend,* ○ *CG1,* ● *CG2,* □ *CG3,* ■ *CG4,* ▷ *CG5 and* ► *CG6.*

In Figure 5.14 are depicted the ratio of the combined contributions from Q2+Q4 and Q1+Q3 $((u'w')_{Q2}+(u'w')_{Q4})/((u'w')_{Q1}+(u'w')_{Q3})$, thus the ratio of positive contributions over the negatives along the dimensionless depth profile (z/d). From the figure, it is obtained that positive contributions gain presence when increasing the height in the profile. Near the bed region, experiments with a low level of turbulence (RG1 to RG5) the positive contribution is higher (3-4) than for the rest which is 2, with a fairly constant value within the roughness region. This shows that near the bed the magnitudes

of the pairs *u'w'* in the Q1 and Q3 also take extreme values, although these decrease with the height more sharply than the Q4 and Q2.

The quadrant fractional method showed that in the outer region of roughness layer (z/d> 0.4), ejections have greater influence than sweeps, but in the inner region, the sweep contribution increases and reaches the same level as the ejections. The effect of bed roughness in changing the balance between ejections and sweeps is important below 0.2-*z/d*.

The significance of the ejections and sweeps events in generating the turbulence near the wall and their contributions to the vertical component of the Reynolds stresses in the main channel is evident. The contributions from the remaining odd quadrants to the total stress are relatively small. The significance of ejections increases in comparison with other events as the distance from the channel bed increases.

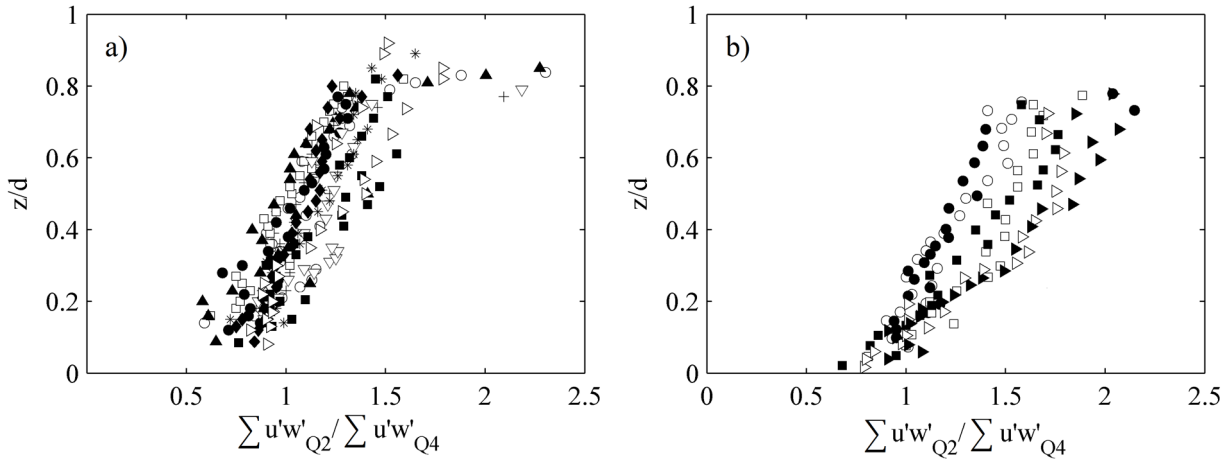

Figure 5.13- Vertical distribution of (a) $(u'w')_{Q2}/(u'w')_{Q4}$ and (b) $((u'w')_{Q2}+(u'w')_{Q4})/((u'w')_{Q1}+(u'w')_{Q3}$ for the (a) RG and (b) CG experiments. *Legend (a), + RG1, ○ RG2, □ RG3, ● RG4, ▲ RG5, ▽ RG6, ✳ RG7, ♦ RG8, ■ RG9 and ▷ RG10. Legend (b), ○ CG1, ● CG2, □ CG3, ■ CG4, ▷ CG5 and ▶ CG6.*

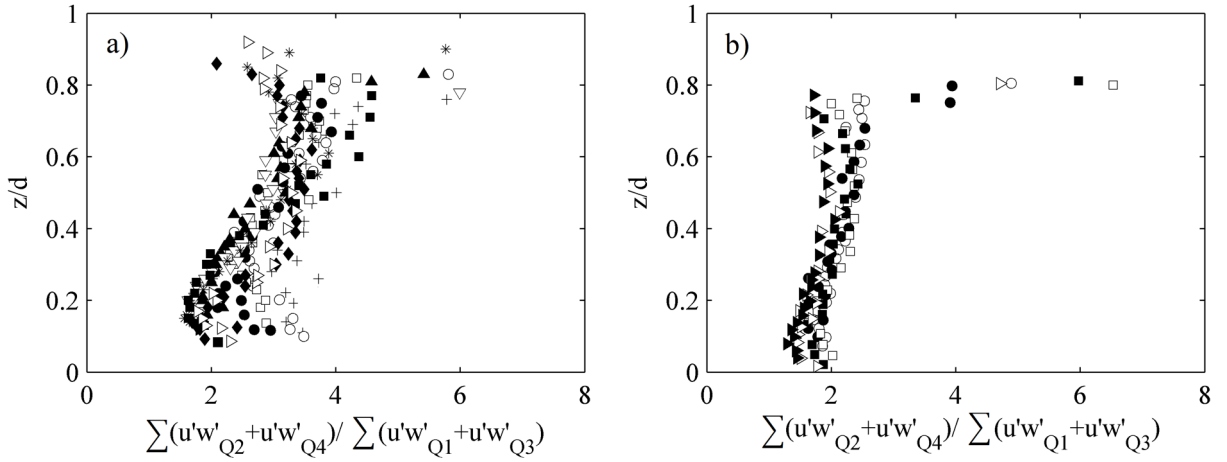

Figure 5.14- Vertical distribution of (a) $(u'w')_{Q2}/(u'w')_{Q4}$ and (b) $((u'w')_{Q2}+(u'w')_{Q4})/((u'w')_{Q1}+(u'w')_{Q3}$ for the (a) RG and (b) CG experiments. *Legend as for Figure 5.13.*

5.5 Gram-Charlier Probability distribution.

The Reynolds shear stress ($\overline{u'w'}$) can be defined statistically as Eq. 5-1, where *P*(*u'*, w') is the joint probability density function (JPDF) of the velocity fluctuations *u'* and *w'*.

$$\overline{u'w'} = \int_{+\infty}^{-\infty} u'w'P(u',w')du'dw' \tag{5-1}$$

If the turbulent components were independently random, a normal PDF, or a Gaussian distribution, determined by the second-order moment, i.e., the turbulence intensity, could describe them. However, turbulent components are never independently random; they are always correlated with each other in both space and time. In a broad sense, one can describe such correlated fluid parcels by the appellation "coherent". Thus, higher-order moments must also be considered in order to obtain more detailed information concerning turbulence.

Several studies (Nakagawa & Nezu 1977; Wu & Yang 2004) have suggested that the Gram-Charlier probability density function (GC JPDF) describes correctly the distribution of near-bed velocity fluctuations. Wu & Jiang (2007) incorporated a Gram-Charlier third-order distribution $g_3(U, W)$, which adjusts the 2D joint probability of $u'w'$ in the near-bed region. The expression $g_3(U, W)$ is defined by Eq. 5-2, where the values of the $g_0(U,W)$ (Eq. 5-3), L1 (Eq. 5-4), L2 (Eq. 5-5), L3 (Eq. 5-6) and L4 (Eq. 5-7), are expressed as function of $U=u'/\sigma_u$; $W=w'/\sigma_w$ normalized velocity fluctuation; with u' and w' instantaneous longitudinal and vertical velocities, σ_u and σ_w standard deviations, $R_{uw} = \overline{u'w'}/\sigma_u\,\sigma_w$ correlation coefficient; $R_u = R_{uw}W - U$; $R_w = R_{uw}U - W$; $S_u = \overline{u'^3}/\sigma_u{}^3$ and $S_w = \overline{w'^3}/\sigma_w{}^3$ skewness factors; and $M_{21} = \overline{u'^2w'}/\sigma_u{}^2\sigma_w$ and $M_{12} = \overline{u'w'^2}/\sigma_u\sigma_w{}^2$ diffusion factors.

$$g_3(U,W) = g_0(U,W)\cdot(1 + L_1 + L_2 + L_3 + L_4) \tag{5-2}$$

$$g_0(U,V) = 1/(2\pi\sqrt{1 - R_{uw}{}^2})\exp\left[-(U^2 - 2R_{uw}UW + W^2)/2(1 - R_{uw}{}^2)\right] \tag{5-3}$$

$$L_1 = \frac{S_u}{3!}\left[-\left(\frac{R_w}{1 - R_{uw}{}^2}\right)^3 + \frac{3R_w}{(1 - R_{uw})^2}\right] \tag{5-4}$$

$$L_2 = \frac{M_{21}}{2!}\left[\frac{3R_{uw}U - 2R_{uw}{}^2W - W}{\left(1 - R_{uw}{}^2\right)^2} - \frac{R_uR_w{}^2}{\left(1 - R_{uw}{}^2\right)^3}\right] \tag{5-5}$$

$$L_3 = \frac{M_{12}}{2!}\left[\frac{3R_{uw}W - 2R_{uw}{}^2U - U}{\left(1 - R_{uw}{}^2\right)^2} - \frac{R_wR_u{}^2}{\left(1 - R_{uw}{}^2\right)^3}\right] \tag{5-6}$$

$$L_4 = \frac{S_w}{3!}\left[-\left(\frac{R_u}{1 - R_{uw}{}^2}\right)^3 + \frac{3R_u}{(1 - R_{uw})^2}\right] \tag{5-7}$$

The values of the main parameters can be obtained from several expressions. The near-bed correlation coefficient R_{uw} are normally in the range from -0.4 to -0.5 (Pope 2000). Wu & Yang (2004) from a compilation of published experimental and simulation data observed that no significant variations of some parameters were observed from the compiled data set. The methods of data acquisition and computation of the analyzed data by Wu & Yang (2004) were Hydrogen-bubble/water, Hot-film/oil, Hot-wire/air, LDA, PIV, LDV, DNS, and LES. For cases of smooth and transitional flows, they proposed the expression $S_u = 0.102\,ln(k_s{}^+)$, with $k_s{}^+ = u^*k_s/\nu$ and $k_s = 2D_{50}$, while in case of rough turbulent flows ($u_*k_s/\nu > 100$) proposed a constant value of $S_u=0.43$. Wu & Jiang (2007) in their study proposed, in the near-bed region, a constant values of R_{uw}=-0.45, $S_w=0$, $M_{12}=0.1$, and $M_{21}=-0.04$.

The Gram-Charlier GC joint probability distribution of near-bed 2D instantaneous velocities is used to replicate the burst events and characterize the turbulence. Conventionally, the values proposed by Wu & Yang (2004) are used for the characterization. However, the near-bed burst events are deeply affected by roughness and relative submergence, thus considering constant values along the depth is considered very imprecise.

In order to throw light on this assumption, the values of R_{uw}, S_u, S_w, M_{21}, and M_{12}, have been computed from the experimental data for each point of the profile and for each experiment, and of de distribution of $g_3(U, W)$ for some points have been represented in a 3D map (Figure 5.15). Moreover, the distribution of the U,W are plotted in a turbulent map (2D), Figure 5.16, where it can be seen that the U,W (points) obtained from the data series are close to the adjusted by the $g_3(U, W)$ (textured colors).

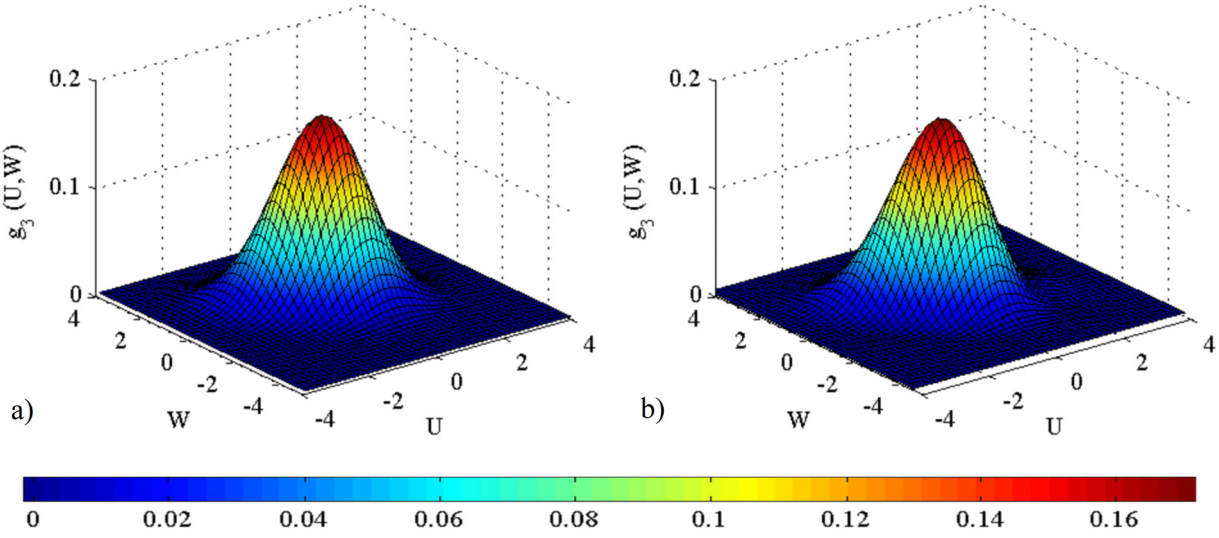

Figure 5.15- Three-dimensional plot showing the third-order Gram–Charlier joint PDF of the normalized velocity fluctuations at height z/d=0.1 (a) RG1 and (b) RG5.

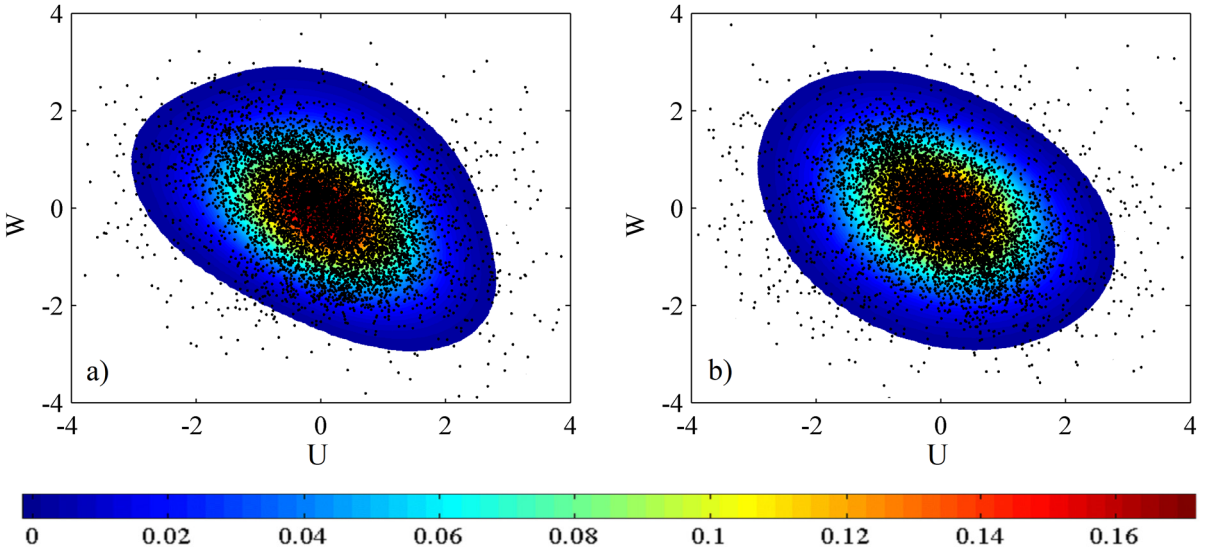

Figure 5.16- Three-dimensional plot showing the third-order Gram–Charlier joint PDF of the normalized velocity fluctuations at height z/d=0.1 (a) RG1 and (b) RG5.

Figure 5.17 shows the different parameters implied in the GC distribution represented along the dimensionless depth for the RG and CG experiments, together with the values proposed by Wu & Yang (2004) for rough turbulent flows (dashed lines). In this figure, all results are gathered without distinction of the experiments so the general trends are visible. It is noticeable how all the variables present a vertical trend, demonstrating that considering constant values subtract important information of the flow turbulence. For a more precise study of the different variables and the use of the $g_3(U, W)$ at different points of the profile, each variable has been characterized along the dimensionless depth, distinguishing between experiments of the same kind.

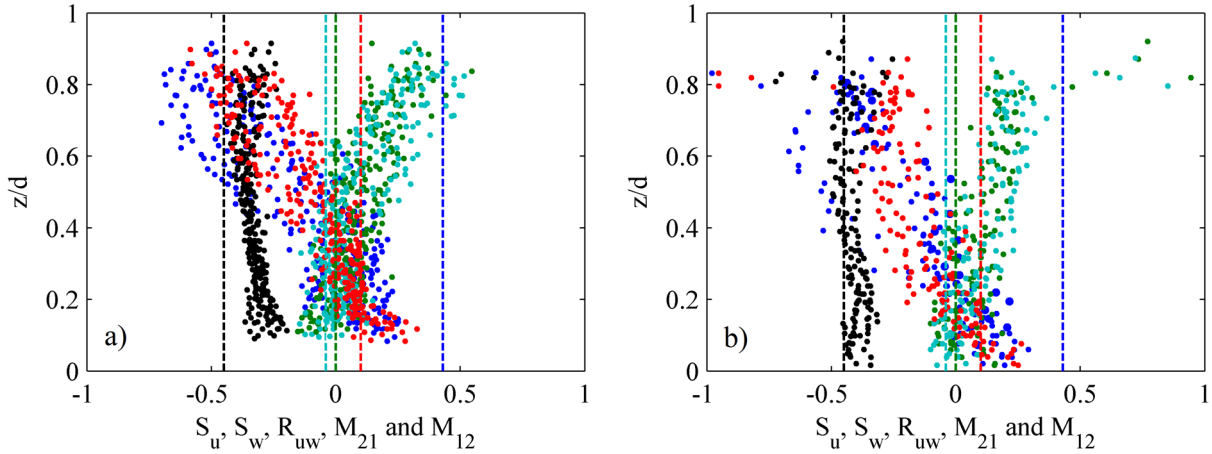

Figure 5.17- Vertical distribution of the Gram-Charlier Parameters for the (a) RG and (b) CG experiments. *Legend,* ● *S_u,* ● *S_w,* ● *Ru_w,* ● *M_{21}, and* ● *M_{12}. Dashed lines represent the values proposed by Wu & Yang (2004) for rough turbulent flows.*

5.5.1 Correlation coefficient

The correlation between longitudinal and vertical turbulent velocities, i.e. the ratio ($\overline{u'w'}/\sigma_u\,\sigma_w$), or correlation coefficient (R_{uw}) of the Reynolds shear stress is an interesting parameter since it involves only turbulence velocities, without the need for estimating other turbulent variables.

As stated before, Wu & Yang (2004) considered that a value of R_{uw}=-0.45 characterizes correctly rough turbulent flows. Nezu (2005) found that in the equilibrium region, $0.1<z/d<0.6$, R_{uw} remains nearly constant, with a value ≈[-0.4,-0.5] in open-channels and boundary layers. Besides, he noted that R_{uw} is universal and independent of the properties of the mean flow and the wall roughness.

Czernuszenko & Rowinski (2008) obtained that R_{uw} does not change greatly until a distance of z/d=0.3 is reached, at which point it begins to decrease. However, Lu and Wilmarth (1973) reported a value of $0.44<z/d<0.6$. In the greater part of the channel flows, the correlation coefficient is in the range from -0.4 to -0.5 as reported by others.

Our results suggest that the parameter R_{uw} is fairly constant vertically compared to the rest of the variables involved in the GC distribution (Figure 5.17). However, by expanding this value a bit in Figure 5.18, certain trends are observed. In this figure, in addition to the experimental results of R_{uw}, are overlapped as well as the proposed value by Wu & Jiang (2007) (R_{uw}=-0.45, dashed line). The experimental values are always between a range of [-0.45, -0.25], thus reaching values below the recommended by Pope (2000) and Wu & Jiang (2007). The value close to the bed surface (on the

roughness crests) has a value close to -0.4, this value decreases until a minimum at approximately *z/d* =0.2 and increases again up to a height of *z/d*=0.6, where it begins to decrease again. This trend is in line with those described by other authors, although lower values (up to -0.2) are obtained within the roughness layer. The results highlight the variability of this parameter along the depth profile, although maintaining a pretty constant value in the near-bed region, which is in agreement with Wu & Jiang (2007).

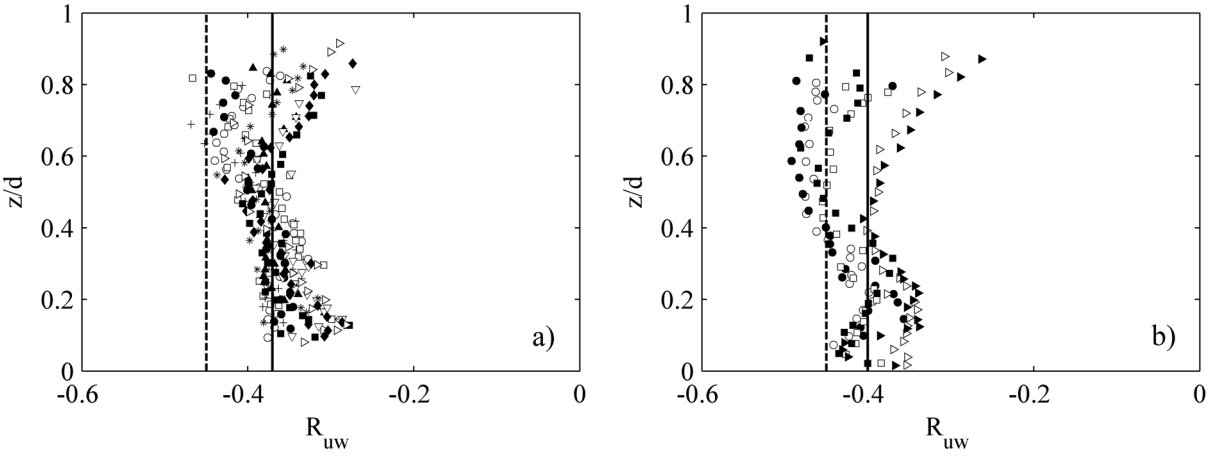

Figure 5.18- Vertical distribution of the correlation coefficient R_{uw} from the (a) RG experiments and (b) CG experiments. *Legend (a), + RG1, ○ RG2, □ RG3, ● RG4, ▲ RG5, ▽ RG6, ∗ RG7, ♦ RG8, ■ RG9 and ▷ RG10. Legend (b), ○ CG1, ● CG2, □ CG3, ■ CG4, ▷ CG5 and ▶ CG6. Solid line, average R_{uw} from experimental data and the dashed line is the value proposed by Wu & Jiang (2007).*

5.5.2 Skewness factors

Third-order correlations are directly correlated to the turbulent coherent structures because of the preservation of their signs, transmitting essential stochastic information on the temporal characteristics of the velocity fluctuations in the form of a flux of the turbulent stresses.

The parameter S_u is a third-order moment correlation of *u'*, also known as the skewness of *u'*, and represents the streamwise flux of the streamwise Reynolds stress (*u'u'*). On the other hand, the S_w is the third-order moment correlation of *w*', defining its skewness, and representing the vertical flux of vertical Reynold stress (*w'w'*). The skewness factors describe the asymmetry in the PDF of turbulent fluctuations, and it is an important factor used to describe bursting events.

Figure 5.19 represents the vertical distribution of the S_u for the (a) RG and (b) CG experiments. The most powerful experiments (RG4 to RG10, and CG3 to CG6) have positive values in the near-bed region (*z/d*<0.4) which changes to negative values with increasing depth. The maximum positive values for these cases occurs inside this region around a height of *z/d*=0.2. This implies that the $\overline{u'u'}$ flux occurs in the streamwise direction within the roughness, and in the upper part of the profile *z/d*>0.4 (out of the roughness region) the flux of $\overline{u'u'}$ occurs in the opposite direction to the flow. In less powerful cases (RG1 to RG3, and CG1 to CG2), this value is closer to zero (or negative) in the near bed region, which means that the transport of flux in the flow direction is lower. It is observed that the leveling of the surface has a little effect on the S_u, achieving values closer to zero in the near bed region (Figure 5.19-b).

From Figure 5.19 it is also obtained that the values of S_u do not match with the proposed by Wu and Yang (2004) for rough turbulent flows, who proposed a positive constant value of 0.43 in the near-bed region (dashed line in Figure 5.19). This value (S_u=0.43) is very far from the values obtained for the present experiments, which averaged values in the near-bed region are between $0<S_u<0.15$ (continuous line in Figure 5.19) increasing with the level of turbulence. However, S_u can be considered constant in the near-bed region.

As commented in the introduction of this section, they proposed an expression of S_u for smooth and transitional flows ($S_u = 0.102\, ln(k_s^+)$), however, this expression does not achieve closer results, being the obtained for our experiments in the range of [0.87-1.07], so that these values are not represented in Figure 5.19.

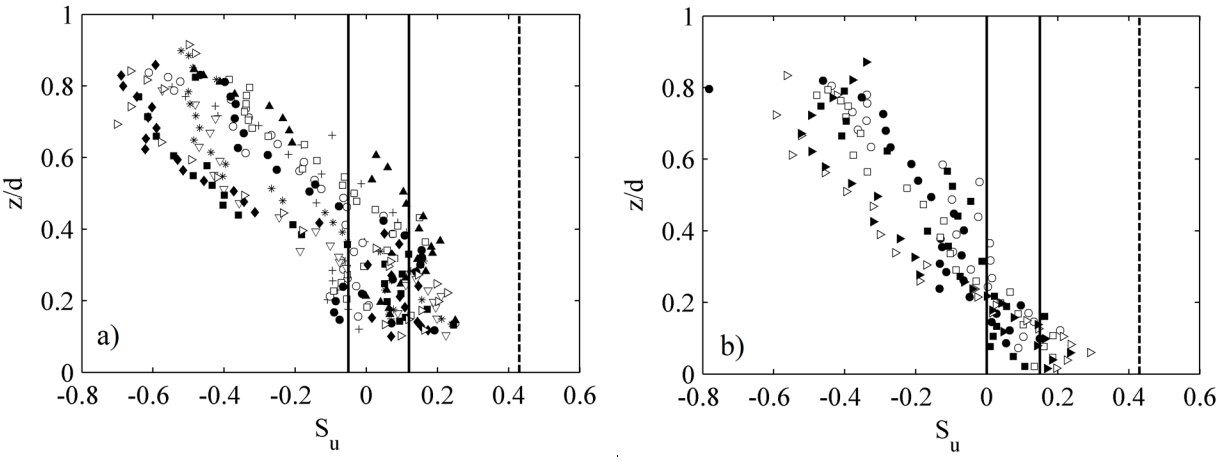

Figure 5.19- Vertical distribution of S_u (a) RG and (b) CG experiments. *Legend (a), + RG1, ○ RG2, □ RG3, ● RG4, ▲ RG5, ▽ RG6, ∗ RG7, ♦ RG8, ■ RG9 and ▷ RG10. Legend (b), ○ CG1, ● CG2, □ CG3, ■ CG4, ▷ CG5 and ► CG6. Solid line, experimental depth-averaged (z/d<0.3) S_u and dashed line is the value proposed by Wu & Yang (2004).*

Figure 5.20 represents the vertical distribution of the S_w for the (a) RG and (b) CG experiments. Contrarily to S_u, S_w reaches negative values inside the roughness region, and positive values with increase in the depth, thus the $\overline{w'w'}$ flux is in downward direction in the near-bed region. The less powerful experiments show more positive values of S_w in the near bed region, while the most powerful have more negative value.

A S_w<0 denotes that the transport of vertical Reynolds stresses (*w'w'*) have a predominantly downward direction, which is due to the high roughness of the bed. This can be seen also in Figure 5.20-b, where the not leveled beds (CG1, CG3, and CG5) show more negatives values of S_w in comparison with the leveled ones (CG2, CG4, and CG6). Nevertheless, the effects from the packing surface roughness are limited to the bed-region.

In this case, the value proposed by Wu & Jiang (2007) is S_w=0 (dashed line in Figure 5.20), which is close to the averaged from our results within the roughness region [-0.015, -0.083] (continuous line in Figure 5.20).

In both parameters (S_u and S_w) it has been obtained that within the region near the bed (z/d<0.4) the values tend to be positive and negative respectively, which despite having a progression with the

distance to the bed (z), the sign is constant within this region and out of it the signs are reversed. This tells us that in the rough layer the transport of the streamwise Reynolds stresses is carried out in the direction of flow, and the vertical stresses in the downward toward the bed. The latter denotes strong sweep (Q4) events, which despite being very compensated with ejections (Q2) in the near-bed region (as we saw in the previous section), the former has greater intensity.

The fact of $S_u>0$ and $S_w<0$ in $z/d<0.4$ become more extreme with the flow rate (higher τ_0) and with greater roughness (irregular surface), which demonstrates that both variables are affected by the level of turbulence. Therefore, the imposition of a constant value for all turbulent flow, especially in the case of the S_u, could misrepresent the reality.

Bigillon et al. (2006), note that for smooth flows $S_u<0$ and $S_w> 0$ in the whole profile, however, near the bed z/d <0.05 these signs were reversed when increasing bed roughness, which is in accordance with the results presented here. On the other hand, Dey et al. (2011) observed that $S_u>0$ below $0.1<z/d$ and from this point on became negative, whereas $S_w>0$ on the whole profile. However, in the presence of sediment transport, the value of S_u became more positive and S_w became negative, in the zone $0.1<z/d$. The reason could be that sediment transport increased the effective roughness of the bed, and so these results are in line with the presented throughout this section.

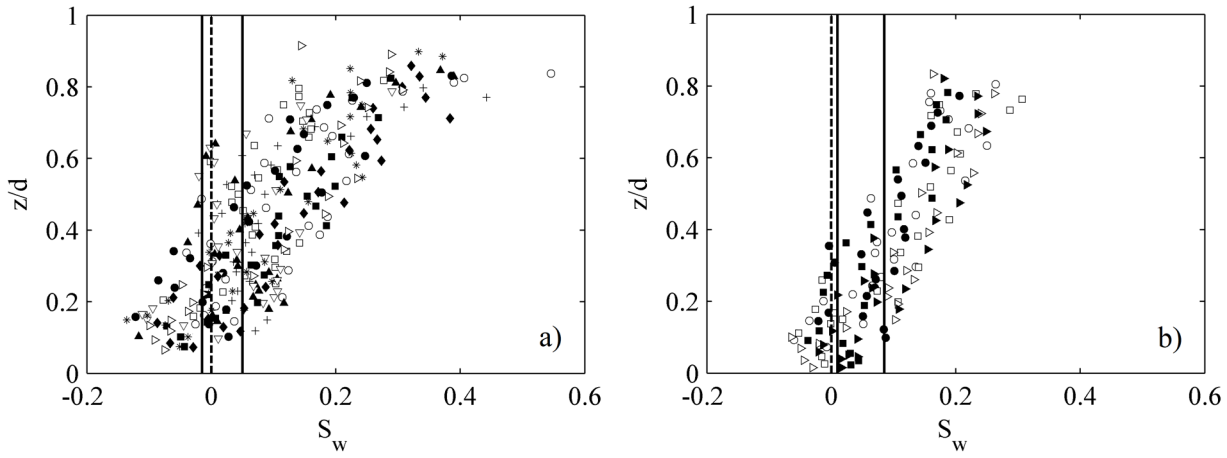

Figure 5.20- Vertical distribution of S_w (a) RG and (b) CG experiments. *Legend (a), + RG1, ○ RG2, □ RG3, ● RG4, ▲ RG5, ▽ RG6, ∗ RG7, ♦ RG8, ■ RG9 and ▷ RG10. Legend (b), ○ CG1, ● CG2, □ CG3, ■ CG4, ▷ CG5 and ► CG6. Solid line, experimental depth-averaged ($z/d<0.3$) S_w and the dashed line is the value proposed by Wu & Jiang (2007).*

5.5.3 Diffusion factors

The third-order moments M_{21} and M_{12} are the diffusion terms of $\overline{u'u'}$ in the vertical direction and $\overline{w'w'}$ in the streamwise direction respectively, therefore, both parameters define the turbulent advection of the normal Reynold stress.

The vertical distribution of M_{12} is depicted in Figure 5.21 for the (a) RG and (b) CG experiments. M_{12} has positive values near the bed (roughness region) for all experiments and starts to become negative with the depth, above $z/d\approx0.3$. The positive value near the bed increases with the level of turbulence, thus with τ_0, and decrease, in the case of the CG experiments, with the packing of the surface, thus

when the roughness decrease. The positive value of M_{12} indicates that the $\overline{w'w'}$ diffusion propagates in the flow direction.

Regarding the third-order moment M_{21}, Figure 5.22 shows values very close to zero in the near-bed region with some deviation to negative values; however, the values become positive with the depth and keep increasing until the water surface. The negative nature of the M_{21} close to the bed increases with the level of turbulence, i.e. the value becomes more deviated from zero for the most powerful RG experiments, from RG5 to RG10, and the not-packed surfaces of the CG experiments in comparison with the packed ones (CG2, CG4, and CG6). Therefore, high values of τ_0 or k_s indicate that value M_{21} become more negative. The negative value of M_{21} indicates that the $\overline{u'u'}$ diffusion occurs in the downward direction.

Wu & Jiang (2007) proposed constant values for both M_{21} and M_{12}, -0.04 and 0.1 respectively (in the near-bed region) which are represented by a dashed line Figure 5.21 and Figure 5.22. The assumption of a constant value in the near-bed region, although no representing the variability of the flow in the depth, it can be considered fairly accurate to represent our experiments. The averaged value of M_{12} in the near-bed region showed a value inside the range [-0.08, 0.1] (solid line Figure 5.21) and of M_{21} from our experiments showed a value inside the range [-0.08, 0.06] (solid line Figure 5.22). Dey et al. (2011) obtained similar vertical distribution of the M_{21} and M_{12}, noting that both values became more negative and positive respectively, in the near bed region, in the presence of sediment transport.

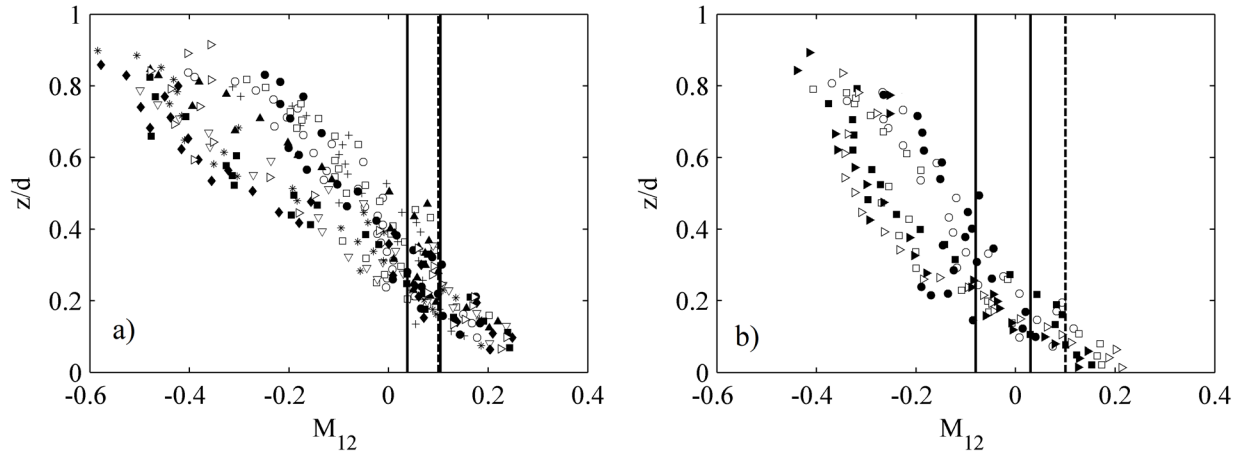

Figure 5.21- Vertical distribution of the Diffusion factor M_{12} (a) RG and (b) CG experiments. *Legend (a), + RG1, ○ RG2, □ RG3, ● RG4, ▲ RG5, ▽ RG6, ✳ RG7, ♦ RG8, ■ RG9 and ▷ RG10. Legend (b), ○ CG1, ● CG2, □ CG3, ■ CG4, ▷ CG5 and ▶ CG6. Solid line, experimental depth-averaged (z/d<0.3) M_{12} and dashed line is the value proposed by Wu & Jiang (2007).*

Smooth boundaries tend to not change the sign of the third-order moments, keeping the values close to zero in the near-bed region, thus there is no change in sign (Keirsbulck et al. 2002). As a conclusion from our experiments, the effects of the roughness conditions have a strong effect on the third-order moments. It has to be underlined that all third-order values do not have a constant value, however, in the near-bed region, the variability is lower.

The fact that both S_w and M_{21} have negative values in the near-bed region indicates that is occurring an inrush of flow toward the bed, due to the strong sweep events (Q4). On the other hand, the positive values of S_u and M_{12} imply that the flow toward the bed is carried away by the flow. Values different

from zero indicates an existence of important turbulent activity, consistent with the occurrence of strong and highly intermittent turbulent events (Nezu and Nakagawa 1977).

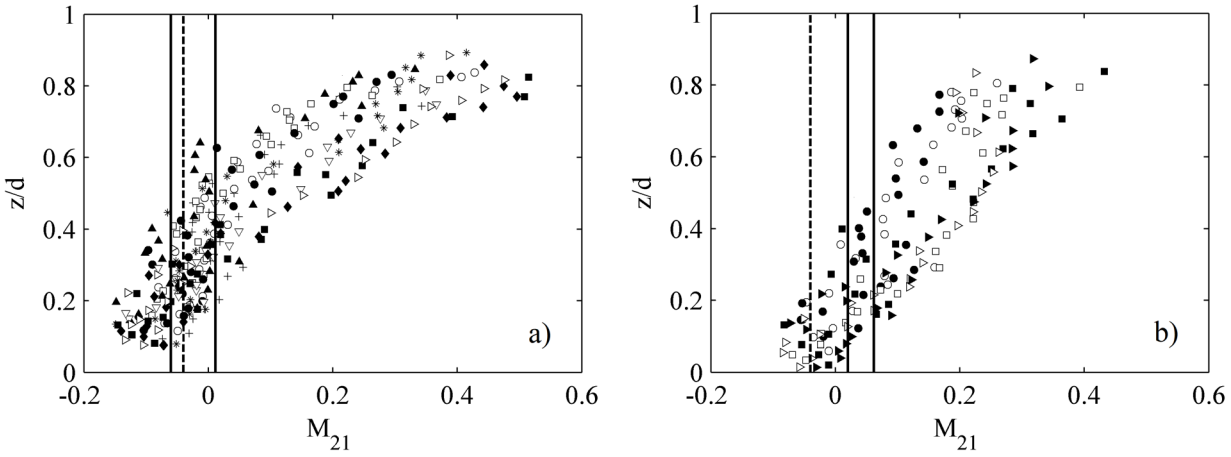

Figure 5.22- Vertical distribution of the Diffusion factor M_{21} (a) RG and (b) CG experiments. *Legend (a), + RG1, ○ RG2, □ RG3, ● RG4, ▲ RG5, ▽ RG6, ✳ RG7, ♦ RG8, ■ RG9 and ▷ RG10. Legend (b), ○ CG1, ● CG2, □ CG3, ■ CG4, ▷ CG5 and ► CG6. Solid line, experimental depth-averaged (z/d<0.3) M_{21} and dashed line is the value proposed by Wu & Jiang (2007).*

5.5.4 Third-order moments ratios

Raupach (1981) found in the measurements from a wind tunnel of smooth and rough surfaces that there is a simple linear relationship between all third-order moments, $S_u \approx C_{21}M_{21} \approx C_{12}M_{12} \approx C_w S_w$, and data from some other authors in open-channel flows confirmed the relationship.

The data analyzed by Bigillon et al. (2006) cover a high range of turbulence levels (Re) and surfaces. The values used as a reference in the present work are presented in Table 5.2. The experiments presented here have Reynolds numbers from $2.69 \cdot 10^5$ (RG1) to $1.13 \cdot 10^6$ (RG10), considerably higher than those exposed Table 5.2.

From a simple linear fitting trend, for all tested data put together independently of the Reynolds number, the coefficients C_{21} = -2.1, C_{12} = 1.86, and C_w = -1.15 were found. From comparison with the studies included in Table 5.2, it can be concluded that for highly turbulent flows, as the presented in this work, the results are similar to the obtained for Nikora (2000). The C_{12} tends to increase while C_{21} tends to decrease. On the other hand, C_w takes lower values, close to -1. Moreover, as the distribution of M_{21} and M_{12} is symmetric means that $C_{21} \approx -C_{12}$ and Nikora (2000). Constant values used by Wu & Jiang (2007) demonstrate that do not match with the results of other studies, included the present. Therefore, it has been corroborated that the third-order moments are related by a simple linear relationship, as long as no constant values for all points are used. The relationship depends on the Reynolds number, thus further investigation is needed to define the trend as a function of the Reynolds number.

Table 5.2 Coefficient connecting the skewness factor Su with the third-order moments M_{21}, M_{12}, and S_w.

	R_e	C_{21}	C_{12}	C_w
Raupach (1981)	1.5·10^5	-2	1.97	-1.7
Lopez (1997)	5.7·10^4	-1.36	1.5	-1.28
Hurther (1981)	8.2·10^4	-1.78	1.43	-0.94
Nikora (2000)	1.3·10^6	-1.9	1.9	-0.9
Bigillon et al. (2006)	1.2·10^4	-1.89	1.79	-1.47
Wu & Jiang (2007)	Fully rough	-10.75	4.3	∞
Present work	2.69·10^5 to 1.13·10^6	-2.1	1.86	-1.15

Figure 5.23 shows the third-order moments M_{21}, M_{12}, and S_w as a function of S_u, obtained from each point of the experiments, and the fitted parameter in each case (showed in Table 5.2). In addition, the values proposed by Wu & Jiang (2007) are also represented as a point (✳) since they proposed constant values for all parameters. From the figure, it is obtained that a lower value of (S_u<0.45) would have been closer to our results, for example, a value of S_u ≈0.15 would match the adjustment.

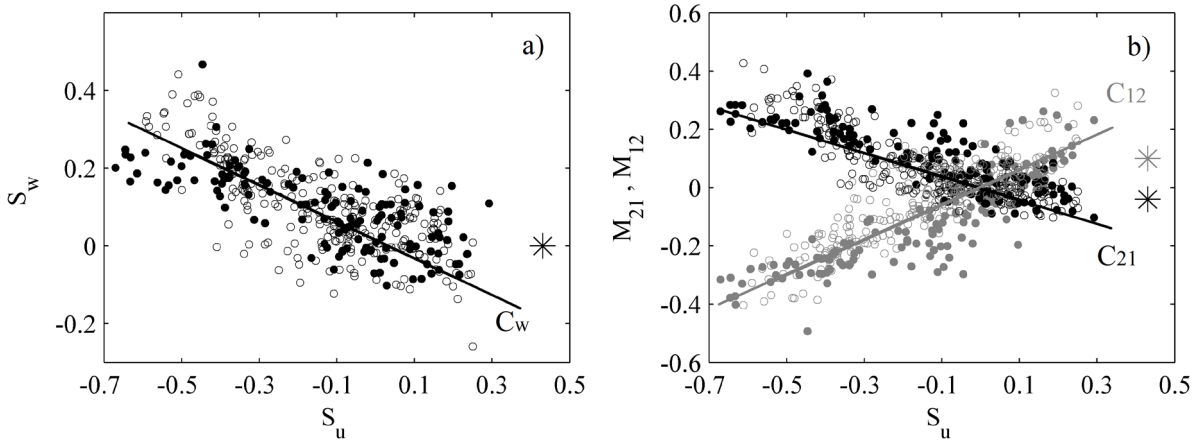

Figure 5.23- Relationship between the third-order moments (a) S_w with S_u, and (b) M_{21} and M_{12}, with S_u. *Legend Markers,* ○ *RG tests,* ● *CG tests,* ✳ *Wu & Jiang (2007). Legend Colors (b),* ● *ratio between (M_{21}, S_u), and* ● *ratio between (M_{12}, S_u).*

5.6 Quadrant sequences

So far, it has been proved that by adjusting the parameters of the GC JPDF it is possible to can achieve velocity series close to reality, however, the GC distribution does not give the series an order, i.e. the velocities are randomly distributed. This may not seem important a priori, however, the results from this section evidence the importance of giving a proper coherent order to the velocity data series.

5.6.1 Sequence of two movements (Trips)

Every time an event (*u',w'*) moves from one quadrant to a new one, or remains in the same, is considered in the present thesis as a "trip", or sequence of two movements. That is to say, a "trip" is the sequence of two consecutive quadrants, thus obtaining a total of 16 trips (Q1-Q1, Q1-Q2, Q1-Q3, Q1-Q4, Q2-Q1, Q2-Q2, Q2-Q3, Q2-Q4, Q3-Q1, Q3-Q2, Q3-Q3, Q3-Q4, Q4-Q1, Q4-Q2, Q4-Q3, and Q4-Q4), see example of Figure 5.24

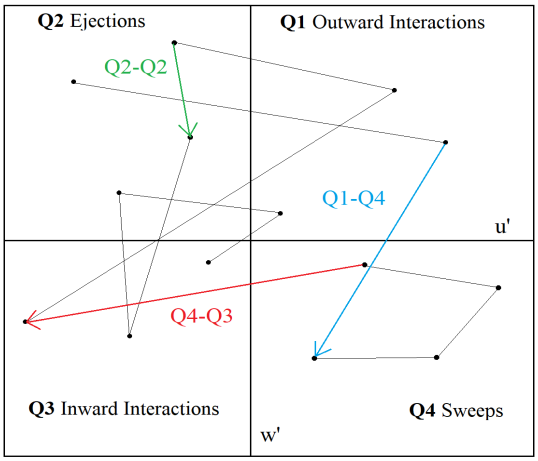

Figure 5.24- Example of trips.

A vector of quadrant position <Q_i> is obtained from the velocity data series for each time step (1/25 Hz=0.04 sec), in which Q_i is an event from a quadrant zone at a time (t), and (i) represents the quadrant zone 1, 2, 3 and 4. From this vector, it is possible to obtain the vector of trips *Qi(t)-Qi(t+1)*, in which the current quadrant and the next one are represented.

The representation of these trips on the quadrant map is depicted below in Figure 5.25-a. In the figure, it is noticeable that each color represents each quadrant *Qi(t)*. The blue markers represent the trips initiated from Q1, the green ones from Q2, the red ones from Q3 and finally the blacks from Q4. On the other hand, the markers represent the next quadrant *Qi(t+1)*, Q1 (×), Q2 (∗), Q3 (+) and Q4 (●), see the legend of Figure 5.25-a. In order to clarify the trip concept Figure 5.25-b show a scheme on the quadrant map, where each of the 16 trips is represented.

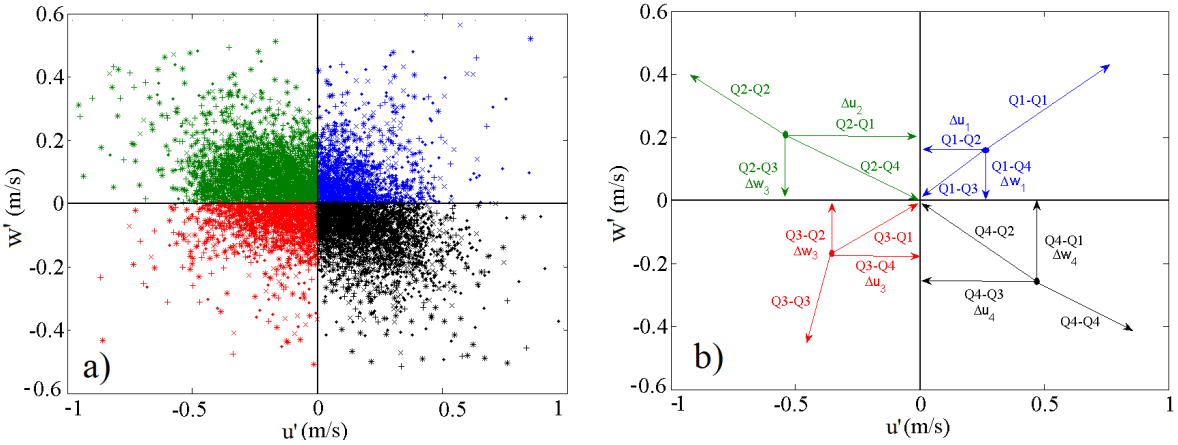

Figure 5.25- Turbulence maps of (a) Trips and (b) scheme of the trips. *Legend,* × *Q1-Q1,* ∗ *Q1-Q2,* + *Q1-Q3,* ● *Q1-Q4,* × *Q2-Q1,* ∗ *Q2-Q2,* + *Q2-Q3,* ● *Q2-Q4,* × *Q3-Q1,* ∗ *Q3-Q2,* + *Q3-Q3,* ● *Q3-Q4,* × *Q4-Q1,* ∗ *Q4-Q2,* + *Q4-Q3, and* ● *Q4-Q4).*

5.6.1.1 Vertical distribution of the Trips TF

The time fraction TF (%) of each trip has been assessed for all the tests, evaluated as the percentage of occurrence in the time series, and it was found that some trips stand out from the rest.

In Figure 5.26 it is depicted the vertical distribution, as a function of the dimensionless depth (*z/d*), of each trip TF just for some experiments from the RG group, and in Figure 5.27, some of the experiments

from the CG group, for the sake of brevity. The conclusion obtained from these graphs is that the trips that clearly soar above the others are those that cover trips inside Q2 and Q4, that is, the trips Q2-Q2 and Q4-Q4, while the Q1-Q1 and Q3-Q3 do not have a considerable probability. The probability of occurrence of the trips Q1-Q1 and Q3-Q3 is even lower than in a random distribution where the probability would have been p=1/16=6.25%. On the other hand, Q2-Q2 and Q4-Q4 have a probability of occurrence of around 15-16%, much higher than 6.25%. Moreover, the TF of the most likely trips (Q2-Q2 and Q4-Q4) follow the same trend that it was found for the vertical distribution of the QTF, meaning that not only these two quadrants are the most probable but also that they contain longer events.

It is observed in Figure 5.26 and Figure 5.27 that some trips stand out from the rest. These trips are Q1-Q4, Q4-Q1, Q2-Q3, Q3-Q2, and specially Q2-Q2, Q4-Q4. Figure 5.28 and Figure 5.29 show the evolution along the profile of these most frequent trips, for the RG and CG experiments respectively. The results show that all trip probabilities have a fairly constant behavior along the profile and very similar value between experiments, regardless of the flow ratio or the flow depth (d).

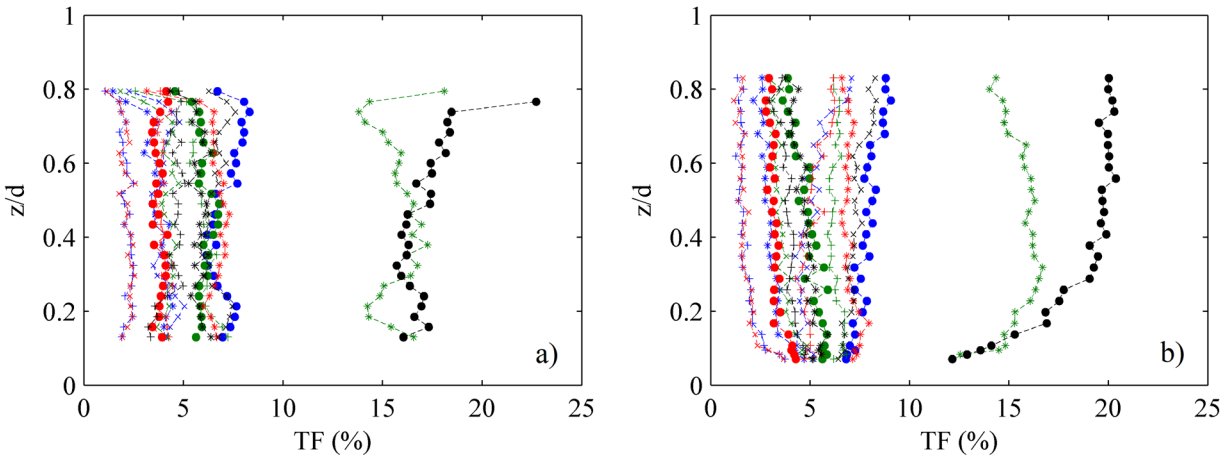

Figure 5.26- Vertical distribution of the trips TF (%) (a) RG1 and (d) RG10. *Legend, × Q1-Q1, ∗ Q1-Q2, + Q1-Q3, ● Q1-Q4, × Q2-Q1, ∗ Q2-Q2, + Q2-Q3, ● Q2-Q4, × Q3-Q1, ∗ Q3-Q2, + Q3-Q3, ● Q3-Q4, × Q4-Q1, ∗ Q4-Q2, + Q4-Q3, and ● Q4-Q4).*

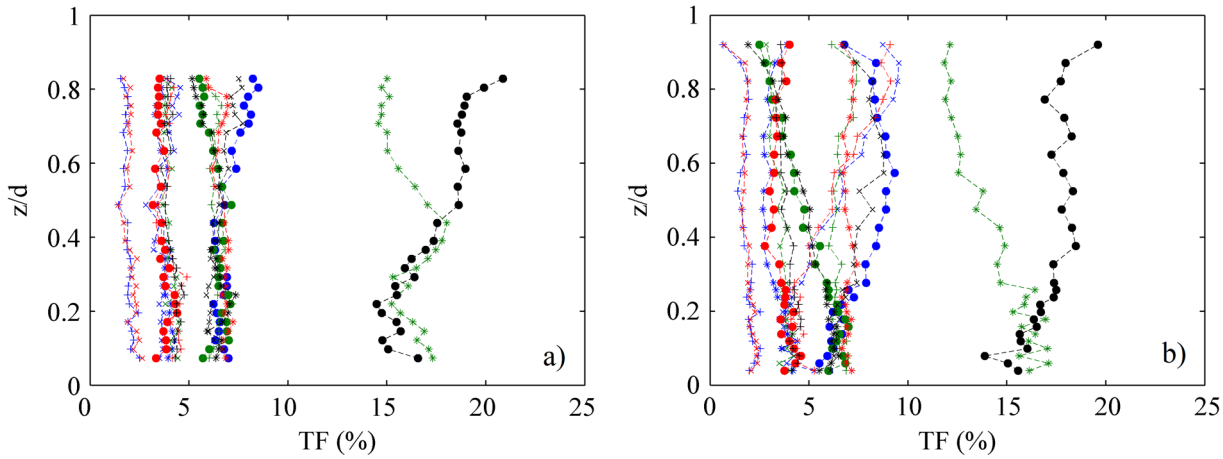

Figure 5.27- Vertical distribution of the trip TF (%) (a) CG1 (b) CG5. *Legend as for Figure 5.26.*

It is seen in both groups of experiments that the most likely trips (Q2-Q2 and Q4-Q4) show some differences depending on the experiment, thus on the flow depth (*d*), while the rest of the trips analyzed, with less probability, stay more constant along the depth profile and show fewer differences between experiments with different flow rate.

While trips Q2-Q2 tend to reduce their appearance in the sample slightly, trips Q4-Q4 increase their appearance, following the same vertical pattern exposed by the Q2-TF and Q4-TF.

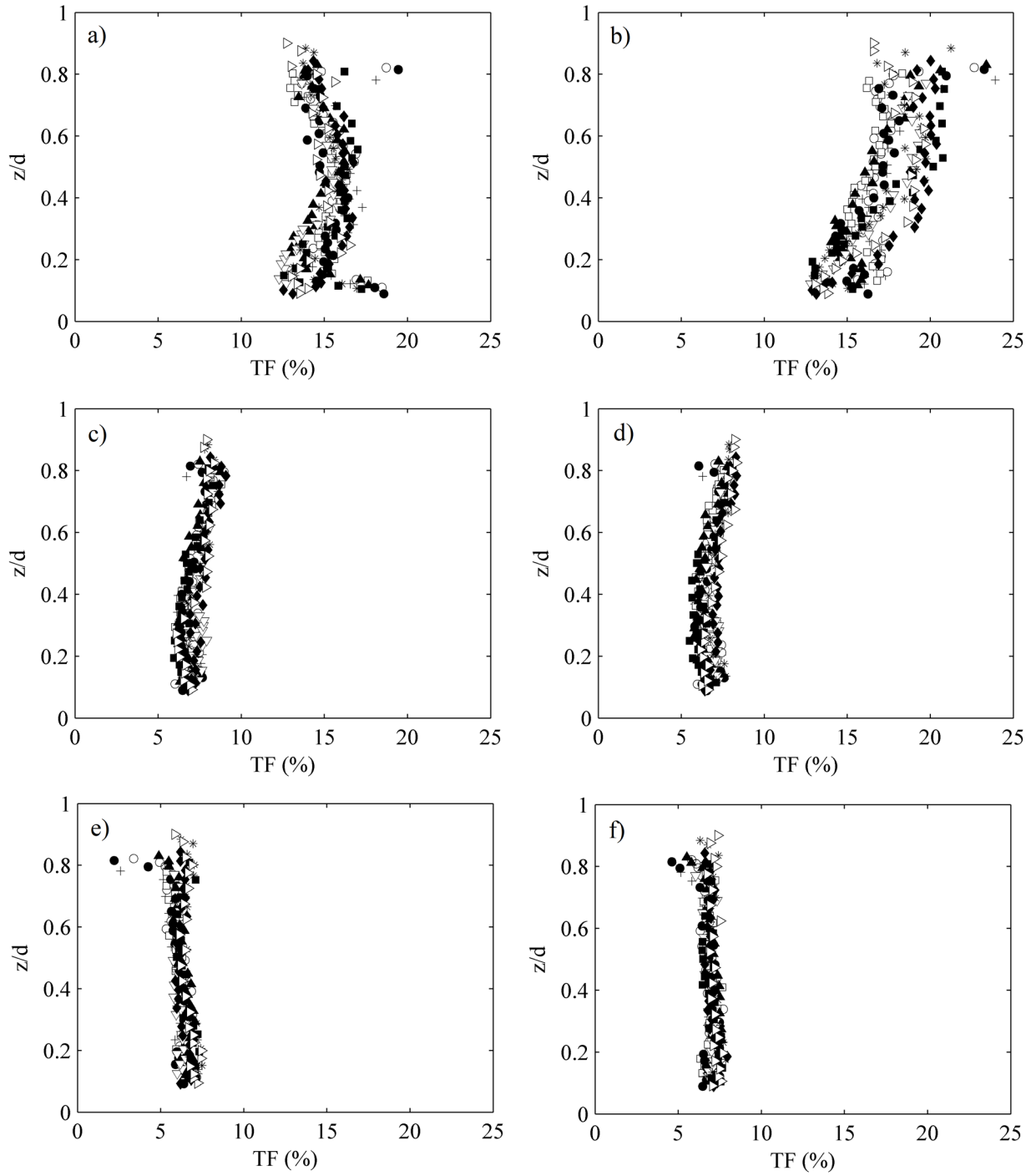

Figure 5.28- Vertical distribution of the trips TF (a) Q2-Q2, (b) Q4-Q4, (c) Q1-Q4, (d) Q4-Q1, (e) Q2-Q3, and (f) Q3-Q2, for all the RG. *Legend,* + *RG1,* ○ *RG2,* □ *RG3,* ● *RG4,* ▲ *RG5,* ▽ *RG6,* ✳ *RG7,* ♦ *RG8,* ■ *RG9 and* ▷ *RG10.*

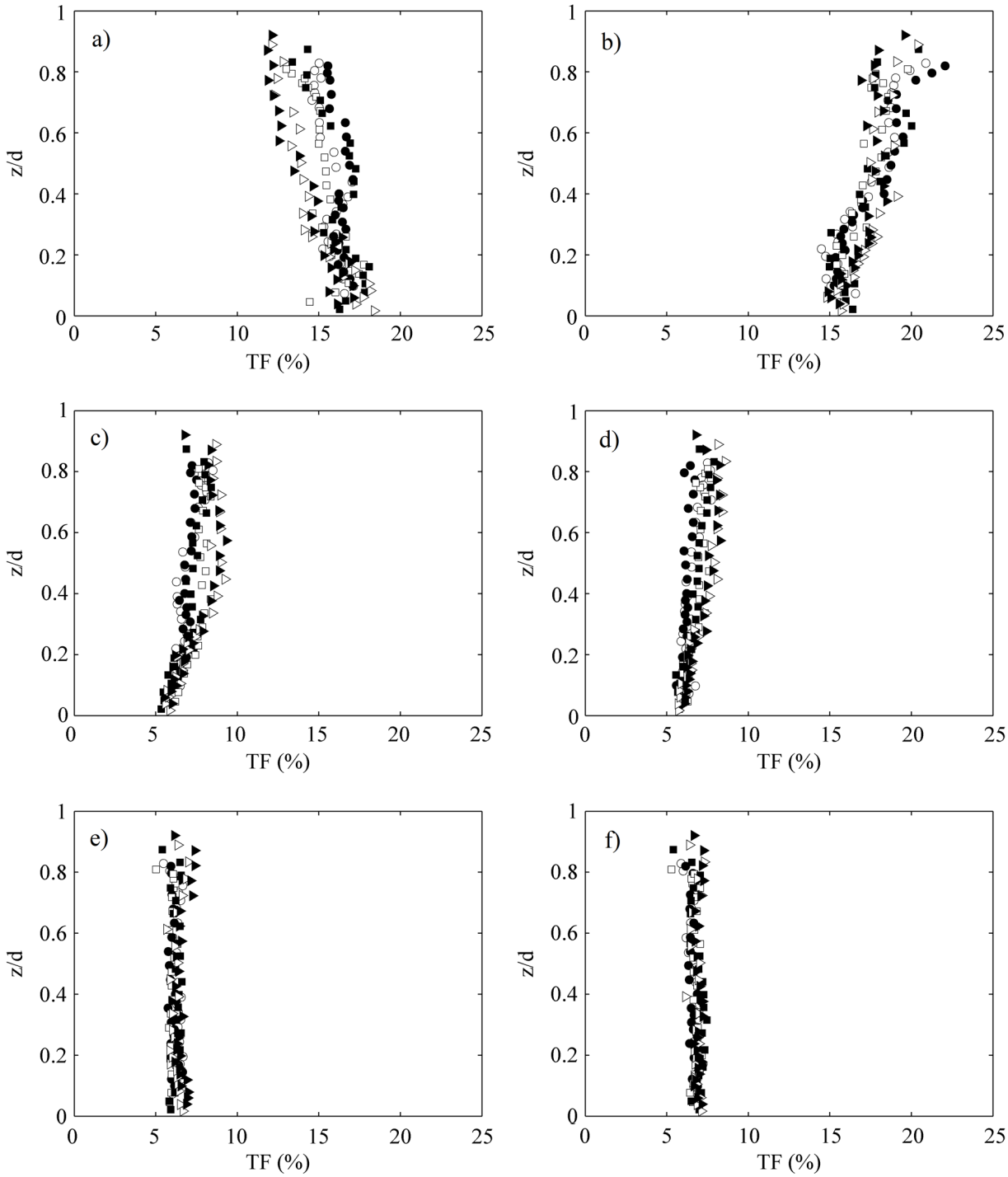

Figure 5.29- Vertical distribution of the trips TF (a) Q2-Q2, (b) Q4-Q4, (c) Q1-Q4, (d) Q4-Q1, (e) Q2-Q3, and (f) Q3-Q2, for all the CG. *Legend,* ○ *CG1,* ● *CG2,* □ *CG3,* ■ *CG4,* ▷ *CG5 and* ▶ *CG6.*

Despite the trends along the depth profile, the value of each trip TF can be considered very stable and it is worthwhile to obtain the depth-averaged for each experiment. In order to distinguish if there is any considerable difference as a function of the flow depth (*d*), and facilitate the comparison between experiments, Table 5.3 shows the depth-averaged TF (%) of each trip for the two groups of experiments.

Table 5.3 Average trip time-fraction results of the two groups of experiments

	1-1	1-2	1-3	1-4	2-1	2-2	2-3	2-4	3-1	3-2	3-3	3-4	4-1	4-2	4-3	4-4
RG1	4,04	3,90	2,22	6,99	4,25	15,96	6,09	6,13	2,21	6,75	4,06	3,78	6,65	5,82	4,44	16,70
RG2	4,44	4,11	2,34	7,07	4,14	14,18	6,63	6,36	2,43	6,81	4,74	4,03	6,96	6,21	4,29	15,25
RG3	4,17	3,96	2,51	6,75	4,31	15,44	6,24	6,01	2,47	6,92	4,56	3,97	6,45	5,67	4,60	15,98
RG4	4,33	4,01	2,37	6,90	4,35	15,48	6,21	6,04	2,46	6,89	4,40	3,82	6,47	5,70	4,58	15,98
RG5	4,43	4,32	2,79	6,44	4,48	14,38	6,78	6,06	2,83	7,30	5,30	4,35	6,24	5,70	4,90	13,68
RG6	4,83	3,89	2,52	7,47	4,37	13,81	6,16	5,83	2,55	6,94	4,71	3,86	6,95	5,54	4,67	15,89
RG7	4,74	3,68	2,32	7,10	3,80	15,28	6,78	5,40	2,37	7,23	5,10	3,73	6,92	5,08	4,23	16,22
RG8	4,79	3,33	2,05	7,56	3,87	15,51	6,30	5,27	2,03	7,07	4,91	3,43	7,04	5,03	4,18	17,63
RG9	4,73	3,66	2,21	6,34	3,77	15,11	6,55	5,52	2,22	6,92	5,26	3,83	6,21	5,27	4,22	18,17
RG10	5,31	3,39	2,35	7,60	3,81	14,51	6,78	4,85	2,28	7,28	5,94	3,56	7,25	4,77	3,98	16,33
Mean	4,63	3,83	2,37	7,02	4,12	14,94	6,45	5,75	2,39	7,01	4,90	3,84	6,71	5,48	4,41	16,16
CG1	3,68	3,85	1,97	6,70	4,08	16,42	6,43	6,48	2,11	6,75	4,10	3,73	6,32	6,39	4,20	16,78
CG2	3,58	3,74	1,93	6,74	4,20	16,46	6,08	6,41	1,99	6,65	3,87	3,67	6,21	6,30	4,31	17,85
CG3	4,64	3,60	1,87	6,78	3,97	16,41	5,99	6,90	1,81	6,56	4,06	3,74	6,36	5,51	4,26	17,82
CG4	4,60	3,64	1,94	6,69	4,00	16,85	6,80	6,83	1,89	6,50	5,18	3,55	6,39	5,33	3,95	16,48
CG5	4,56	3,35	1,82	7,30	3,78	15,94	6,16	6,01	1,91	6,79	4,65	3,64	6,78	5,81	4,36	17,12
CG6	4,79	3,50	1,99	7,25	3,77	15,30	6,48	5,80	2,01	6,93	4,99	3,67	6,96	5,63	4,14	16,78
Mean	4,31	3,61	1,92	6,91	3,97	16,23	6,32	6,41	1,95	6,70	4,48	3,67	6,50	5,83	4,20	17,14

To see the results more graphically Figure 5.30 depicts the average trip value of each experiment as a function of the flow depth (*d*). The graphic result shows that the depth-averaged TF depend slightly on the flow depth (*d*), above all the Q2-Q2 and the Q4-Q4 trips, the first decreasing and the second increasing with *d*.

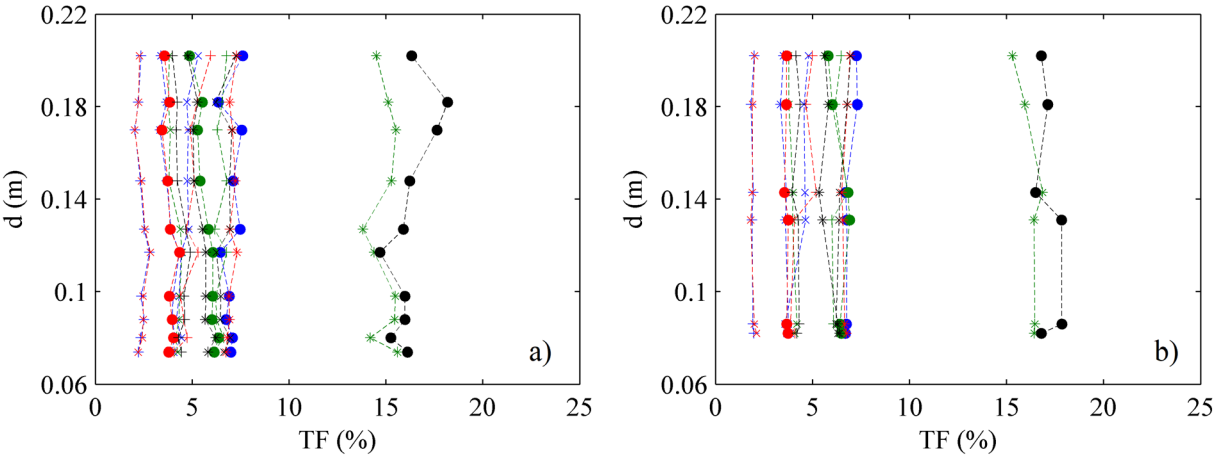

Figure 5.30- Depth-averaged trip TF (%)as a function of the flow depth (*d*), (a) RG and (b) CG experiments. *Legend,* × *Q1-Q1,* ∗ *Q1-Q2,* + *Q1-Q3,* ● *Q1-Q4,* × *Q2-Q1,* ∗ *Q2-Q2,* + *Q2-Q3,* ● *Q2-Q4,* × *Q3-Q1,* ∗ *Q3-Q2,* + *Q3-Q3,* ● *Q3-Q4,* × *Q4-Q1,* ∗ *Q4-Q2,* + *Q4-Q3, and* ● *Q4-Q4).*

5.6.2 Sequences of three movements

The bursting process consists of an intermittent quasi-cyclic sequential occurrence of events (Nezu and Nakagawa, 1977) following a kind of duty cycle (Brodkey et al. 1974). Therefore, longer sequences of events have to be studied. In this sense, sequences of three consecutive quadrants (64 sequences, permutations with repetition of four quadrants in a three quadrant chain) have been analyzed since the consideration of more than three consecutive quadrants do not show any highlighted sequence probability

5.6.2.1 Vertical distribution of the sequences TF

In Figure 5.31, the vertical patterns evolution of the 64 sequences, as a function of the dimensionless depth (*z/d*) are depicted for the RG and CG experiments respectively. In the figure, just four sequences have been highlighted, Q1-Q1-Q1, Q2-Q2-Q2, Q3-Q3-Q3, and Q4-Q4-Q4, thus the sequences that represent three consecutive events in the same quadrant, two of which, Q2-Q2-Q2 and Q4-Q4-Q4, are the most frequent sequences among all the sequences as can be seen in the figure.

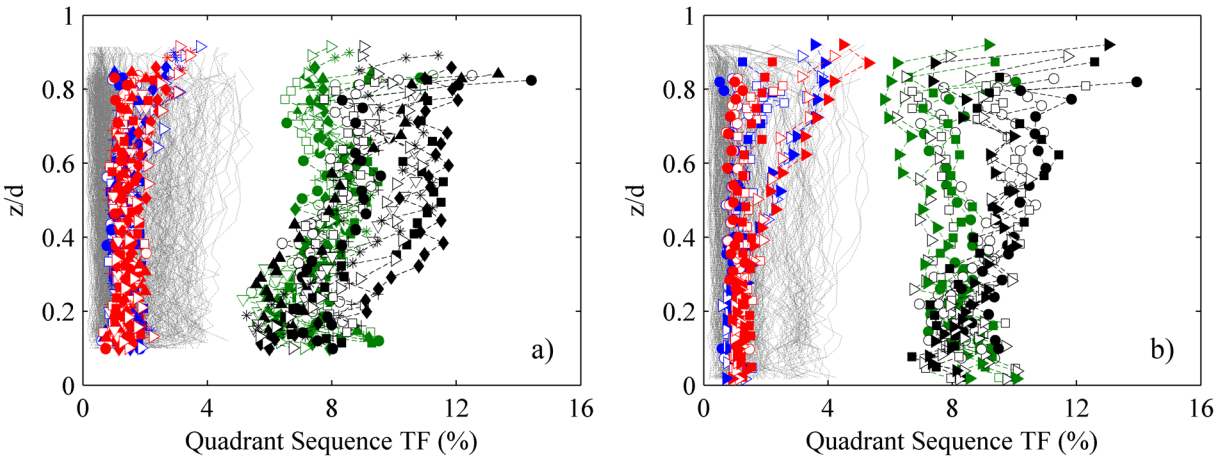

Figure 5.31- Vertical distribution of the Quadrant Sequence TF (%), for the (a) RG and (b) CG experiments. *Legend Markers (a),* + *RG1,* ○ *RG2,* □ *RG3,* ● *RG4,* ▲ *RG5,* ▽ *RG6,* ∗ *RG7,* ♦ *RG8,* ■ *RG9 and* ▷ *RG10. Legend Markers (b) ,* ○ *CG1,* ● *CG2,* □ *CG3,* ■ *CG4,* ▷ *CG5 and* ► *CG6. Legend colors,* ● *sequence 111,* ● *222,* ● *333,* ● *444, and* ● *the rest.*

The TF of the sequence Q4-Q4-Q4 gains importance in the outer region of the roughness layer, above all in the most powerful experiments, in contrast, the rest of the sequences maintain similar values in the different experiments. It is also observed that the packing of the bed particles does not show substantial differences between sequences in the near-bed region.

The sequences show a continuous pattern along the profiles demonstrating a quasi-cyclic behavior in space and time. In all sequences, especially in the less likely sequences, it is noticeable how they maintain their value very constant regardless of the flow rate and the height in the flow depth. Therefore, it is possible to obtain the average value in the depth, for each experiment, and for each sequence and relate this value to the flow depth (*d*) from each experiment. In Figure 5.32, the depth-averaged values of the most probable sequences, with a higher presence in the samples, are depicted as a function of the flow depth (*d*) in each experiment.

These sequences turned out to be, arranged in increasing order as Q4-Q4-Q4, Q2-Q2-Q2, Q1-Q4-Q4, Q4-Q4-Q1, Q3-Q2-Q2, Q2-Q2-Q3, Q2-Q3-Q2, Q2-Q4-Q4, Q2-Q2-Q4, Q4-Q2-Q2, Q2-Q3-Q2, and Q4-Q4-Q3.

From the list above, it can be assumed that when an event is placed in the Q2 and Q4, the current quadrant is the most likely. That is to say, an event tends to stay in those quadrants, since the most probable sequences are Q2-Q2-Q2 and Q4-Q4-Q4, and after these sequences, sequences, which imply a trip of Q4-Q4 or Q2-Q2, are more present in the series than the rest. Regarding the distribution of the mean value based on *d*, it must be mentioned that in most cases there is no substantial difference, only in the case of the two most likely sequences in which the value fluctuates, same as we saw with the trips, slightly increasing the Q4-Q4-Q4 and decreasing Q2-Q2-Q2 with the flow depth (*d*).

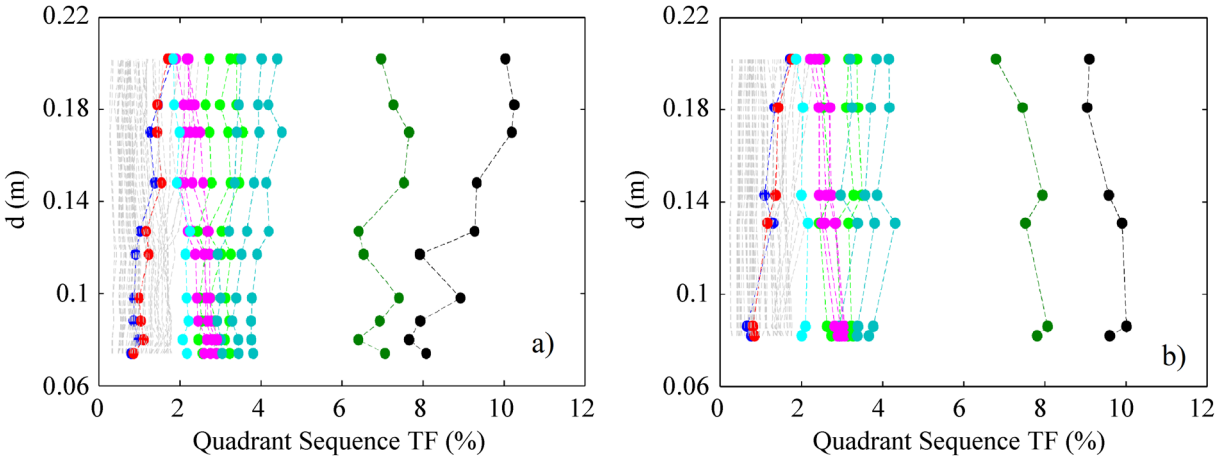

Figure 5.32- Depth-averaged Quadrant Sequence TF (%) as a function of the flow depth (d), for the (a) RG and (b) CG experiments. *Legend,* ● *sequence 111,* ● *222,* ● *333,* ● *444,* ● 223-232-322, ● *224-244-422-442,* ● *144-414-441, and* ● *the rest.*

5.6.3 Markov process

From the quadrant sequence analysis, it has been already demonstrated that the fluid motions are far from being completely chaotic, showing an organized behavior.

Keshavarzi & Shirvani (2002) found that the first-order Markov process is the most appropriate model to define the occurrence of the bursting process, due to its stochastic nature. The Markov model considers that the probability of a quadrant event depends only on current quadrant. This lack of memory is known as the Markov property. The method receives its name from the Russian mathematician Andréi Márkov (1856-1922), who introduced it in 1907.

5.6.3.1 First-order Markov process

The Markov process is governed by a set of probabilities, called transition probabilities (P_{ij}). In the present section, it is evaluated the suitability of the first-order Markov chain to model the transition probabilities of the events from a quadrant to the next one (16 trips).

The transition probabilities are defined as $P_{ij} = P\{Q(t+1) = j | Q(t) = i\}$, with i, j=1, 2, 3, 4 (quadrants). The transition probabilities (P_{ij}) are used to compose the transition matrix 4x4 (P_{IJ}). Figure 5.33 show the scheme of the transition probabilities.

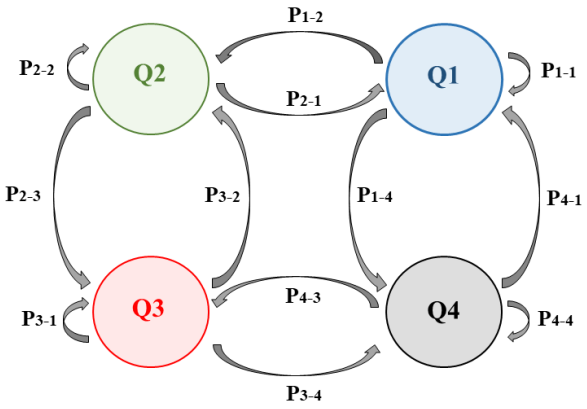

Figure 5.33- Markov Trip probability scheme

An example of a transition matrix (P_{IJ}) can be obtained using the mean TF of each trip obtained from experimental data (Table 5.3). The mean TF (probability) of trips between all experiments were similar so that the mean value for all experiments shown in the last row of Table 5.3 can be considered universal for the group of tests. This time fraction represents the probability that each trip has to occur, however, these values (Table 5.3) cannot be used directly to assemble the transition probability matrix (P_{IJ}). The P_{ij} values are the probability of each trip once the first quadrant has been established, therefore, to obtain each P_{ij} value, the TF trip has to be divided by the mean quadrant TF, or $P(Q_i)$, from the Table 5.1 (MEAN row), $P(Q_i)$=[0.178, 0.313, 0.181, 0.328]. In this way, the sum of the elements of the rows of P_{IJ} is equal to the unity. Below it is shown the transition probability matrix P_{IJ} obtained from experimental data.

$$P_{IJ} = \begin{vmatrix} P_{11} & P_{12} & P_{13} & P_{14} \\ P_{21} & P_{22} & P_{23} & P_{23} \\ P_{31} & P_{32} & P_{33} & P_{34} \\ P_{41} & P_{42} & P_{43} & P_{44} \end{vmatrix} = \begin{vmatrix} 0.259 & 0.214 & 0.133 & 0.393 \\ 0.132 & 0.478 & 0.206 & 0.184 \\ 0.131 & 0.387 & 0.270 & 0.212 \\ 0.205 & 0.167 & 0.135 & 0.493 \end{vmatrix}$$

The current quadrant probability at the time (t) is defined by the state vector $V_0 = P\{Q_i(t)\}$, with i=1, 2, 3, 4, and corresponds to the current quadrant. Therefore depending on the departing quadrant, the vector is defined as; $Q_i(t)$=1, $V_0 = \{1 \quad 0 \quad 0 \quad 0\}$, $Q_i(t)$=2, $V_0 = \{0 \quad 1 \quad 0 \quad 0\}$, $Q_i(t)$=3, $V_0 = \{0 \quad 0 \quad 1 \quad 0\}$, $Q_i(t)$=4, $V_0 = \{0 \quad 0 \quad 0 \quad 1\}$. Starting from the current situation (V_0) and using the matrix (P_{IJ}), it is possible to obtain the next quadrant probability $V_1 = P\{Q_i(t+1)\}$, by multiplying the transition matrix by the current situation vector, $V_1 = V_0 \cdot P_{IJ}$ and, thereby, the following states can be obtained as $V_n = V_0 \cdot {P_{IJ}}^{n+1}$.

The first observation is that the mean quadrant probability ($P(Q_i)$) is an invariant of a Markov chain because it fulfills the condition $V_0 = V_0 \cdot P_{IJ}$, when $V_0 = P(Q_i)$. In fact, every probability vector V_0 achieves a stationary process, when $\rightarrow \infty$, $V_n = V_0 \cdot {P_{IJ}}^{n+1} = P(Qi)$, in this case for n>8, no matter the value of V_0.

To check the suitability of the first-order Markov chain to represent the bursting process the transition matrix (P_{IJ}) is evaluated only using the mean quadrant probability $P(Q_i)$ obtained from Table 5.1, by means of Eq. 5-8. That is to say, if the transition matrix obtained considering only the $P(Q_i)$ is equivalent to the one obtained from the trip TF (experimentally), the process can be considered to follow a first-order Markov chain.

$$P_{ij} = \mathrm{P}(Q_{n+1} = j \,/\, Q_n = i) = (P_i \cdot P_j)/P_i \tag{5-8}$$

From Eq. 5-8 the obtained transition matrix P_{IJ} is the following:

$$P_{IJ} = \begin{vmatrix} 0.178 & 0.307 & 0.178 & 0.336 \\ 0.178 & 0.307 & 0.178 & 0.336 \\ 0.178 & 0.307 & 0.178 & 0.336 \\ 0.178 & 0.307 & 0.178 & 0.336 \end{vmatrix}$$

The result indicates that the probability of trips (P_{ij}) does not depend only on the quadrant probability $P(Q_i)$. The next matrix shows the percentage of error obtained from P_{IJ} (Eq. 5-8) with respect to the transition matrix obtained from the laboratory data ($P_{IJ,}$ Table 5.3).

$$\%\ of\ error = \begin{vmatrix} 31.31\% & -43.22\% & -34.20\% & 14.48\% \\ -35.19\% & 35.70\% & 35.70\% & -82.85\% \\ -35.24\% & 20{,}48\% & 20.48\% & -58.88\% \\ 13.01\% & -83.71\% & -83.71\% & 31.82\% \end{vmatrix}$$

The differences between both matrices display a relative error of between -83.7 and 35.70% showing that both transition matrices are far from being equivalent and therefore the probability to travel to a certain quadrant seem to depend not only on the current quadrant.

5.6.3.2 Second-order Markov process

As we have seen in the preceding section, the bursting process seems to have more memory than the immediately preceding quadrant. Therefore is possible to perform a second-order Markov chain where the probability of a sequence of three events (64 sequences) is represented instead of the trip probability. The transition probabilities are defined as $P_{ijk} = P\{Q(t+1) = k | Q(t-1) = i \ \&\ Q(t) = j\}$ (with i, j, k=1, 2, 3, 4), resulting in a 16x16 matrix (P_{IJK}). The Table 5.4 show the scheme of the transition matrix (converted as a first-order matrix transition) of the sequences of three events. Note that sequences of three events in the same quadrant compose the diagonal of the matrix.

Table 5.4 Scheme of a transition matrix P_{IJK}

	1-1	**1-2**	**1-3**	**1-4**	**2-1**	**2-2**	**2-3**	**2-4**	**3-1**	**3-2**	**3-3**	**3-4**	**4-1**	**4-2**	**4-3**	**4-4**
1-1	**111**	112	113	114	0	0	0	0	0	0	0	0	0	0	0	0
1-2	0	**0**	0	0	121	122	123	124	0	0	0	0	0	0	0	0
1-3	0	0	**0**	0	0	0	0	0	131	132	133	134	0	0	0	0
1-4	0	0	0	**0**	0	0	0	0	0	0	0	0	141	142	143	144
2-1	211	212	213	214	**0**	0	0	0	0	0	0	0	0	0	0	0
2-2	0	0	0	0	221	**222**	223	224	0	0	0	0	0	0	0	0
2-3	0	0	0	0	0	0	**0**	0	231	232	233	234	0	0	0	0
2-4	0	0	0	0	0	0	0	**0**	0	0	0	0	241	242	243	244
3-1	311	312	313	314	0	0	0	0	**0**	0	0	0	0	0	0	0
3-2	0	0	0	0	321	322	323	324	0	**0**	0	0	0	0	0	0
3-3	0	0	0	0	0	0	0	0	331	332	**333**	334	0	0	0	0
3-4	0	0	0	0	0	0	0	0	0	0	0	**0**	341	342	343	344
4-1	411	412	413	141	0	0	0	0	0	0	0	0	**0**	0	0	0
4-2	0	0	0	0	421	422	423	424	0	0	0	0	0	**0**	0	0
4-3	0	0	0	0	0	0	0	0	431	432	433	434	0	0	**0**	0
4-4	0	0	0	0	0	0	0	0	0	0	0	0	441	442	443	**444**

An example of a transition matrix (P_{IJK}) is shown in Table 5.5. The values have been obtained from the mean sequence (of three quadrants) time fraction from experimental data, especially from the depth-averaged value of each sequence from Figure 5.32-a (section 5.6.1.1). This TF of each sequence have to be normalized by dividing by the mean trip TF (last row of Table 5.3) so that the sum of the elements of the rows of P_{IJK} is equal to the unity. In other words, it shows the probability of P_{ijk} given that P_{ij}=1.

Table 5.5 Example of a transition matrix $P_{IJK,}$ from experimental data.

	1-1	**1-2**	**1-3**	**1-4**	**2-1**	**2-2**	**2-3**	**2-4**	**3-1**	**3-2**	**3-3**	**3-4**	**4-1**	**4-2**	**4-3**	**4-4**
1-1	0,260	0,174	0,116	0,450	0	0	0	0	0	0	0	0	0	0	0	0
1-2	0	0	0	0	0,167	0,402	0,197	0,234	0	0	0	0	0	0	0	0
1-3	0	0	0	0	0	0	0	0	0,149	0,346	0,242	0,263	0	0	0	0
1-4	0	0	0	0	0	0	0	0	0	0	0	0	0,214	0,139	0,117	0,529
2-1	0,226	0,227	0,146	0,402	0	0	0	0	0	0	0	0	0	0	0	0
2-2	0	0	0	0	0,113	0,500	0,212	0,175	0	0	0	0	0	0	0	0
2-3	0	0	0	0	0	0	0	0	0,120	0,414	0,264	0,201	0	0	0	0
2-4	0	0	0	0	0	0	0	0	0	0	0	0	0,198	0,200	0,151	0,451
3-1	0,216	0,243	0,154	0,387	0	0	0	0	0	0	0	0	0	0	0	0
3-2	0	0	0	0	0,122	0,479	0,218	0,182	0	0	0	0	0	0	0	0
3-3	0	0	0	0	0	0	0	0	0,115	0,414	0,276	0,196	0	0	0	0
3-4	0	0	0	0	0	0	0	0	0	0	0	0	0,199	0,217	0,169	0,416
4-1	0,255	0,185	0,117	0,444	0	0	0	0	0	0	0	0	0	0	0	0
4-2	0	0	0	0	0,167	0,404	0,190	0,239	0	0	0	0	0	0	0	0
4-3	0	0	0	0	0	0	0	0	0,151	0,354	0,244	0,251	0	0	0	0
4-4	0	0	0	0	0	0	0	0	0	0	0	0	0,212	0,148	0,120	0,520

The state vector is defined by the current trip at a time (t), $V_0 = P\{Q_i(t)Q_j(t)\}$. Same as for the first-order process, starting from the current situation (V_0) and using the matrix (P_{IJK}), it is possible to obtain the next trip probability $V_1 = P\{Q_i(t+1)Q_j(t+1)\}$, by multiplying the transition matrix by the current state vector $V_1 = V_0 \cdot P_{IJK}$, and the following states can be obtained as $V_n = V_0 \cdot {P_{IJK}}^{n+1}$.

The mean trip TF (last row of Table 5.3), or $P(Q_iQ_i)$, obtained through the analysis of experimental data is also an invariant vector of the Markov chain since it fulfills the condition $V_0 = V_0 \cdot P_{IJK}$, $V_0 = P(Q_iQ_i)$. In addition, all probability vectors V_0 reach a steady state for n> 5, fulfilling $V_n = V_0 \cdot {P_{IJK}}^{n+1} = P(QiQi)$ when $n \to \infty$, no matter the value of $V_{0.}$

As in the case of the first order Markov process, it is possible to check if the probability of a quadrant at the time (t + 2) can be achieved only considering the probability of the previous quadrant (t + 1) and the current quadrant (t). If the transition matrix P_{IJK} calculated by means of the experimental trip probabilities (Eq. 5-9) is equivalent to the obtained directly from the experiments (Table 5.5) the bursting process will be well represented by a second-order Markov chain. The transition matrix from Eq. 5-9 is shown below (Table 5.6).

$$P_{ijk} = \mathrm{P}(Q_{n+1} = k \,/\, Q_{n-1} = i \,\&\, Q_n = j) = (P_{ij} \cdot P_{jk})/P_{ij} \tag{5-9}$$

Table 5.6 Transition matrix P_{IJK} obtained from the trip probabilities.

	1-1	1-2	1-3	1-4	2-1	2-2	2-3	2-4	3-1	3-2	3-3	3-4	4-1	4-2	4-3	4-4
1-1	0,259	0,215	0,133	0,393	0	0	0	0	0	0	0	0	0	0	0	0
1-2	0	0	0	0	0,132	0,478	0,206	0,184	0	0	0	0	0	0	0	0
1-3	0	0	0	0	0	0	0	0	0,132	0,386	0,270	0,212	0	0	0	0
1-4	0	0	0	0	0	0	0	0	0	0	0	0	0,205	0,167	0,135	0,493
2-1	0,259	0,215	0,133	0,393	0	0	0	0	0	0	0	0	0	0	0	0
2-2	0	0	0	0	0,132	0,478	0,206	0,184	0	0	0	0	0	0	0	0
2-3	0	0	0	0	0	0	0	0	0,132	0,386	0,270	0,212	0	0	0	0
2-4	0	0	0	0	0	0	0	0	0	0	0	0	0,205	0,167	0,135	0,493
3-1	0,259	0,215	0,133	0,393	0	0	0	0	0	0	0	0	0	0	0	0
3-2	0	0	0	0	0,132	0,478	0,206	0,184	0	0	0	0	0	0	0	0
3-3	0	0	0	0	0	0	0	0	0,132	0,386	0,270	0,212	0	0	0	0
3-4	0	0	0	0	0	0	0	0	0	0	0	0	0,205	0,167	0,135	0,493
4-1	0,259	0,215	0,133	0,393	0	0	0	0	0	0	0	0	0	0	0	0
4-2	0	0	0	0	0,132	0,478	0,206	0,184	0	0	0	0	0	0	0	0
4-3	0	0	0	0	0	0	0	0	0,132	0,386	0,270	0,212	0	0	0	0
4-4	0	0	0	0	0	0	0	0	0	0	0	0	0,205	0,167	0,135	0,493

To assess the differences between the two transition matrices, obtained directly from the experiments (Table 5.5) and obtained by the trip TF (Table 5.6), the relative error matrix (Table 5.7) is obtained below. The differences between both matrices cover a relative error from -23.3 to 23%. This shows that, although there are differences, a certain proportionality is followed between both matrices (Table 5.5 and Table 5.6). Therefore, a Markov chain of second order better determines the quadrant time series than a first order process.

Table 5.7 Error of calculation of P_{IJK}.

	1-1	1-2	1-3	1-4	2-1	2-2	2-3	2-4	3-1	3-2	3-3	3-4	4-1	4-2	4-3	4-4
1-1	0,2%	-23,3%	-14,5%	12,6%	0	0	0	0	0	0	0	0	0	0	0	0
1-2	0	0	0	0	21,1%	-18,9%	-4,7%	21,4%	0	0	0	0	0	0	0	0
1-3	0	0	0	0	0	0	0	0	11,6%	-11,7%	-11,6%	19,5%	0	0	0	0
1-4	0	0	0	0	0	0	0	0	0	0	0	0	4,3%	-20,3%	-15,1%	6,8%
2-1	-14,8%	5,5%	9,1%	2,2%	0	0	0	0	0	0	0	0	0	0	0	0
2-2	0	0	0	0	-16,6%	4,4%	2,7%	-5,1%	0	0	0	0	0	0	0	0
2-3	0	0	0	0	0	0	0	0	-9,8%	6,7%	-2,3%	-5,3%	0	0	0	0
2-4	0	0	0	0	0	0	0	0	0	0	0	0	-3,4%	16,4%	10,9%	-9,4%
3-1	-20,1%	11,7%	13,8%	-1,6%	0	0	0	0	0	0	0	0	0	0	0	0
3-2	0	0	0	0	-8,0%	0,2%	5,4%	-1,1%	0	0	0	0	0	0	0	0
3-3	0	0	0	0	0	0	0	0	-14,6%	6,7%	2,1%	-8,0%	0	0	0	0
3-4	0	0	0	0	0	0	0	0	0	0	0	0	-2,9%	22,9%	20,3%	-18,6%
4-1	-1,7%	-16,0%	-13,5%	11,4%	0	0	0	0	0	0	0	0	0	0	0	0
4-2	0	0	0	0	21,1%	-18,3%	-8,6%	23,0%	0	0	0	0	0	0	0	0
4-3	0	0	0	0	0	0	0	0	12,7%	-9,2%	-10,7%	15,7%	0	0	0	0
4-4	0	0	0	0	0	0	0	0	0	0	0	0	3,4%	-13,0%	-12,2%	5,1%

5.7 Poincare Maps

Around the same time that Reynolds was proposing a random description of turbulent flow, Poincaré (1899) was finding a deterministic view of simple nonlinear dynamic systems that exhibit a chaotic behavior. Yet, it will be 70 years later when Lorenz (1963), an American meteorologist, proposed links between "deterministic chaos" and turbulence.

The state of a continuous dynamic system is the smallest set of variables that allows knowing the evolution of a system when the inputs of this are known. The set of all states is known as the state space. A Poincaré map gives the location of the next step of a path through a Poincaré section based on the current location of the path. It is, therefore, the intersection of a periodic orbit in the state space of a continuous dynamic system with a certain subspace of smaller dimensions, called the Poincaré section, transverse to the flow of the system. They provide mainly a qualitative description of the general behavior of a dynamic system; but because they are relatively simple, it has been suggested that they could have the potential for use in turbulence models.

We use the Poincaré maps here trying to find a hint of the deterministic behavior of turbulence. The Poincare map is defined as the representation of the instantaneous velocity *u'* (X-coordinate) with its velocity variation Δu (Y-coordinate). The velocity variation (or velocity increment) represents the acceleration (a) but multiplied by the time interval ($\Delta u = a \cdot \Delta t$). It has been done this way so that both axes (u', Δu) have the same units and the continuous value of the time-interval Δt=0.04 s allows it. The Phase-state maps, or Poincare maps, are the representation of the velocity variation (Δu) that occurs inside each burst or event as a function of the instantaneous velocity (u).

5.7.1 Quadrant-events on the Poincaré maps

Figure 5.34 shows the Poincaré maps, phase-state map (u', Δu), obtained at two different heights (z=10 mm and z=35 mm) for three different experiments (RG1, RG5, and RG10). On the other hand, Figure 5.35 shows the phase state map of the vertical velocity fluctuation (w', Δw), for the same experiments.

In Figure 5.34, each event is represented by a pair (u', Δu), where u' is the instantaneous streamwise fluctuation and Δu the subsequent velocity variation. This value represents the acceleration ($a = \Delta u / \Delta t$); however, because the time interval Δt has a constant value (Δt=1/25 Hz=0.04 s), it is preferred to keep Δu instead of the acceleration, since it has same units than the velocity (m/s), so that it can be obtained a fitted slope of the cloud of events.

The maps from the point inside the near-bed region (z=10 mm), Figure 5.34-a-b-c, display more extreme values than at height of z=35 mm, Figure 5.34-d-e-f, denoting that the most extreme turbulence fluctuations occur inside this region with higher accelerations. In the same way, at the same height z more extreme values are obtained from the experiments with a higher level of turbulence, RG10 (Figure 5.34-c) in comparison with RG1 (Figure 5.34-a).

It can be seen that the left side of the ordinate axis corresponds to negative velocity fluctuations $u' < 0$ ($u < \bar{u}$), thus these velocities would correspond to quadrants Q2 (green) and Q3 (red), in the turbulent velocity maps (see in section 5.2). At the right side, we found the positive values of u', corresponding to Q1 (blue) and Q4 (black).

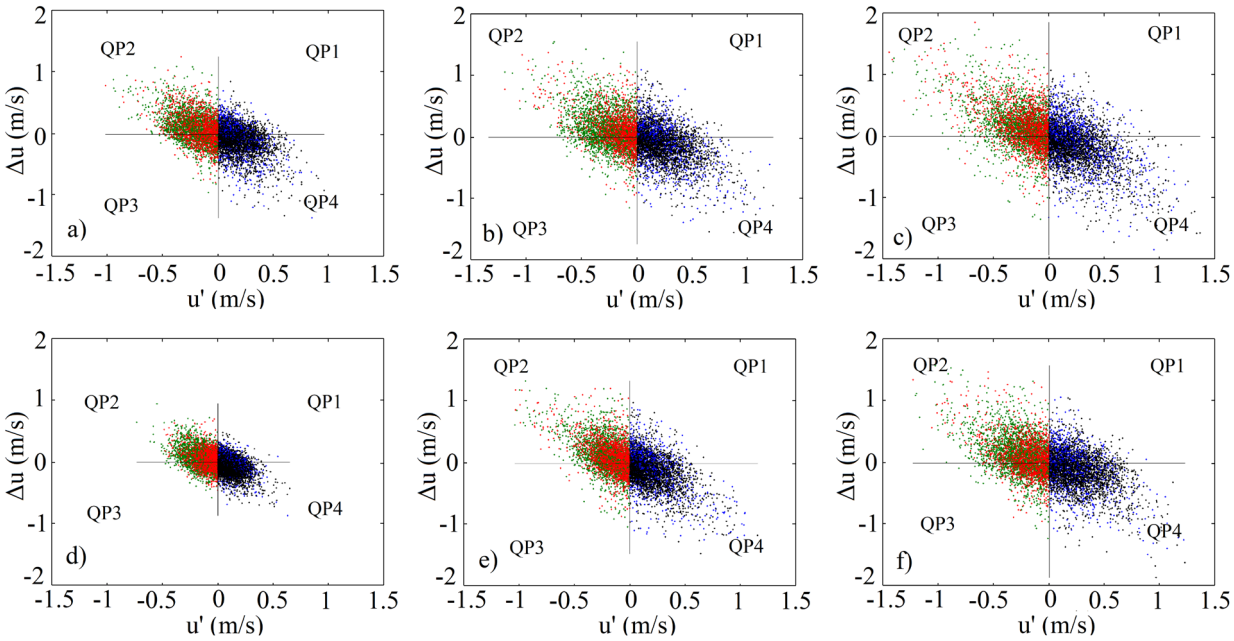

Figure 5.34- Phase state maps of *(u', Δu)* for (a) RG1 at *z*=10 mm, (b) RG5 at *z*=10 mm, (c) RG10 at *z*=10 mm, (d) RG1 at *z*=35 mm, (e) RG5 at *z*=35 mm, (f) RG10 at *z*=35 mm. *Legend,* ● *Q1,* ● *Q2,* ● *Q3, and* ● *Q4.*

If the phase-state map is interpreted by quadrants (QP1 ($u > \bar{u}$, $\Delta u>0$), QP2 ($u < \bar{u}$, $\Delta u>0$), QP3 ($u < \bar{u}$, $\Delta u<0$) and QP4 ($u > \bar{u}$, $\Delta u<0$)), it is noticeable that the density of points is higher in QP2 and QP4. That is to say, the cloud of points is biased with a negative value of the fitted slope in all cases, thus positive velocity fluctuations ($u'>0$) in QP4 ($u'>0$, $\Delta u<0$) are likely to be followed by a negative velocity variation ($\Delta u < 0$), that is, u tends to decelerate in QP4. On the other hand, for the events at QP2 ($u'<0$, $\Delta u>0$), with negative fluctuation $u'<0$, are more likely to be followed by a positive velocity increments, thus u tends to accelerate. The latter seems logical and shows the turbulent nature of the flow.

In Figure 5.35, the same points of the profiles displayed in Figure 5.34are now represented on the Phase-state maps of vertical velocities (w', $\Delta w'$). The figure shows the same logical effect, extreme vertical v elocity fluctuations (w') are followed by a high vertical velocity variation ($\Delta w'$) with an opposite sign. Equal than Figure 5.34, the cloud of point becomes more accentuated with increasing turbulence, at the near-bed region, and for the most powerful experiments, with higher density in QP2 and QP4. In this case, the left side of the map hosts the events in quadrants Q3 (red) and Q4 (black) and the right side the Q1 (blue) and Q2 (green).

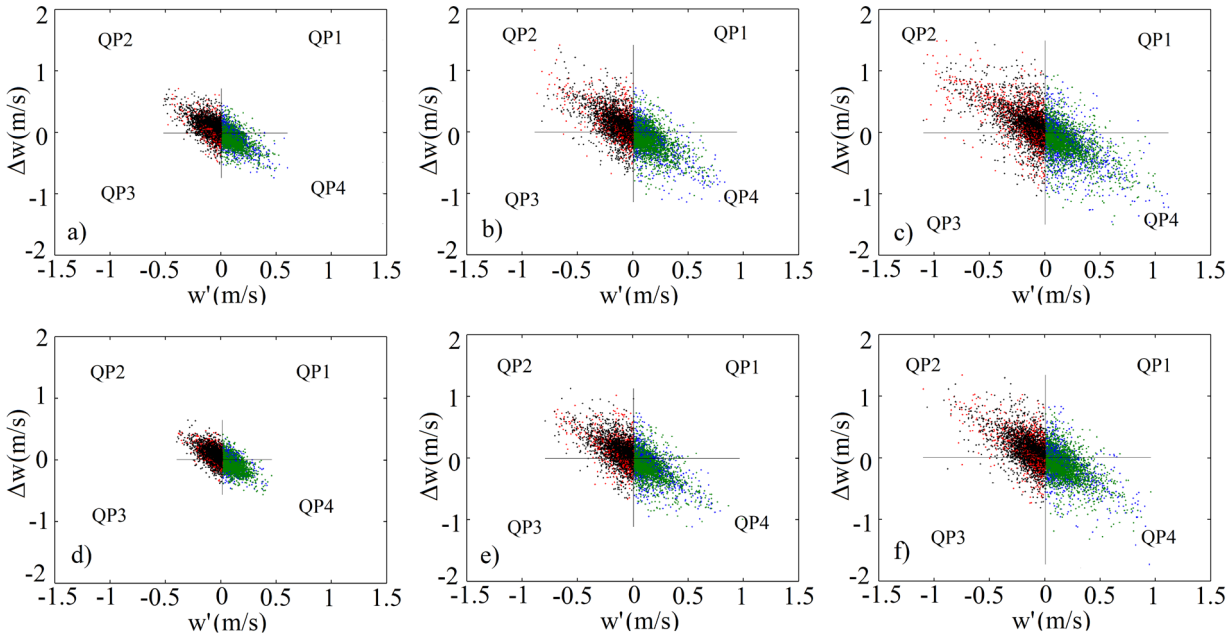

Figure 5.35- Phase state maps of *(w',Δw)* for (a) RG1 at *z*=10 mm, (b) RG5 at *z*=10 mm, (c) RG10 at *z*=10 mm, (d) RG1 at *z*=35 mm, (e) RG5 at *z*=35 mm, (f) RG10 at *z*=35 mm. *Legend,* ● *Q1,* ● *Q2,* ● *Q3, and* ● *Q4.*

5.7.2 Vertical distribution of the Poincaré slope

Although in all cases the cloud of points is biased to QP2 and QP4 (Figure 5.34, Figure 5.35), the fitted slope (*m*) slightly varies for each height (*z*) in the depth profile. In the near-bed region, *m* reaches negative maximum values and starts to decrease, approaching zero value with the height in the profile. The more negative is *m* (steeper), the more extreme are the velocity increments. However, when *m* approaches zero, the point cloud becomes more horizontal, with less extreme velocity variations (accelerations).

In order to see graphically the evolution of this fitted slope (*m*) along the depth profile, Figure 5.36 and Figure 5.37, show the vertical distribution of *m* obtained from the Poincaré maps (*u', Δu'*) and (*w', Δw'*) respectively, for the two groups of experiments. From Figure 5.36, it is observed that the negative nature of *m* becomes more accentuated in the near-bed region for high flow rates (high level of turbulence) in the RG experiments (from RG6 to RG10). The fitted slope seems to reach a little higher value in the well-packed beds (CG2, CG4, and CG6) in comparison to the not-packed beds (CG1, CG3, and CG5), thus with the increase of the roughness the accelerations of *u*' are damped, although the differences are minimal.

For the low turbulent cases, (RG1 to RG5) and (CG1 and CG2), the value of the slope has a constant value along the roughness region, showing a maximum at *z/d* =[0.2-0.3], and decrease slowly and progressively to the water surface. On the other hand, the most turbulent experiments (RG6 to RG10) have a descending slope until the bed, showing that as the distance to the bed increase (*z*) the accelerations decay more. In the case of the CG experiments where it was possible to get closer to the boundary, the experiments with a higher level of turbulence (CG3 to CG6) it is observed that the maximum slope value is not reached just at the surface of the roughness but at a height of *z/d* =0.15 approximately.

It is has been demonstrated that the streamwise accelerations are greater in the region near the bed and maintaining a fairly constant value throughout the roughness region. However, this value can decrease slightly in the crests of the roughness, due to the interaction of the fluid-roughness; the streamwise accelerations seems to be a little greater in the case of the well-packed surfaces, which is consistent with the results of turbulent intensity from chapter 4.

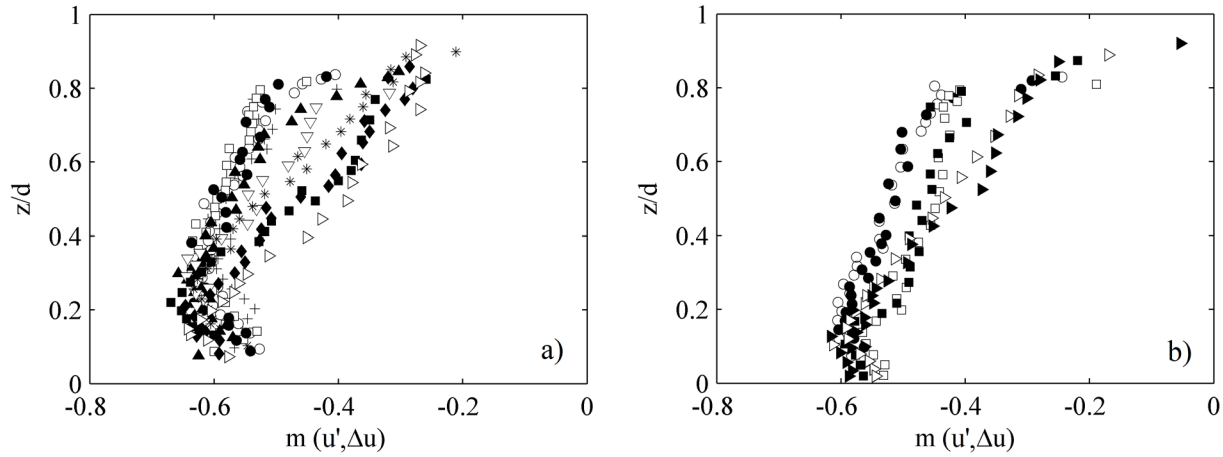

Figure 5.36- Vertical distribution of the fitted slopes (m) from the points cloud *(u', Δu)* for (a) RG and (b) CG experiments. *Legend (a), + RG1, ○ RG2, □ RG3, ● RG4, ▲ RG5, ▽ RG6, ✳ RG7, ♦ RG8, ■ RG9 and ▷ RG10. Legend (b), ○ CG1, ● CG2, □ CG3, ■ CG4, ▷ CG5 and ▶ CG6.*

In the case of the fitted slope (*m*) of the events cloud on the Poincaré map (*w', Δw'*) (Figure 5.37), it is noticeable the same slope pattern, the negative value decreases, thus denoting the acceleration decrease on the vertical axis toward the water surface. However, the decrease occurs in a more slowly manner, remaining far from zero even near the water surface. This shows that accelerations are high throughout the whole profile; there is much exchange of momentum in the vertical direction. Nevertheless, these accelerations are higher in the near-bed region, due to the interaction of the fluid with the particles.

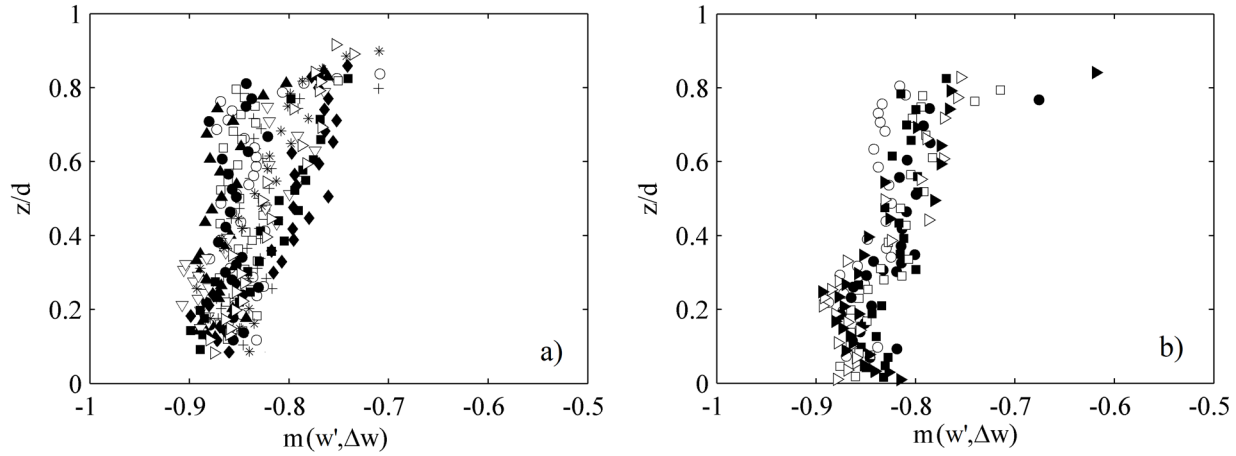

Figure 5.37- Vertical distribution of the fitted slopes from the point clouds (*w', Δw*) for (a) RG and (b) CG experiments. *Legend (a), + RG1, ○ RG2, □ RG3, ● RG4, ▲ RG5, ▽ RG6, ✳ RG7, ♦ RG8, ■ RG9 and ▷ RG10. Legend (b), ○ CG1, ● CG2, □ CG3, ■ CG4, ▷ CG5 and ▶ CG6.*

The vertical acceleration (or *Δw')* turns out to be a little more pronounced close to the bed for cases of equal level of turbulence but with not-packed surfaces, in comparison with those with smoother surfaces, that is to say, the experiments CG1, CG3 and CG5 against CG2, CG4, and CG6. The latter is probably due to the interaction of the roughness crests, reaching higher *w'* and *Δw',* which is consistent with the results of turbulent intensity from chapter 4.

5.7.3 Trajectories of the events on the Poincaré maps

It is possible to analyze the Poincaré maps by frames of time intervals as we did with for the turbulent velocity maps. The trajectories in the phase-state maps have been investigated by observing its evolution in time.

In Figure 5.38, some of the frames covering a period of 0.48 seconds (12-time intervals of *Δt*=0.04 sec) of the Phase-state (*u', Δu'*) are shown. It is observed how the movements are rather ordered and seem to follow a clockwise rotation. The trajectory seems to be stable for low streamwise velocity fluctuations, below the mean velocity, while is more erratic for higher velocities. However, no differentiated pattern seems to stand out.

In the case of the period frames of the phase-state map (*w', Δw'*), Figure 5.39, the behavior seems to follow the same clockwise direction but with the trajectories closer to the center of coordinates and with a higher frequency of appearance.

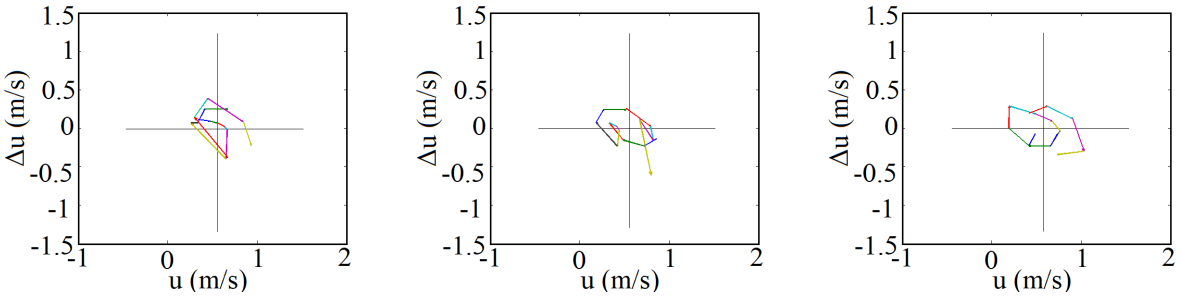

Figure 5.38- Phase state maps (u, Δu) for different frames of 0.48 s from the RG1 at a height of z=1 mm.

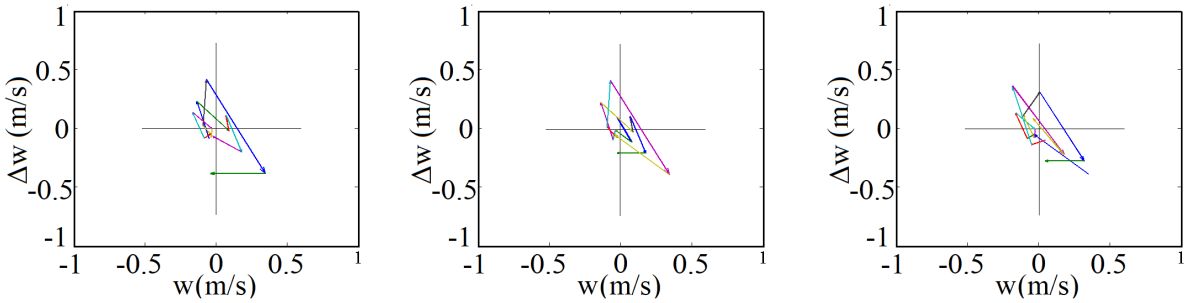

Figure 5.39- Phase state maps (w, Δw) for different frames of 0.48 s from the RG1 at a height of z=1 mm.

5.7.4 Probabilities of events on the Poincaré Maps

As mentioned before, a synthetic velocity data series is far from representing the nature of the phenomenon if the series is not given a certain order, since the experimental data show conclusive results of following a coherent order.

In order to shed some light on the mechanism of development of turbulent events, this section shows the density maps of these events on the phase-state maps, with the purpose of seeing if quadrant-events (section 5.7.1) and their sequences (section 5.6) show some incidence zone in the phase-state maps.

5.7.4.1 Density Maps of quadrant-events

Figure 5.40 depicts the quadrant-events density (heat map) on the phase-state map (*u', Δu'*), that is to say, the probability that a pair (*u', Δu')* have to belong to a certain quadrant. The figure demonstrates that all events have a higher density close to the equilibrium (origin of coordinates). Therefore, low-velocity fluctuations are followed by low-velocity variations. The density map shows that events from Q1 and Q2 have similar distribution on the Poincaré maps, as well as the Q4 and Q3 have it. However, events from Q2 and Q4 reach higher accelerations and have higher density, because as it was verified they have higher TF in the data series.

The height point (*z*) represented in Figure 5.40 pertain to the near-bed area where the QTF are distributed as Q1-TF=17.69%, Q2-TF=31.94% Q3-TF=16.36% Q4-TF=34%, thus the percentage of appearance of Q4 events (sweeps) is similar to the Q2 (ejections). In Figure 5.40-a the density of Q4 events (sweeps) is concentrated close to the origin of coordinates, while the Q2-events (ejections) are more spread out.

On the other hand, Figure 5.41 depicts the density of the quadrant events on the Poincaré map (*w', Δw'*). Same as in Figure 5.40, all events have a higher density close to the equilibrium (origin of coordinates). The density map also shows that the quadrant events have a similar distribution in the Poincaré maps (*w', Δw'*) for quadrants Q4-Q3 and Q2-Q1.

Both maps, Figure 5.40 and Figure 5.41, show that each quadrant-event has a probability on each position on the Poincaré maps, and that could be very useful in the goal of generating synthetic velocity series. However, it should be noted that the probabilities on the Poincaré Map would vary depending on the level of turbulence and the height in the depth profile, so the density map must be characterized by levels of turbulence and height in the depth profile.

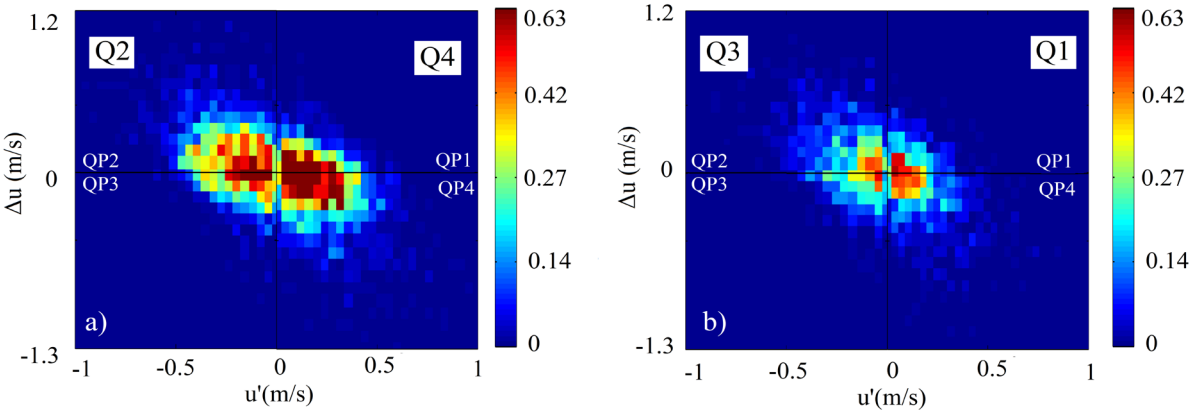

Figure 5.40- Density of the quadrant-events (a) Q2 and Q4 and (b) Q3 and Q1, on the Poincaré Map (*u', Δu*). Experiment RG1 at *z*=10 mm.

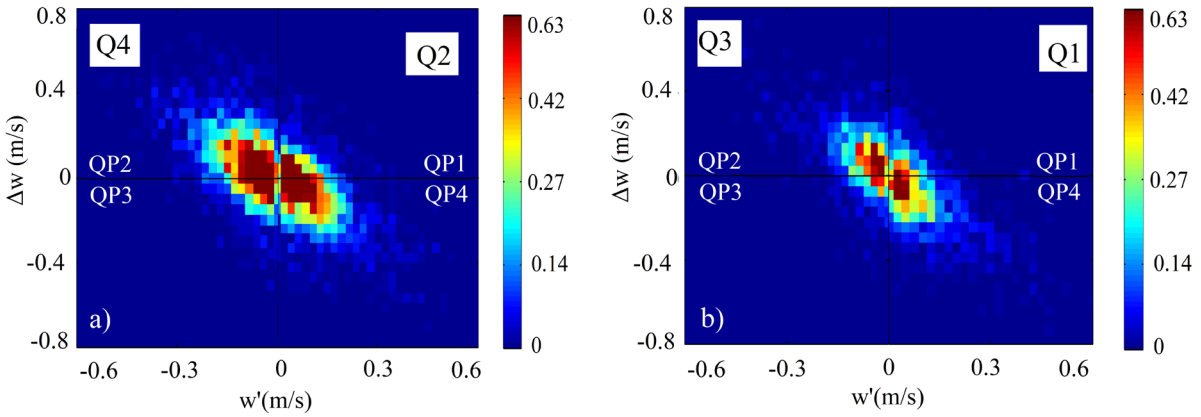

Figure 5.41- Density of the quadrant-events (a) Q2 and Q4 and (b) Q3 and Q1 on the Poincaré Map (*w', Δw*). Experiment RG1 at *z*=10 mm.

5.7.4.2 Density Maps of Trips

With the aim of analyzing more accurately the trajectory of the events on the Poincaré maps, each event on the maps (*u', Δu'*) and (*w', Δw'*), has been named after the trip between quadrants that it makes. As a result, Figure 5.42 and Figure 5.43 show an example of the trips on the Poincaré maps of (*u', Δu'*) and (*w', Δw'*) respectively.

The same strategy for the symbols used in the section 5.6.1 has been used for the representation of the trips. That is, if a trip is represented as $Q_i(t)$-$Q_i(t+1)$, the color represents the departure quadrant $Q_i(t)$, Q1 (blue), Q2 (green), Q3 (red) and Q4 (black); and the markers represent the arrival quadrant $Q_i(t+1)$, Q1 (×), Q2 (∗), Q3 (+) and Q4 (●) (see legend of Figure 5.42).

In Figure 5.42-a, Poincare map (*u', Δu'*), it makes sense that the positioning of the trips depends on the departing quadrant $Q_i(t)$. The trips departing from Q1 and Q4 are inside the right side of the ordinate axis (zone A) since both have positive velocity fluctuation $u'>0$ ($u>\bar{u}$). In the same manner, trips departing from Q2 and Q3, thus with $u'<0$ ($u<\bar{u}$), are located on the left side (zone B). It can be also observed that depending on the arrival quadrant $Qi(t+1)$ (Figure 5.42-b) the trips are again divided into two zones defined by the diagonal dashed line (C and D). The zone C include the arrival quadrants Q1 and Q4, and zone D hosts the trips with arrival quadrants Q2 and Q3. The diagonal comes from the imposition $\Delta u=u'$, obtaining an inclination of 45º with the horizontal axis. If $\Delta u< u'$ (zone C), the event will not have enough Δu to change its quadrant position. Contrarily, when $\Delta u>u'$ (zone D) the event will move from its current quadrant $Q_i(t)$ to a different quadrant $Qi(t+1)$. From this observation, the trips are then organized in the Poincaré map (*u', Δu*) as shown in Figure 5.33-a.

In the case of Figure 5.43, Poincare map (*w', Δw*), a similar sort distribution is found. In Figure 5.43-a, the vertical axis separate zones where the trips depart. The right zone (A) hosts the departing quadrants $Q_i(t)$ Q1 and Q2, both with $w'>0$, and the left zone (B) include the departing quadrants Q3 and Q4 ($w'<0$). On the other hand Figure 5.43-b show the zones defined by the arrival quadrants $Q_i(t+1)$ by means of a diagonal with an angle of 45º with the horizontal axis, due to the imposition of $\Delta w=w'$. The summary of trips distribution in the Poincare map (*w', Δw*) is shown in Figure 5.33-b.

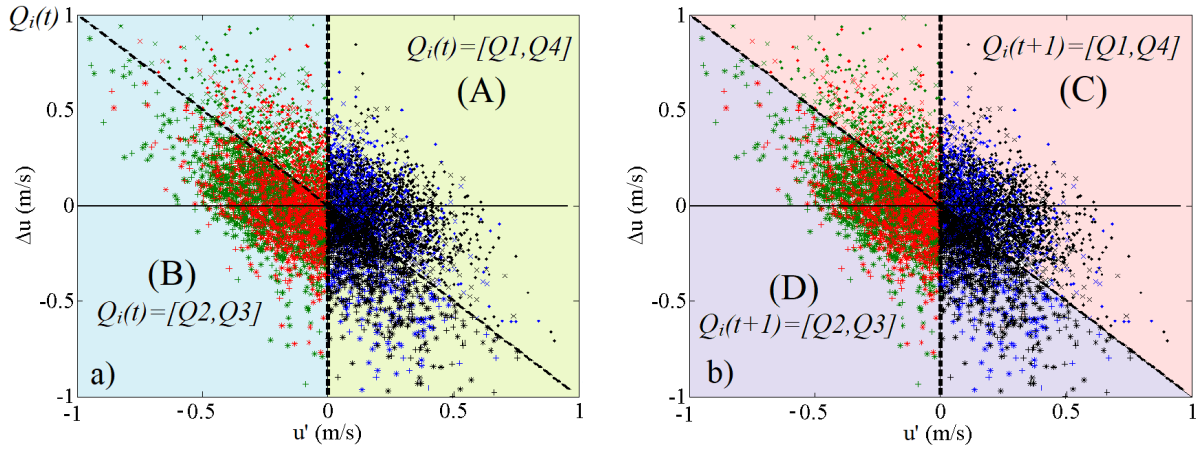

Figure 5.42- Trips represented on the Poincaré map in the axes (*u', Δu'*). *Legend,* × *Q1-Q1,* ∗ *Q1-Q2,* + *Q1-Q3,* ● *Q1-Q4,* × *Q2-Q1,* ∗ *Q2-Q2,* + *Q2-Q3,* ● *Q2-Q4,* × *Q3-Q1,* ∗ *Q3-Q2,* + *Q3-Q3,* ● *Q3-Q4,* × *Q4-Q1,* ∗*Q4-Q2,* + *Q4-Q3, and* ● *Q4-Q4).*

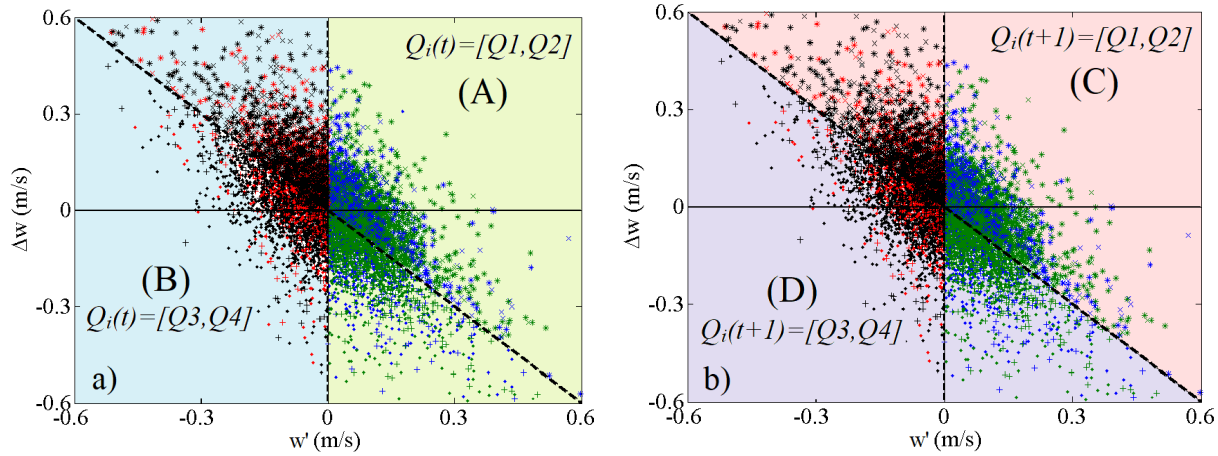

Figure 5.43- Trips represented on the Poincaré map in the axes (*w', Δw'*). *Legend,* × *Q1-Q1,* ∗ *Q1-Q2,* + *Q1-Q3,* ● *Q1-Q4,* × *Q2-Q1,* ∗ *Q2-Q2,* + *Q2-Q3,* ● *Q2-Q4,* × *Q3-Q1,* ∗ *Q3-Q2,* + *Q3-Q3,* ● *Q3-Q4,* × *Q4-Q1,* ∗*Q4-Q2,* + *Q4-Q3, and* ● *Q4-Q4).*

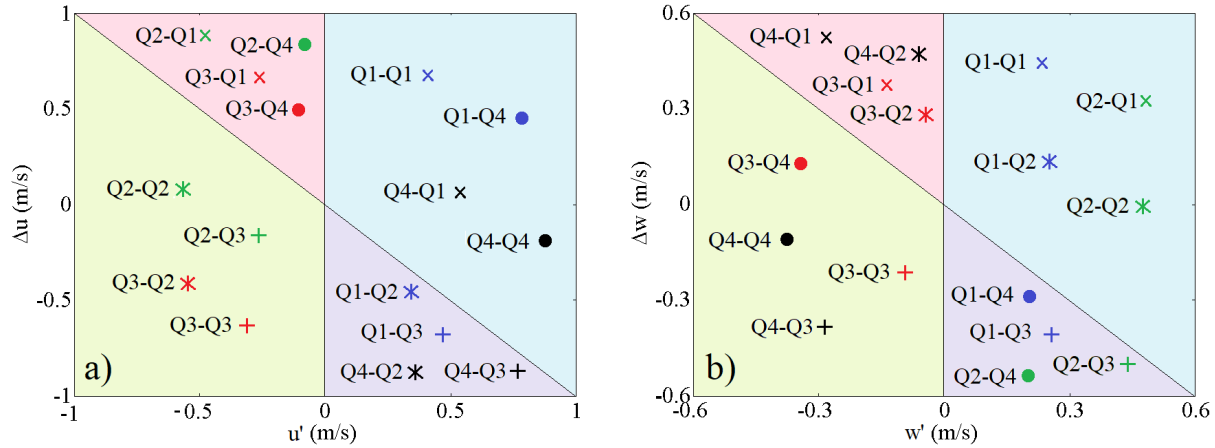

Figure 5.44- Ditribution of the trips on the Poincaré map (a) (*u', Δu'*) and (b) (*w', Δw'*). *Legend,* × *Q1-Q1,* ∗ *Q1-Q2,* + *Q1-Q3,* ● *Q1-Q4,* × *Q2-Q1,* ∗ *Q2-Q2,* + *Q2-Q3,* ● *Q2-Q4,* × *Q3-Q1,* ∗ *Q3-Q2,* + *Q3-Q3,* ● *Q3-Q4,* × *Q4-Q1,* ∗*Q4-Q2,* + *Q4-Q3, and* ● *Q4-Q4).*

In the same way, as it was done with the quadrant-events, the density maps on the Poincaré maps can be obtained for each trip. Figure 5.45 and Figure 5.46 show these density maps, where each trip is located in an area resulting from the division of the map by the ordinate axis, ($u'<0$, $u'>0$) and (w'<0, $w'>0$), and the diagonal, ($\Delta u <u', \Delta u>u'$) and ($\Delta w <w', \Delta w>w'$) defined in Figure 5.44.

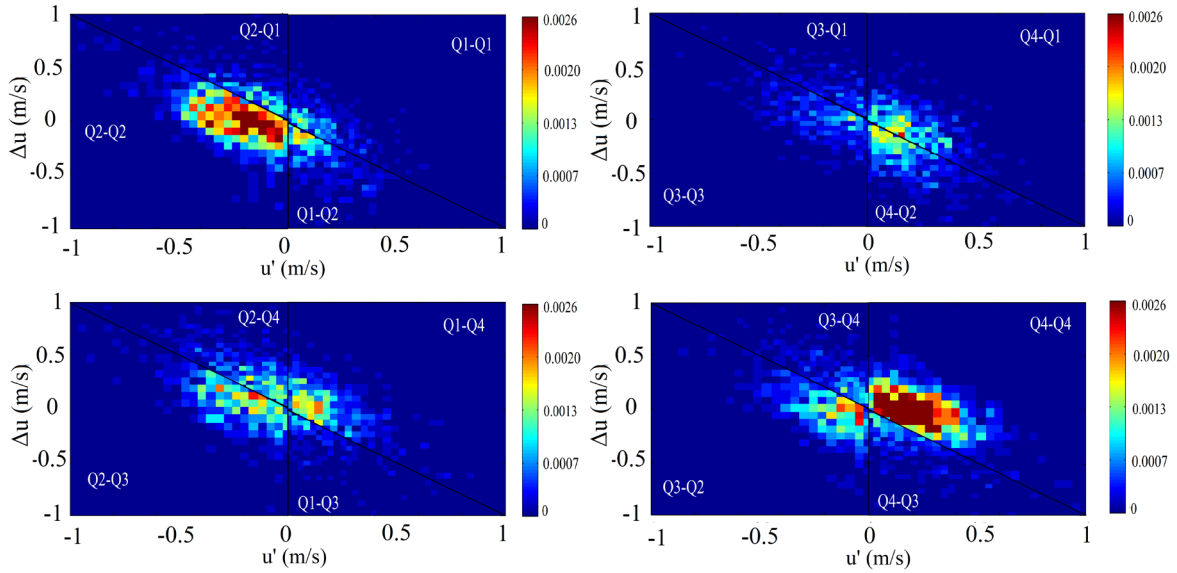

Figure 5.45- Density of the trips on the Poincaré Map (u', Δu). Experiment RG1 at z=10 mm.

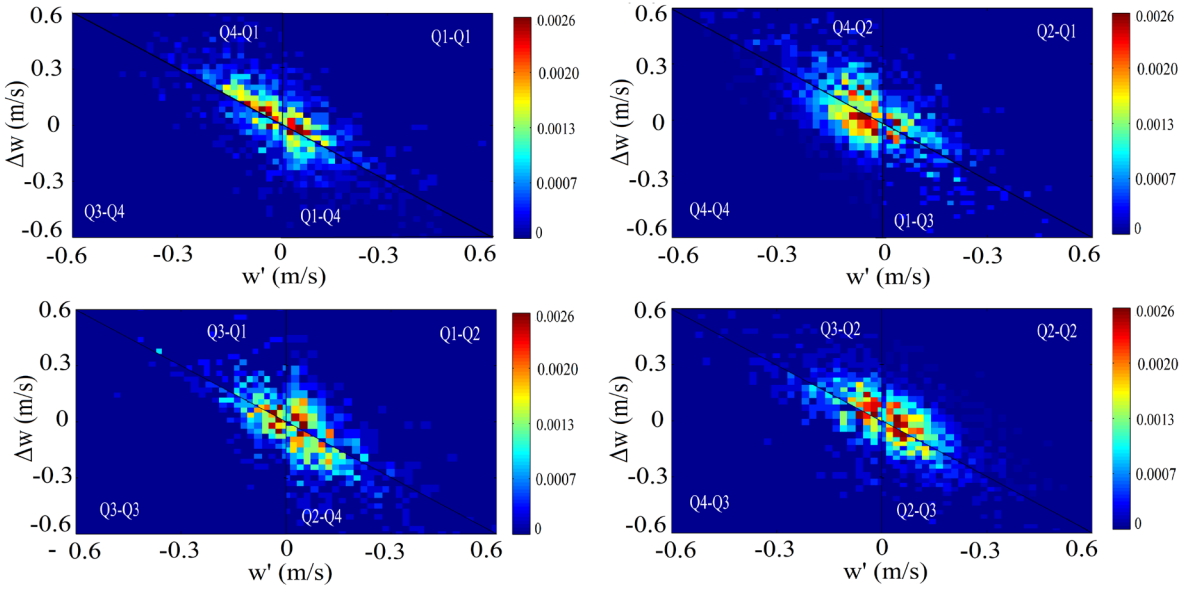

Figure 5.46- Density of the trips on the Poincaré Map (w', Δw). Experiment RG1 at z=10 mm.

5.8 Synthetic velocity series

As seen in section 5.5, Wu & Jiang (2007) demonstrated that by means of the third order Gram-Charlier JPDF the synthetic velocity series faithfully represented the QTF obtained in experimental data of Nelson et al. (1995), as well as the Reynolds shear stresses and the contribution of the quadrants to sediment entrainment. In the present chapter, it has been shown that the variables proposed by Wu & Jiang (2007) and Wu & Yang (2004) can only be considered constant in the region near the bed, despite

having certain evolution also in this area. Therefore, the distribution could be improved by the description of these variables through the depth profile.

On the other hand, the quadrant analysis has shown that not only the intensity and time fraction of the events is important, but also the order in which they occur, with an evolution along the depth profile. Therefore, the GC JPDF does represent well the density of velocities in a turbulent map (*u',w'*) but do not give them an order of appearance.

Together with the consideration of the description of the GC variables and the timewise statistics of events, it is possible to achieve an enhanced tool to reproduce velocity series, representing better the nature of turbulence. That requires a methodology that also considers the distribution of the velocity increments.

It is possible to generate a velocity series by means of the GC JPDF, which represents well the turbulent properties of a flow and to take one pair of (*u', w'*) of the obtained series as a departing point. This pair of (*u', w'*) has an associated distribution of Δu and Δw which can be found by the vertical defined by a certain value of *u'* and *w'* in the density map of Poincaré, see Figure 5.47. In this figure, it is shown an example of the density maps of Poincaré discretized by contours (level curves), obtained from experimental data. The intersection of the departing pair (*u'* and *w')* with the maps (Figure 5.47) defines the probability distribution of Δu and Δw, Figure 5.48-a, and the cumulative distribution function (Figure 5.48-b).

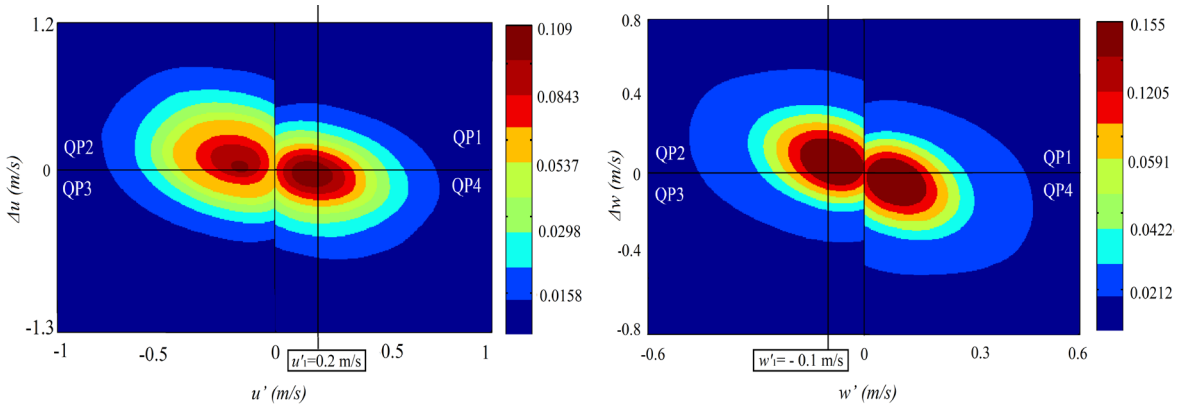

Figure 5.47- Example of Probability level curves of the Poincaré Map (a) (*u', Δu*) and (b) (*w', Δw*).

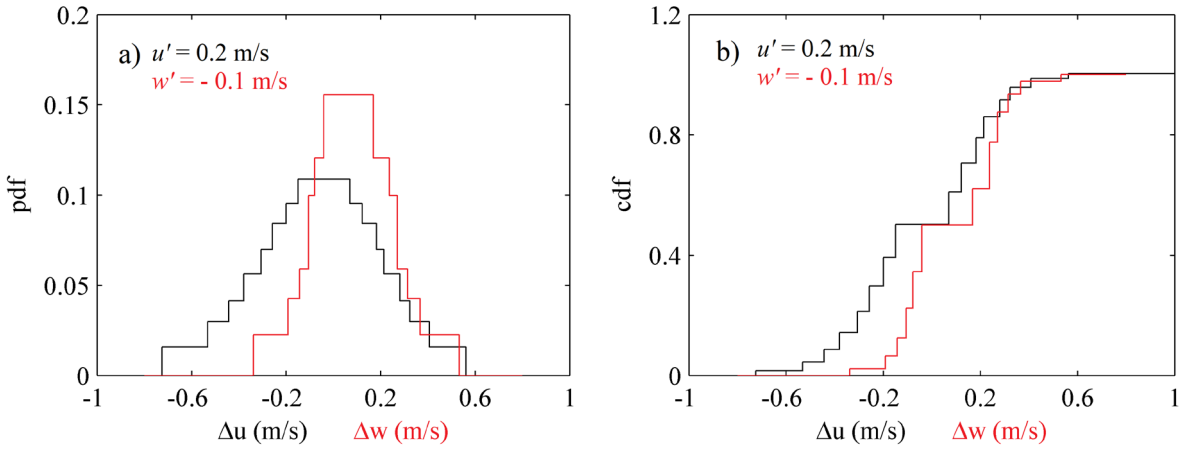

Figure 5.48- Probability density function (PDF) and (b) cumulative density function (CMF) of Δu for *u'*=0.2 m/s and Δw for *w'*=-0.1 m/s

By means of a random number (between 0 and 1) generator, two numbers are assigned to the first pair (u', w'), determining the value of Δu and Δw associated from Figure 5.48-b. These values determine the next pair ($u'(t+1)$, $w'(t+1)$), Eq. 5-10 and Eq. 5-11. However, the pair that better fits the obtained from this methodology has to be found in the initial velocity series adjusted using the GC JPDF, so that the values of the series *u'w'* defined by the GC distribution are concatenated.

$$u'(t+1) = u' + \frac{\partial u}{\partial t}\Delta t = u' + \Delta u \tag{5-10}$$

$$w'(t+1) = w' + \frac{\partial w}{\partial t}\Delta t = w' + \Delta w \tag{5-11}$$

The probability distributions of (u', Δu) and (w', Δw) (Poincaré maps) shown in Figure 5.47 come from experimental data and only correspond to a specific point. It is suggested a detailed study of these distributions for different flows and different depth heights in order to determine a joint probability density function (3D) that best fits the points in a plane (u', Δu) and (w', Δw). The methodology could be validated by comparing sequences and trips between quadrants with the experimental results obtained in this thesis.

On the other hand, given the differences observed between velocity series taken with different configurations it might be possible to reproduce a series of velocities associated with a certain frequency (FDC).

Chapter 6: Pulse Analysis

6.1 Pulse definition

From the results obtained so far we have observed the tendency of an event to remain in a quadrant, therefore, it is considered necessary to know the residence time of all events belonging to a particular quadrant. The events that remain in the same quadrant are called henceforth as "pulses", in which the residence time inside the quadrant is also considered. Thus, a pulse is considered here as the uninterrupted time spent in the same quadrant before moving to the next one, see Figure 6.1.

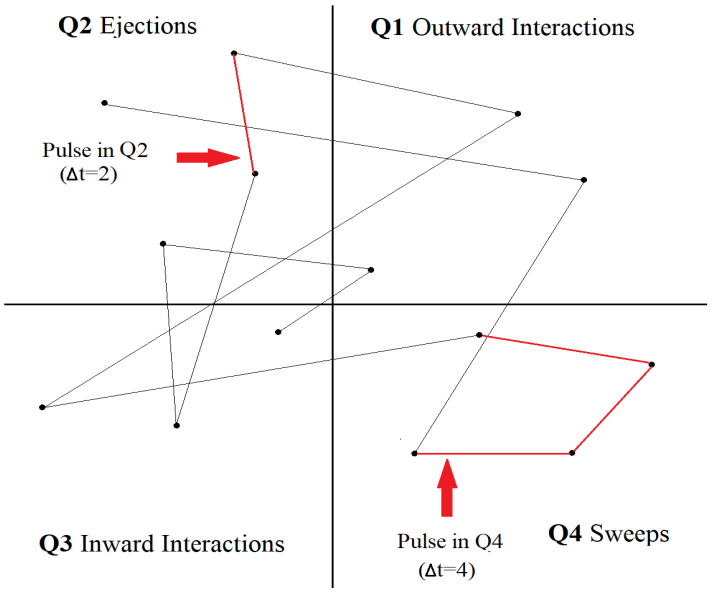

Figure 6.1- Pulse sketch on the quadrant map.

6.2 Pulse duration distribution

6.2.1 Pulse duration histograms

The pulse duration histogram (PDH) describes the distribution of the dwell time in a specific quadrant, where the pulse is contained, based on the pulse duration (T_p). That is, it explains how much time each pulse duration represents, as a time fraction TF (decimal fraction) of the total time-sample. Figure 6.2 shows two examples of these histograms for a point located at 3 cm from the bed surface, for two different experiments, RG1 and RG10 respectively. From the figures, it is obtained that both histograms are quite similar although they are two experiments with different level of turbulence.

In order to see if there are differences between these PDH along the profile of the same experiment, the histograms of all the points have been overlapped on a single graph. In Figure 6.3-a it can be seen the superposition of these histograms, now defined by a line for a correct visualization, for the RG3 experiment. What is obtained from this graph is quite curious since all the points in the same profile show a very similar, almost coincident distribution of pulses as if it were a universal behavior. However, not all the experiments produce the same distribution. For example, Figure 6.4 shows three different experiments and the superposition of all the PDH in the profile. It has been differentiated between the histograms obtained for points at height $z/d<0.5$ (red lines) and points at a height $z/d>0.5$

(black lines). What is obtained from these graphs is that the distribution of T_p remains fairly constant at points near the bed. However, as the points are located away from the bed surface, the distribution flattens out, that is, the pulses of shorter durations ($1\Delta t$=0.04 s , $2\Delta t$=0.08 s , and $3\Delta t$=0.12 s) reduce their presence in the sample while the presence of longer durations increase. This effect is accentuated for the most turbulent flows, due to the fact that the hydraulic depth is greater, and therefore they are placed further away from the bed.

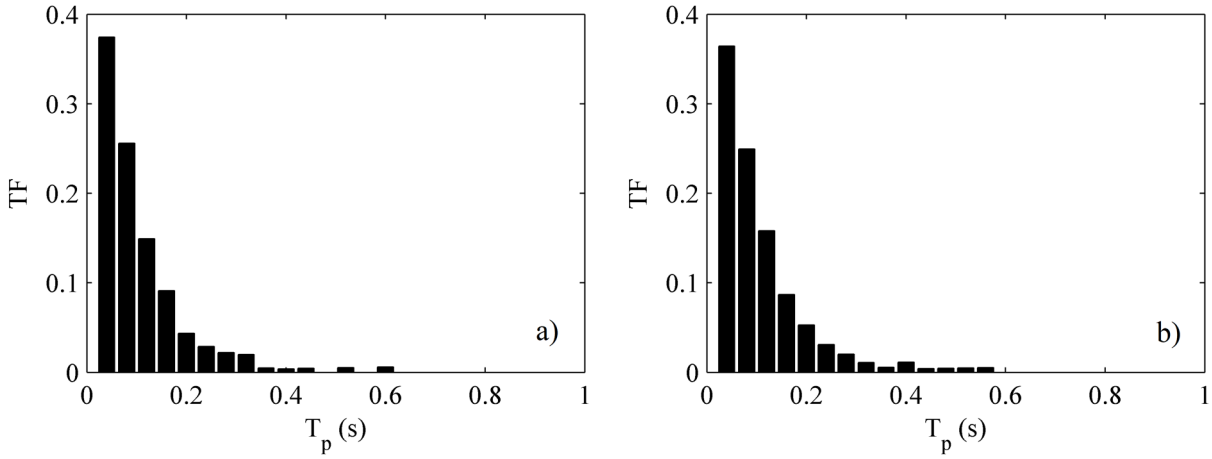

Figure 6.2- PDH of a point at height of z=3 cm, (a) RG3 and (b) RG10.

Finally, Figure 6.3-b shows the PDH separated by quadrants, that is to say, distinguishing the quadrant where each pulse appears. This graph is very interesting since it is observed that not only there is a pattern of the T_p distribution in the data series, but also each quadrant shows its own pattern, being very similar along the profile. The pulses that occur in Q1 and Q3 show a higher TF of short pulses ($1\Delta t$=0.04 s), while the TF of pulses over this duration (>$1\Delta t$) decrease. In the case of Q2 and Q4 this behavior is opposite, being the value of pulses of duration $1\Delta t$ = 0.04 s lower, and pulses above this (>$1\Delta t$) more present in the sample in comparison with the other two quadrants.

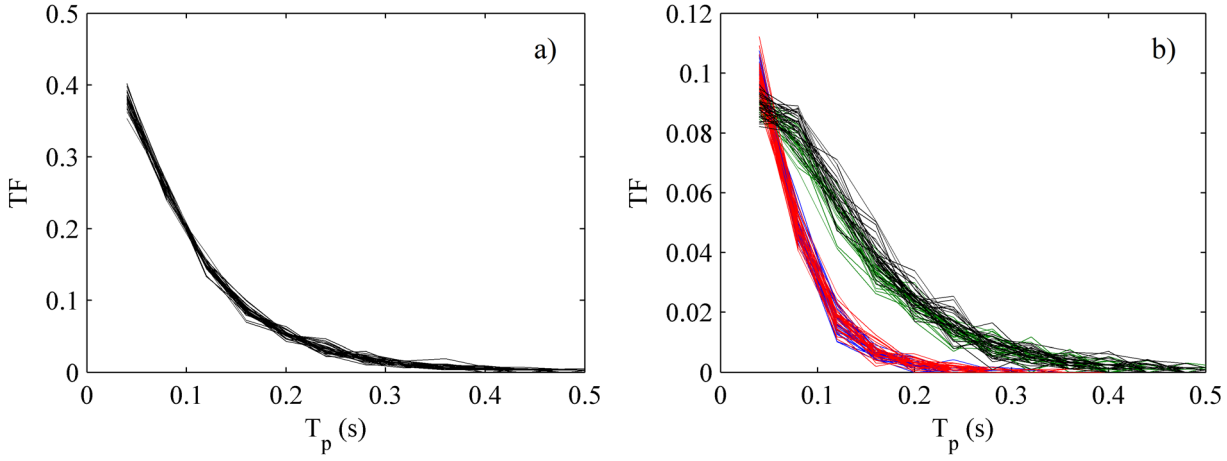

Figure 6.3- PDH of all points from RG3, (a) without distinction between quadrants and (b) separated by quadrants. *Legend (b),* ● *Q1,* ● *Q2,* ● *Q3, and* ● *Q4.*

Ferreira et al. (2009) have studied the statistics of quadrant events in mobile and immobile rough beds. However, its study (duration of the events, intensity and frequency) is based on the hole size H (Willmarth & Lu 1972) which is not considered here by the reasons exposed in section 5.4. They found

that the momentum transported by very strong sweeps and by extreme ejections increase in the mobile bed case. However, they found no important differences in the duration and frequency of the events.

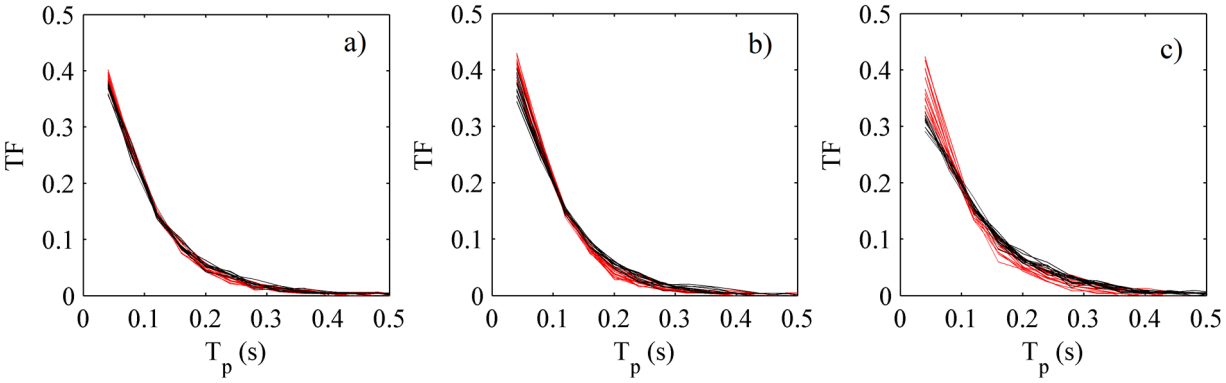

Figure 6.4- PDH regardless the quadrant, for the experiments (a) RG1, (b) RG5, and (c) RG10. *Legend, points at height of* ● *z/d<0.5, and z/d>0.5.*

6.2.2 Vertical distribution of the T_p TF

Figure 6.5-a and Figure 6.5-b show the TF that the most relevant T_p (from 1Δt to 5Δt) represent over the total time-sample, for the RG and CG experiments, respectively. As mentioned above, all T_p show a similar percentage of appearance along the profile. It can be observed that except pulses of $T_p = 1\Delta t$, the rest show a fairly constant vertical distribution. It is also observed for experiments with large hydraulic depth (d) (RG6 to RG10, in the case of the RG tests and the CG5 and CG6 tests of the CG experiments) it is noticeable a more noticeable decrease of the short pulses $T_p = 1\Delta t$ as the distance to the bed increases. This decrease is possible thanks to the increase in the TF of all pulse durations above 1Δt (>1Δt).

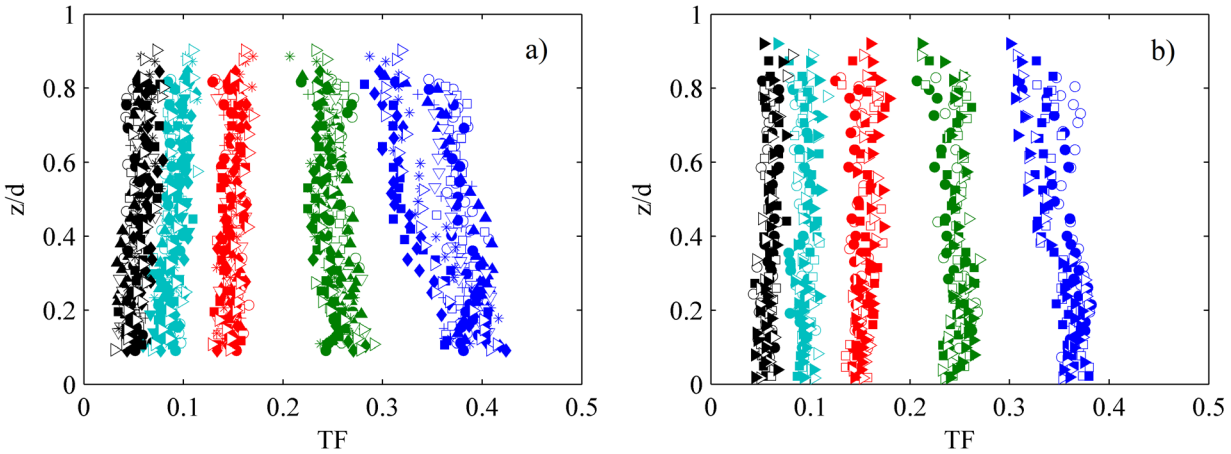

Figure 6.5- Vertical distribution of the total TF of pulses with a T_P of 1Δt, 2Δt, 3Δt, 4Δt, and 5Δt, for the (a) RG experiments and (b) CG experiments. *Legend Markers (a),* + *RG1,* ○ *RG2,* □ *RG3,* ● *RG4,* ▲ *RG5,* ▽ *RG6,* ✳ *RG7,* ♦ *RG8,* ■ *RG9 and* ▷ *RG10. Legend Markers (b),* ○ *CG1,* ● *CG2,* □ *CG3,* ■ *CG4,* ▷ *CG5 and* ▶ *CG6. Legend colors,* ● *1Δt,* ● *2Δt,* ● *3Δt,* ● *4Δt, and* ● *5Δt.*

However, as it has been seen in the previous section, the pulses of short duration ($1\Delta t$) tend to belong to quadrants Q1 and Q3. With the aim of seeing how the TF of pulses from the different quadrants evolves along the profile and discerning the differences between patterns, the same vertical distribution

profiles of the T_p TF separated by quadrants are shown in Figure 6.6 and Figure 6.7, for the RG and CG experiments respectively.

Figure 6.6 and Figure 6.7 show the TF of T_p (from $1\Delta t$ to $5\Delta t$) that are placed in each quadrant, for each group of experiments respectively. In the graphs it can be appreciated how quadrants Q1 and Q3 have the distribution of each T_p clearly differentiated from each other, having the pulses of T_p=$1\Delta t$ (blue markers) a TF clearly greater than the rest. Both Q1 and Q3 show a tendency of decrease in the TF of short pulses ($1\Delta t$) along the profile, towards the water surface, however, a more marked diminution is observed in Q3, while in the Q1 a more constant vertical value is maintained. In both cases, though, the decrease is more pronounced for experiments with large depth flows (d), as the distance to the bed increases.

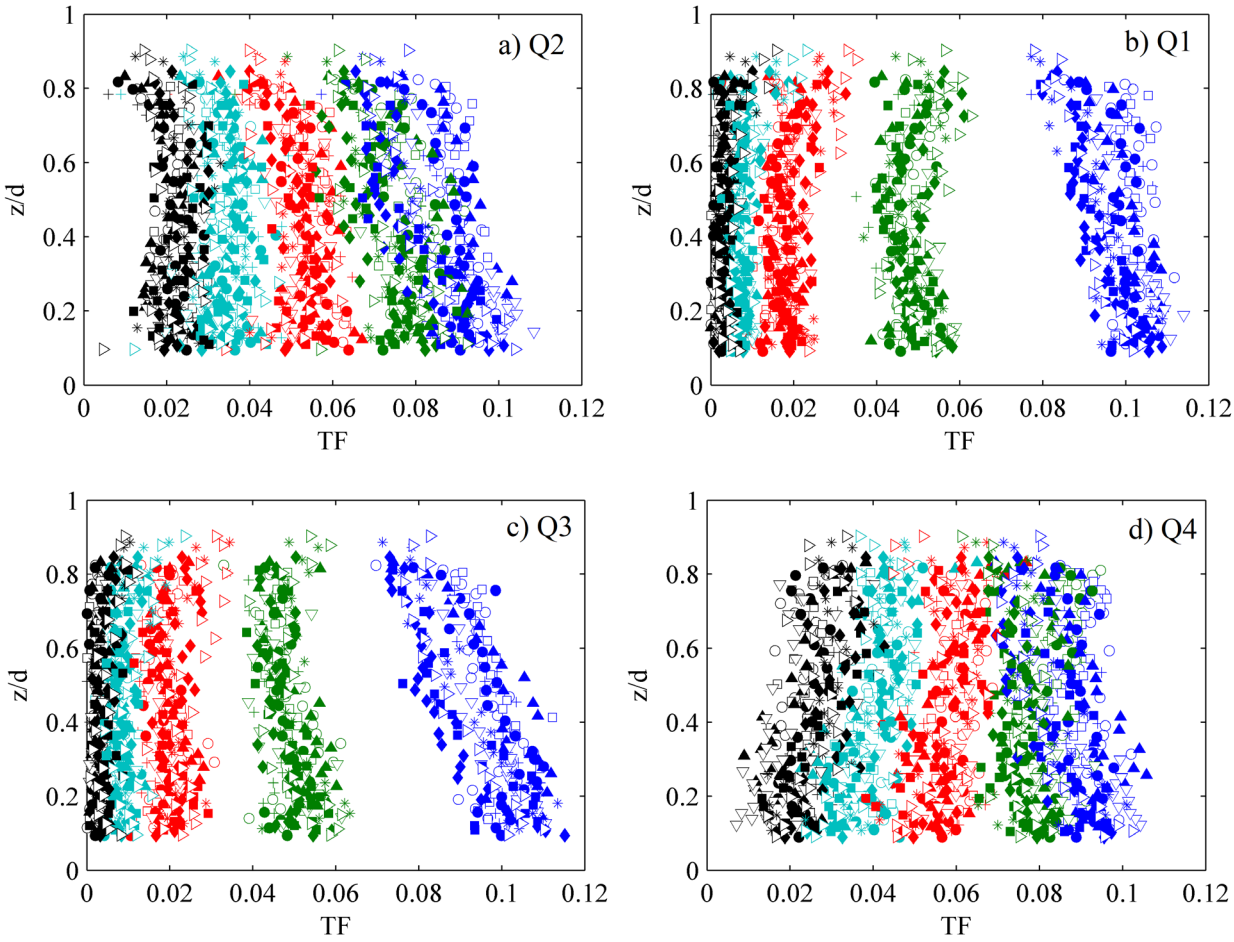

Figure 6.6- Vertical distribution of the total TF of pulses with a T_P of 1Δt, 2Δt, 3Δt, 4Δt, and 5Δt, separated by quadrants (a) Q2, (b) Q1, (c) Q3, and (d) Q4. (RG experiments). *Legend Markers, + RG1, ○ RG2, □ RG3, ● RG4, ▲ RG5, ▽ RG6, ∗ RG7, ♦ RG8, ■ RG9 and ▷ RG10. Legend colors, 1Δt, 2Δt, 3Δt, 4Δt, and 5Δt.*

In the case of the other two quadrants (Q2 and Q4), it is obtained, first of all, that all T_p show more differences from one test to another, especially at the points furthest from the bed. On the other hand, fewer differences between the different T_p-TF are seen, that is to say, the percentage of T_p=$1\Delta t$ is closer to the rest. Both quadrants display very similar trends, although some differences between them can be highlighted. In the T_p-TF in Q2, short pulses ($1\Delta t$) decrease a little more sharply with the distance

to the bed than in the Q4, especially for tests of greater hydraulic depth (d), where the value is further reduced in the second part of the profile (z/d>0.5). The rest of pulse-durations in Q2 remain fairly constant with a slight TF decrease when ascending in the profile, while in the Q4 the durations ($3\Delta t$, $4\Delta t$, and $5\Delta t$) tend to increase slightly higher. The increase in pulses of long duration is explained by the decrease of the short pulses, thus the events tend to spend more time in a quadrant when the distance to the bed is increased. Regarding the experiments type RG or type CG, both show the same described behavior.

Regarding the effects of the turbulence levels on these TFs, it should be noted that in all cases the experiments with low level of turbulence, thus with low d, have higher TF of short pulses (1Δt) in quadrants Q1 and Q3, and lower TF of T_p>$1\Delta t$, while for quadrants Q2 and Q4 this trend is not observed so clearly. The leveling of the bed surface does not return worth differences to be highlighted, just a slight increase in the TF of pulses T_p>$2\Delta t$ is observed very close to the bed (z/d<0.15) in quadrants Q2 and Q4, maintaining a very similar value in Q1 and Q3.

It should be mentioned again that at some points near the water surface the behavior could vary drastically due to the disturbance of the water surface by the apparatus.

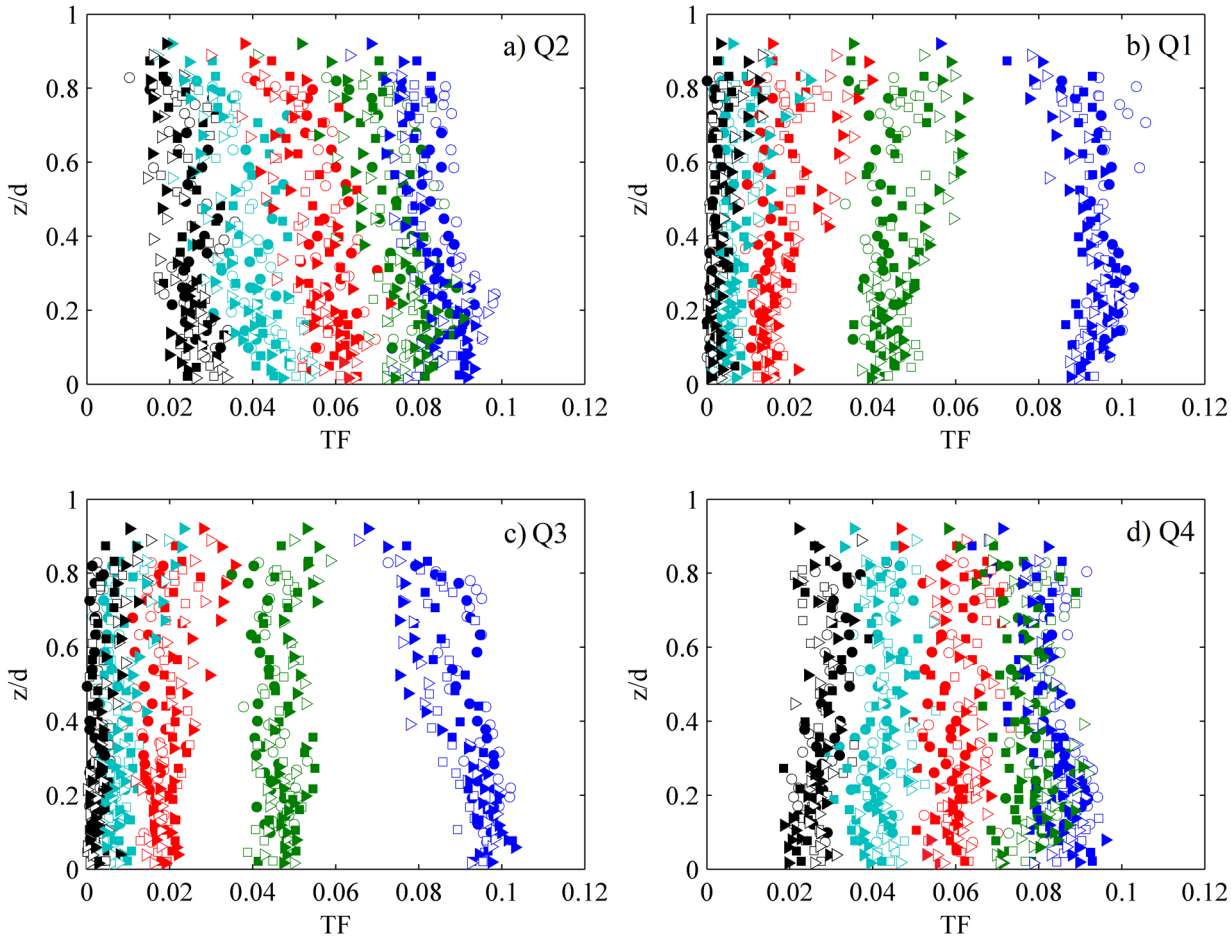

Figure 6.7- Vertical distribution of the total TF of pulses with a T_P of 1Δt, 2Δt, 3Δt, 4Δt, and 5Δt, separated by quadrants (a) Q2, (b) Q1, (c) Q3, and (d) Q4. (CG experiments). *Legend Markers,* ○ *CG1,* ● *CG2,* □ *CG3,* ■ *CG4,* ▷ *CG5 and* ► *CG6. Legend colors,* ● *1Δt,* ● *2Δt,* ● *3Δt,* ● *4Δt, and* ● *5Δt.*

6.2.3 Return period of the pulses

The return period tells us about the frequency of occurrence that has a certain T_p, that is, the distribution of the pulse over the measurement time.

In this section, the return periods of three different pulse durations ($1\Delta t$, $2\Delta t$, and $3\Delta t$) have been evaluated, for the RG experiments in Figure 6.8, and the CG tests in Figure 6.9. In this case, for the sake of simplicity, no distinction between experiments within each group has been made, although it has been considered a distinction between quadrants.

The return periods are measured in time periods Δt, which represent the average time that a certain pulse duration takes to appear, and correspond to averaged values of the return period at each height (z), obtaining the vertical distribution in the depth profile.

The short pulses (T_p=$1\Delta t$) show similar return periods in the four quadrants, being slightly lower in the case of Q1 and Q3, as expected since their TF is higher. However, more differences between quadrants appear when the T_p is longer, observing a considerable increase in the return period of the pulses of duration $2\Delta t$ and $3\Delta t$, especially for the quadrants Q1 and Q3. It is also noted that the return periods of the three pulse durations maintain a more stable value along the profile for quadrants Q2 and Q4 (green and black).

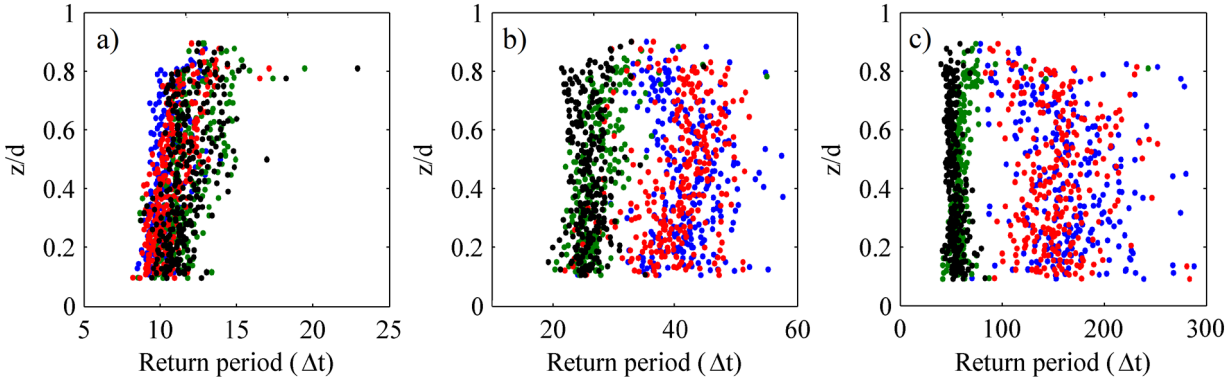

Figure 6.8- Vertical distribution of the Return Period of the pulses of (a) T_p=1Δt, (b) T_p=2Δt, and (c) T_p=3Δt, separated by quadrants. All RG experiments included. *Legend,* ● *Q1,* ● *Q2,* ● *Q3, and* ● *Q4.*

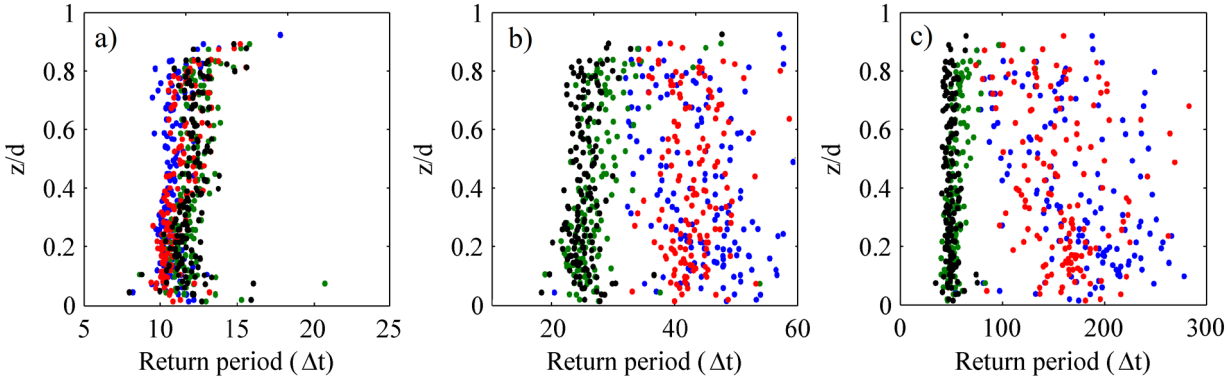

Figure 6.9- Vertical distribution of the Return Period of the pulses of (a) T_p=1Δt, (b) T_p=2Δt, and (c) T_p=3Δt, separated by quadrants. All CG experiments included. *Legend,* ● *Q1,* ● *Q2,* ● *Q3, and* ● *Q4.*

6.3 Characteristic velocity of the pulses

6.3.1 Fluctuating terms u' and w'

Up to this point, only the duration of the pulses has been evaluated. In this section, we will delve into the differences in terms of velocity from each pulse duration. As it has been exposed, a pulse is a time in which an event ($u'w'$) remains within the same quadrant. Each pulse is composed for one or more events, and each one of these events has associated its fluctuating terms u' and w'. Therefore, it is possible to obtain average velocities of the terms u' and w' for each pulse.

Figure 6.10 shows two examples of the average pulse velocity on the turbulent map, for two points of the experiment RG3 at different heights, z=1 cm (Figure 6.10-a) and z=3 cm (Figure 6.10-b). The pulses have been grouped by intervals of T_p, (*1*Δt, *[2-4]*Δt, *[5-8]*Δt, *[9-16]*Δt, *[17-32]*Δt, *>32*Δt). It is observed that pulses of long durations tend to stay away from the origin of coordinates since staying longer in the same quadrant allows them to get further from the origin of coordinates, and therefore reach higher velocities. However, that does not mean that pulses of short T_p cannot reach far too. Regarding the height in the depth, it is emphasized that as we separate from the bed (Figure 6.10-b), fewer extreme events of short duration are obtained.

It should be noted that Figure 6.10 displays average velocities of pulses, and it is not clear if a greater velocity is actually reached within the pulse. To clarify this aspect we refer to Figure 6.11, which shows the maximum instantaneous velocities reached for pulses inside in the same T_p intervals of Figure 6.10. In Figure 6.11 it is clearly observed that long pulses reach higher maximum velocities, arriving further from the origin of coordinates in the quadrant map.

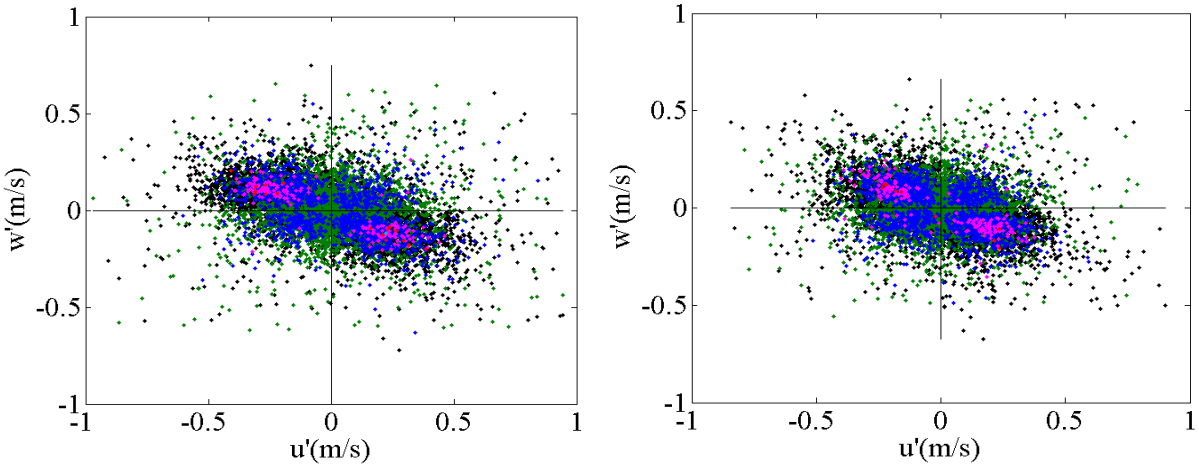

Figure 6.10- Mean velocities (*u',w'*) of pulses of T_p from 1*Δt* (0.04 s) to 32*Δt* (0.128 s) on the Turbulent map for points at height of (a) z=1 cm, and (b) z=3 cm. Experiment RG3. *Legend,* ● *1Δt,* ● *[2-4]Δt or [0.08-0.16]s* , ● *[5-8]Δt or [0.2-0.32]s* , ● *[9-16]Δt or [0.36-0.64]s* , ● *[17-32]Δt or [0.68-1.28]s* , ● *>32Δt or 1.28 s* .

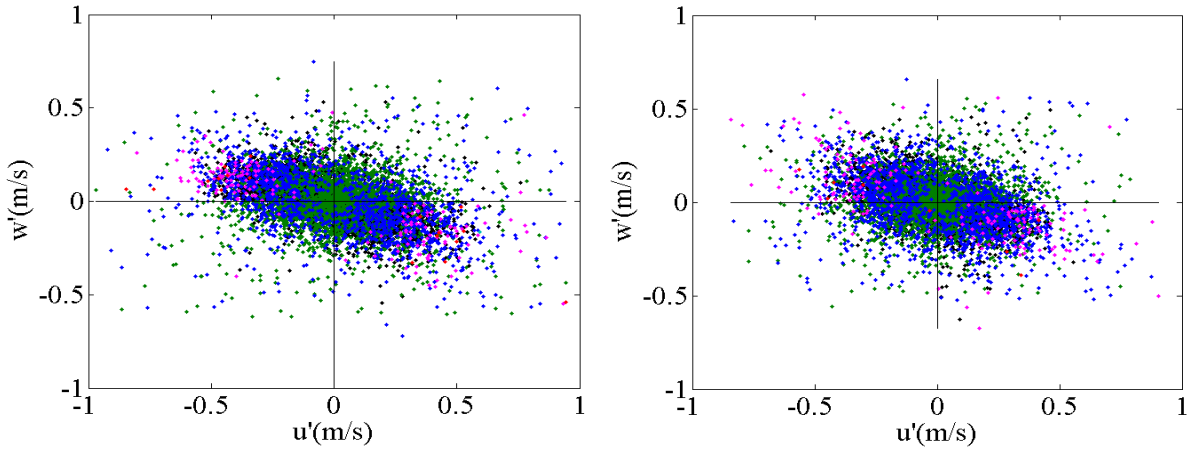

Figure 6.11- Mean velocities (*u',w'*) of pulses of T_p from 1Δt (0.04 s) to 32Δt (0.128 s) on the Turbulent map for points at height of (a) z=1 cm, and (b) z=3 cm. Experiment RG3. *Legend,* ● *1Δt,* ● *[2-4]Δt or [0.08-0.16]s* , ● *[5-8]Δt or [0.2-0.32]s* , ● *[9-16]Δt or [0.36-0.64]s* , ● *[17-32]Δt or [0.68-1.28]s* , ● *>32Δt or 1.28 s* .

The following figures (Figure 6.12-a and Figure 6.12-b) show the vertical distribution of the average fluctuating velocity (*u'*) for pulses of duration T_p=1Δt (black), T_p=3Δt (blue), and T_p=5Δt (red), for the experiments RG and CG respectively.

As expected, the average velocity associated with each height is centered on a zero value, since positive and negative deviations of the local velocity (*u*) are compensated. However, a decreasing tendency is observed with the distance to the bed. Therefore, despite the average local velocity ($\bar{u}$) increases when ascending in the depth profile, the fluctuating term *u'* is diminished. This effect is more noticeable in the case of pulses of duration T_p=1Δt and T_p=3Δt, while pulses of duration T_p=5Δt show more extreme values along the whole depth. The near-bed region z/d<0.3 although having more amount of *u'*<0, as seen in the previous chapter, the more extreme character of sweeps make the mean *u'* of pulses to be positive for T_p=1Δt, while the longer pulses alternate positive and negative values. In reference to the bed leveling (CG experiments), it is worth mentioning that slightly higher velocities are observed in the case of the not-leveled bed, for pulses of T_p=3Δt and T_p=5Δt. Therefore, although the local velocity ($\bar{u}$) it was seen to increase with the decrease of k_s, the fluctuations *u'* become lower.

In Figure 6.13 we find the same distribution, but in this case, the maximum value of the fluctuation *u'* within the pulse has been represented, that is, the average of the maximum values found for pulses of T_p=1Δt (black), T_p=3Δt (blue), and T_p=5Δt (red). The patterns are very similar that in the case of the average velocity within the pulse; however, velocities from pulses of T_p=3Δt and T_p=5Δt become extreme. In the first half of the depth profile z/d<0.5 the fluctuations appear on both sides of the zero value (*u'*=0), positive and negative, while in the second half z/d>0.5 appear more in the negative direction (*u'* <0). This is interesting because in this area of the profile there are more sweeps (Q4, *u'*>0), therefore, these high fluctuations must come from Q2 (*u'* <0) even though they do not increase their presence in comparison with the first half z/d<0.5.

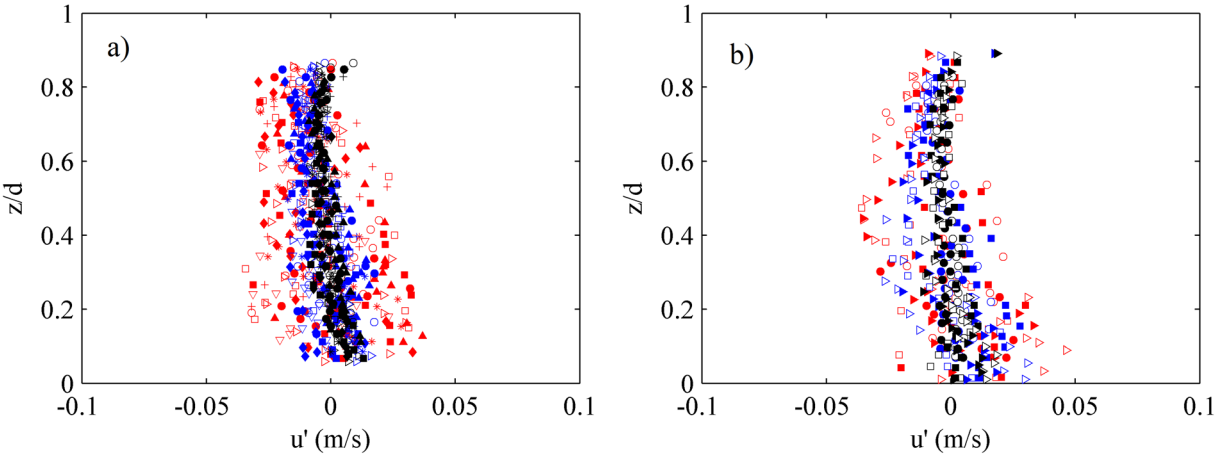

Figure 6.12- Vertical distribution of the average fluctuation *u'* ($u = \bar{u} + u'$) inside pulses of T_p=1Δt, T_p=2Δt, and T_p=3Δt. Experiments (a) RG and (b) CG. *Legend Markers (a), + RG1, ○ RG2, □ RG3, ● RG4, ▲ RG5, ▽ RG6, ∗ RG7, ♦ RG8, ■ RG9 and ▷ RG10. Legend Markers (b), ○ CG1, ● CG2, □ CG3, ■ CG4, ▷ CG5 and ▶ CG6. Legend colors,* ● *1Δt,* ● *3Δt, and* ● *5Δt.*

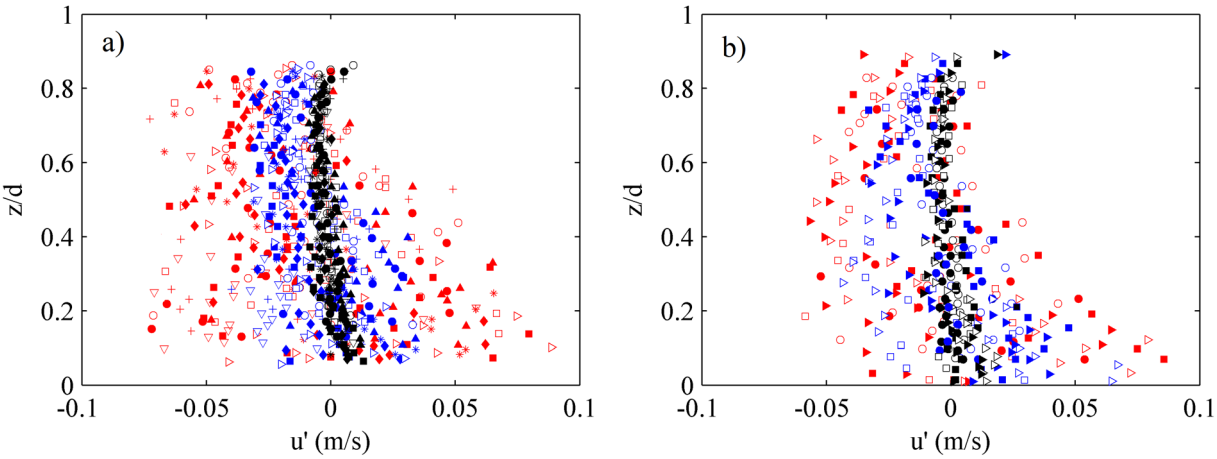

Figure 6.13- Vertical distribution of the maximum fluctuation u' ($u = \bar{u} + u'$) inside pulses of T_p=1Δt, T_p=2Δt, and T_p=3Δt. Experiments (a) RG and (b) CG. *Legend as for Figure 6.12.*

The same procedure has been used to assess the vertical velocity fluctuations (*w'*) along the depth profile. Figure 6.14 and Figure 6.15 represent the vertical distribution of the mean and maximum fluctuations *w'* inside pulses of duration T_p=1Δt, T_p=3Δt, and T_p=5Δt. In the case of the mean value of *w',* the distribution turns out to be more centered at *w'*=0, mainly for durations T_p=1Δt and T_p=3Δt, with greater variations observed in the case of pulses T_p=5Δt. In the case of the vertical distribution of the maximum *w'* inside pulses, it is obtained that the pulses of duration T_p=5Δt have values as high as *u'*. However, in this case the positive (*w'*>0) and negative fluctuations (*w'*<0) are present in the whole profile, with a positive tendency in the second half of the profile (*z/d*>0.5), confirming that it is the ejections (Q2) that become more intense in this zone. The effects of shaping the bed surface are not appreciable, though, more extreme values of w' are observed for the non-shaped case. Both *u'* and *w'*, reach greater fluctuations with the increase of the average flow velocity.

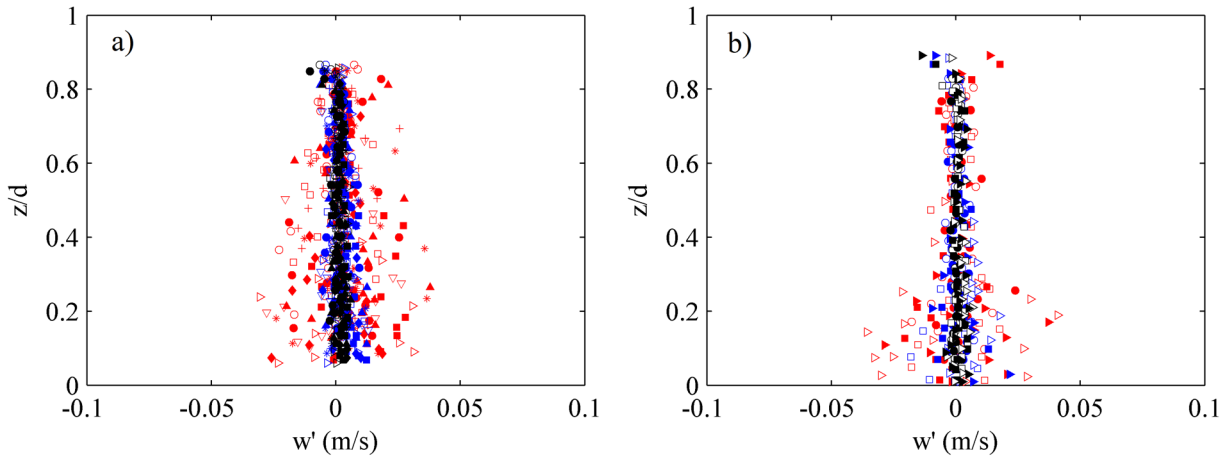

Figure 6.14- Vertical distribution of the average fluctuation w' ($w = \overline{w} + w'$) inside pulses of T_p=1Δt, T_p=2Δt, and T_p=3Δt. Experiments (a) RG and (b) CG. *Legend Markers (a), + RG1, ○ RG2, □ RG3, ● RG4, ▲ RG5, ▽ RG6, ∗ RG7, ♦ RG8, ■ RG9 and ▷ RG10. Legend Markers (b), ○ CG1, ● CG2, □ CG3, ■ CG4, ▷ CG5 and ▶ CG6. Legend colors, ● 1Δt, ● 3Δt, and ● 5Δt.*

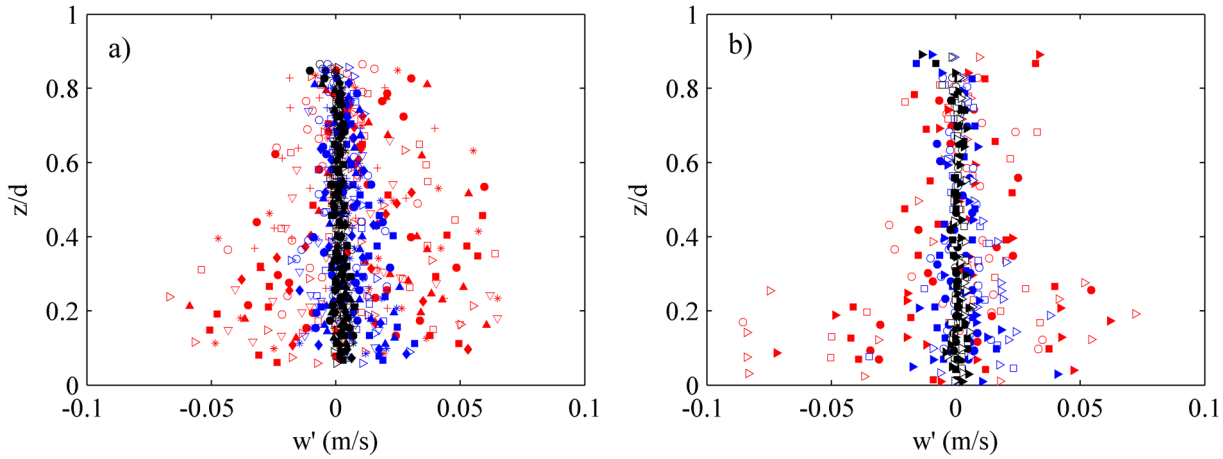

Figure 6.15- Vertical distribution of the average fluctuation w' ($w = \overline{w} + w'$) inside pulses of T_p=1Δt, T_p=2Δt, and T_p=3Δt. Experiments (a) RG and (b) CG. *Legend as for Figure 6.14.*

Up to this point, we have not differentiated between quadrants, for this reason, the fluctuations were centered in zero value. In the following graphs (from Figure 6.16 to Figure 6.19) the same variables have been represented, also for the three pulse durations, T_p=1Δt, T_p=3Δt, and T_p=5Δt, but separated by quadrants of appearance (Q1, u'>0 and w'>0), (Q2, u'<0 and w'>0), (Q3, u'<0 and w'<0), (Q4, u'> 0 and w'<0).

Figure 6.16 and Figure 6.17, represent the vertical distribution of the average fluctuations u' of pulses of duration T_p=1Δt, T_p=3Δt, and T_p=5Δt, for the experiments RG and CG respectively. The four quadrants show a descending progression of u', both the mean and maximum value. In other words, the value of u' is indirectly proportional to the local mean velocity (u) along the depth profile, reaching lower values as u increases. However, as previously mentioned, the pulses produced in the Q2 reach a greater fluctuation u' (in comparison with the other quadrants) in the second half of the profile z/d>0.5.

In both groups of experiments, it is observed that the maximum value is not located on the surface of the bed, but at a height of approximately z/d=0.2-0.3. By definition the u'> 0 are placed in Q1 and Q4

(blue and black respectively), but in the case of Q4 they are considerably larger. In the opposite case, the $u'<0$ are greater in Q2 than in Q3. The above is accentuated for long pulse durations. In general, higher flow rates reach higher *u'* along the whole profile.

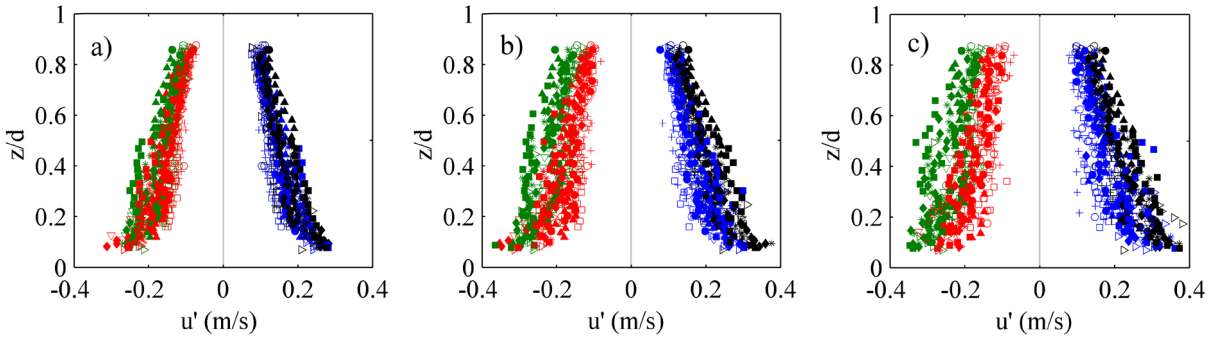

Figure 6.16- Vertical distribution of the average fluctuation *u'* ($u = \bar{u} + u'$) inside pulses of (a) T_p=1Δt, (b) T_p=3Δt, and (c) T_p=5Δt, separated by quadrants. Experiments RG. *Legend Markers, + RG1, ○ RG2, □ RG3, ● RG4, ▲ RG5, ▽ RG6, ∗ RG7, ♦ RG8, ■ RG9 and ▷ RG10. Legend colors,* ● *Q1,* ● Q2, ● *Q3, and* ● *Q4.*

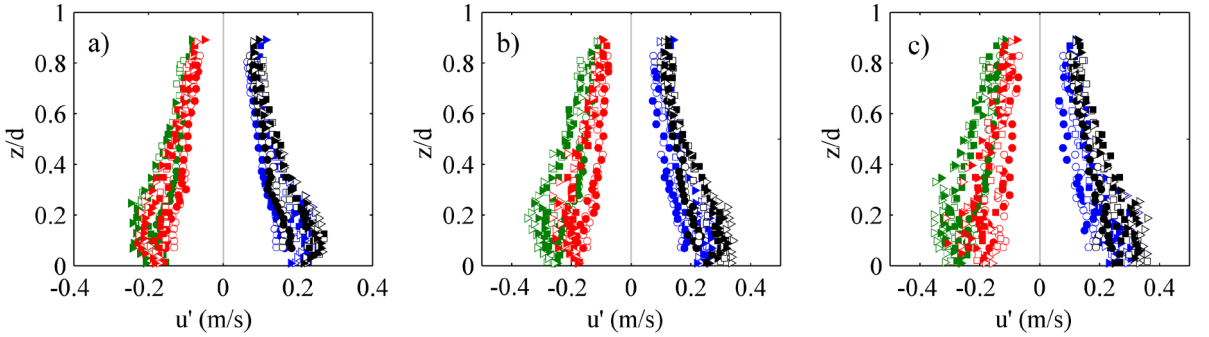

Figure 6.17- Vertical distribution of the average fluctuation *u'* ($u = \bar{u} + u'$) inside pulses of (a) T_p=1Δt, (b) T_p=3Δt, and (c) T_p=5Δt, separated by quadrants. Experiments CG. *Legend Markers, ○ CG1, ● CG2, □ CG3, ■ CG4, ▷ CG5 and ► CG6. Legend colors,* ● *Q1,* ● *Q2,* ● *Q3, and* ● *Q4.*

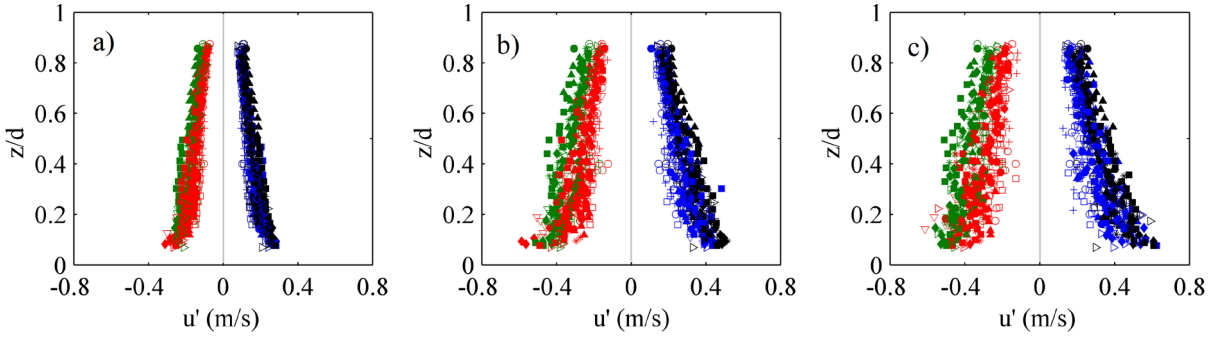

Figure 6.18- Vertical distribution of the maximum fluctuation *u'* ($u = \bar{u} + u'$) inside pulses of (a) T_p=1Δt, (b) T_p=3Δt, and (c) T_p=5Δt, separated by quadrants. Experiments RG. *Legend Markers, + RG1, ○ RG2, □ RG3, ● RG4, ▲ RG5, ▽ RG6, ∗ RG7, ♦ RG8, ■ RG9 and ▷ RG10. Legend colors,* ● *Q1,* ● Q2, ● *Q3, and* ● *Q4.*

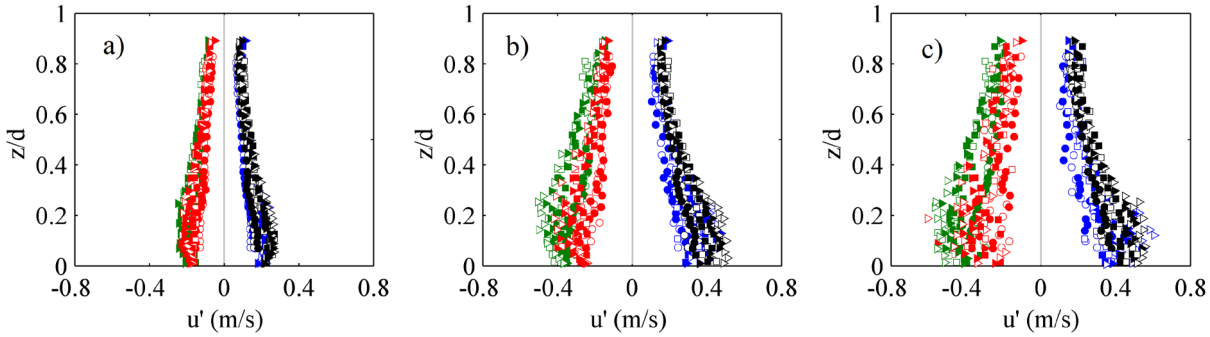

Figure 6.19- Vertical distribution of the maximum fluctuation u' ($u = \bar{u} + u'$) inside pulses of (a) T_p=1Δt, (b) T_p=3Δt, and (c) T_p=5Δt, separated by quadrants. Experiments CG. *Legend Markers,* ○ *CG1,* ● *CG2,* □ *CG3,* ■ *CG4,* ▷ *CG5 and* ► *CG6. Legend colors,* ● *Q1,* ● *Q2,* ● *Q3, and* ● *Q4.*

It is now the turn of the vertical velocity fluctuations w', which its average and maximum value are represented for the pulses of duration T_p=1Δt, T_p=3Δt, and T_p=5Δt in the figures below. Figure 6.20 and Figure 6.21 represent the average values of w' for the two groups of experiments, while Figure 6.22 and Figure 6.23 represent the maximum value w'.

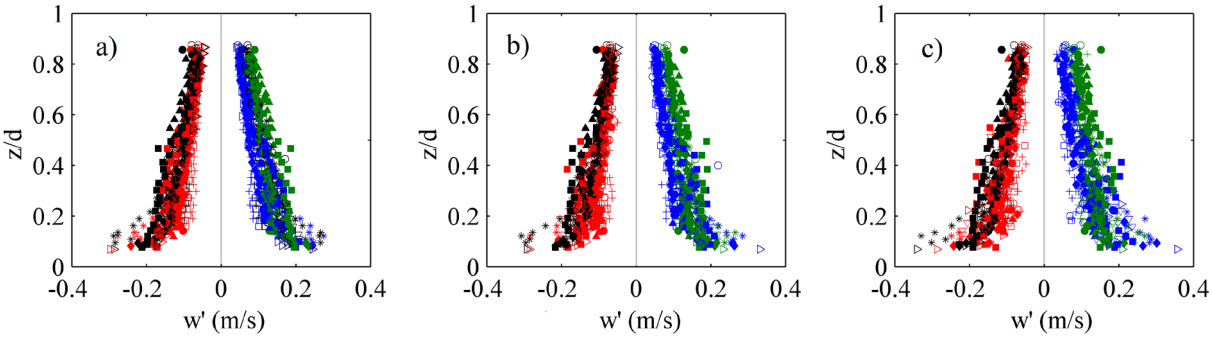

Figure 6.20- Vertical distribution of the average fluctuation w' ($w = \bar{w} + w'$) inside pulses of (a) T_p=1Δt, (b) T_p=3Δt, and (c) T_p=5Δt, separated by quadrants. Experiments RG. *Legend Markers,* + *RG1,* ○ *RG2,* □ *RG3,* ● *RG4,* ▲ *RG5,* ▽ *RG6,* ∗ *RG7,* ♦ *RG8,* ■ *RG9 and* ▷ *RG10. Legend colors,* ● *Q1,* ● Q2, ● *Q3, and* ● *Q4.*

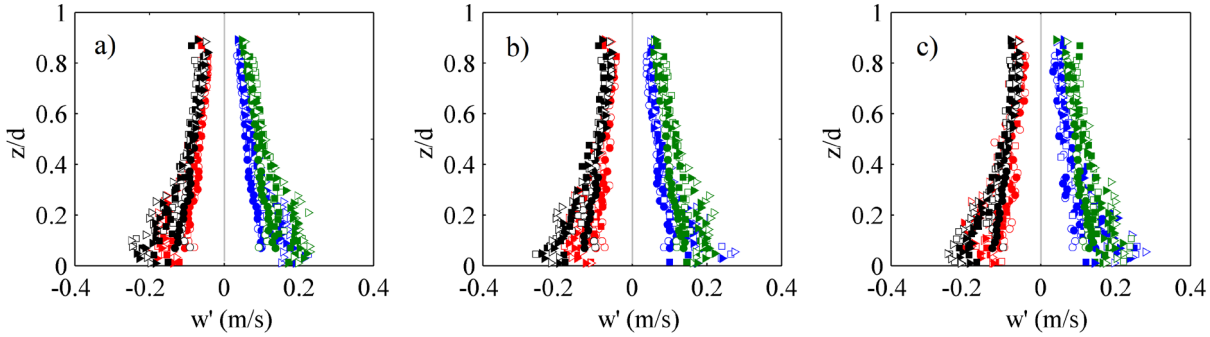

Figure 6.21- Vertical distribution of the average fluctuation w' ($w = \bar{w} + w'$) inside pulses of (a) T_p=1Δt, (b) T_p=3Δt, and (c) T_p=5Δt, separated by quadrants. Experiments CG. *Legend Markers,* ○ *CG1,* ● *CG2,* □ *CG3,* ■ *CG4,* ▷ *CG5 and* ► *CG6. Legend colors,* ● *Q1,* ● *Q2,* ● *Q3, and* ● *Q4.*

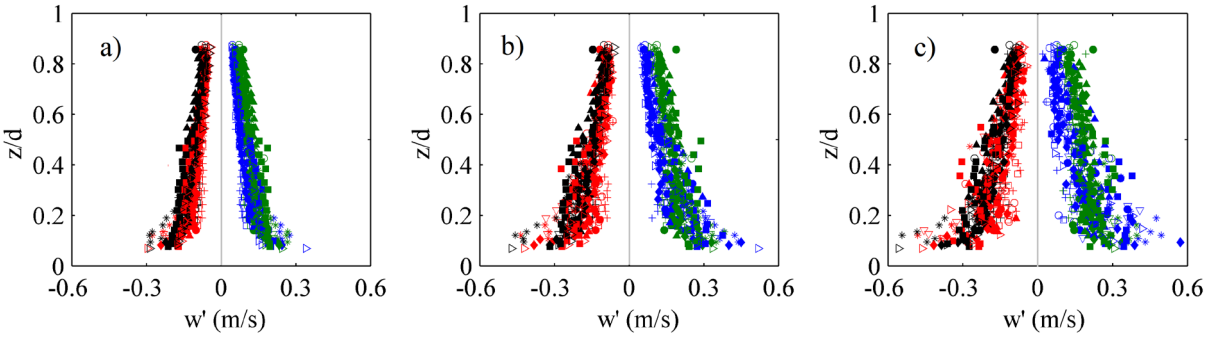

Figure 6.22- Vertical distribution of the maximum fluctuation *w' (*$w = \bar{w} + w'$*)* inside pulses of (a) T_p=1Δt, (b) T_p=3Δt, and (c) T_p=5Δt, separated by quadrants. Experiments RG. *Legend Markers, + RG1, ○ RG2, □ RG3, ● RG4, ▲ RG5, ▽ RG6, ∗ RG7, ♦ RG8, ■ RG9 and ▷ RG10. Legend colors, ● Q1,* Q2, *● Q3, and ● Q4.*

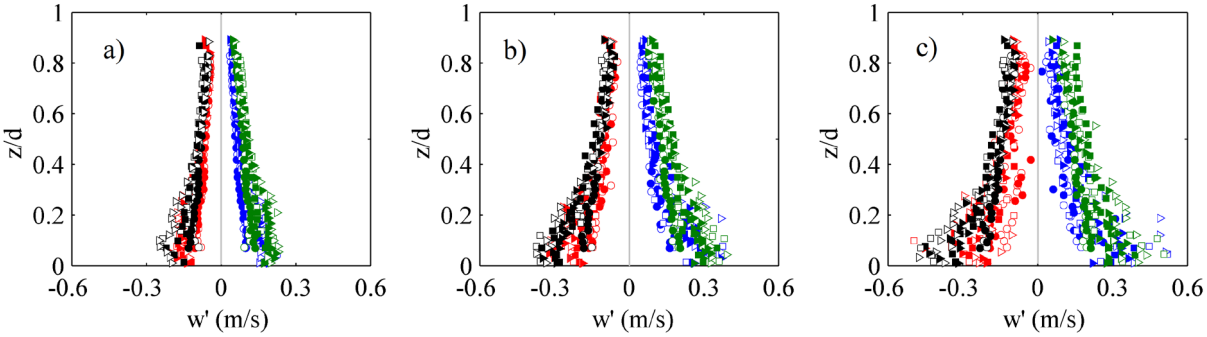

Figure 6.23- Vertical distribution of the maximum fluctuation *w' (*$w = \bar{w} + w'$*)* inside pulses of (a) T_p=1Δt, (b) T_p=3Δt, and (c) T_p=5Δt, separated by quadrants. Experiments CG. *Legend Markers, ○ CG1, ● CG2, □ CG3, ■ CG4, ▷ CG5 and ► CG6. Legend colors, ● Q1, ● Q2, ● Q3, and ● Q4.*

From the figures, it is observed that as in the case of u', the values of w' of each pulse-quadrant is decreasing as increasing the distance to the bed. However, now the larger values of each distribution are located closer to the bed. As for the fluctuations u', the w' are greater in the quadrants Q2 and Q4, with respect to the other two (Q1 and Q3), being as well increased with the mean velocity $\bar{u}$ of the flow. The Q2 shows the same predominance of the w' values in the second half of the profile, showing the more extreme behavior of ejections in comparison with the rest. Regarding the effects of the bed roughness on the fluctuations, it is noteworthy that values of *w'* are increased (near the bed) in the case of not-leveled beds (CG experiments), mainly for the fluctuations of Q2 and Q4 and for pulses of T_p>3Δt.

The following conclusions can be summarized from the velocity fluctuations (*u', w'*) distributions. Quadrants Q2 and Q4 are those that show higher fluctuations in both the vertical plane w' and horizontal plane u'. However, it is the fluctuations of Q2 events that remain high along the profile (mainly u') while those from the Q4 events show a clearer pattern of decay, obtaining minimum values near the water surface.

6.3.2 Velocity Fluctuation module $\overrightarrow{u'w'}$

6.3.2.1 Vertical distribution of $\overrightarrow{u'w'}$

So far, we have analyzed the fluctuations of u' and w' separately, but if we consider that both act together, and so defining a direction on the quadrant map, it is possible to obtain the vector module $\overrightarrow{u'w'}$ on a plane (u', w') resulting from both fluctuation terms. The fluctuation module is interesting because it allows associating each pulse duration with a single fluctuation, which is also positive.

Figure 6.24 shows the vertical distribution of $\overrightarrow{u'w'}$ associated to three pulse durations (T_p=1Δt, T_p=3Δt, and T_p=5Δt) for the two sets of experiments. As expected, the pulses of longer duration obtain a higher velocity module ($\overrightarrow{u'w'}$). Since all velocities are positive now, the progressive decrease of $\overrightarrow{u'w'}$ can be observed for all pulse durations with the distance to the bed, demonstrating once again that the events turn out to be extreme especially in the near-bed region. In the CG experiments (Figure 6.24-b), it can be seen that these velocities remain rather constant in the roughness layer (z/d<0.3). The velocities ($\overrightarrow{u'w'}$) are greater as the level of turbulence of the experiments is increased. In addition, it is detected that in experiments of equal turbulent level but with not-packed bed surface (CG1, CG3 and CG5), thus with higher relative roughness (k_s) in comparison with CG2, CG4 and CG6, obtain greater velocities.

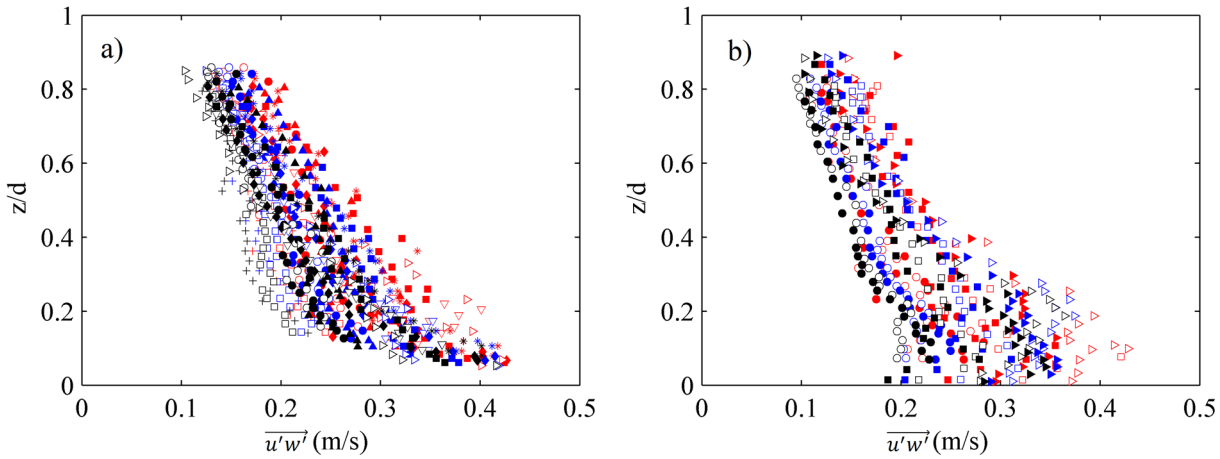

Figure 6.24- Vertical distribution of the average fluctuation modulus inside pulses of duration 1Δt, 3Δt, 5Δt, without distinction between quadrants, for (a) RG and (b) CG experiments. *Legend Markers (a), + RG1, ○ RG2, □ RG3, ● RG4, ▲ RG5, ▽ RG6, ∗ RG7, ♦ RG8, ■ RG9 and ▷ RG10. Legend Markers (b), ○ CG1, ● CG2, □ CG3, ■ CG4, ▷ CG5 and ▶ CG6. Legend colors, ● 1Δt, ● 3Δt, and ● 5Δt.*

In the same way, as done in the previous section, it is possible to characterize the average ($\overrightarrow{u'w'}$) of each pulse duration depending on the quadrant in which it appears. The following figures show the decomposition of the average velocities ($\overrightarrow{u'w'}$) of the three pulses (T_p=1Δt, T_p=3Δt, and T_p=5Δt) in each quadrant of appearance (by colors), see Figure 6.25 (RG tests) and Figure 6.26 (CG tests). From the disaggregation of the quadrants, it can be seen that the most extreme $\overrightarrow{u'w'}$ are those of pulses located in quadrants Q2 and Q4. In addition, it can be observed how the velocities become more fluctuating, reaching maximum and minimum values as the pulse duration T_p increases.

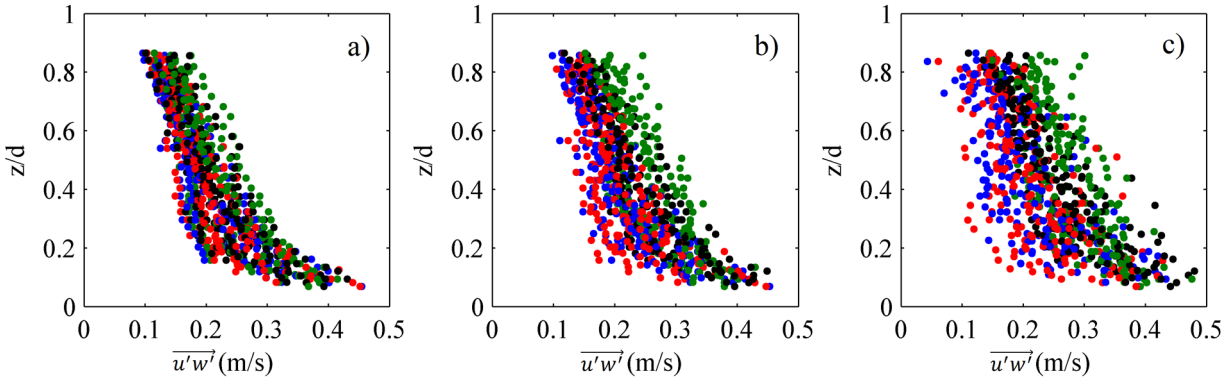

Figure 6.25- Vertical distribution of the average $\overline{u'w'}$ inside pulses of (a) T_p=1Δt, (b) T_p=3Δt, and (c) T_p=5Δt, separated by quadrants. Experiments RG. *Legend,* ● *Q1,* ● *Q2,* ● *Q3, and* ● *Q4.*

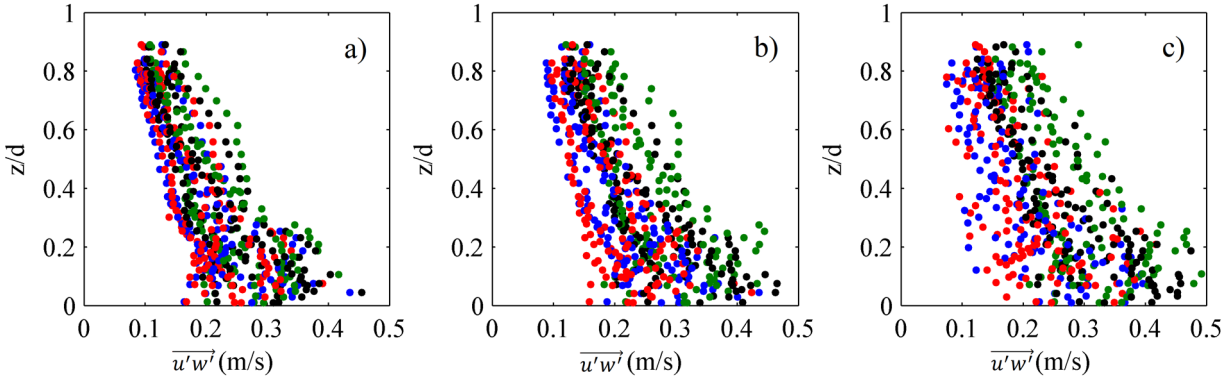

Figure 6.26- Vertical distribution of the average $\overline{u'w'}$ inside pulses of (a) T_p=1Δt, (b) T_p=3Δt, and (c) T_p=5Δt, separated by quadrants. Experiments CG. *Legend,* ● *Q1,* ● *Q2,* ● *Q3, and* ● *Q4.*

6.3.2.2 Velocity- Duration-Density maps

In section 6.2.1 we have analyzed pulse durations by means of the pulse-duration Histograms (PDH), the return period associated, and the analysis of the velocity terms (*u',w'*) associated with some pulse durations, in all cases also distinguishing between quadrants of appearance. What is intended in this section is the union of the three concepts through the Velocity-Duration-Density (VDD) maps. In these maps, the density distribution (or frequency) of the pulse durations (T_p) expressed as time steps (ΔT) is represented as a function of the velocity module ($\overline{u'w'}$), with one map by quadrant.

As seen in section 6.2.1, the PDH defined in each quadrant, turn out to be very consistent along the depth profile, that is, the pulse durations were little affected by the distance to the bed, as long as the water depth (d) of the experiment was relatively small.

The aim of the VDD maps is to see if there is a type pulse (of a certain T_p and $\overline{u'w'}$) of greater occurrence. In Figure 6.27 an example of these maps (for each quadrants) is shown, for a point located at a height of z =1 cm from the experiment RG3. Figure 6.28 shows a point at a height of z=3 cm from the same experiment.

Quadrants Q2 and Q4 obtain the highest density of events of pulses of T_p=2Δt with a fluctuation velocity module ($\overline{u'w'}$) of approximately 0.2 m/s, while the other two quadrants (Q1 and Q3) have a greater density of pulses of T_p=1Δt with a lower velocity module ($\overline{u'w'}$).

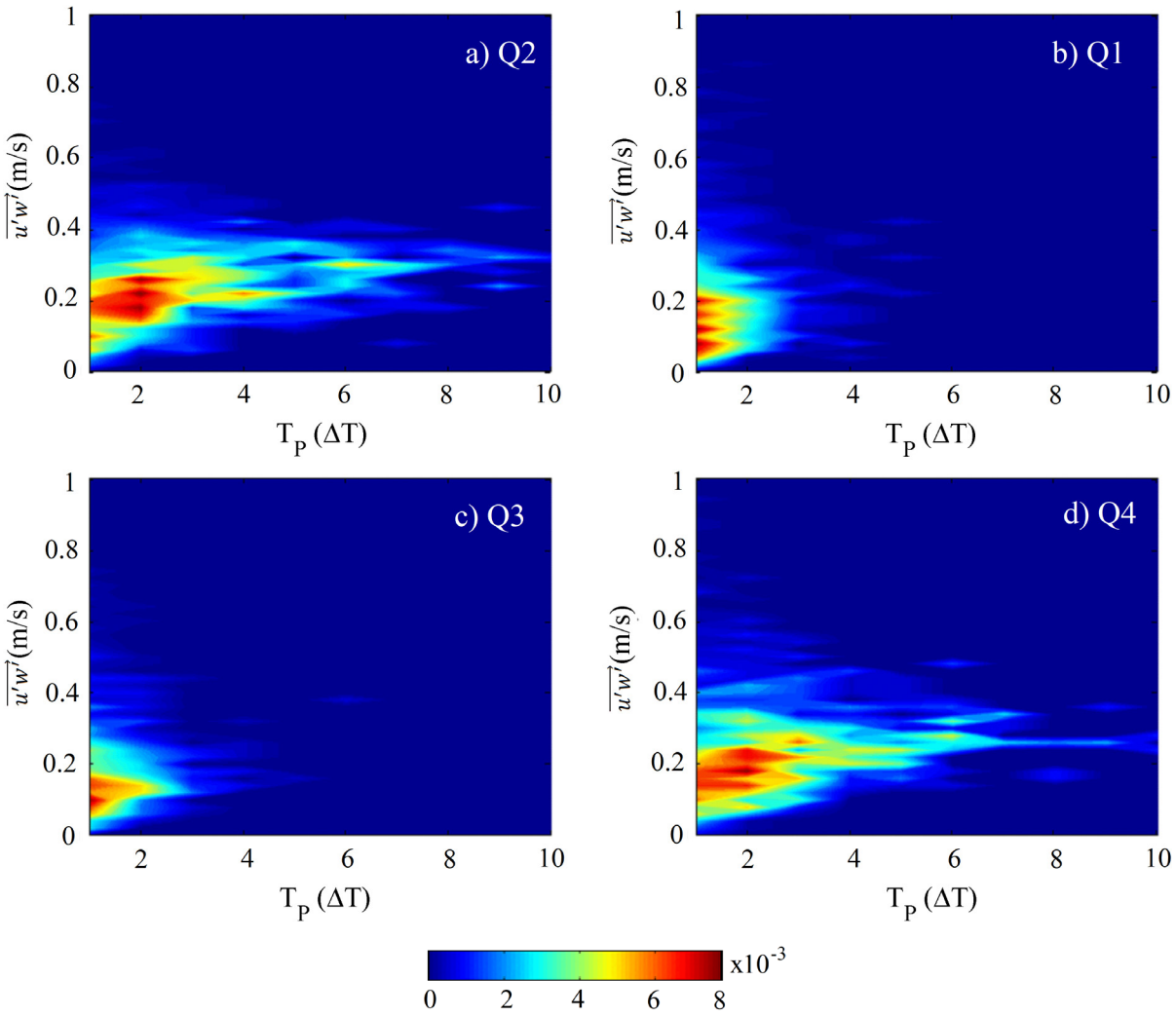

Figure 6.27- VDD maps from quadrants (a) Q2, (b) Q1, (c) Q3, and (d) Q4. Experiment RG3 at height z=1 cm.

At a glance of Figure 6.27 and Figure 6.28, it is observed that the VDD maps are also quite consistent for the two represented points, located at a different height, where the same T_p prevails in the quadrants. Possibly a higher concentration of events is observed at slightly lower velocities compared to the point closest to the bed because as we saw earlier, the velocity fluctuations are reduced when ascending through the profile.

By only visual inspection of the maps, it is very difficult to detect patterns. For this reason, in Figure 6.29 and Figure 6.30 it is depicted the vertical distributions obtained from the VDD maps for the two groups of experiments respectively. In the figures, the $\overline{u'w'}$ as a function of the T_p (indicated by color) of the highest density of events from the VDD maps, of each height point (z/d) has been represented for each experiment, separated by quadrant of appearance. That is to say, the vertical distribution of $\overline{u'w'}$ from the most likely pulses.

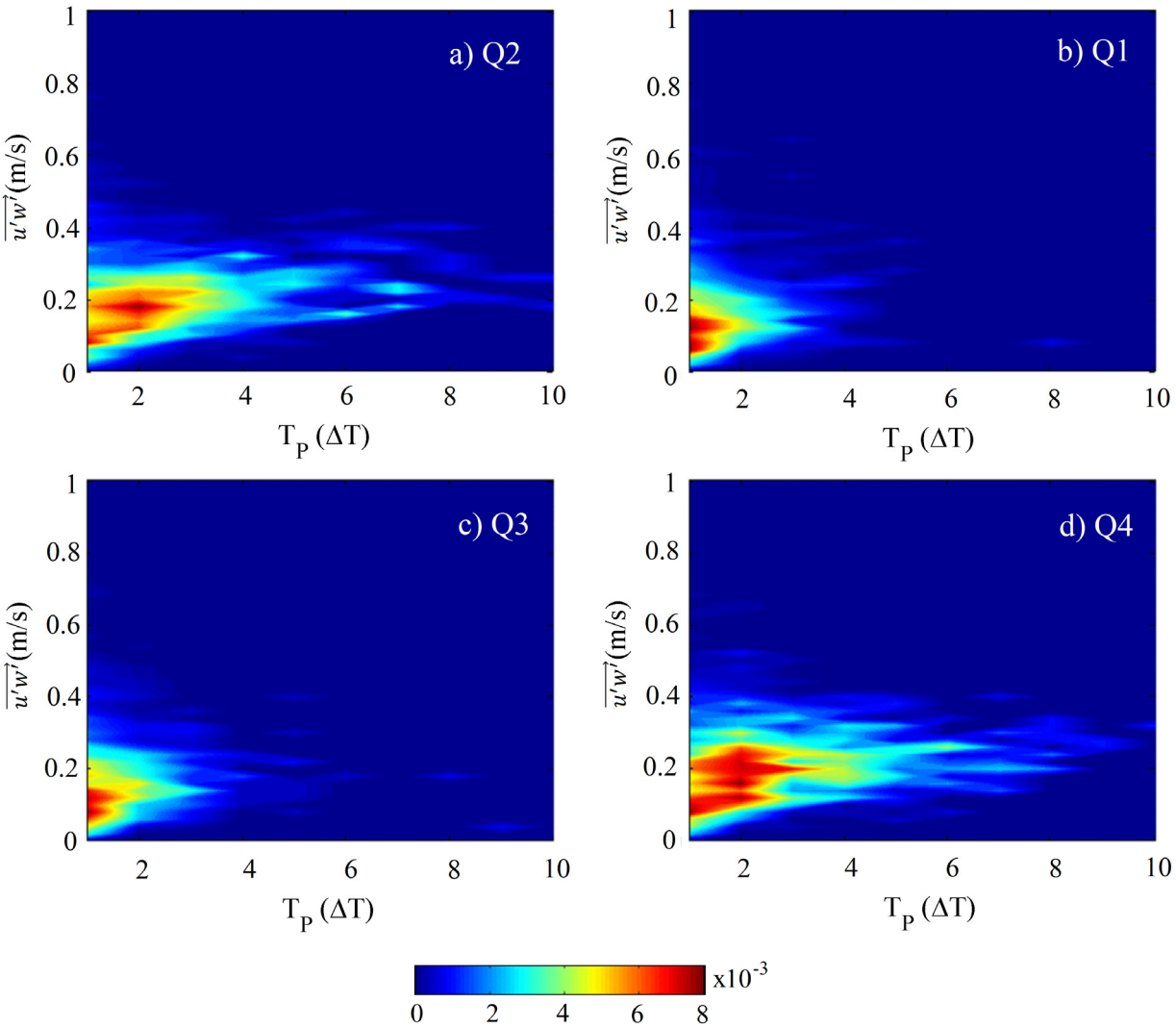

Figure 6.28- VDD maps from quadrants (a) Q2, (b) Q1, (c) Q3, and (d) Q4. Experiment RG3 at height z=3 cm.

From the figures, it can be seen that quadrants Q1 and Q3 show lower ($\overline{u'w'}$), as we had already verified by means of the study of u' and w' separately; moreover, the highest density of pulses is located in pulses of duration T_p=1Δt. However, quadrants Q2 and Q4, in addition to obtaining higher velocities ($\overline{u'w'}$) in the pulse, these pulses have a tendency to be longer than T_p >2Δt, concentrating in some cases the highest density of events, in pulses of T_p=3Δt or even up to T_p=5Δt. This usually happens for high levels of turbulence (high flow rate) and inside the bed region. Quadrant Q4 shows a zone of high ($\overline{u'w'}$) in the region near the bed z/d<0.3, while the Q2 shows greater velocities along the whole profile. The velocities in the other two quadrants, although decreasing with the height (z/d), have a slow and progressive decay.

Both figures, Figure 6.29 and Figure 6.30, show that the velocities ($\overline{u'w'}$) are greater near the bed and that they progressively decrease with the height in the profile. In reference to the flattening of the bed surface (CG experiments), it seems that the experiments with not-packed beds obtain higher ($\overline{u'w'}$), however, as it has been mentioned previously, given the differences between all the tests, these variations cannot be attributed to the change in roughness.

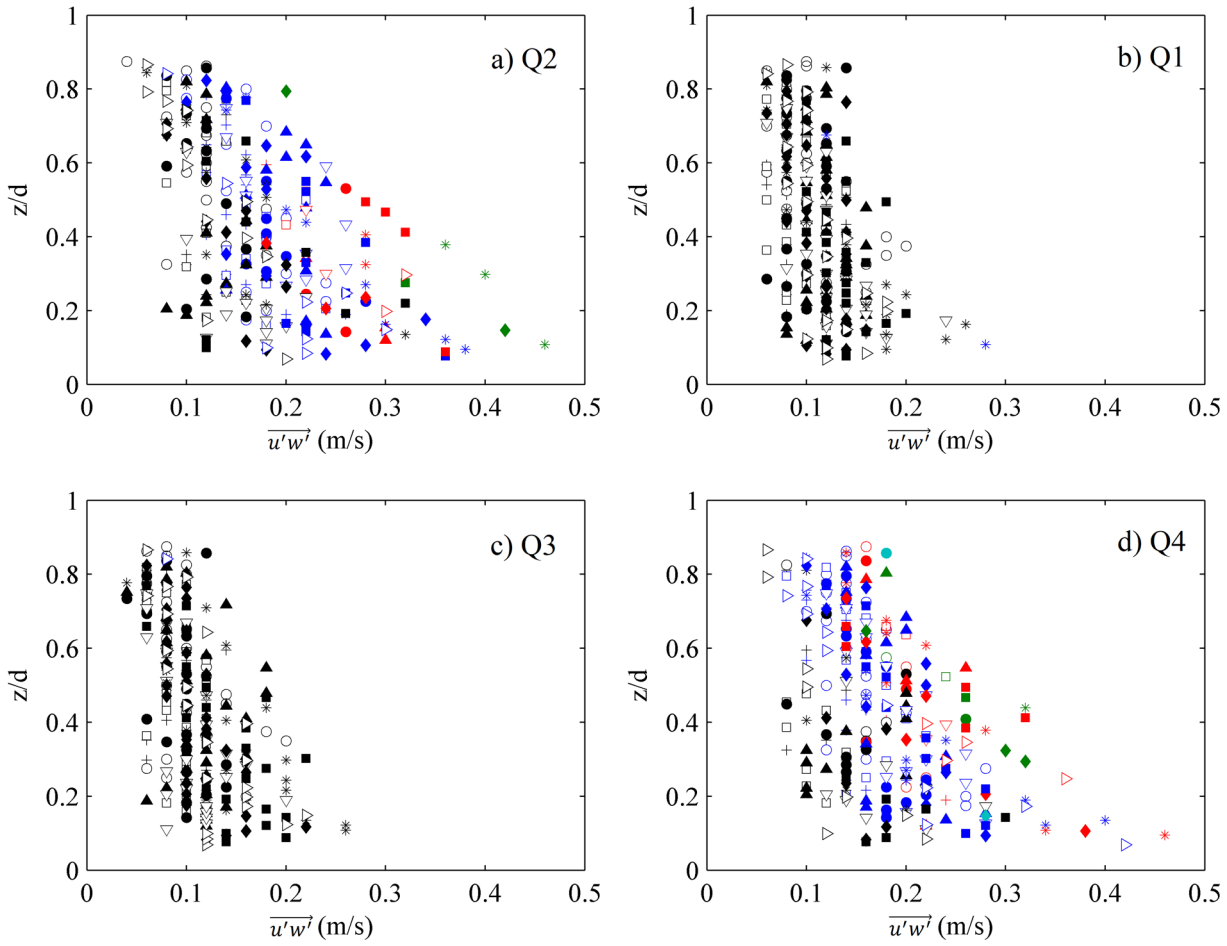

Figure 6.29- Vertical distribution of the average $\overline{u'w'}$ of the most frequent T_p, separated by quadrants (a) Q1, (b) Q2, (c) Q3, and (d) Q4. RG experiments. *Legend Markers,* + *RG1,* ○ *RG2,* □ *RG3,* ● *RG4,* ▲ *RG5,* ▽ *RG6,* ∗ *RG7,* ♦ *RG8,* ■ *RG9 and* ▷ *RG10. Legend colors,* ● *1Δt,* ● *2Δt,* ● *3Δt,* ● *4Δt, and* ● *5Δt.*

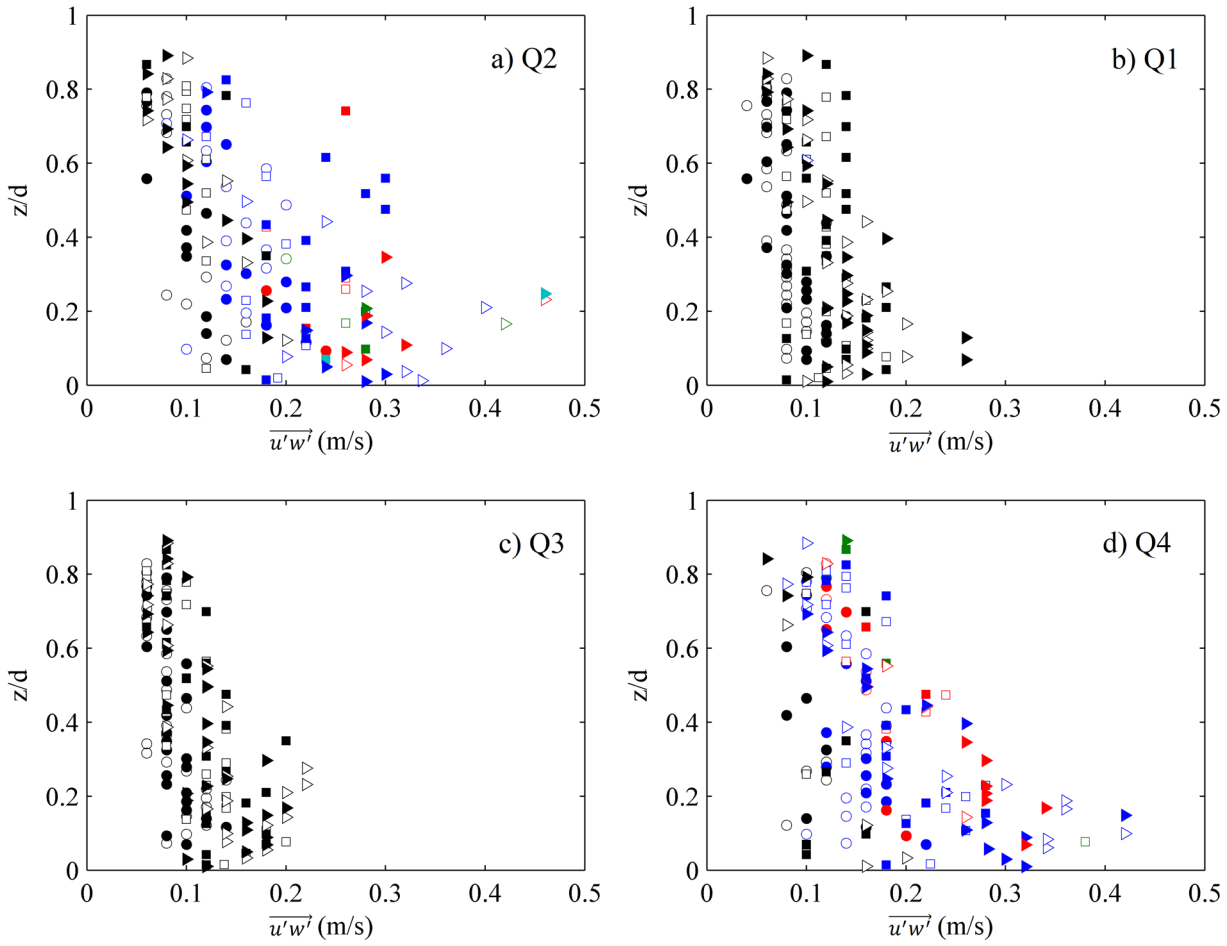

Figure 6.30- Vertical distribution of the average $\overline{u'w'}$ of the most frequent T_p, separated by quadrants (a) Q1, (b) Q2, (c) Q3, and (d) Q4. CG experiments *Legend Markers,* ○ *CG1,* ● *CG2,* □ *CG3,* ■ *CG4,* ▷ *CG5 and* ▶ *CG6. Legend colors,* ● *1Δt,* ● *2Δt,* ● *3Δt,* ● *4Δt, and* ● *5Δt.*

6.4 Pulse Sequences

Due to the analysis of the quadrant sequences (Chapter 5, section 5.6); the importance of the duration of the events within the same quadrant was emphasized, arousing an exhaustive analysis of the pulse statistics. At this point, it is necessary to rethink again if there are certain sequences, of pulses in this case, which has a predominance with respect to the rest. For this, sequences of three consecutive pulses have been analyzed, since the consideration of larger sequences did not yield the predominance of any sequence with respect to the rest sufficiently significant to be taken into account.

In the case of quadrant sequences, chapter 5 section 5.6.2, we obtained a total of 64 sequences, from permutations with repetition of the four quadrants in a chain of 3 events). However, in a pulse sequence, two quadrants cannot be consecutive in the chain since pulses already consider all the events that occur consecutively in a quadrant. Therefore, a total of 36 sequences is obtained.

6.4.1 Vertical distribution of the pulse-sequences

Figure 6.31 shows the vertical distribution of the TF that each sequence (36) has in the data series, yet only the sequences with a certain predominance in the data series have been highlighted by colors for sake of simplicity. It is observed that the sequences with high predominance are those that involve trips between quadrants Q1 and Q4 (Q4-Q1-Q4 and Q1-Q4-Q1), with a clear tendency to increase their presence when approaching the water surface (z/d>0.5). The following sequences of greater TF in the data series are those that include trips between quadrants Q2 and Q3, (Q2-Q3-Q2 and Q3-Q2-Q3), keeping these a more constant distribution along the depth profile than the previous ones. Nevertheless, all show a rather constant value in the region near the bed (z/d<0.3).

In Figure 6.31 have been also highlighted the sequences of pulses between quadrants Q2 and Q4, (Q4-Q2-Q4 and Q4-Q2-Q4), due to the importance that these quadrants have revealed throughout the thesis development, observing that although they have a certain importance, they do not predominate over those already mentioned. They also show a certain steadiness in the near-bed region, but outside the roughness area, they show a tendency to decrease.

We had already seen that the quadrant TF that grows the most compared to the rest with the height in the depth profile (z) is the Q4. Therefore, pulses in the near-bed region that belong to Q4 have a closer probability of belonging to the sequences Q4-Q1-Q4, Q1-Q4-Q1, Q4-Q2-Q4, and Q4-Q2-Q4 since the TF pulse-sequences remain close and constant in this region. However, in the second half of the depth profile (z/d>0.5) pulses from Q4 are more likely to be part of the sequences Q1-Q4-Q1 and Q4-Q1-Q4, because the TF of these two pulse-sequences increase considerably along the water depth. On the other hand, the rest of the sequences have less probability of occurrence and display a constant TF distribution along the profile.

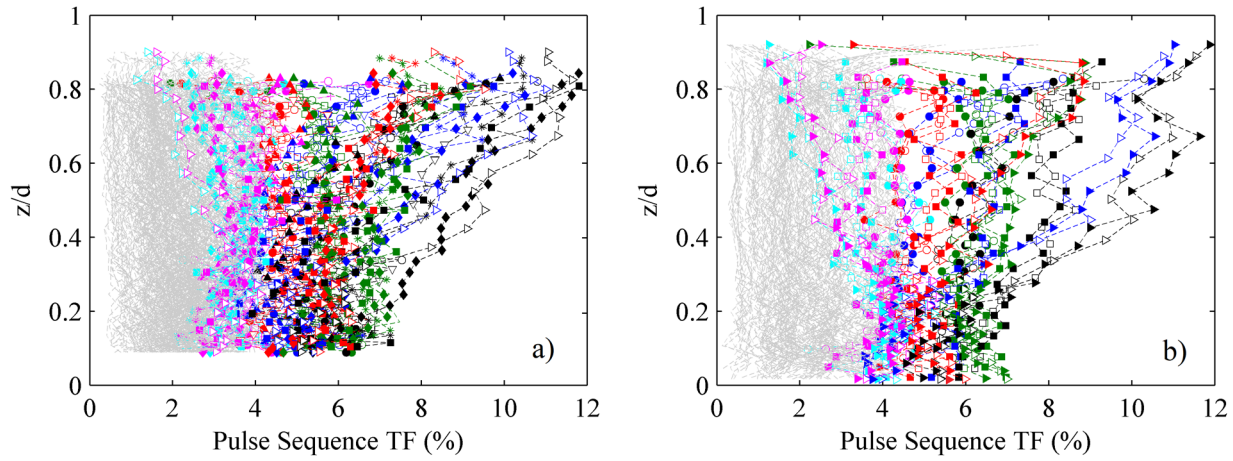

Figure 6.31- Vertical distribution of the pulse-sequences TF, for the experiments (a) RG and (b) CG. *Legend Markers (a), + RG1, ○ RG2, □ RG3, ● RG4, ▲ RG5, ▽ RG6, ∗ RG7, ♦ RG8, ■ RG9 and ▷ RG10. Legend Markers (b) , ○ CG1, ● CG2, □ CG3, ■ CG4, ▷ CG5 and ▶ CG6. Legend colors, ● sequence 141, ● 232, ● 242, ● 323, ● 414, ● 424, and ● the rest.*

The depth-averaged TF of the pulse-sequences for all experiments are shown in Table 8.1, where it can be seen that the mean values from one experiment to another are quite congruent. However, for a better visualization of the results, Figure 6.32 represents graphically the results of Table 8.1. In these

graphs, the tendency of the depth-averaged values of TF (or probability) of each sequence as a function of the hydraulic depth (*d*) of the experiment is observed.

The sequences Q4-Q1-Q4 and Q1-Q4-Q1 tend to increase when the water depth (*d*) is greater because they grow when approaching the water surface, like the sequences Q2-Q3-Q2 and Q3-Q2-Q3. The rest of the sequences have a tendency to decrease when the water depth (*d*) increases. Thanks to the graph of the depth-averaged values, it can now be elucidated which are the sequences with the least presence in the sample, Q1-Q3-Q1, and Q3-Q1-Q3.

Table 6.1 Pulse-sequence time fraction results for all experiments.

SEQ	RG1	RG2	RG3	RG4	RG5	RG6	RG7	RG8	RG9	RG10	CG1	CG2	CG3	CG4	CG5	CG6
121	1,62	1,50	1,57	1,60	1,63	1,53	1,51	1,46	1,18	1,47	1,53	1,45	1,4	1,54	1,42	1,47
123	2,10	2,20	2,18	2,09	2,30	1,98	2,12	1,90	1,72	2,05	2,3	2,28	1,95	2,19	1,93	2,14
124	2,46	2,46	2,36	2,40	2,38	2,25	2,13	2,02	2,08	1,86	2,42	2,43	2,23	2,2	2,1	2,23
131	0,71	0,73	0,77	0,71	0,79	0,76	0,70	0,60	0,59	0,72	0,61	0,56	0,57	0,57	0,6	0,64
132	1,80	1,79	1,97	1,82	1,92	1,77	1,68	1,64	1,44	1,70	1,68	1,65	1,47	1,72	1,46	1,65
134	1,23	1,20	1,30	1,29	1,36	1,28	1,21	1,13	1,28	1,26	1,05	1,07	1,03	1,06	1,13	1,17
141	5,08	5,19	4,93	5,19	4,99	5,89	6,80	7,18	7,28	7,76	4,91	4,86	6,46	5,63	7,01	7,21
142	3,92	4,03	3,77	3,80	3,63	3,81	3,39	3,68	3,74	3,42	4,15	4,05	4,02	3,75	3,79	3,55
143	3,23	3,04	3,29	3,31	3,02	3,33	2,96	3,20	3,08	2,89	2,82	2,95	3,18	2,89	2,94	2,83
212	2,01	1,82	2,00	2,03	2,07	1,78	1,78	1,72	1,39	1,61	1,92	2,06	1,71	1,84	1,66	1,68
213	1,24	1,17	1,35	1,23	1,35	1,17	1,17	1,07	0,97	1,15	1,09	1,09	0,92	1,09	1,01	1,06
214	3,72	3,63	3,68	3,53	3,31	3,60	3,16	3,61	3,05	3,26	3,68	3,68	3,76	3,55	3,46	3,48
231	1,58	1,77	1,74	1,66	1,81	1,60	1,64	1,47	1,36	1,62	1,74	1,56	1,42	1,58	1,48	1,59
232	5,52	5,40	5,52	5,31	5,72	5,44	6,84	6,81	6,42	7,05	5,98	5,82	5,81	6,61	6,33	6,51
234	2,72	3,02	2,67	2,72	2,91	2,77	2,82	2,62	2,69	2,87	3,01	2,97	2,78	3,09	2,96	2,98
241	4,01	4,03	3,77	3,82	3,75	3,90	3,56	3,68	3,30	3,35	4,07	3,93	3,97	3,75	3,53	3,59
242	3,72	3,79	3,66	3,71	3,59	3,39	3,12	3,05	3,02	2,79	4,16	4,39	3,79	3,71	3,37	3,15
243	2,80	2,67	2,81	2,83	2,87	2,65	2,44	2,37	2,21	2,20	2,67	2,8	2,62	2,56	2,57	2,37
312	1,13	1,14	1,22	1,17	1,30	1,14	1,17	0,95	0,98	1,02	1,11	1,05	0,89	1,02	0,96	1,1
313	0,67	0,67	0,76	0,73	0,87	0,75	0,73	0,61	0,68	0,77	0,63	0,56	0,51	0,58	0,57	0,66
314	1,90	2,08	2,07	2,02	1,99	2,00	1,80	1,81	1,74	1,85	1,87	1,79	1,8	1,72	1,8	1,74
321	2,70	2,50	2,85	2,61	2,59	2,46	2,36	2,50	2,29	2,34	2,51	2,58	2,46	2,52	2,21	2,3
323	4,34	4,42	4,45	4,31	4,80	4,66	6,06	5,93	5,90	6,44	4,56	4,32	4,68	5,45	5,62	5,73
324	4,05	3,95	4,02	3,99	4,00	3,86	3,61	3,72	3,60	3,37	4,23	4,28	3,96	4,05	3,69	3,54
341	2,40	2,42	2,37	2,46	2,39	2,37	2,34	2,20	2,50	2,35	2,19	2,26	2,29	2,37	2,37	2,37
342	2,39	2,44	2,34	2,34	2,46	2,38	2,24	2,14	2,29	2,15	2,45	2,52	2,29	2,38	2,25	2,28
343	1,69	1,65	1,79	1,90	2,00	1,87	1,89	1,67	1,75	1,86	1,6	1,62	1,7	1,76	1,95	1,78
412	3,05	3,20	2,89	2,89	2,95	2,85	2,80	2,72	2,60	2,75	3,21	3,04	2,97	3,07	2,82	3,06
413	1,83	1,89	1,93	1,85	1,85	1,89	1,70	1,70	1,67	1,75	1,63	1,62	1,65	1,68	1,6	1,74
414	6,61	6,55	6,25	6,74	6,45	7,43	8,19	8,65	8,76	8,96	6,33	6,39	8,1	7	8,49	8,38
421	2,64	2,61	2,61	2,58	2,51	2,56	2,23	2,44	2,36	2,20	2,64	2,8	2,53	2,43	2,51	2,44
423	3,37	3,56	3,30	3,29	3,35	3,18	3,13	3,07	3,14	3,05	3,87	3,75	3,37	3,64	3,22	3,21
424	4,02	4,08	3,85	3,98	3,83	3,83	3,38	3,36	3,28	3,12	4,24	4,4	4,19	3,77	3,67	3,34
431	1,42	1,39	1,53	1,56	1,55	1,51	1,35	1,29	1,44	1,31	1,26	1,28	1,22	1,17	1,25	1,28
432	3,77	3,67	3,83	3,77	3,75	3,77	3,51	3,69	3,53	3,39	3,65	3,72	3,83	3,7	3,73	3,42
434	2,52	2,30	2,52	2,70	2,58	2,56	2,43	2,27	2,27	2,24	2,18	2,37	2,46	2,35	2,48	2,29

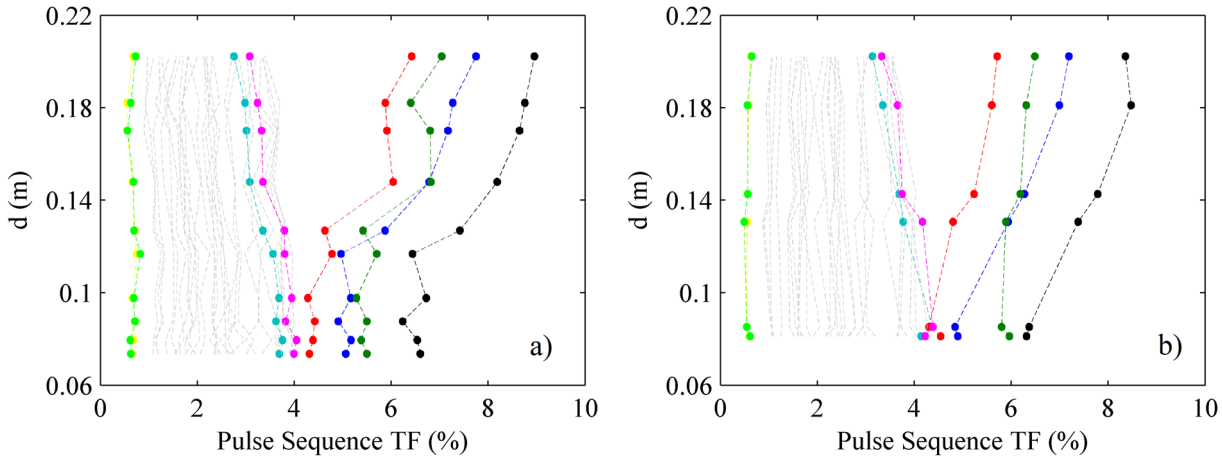

Figure 6.32- Depth-averaged TF for each pulse-sequence, as a function of *d* for the experiments (a) RG and (b) CG. *Legend,* ● *sequence 131,* ● *141,* ● *232,* ● *242,* ● 313, ● *323,* ● *414,* ● *424, and* ● *the rest.*

6.4.2 Return period of the pulse-sequences

In addition to the representation of the pulse-sequence TF, in Figure 6.33 the vertical distributions of the average return periods associated to each pulse-sequence have been characterized, where the same sequences as in Figure 6.31 have been highlighted. The figure shows that the average return period of each sequence is indirectly proportional to the time fraction that they represent in the data series. All return periods show a constant distribution in the region near the bed $z/d<0.3$ and a slightly decreasing trend towards the water surface.

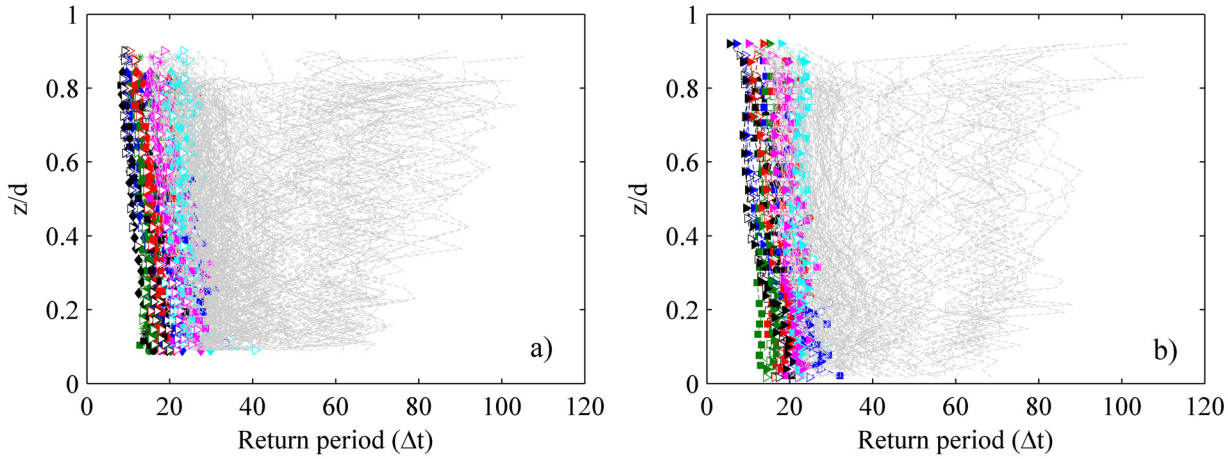

Figure 6.33- Vertical distribution of the Return period of each pulse-sequence, for the experiments (a) RG and (b) CG. *Legend Markers (a),* + *RG1,* ○ *RG2,* □ *RG3,* ● *RG4,* ▲ *RG5,* ▽ *RG6,* ✶ *RG7,* ♦ *RG8,* ■ *RG9 and* ▷ *RG10. Legend Markers (b) ,* ○ *CG1,* ● *CG2,* □ *CG3,* ■ *CG4,* ▷ *CG5 and* ▶ *CG6. Legend colors,* ● *sequence 141,* ● *232,* ● *242,* ● *323,* ● *414,* ● *424, and* ● *the rest.*

The sequences have a length of three consecutive pulses (P_1-P_2-P_3). However, the duration of the sequence depends on the duration of each pulse that composes the sequence P_1-P_2-P_3. In Figure 6.34 and Figure 6.35, the vertical distribution of the mean T_p of the (a) P_1, (b) P_2 and (c) P_3 (first, second and third pulse in the sequence) have been represented, distinguishing between quadrants. Figure 6.34 depicts the results of the RG experiments and Figure 6.35 from the CG experiments.

The results show that pulses inside the quadrants Q1 and Q3 have a mean duration of T_p=1.3Δt (0.052 s), and are very constant along the profile, and pulses in the Q2 and Q4 have a mean duration of T_p=1.9Δt (0.076 s) with a trend of extending the T_p with the height in the depth profile (z/d). For all pulses no matter the position in the sequence (P_1-P_2-P_3), the mean T_p of the pulse is consistent.

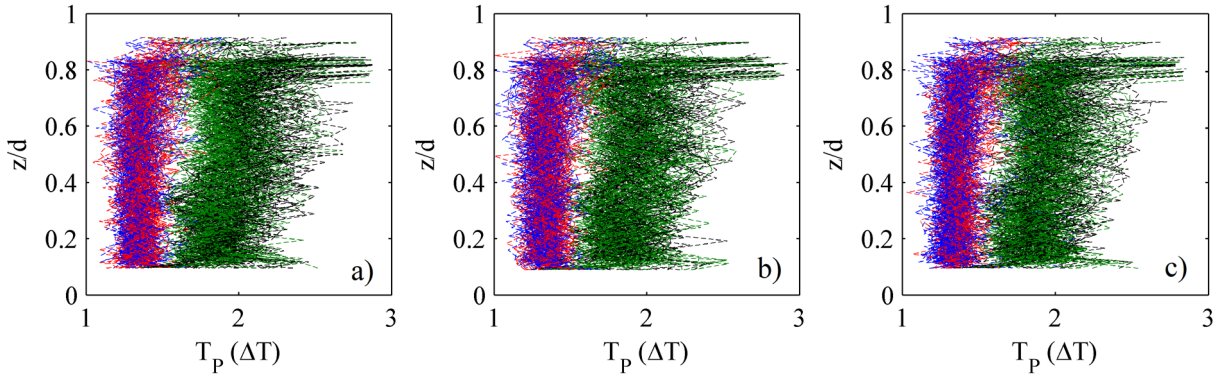

Figure 6.34- Vertical distribution of the average T_p of the (a) P_1, (b) P_2, and (c) P_3 in the pulse-sequence (P_1-P_2-P_3), separated by quadrant of appearance. RG experiments. *Legend, Q1, Q2, Q3, and Q4.*

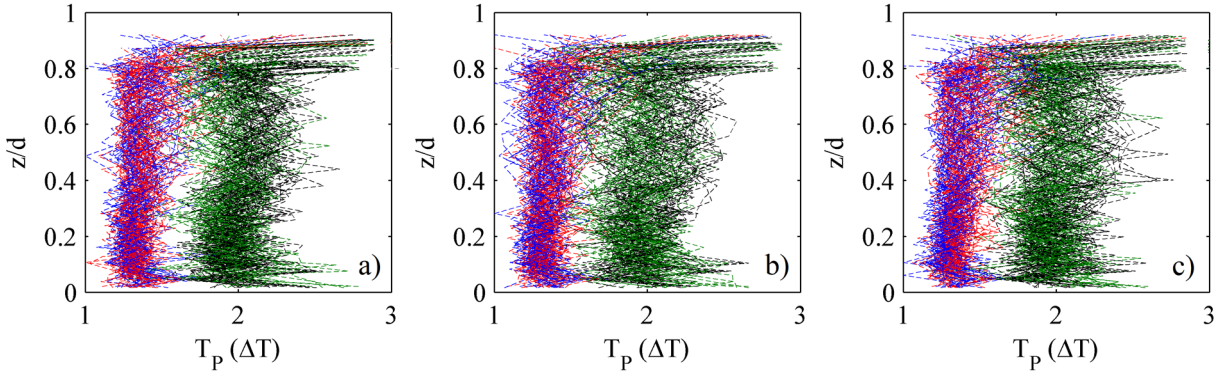

Figure 6.35- Vertical distribution of the average T_p of the (a) P_1, (b) P_2, and (c) P_3 in the pulse-sequence (P_1-P_2-P_3), separated by quadrant of appearance. CG experiments. *Legend, Q1, Q2, Q3, and Q4.*

6.5 Contribution to Reynold stress

6.5.1 Contribution of the pulse durations

In the same way that the quadrant contribution to the Reynolds stress was obtained in the previous chapter, the contribution of each pulse duration is evaluated in this section. Figure 6.36 shows the vertical distribution of the contribution to the Reynolds stress (decimal fraction) of the pulses of duration T_p=1Δt (blue), T_p=2Δt (red), and T_p=3Δt (black). No distinction has been made between experiments, only between the two large groups RG (Figure 6.36-a) and CG (Figure 6.36-b), for sake of simplicity.

From the graph, it is obtained that the short pulses, T_p=1Δt (blue), have a contribution to the Reynolds stress of approximately 30%, which is logical since they represent around 35-40% (TF) of the data series (Figure 6.5). The contribution of the pulses T_p=2Δt (green) and T_p=3Δt (red) is very similar, being around 10-20%. However, in Figure 6.5 we saw that the TF of these two pulse durations was well differentiated, with a TF=0.25 (25%) from T_p=2Δt, while that of the T_p=3Δt was TF=0.15.

Therefore, pulses of $T_p=3\Delta t$ are able to increase in the same proportion even though they have less presence in the sample, denoting the most extreme character of the pair ($u'w'$) of $T_p=3\Delta t$.

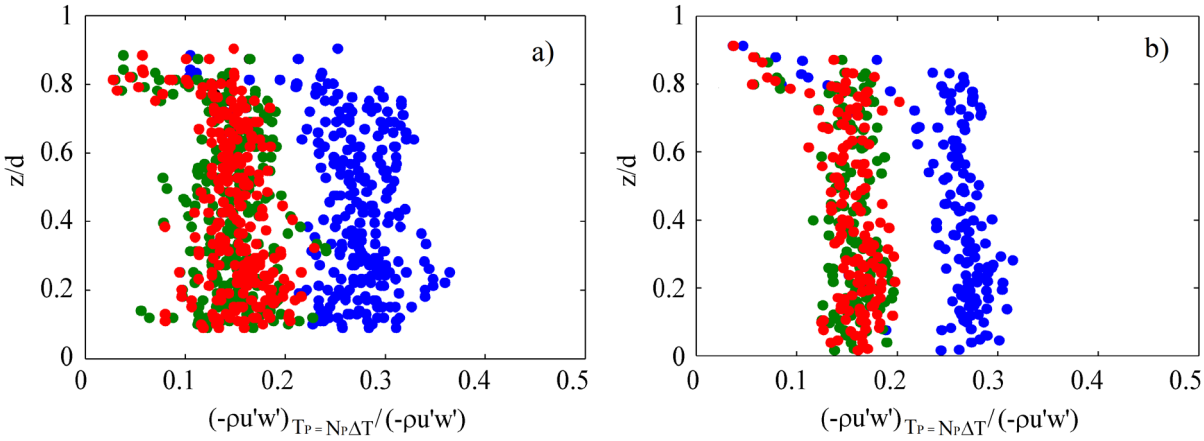

Figure 6.36- Vertical distribution of the contribution to Reynold stress of $T_p=1\Delta t$, $Tp=2\Delta t$, and $Tp=3\Delta t$, for the experiments (a) RG and (b) CG. *Legend colors,* ● $T_p=1\Delta t$, ● $Tp=2\Delta t$, *and* ● $Tp=3\Delta t$.

The same contributions are shown in the figures below, but in this case, we have distinguished between experiments of each kind and separated the contribution of each pulse duration in a different graph. All contributions have a rather constant behavior along the depth profile. The RG experiments allow seeing the differences between experiments with the same bed roughness but different flow rate and hydraulic depth (d). From them, it is observed that in the cases $T_p=1\Delta t$ (Figure 6.37-a) and $T_p=2\Delta t$ (Figure 6.38-a), the contributions tend to be a little higher for cases of lower turbulent level (lower flow rate and d), while the contribution of $T_p=3\Delta t$ (Figure 6.39-a) is higher in cases of higher turbulent level. This may be due to the fact that in cases whit high level of turbulence (d>>) the TF of pulses $T_p=1\Delta t$ were more diminished along the profile (Figure 6.5) since this decreases with distance to the bed. Therefore, the contribution of longer duration pulses ($T_p>1\Delta t$) becomes more noticeable. This effect can also be observed in the fact that for the points located at z/d>0.5, while $T_p=2\Delta t$ (Figure 6.38) and $T_p=3\Delta t$ (Figure 6.39) seem to converge towards a stable contribution of 0.15 (15%), in the case of $T_p=1\Delta t$ (Figure 6.37) the values do not converge, because the pulse duration $T_p=1\Delta t$ shows more TF differences along the profile (Figure 6.5).

It is difficult to assess the effects that the packing of the bed surface has on the different variables since there are few conclusive data available. However, it is observed that for the cases where the surface of the bed has been shaped, and especially in the cases where the bed-diameter is great conferring substantial difference in the relative roughness (tests CG4 and CG6), there seems to be a decrease in the pulses $T_p=1\Delta t$, while longer pulses ($T_p>1\Delta t$) increase. This suggests that the interactions of the roughness crests produce shorter pulses in the region near the bed as if breaking the coherence of the long pulses.

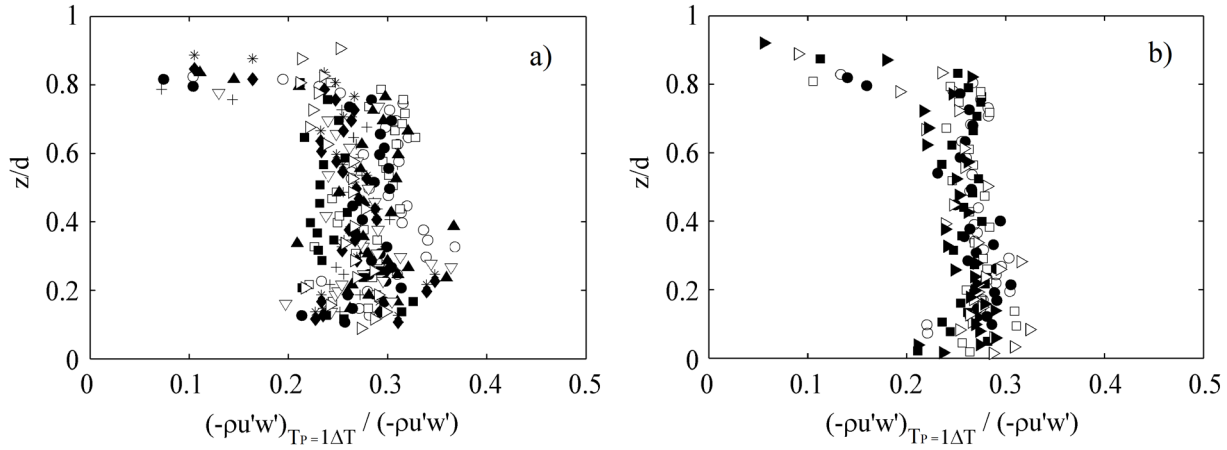

Figure 6.37- Vertical distribution of the contribution to Reynold stress of pulses of duration $T_p=1\Delta t$, for the experiments (a) RG and (b) CG. *Legend (a), + RG1, ○ RG2, □ RG3, ● RG4, ▲ RG5, ▽ RG6, ∗ RG7, ♦ RG8, ■ RG9 and ▷ RG10. Legend (b), ○ CG1, ● CG2, □ CG3, ■ CG4, ▷ CG5 and ▶ CG6.*

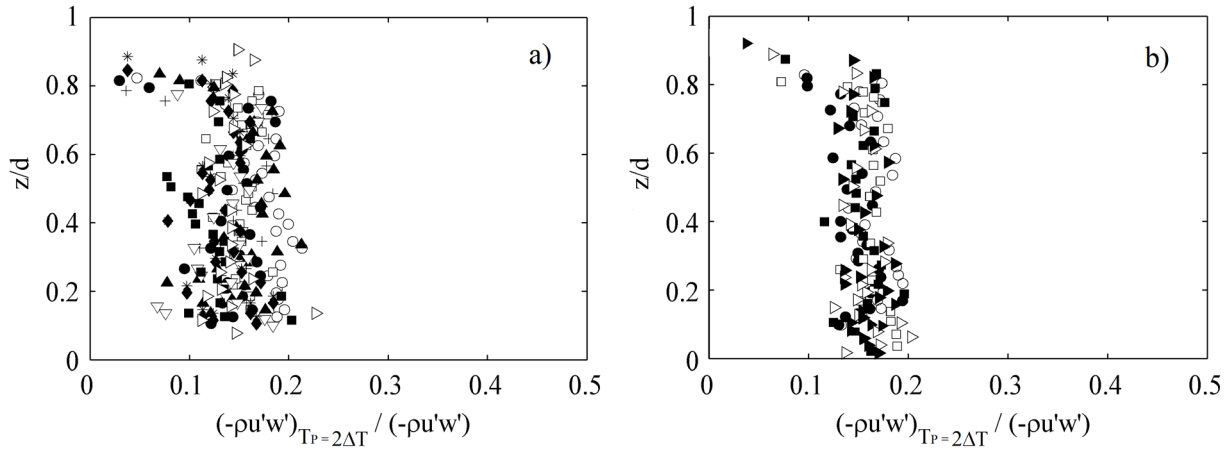

Figure 6.38- Vertical distribution of the contribution to Reynold stress of pulses of duration $T_p=2\Delta t$, for the experiments (a) RG and (b) CG. *Legend as for Figure 6.37.*

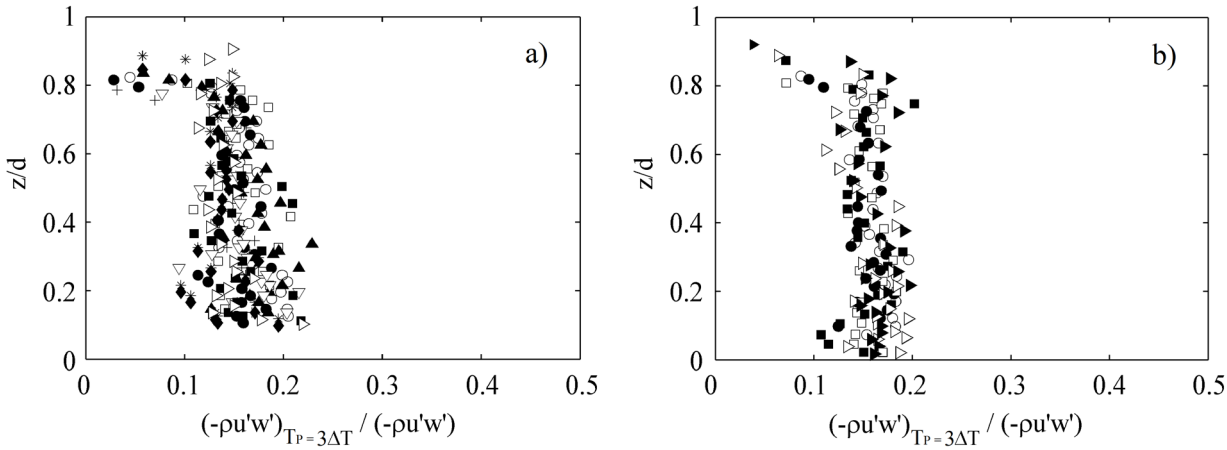

Figure 6.39- Vertical distribution of the contribution to Reynold stress of pulses of duration $T_p=3\Delta t$, for the experiments (a) RG and (b) CG. *Legend as for Figure 6.37.*

The figure below (Figure 6.40) shows the distribution of the contributions to the Reynolds stress of pulse durations from T_p=1 to T_p=10 of all the measurement points of the experiments RG1 (Figure 6.40-a) and RG10 (Figure 6.40-b). In addition, we have distinguished between the points located at a height of z/d<0.5 (red) and z/d>0.5 (black). The figure shows that there is a consistent pattern along the profile, although it is observed that points at z/d<0.5, the contribution of short pulses ($T_p=1\Delta t$) is greater than that of long pulses ($T_p>1\Delta t$), in both cases (Figure 6.40-a and Figure 6.40-b). This behavior is logical since we had seen that the $T_p=1\Delta t$ have a tendency to decrease with the height in the profile, in addition, the fluctuations decrease with the distance to the bed. This is observed better in the distribution of RG10 (Figure 6.40-b) because the depth is greater, the contributions of $T_p=1\Delta t$ are lower in cases z/d>0.5.

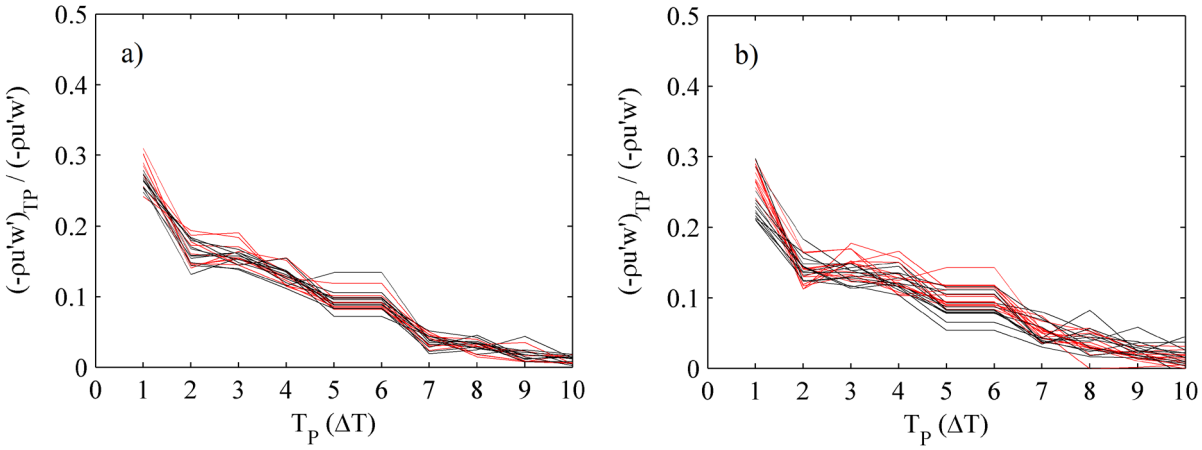

Figure 6.40- Distribution of the contributions to Reynolds stress of pulses from $T_p=1\Delta t$ to $T_p=10\Delta t$, for experiments (a) RG1 and (b) RG10. *Legend, contribution of points at height of* ● *z/d<0.5, and* ● *z/d>0.5.*

The above figures recall the figures shown in the TF distribution as a function of T_p shown in section 6.2.1 (Figure 6.4). That is, the contribution of each pulse duration is linked to its presence in the data series. To facilitate the comparison between both distributions (TF and contributions) they have been overlapped in Figure 6.41 for three different experiments (RG1, RG5, and RG10). This figure allows to see how, from pulses of duration $T_p>3\Delta t$, both distributions differ, because, although the TF is small, the intensity of the fluctuations of these pulses ($T_p>3\Delta t$) makes the contribution to the Reynolds stress greater, being not proportional to the TF.

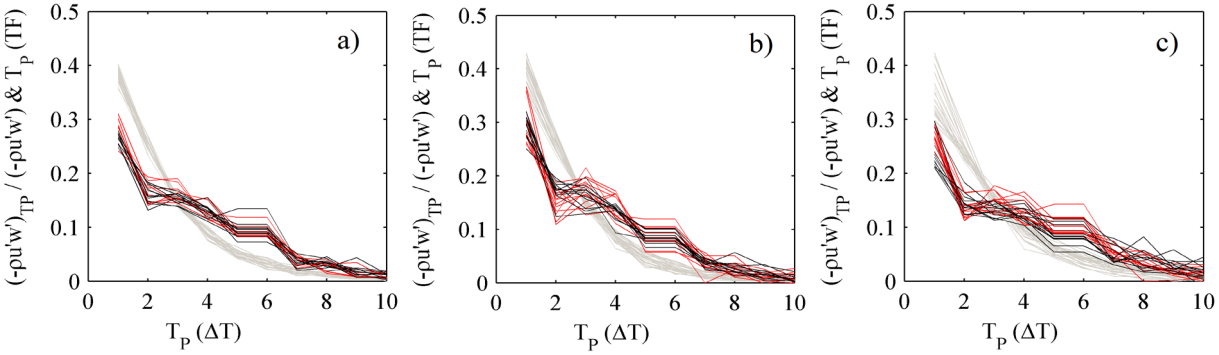

Figure 6.41- Overlapping of the PDH (TF of pulses from Tp=1Δt to Tp=10Δt, Figure 6.4) and the distribution of the contributions to Reynolds stress (from Tp=1Δt to Tp=10Δt) from Figure 6.40, for experiments (a) RG1 and (b) RG10. *Legend, contributions of points at height of* ● *z/d<0.5,* ● *z/d>0.5, and* ● *PDH.*

6.5.2 Contribution of the pulse sequences

Although, as we saw in section 6.4.1, the sequences of pulses with the highest TF were the sequences Q4-Q1-Q4, Q1-Q4-Q1, Q2-Q3-Q2 and Q3-Q2-Q3, the pulses that make up these sequences have a different sign contribution to the Reynolds shear stress. The sign of the contribution of each pulse would be as follows: Q4(+)Q1(-)Q4(+), Q1(-)Q4(+)Q1(-), Q2(+)Q3(-)Q2(+) y Q3(-)Q2(+)Q3(-). For this reason it has been preferred to account only for the contribution of sequences that obtain the same sign of $-\rho u'w'$, i.e. Q4(+)Q2(+)Q4(+), Q2(+)Q4(+)Q2(+), Q1(-)Q3(-)Q1(-) and Q3(-)Q1(-)Q3(-). It is worthwhile to mention that while the sequences involving Q2 and Q4 are the most frequent sequences after those mentioned in the first instance, the sequences involving Q1 and Q3 have the lowest TF in the data series, see section 6.2.1.

In Figure 6.42 it is shown the vertical distribution of the contributions without distinguishing between experiments, only between the two large groups of tests RG (Figure 6.42-a) and CG (Figure 6.42-b). The characterization of each sequence by color (Q1Q3Q1 (blue), Q3Q1Q3 (green), Q2Q4Q2 (red), and Q4Q2Q4 (black)) allows seeing the vertical pattern (depth profile) that they follow.

In the first place, it is worth mentioning that, as we saw in Figure 6.31 and Figure 6.32 (vertical distribution of the sequences TF), the sequence Q3Q1Q3 and Q1Q3Q1 remain very stable throughout the depth profile, not being dependent on the depth (d) of the experiment. However, the depth-averaged value of sequences Q4Q2Q4 and Q2Q4Q2 (Figure 6.32) depends very much on d, since they have a tendency to decrease their presence (TF) in the data series when approaching the water surface as increasing the depth (d).

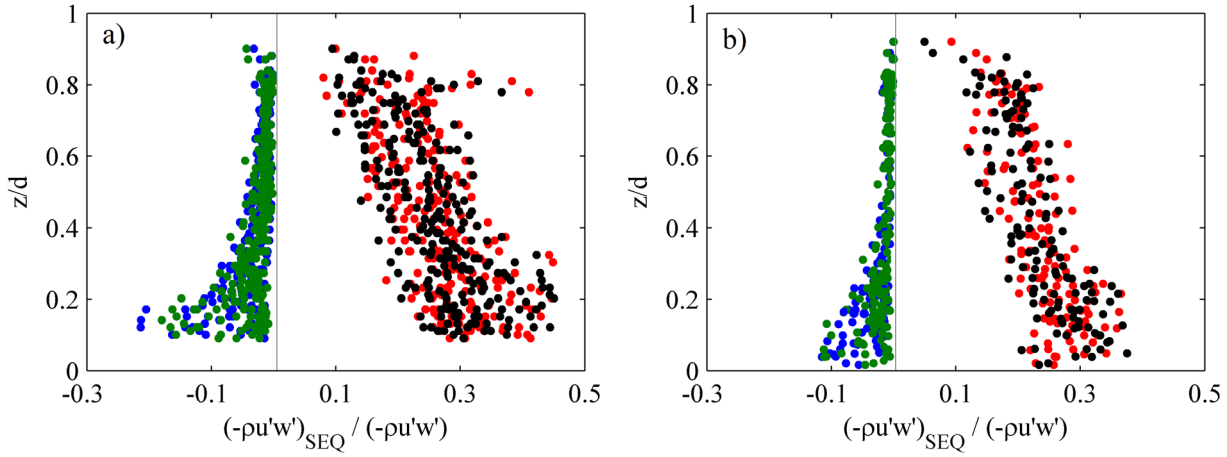

Figure 6.42- Vertical distribution of the contribution to Reynold stress of pulse-sequences Q1-Q3-Q3, Q3-Q1-Q3, Q2-Q4-Q2, and Q4-Q2-Q4, for experiments (a) RG and (b) CG. *Legend colors,* ● *sequence 131,* ● *313, ,* ● *242,* ● *424.*

From Figure 6.42 it is obtained that all the contributions diminish their value with the distance to the bed, due to the decrease of the fluctuations ($u'w'$). In the case of the sequences Q1Q3Q1 (blue) and Q3Q1Q3 (green) the contribution is clearly greater in the region near the bed (z/d<0.3). Since the TF remains constant in the profile, the decrease in $u'w'$ is very marked in the profile, obtaining contributions close to zero for all the experiments in the region near the water surface. In the case of the sequences Q2Q4Q2 and Q4Q2Q4, there is also a decrease along the profile as is logical because of the decrease of $u'w'$. However, a lower steep decrease is observed between regions z/d>0.5 and

z/d<0.5 than in the previous case. This is due to the fact that the velocities inside pulses of Q2 maintain a higher value with respect to the rest in the second half of the profile *z/d*> 0.5, although it also decreases with increasing *z*.

Figure 6.43 and Figure 6.44 (RG and CG) show the same contributions, but in this case, each figure represents each sequence with a distinction between experiments within each group. In the figures, it is observed that for cases where the level of turbulence is high, (RG5 to RG10) and (CG4 to CG6) the contributions of the sequences Q1Q3Q1 and Q3Q1Q3 are greater in the whole profile.

In the case of Q2Q4Q2 and Q4Q2Q4, for cases of greater flow rate (level of turbulence), the value of the contribution is higher in the lower half of the profile, while in the upper half (*z/d*> 0.5) the contributions are greater for cases of lower flow rate (RG1 to RG5 and CG1-CG2). The above is because, as said before, when the *d* is high, the TF of the sequences involving Q2 and Q4 are more diminished along the depth profile. Regarding the effects that the packing of the surface has on the sequences, it seems that in the area very close to the bed surface (*z/d* <0.2), on the crests of the roughness, there is a lower contribution by these sequences to the Reynolds shear stress, (Figure 6.44). This must be due to the increase of Q2-TF and Q4-TF, reaching more extreme pulses, especially in the second case, when increasing the relative roughness.

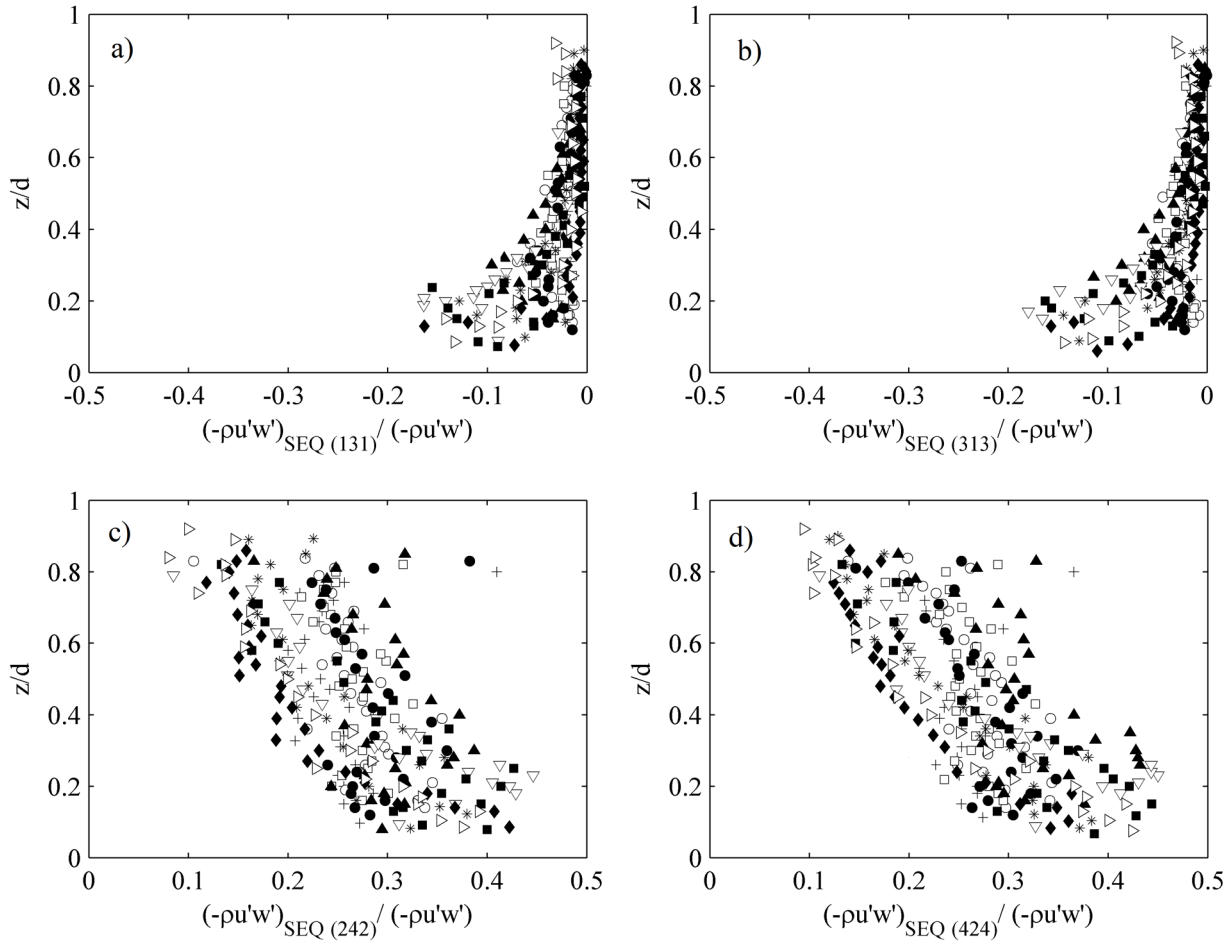

Figure 6.43- Vertical distribution of the contribution to Reynold stress of pulse-sequences (a) Q1-Q3-Q3, (b) Q3-Q1-Q3, (c) Q2-Q4-Q2, and (d) Q4-Q2-Q4, for the RG experiments. *Legend, + RG1, ○ RG2, □ RG3, ● RG4, ▲ RG5, ▽ RG6, ∗ RG7, ♦ RG8, ■ RG9 and ▷ RG10.*

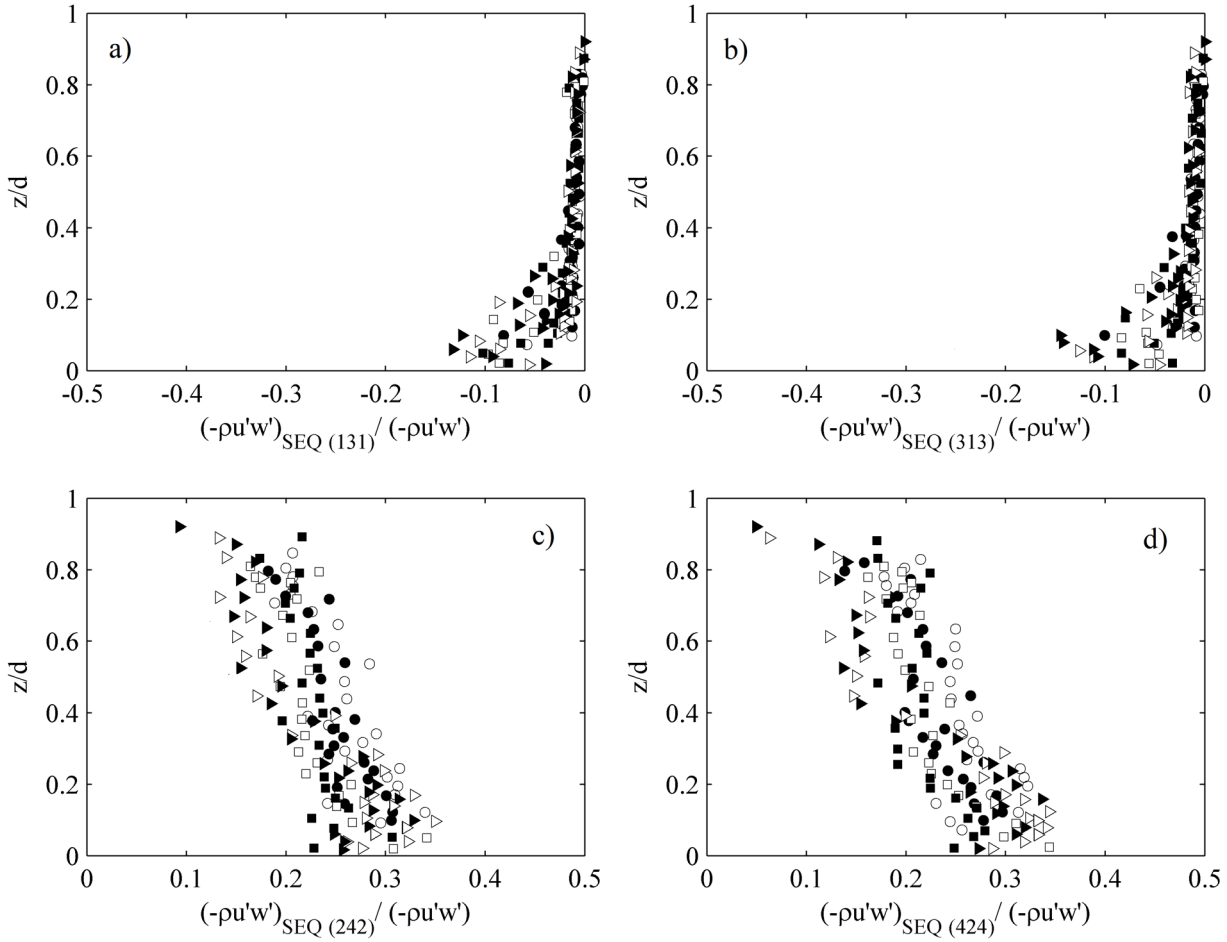

Figure 6.44- Vertical distribution of the contribution to Reynold stress of pulse-sequences (a) Q1-Q3-Q3, (b) Q3-Q1-Q3, (c) Q2-Q4-Q2, and (d) Q4-Q2-Q4, for the CG experiments. *Legend,* ○ *CG1,* ● *CG2,* □ *CG3,* ■ *CG4,* ▷ *CG5 and* ► *CG6.*

In the present chapter, all the analyzed experiments were performed with the same ADV and with the same configuration, with a frequency of data acquisition (FDC) of 25 Hz. Therefore, the pulse duration (T_p) can be accounted in time steps $1\Delta t$=1/FDC=0.04 s . In appendix C "ADV Configuration Analysis" this duration is analyzed according to the steps represented by the sign δ (pulse length). In this way, the PDH is done as a function of the length δ, so that experiments taken at different FDC can be compared with each other. This clarification is made to mention that the histograms of T_p, despite being slightly modified by the FDC or the variation of the control volume (CV), showed very similar patterns, see section C.8 of the mentioned appendix. Therefore, the statistical distribution of the pulse duration can be considered independent of sampling, maintaining a certain proportionality. This behavior is reminiscent of Kolmogorov's third hypothesis, which says that statistics in the inertial range are scale-invariant and self-similar.

Chapter 7: Threshold of motion

7.1 Introduction

Essential to the study of sediment transport is the prediction of threshold conditions and incipient motion. The critical condition, which is the limit state to initiate sediment motion, is termed threshold of motion. Incipient motion of bed material refers to the commencement of movement of bed particles that previously were at rest and is associated with changing river flow conditions. The condition of incipient motion is needed to set a lower bound on the transport of bed material

7.1.1 Deterministic view

The onset of sediment movement has been historically treated in a deterministic manner, assuming that there is a univocal relationship between a threshold condition (critical) and incipient motion. The threshold concept was first developed by Shields (1936), although the initial idea was introduced by Dubuat (1779). Shields (1936) concluded that the dimensionless Shields stress (τ^*), Eq. 7-1, as a function of the time-space averaged bed shear stress (τ_o), Eq. 7-2, and mean bed particle D_{50} is the most suitable parameter for predicting threshold conditions.

$$\tau^* = \frac{\tau_0}{g \cdot (\rho_s - \rho_w) \cdot D_{50}} \tag{7-1}$$

$$\tau_0 = \gamma \cdot R \cdot S_f \tag{7-2}$$

$$Re^* = \frac{u^* \cdot D_{50}}{\nu} \tag{7-3}$$

The Shields stress can be thought as the ratio of the destabilizing force (applied hydraulic force) and the stabilizing force (resisting force by a particle located at the bottom of a stream). Accordingly, it can be assumed that the critical shear stress is reached when the movement of a particle occurs thus $\tau_o = \tau_{cr}$. For gravels and coarser, Shields suggested a constant value of $\tau^* = 0.06$ (which was discussed by Prandtl (1952) for being "remarkably low"), and therefore independent on the particle Reynolds number (Re^*) (Eq. 7-3), as long as $Re^* > 5 \cdot 10^3$. Other authors have considered the threshold condition defined by the mean local velocity of the flow on the particles ($\overline{u_p}$), Neill et al. (1969).

The deterministic view cannot account for the turbulent fluctuations of the flow, which cause high instantaneous variations in both the local flow velocity and instantaneous Reynolds shear stress. Besides, they do not consider the non-homogeneity of the hydraulic characteristics along the depth profile, but only average values. Several researchers, Grass (1983), Naden (1987), Buffington & Montgomery (1997), Parker (2008) etc., have observed from laboratory and field studies that, for hydraulically rough beds, a variability of more than an order of magnitude of the Shields criterion.

Moreover, various roughness geometries may produce the same effect on the mean velocity profile, but turbulent characteristics (e.g., Reynold stress, the microstructure of turbulence) may differ significantly (Krogstad et al. 1992). The time-averaged characteristics of flow may be inadequate to describe the effects of roughness on flow characteristics. Therefore, incipient motion criteria based solely on time-averaged flow properties may unpredict sediment transport.

7.1.2 Stochastic view

In contrast to the deterministic view, stochastic methods are based on the concept that the particle motion is governed by the intermittent nature of near-bed turbulence. Thus, considering turbulent variables (stresses or velocities) as responsible for the initial dislodgement of sediment.

Einstein & El-Sammi (1949), who measured pressure fluctuations with a pitot tube on a rough wall and related them to the drag force, modeled the effect of turbulence on sediment transport for the first time in detail. Prandtl (1952) promoted the important role of turbulent fluctuation in particle dislodgement. He concluded that the peak velocity values, and the resulting applied forces near threshold conditions, are the responsible for the initiation of movement. Others have detected that increases in the turbulence level of the bed shear stress, although with the same average value, resulting in significantly higher bed transport rates (e.g. Sumer et al. 2003, Schmeeckle & Nelson 2003).

7.1.2.1 The role of near-bed coherent structures

With the emphasis on the study of individual grains, the interaction grain-fluctuation induced by coherent flow structures, with both spatial and temporal coherence (Adrian 2007), is considered responsible for grain entrainment at near incipient conditions. Turbulent bursting constitutes a near-bed coherent flow structure in open-channel flows (Nezu & Nakagawa 1993).

Since the definition of bursting turbulence presented by Kline (1967), a big interest about structures in the turbulent boundary layer and its applicability in the entrainment phenomenon has been developed. The concept of "bursting turbulence" is closely related to the generation of turbulent energy, Reynolds shear stress in the region near-bed and entrainment process (Grass 1983, Williams et al. 1989). As explained in chapter 5, burst events are divided into four quadrants, outward interactions (Q1, u'>0 and w'>0), ejections (Q2, u'<0 and w'>0), inward interactions (Q3 u'<0 and w'<0) and sweeps (Q4 u'>0 and w'<0).

Conventionally, sweeps (u'>0, w'<0) and ejections (u'<0, w'>0) have been considered as responsible for sediment transport, to contribute positively to the bed shear stress (τ_0), since their contribution to Reynolds shear stress ($-\rho\overline{w'u'}$)) is positive, Sumer & Deigaard (1981), Bridge & Bennet (1992), Chiew & Cheng (1998), Kleinhans & Van Rijn (2002) etc. The main reason for the attention paid to the term (u'w') is because is the only term that cannot be eliminated after the time average of the Navier Stokes equations. Some researchers identified sweeps as the cause of the initiation of bed motion and ejections are mostly responsible for sediment entrainment (e.g, Grass 1983, Niño & Garcia 1996, Dey et al. 2011 and Celik et al. 2014).

On the other hand, other investigators observed in their experiments that Reynolds shear stress may not be the most relevant factor for sediment transport, finding instead that instantaneous streamwise velocity (u) correlated well with sediment transport (Paintal 1971, Nakagawa & Nezu 1981, Grass 1983, Naden 1987). Other authors found that normal Reynolds stresses ($\rho\overline{u'^2}$) ($\rho\overline{w'^2}$) might be more significant for sediment transport than the shear stress component ($-\rho\overline{wu}$) (Clifford et al. 1991, Sterk et al. 1998, Papanicolau et al. 2001). Sumer et al. (2003) have justified a considerable increase in sediment transport under conditions of unstable flow, attributing the transport of particles to the streamwise turbulent intensity TI_X near the bed.

The consideration of (u) as an engine agent derives from the concept of drag force and particle stability. From this assumption, it follows that "sweeps" and "outward interactions" contribute positively to this force since u'> 0 (Celik et al. 2010, Melville et al 2012). Nelson et al. (1995) demonstrated that the increase of outward interactions ($u'>0$, $w'>0$) respect the other events yields an increase of the sediment flux, although the magnitude of Reynolds shear stress decay. Besides, he pointed out that the transport is not necessarily well predicted by the (u), although they are well correlated, due to the duration of sweep and outward interaction events influence the transport process.

On the other hand, in highly turbulent flows, it is reasonable to consider that the fluctuations in drag and lift forces result from the grain pressure distribution (e.g. Hofland et al. 2005, Detert et al. 2010, Celik et al. 2013). However, the measurement of detailed turbulent pressures is a difficult task due to the lack of resolution in small-scale measurement devices. The studies concluded the existence of Q4 events (sweeps) near the time of entrainment and high drag forces. Dwivedi et al. (2010) suggest that a positive lifting force followed by a "sweep" event that gives the final push initiates the movement of the particles, generating drag force on the particle. Dwivedi et al. (2011) observed that large sweep (Q4) events predominate in grain entrainment. They speculated that these sweeps were caused by retrograde vortices. Cameron (2006) in his experimental research has made similar observations and relates u'>o followed by vortices near the bed before the initiation of particle movement.

Celik et al. (2014) studied the surface pressures and resultant forces on a grain whose size is comparable to the turbulent flow scales in a hydraulic channel to see the flow-grain interaction, observing that events with a positive streamwise velocity fluctuation ($u'>0$) where directly related to the forces and distribution of pressure on the particles. Moreover, they indicated the importance of the duration of the event, the impulse exerted on the particle, as it is explained in the next section.

7.1.2.2 Impulse concept

The latest findings have provided enough evidence that not average forces, but the instantaneous forces move the particles. In addition, these studies corroborate that beyond the magnitude of the applied force, their duration is important in order to determine the entrainment of a particle (e.g. Diplas et al. 2008, Celik et al. 2010, Celik et al. 2013, Valyryakis et al 2013, Celik et al. 2014), i.e. the impulse applied by the force. They provided evidence that impulse imparted by near-bed turbulent events have to be larger than a critical impulse value to entrain a grain from rest. Understanding the statistical characteristics of impulse imparted by near-bed turbulent events over several grain-size beds is essential for describing the effect of the bed on the sediment entrainment process.

The concept is based on the first Newton's Law. When a particle is at rest, its Momentum (p) is zero. However, when it starts to move there is an increment of momentum (Δp), applied by an exerted force ($\vec{F} = dp/dt$). The impulse (I) exerted by the force to the particles is defined as the variation of the momentum ($\overrightarrow{\Delta p}$) as a function of time. Integrating the force function $\vec{F}(t)$, which describes the time history of hydrodynamic force acting upon a bed Surface, between times t_1 and t_2, the applied momentum or impulse is found by the Eq. 7-4.

$$I = \overrightarrow{\Delta p} = \int_{t1}^{t2} \vec{F}\,(t)dt = F \cdot \Delta t \qquad (7\text{-}4)$$

7.2 Conceptual model

Regardless of the role that bursting events play in the sediment transport, the scale of these events remains unclear, in particular for highly turbulent flows. Further evidence about how the structure of turbulence is organized in steep rough beds, depending on the relative submergence and presence of large roughness geometry, is approached in this study. The attention is placed on the description of the near-bed turbulence characteristics and quadrant/pulse analysis.

In the present section, a methodology using simple arguments from mechanics to insight the bursting cycle and incipient motion is developed. Here, following the line to date by the deterministic vision, it is considered the Reynolds shear stress ($-\rho u'w'$) responsible for the incipient motion of the particles. However, to link with stochastic vision, and consider the impulse applied by the hydrodynamic forces, the impulse exerted by these shear stresses on the particle has been considered. The impulse exerted by the Reynolds shear stress is equivalent to the term 'transported momentum' of Franca et al. (2014).

The criterion accounts for both the duration and the magnitude of flow events, introducing a dynamical perspective for the incipient entrainment of particles. It is based on considering that there is a certain critical impulse (I_{cr}), related to the energy scheme of the particles that when overcome by the impulse exerted by the flow (I_i) sets the particles in motion. Below, the simple methodology for its evaluation is exposed.

7.2.1 Critical Particle Impulse

The critical impulse (I_{cr}) is necessary to know the minimum impulse that sets in motion the particle. In Figure 7.1 a particle of mass (m), Eq. 7-5, is located on the bed surface among other particles. The particle is at rest until a net force (accounting for gravity) applied over a time interval ΔT imparts momentum (p) to the particle. The variation of the momentum of the particle Δp corresponds to the impulse applied as it was described in Eq. 7-4, ($I = \overrightarrow{\Delta p}$).

The work exerted by the force, Eq. 7-6, corresponds to the energy expense (ΔE) to rise a particle a distance of ΔZ (minimum displacement required for particle dislodgement), where the particle is swept by the shear velocity. This shear velocity corresponds to the obtained from the critical shear stress (τ_{cr}), named as critical shear velocity u_{cr}, Eq. 7-7 and Eq. 7-8 respectively. The energy required (ΔE) to set the particle in motion can be obtained by the sum of the kinetic energy (ΔE_k) applied by u_{cr} and the potential energy (ΔE_p) increase from ΔZ, Eq. 7-9. Using all the latter equations, an expression of the critical impulse (I_{cr}) and the critical displacement ΔZ is shown in Eq. 7-10.

Each particle size has a critical impulse associated. Throughout this chapter, three size diameters have been considered (D_{50}, $D_{max,}$ and D_{min}), for the calculations of both, critical impulse (I_{cr}) and impulse exerted by the flow to the particles (I_i).

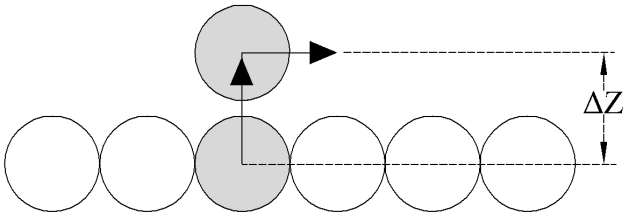

Figure 7.1- Scheme of a mobile particle.

$$m = (\rho_s - \rho_w) \cdot \frac{4}{3} \cdot \pi \cdot \left(\frac{D}{2}\right)^3 \quad (7\text{-}5)$$

$$W = \int F \cdot u \, dt = I \cdot u_{cr} = \Delta E \quad (7\text{-}6)$$

$$\tau_{cr} = \tau^* \cdot (\rho_s - \rho_w) \cdot D \cdot g \quad (7\text{-}7)$$

$$u_{cr} = \sqrt{\tau_{cr}/\rho_w} \quad (7\text{-}8)$$

$$\Delta E = \Delta E_k + \Delta E_p = \frac{m \cdot {u_{cr}}^2}{2} + m \cdot g \cdot \Delta z \quad (7\text{-}9)$$

$$I_{cr} = m\left(\frac{u_{cr}}{2} + \frac{g \cdot \Delta Z}{u_{cr}}\right) \quad (7\text{-}10)$$

With the methodology described in this section, we can obtain τ_{cr}, u_{cr}, and I_{cr} for each particle size (D_{50}, D_{max}, *and* D_{min}). As mentioned, the threshold of motion can only be evaluated in the CG tests, since it was possible to obtain results of particle displacements associated with each tested flow. Table 7.1 shows the critical values (τ_{cr}, u_{cr}, and I_{cr}) associated with each experiment.

Table 7.1- Critical values for the CG experiments

Nº TEST	Flow R.	Particle diameter			Critical stress (τ_{cr})			Critical velocity u_{cr}			Critical Impulse (I_{cr})		
		D_{50}	Dmax	Dmin	D_{50}	Dmax	Dmin	D_{50}	Dmax	Dmin	D_{50}	Dmax	Dmin
	l/s	mm	mm	mm	N/m2	N/m2	N/m2	m/s	m/s	m/s	N·s	N·s	N·s
CG1	61,6	17,82	27,32	6,51	16,77	25,70	6,12	0,13	0,16	0,08	0,0067	0,0299	0,0002
CG2	65,24	17,82	27,32	6,51	16,77	25,70	6,12	0,13	0,16	0,08	0,0067	0,0299	0,0002
CG3	137,4	30,02	44,61	12,96	28,24	41,97	12,19	0,17	0,20	0,11	0,0415	0,1663	0,0022
CG4	157,84	30,02	44,61	12,96	28,24	41,97	12,19	0,17	0,20	0,11	0,0415	0,1663	0,0022
CG5	231,41	51,08	62,04	20,16	48,06	58,37	18,97	0,22	0,24	0,14	0,2672	0,5276	0,0103
CG6	260,38	51,08	62,04	20,16	48,06	58,37	18,97	0,22	0,24	0,14	0,2672	0,5276	0,0103

7.2.2 Impulse exerted by the flow

As explained, the impulse is the product of a force and the time during which it is applied. Therefore, duration and the magnitude of flow events are involved in impulse criterion.

Considering the Reynolds shear stress ($-\rho \cdot u' \cdot w'$), force per unit area, as responsible of sediment transport, sweeps (Q4, u'>0 and w'<0) and ejections (Q2, u'<0 and w'>0) contribute positively to fluctuating Reynold stress, and consequently the impulse applied it is positive. Whereas outward interaction (Q1, u'>0 and w'>0) and inward interactions (Q3, u'<0 and w'<0) contribute negatively and hence exert a negative impulse. In this sense, it is possible to consider that whilst a bursting event remains inside a quadrant (pulse) the direction of the applied stress (τ_{xz}) is the same, thus with the same impulse sign. That is to say, every pulse exerts an impulse.

This approach allows obtaining the signal impulse (per unit area), Figure 7.2-a, by means of Eq. 7-11, where p is the momentum (or amount of motion), $\langle F/A \rangle$ is the force-time average per unit area over

duration ΔT, the term $\overline{-\rho u'w'}_i$ is the average Reynolds shear stress of each pulse, and T_p is the time duration pulse. In Figure 7.2-b it is represented the distribution of the average impulse (N·s/m^2) by pulse duration.

$$I_i/m^2 = \overrightarrow{\Delta p}/m^2 = \int \overrightarrow{F/A}\, dt = -\overline{\rho u'w'}_i \cdot T_p \qquad (7\text{-}11)$$

Figure 7.3-a show the distribution of the impulse per unit area of three experiments (RG1, RG5 and RG10) where the red markers represent points located at a distance *z/d*<0.5. Figure 7.3-b represent all RG experiments, with the same marker, but distinguishing between points at height *z/d*<0.5 (red) and points at *z/d*>0.5 (black). From them, it can be easily seen that points located closer to the bed exert a higher impulse (per unit area) than points higher in the depth profile. As seen in the previous chapter, although the pulses near the bed tend to be shorter, the Reynold stress have an extreme behavior, obtaining thus higher impulses.

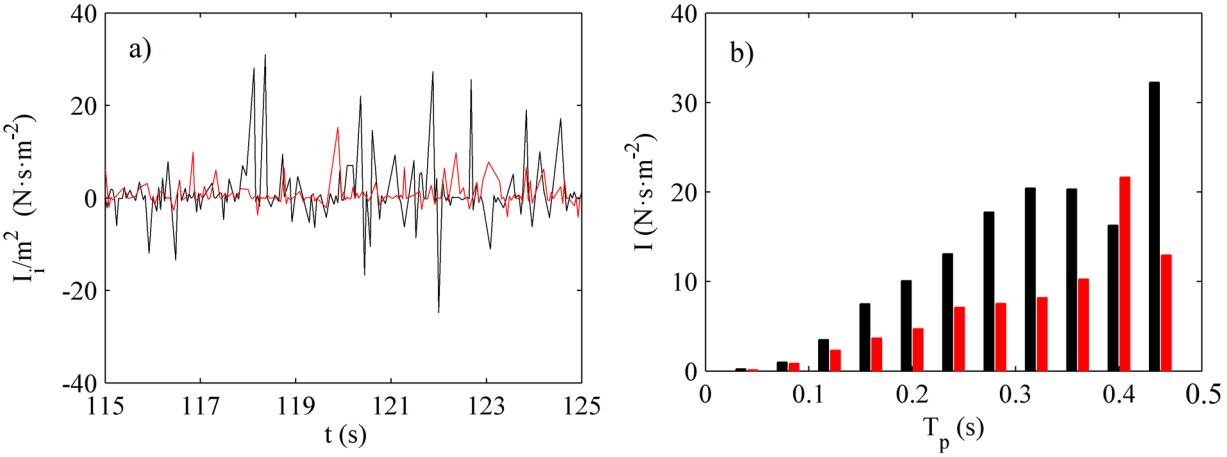

Figure 7.2- Figure (a) represents the signal of impulse per unit area, from two experiments, CG1 and CG6, and Figure (b) represents the impulse per unit area associated to each pulse duration, z/d=0.075. Legend, ● *CG1, and* ● *CG6.*

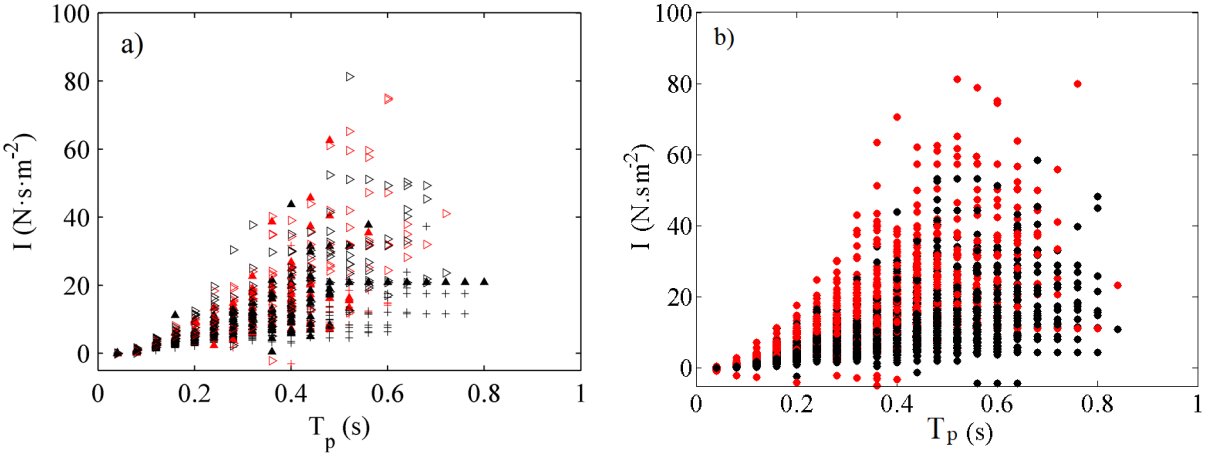

Figure 7.3- Impulse per unit area exerted by the flow as a function of the pulse duration, Figure a, experiments RG1, RG5, and RG10. Figure b, all RG experiments. *Legend Markers (a), + RG1,* ▲ *RG5and* ▷ *RG10. Legend colors,* ● *points at z/d<0.5, and* ●, *points at z/d<0.5* .

As explained before, sweeps (Q4) and ejections (Q2) contribute positively to fluctuating Reynold stress thus to the impulse applied by it. This can be seen in Figure 7.4-a, and Figure 7.4-b, where the impulse exerted by each pulse has been discretized by quadrant of appearance for two experiments. The figures show that sweeps and ejections reach positive values and longer pulses durations.

Therefore, if pulses from Q2 and Q4 reach the same direction of shear stress, thus a positive impulse, it might be convenient to consider that concatenate pulses from these two quadrants still apply the force in the same direction and thus the same impulse. Accordingly, we can consider that sequences Q2-Q4, Q4-Q2, Q2-Q4-Q2, and Q4-Q2-Q4 apply the same positive impulse and, in the same way, sequences Q1-Q3, Q3-Q1, Q1-Q3-Q1, and Q3-Q1-Q3 apply the same negative impulse. The assumption of considering both, pulses and the mentioned sequences, it is henceforth called impulse by "packets".

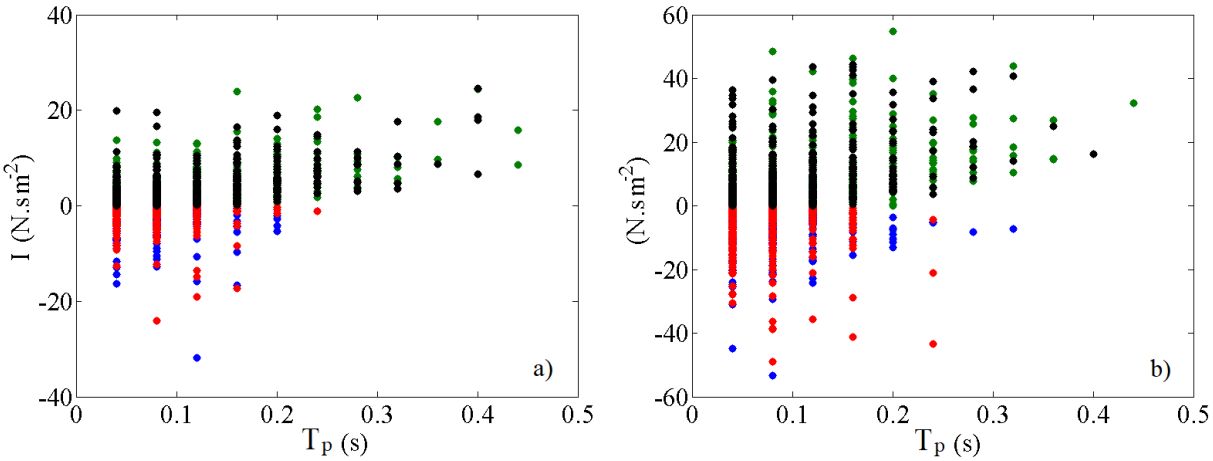

Figure 7.4- Impulse per unit area exerted by the flow as a function of the pulse duration and appearance quadrant. Figure a, experiments CG1 and Figure b, experiment CG6. *Legend,* ● *Q1,* ● *Q2,* ● *Q3, and* ● *Q4.*

Figure 7.5 shows the impulse signals of the same point (*z/d*=0.075, CG1) by considering the two hypothesis, impulse applied by pulses (red) and impulse applied by pulses and sequences "packets" (black), where is noticeable how considering packets reach higher impulse values.

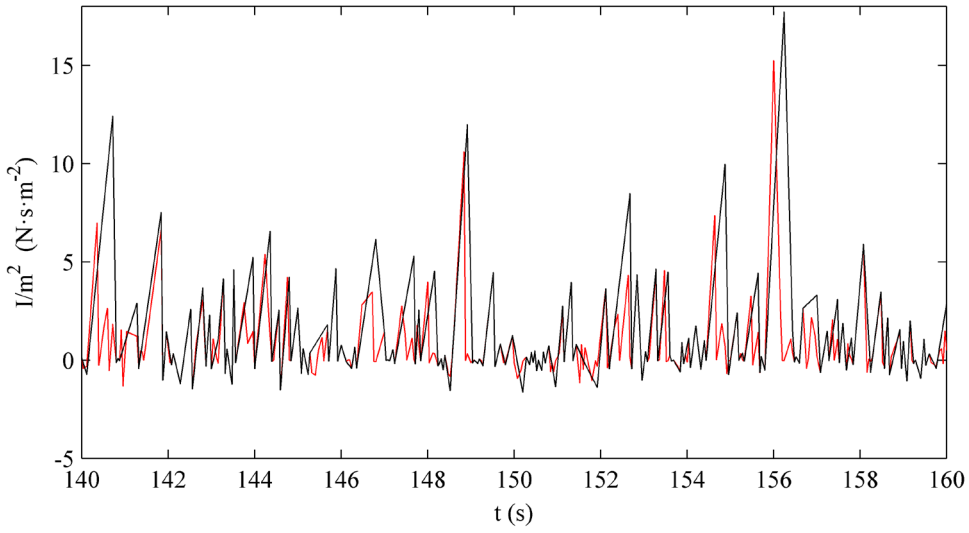

Figure 7.5- Impulse (N·s/m^2) signals by considering impulse exerted by pulses and packets. Experiment CG1, z=0.012-m. *Legend,* ● *pulses, and* ● *packets.*

In order to considerate the impulse exerted to a single particle, the area of the particle exposed to the flow is considered so that the impulse exerted to different size particles can be calculated, Eq. 7-12. In this section, three size diameters have been considered (D_{50}, D_{max}, and D_{min}), and three different impulse signals (one per diameter) are obtained for each point in the profile. Figure 7.6 shows three different histograms of the impulse (N·s) exerted by the flow to the three diameters considered.

$$I_i = \left(\tau_{xz_i} \cdot \Delta t\right) \cdot A_p \tag{7-12}$$

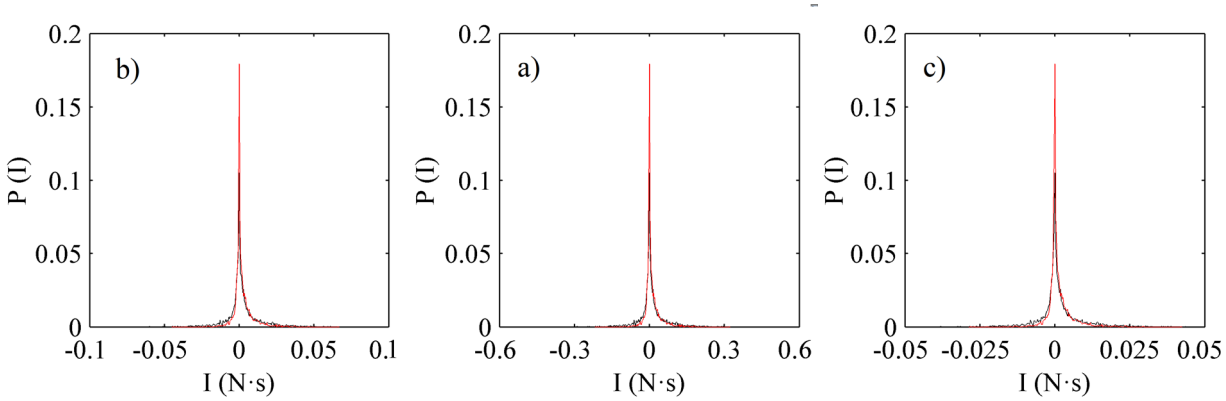

Figure 7.6- Histogram of impulse exerted by the flow to a particle of size (a) D_{max}, (b) D_{50} and (c) D_{min}. *Legend,* ● *RG1, and* ● *RG10.*

7.2.3 Balance of Impulses

Once the critical impulse (I_{cr}) and the impulse signal $\{I_i\}$ have been obtained for each particle size, they can be compared. In the figures below the two impulse signals $\{I_i\}$, first by considering the impulse exerted by pulses (a) and second by packets (b), obtained for the CG1 test (z/d=0.075) are represented for the three particle size (D_{50}, D_{max}, and D_{min}), Figure 7.7, Figure 7.8, and Figure 7.9 respectively. Besides, the critical impulse (dashed red line) associated with each particle size is included.

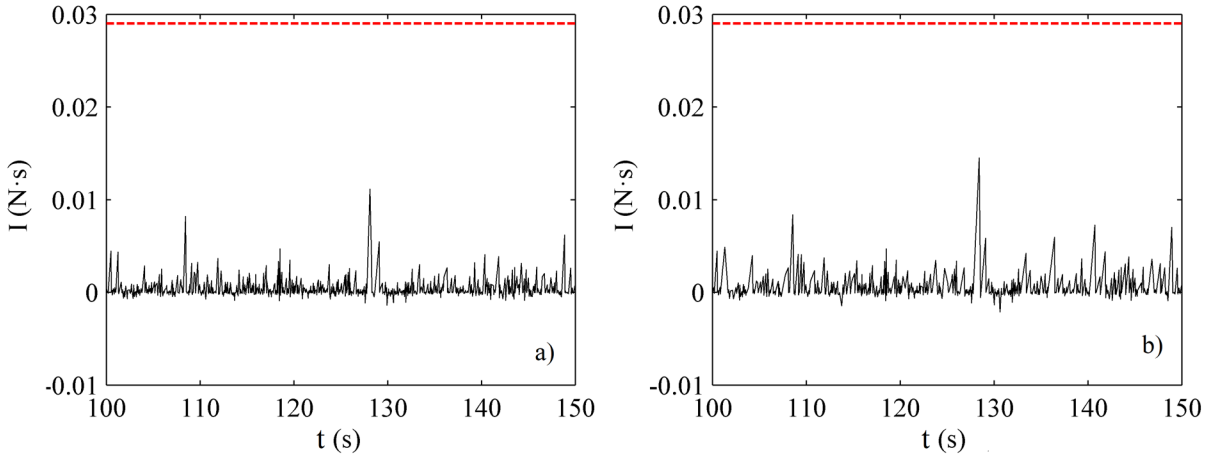

Figure 7.7- Signal of impulse exerted by the (a) the pulses and (b) pulses and sequences (packets), considering a particle size of D_{max} (CG-D1). Test CG1 z=0.012-m. *Legend,* ● *Critical impulse, and* ● *Impulse signal.*

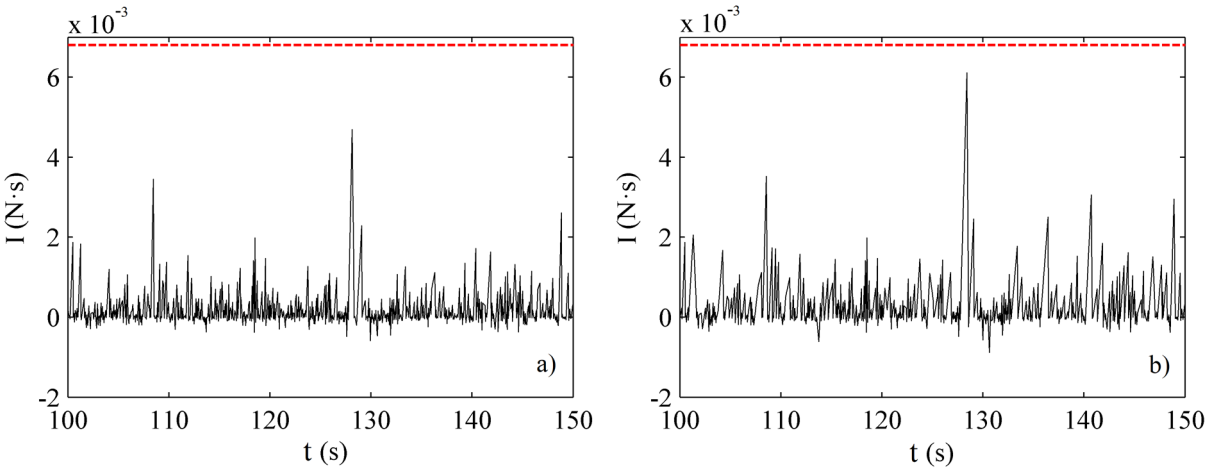

Figure 7.8- Signal of impulse exerted by the (a) the pulses and (b) pulses and sequences (packets), considering a particle size of D_{50} (CG-D1). Test CG1 z=0.012-m. *Legend,* ● *Critical impulse, and* ● *Impulse signal.*

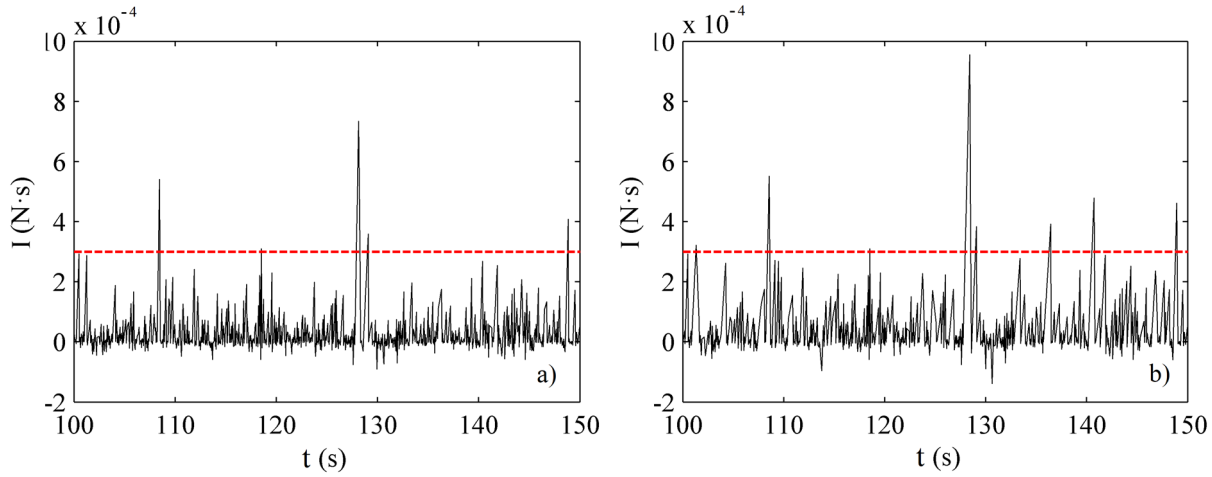

Figure 7.9- Signal of impulse exerted by the (a) the pulses and (b) pulses and sequences (packets), considering a particle size of D_{min} (CG-D1). Test CG1 z=0.012-m. *Legend,* ● *Critical impulse, and* ● *Impulse signal.*

It is observed that in the case of D_{max} and D_{50}, the critical impulse necessary to set a particle of such size in motion is unattainable by the both of the impulse signals (Figure 7.7 and Figure 7.8). However, the critical impulse of a particle of size D_{min} has a higher probability of being exceeded for both signals. The impulse signal $\{I_i\}$ by pulses (Figure 7.9-a) exceeds the value on five occasions while the impulse signal $\{I_i\}$ by packets (Figure 7.9-b) exceeds this critical value eight times.

7.2.4 Limitations of the conceptual model

The detected movements of the particles, those that have been displaced from their position, cannot be related to a specific event, since the video was not synchronized with the data collection of the ADV, and even if it had been, it would not have been possible to measure around each particle set in motion since the study area is too big ($0.8 \cdot 0.8 = 0.64$-m^2).

As the recorded videos have not enough resolution, we have not been able to detect at which velocity the particles set in motion. Therefore, the assumption that they are moved by a velocity equal to u_{cr} is a big simplification, made in order to obtain numerical results; consequently, the evaluation is purely qualitative.

In many occasions, the particles vibrate without moving from its place. However, only those movements that involve a displacement detected visually have been considered, in order to check the conceptual model. Therefore, these destabilizations do not fall within the account of movements, although being very close to the threshold of motion.

There are numerous uncertainties that cannot be considered quantitatively, such as the uniformity of the sediment, shape, and density, which can affect the hydrodynamic effects on a particle in two different ways, smaller particles remain hidden in the wake of larger particles, consequently, the smaller particles move later than they should and the larger ones earlier than they should. The shape and density also modify the thresholds.

Other uncertainties are associated with the packing density of the bed. Under the conceptual model presented here, two experiments with the same particle size (CG1 and CG2, CG3 and CG4, CG5 and CG6) would obtain the same critical impulse, because the sediment is the same. However, it has been found that a compacted/shaped bed (well-packed) supports better the actions of the flow, obtaining less amount of particle displacements.

Finally, the conceptual model is extremely simple and does not consider additional forces of holding between particles.

7.3 Evaluation of the velocity data series

7.3.1 Methodology

In this section, the potential sediment transport of the CG experiments is analyzed by following the described conceptual model. The critical impulse (I_{cr}) of each test was represented in Table 7.1, and the impulse exerted by the flow $\{I_i\}$ to each particle size (D_{50}, $D_{max,}$ and D_{min}) have been calculated by means of the methodology described at section 7.2.2, considering the impulse exerted by pulses on the one hand, and considering both pulses and sequences packets on the other.

Whether the first (impulse by pulses) is considered, the number of pulses that exceed I_{cr} ($I_i > I_{cr}$) are obtained as well as the fraction of these extreme impulses that belong to Q2 (ejection pulse) and to Q4 (sweep pulse), and the fraction that belongs to the pulse durations (T_p) of ($1\Delta T$, $2\Delta T$, $3\Delta T$, and $\geq 4\Delta T$).

When the impulse exerted is obtained from packets (pulses and sequences), in addition to the number of packets that exceed I_{cr} ($I_i > I_{cr}$), it is obtained the fraction of them that corresponds to the packets Q2-Q4, Q4-Q2, Q2-Q4-Q2, and Q4-Q2-Q4. The probability that an impulse exerted exceeds this critical value, $P(I_i > I_{cr})$, or impulse rate (*Imp. R.*), Eq. 7-13, has been obtained in all cases.

$$P(I_i > I_{cr}) = Imp.R. = \frac{\sum I(I_i > I_{cr})}{\sum_{i=1}^{n} I_i} \tag{7-13}$$

In almost all the analyzed experiments, the balance of impulses that affect D_{max} did not obtain any result, $P(I_i > I_{cr}/D_{max})=0$, the impulses capable of mobilizing the D_{50} were very reduced, while the balance of impulses for D_{min} obtained a good distribution. The tables of results obtained for each one of the tests, considering the two mentioned methods (impulse exerted by pulses and exerted by packets) are shown in Appendix D (section D.1) At the end of this section, there is a summary of results and their discussion.

7.3.2 Summary of results

Table 7.2 shows a summary of the results averaged at a variable height interval (z^*), according to the particle size. The table shows the distribution of pulses that comply ($I_i > I_{cr}$) for both cases, considering that the impulse is exerted by pulses and by packets, for the particle size D_{min}, since it is the most affected particle size by impulses.

In the first case, impulse exerted by pulses, the fraction of pulses the Q2 and Q4 that comply ($I > Icr$), as well as the fraction of pulses that belong to a pulse with $T_p > 4\Delta T$ are shown in Table 7.2. In the second case, impulse by packets, the fraction of pulses belonging to a pulse chain (sequence) of two pulses (*2P*), (Q2-Q4 and Q4-Q2), and a sequence of three pulses (*3P*), (Q2-Q4-Q2 and Q4- Q2-Q4). In general, impulses have a higher probability of belonging to Q4 than to Q2, especially in cases where the bed is not leveled (CG1, CG3, and CG5). In addition, a high percentage of pulses (45-75%), with the potential to mobilize particles (D_{min}), belong to long pulses ($T_p \geq 4\Delta T$), which makes sense given the definition of momentum.

Table 7.2- Average probability to exceed the critical impulse

Nº	z*	Impulse by pulse			Impulse by packets	
TEST	m	P(I>Icr/Q2)	P(I>Icr/Q4)	P(I>Icr/$T_p \geq 4\Delta T$)	P(I>Icr/*2P*)	P(I>Icr/*3P*)
CG-1	(0,06-0,012)	0,456	0,544	0,621	0,275	0,123
CG-2	(0,085-0,0125)	0,445	0,555	0,610	0,253	0,107
CG-3	(0,06-0,02)	0,487	0,513	0,482	0,263	0,097
CG-4	(0,03-0,021)	0,554	0,441	0,465	0,260	0,089
CG-5	(0,03-0,031)	0,371	0,629	0,744	0,268	0,123
CG-6	(0,08-0,03)	0,476	0,524	0,690	0,229	0,087

Table 7.3 shows the results of the *Imp. R*, averaged for an interval height (z^*), for the experiments. As can be seen in this table, as well as in the results tables of each experiment, there are no pulses able to displace a particle of size (D_{max}), only at some point of the near-bed region when the impulses are calculated exerted by packets. In the case of the D_{50}, there are some impulses of sufficient intensity to set them in motion; however, just in some points of the profile, thus the average over z^* is not representative. Conversely, when analyzing the minimum particle size (D_{min}), a good distribution is obtained along the depth profile.

Figure 7.10 shows the vertical distribution of the *Imp. R* (associated to D_{min}), all along the dimensionless profile (z/d), obtained by the pulse method (Figure 7.10-a) and by the packets method (Figure 7.10 -b), for all CG experiments. It is observed that the *Imp. R.* is higher in the region near the bed, while it tends to be zero from $z/d > 0.4$. Moreover, the *Imp. R.* is significantly greater, more than double when the sequences are considered responsible for the impulses exerted.

On the other hand, the experiments in which the bed has been shaped (CG2, CG4, and CG6) show a lower *Imp. R.* in the region near the bed compared to the experiments in which the bed has not been leveled (CG1, CG3, and CG5), showing that impulses (at least those that occur inside quadrants Q2 and Q4) have an extreme value as the roughness increases, due to a rise of vertical turbulence intensity (chapter 4, section 4.5).

Table 7.3- Average Impulse rate

			Impulse by pulse			Impulse by packets		
Nº TEST	**Z* m**		**Dmax Imp R.**	**D50 Imp R.**	**Dmin Imp R.**	**Dmax Imp R.**	**D50 Imp R.**	**Dmin Imp R.**
CG1	(0,03-0,018)	1800	-	0,021%	0,889%	0,031%	0,042%	1,978%
CG2	(0,035-0,0175)	1800	-	0,022%	0,596%	-	0,057%	1,535%
CG3	(0,03-0,03)	697	-	0,058%	0,650%	0,040%	0,104%	1,435%
CG4	(0,02-0,03)	697	-	0,022%	0,488%	-	0,059%	1,263%
CG5	(0,02-0,05)	295	-	-	0,049%	-	-	0,197%
CG6	(0,02-0,05)	295	-	-	0,038%	-	-	0,147%

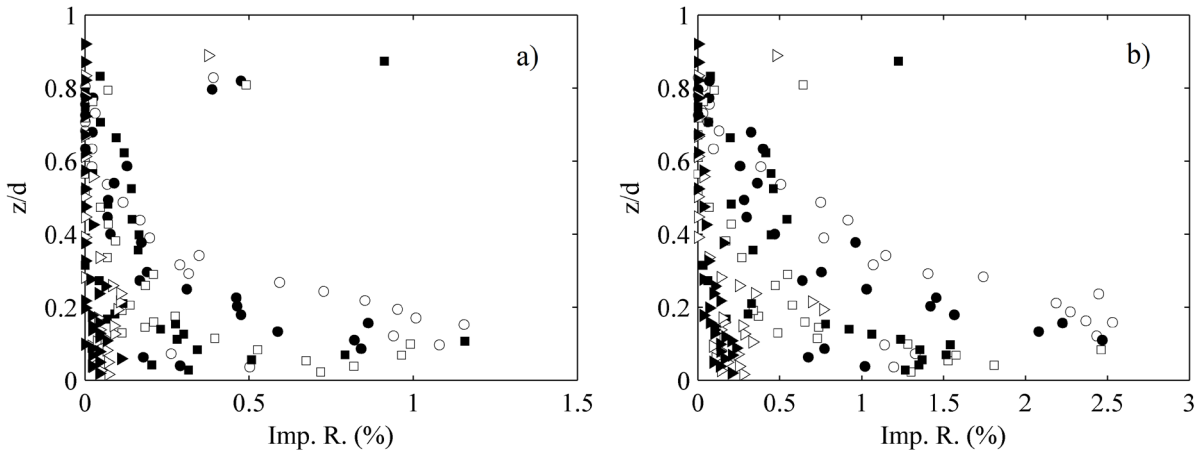

Figure 7.10- Vertical distribution of the *Imp. R.* from the RG experiments considering impulse exerted by (a) pulses or (b) packets (sequences and pulses) to particles of D_{min} size. *Legend,* ○ *CG1,* ● *CG2,* □ *CG3,* ■ *CG4,* ▷ *CG5 and* ► *CG6.*

7.3.3 Motion Rate

So far, it has been evaluated the probability that a certain size-grain has to be set in motion, however, the sediment of our experiments has an extended granulometry, as we saw in the sieve analysis included in the second chapter (section 3.2.2). In order to assess the ability of the flow to mobilize the sediment, the granulometry has been divided into 10 classes (n_x=10), thus obtaining a simpler distribution of sizes.

Using a simple rule of three and knowing the number of particles exposed in each experiment, it is possible to obtain the number of particles of each class that are exposed in the experiments, thus subject to motion. Figure 7.11-a shows the sediment distribution of the three bed-sediments used in the experiments (CG-D1, CG-D2, and CG-D3), but now divided into 10 classes, and Figure 7.11-b shows the probability of the sediment of having a certain size D_X, thus $P(D_X)$. In this way, it is possible to obtain the *Imp. R.* associated with each particle size, as shown in Figure 7.12. In the figure, it is noticed how points close to the bed (red points) have a higher impulse rate. Moreover, for large sediment sizes (CG-D2 and CG-D3) it is perceptible a greater *Imp. R.* for near-bed points in not leveled beds, CG3 (Figure 7.12-b) and CG5 (Figure 7.12-c), in contrast to the leveled ones (CG4 and CG6).

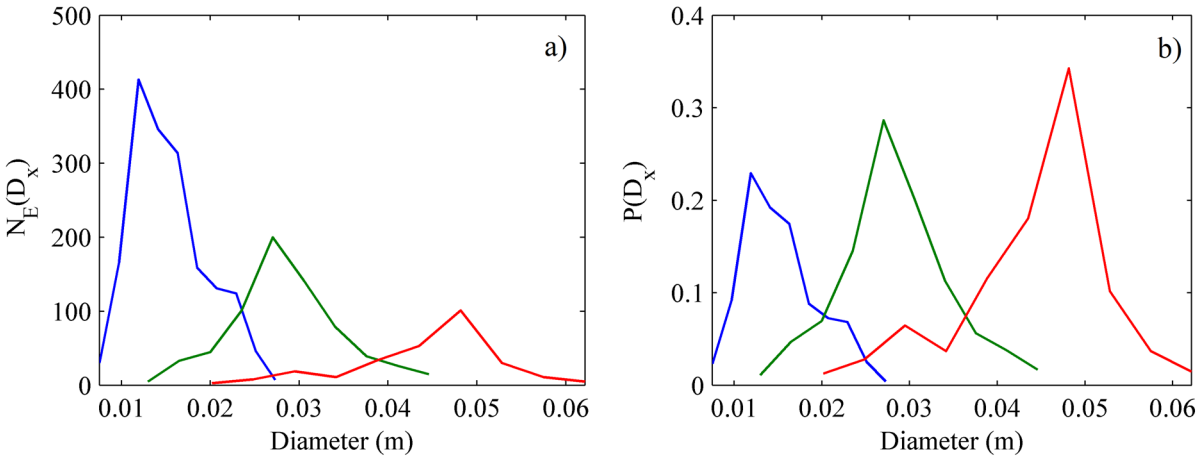

Figure 7.11- Three sediment gradations (CG-D1, CG-D2, and CG-D1) class division. (a) Number of exposed particles of each gradation and (b) probability of each class. *Legend, , — CG-D1, — CG-D2, and — CG-D1.*

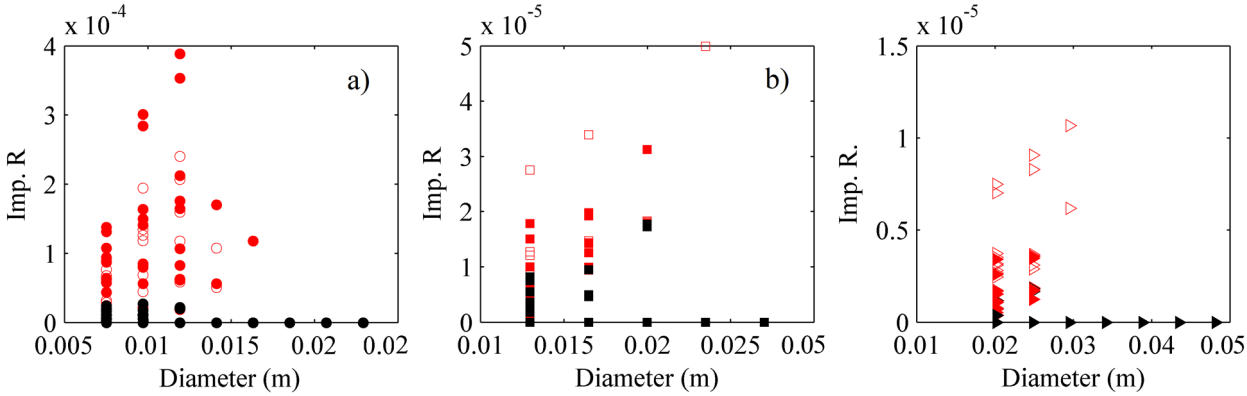

Figure 7.12- Impulse Rate at each point of the profile, as a function of the D_x of each granulometry, for the experiments (a) CG1 and CG2 (CG-D1), (b) CG3 and CG4 (CG-D2), (c) CG5 and CG6 (CG-D3). *Legend Markers (a), ○ CG1 and ● CG2. Legend Markers (b), □ CG3 and ■ CG4. Legend Markers (c), ▷ CG5 and ▶ CG6. Legend colors, ● points with elevation z/d<0.5, and ● points with elevation z/d>0.5.b*

In order to standardize the results obtained by the evaluation of impulses, the Motion Rate (*Motion R.*) is defined by Eq. 7-19. In this manner, the results can be compared with the data obtained from the visualization of particle mobilization, which can be found in the following section. The *Motion R.* is analyzed only for the case of impulse exerted by sequences for sake of simplicity. This rate tries to represent the fraction of particles mobilized per minute, by considering that the sum of ($I_i > I_{cr}$) are the times that a particle of size (D_x) is set in motion. Although as mentioned, this may be too ostentatious due to the limitations of the model (section 7.2.4).

It is further considered that the distribution of pulses throughout the test area is equivalent to that of the measurement control volume (CV). Therefore, each particle receives a pulse distribution statistically comparable to that of the CV. The number of particles of a certain size D_X that are exposed to the flow $N_E\ (D_X)$ is obtained by multiplying the total number of exposed particles (N_T) by the probability of a certain particle size $P(D_X)$, Eq. 7-14. If there are impulses that comply $I_i > I_{cr}\ (D_X)$, thus able to mobilize particles of size D_X, then the particles set in motion of this size ($N_D(D_X)$) is equal to the total of exposed particles $N_E(D_X)$, since it is not possible to mobilize more than those that are available, Eq. 7-15. Contrarily, if any impulse has sufficient intensity for the mobilization of D_X, the number of displaced particles $N_D(D_X)$ is equal to zero, Eq. 7-16.

The total number of displaced particles, including all sizes, corresponds to the sum of displaced particles of each size $N_D(D_X)$, Eq. 7-17, where n_x is the number of classes in which the granulometry has been divided. The fraction of particles set in motion during the measurement is defined by the *Motion I.* (Eq. 7-18) which represents the ability of the flow to mobilize a given granulometry. Obviously, the greater the number of classes in which the sediment granulometry is divided, the more precise this index will be.

However, the duration of the measurement plays an important role, so the Motion Rate (*Motion R.*) is defined, which is the *Motion I.* per unit of time, Eq. 7-19. In this way, all the experiments can be compared with each other, as well as with the evaluation of sediment transport results obtained from the visualization of the laboratory tests.

Figure 7.13 shows the result obtained for all tests, in each point of the profile, where it is observed that the *Motion R.* is superior in the zone near the bed z/d <0.3. As mentioned, the *Motion R.* represent the potential of the flow to mobilize the particles. This index will be compared with that obtained through the laboratory test visualization, which is analyzed in the next section.

$$N_E(D_x) = N_T \cdot P(D_x) \tag{7-14}$$

$$\sum_{i=1}^{n}(I_i > I_{cr})_{D_x} \neq 0 \qquad N_D(D_x) = N_E(D_x) \tag{7-15}$$

$$\sum_{i=1}^{n}(I_i < I_{cr})_{D_x} = 0 \qquad N_D(D_x) = 0 \tag{7-16}$$

$$N_D = \sum_{x=1}^{nx} N_D(D_x) \tag{7-17}$$

$$Motion\ I. = \frac{N_D}{N_T} = \frac{\sum_{x=1}^{nx} N_D(D_x)}{N_T} \tag{7-18}$$

$$Motion\ R. = \frac{Motion\ I.}{T_f} \tag{7-19}$$

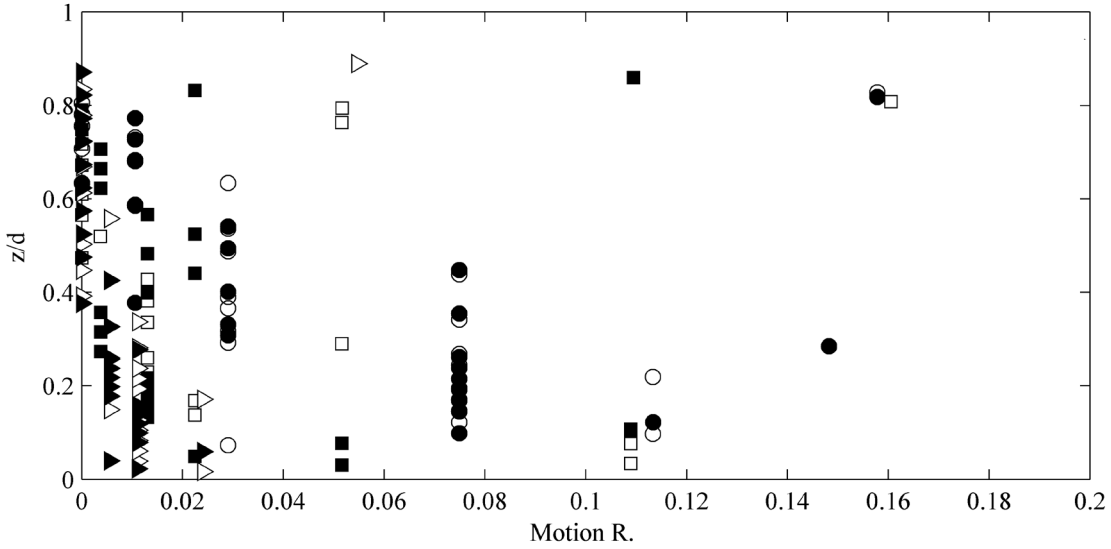

Figure 7.13- Vertical distribution of the Motion R. of the CG tests. *Legend Markers, ○ CG1, ● CG2, □ CG3, ■ CG4, ▷ CG5 and ► CG6.*

7.4 Evaluation of the experimental particle motions

7.4.1 Methodology

As discussed in chapter two (section 2.5.2, Experimental methodology) the tests were carried out by means of a progressive increase in the flow rate until reaching the incipient motion. For each flow rate step, it has been noted the hydraulic characteristics and the number of dislodged particles (N_D).

The results tables from some of the flow rates tested in each experiment are presented below, where the main hydraulic characteristics (d, R, S_f, and τ_o) obtained from gauge measurements are recalled. In addition, it is included the critical shear stress (τ_{cr}) associated with each mean diameter (D_{50}) by means of the Eq. 7-7, considering a dimensionless critical stress (τ^*) of 0.06 since all the experiments turned out to be in hydraulically rough regime Re^*> 1000. The rate τ_o / τ_{cr} belonging to each flow rate is presented in the tables.

In the Appendix D (section D.2) are presented the results from the experimental visualization, the number of dislodged particles (N_D), the application time of each flow rate (T_f), and the fraction of displaced particles (*Motion I.*); which can be also thought as the probability of motion of a single particle (Eq. 7-20), where N_T is the number of total particles exposed. Finally, the tables show the *Motion R.*, which represents the *Motion I.* per unit of time (min), in order to standardize all flow results regardless of the tested time, Eq. 7-21.

$$Motion\ I. = \frac{N_D}{N_T} \tag{7-20}$$

$$Motion\ R. = \frac{Motion\ I.}{T_f} = \frac{N_D}{N_T} \cdot \frac{1}{T_f} \tag{7-21}$$

7.4.2 Summary of results

Results from the visualization of the incipient motion experiments are gathered in this section. The main hydraulic characteristics of the final flow rate for each test are shown below in Table 7.4. This table shows the results of the last situation of the CG, that is when the threshold of motion is reached. In addition to the hydraulic characteristics the values of τ_0 (Eq. 7-2), τ_{cr} (Eq. 7-7) considering a value of τ^*=0.06 (rough flows), Re^* (Eq. 7-3) and the real value of τ^* (Eq. 7-1) are indicated in Table 7.4. These values allow graphing the experiments in the Shields graph (Figure 7.14).

Table 7.5 shows the summary of sediment movements during the ADV measurements along the depth profile once the threshold of motion was achieved in each experiment. From the visual evaluation of the experiments, it is obtained that the leveling of the bed surface obtains a significantly lower Motion R. than in the case of loose bed, thus reaching a higher percentage of the Shields critical stress at the incipient motion conditions. Although in all the experiments the τ_0 is very close to the τ_{cr}, the experiments of smaller diameter show mobilization of the particles at a bed shear stress (τ_0) slightly higher than the critical (τ_{cr}) (115-118%), while those of greater diameter do so at a τ_0 slightly lower than the critical τ_{cr} (87-95%).

Finally, Figure 7.15 depicts the evolution of the *Motion R.* as the flow rate is increased in each experiment. In this figure, it can be seen how in the cases of the smallest particles (CG1 and CG2), the

Motion R. has a similar evolution in both cases, although the experiment with leveled bed (CG2) being slightly lower. However, for cases of larger particles, where the fact of shaping the particles gives them a better hold between them, the *Motion R.* is clearly diminished.

Table 7.4- CG test description summary

TEST	Flow R. (l/s)	D_{50} (mm)	S_f m/m (m/m)	d (m)	R (m)	U (m/s)	u^* (m/s)	τ_o (N/m²)	τ_{cr} (N/m²)	Re^*	real τ^*
CG1	61,60	17,82	0,027	0,082	0,073	1,082	0,139	19,32	16,77	2477	0,0691
CG2	65,24	17,82	0,028	0,086	0,076	1,085	0,136	18,62	16,77	2432	0,0666
CG3	157,84	30,02	0,027	0,131	0,108	1,605	0,173	29,99	28,24	5199	0,0637
CG4	137,4	30,02	0,028	0,13	0,108	1,41	0,181	32,81	28,24	5438	0,0697
CG5	231,41	51,08	0,03	0,181	0,141	1,582	0,204	41,45	48,06	10400	0,0518
CG6	260,38	51,08	0,029	0,202	0,154	1,549	0,209	43,77	48,06	10686	0,0546

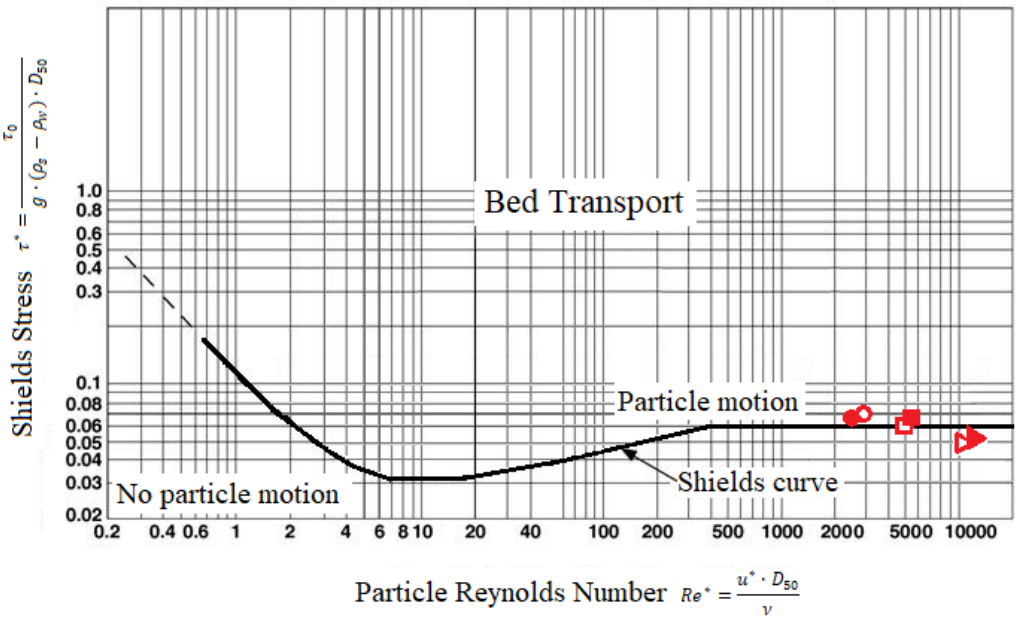

Figure 7.14- Representation of the CG experiments on the Shields graph. *Legend,* ○ *CG1,* ● *CG2,* □ *CG3,* ■ *CG4,* ▷ *CG5 and* ► *CG6.*

Table 7.5- Summary of results

TEST	Flow R. (l/s)	Bed Leveling	N_T (num.)	N_D (num.)	T_f (min)	*Motion I.* (%)	*Motion R.* (%/min)	τ_0/τ_{cr} (%)
CG1	61,6	D	1800	338	198	18,8%	0,0948%	115,2%
CG2	65,24	P	1800	314	210	17,4%	0,0831%	111,1%
CG3	137,4	D	697	103	246	14,8%	0,0601%	106,2%
CG4	157,84	P	697	92	245	13,2%	0,0539%	116,2%
CG5	231,41	D	295	22	282	7,4%	0,0264%	86,3%
CG6	260,38	P	295	15	294	5,1%	0,0173%	91,1%

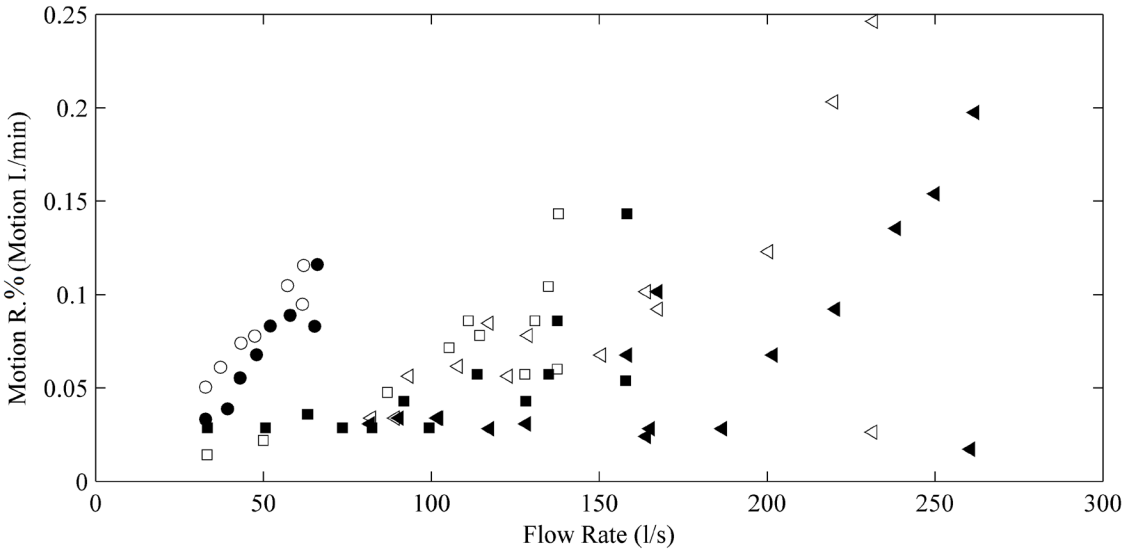

Figure 7.15- Motion R. as a function of the flow rate *Legend,* ○ *CG1,* ● *CG2,* □ *CG3,* ■ *CG4,* ▷ *CG5 and* ▶ *CG6.*

7.5 Critical shear stress

Finally, this section shows the quantitative evaluation that has the flow of overpassing the critical shear stress obtained from the deterministic methodology of Shields, Eq. 7-7.

We have seen in the analysis of visualization tests, section 7.4, that in general, for the theoretical calculation values (τ_0 and τ_{cr}) the initiation of movement of the particles occurs when $\tau_0 \sim \tau_{cr}$. However, from experimental results of chapter 4, it was seen that the calculated shear stress (τ_{xz}) was significantly lower than the theoretical one (τ_0), possibly due to the lack of accuracy of the Frequency data collection (small FDC) that softens the peaks of the instantaneous velocities.

The percentage of Reynolds shear stress events ($-\rho u'w'$) that exceed the theoretical value of τ_{cr} (Shields) has been evaluated, despite the fact that the average value thereof is lower, i.e. $\overline{\tau_{xz}} < \tau_{cr}$. The results obtained are shown below.

Figure 7.16-a shows the percentage of ($-\rho u'w'$) events that exceed τ_{cr} for the CG experiments. It can be seen that this percentage is greater in the near-bed region, reaching values close to 30% in all the analyzed cases. According to the consideration that provided that $\tau_o > \tau_{cr}$ a particle mobilization is produced, this occurs in 30% of the events ($u'w'$). Since a single measure lasts 5 minutes, there are 7500 (5·60·25-Hz) registered turbulent events, thus, around 2250 (30%) events are able to mobilize the particles, which would suppose a complete sweep of the bed sediment. This is why it is necessary to define a more precise way the limit value to be exceeded by turbulence.

Figure 7.16-b, Figure 7.16-c, and Figure 7.16-d depict only the percentage of events; with a pulse duration (T_p) equal to $1\Delta T$, $2\Delta T$ and $3\Delta T$ (remember that $1\Delta T = 1/FDC$), that manage to overcome τ_{cr}. In the area near the bed (z/d <0.3), around 25% of events of $T_p = 1\Delta T$ exceed the value of τ_{cr}, 11% of the events that belong to a $T_p = 2\Delta T$, and 15% in the case of events that belong to a $T_p = 3\Delta T$. Therefore, it seems that shorter events overpass more times the τ_{cr} than longer pulse-durations. Regarding the

leveling of the surface, there are significant differences for events of T_p=2ΔT and T_p=3ΔT when leveling the bed surface, decreasing the probability of overcoming the τ_{cr} in the near-bed region.

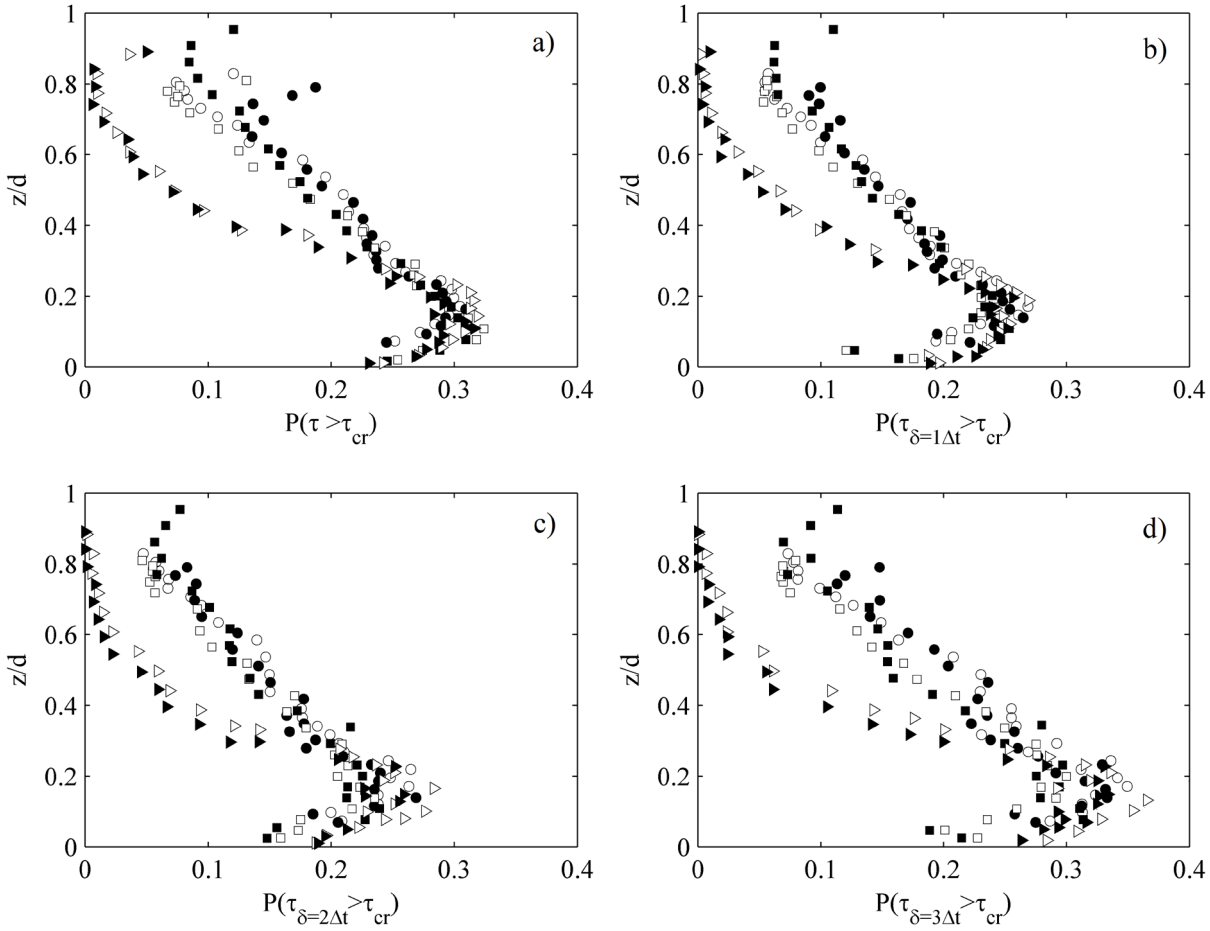

Figure 7.16- Probability that τ_{xz} overpasses the τ_{cr} ($P(\tau_{xz} > \tau_{cr})$) for (a) all events, (b) pulses of T_P=1ΔT, (c) pulses of T_P=2ΔT, and (d) pulses of T_P=3ΔT. *Legend,* ○ *CG1,* ● *CG2,* □ *CG3,* ■ *CG4,* ▷ *CG5 and* ▶ *CG6.*

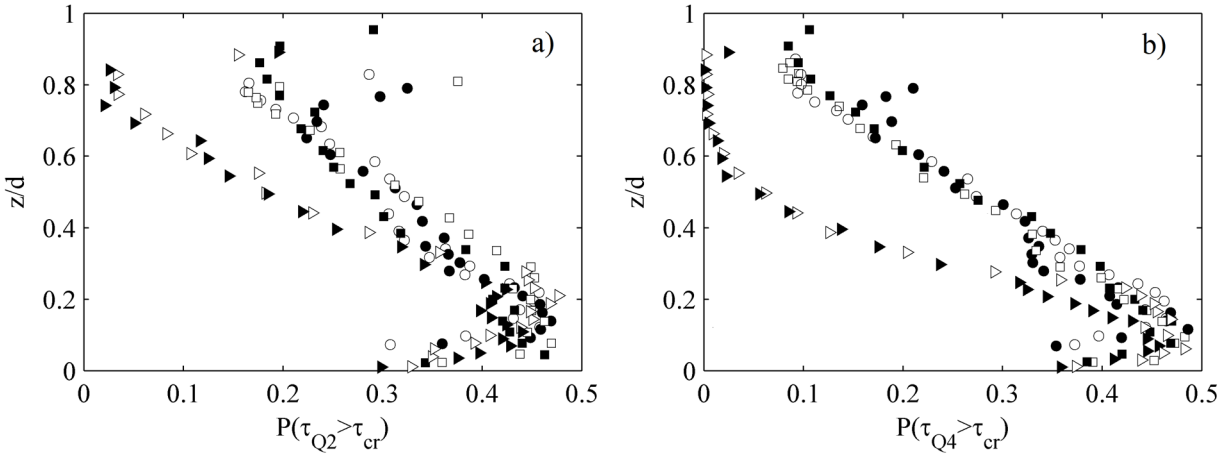

Figure 7.17- Probability that τ_{xz} from (a) Q2, and (b) Q4, overpasses the τ_{cr} $P(\tau_Q > \tau_{cr})$. *Legend,* ○ *CG1,* ● *CG2,* □ *CG3,* ■ *CG4,* ▷ *CG5 and* ▶ *CG6.*

The number of events from Q2 and Q4 that exceed τ_{cr} is also analyzed. Figure 7.17 depicts the fraction of Q2 and Q4 events that reach to overpass τ_{cr}. Both quadrants show a similar behavior with 45% of

events greater than τ_{cr} in the near-bed region, with a little increase of the Q4 events exceeding the τ_{cr} when the bed has not been leveled.

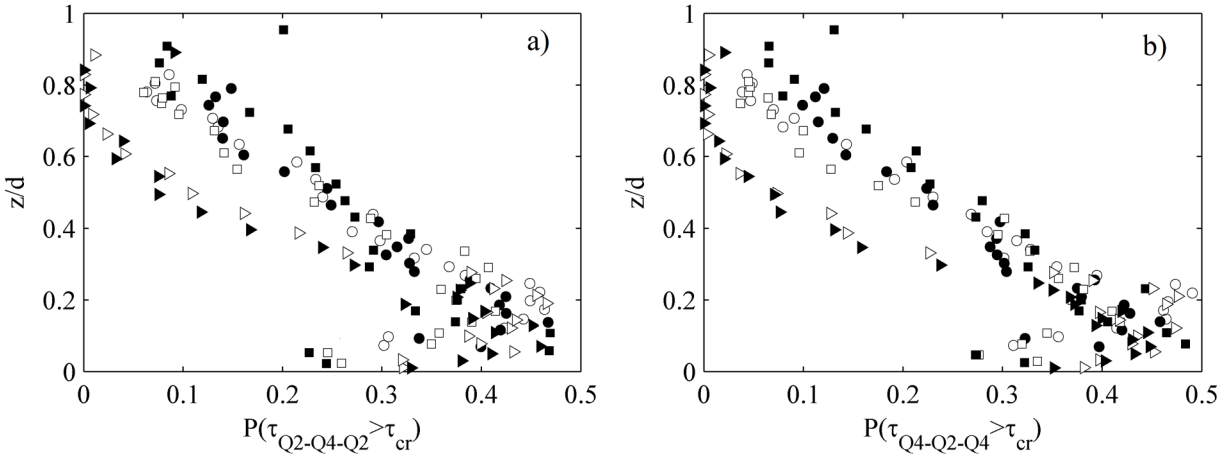

Figure 7.18- Probability that τ_{xz} from the sequences (a) Q2-Q4-Q2, and (b) Q4-Q2-Q4, overpasses the τ_{cr} $P(\tau_{SEQ} > \tau_{cr})$. *Legend,* ○ *CG1,* ● *CG2,* □ *CG3,* ■ *CG4,* ▷ *CG5 and* ▶ *CG6.*

Finally, those events that belong to the main sequences that contribute positively to the increase of the Reynolds shear stress have been calculated. The results show that around 25-35% of the events within the sequence Q2-Q4-Q2, in the near-bed region, exceed the value of τ_{cr}, and a similar percentage is obtained for events belonging to the sequence Q4-Q2-Q4 with a percentage of 25-40% of events that exceed the critical value.

7.6 Discussion of results

In this section, the results obtained from the visualization and counting of particles during the execution of the tests, and the mobilization potential obtained from the impulse analysis are unified. Table 7.6 shows the Motion R. obtained in each of the cases. It is emphasized that, in the case of the impulse analysis, this value corresponds to the average obtained in the area of action of the flow in each case.

From the results of both analyses, it is concluded that the comparison between them is very subjective since there are differences of up to an order of magnitude between the results from visualization and results from impulse analysis, although similar trends are observed.

Experiments CG1 and CG2, show a similar *Motion R*. in both analyses, due to the similar k_s they have because of the low D_{50}. Nonetheless, in the other cases, a significant decrease of mobilization is observed for the cases in which the bed has been shaped (CG4 and CG6) with respect to the cases in which the sediment is simply poured (CG3 and CG5). The reason that the *Motion R.* obtained from the impulses is significantly higher than that obtained by laboratory visualization (counting) is due to the limitations of the conceptual model.

It has to be pointed out that when no consideration of the application time of the shear stress is considered, but only the value of τ_{cr} (section 7.5) the results suggest that a complete sweep of the bed sediment would occur, which obviously did not happen.

Table 7.6- Unification and standardization of results.

TEST	Flow R. (l/s)	Visualization results	Impulse analysis	
		Motion R.	***Z****	***Motion R.***
CG1	61,6	0,09%	(0,06-0,012)	8.13%
CG2	65,24	0,08%	(0,085-0,0125)	7.89%
CG3	137,4	0,06%	(0,06-0,02)	5,14%
CG4	157,84	0,05%	(0,03-0,021)	2,95%
CG5	231,41	0,03%	(0,03-0,031)	1,14%
CG6	260,38	0,02%	(0,08-0,03)	0,94%

During the experiments, it was observed certain instability of some particles in the bed surface, despite remaining in place, that makes them vibrate in their pocket. Some of them are finally set in motion, while others manage to stabilize or continue to vibrate without moving. This may be due to the fact that the impulse exerted is close to the critical impulse, or even goes beyond it, but there are clamping forces between particles that have not been considered in the conceptual model. The conceptual model is too simple to be able to quantitatively equate the results obtained from both analyses, however, in a qualitative way a similar trend is obtained.

The results obtained from the analysis of the ADV configuration may compromise some of the hypotheses made in this chapter. Although the statistics of quadrant and pulse analysis have demonstrated to be very robust, regardless of the frequency of data acquisition (FDC), the FDC defines the Δt of the T_P. Therefore, despite a low FDC could reduce the shear stress around a 30-40%, the duration of the pulses in time (not in length steps) would increase by definition $\Delta t=1/FDC$, and so different results would be obtained. However, as discussed before, Valyryakis et al. (2013) determined that the total displacement of the particles was produced by those flow structures that were at least twice the grain size. Therefore, measuring with a high FDC, thus oversampling the flow velocity, might compromise the analysis by introducing non-essential high-frequency velocity fluctuations.

This suggests that the signals should be measured at the FDC corresponding to each particle size, or be measured at a high FDC and later filtered by a low-pass filter, depending on the particle size to be studied, which would allow evaluating with the same velocity signal the impulse applied to the different particles. However, this would modify the signal obtained, and the number of total pulses from one signal to another would vary.

In the present study, the measurements were performed at 25-Hz. Measuring at 25-Hz (FDC), it was found that the integral length L_X in the region that affects the sediment was about twice the sediment size D_{50} in each case, see chapter 4, section 4.11.1. Specifically, CG1 and CG2 with D_{50}=0.0177-m have an L_X of 0.033-m and 0.038-m respectively, averaged in z=[0-0.018]-m. Experiments CG3 and CG4 (D_{50}=0.03-m) a L_X of 0.059-m and 0.054-m, averaged in z=[0-0.03]-m. Finally, experiments CG5 and CG6, with a bed-sediment of D_{50}=0.05-m, have a mean L_X of 0.096-m and 0.085-m respectively, averaged in z=[0-0.05]-m. Therefore, the analyzed signal can be considered suitable for the analysis of sediment entrainment of the bed diameters, although as mentioned, the impulse analysis that complies ($I > Icr$) is still far from being quantitatively assessed.

Chapter 8: Conclusions

8.1 ADV Measurements

Measurements in highly turbulent flows usually yield some uncertainties, such as a significant amount of spikes, low signal-noise ratios, and low correlation values. Under the suspicion that low-COR values may not be considered wrong, arose the necessity of further understanding about the ability of the ADV to solve highly turbulent flows in an accurate way, suggesting a broader examination of the nature of the spikes and the low COR values.

8.1.1 Data quality and filtering

No effects of steadiness have been detected in the series and, therefore, no affections of low frequencies outside the system are found. The Doppler noise contribution to the total measured energy remains under 10%, as predicted by Garcia et al. (2005) in highly turbulent flows.

The data series showed a stable value of SNR along the depth profile, far above the minimum suggested by Wahl (2000) (SNR>15), with a robust value of σ_{SNR} (<4.5), validating the particular placement of the ADV (upside down), opposite to the conventional way, so that there were no contaminating bubbles in the CV.

It has been observed that the COR parameter has an evolution of growth along the depth profile, maintaining a fairly constant value near the bed region (z/d <0.3), being closely related to the level of turbulence. Therefore, the more turbulent the series, the less correlation can be expected. In all cases, the mean COR values do not achieve the minimum value suggested by Wahl (2000) (COR>70). Moreover, by increasing the limit of COR_{CR} until 40, more than 50% of data were removed within the near-bed region, resulting in high filtering effects such as the decrease of the main turbulent properties (Reynold shear stresses, TIs, TKE, ε, etc.), due to the high energy being erased and biased toward the mean value. On the other hand, the quadrant analysis was also affected by filtering (COR_{CR}=40), increasing the time fraction in the data series of quadrants Q2 and Q4 at the expense of the Q1 and Q3, and lessening the peak values of all quadrant events. The effects on the distribution of pulse durations are overwhelming, with a marked decrease of short pulses T_P=1Δt (from 40% to 18%) and an increase of pulses T_P>1Δt, due to the replacement of data. From the three methods of replacement analyzed, the linear interpolation has shown to affect more all turbulent properties, especially the pulses distribution. It is recommended the use of a third-order polynomial using two points at each side of the value since it better respects the nature of turbulent flows.

The examination of the nature of the spikes and the low-COR values ("bad" data) showed that low-COR data has a normal behavior in comparison with "good" data. In fact, low-COR velocities follow better the trend of the "good data" than the velocities obtained after filtering and replacement by any of the methods assessed here. On the other hand, the spikes have shown a particular behavior in comparison with "good data", but do not always show the aspect of aliasing data defined by Goring & Nikora (2002).

Moreover, the spikes are not related to the low-COR values since the former has a well-sorted distribution of COR values. Therefore, discarding low-COR velocities removes a significant amount of useful data and distorts results related to the history of the velocity signal, breaking the natural trend of highly turbulent events while retaining a portion of spikes. Besides, it does not eliminate the necessity of applying the Despiking filter.

The arbitrary operation of filtering methods shows that the filter should not be applied without prior study of suitability. It is recommendable a previous visual inspection of the data series to detect points where aliasing is occurring and apply the Despiking filter. It has to be mentioned that the application of Despiking does not solve the "interpolating" effect observed in some of the points near the water surface, due to the distortion caused by the ADV. This highlights the necessity for a filtering method that takes into account not only the velocity increments ($\Delta u, \Delta w$) but also their time-wise distribution.

8.1.2 ADV configuration

In order to validate the ADV configuration used to the data acquisition, a further study was conducted to evaluate the effects of the device configuration on the results. This evaluation is based on other experiments (FRITZ experiments) since the ADV used in this work did not allow varying the configuration. In the FRITZ experiments, the channel configuration did not allow a higher specific flow (FRITZ channel, Lehigh University), so the level of turbulence was lower. Additionally, the effects on the CUBE experiments (from "the cube" channel) were evaluated by means of the performance curves using averaging methods, although only configurations of lower precision than the real ones can be reproduced by these methods. The main parameters studied here were the CV height (h) and the FDC. If the FDC is increased, it means that the definition is higher, that is, an FDC =100-Hz takes 100 velocities per second, while an FDC=25-Hz takes only 25. Therefore, the second FDC is able to break down into four velocities a result of the first working as a "magnifying glass". The CV height (h) is the portion of the flow that is measured.

While the data quality is not strongly affected by the configuration of the ADV, the attenuation of the peak velocity due to the decrease of the FDC or the increase of the CV height (h) reduces the intensity of the turbulent properties, such as Reynold shear stresses, TKE or dissipation rate etc., while the length scales are augmented. The performance curves of the CUBE experiments show that these variations are more pronounced the higher is the level of turbulence of each scenario.

The PSD is also affected by the ADV configuration, with the closest slope to the Kolmogorov (-5/3) with an FDC of 25-Hz and a CV height of h=7-mm, for the FRITZ experiments. The spectrum indicates the energy level associated with each size vortex, therefore it seems that providing that a large range of coherent structures are represented in the signal, the PSD achieves the theoretical slope. Nonetheless, this cannot be assumed for cases with a different level of turbulence.

The configuration of the device has the ability to favor the representation of small or large flow structures in the measured data series. Therefore, the configuration of the device should be studied in the first instance for each scenario and level of turbulence, and determine whether the accuracy of big or small flow structures has to be prioritized. For example, in sediment transport of big stones, it could be useful to detect how big vortices grow through the depth. Valyryakis et al. (2013) stated that full grain entrainment is due to flow structures as large as at least twice the grain size, and so oversampling

the velocity might compromise the analysis by introducing non-essential high-frequency fluctuations (increasing the number of spikes) that will have to be removed to bring out the most impactful structures.

On the other hand, the quadrant time fraction (QTF) is a robust characteristic, which depends very little on the precision of the measurement; the same applies to the trips and sequences. That is to say, as much as the data series is disintegrated in increasingly smaller time intervals, the QTFs in the data series do not change much. However, Q4 is a little increased by decreasing the FDC or increasing the CV, showing a link between the growth of the Q4 events and large structures.

On the other hand, although the analysis of pulse durations between data series taken with different FDC is a bit more complicated, since the duration between events is different, if the time between two quadrant events is considered as a step (1δ, 2δ, 3δ...) instead of duration, the histograms of pulse durations (T_p) from two different FDC data series overlaps in the same pattern. Therefore, in terms of quadrant trajectories, QTF, pulses and pulse sequences, the data series shows a robust trend that is very little sensitive to the accuracy of the measurement. As the velocity series is temporarily disintegrated, the same structures appeared, responding to a proportional behavior. This effect is tremendously interesting because it is possible to rely on data from quadrants and trajectories as if they are a timeless property.

8.2 Turbulent Characterization

8.2.1 Velocity profile distribution and flow resistance

It has been determined that the assumption of a value of k_s unique for each bed diameter (*i*) or unique for each experiment (*ii*) yield similar logarithmic description, fitting well above the roughness layer and below the outer region. As the level of turbulence increases (u^*, U), the mean local velocity $\bar{u}$ inside the roughness region takes a more linear behavior distancing itself from the logarithmic description, obtaining a greater velocity than the one defined by the log-profile. The adjustment (*i*) obtains a higher k_s for experiments with low relative submergence ($<<R/D_{50}$) and a lower k_s for experiments with high relative submergence ($>>R/D_{50}$), in comparison with the ones obtained by (*ii*). However, both descriptions, (*ii*) and (*i*), reach similar log-profile and mean velocity U, since the adjustment compensate the decrease or increase of k_s with a decrease or an increase of u^*.

The results show that the measured u^* is closer to the one obtained from the second adjustment (*ii*), with k_s increasing with the flow rate for experiments with the same D_{50}, thus by increasing R/D_{50}.

The value of k_s turns out to be correlated with the turbulence level (τ_0) besides with R/D_{50}, demonstrating that D_{50} may not be representative of the relative roughness by itself. That is, it should not be expected that for flows with same R/D_{50} but different u^*, the same relative roughness k_s would be obtained. The latter applies also to α ($\alpha = k_s/D_{50}$). The values reached by α in both adjustments are below the ones obtained by the different authors (Bathurst 1985, Papanicolau & Maxwell 2000 etc.). However, it has to be taken into account that the approaches made by the different authors come mostly from field measurements in actual rivers, where also the curvature of the river, the macro-roughness (dunes, pools etc.), or the sediment transport could be included.

Regarding the packing of the bed surface (CG experiments), it affects the k_s reducing its value when the bed has been shaped. The leveling of the surface and consequently reduction of k_s yields higher experimental shear velocities (u^*) near the bed, for both descriptions (*i*) and (*ii*), making evident the need that has to be evaluated for each scenario, regardless they share the same bed diameter. Consequently, α is dependent on the packing effects and level of turbulence.

The flow resistance coefficient has been evaluated using different formulas by means of the hydrodynamic values, and from both logarithmic adjustments by means of the dimensionless Chezy coefficient $C^*(u^*, k_s)$ and Manning coefficient (n). The results suggest that the formula that best fits the experimental results of this study is Papanicolau & Maxwell (2000), above all in cases where $R/D_{84}<2$. The reason is that the experiments were inside the range of application of this formula, while the range of the rest of the approaches is much larger. As the R/D_{50} increases, the values differ from Papanicolau & Maxwell (2000) and become closer to Bathurst (1985), because the range of relative submergence (d/D_{84}) defined by Bathurst reaches a higher range [0.4-11.4].

The value of the Manning coefficient (n) obtained from the adjustments, although showing a decrease with the increase of R/D_{50}, remains more stable than the one obtained from the authors. However, it is noticeable that the adjustment that considers k_s as a constant (*i*) shows a little steeper decrease as R/D_{50} increases compared to the adjustment (*ii*), trying to follow the coefficients (n) defined by the authors since they also consider a constant k_s. The flow resistance was found to decline a little with the leveling of the bed, i.e. by reducing k_s.

All the results seem to be in accordance with the conclusion that the characteristic property used to calculate flow resistance is not only the mean bed diameter or the relative submergence but also the turbulent level (U, u^*, d, τ_0).

8.2.2 Turbulence intensities, TKE, and shear stress

The vertical distribution of the TI_X follows the same trend as the exponential decay function of Nezu and Nakagawa (1993), decreasing with the distance from the bed. All TI patterns reveal a layer of highly turbulent flow in the near-bed region, above all for the TI_Z, where the greatest turbulence intensities occur within the near-bed region ($0.2 \approx z/d$) although showing a stable behavior. This is probably due to the near-bed roughness that dampens the turbulence. The TKE has the same behavior than the one described by the TI_Z. There is a region near the bed ($z/d<0.3$) where the values of TKE keep rather constant until reaching the bed surface. The peak value of the TKE is located around $z/d \approx 0.2$, elevating its position z as the flow rate is increased. The Reynolds shear stress ($-\rho\overline{u'w'}$) reaches a maximum value around ($0.15 \approx z/d$), denoting the existence of a continuous band of high turbulent stresses across the near-bed region. As the flow rate is increased, the roughness layer increases in size (δ), thus the maximum $\rho\overline{u'w'}$ is located further from the bed.

The leveling of the bed surface has also little implications, decreasing the TI_Z in the near-bed region and TKE while increasing the TI_X. Moreover, the band of high Reynolds stresses becomes thinner and the maximum decreases.

Finally, it is noteworthy to remind that the ADV configuration has an impact on the turbulence quantities analyzed here, decreasing its value when an FDC or high CV is used, thus it could be expected higher values of these properties if more precision had been set.

8.2.3 Power Spectrum and dissipation

The obtained energy spectrums do not match with the theoretical -5/3 Kolmogorov's universal slope, or better said, they just follow this slope in a narrow range [1-3]-Hz. The wide variations in the PSD for frequencies over 3-Hz evidence a high energy inside the smallest frequencies that do not follow the theoretical -5/3 and this effect becomes more accentuated in the near-bed region, where the energy fluctuates more intensely.

This can be due to an incorrect ADV configuration. However, in the configuration analysis, an FDC of 25-Hz was enough to represent the FRITZ experiments correctly. The high turbulence of the CUBE experiments generates a greater range of size vortices that may not be well represented with this configuration. As a result, the data series do not account for a large range of structures and part of the energy from these not represented vortices is allocated to the represented ones.

Among all the methods used to describe the dissipation rate (ε), the structure functions method has shown a closer value to the actual dissipation in the channel, defined by the power channel (W). However, all methods display the same trend of increase as approaching to the bed surface, with a maximum close to the near-bed region and a band of almost constant dissipation rate ($0.3<z/d$).

8.2.4 Length Scales

All the structures are generated in the near-bed region, where the dissipation takes place; large and small length scales increase their size as they move towards the water surface. Taylor's (λ) scale shows similar lengths for all the experiments in the near-bed region regardless the flow rate, while the integral (L_X) and Kolmogorov scale (η) yields higher and smaller lengths for the highest turbulent flows, which explains the more energy dissipation.

The integral length scale exceeded the theoretical Von Karman mix length, which is defined in terms of the height (z) and the Von Karman constant K=0.4 ($L=K\cdot z$), reaching a value of K of 1.2 instead of the 0.4 in the near-bed region. The integral length scale is enlarged by increasing the turbulence regardless of the height in depth (z), contrarily to the η that is reduced. The effects of the k_s decrease (by leveling the bed surface) are the opposites, with a decrease of L_X ad increase of η, although the changes are low. Therefore, turbulent flows over high roughness beds develop macroturbulent flow structures that are initiated at the bed and grow towards the water surface. It has also to be considered that all length scales are affected by the ADV configuration, reaching higher values of the three length scales when the FDC is low, because of the lessening of the velocity signal peaks.

The assumption of a thick layer above the boundary where the amount of small coherent structures (SCS) is higher than out of it has been corroborated by all the results of this thesis.

8.3 Quadrant Analysis

8.3.1 Quadrant time fractions and contributions to Reynolds shear stress

The vertical distribution of the quadrants time fractions (QTF) along the depth profile has shown a consistent pattern for all experiments. Outward and inward interactions, Q1 (*u',w'*) and Q3 (*-u',-w'*) respectively, are the least likely quadrant-event in the depth profile, with a similar trend along the depth, in contrast to ejections and sweep events, Q2 (*-u',w'*) and Q4 (*u',-w'*), which are the most present in the data series but both showing a different vertical trend. While the sweeps increase their presence in the data series when approaching the water surface, the ejections show a trend of decrease. The Q2-TF is a little higher than Q4-TF only close to the bed surface, and from $z/d \approx 0.4$ the Q4-TF takes advantage obtaining its maximum value close to the water surface, while the Q2-TF reaches its minimum.

In the roughness region ($z/d<0.3$) Q2 and Q4 events are the dominant ones, and this seems to be linked with the turbulent energy production. Moreover, here Q2-TF>Q4-TF and Q3-TF>Q1-TF, denoting the predominance of negative streamwise fluctuations ($u'<0$), thus the flow is being decelerated due to the roughness ejecting streaks of low-momentum, while in the zone with $z/d>0.3$ the effect is the opposite. As the distance to the bed (z) is increased, the effect of the bed surface decreases and the increase of the local mean streamwise velocity pushes the vertical velocities downwards, generating an increase of Q4-TF. The trends of the four QTF are inverted along the height $0.2<z/d<0.4$. Towards the water surface, the QTFs tend to a value of 0.25 (25%), except the Q4-TF that, despite decreasing in the last zone ($z/d>0.7$), fails to reach a value of 0.25. Therefore, far from the bed, it seems that the quadrants tend to equalize, which reflects the lack of correlation in the quadrant map and consequent decrease of the Reynolds shear stress. This decrease in correlation can also be interpreted as vortices, which in addition to increasing in size with increasing z, also become more rounded, thus losing their ability to transport kinetic energy but maintaining their dissipative capacity. This corroborates the fact that turbulent flows moving over rough beds develop macroturbulent flow structures, that are initiated at the bed, and grow and dissipate as they move upward through the flow depth.

The quadrants Q2 and Q4 are ejections of low-momentum flux upwards and high-momentum flux downwards respectively, slowing the flow above and accelerating it below, thus increasing the stress in the flow direction. In the near-bed region, the contributions to the Reynolds shear stress of the sweeps (Q4) are higher than those from the ejections (Q2). Therefore, despite being smaller in number (TF) the Q4 events are more intense than the Q2 events. However, out of this region ($z/d>0.4$) the contributions of the ejections (Q2) increase and dominate over the sweeps (Q4). Therefore, although the Q2 events become less present in the sample as increasing z, they become more intense than sweeps (Q4). The maximum contribution of the four quadrants occurs in all experiments around $0.1<z/d<0.3$, coinciding with the height where the maximum Reynold shear stress value occurs.

The effects of the level of turbulence produce an increase in the presence of sweeps and ejections and the augment of all quadrants contributions to shear stress (positive and negative) because the events become more extreme. A tendency to decrease of the sweeps and ejections (Q2 and Q4) inside the roughness layer has been observed when leveling the bed, as well as the decrease of the contribution of both events to the Reynolds stress, showing a greater decrease of the contribution of Q4. Therefore,

a higher turbulence level and a greater roughness cause that sweeps events (Q4) and ejections (Q2) become more present, with a higher increase in the intensity of the first. On the other hand, it has been seen that QTF are also a little affected by the configuration of the device, where the Q4-TF is increased at expenses of the Q1-TF and Q3-TF, inside and outside the roughness region respectively, by configurations giving more importance to big structures. Therefore, it seems that events in Q4 are related to large structures, although also small ones can be present as well.

8.3.2 Quadrant sequences

The study of quadrant sequences has shown that there are also marked patterns along the profile that are repeated for all experiments. The most frequent sequences of two and three consecutive quadrants are those that involve quadrants Q2 and Q4 with a clear predominance of trips Q2-Q2 and Q4-Q4 and the sequences of Q2-Q2-Q2 and Q4-Q4-Q4. Therefore, quadrant events tend to stay in the same quadrant more than one time-interval. The trend of these sequences along the depth profile is similar to the one followed by their QTF, showing a change of behavior out of the roughness layer.

Near the bed surface, it seems that the events in Q2 tend to stay longer in cases of higher roughness but similar flow rate (CG experiments), while the rest of quadrant events do not show this trend, due to the roughness-flow interaction ejecting streaks of low-momentum for longer periods.

On the other hand, it has been discarded that the quadrant sequences follow a first-order Markov process, that is to say, the next quadrant cannot be predicted only with the probability of the current one. When the Markov process is elevated to another order, thus considering the current quadrant and the preceding one to predict the next quadrant (second-order Markov process), the quadrant sequences seem to be better represented.

8.3.3 Gram-Charlier

It has been verified the suitability of the third-order Gram-Charlier (GC) distribution to represent a series of velocities (u',w') in the region near the bed by mean of the description of Wu & Jiang (2007). Although all the variables describing this method (R_{uw}, S_u, S_w, $M_{21,}$ and M_{12}) have a trend along the depth profile, in the region near the bed they could be considered constant. However, it is worthwhile the revision of the values proposed by Wu & Yang (2004), which are somewhat dependent on the level of turbulence in each case and do not always match with the obtained from this analysis. However, it has to be mentioned that the data used by Wu & Yang (2004), and Wu & Jiang (2007) were not taken in any case with an ADV.

The values obtained show that within the roughness region the flux of streamwise Reynolds stress $\overline{u'u'u'}$ (S_u) occurs in the streamwise direction, and in the upper part of the profile (z/d>0.3), out of the roughness region, the flux occurs in the opposite direction to the flow. This effect becomes more intense for a higher level of turbulence and a greater roughness. Contrarily, the flux of vertical Reynolds stresses $\overline{w'w'w'}$ (S_w) occurs in a downward direction in the roughness region, changing the direction out of this layer, with this effect increased as the turbulence level or roughness augments.

The vertical Reynolds stress diffuses $\overline{w'w'u'}$ (M_{21}) in the flow direction inside the roughness region (z/d<0.3) for all the experiments. Out of this layer, the diffusion is in the counter-flow direction. The

diffusion factor is increased with the level of turbulence and bed roughness. On the other hand, the streamwise Reynolds stress $\overline{u'u'w'}$ (M_{12}) diffuses downward inside the roughness region, while it diffuses upward out of it. The diffusion becomes more accentuated for higher levels of turbulence and with the roughness height. Moreover, these quantities are also related to each other by some coefficients, as already demonstrated Raupach (1981).

The trend of S_w and M_{21} indicates that inside the roughness region an inrush of flow toward the bed occurs, due to the strong sweep events (Q4), and the behavior of S_u and M_{12} implies that the flow toward the bed is carried away by the flow, both indicating the occurrence of strong and highly intermittent turbulent events.

8.3.4 Poincaré maps

The quadrant events have also shown certain patterns when they are characterized on a phase-state plane (Poincaré map), in which each fluctuation is represented with the subsequent velocity variation ($\Delta u'$) (or acceleration, being the time interval always the same).

The streamwise and vertical accelerations are greater in the region near the bed and maintain a rather constant value throughout the roughness region, both decreasing towards the water surface. The increase of the flow rate results in a rise of these accelerations because velocity fluctuations increase. However, the augment of the roughness height dampens a little the $\Delta u'$ while raising the $\Delta w'$, due to the flow interaction with the roughness crests.

8.3.5 Synthetic velocity series

The third-order GC JPDF has demonstrated to be an important tool when obtaining synthetic velocity series since it fits well the turbulent properties associated with the turbulence of the flow. However, the analysis of quadrants has shown that it is also important the order in which they occur; moreover, this order may change also with the distance to the bed. Therefore, together with the consideration of the vertical patterns of the CG pdf variables and the statistics of the sequence of events, it is possible to achieve a more sophisticated tool to generate velocity series that better adjusts to the reality of a turbulent velocity.

In addition, it has been seen that there is also a coherent distribution of the turbulent events (and trips) on the Poincaré planes (u', $\Delta u'$) (w', $\Delta w'$). These maps can be also a useful tool in the process of obtaining the synthetic velocity series.

8.4 Pulse Analysis

The analysis of pulse durations (uninterrupted time spent by an event within a quadrant) along the depth profiles has also revealed certain patterns that seem to be mandatory for flows. Although the presence of each pulse duration in the sample seems to vary with its height in the profile (z), these variations are much smaller than in other properties seen in the thesis. There is a general tendency for the short pulses (T_p=1Δt) to decrease their presence in the data series with the distance from the bed, that is, the pulses become longer, especially the sweep pulses (Q4). As Q4-TF increase with the distance to the bed, this increase occurs thanks to the lengthening of pulses contained in Q4. The

differences in the distribution of pulses determined by the increase of the bed roughness is a little increase in the TF of the Q2 pulses (T_p>1Δt) near the bed region. That is to say, the roughness height provokes longer Q2 events.

The analysis of velocities associated with the pulses reveals that long pulses (T_p>2Δt) have higher *u'* and *w'* than short pulses (T_p=1Δt), because they have more time to reach further inside the quadrant map (*u'w'*). Within the bed region *(z/d*<0.3) it is obtained that the highest fluctuations (*u ',w'*) are those produced in Q4, while for *z/d*>0.3 the fluctuations (*u ',w'*) associated with Q2 pulses are superior to the rest. The ejections (Q2) reduce their fluctuations (*u ',w'*) less on their way to the water surface than the rest. In both cases, Q2 and Q4 show higher fluctuations for a longer duration of pulses. Regarding the effects that the high roughness has on the fluctuations, it is noteworthy that values of *w'* are increased near the bed, mainly for the fluctuations of Q2 and Q4 and for pulses of T_p>3Δt.

The fluctuation module ($\overrightarrow{u'w'}$) has a constant tendency within the roughness region, increasing with the level of turbulence and the bed roughness, being very similar in the case of sweeps (Q4) and ejections (Q2) near the bed-region (*z/d*<0.3), while outside of it ejections show a greater ($\overrightarrow{u'w'}$). The events seem to concentrate on a certain pulse duration and a certain ($\overrightarrow{u'w'}$) at each point of the profile. The quadrants Q1 and Q3 show greater density of short pulses (T_p=1Δt) with a low fluctuation module between 0.08-0.25 m/s in *z/d*<0.3, while Q2 and Q4 have a higher density of pulses of T_p=2Δt and T_p=3Δ, in some cases even up to T_p=5Δt, with a fluctuation module value between 0.08<$\overrightarrow{u'w'}$ <0.4. In reference to the leveling of the bed surface (CG experiments), it seems that the experiments with not-packed beds obtain higher ($\overrightarrow{u'w'}$); however, given the differences between all the tests, these variations cannot be attributed to the change in roughness.

The contributions of the pulses to the Reynolds shear stress show a clear predominance of the pulses of T_p=1Δt because they are the most present in the sample. However, even though pulses of T_p=2Δt have a higher TF than the pulses of T_p=3Δt both contributions are almost equal. In general, it is obtained that although long pulses have low TF its contribution to Reynolds stress is high.

The sequences of pulses have revealed that the most frequent sequences are those involving trips between quadrants Q1 and Q4 (Q4-Q1-Q4 and Q1-Q4-Q1), with a clear tendency of increasing their presence when approaching the water surface (*z/d*>0.5), due to the increase of Q4 events and pulse durations. The following sequences with greater presence are those that include trips between quadrants Q2 and Q3, (Q2-Q3-Q2 and Q3-Q2-Q3), keeping these a more constant distribution along the depth profile than the previous ones. Nevertheless, all show a rather constant value in the region near the bed (*z/d*<0.3).

The contribution of the sequences to the Reynolds shear stress has only been evaluated for those in which the three pulses obtain the same sign of contribution, that is, Q1-Q3-Q3, Q3-Q1-Q3, Q2-Q4-Q2, and Q4-Q2-Q4. All the contributions show a decrease along the depth profile with a fairly constant value in the roughness region, with a predominance of sequences Q2-Q4-Q2 and Q4-Q2-Q4. However, the contribution of Q1-Q3-Q3 and Q3-Q1-Q3 approaches zero rapidly from *z/d*>0.3 while the decrease of Q2-Q4-Q2 and Q4-Q2-Q4 is softer. It is hard to assure if the differences near the bed surface between the CG experiments is due to the flattening of the bed surface. However, in cases of not-packed beds, the contribution of the sequences of pulses that involves Q2 and Q4 is greater.

From the analysis of pulses, both the pulse duration distributions and the velocities associated with each pulse can also be a useful tool for simulations of synthetic velocity series or at least an instrument for assessing its correct description.

The statistical distribution of the pulse durations can be considered independent of the FDC sampling, maintaining a certain proportionality, when the pulse duration is considered in steps (δ). The robustness of the pulse duration histograms between experiments, height in the profile and FDC of data acquisition, is reminiscent of Kolmogorov's third hypothesis, which says that statistics in the inertial range are scale-invariant and self-similar.

8.5 Sediment transport

One of the stated objectives of the thesis was the development of a methodology to assess the initiation of movement of the bed particles by means of the examination of the role that Reynolds shear stress plays on the commencement of sediment motion. For this purpose, the coupling of the impulse applied by the Reynolds shear stress (exerted by packets of pulses) with the rate of the entrained sediment obtained from the CG experiments visualization is assessed. These experiments have been also analyzed by means of a conceptual model, using simple arguments from mechanics based on the consideration that there is a certain critical impulse (I_{cr}), related to the energy balance of the particles that, when overcome by the impulse exerted by the flow (I_i), set the particles in motion.

It has been verified by the experimental results of displaced particles that, by reducing the roughness of the bed k_s by shaping the bed surface, the actions of the flow are supported better, obtaining less amount of particle displacements, mainly because of the additional clamping forces between particles and less exposition to the flow. Moreover, the implementation of the methodology developed by the conceptual model has shown that the experiments in which the bed has been shaped show a lower *Imp. R.* in the region near the bed compared to the experiments in which the bed has not been leveled, due to the decrease and attenuation of sweep (Q4) and ejection (Q2) events.

It has to be pointed out that when the time application of the shear stress is not considered, but only the value of τ_{cr} is taken into account, the results suggest that a complete sweep of the bed sediment would occur, since almost a 30% of the events can exceed τ_{cr}, which obviously did not happen. On the other hand, the not leveled beds (higher k_s) show more percentage of pulses exceeding τ_{cr}, mostly for durations of $T_P > 2\Delta t$.

From the results, it is concluded that the comparison between the real entrainment observed in the experiments and the obtained from the conceptual model is very subjective. Although similar trends are observed, there are differences of up to an order of magnitude between Motion Rates. This must be due to the simplicity of the conceptual model not being able to equate quantitatively the results obtained from both analyses, although in a qualitative way a similar trend is obtained. The latter is due to the uncertainties linked to this methodology, some related to the conceptual model and other to the coupling of data acquisition and displaced particles.

On the other hand, the results obtained from the analysis of the ADV configuration may compromise some of the hypotheses made in the conceptual model. Although the statistics of quadrant and pulse analysis have demonstrated to be very robust, maintaining a proportional behavior regardless the

frequency of data acquisition (FDC), the FDC compromise the intervals of the pulse durations in addition to the peak values of the events.

However, the methodology is supported by the stated by Valyryakis et al. (2013), as mentioned before. They observed that a particle can only be moved through a structure at least twice its diameter. This suggests that the signals should be measured at the FDC that represents the flow structures of a certain size corresponding to the mean particle diameter. Other option could be to measure with a high FDC and later filtered by a low-pass filter, depending on the particle size to be studied, which would allow evaluating with the same velocity signal the impulse applied to the different particles.

From the experiments analyzed here (with an FDC=25-Hz), the results show that the integral scale in the near-bed region was about twice the sediment size D_{50} in each case, being this length also raised when the roughness was increased, evidencing a greater erosive capacity of a greater roughness. The latter provides reliability to the used methodology, although, as mentioned, the rate of displaced particles by means of the conceptual model is still far from being quantitatively assessed.

8.6 Recommendation for Future Work

On the basis of above conclusions and understanding of microturbulence of the high turbulent open channel flow, many different paths to be explored have shown up. The following recommendations are relevant to future work. It is suggested to:

- Study filtering methods based on the velocity increments time-distribution, so that undesired effects such as those observed near the water surface due to the distortion produced by the ADV can be avoided. The analysis of quadrants and pulses presented here can be a tool for assessing the correct filtering;
- Perform experiments using other measurement systems such as PIV or LDV to accredit the results of quadrants and pulses obtained with ADV;
- Resort to the sophistication of the third-order GC distribution by considering the vertical distribution along the depth profile of the variables that define it;
- Investigate the generation of synthetic velocity signals that takes into account the distributions of velocity increments and quadrant-pulse sequences, by means of the coupling of the third-order GC and density maps of events obtained on the phase-state planes;
- Improve the methodology of sediment entrainment developed in this thesis through the complexity of the conceptual model, and by considering the impulses imparted by the force of drag. In addition to its evaluation, resort to idealized experiments in which the particle motions are synchronized with the velocity signal;
- Finally, it would be of great interest to the community of fluvial engineers to apply these concepts of turbulence to the formulation of riprap design, especially for high mountain rivers.

References

Aberle, J., & Smart, G. M. (2003), 'The influence of roughness structure on flow resistance on steep slopes'. *J. Hydraul..Res.* 41, 259-269.

Adrian, R.J. (2007), 'Hairpin vortex organization in wall turbulence'. *Physics of Fluids* 19, 1-16.

Antonia, R. & Krogstad, P. (2001), 'Turbulent structure in boundary layers over different types of surface roughness'. *Fluid Dynamics* 28, 139-157.

Balachandar, R. & Bhuiyan, F. (2007), 'Higher-order moments of velocity fluctuations in an open channel flow with large bottom roughness'. *J. Hydraul. Eng.*133(1), 77-87.

Barkdoll, B. (2002), Discussion of 'Mean flow and turbulence structure of open-channel flow through non-emergent vegetation', Lopez F., Garcia M. *J. Hydraul. Eng.*128(11), 1032.

Bathurst, J. C. (1985), 'Flow resistance estimation in mountain rivers'. *J. Hydraul. Eng.*111, 625-643.

Bigillon, F., Niño Y., & Garcia M. (2006), 'Measurements of turbulence characteristics in an open-channel flow over a transitionally-rough bed using particle image velocimetry'. *Exp. Fluids* 41(6), 857-867.

Bray, D.I. (1983), 'Flow resistance in gravel-bed rivers'. In Hey, R. D., Bathurst, J.C. and Thorne, C.R. Gravel river beds. Wiley, 109-137.

Bridge, J. S. & Bennett, S. J. (1992), 'A Model for the Entrainment and Transport of Sediment Grains of Mixed Sizes, Shapes, and Densities'.Water Resources Research 28(2), 337-363.

Brodkey R.S., Wallace J.M. & Eckelmann H. (1974), 'Some properties of truncated turbulence signals in bounded shear flows'. *J. Fluid Mech.* 63, 209-24.

Buffin-Bélanger, T. & Roy A.G. (1998), 'Effects of a pebble cluster on the turbulent structure of a depth-limited flow in a gravel-bed river'. *Geomorphology 25*, 249-67.

Buffington, J. R., & Montgomery, D. R. (1997), 'A systematic analysis of eight decades of incipient motion studies, with special reference to gravel-bedded rivers'. *Water Resour. Res.,* 33, 1993-2029.

Cameron, S. M. (2006), 'Near-boundary flow structure and particle entrainment'. PhD thesis, University of Auckland, New Zealand.

Cantwell, B. J. (1981), 'Organized motion in turbulent flow'. *Ann. Rev. Fluid Mech. 13*, 457.

Cao, H.H. (1985), 'Résistance hydraulique d'un lit de gravier mobile à pente raide'. PhD thesis 589. École Polytechnique Fedérale de Lausanne.

Cea, L., Puertas, J., & Peña, L. (2007), 'Velocity measurements on highly turbulent free surface flow using ADV'. *Exp. Fluids,* 42(3), 333-348.

Celik, A. O., Diplas, P., Dancey, C. L. & Valyrakis, M. (2010), 'Impulse and particle dislodgement under turbulent flow conditions'. *Phys. Fluids* 22.

Celik, A.O., Diplas, P. & Dancey, C.L. (2013), 'Instantaneous turbulent forces and impulse on a rough bed: Implications for initiation of bed materialmovement'. *Water Resources Research*, 49(4), 2213-2227.

Celik, A.O., Diplas, P., Dancey, C.L. & Valyrakis, M. (2010), 'Impulse and particle dislodgement under turbulent flow conditions'. *Physics of Fluids* 22, 1-13.

Celik, O., Diplas, P. & Dancey, L. (2014), 'Instantaneous pressure measurements on a spherical grain under threshold Low conditions'. *J. Fluid Mech.* 741, 60-97.

Chamberlain, A. C. (1983), 'Roughness length of sea, sand, and snow'. *Boundary-Layer Meteorology*, 25, 405-409.

Cheng S. & Chiew M. (1998), 'Pick-up probability for sediment entrainment'. *J. Hydraul. Eng*. 124(2), 232-235.

Clifford, N. J., McClatchey, J. & French, J. R. (1991), 'Measurements of turbulence in the benthic boundary layer over a gravel bed and comparison between acoustic measurements and predictions of the bedload transport of marine gravels'. *Sedimentology,* 38(1), 161-171.

Clifford, N. J., Robert, A., & Richards, K. S. (1992), 'Estimation of flow resistance in gravel-bedded rivers: A physical explanation of the multiplier of roughness length'. *Earth Surf. Processes Landforms* 17, 111-126.

Corino ER & Brodkey RS. (1969), 'A visualization of the wall region in turbulent flow'. *J. Fluid Mech.* 37, 1-30

Czernuszenko W. & Rowinski P. M. (2008), 'Reynolds stresses in a compound open channel flow-flume experiments. *International Conference on Fluvial Hydraulics. Cesme-Izmir,Turkey. River Flow 1,* 289–297.

Davidson P. A. (2004), Tubulence. University press.

Detert, M., Weitbrecht, V. & Jirka, G. H. (2010), 'Laboratory measurements on turbulent pressure fluctuations in and above gravel beds'. *J. Hydraul. Eng.* 136, 779-789.

Dey S., Sarkar S., & Solari L. (2011), 'Near-Bed Turbulence Characteristics at the Entrainment Threshold of Sediment Beds'. *J. Hydraul. Eng*. 137(9), 945-958.

Diplas, P., Dancey, C. L., Celik, A. O., Valyrakis, M., Greer, K. & Akar, T. (2008), 'The role of impulse on the initiation of particle movement under turbulent flow conditions'. *Science* 322, 717-720.

Dubuat, L. G. (1779), 'Principes d'Hydraulique et de Pyrodynamique'. Paris.

Dwivedi, A., Melville, B., & Shamseldin, A. (2010), 'Hydrodynamic forces generated on a spherical sediment particle during entrainment'. *J. Hydraul. Eng.,* 136(10), 756-769.

Einstein, H. A. & El-Samni E. A. (1949), 'Hydrodynamic Forces on a Rough Wall'. *Review of Modern Physics* 21, 520-524.

Ferguson, R. I., Kirkbride A. D., & Roy A. G. (1996), 'Scales of turbulent coherent flow structures in gravel bedded river'. John Wiley, *Coherent Flow Structures in Open Channels*, 165 -184.

Ferreira, R.M.L., Amatruda M., Ricardo A.M., Franca M.J. & Di Cristo C. (2010), 'Production and dissipation of turbulent kinetic energy in the roughness layer'. Proceedings of the I European IAHR conference, Edinburgh.

Ferreira, R.M.L., Franca, M.J., Leal, J.G.B. & Cardoso, A.H. (2009). 'Organized turbulence over mobile and immobile hydraulically rough boundaries'. In proc. 35rd IAHR Congress, Vancouver, British Columbia, Canada, 36-43.

Finelli, C. M., Hart, D. D. & Fonesca, D. M. (1999), 'Evaluating the spatial resolution of an acoustic Doppler Velocimeter and the consequences for measuring near-bed flows'. *Limnol. Oceanogr.* 44, 1793-1801.

Franca, M. J., Santos B.O, Antico F., & Ferreira R. M. L. (2014). 'Quadrant analysis of shear events in open channel flows over mobile and immobile hydraulically rough beds'. *Ercoftac Bull.,* 100 (100), 29-36.

G. Taylor. (1935), 'Statistical theory of turbulence'. *Proceedings of the Royal Society of London. Series A, Mathematical and Physical Science*s, 151(873), 421-444.

Garcia, C., Cantero, M. I., Jackson, P.R., & Garcia, M. (2004), 'Characterization of the flow turbulence using water velocity signals recorded by acoustic Doppler Velocimeters'. *Hydraul. Eng. Studies*, nº 75.

Garcia, C., Cantero, M. I., Niño, Y., & Garcia, M. (2005), 'Turbulence measurements with acoustic Doppler Velocimeters'. *J. Hydraul. Eng.* 131 (12), 1062-1073.

Garcia, M. (1996), 'Resistencia al flujo en ríos de montaña'. *XVII Congreso Latinoamericano de hidráulica. Guayaquil, Ecuador,* 105-116.

Goring, D., & Nikora, V. (2002), 'Despiking Acoustic Doppler Velocimeter data'. *J. Hydraul. Eng.* 128(1), 117-126.

Grass, A. J. (1971), 'Structural features of turbulent flow over smooth and rough boundaries'. *J. Fluid Mech*. 50, 233-255.

Grass, A. J. (1983), 'The Influence of Boundary Layer Turbulence on the Mechanics of Sediment Transport'. *Mechanics of Sediment Transport. Proceedings Euromechanics* 156, 3-18.

Grass, A. J., Stuart R. J., & Tehrani M. M. (1991), 'Vortical Structures and Coherent Motion in Turbulent Flow Over Smooth and Rough Boundaries'. *J.Fluid Mech.* 336, 35-65.

Hardy, R. J., Best J. L., Lane S. N., & Carbonneau P. E. (2009), 'Coherent flow structures in a depth-limited flow over a gravel surface: the role of nearbed turbulence and influence of Reynolds number'. *J. Geophys. Res*. *114, F01003*.

Hardy, R. J., Best J. L., Lane S. N., & Carbonneau P. E. (2010), 'Coherent flow structures in a depth-limited flow over a gravel surface: the influence of surface roughness'. *J. Geophys. Res. 115, F03006.*

Hardy, R. J., Lane S. N., Ferguson R. I. & Parsons D. R. (2007), 'Emergence of coherent flow structures over a gravel surface: A numerical experiment'. Water Resourc. Res. 43, W03422.

Hardy, R. J., Lane S. N., Lawless M. R., Best J. L., Elliott L. & Ingham D. B. (2005), 'Development and testing of a numerical code for treatment of complex river channel topography in three-dimensional CFD models with structured grids'. *J. Hydraul. Res. 43*, 468-80.

Hey, R. D. (1979), 'Flow resistance in gravel-bed rivers'. *J. Hydraul. Div.* 105(4), 365-379.

Hofland, B. (2005), 'Rock & roll: turbulence-induced damage to granular bed protections'. *PhD. Technologic university tu Delft.*

Hurther, D., & Lemmin, U. (2000), 'A correction method for turbulence measurements with a 3D acoustic Doppler velocity profiler'. *J. Atmos. Ocean. Technol*. 18, 446-458.

Islam, M. R., & Zhu, D. Z. (2013), 'Kernel Density-Based Algorithm for Despiking ADV Data'. *J. Hydraul. Eng.* 139(7), 785-793.

Jimenez J. (2004), 'Turbulent flows over rough walls'. *Annu Rev Fluid Mech* 36, 173-96.

Keshavarzi A & Shirvani A. (2002), 'Probability analysis of instantaneous shear stress and entrained particles from the bed'. *CSCE/EWRI of ASCE environmental engineering conference. Niagara.*

Keulegan, G. H. (1938), 'Laws of Turbulent Flow in Open Channel'. *U.S. National Bureau of Standards, Journal,* 21(1151), 707-741.

Kim H.T., Kline S.J. & Reynolds W.C. (1971), 'The production of turbulence near a smooth wall in a turbulent boundary layer'. *J. Fluid Mech.* 50, 133-60.

Kirkbride, A. (1993), 'Observations of the influence of bed roughness on turbulence structure in depth limited flows over gravel beds'. Perspectives on flow and sediment transport. N. J. Clifford, J. R. French, and J. Hardisty, eds., *Wiley, New York,* 185-196.

Kleinhans G. & Van Rijn L. (2002), 'Stochastic Prediction of Sediment Transport in Sand-Gravel Bed Rivers'. *J. Hydraul. Eng.* 128, 412-425.

Kline, S. J., Reynolds, W. C., Schraub, F. A., & Rundstadler, P. W. (1967), 'The Structure of Turbulent Boundary Layers'. *J. Fluid Mech.* 30, 741-773.

Kolmogorov, A.N. (1941), 'Dissipation of Energy in the Locally Isotropic Turbulence'. *Proceedings of the USSR Academy of Sciences* 32, 16-18.

Kresta S.M. & Wood P.E. (1993), 'The flow field produced by a pitched blade turbine: characterization of the turbulence and estimation of the dissipation rate'. *Chem. Eng. Sci.* 48, 1761-1774.

Krogstad P.A., Antonia R.A., Browne L.W.B. (1992), 'Comparison between rough- and smooth-wall turbulent boundary layers'. *J. of Fluid Mech.* 245, 599-617.

Lane, S. N., Biron, P. M., Bradbrook, K. F., Butler, J. B., Chandler, J. H., Crowel, M. D., McLelland, S. J., Richards, K. S. & Roy, A. G. (1998), 'Three-Dimensionalm Measurement of River Channel Flow Processes Using Acoustic Doppler Velocimetry'. *Earth Surf. Proc. and Land.* 23, 1247-1267

Lee, A. J. & Ferguson R. I. (2002), 'Velocity and flow resistance in step-pool streams, *Geomorphology* 46, 59-71.

Lhermitte, R. & Lemmin U. (1994), 'Open-channel flow and turbulence measurement by high-resolution Doppler sonar'. *J. Atmos. Oceanic Technol.*11, 1295-1308.

Limerinos, J. T. (1970), 'Determination of the Manning coefficient from measured bed roughness in natural channels'. *U.S. Geol. Surv. Water Supply* 1898-B.

Liu, M., Zhu, D. Z. & Rajaratnam, N. (2002), 'Evaluation of ADV measurements in bubbly two-phase flow'. *Proc., Hydraulic Measurements and Experimental Methods Conf., ASCE, Reston, VA.*

Lohrman, A., Cabrera, R., & Kraus, N.C. (1994), 'Acoustic Doppler velocimeter ADV for laboratory use'. Proc., on Fundamentals and Advancements in Hydr. Measurements and Experimentation, C. A. Pugh, ed., ASCE, New York, 351-356.

López, R. & Barragan, J. (2003). 'Expresiones para la determinación del factor de fricción en ríos de fuerte pendiente'. Ingeniería civil 130, 43-50.

Lorenz, E.N. (1963), 'Deterministic Nonperiodic flow'. *J. of the Atmospheric Sciences* 20, 130-411.

Martin, V., Fisher, T., Millar, R., & Quick, M. (2002), 'ADV data analysis for turbulent flows: Low correlation problem'. *Proc., ASCE/ EWRI and IAHR Int. Conf. on Hydraulic Measurements and Experimental Methods* 113, 101-111.

Maynord, S. (1991), 'Flow Resistance of Riprap'. *J. of Hydraul. Eng.*117(6), 687-696.

Melville, B., Dwivedi, A., Raudkivi, A., Shamseldin, A. & Chiew, Y. (2012), 'Role of Turbulence and Particle Exposure on Entrainment of Large Spherical Particles in Flows with Low Relative Submergence'. J. Hydraul. Eng. 138(12), 1022-1030.

Millar, R. G. (1999), 'Grain and form resistance in gravel-bed rivers'. *J. Hydraul. Res.* 37, 303-312.

Mujal-Colilles A., Christensen, K. T., Bateman, A., & Garcia, M. (2016), 'Coherent structures in oscillatory flows within the laminar-to-turbulentvtransition regime for smooth and rough walls'. *J. Hydraul. Res*. 54 (5), 502-515

Naden, P. (1987), 'An Erosion Criterion for Gravel-Bed Rivers'. *Earth Surf. Proc. Land.* 12, 83-93.

Nakagawa, H., & I. Nezu. (1977), 'Prediction of the Contributions to the Reynolds Stress from Bursting Events in open-Channel Flows'. *J. of Fluid Mech.* 80, 99-128.

Nakagawa, H., & Nezu I. (1977), 'Prediction of the Contributions to the Reynolds Stress from Bursting Events in open-Channel Flows'. *J. of Fluid Mech.* 80, 99-128.

Nakagawa, H., Nezu, I. & Ueda, H. (1975), 'Turbulence of open channel flow over smooth and rough beds'. *J. of Japan Society of Civil Engineers* 241, 155-168.

Nakagawa. H & I. Nezu. (1981), 'Structure of space-time correlations of bursting phenomena in open channel flows'. J. F'luid. Mech. 104, 1-43.

Neill, C. R., Yalin, M. S. (1969), 'Qualitative definition of beginning of bed movement'. *J. Hydraul. Division* 95, 585-587.

Nelson, J. M., Shreve, R. L., Maclean, S. R. & Drake, T. G. (1995). 'Role of near-bed turbulence structure in bed load transport and bed form mechanics'. *Water Resourc. Res.* 31(8) 2071-2086.

Nezu, I., Tominaga, A. & Nakagawa, H. (1993), 'Fields measurements of secondary currents in straight rivers'. *J. Hydr. Eng.* 119, 598-614.

Nikora, V. & Goring, D. (1998), 'ADV measurements of Turbulence: Can we improve their interpretation?' *J.Hydr. Eng* 124(6), 630-634.

Nikora, V. I., Koll K.., McEwan, I.,McLean, S., & Dittrich, A. (2004), 'Velocity distribution in the roughness layer of rough-bed flows'. *J. Hydraul. Eng.*, 130, 1036–1042.

Nikora, V., & Goring, D. (2000), 'Flow turbulence over fixed and weakly mobile gravel beds'. *J. Hydraul. Eng.* 126(6), 679-690.

Nikora, V., Goring D., I. McEwan, & G. Griffiths. (2001), 'Spatially averaged openchannel flow over rough bed'. *J. Hydraul. Eng*. 127(2), 123-133.

Nikuradse, J. (1933), 'Strömungsgesetze in rauhen Rohren' *Forschg. Arb. Ing*. 361.

Niño Y., Garcia M. (1996), 'Experiments on particle–turbulence interactions in the near-wall region of an open channel flow: implications for sediment transport'. *J Fluid. Mech.* 326, 285-319.

Nortek. (2004), Vectrino velocimeter, User Guide, 625-641.

Paintal, A. S. (1971), 'Concept of Critical Shear Stress in Loose Boundary Open Channels'. *J. of the Hydraulics Division*, 9, 91-114.

Papanicolaou, A. N., Diplas, P., Dancey, C. L., & Balakrishnan, M. (2001), 'Surface roughness effects in near-bed turbulence: Implications to sediment entrainment'. *J. Eng. Mech.* 127(3), 211-218.

Papanicolaou, A.N., Kramer C.M., Tsakiris G. M., Stoesser T., Bonnaninayuni S. & Chen Z. (2012), 'Effects of a Fully Submerged Boulder within a Boulder Array on the Mean and Turbulent Flow Fields: Implications to Bedload Transport'. *Acta Geophysica.* 60(6), 1502-1546.

Papanicolau A. N.T. & Maxwell A. (2000), 'Equilibrium geomorphological conditions for high gradient bed streams'. *Washington State University.*

Parker, G. (2008), 'Transport of gravel and sediment mixtures. In Sedimentation engineering. Processes, measurements, modeling and practice'. *ASCE, Reston,* VA, 3, 165-251.

Parsheh, M., Sotiropoulos, F., & Porte-Agel, F. (2010), 'Estimation of power spectra of acoustic-Doppler velocimetry data contaminated with intermittent spikes' *J. Hydraul. Eng.* 136(6), 368-378.

Pope. S. B. (2000), 'Turbulent flows'. *Cambridge university press*

Prandtl, L. (1926), 'Über die ausgebildete Turbulenz'. ZAMM, 5-136.

Raupach, M. R., Thom A. S., & Edwards I. (1981), 'A Wind-Tunnel Study of Turbulent Flow Close to Regularly Arrayed Rough Surfaces'. *Boundary-Layer Meteorology* 18, 373-397..

Raupach, M.R., Antonia, R.A., & Rajagopalan, S. (1991), 'Rough-Wall Turbulent Boundary Layers'. Applied Mechanics Review 44, 1-25.

Richardson, L. F. (1922), 'Weather Prediction by Numerical Process'. *Cambridge University Press.*

Roberson, J. & Crowe, C. (1993), 'Engineering Fluid Mechanics', John Wiley, New York, 823..

Robinson, S.K. (1991), 'Coherent motions in the turbulent boundary layer'. *Annual Review of Fluid Mechanics* 23, 601-639.

Roy, A.G, Buffin-Belanger T., Lamarre H., Kirkbride A.D. (2004), 'Size, shape and dynamics of large-scale turbulent flow structures in a gravel-bed river'. *J. Fluid Mech. 500*, 1-27.

Rusello, P. J. (2009), 'A practical primer for pulse coherent instruments'. *Technical Note* TN-027, Nortek, Norway.

Sambrook Smith, G. H., & Nicholas A. P. (2005), 'Effect on flow structure of sand deposition on a gravel bed: Results from a two-dimensional flume experiment'. *Water Resour. Res.* 41, W10405.

Schmeeckle, M.W & Nelson, J.M. (2003), 'Direct numerical simulation of bedload transport using a local dynamic boundary condition'. *Sedimentology* 50, 279-301.

Shen, C. & Lemmin, U. (1999), 'Application of an acoustic particle flux profiler in particle-laden open channel flow'. J. *Hydr. Res., IAHR, Delft,* The Netherlands 37(3) 407-419.

Shields, A. (1936), 'Anwendung der Aehnlichkeitsmechanik und der Turbulenzforschung auf die Geschiebebewegung'. Mitt. 26, Preuss. Versuchsanst. fuerWasserbau und Schiffbau, Berlin.

Shvidchenko, A. B., & Pender G. (2001), 'Macroturbulent structure of open-channel flow over gravel beds'. *Water Resour. Res*. 37, 709-719.

Smart, G. M. (1999), 'Turbulent velocity profiles ad boundary shear in gravel bed rivers'. *J. Hydraul. Eng*. 125, 106-116.

Song, T., Graf, W. H., & Lemmin, U. (1994), 'Uniform flow in open channels with movable gravel bed'. *J. Hydr. Res.* 32(6), 861-876.

SonTek Technical Notes. (1997), 'Pulse coherent Doppler processing and the ADV correlation coefficient'.

Sterk, G., Jacobs, A. F. G., & van Boxel, J. H. (1998), 'The effect of turbulent flow structures on saltation sand transport in the atmospheric boundary layer'. *Earth Surf. Processes Landforms* 23(10), 877-887.

Strickler, A. (1923), 'Beitrage zur Frage der Geschwindigheits-formel un der Rauhigkeitszahlen fur strome, Kanale und Geschlossene Leintungen'. *Mitteilunge des Eidgenossischer Amtes fur Wassewirtschaft*. Berna, Suiza.

Strom, K. B. & Papanicolau, A.P. (2007), 'ADV Measurements around a Cluster Microform in a Shallow Mountain Stream'. *J. Hydraul. Eng.* 133, 1379-1389.

Sumer M., Chua L.H.C., Cheng N.S, & Fredsøe J. (2003), 'Influence of turbulence on bed load sediment transport'. *J. Hydraul. Eng.* 129, 585-596.

Sumer, B. M., & Deigaard R. (1981), 'Particle Motions Near the Bottom in Turbulent Flow in an Open Channel'. *J. Fluid Mech.* 109, 311-338.

Taylor, G.I. (1935), 'Statistical theory of turbulence'. Parts I-IV. *Proc. of Royal Soc. se*ries A, 151(873).

Townsend A.A. (1976), 'The structure of turbulent shear flow'. *Cambridge University press.*

Tritico, H. M., & Hotchkiss, R. H. (2005), 'Unobstructed and obstructed turbulent flow in gravel-bed rivers'. *J. Hydraul. Eng.* 13 (8), 635-645.

Tritton, D.J. (1988), 'Physical Fluid Dynamics' 2nd Ed. *Oxford University Press,* 519.

Ugarte, A. & Méndez, R. (1994), 'Resistencia al flujo en ríos de Montaña'. *XVI Congreso Latinoamericano de Hidráulica, Santiago de Chile*, 503-514.

Valyrakis, M., Diplas P. & Dancey C. L. (2013), 'Entrainment of coarse particles in turbulent flows: An energy approach'. *J. of Geophysical Res. Earth Surface* 118(1), 42-53.

Van Rijn, L. C. (1982), 'Equivalent roughness of alluvial bed'. *J. Hydr. Eng.* 108(10), 1215-1218.

Voulgaris, G. & Trowbridge, J. H. (1998), 'Evaluation of the Acoustic Doppler Velocimeter (ADV) for turbulence measurements'. *J. of Atmospheric and Oceanic Technology* 15, 272-289.

Wahl T. L. (2000), 'Analyzing ADV data using WinADV'. Proc. Joint Conference on Water Res. Eng. and Water Res. Planning and Management, Minneapolis, Minnesota. (WinADV Version 1.845 in http://www.usbr.gov/wrrl/twahl/winadv/).

Wahl, T. (2003), 'Discussion of 'Despiking Acoustic Doppler Velocimeter Data' by Goring D. & Nikora V.". *J.Hydr. Engr.* 129 (6), 484-487.

Wallace J.M., Brodkey R.S. & Eckelmann H. (1972), 'The wall region in turbulent shear flow'. *J. Fluid. Mech.* 54, 39-48

Wernersson, E. S. & Trägårdh C. (2000), 'Measurements and analysis of high-intensity turbulent characteristics in a turbine-agitated tank'. *Experiments in fluids* 28 (6), 532-545.

Wiberg, P. L. & Smith J. D. (1991), 'Velocity distribution and bed roughness in high-gradient streams'. *Water Resourc. Res. 27*, 825-38.

Williams, J. J., Thorne P. D., & A. D. Heathershaw. (1989), 'Measurements of Turbulence in the Benthic Boundary Layer over a Gravel Bed'. *Sedimentology,* 36, 959-971.

Willmarth, W.W. & Lu, S.S. (1972). 'Structure of the Reynolds stress near the wall'. *J. of Fluid Mech.*55 (03) 65-92.

Wu H., Patterson G. K. & Van Doorn M. (1989), 'Distribution of turbulence energy dissipation rates in a Rushton turbine stirred mixer'. *Experiments in Fluids* 8, 153-160.

Wu, F.C & Jiang M.R. (2007), 'Numerical Investigation of the Role of Turbulent Bursting in Sediment Entrainment'. *J. of Hidraul. Eng.*334.

Wu, F.C. & Yang K.H. (2004), 'Entrainment Probabilities of Mixed-Size Sediment Incorporating Near-Bed Coherent Flow Structures'. *J. of Hidraul. Eng.* 1197.

APPENDIX A. FILTERING EFFECTS

Table of Contents

Appendix A: Filtering Effects

A.1 Introduction

As a consequence of the low correlation obtained in the experiments, the use of the conventional value of COR_{CR}=70 proposed by Wahl (2000) (see chapter 3 section 3.4.1.2) yields in the elimination of more than 50% of the time series velocities.

Strom & Papanicolau (2007) made the hypothesis of normality for the real velocity signal. They found the correct critical values of COR and SNR to apply the filter by applying Shapiro-Wilks test statistics to check the normality of the filtered data for various assumptions of critical COR and SNR values (COR_{CR} and SNR_{CR}), once the despiking (see chapter 3 section 3.4.1.1) was applied. The study concluded COR_{CR}=50 and SNR_{CR}=10 for their experiments in a river with cluster bedforms.

On the other hand, Martin et al. (2002) assured that data edited with COR_{CR}=40 could be used to determine bed shear stresses (τ_0) if less than 30% of data is removed after filtering. Therefore, when ADV is used to measure highly turbulent flows in macro-roughness beds, low values of COR seem to be reasonable in clear water and gravel-beds, Tritico & Hotchkiss (2005).

However, according to the experiments carried out in the present work a critical value of COR_{CR}=40 is still restrictive in the high turbulence experiments since more than 50% of data is considered as "bad" under this assumption, mostly in the near-bed region (z/d<0.3). For this reason, the first goal is to find a reasonable value for COR_{CR} for the experiments. Once that value is found, the application of both filters, the Despiking filter and the filter based on COR_{CR} and SNR_{CR}, is discussed through the effects on the most typical turbulent quantities.

The first part of the evaluation is focused on the main turbulent parameters typically used to characterize the flow. However, the present appendix is a compilation of various analysis completed during the research, that is to say, in each step forward of the analysis, the effects of the filters were recursively evaluated. The reason is that some values, generally average values such as mean velocity are not affected, but as the analysis becomes more specific, more attention to data has to be paid. As a consequence of that, a more profound evaluation of the effects of filtering on the quadrant analysis, i.e., "bursting turbulence" and pulse analysis developed in this thesis, has been assessed in the second part in order to validate the suitability of the data to this methodology.

A.2 Percentage of bad data

The present section has the purpose of finding a reasonable value for COR_{CR} to impose in the SNR-COR filter. The first criterion to achieve this by means of the percentage of filtered data since the data series has to have enough data velocities to describe the average and turbulent statistics accurately. Moreover, a high percentage of removed data can misrepresent the results and break down the history of the velocity signal, which has been demonstrated along the thesis to be very important in the velocity series characterization and is the primary target of the present appendix.

Figure A.1-a plots the percentage of removed data by each filter considered, (i) Despiking and SNR_{CR}=15 together with (ii) COR_{CR}=0, (iii) COR_{CR}=10, (iv) COR_{CR}=20, (v) COR_{CR}=30 and (vi)

COR_{CR}=40) as a function of the dimensionless depth (*z/d*), for the test RG3. The COR_{CR} value is set until 40 because it was seen that from that value more than 50% of the data was removed.

The figure shows that the application of only the SNR_{CR}=15 and COR_{CR}=0 criterion does not affect the results, except in the last points close to the surface where the disturbance of the water surface by the device could appear. The Despiking filter removes between 3 and 5% from all data points, this range remaining steady along the profile; hence, no more data is removed near the bed.

On the other hand, for the SNR-COR filters, no matter how high the value of COR is imposed, there is a decrease of the detected "bad" data with the distance to the bed (*z/d*), as it was expected because of the low correlation problem at the near-bed region. When a COR_{CR}=10 is set, around 2-9% of data is considered wrong, while in the case of COR_{CR}=20 around 20-30% of data near the bed (*z/d* <0.40) is removed. Finally, more than 50% data is considered as wrong near the bed for COR_{CR}=30 thus the maximum COR_{CR} applicable to retain more than 50% of data is 30. It is worthwhile to remark that the percentage of removed data for all COR_{CR} remains stable up to a height of *z/d*=0.40 (3.5 cm).

In Figure A.1-b the effects that applying Despiking after the rest of filters is assessed, in order to see the capability of COR-SNR filters to detect the spikes. The figure shows that the application of COR_{CR} before the Despiking change a little the percentage of detected spikes by Despiking.

The percentage of removed data by applying just the Despiking filter is around 3-5%, and this percentage is barely changed by applying COR_{CR}=10, besides, it is very constant through the profile and barely increases with the mean velocity. When a COR_{CR}=30 is used, despite erasing between 19-50% of data, Figure A.1-a, some spikes remain in the signal, being around 1-2% (Figure A.1-b), very similar to applying COR_{CR}=20. Finally, setting a COR_{CR}=40 reaches an even high percentage of detected spikes by the Despiking filter, since a large amount of replaced data creates new spikes, not real spikes though. Therefore, the ability of the COR-SNR filter to erase spikes is insufficient.

The fact of applying the Despiking before COR-SNR filter is not assessed here since the first is not changing the correlation value, which is the criterion used by the second instead of the velocity value.

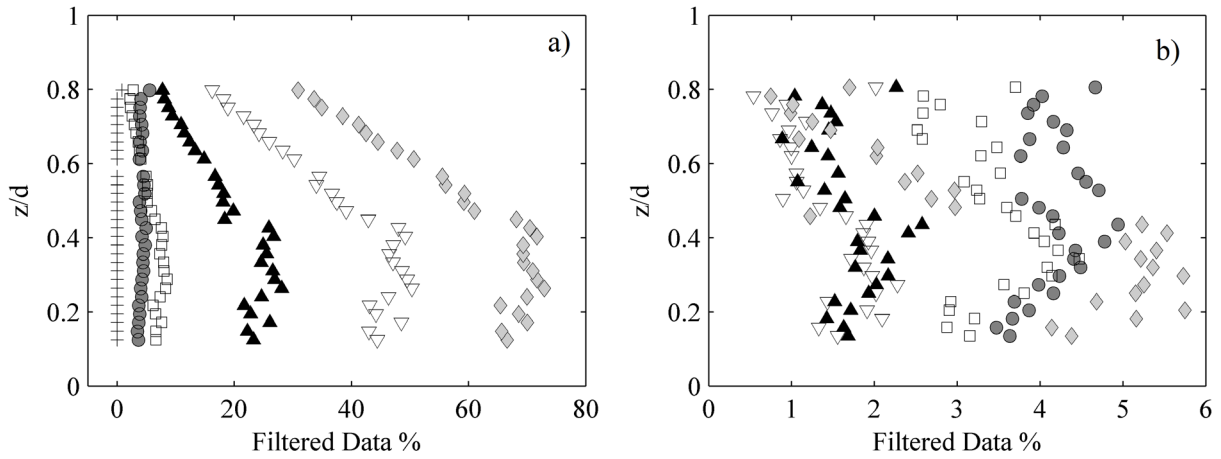

Figure A.1- Vertical distribution of the filtered data (%) by (a) Despiking and COR-SNR filters (with different COR_{CR}), and (b) by the Despiking filter once the SNR-COR filters were applied. Test RG3. *Legend,* ● *Despiking,* + COR_{CR}*=0,* □ COR_{CR}*=10,* ▲ COR_{CR}*=20,* ▽ COR_{CR}*=30,* ◇ COR_{CR}*=40.*

In the next figures (Figure A.2 and Figure A.3), the percentage of removed data by the mentioned filters is evaluated in all the RG experiments. The Despiking filter (Figure A.2-a) tends to erase around 2-6% of data in all RG tests maintaining a rather constant value over the depth. However, the COR-SNR filter (COR_{CR}=10 (Figure A.2-b), COR_{CR}=20 (Figure A.3-a), and COR_{CR}=30 (Figure A.3-b)) remove more data near the bed even for the COR_{CR}=10.

In all cases, the percentage of filtered data in the near-bed region rises as the flow rate increase (with the level of turbulence) however, starting from the height *z/d*=0.40 approximately up to the water surface this percentage begins to decrease with a similar trend for all experiments. That could be expected from the distribution of the mean COR value showed in chapter 3, section 3.3.1, where all experiments showed a similar behavior of the mean COR value along the depth, which is explained by the normality of the COR values in the points as seen in the same section.

When a COR_{CR}=20 is set, Figure A.3-a, a range between 18 and 50% of data is erased in the experiments in the near-bed region and this interval increases until 30-75% if the COR_{CR} is increased until 30 (Figure A.3-b). In both cases, the removed data shows that it is not a viable option since more than 30% of data is erased (Martin et al. 2002). Besides, the velocity data series will be distorted by the replacement of the "bad" data.

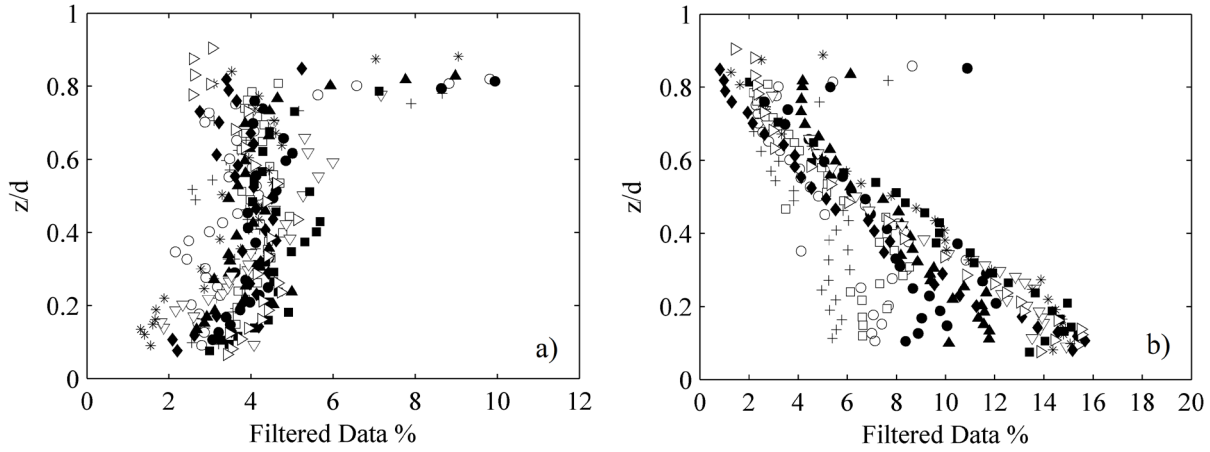

Figure A.2- Vertical distribution of the removed data fraction by (a) Despiking and (b) COR_{CR}=10. Tests RG1 to RG10. *Legend, + RG1, ○ RG2, □ RG3, ● RG4, ▲ RG5, ▽ RG6, ✷ RG7, ♦ RG8, ■ RG9, ▷ RG10.*

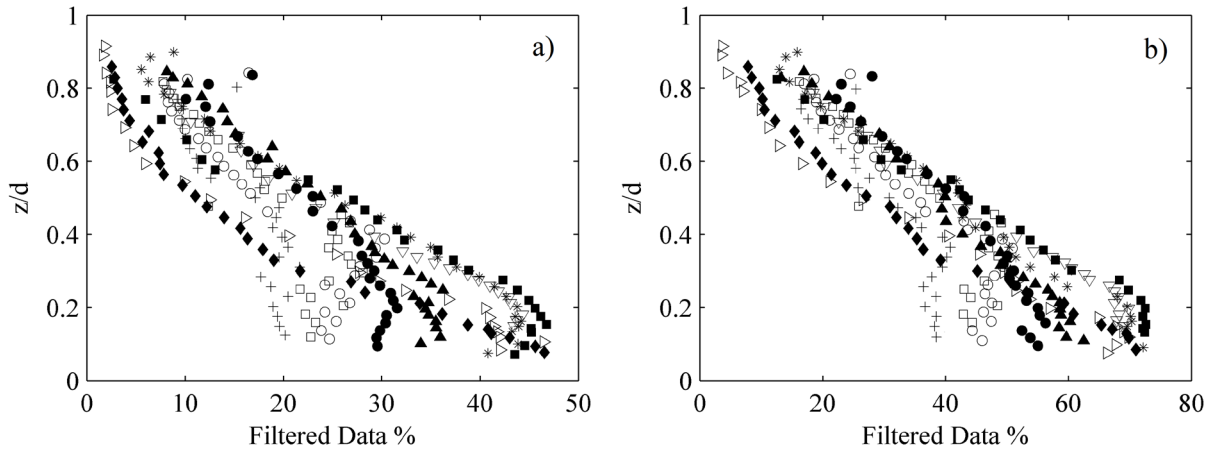

Figure A.3- Vertical distribution of the removed data fraction by (a) COR_{CR}=20 and (b) COR_{CR}=30. Tests RG1 to RG10. *Legend, + RG1, ○ RG2, □ RG3, ● RG4, ▲ RG5, ▽ RG6, ✷ RG7, ♦ RG8, ■ RG9, ▷ RG10.*

A.3 Effects on the main turbulent parameters

The effects of applying the filter are numerous; some of them are described henceforth by comparing some turbulent parameters obtained from the series after filtering with the original series (OS) (raw data), for the experiment RG3. It should be pointed out that in the present appendix only the evaluation of the changes produced by the data treatment is commented since the analysis of the characterization of the flow under different flow conditions it is examined in chapter 4.

The replacement method of the "bad" data used during filtering has been the linear interpolation. This method was highly recommended by Cea et al. (2007) for highly turbulent flows, with data poorly correlated. However, it has been detected that the method of replacement affects the turbulent parameters and the history of the velocity data. For this reason, an evaluation of how the replacement of the bad data affects the turbulent parameters and the history of the velocity data was carried out afterward this evaluation, and it is included in Appendix B.

A.3.1 Basic turbulence statistics

Usually, the fluctuating turbulence is represented by its Turbulent Intensity (TI), by means of the root mean square value (RMS) of each velocity component (u',v',w') and normalized by the local mean velocity of each axis ($\bar{u},\bar{v},\bar{w}$), see Eq. 4-11 of chapter 4. A Gaussian distribution could describe the turbulent components by its second-order moment, thus by the TI. Turbulent components are random; they have a correlation to each other. Consequently, third and fourth moments have to be considered together so that more information about turbulence can be obtained.

Typical TI profiles of the three axes are represented in Figure A.4. The graphic shows that there is a little difference between TIs of the original signal and after filtering by Despiking and COR_{CR}=10, in fact having similar results. For all filters, the streamwise TI (TI_X) (Figure A.4-a) decreases sharply up to about z=3.5 cm (z/d=0.40), then keep decreasing but more gently up to the free surface. As the COR_{CR} is increased, the TI_X is decreased especially for z<3.5 cm. In the case of transversal TI (TI_Y), Figure A.4-b, a very little decrease is shown by the use of filters, remaining steady in the region z<4 cm and start to decrease gradually from this point to the water surface, for all cases. The vertical TI (TI_Z) (Figure A.4-c), show a similar pattern along the depth profile to the TI_Y and a similar pattern of decrease despite the application of the filter is observed.

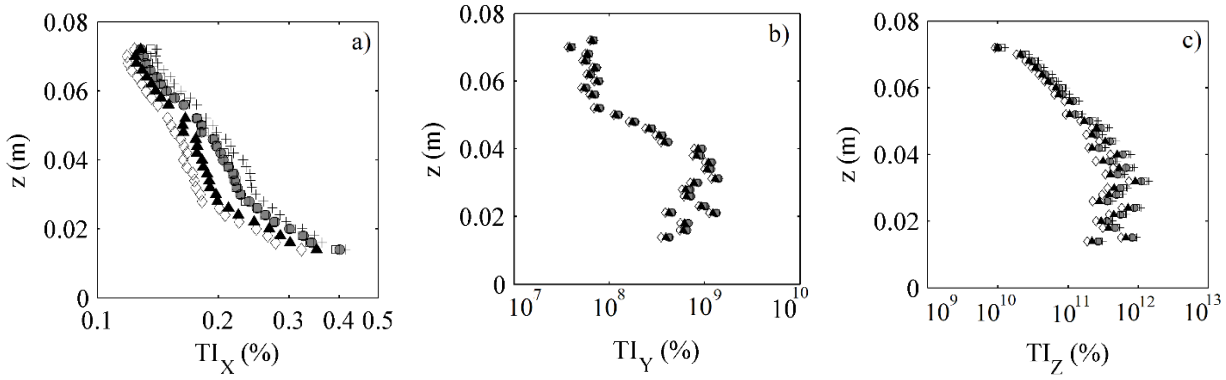

Figure A.4- Vertical distribution of (a), TI_X, (b), TI_Y and (c) TI_Z, before and after filtering. Test RG3. *Legend: + OS, ● Despiking filter, □ COR_{CR}=10, ▲ COR_{CR}=20, ◊ COR_{CR}=30.*

The third-order moment, the skewness factor (S), defines the asymmetry of the probability density function (PDF) of turbulent fluctuations. Figure A.5-a shows the vertical distribution of the streamwise S (S_X), where the same pattern for all filters is found with very little differences between them. All filters enlarge negative S_X and reduce the positive in the region z<4 cm, therefore, taking over the high positive velocity values, from that point, the positive S_X is slightly extended. The transversal direction (S_Y), (Figure A.5-b), is decreased by all filters. In the case of vertical skewness (S_Z) depicted in Figure A.5-c, the Despiking filter achieves a uniform profile, biasing the values to low positive values along the depth, showing the ability of the Despiking filter to erase peak values of vertical velocity (w). Only the COR_{CR}=30 shows similar behavior than Despiking, although a more irregular profile is obtained.

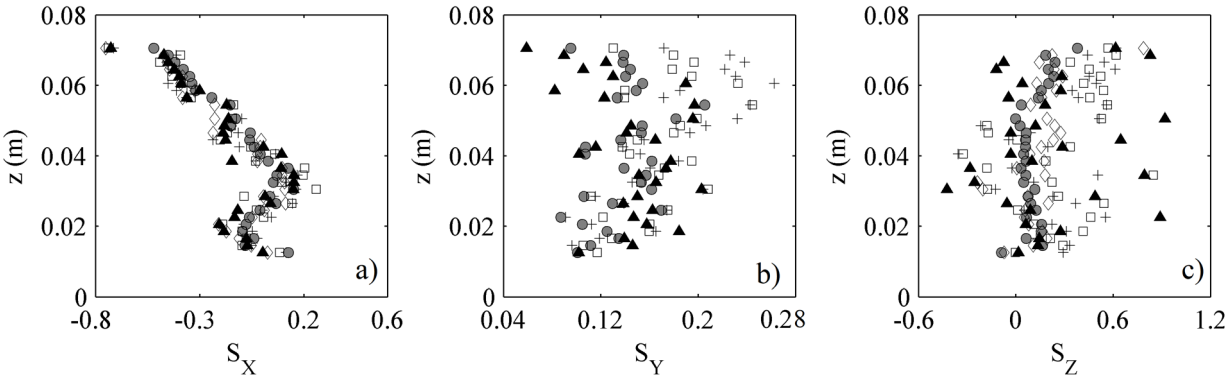

Figure A.5-Vertical distribution of (a) S_X, (b) S_Y and (c) S_Z, before and after filtering. Test RG3. *Legend: + OS, ● Despiking filter, □ COR_{CR}=10, ▲ COR_{CR}=20, ◊ COR_{CR}=30.*

The fourth-order moment, i.e., flatness factor (F) (or Kurtosis), describes the intermittency of turbulence, Nezu & Nakagawa (1993). The streamwise F (F_X), Figure A.6-a, of the OS shown a leptokurtic behavior (F >3) along the depth with lower values at the near-bed region z<4 cm, showing a concentration of velocities around the mean value. In this case, the Despiking filter shows a similar behavior than COR_{CR}=30; the F_X is decreased along the depth, the series becomes more Gaussian (F=3), despite showing the same pattern of variation along the depth. The transversal flatness factor (F_Y), Figure A.6-b, shows a similar comportment along the depth for all data series, with filters applying little effects. However, the vertical F (F_Z), Figure A.6-c, is deeply affected by the application of filters. The OS shows a clear trend of increase with z thus the velocities are more similar to the mean value. While COR_{CR}=10 does not change the values, as it is increased the COR_{CR} the F_Z decreases until a constant value of five and showing a smooth progression.

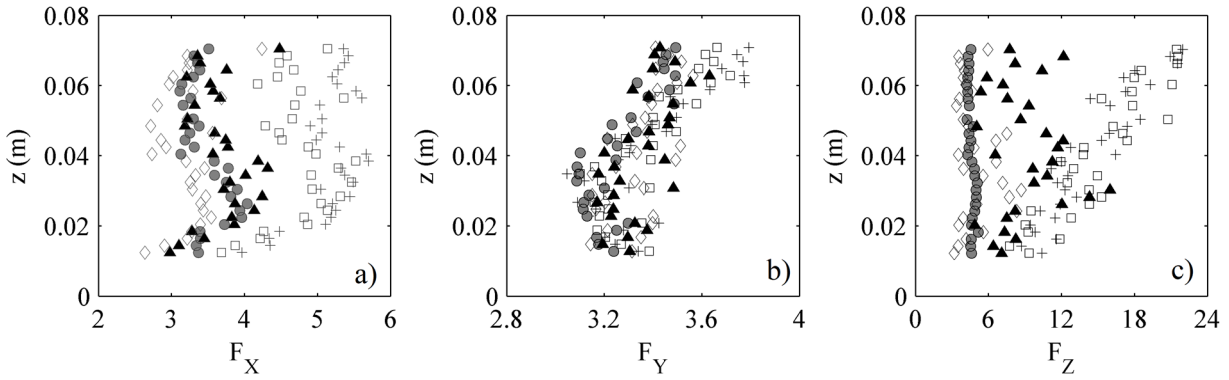

Figure A.6- Vertical distribution of (a) F_x, (b) F_y and (c) F_z, before and after filtering. Test RG3. *Legend: + OS, ● Despiking filter, □ COR_{CR}=10, ▲ COR_{CR}=20, ◊ COR_{CR}=30.*

Despite the amount of filtered data by the despiking filter being much lower than the rest of the filters, it managed to reach similar changes. The replaced data in each point plays a substantial improvement, unlike the others filters that do not follow a consistent trend.

A.3.2 Mean streamwise velocity and Reynolds Shear Stress

Mean velocity appears to be less sensitive than mean Reynolds shear stress ($\overline{-\rho u'w'}$) to COR-SNR and Despiking filters. An adjustment with logarithmic-law shows the effects of filtering on the adjustment parameters. In all cases both shear velocity u^* and k_s variates less than 0.2%. According to Martin et al. (2002), in the region close to the bed, the value of the mean velocity increases when the critical value of correlation decreases, nevertheless the difference can be negligible here.

Table A.1- Log-law parameters obtained after filtering. Test RG3.

Data series	α	k_s	C^*	u^*	$\overline{u}$
OS	1.494	0.082	6.060	0.164	1.110
Despiking Filter	1.551	0.085	6.020	0.165	1.110
COR-SNR filter (COR_{CR}=10)	1.517	0.083	6.040	0.164	1.105
COR-SNR filter (COR_{CR}=20)	1.571	0.086	5.990	0.166	1.100
COR-SNR filter (COR_{CR}=30)	1.593	0.089	5.890	0.168	1.097

The value of ($\overline{-\rho u'w'}$), Figure A.7, generally decrease with the application of all filters. The Despiking filter, as well as giving the lowest value of COR_{CR}, shows a moderate decrease of the average Reynolds shear stress, and the lessening decrease inversely proportional to COR_{CR} value.

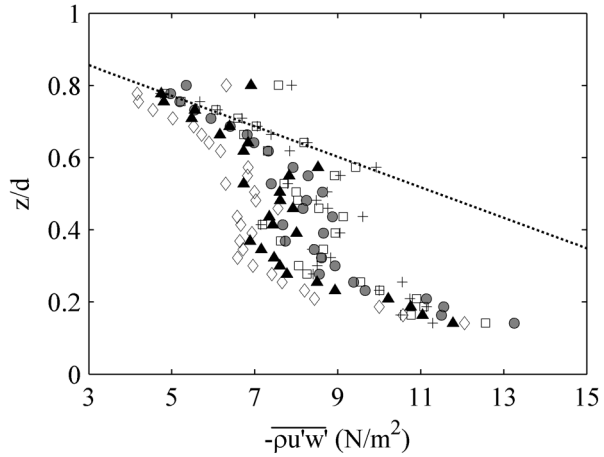

Figure A.7- Vertical distribution of $\overline{-\rho u'w'}$ before and after filtering. Test RG3. *Legend: + OS, ● Despiking filter, □ COR_{CR}=10, ▲ COR_{CR}=20, ◊ COR_{CR}=30.*

The viscous stresses did not change significantly using either of filters. Therefore, application of filters seems to be more influential on the turbulent properties such as Reynolds shear stress, TKE, energy dissipation rate (ε), Turbulence intensities and etc., as it is shown in the next paragraphs.

A.3.3 Autocorrelation function and length scales

The application of filters generally increases the autocorrelation (R_{xx}) of the signal. Figure A.8 depicts the autocorrelation values as a function of the time scale (defined by time intervals or steps (Δt=0.04

s), for three different points of the test RG3. One can see how this autocorrelation is notably increased by applying a COR_{CR}, but this is at expenses of erasing more than 30% of data in some points near-bed. However, even though the Despiking filter erases around 3-5% of data, is increasing the autocorrelation value as much as COR_{CR}=10 which erases until 9% in some points near the bed.

The autocorrelation of the longitudinal velocity signal is the correlation of the signal with itself. From the derivation of the autocorrelation is obtained the integral time scale, which is the specific period of the vortex with average kinetic energy. Thanks to the frozen vortex theory of Taylor, the characteristic period is translated in the characteristic length of the vortex, defining the integral length scale (L_X). Therefore, an increase of R_{xx} is translated into a growth of L_X, Figure A.9-a, thus larger vortices stand out of the signal while the little ones are removed.

The integral length scale increases with the depth, like the mixing length of Von Karman, thus shorter turbulent structures are expected in the near-bed region, where the correlation is lower. Figure A.9-a plots the variation of L_X by applying filters, showing longer lengths if the percentage of erased data is large. Thus, it means that filters are probably removing information about small turbulent structures, and so they are related to low-COR values and spikes. Not only the Integral length scale but also Taylor and Kolmogorov length scales (Figure A.9-b) are increased by the use of filters.

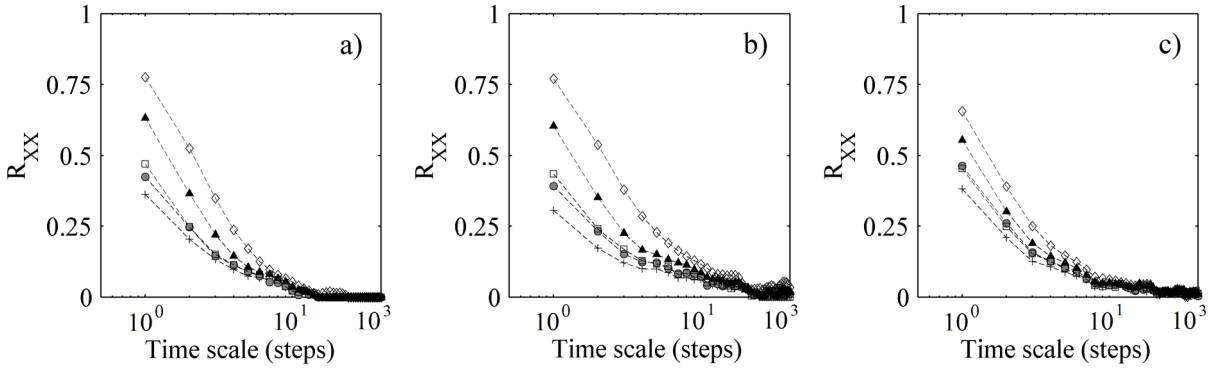

Figure A.8- R_{xx} of the points (a) z/d=0.15, (b) z/d=0.35, (c) z/d=0.70 before and after filtering. Test RG3. *Legend: + OS, ● Despiking filter, □ COR_{CR}=10, ▲ COR_{CR}=20, ◊ COR_{CR}=30.*

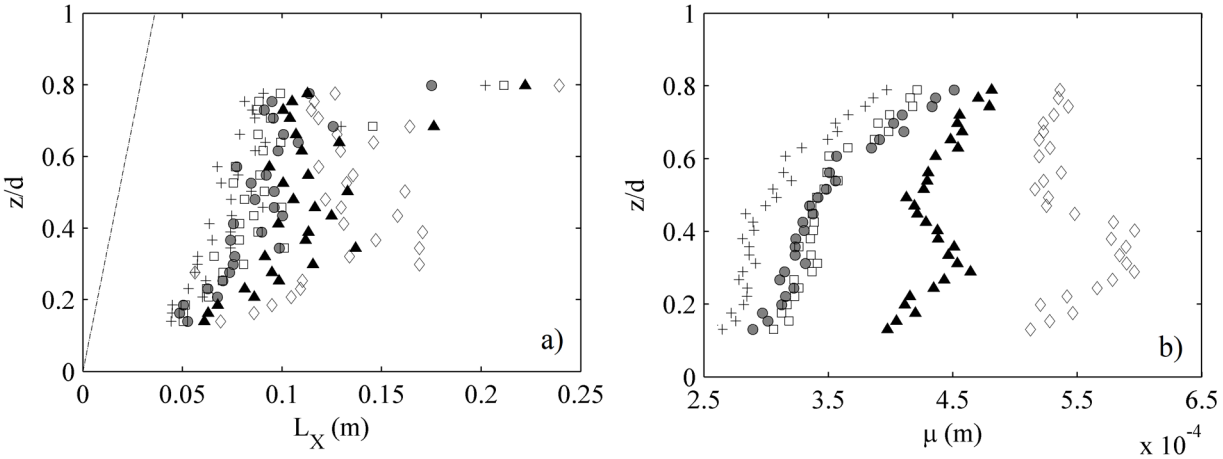

Figure A.9- Vertical distribution of the mean values of (a) L_X (m) and (b) μ (m), before and after filtering. Test RG3. *Legend: + OS, ● Despiking filter, □ COR_{CR}=10, ▲ COR_{CR}=20, ◊ COR_{CR}=30.*

A.3.4 Turbulent Kinetic Energy and Energy Dissipation rate

As commented before, all turbulent characteristics decrease when the spikes and the low-COR values are removed from the signal. Figure A.10 shows the variation of the turbulent kinetic energy (TKE) along the depth profile, as a function of the dimensionless depth (*z/d*), for the OS and the series after the application of the filters. The TKE profile displays a trend of decrease from the bed to the water surface, with a region of constant value around *z/d*= [0.3-0.45].

On the other hand, the energy dissipation rate (ε) is obtained by means of the structure functions (see chapter 4, section 4.9) after the application of filters. Figure A.10 shows the vertical distribution along the dimensionless depth profile (*z/d*) of ε after filtering by the different methods. The modifications are similar to the TKE, where there is a proximity for Despiking, and COR_{CR}=10 and as the critical COR value is increased, the energy contained at small eddies decreases and therefore the ε decreases.

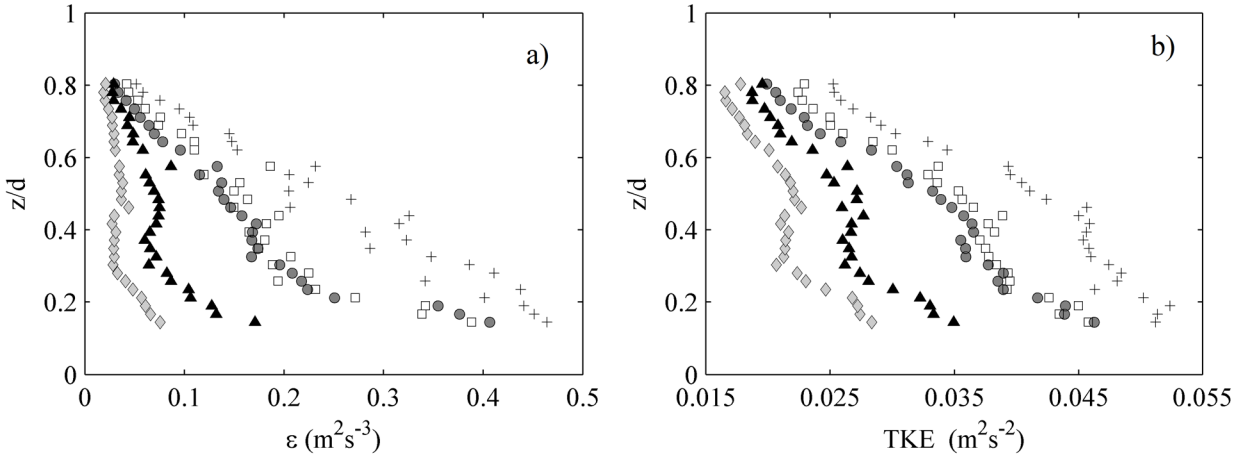

Figure A.10- Vertical distribution of the mean values of (a) TKE and (b) Dissipation rate, before and after filtering. Test RG3. *Legend: + OS, ● Despiking filter, □ COR_{CR}=10, ▲ COR_{CR}=20, ◊ COR_{CR}=30.*

A.3.5 Power Spectral Density

The power spectrum explains how the turbulent energy (per second) of the signal is decomposed in the different frequencies (*f*). The resulting power spectral density (PSD), before and after filtering, is plotted in Figure A.11 as a function of (*f*) for points at a height of *z/d*=0.16 and *z/d*=0.34 (tests RG3).

Comparing the spectrum of the OS to the reconstructed spectra after filtering suggests that values of COR_{CR}>20 can work well for highly turbulent flows since the data shows the expected –5/3 slope up to a frequency of 10-Hz. The spectrums obtained after applying COR_{CR}=30 or COR_{CR}=20 show a decay of energy for frequencies over 4-Hz, the experimental slope of the spectrum becomes steeper, meaning a drop of the energy contained at the lowest frequencies.

On the other hand, applying the Despiking filter and COR_{CR}=10 does not considerably change the PSD in comparison to the OS, due mainly to the low amount of filtered data. Nevertheless, the three patterns seem to follow the universal Kolmogorov slope -5/3 in the range of frequencies [1-3]-Hz and start to separate around 4-Hz, reaching less energy for frequencies over these after filtering.

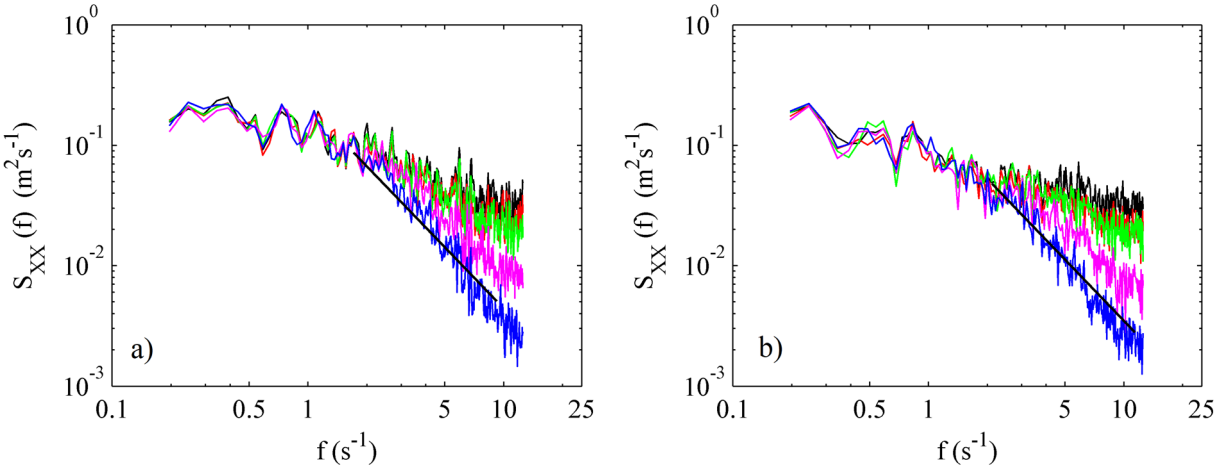

Figure A.11- S_{XX} as function of the frequency (f) before and after filtering, from points at (a) z/d=0.16, and (b) z/d=0.34. Test RG3. *Legend:* ▬ *OS,* ▬ *Despiking filter,* ▬ COR_{CR}*=10,* ▬ COR_{CR}*=20,* ▬ COR_{CR}*=30.*

Figure A.12 illustrates the value of the fitted slopes obtained from the PSD along the depth profile, from the OS, and from each filter. The first slope (Figure A.12-a) covers the range frequencies below 1-Hz and the second the frequencies above 1-Hz. One can see how there are no remarkable changes in the first slope after the application of the filters. However, there are significant variations in the energy for frequencies over 1-Hz.

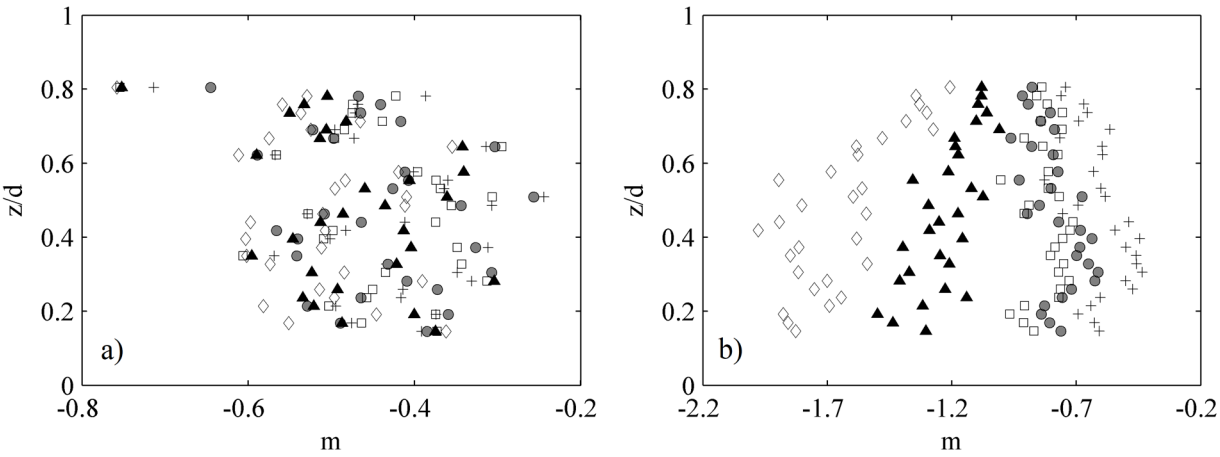

Figure A.12-Vertical distribution of the PSD slope (m) before and after filtering, for frequencies of (a) f<1-Hz and (b) f>1-Hz. Test RG3. *Legend: + OS, ● Despiking filter,* □ COR_{CR}*=10,* ▲ COR_{CR}*=20,* ◊ COR_{CR}*=30.*

Focusing on the second slope in Figure A.12-b, where usually starts to appear the universal Kolmogorov slope (Inertial range), and the lowest values of the slope are always obtained for the OS. Therefore, more energy is contained in the vortices, but the results do not match with the theoretical of -5/3 predicted by Kolmogorov. After the application of the filters, the most similar slope to the theoretical was the one obtained from the critical value of COR of 30. The results after Despiking and COR_{CR}=10 yield similar profiles.

It is important to emphasize that although the spectrum of the series after the COR-SNR filter with a COR_{CR}=30, fits well the slope of -5/3, the significant amount of filtered (>50%) data can distort other results related to the history of the velocity signal.

A.4 Effects on the quadrant analysis

The concept of “bursting turbulence” was presented by Kline (1967) and since then great has developed in structures in the turbulent boundary layer and its applicability in the entrainment phenomenon. Burst events are divided into four quadrants, 1st quadrant ‘Q1’ (u’>0, w’>0) named outward interactions, 2nd quadrant ‘Q2’ (u’<0, w’>0) called ejections, 3rd quadrant ‘Q3’ (u’<0, w’<0) named inward interactions and the 4th quadrant ‘Q4’ (u’>0, w’<0) named as sweeps. The concept "bursting turbulence" is closely related to the generation of turbulent energy and the Reynolds shear stress in the near-bed region and entrainment process, Grass (1983); Williams et al. (1989). The spurious spikes in the ADV signal, obtained in rough beds, have a high influence in bursting turbulence. Quadrant analysis is useful for the study of turbulent structures through bursting events, see chapter 5; hence, this section analyzes the effect caused by the application of filters.

A.4.1 Quadrant time fraction

The quadrant time fraction (QTF) analyzes the time fraction TF (decimal fraction) that the velocity time series, each pair of (*u’w’*) spend in each quadrant. Figure A.13 depicts the vertical distribution of the QTF of the four quadrants (outwards-Q1, ejections-Q2, inwards-Q3, and sweeps-Q4) obtained from the OS and filtered velocity series, for the experiment RG3.

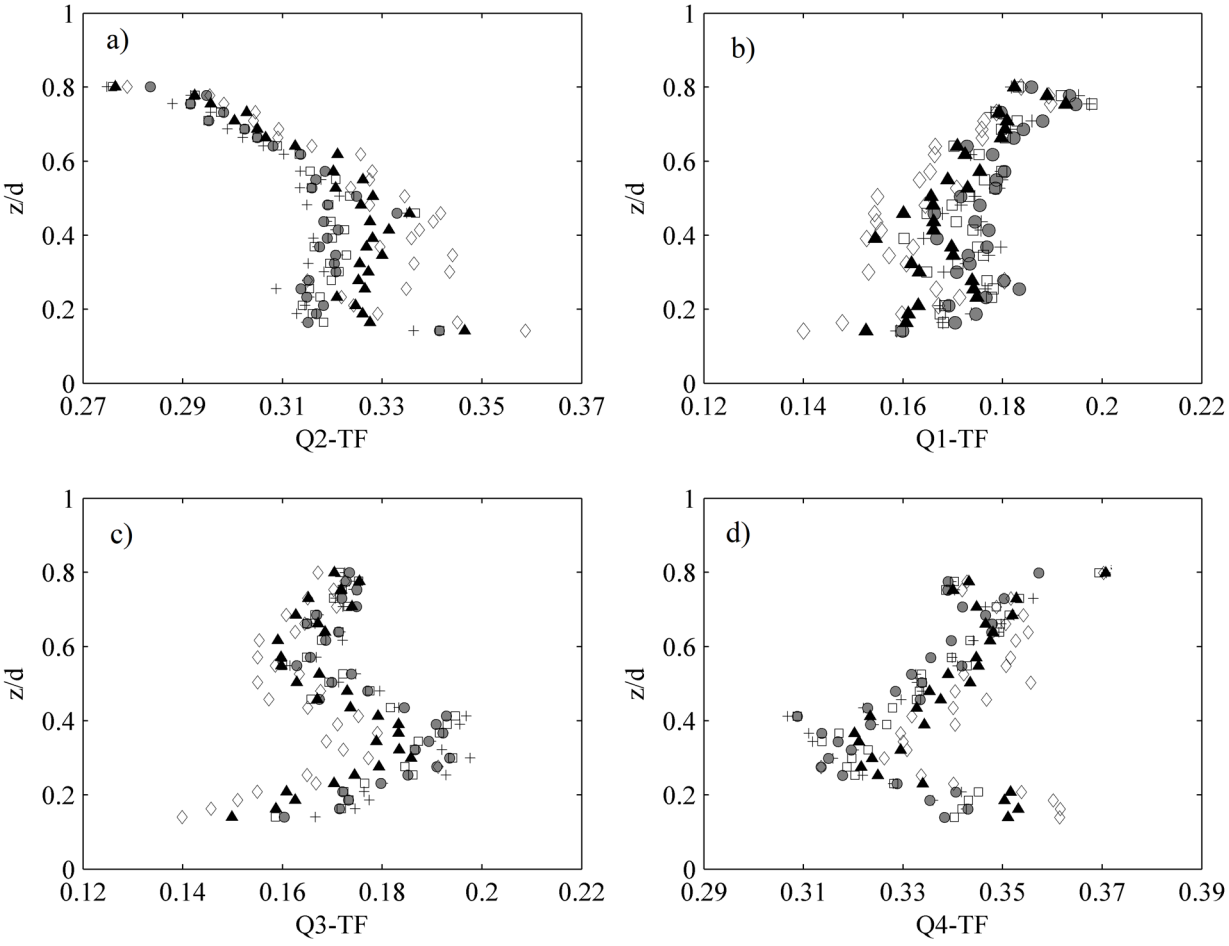

Figure A.13- Vertical distribution of the QTF of quadrants (a) Q2, (b) Q1, (c) Q3 and (d) Q4, before and after filtering. Test RG3. *Legend: + OS, ● Despiking filter, □ COR_{CR}=10, ▲ COR_{CR}=20, ◊ COR_{CR}=30.*

It was seen in Figure A.7 that Reynolds shear stress ($\overline{-\rho u'w'}$) decreased by the use of filters, probably caused by the elimination of spikes or low-COR values, especially at the near-bed region. That suggests that the removed data must belong to Q2 and Q4 since they contribute to increasing the value of $\overline{-\rho u'w'}$. However, Figure A.13 shows that Q2 and Q4, ejections and sweeps respectively, increase after filtering at expenses of the Q1 and Q3, which decrease. All filters produce changes between quadrants, these being more remarkable as the COR_{CR} increases. The Despiking filter modifies the values very little, which makes sense due to the low amount of removed data.

Given that the Q2 and Q4 contribute positively to the Reynolds shear stress and the other two, Q1 and Q3, do it negatively, it seems reasonable to think that $\overline{-\rho u'w'}$ must increase after filter application; unlike it was in section A.3.2. In order to clarify this issue, Figure A.14 shows the contributions to the $\overline{-\rho u'w'}$ of each of the quadrants. The sum of the fractional contributions of all four quadrants is the unity. On the one hand, both Q1 and Q3 represent the negative contribution to the Reynolds Stress. The contribution of the Q1 is higher in the near-bed region and decreases as getting close to the water surface. The negative contribution of this quadrant (makes lower the Reynolds shear stress) increases as the filtered data increases (decrease the negative value). In the case of the Q3, the contributions are steadier along the depth, and likewise the Q1, the negative contribution increases with the percentage of filtered data.

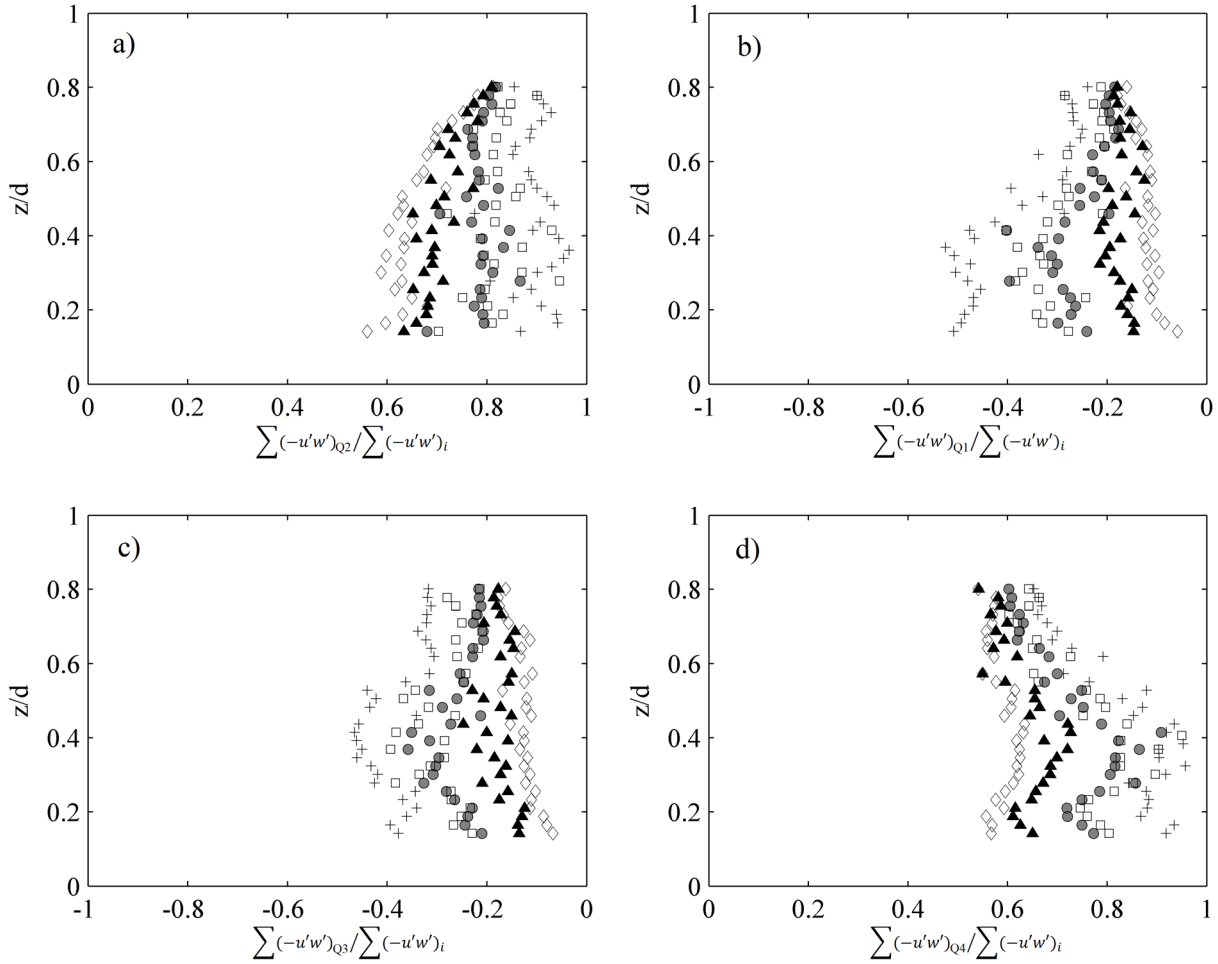

Figure A.14- Vertical distribution of the contribution to $\overline{-\rho u'w'}$ of quadrants, (a) Q2, (b) Q1, (c) Q3 and (d) Q4, before and after filtering. Test RG3. *Legend: + OS, ● Despiking, □ COR_{CR}=10, ▲ COR_{CR}=20, ◊ COR_{CR}=30.*

On the other hand, the contributions to $-\overline{\rho u'w'}$ of Q2 and Q4 decrease with as the percentage of filtered data increase. Thus, after filtering Q1 and Q3 have less effect on the Reynolds shear stress, they are controlled by the events on quadrants Q2 and Q4. Therefore, despite Q2 and Q4 gained importance, the lessening of the peak values yields a decrease of the Reynolds Stress(Figure A.7). That is to say; the Reynolds shear stress decrease could be due to the decrease of the sweep and ejection extreme ($u'w'$) values rather than their QTF since peak velocities tend to belong to these quadrants.

Figure A.15 depicts the quadrant maps of three points from the test RG3. The application of filters produces the elimination of the peak values, mostly placed in the Q2 and Q4 especially for points near the bed. The figures show that the Despiking filter removes the spikes, those placed out of a specific zone, while COR-SNR filters also remove data inside the ellipse and leave some points outside, thus, spikes not always have a low correlation. These issues are deeply studied in Appendix B.

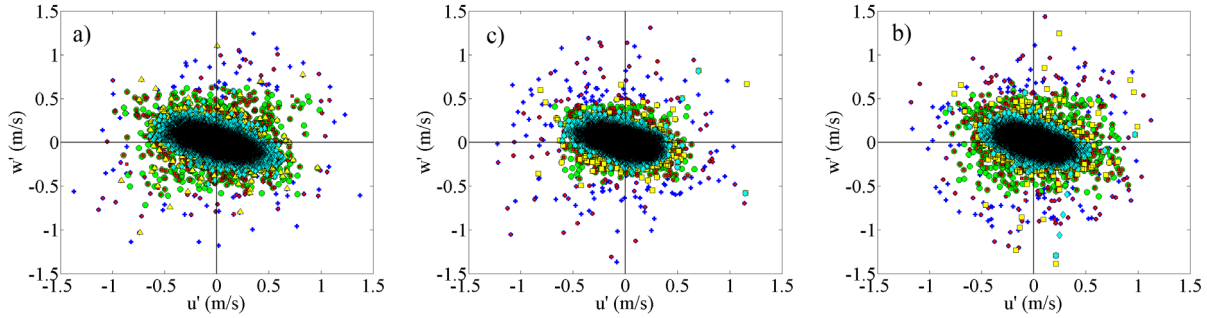

Figure A.15-Turbulent map of points at height of (a) z/d=0.16, (b) z/d=0.35 and (c) z/d=0.70, before and after filtering. Test RG3. *Legend,* + *OS,* ● *Despiking filter,* ■ COR_{CR}=10, ▲ COR_{CR}=20, ♦ COR_{CR}=30.

A.4.2 Phase-state maps

The Phase-state map is the representation of the streamwise velocity increment (Δu) that occurs from one burst event to the next one, as a function of the streamwise fluctuation velocity (u') (see chapter 5, section 5.7). The horizontal axis represents u' while the vertical axis characterizes Δu. In the figures below, the Poincare maps of RG3 for three points are represented, before and after filtering.

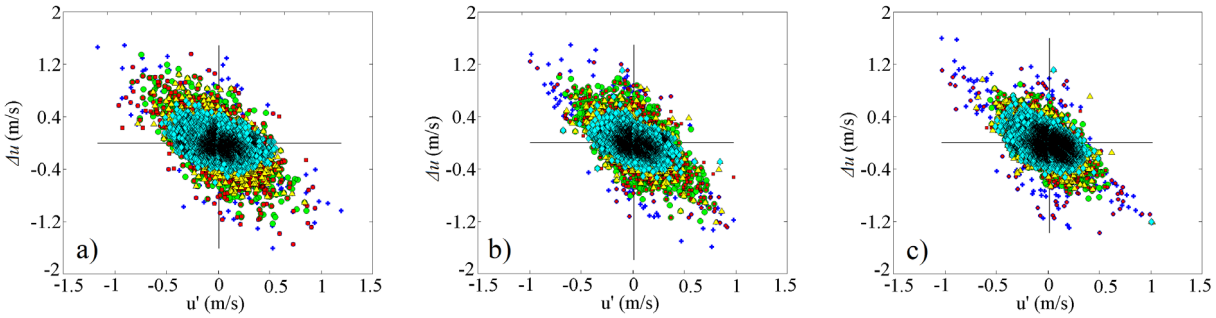

Figure A.16- Poincare Maps of the points (a) z/d=0.16, (b) z/d=0.35 and (c) z/d=0.70, before and after filtering. Test RG3. *Legend,* + *OS,* ● *Despiking filter,* ■ COR_{CR}=10, ▲ COR_{CR}=20, ♦ COR_{CR}=30.

After the application of the filters, it is reduced the Δu between events, thus the fitted slope (m) of the point cloud becomes plainer. Figure A.17 shows the evolution of the mentioned slope along the profile and demonstrates that the application of a filter with COR_{CR}>10 makes decrease this slope; therefore the accelerations between burst events are reduced. Moreover, it changes the pattern followed by the slope along the depth profile.

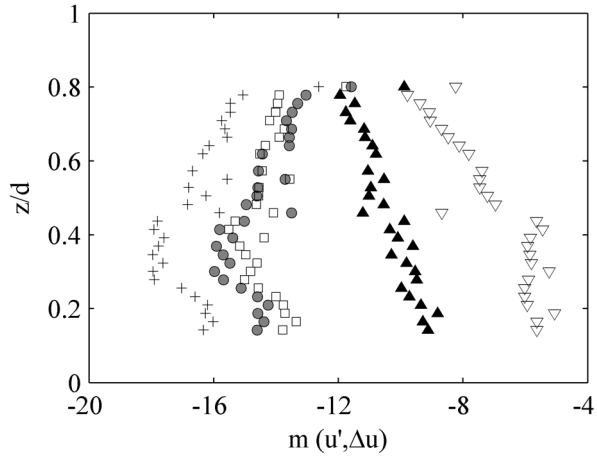

Figure A.17- Vertical distribution of the fitted slope (m) from the points cloud (*u', Δu*), before and after filtering. Test RG3. *Legend: + OS, ● Despiking filter, □ COR_{CR}=10, ▲ COR_{CR}=20, ◊ COR_{CR}=30.*

A.4.3 Trips between quadrants

Regarding the importance of the quadrant events and their sensitivity to filters, the distribution over the time of these events has been studied. The most likely next event (or quadrant) from each quadrant has been studied, called as "trip" (see chapter 5, section 5.6.1) the TF of each "trip" has been calculated.

Figure A.18 shows the vertical distribution along the dimensionless depth of the trips TF (%) obtained from each velocity series (before and after filtering) for the experiment RG3. The figure shows that the most common trip, with the highest percentage, is from Q4 to Q4 (Q4-Q4), increasing also with the depth, followed by Q2 to Q2 (Q2-Q2), in this case decreasing with the depth. In the original series (OS), for example, the sum of these two trips, among the 16 possible trips, represents 30% of the total time. Therefore, when the velocity drops into the Q2 or Q4, the most likely next quadrant is itself, as seen in chapter 5. As the COR_{CR} increases these most common trips also increase reaching a TF of 50% for COR_{CR}=30. The least frequent trips are from Q1 to Q3 (Q1-Q3) and Q3 to Q1 (Q3-Q1) and remaining constant through the depth. Then the Q2 and Q4 are not just the most likely but also the longest events since the probability of staying in the same quadrant is higher than in the other two quadrants.

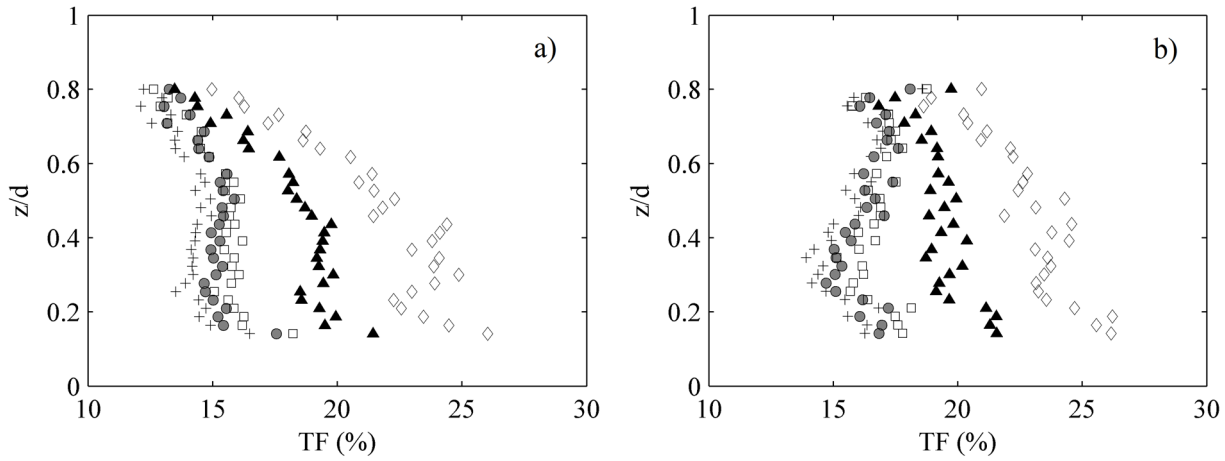

Figure A.18- Vertical distribution of the trip time-fraction, between quadrants (a) Q2-Q2 and (b) Q4-Q4, before and after filtering. Test RG3. *Legend: + OS, ● Despiking filter, □ COR_{CR}=10, ▲ COR_{CR}=20, ◊ COR_{CR}=30.*

The application of filters changes the distribution of the trips between quadrants. The trips with less probability of occurrence do not considerably change; however, the TF of the Q2-Q2 and Q4-Q4 trips are more sensible to filters, where the increase becomes notable by the application of COR_{CR} over 10. These variations on the trips also have other repercussions, as it is demonstrated in the next section.

A.5 Effects on the pulse analysis

Flow motions at a region near the wall are "far from being completely chaotic in nature" revealing a definite "sequence of ordered motions", Clifford et al. (1991), Grass et al. (1991).

One pulse is considered here as the uninterrupted time spent in the same quadrant before moving to the next one, i.e., the time of no quadrant change. This concept is further discussed in chapter 6, where the implications on the turbulent characterization are deeply studied. However, the concept is called in this section in order to validate the pulse concept with the current analysis.

The question addressed in this section is, are the variations seen in the time fraction of the quadrants and trips breaking apart the pulses? The answer is yes. The filter effects on the Pulse Duration Histograms (PDH) and pulse-velocities are investigated in this section.

A.5.1 Pulse duration histograms

Figure A.19-a represents the PDH, i.e., the distribution of the TF that each pulse duration T_p represents on the velocity time series. In the figure, three different points of the experiment RG3 are depicted. The horizontal axis represents the T_p measured by time intervals (Δt) with $1\Delta t$=0.04 s, and the vertical axis the TF that they represent in the data series.

The original series (OS) shows a similar pattern for the three points no matter the height in the depth profile they have. The application of all the filters shows a decrease of the short pulses (T_p=$1\Delta t$), from [38-42]% (OS) to [15-24]% (COR_{CR}=30), and an increase in the TF of pulses over 3Δt of duration (T_p >3Δt). The effect becomes more accentuated for points near the bed, due to the percentage of data removed by the criterion of COR_{CR} being higher. For this reason, the variations from the OS are more significant as increases the COR_{CR} value. When spikes are removed from the signal by the Despiking filter, the histograms are less modified; however, considering that the "bad" data removed for this filter is very low, the variations may not be ignored.

Another way to represent the distribution of the TF of the different pulse durations (T_p) is depicted in Figure A.19-b. The figure shows the vertical distribution along the depth of the TF of pulse durations (from T_p=1Δt to T_p =5Δt) obtained from the OS and after filtering by the different methods. From the figure, it is noticeable how pulses with T_p =1Δt (blue lines) are intensely decreased in the region near the bed (z<4 cm=. Pulses of duration T_p =2Δt also suffer a reduction, albeit less substantially. The rest of the pulse-durations (T_p >3Δt), are increased along the depth. Regarding quadrant-events, the filter effects are much more evidenced in time-wise (pulse durations do show a considerable modification) than in TF (Figure A.13).

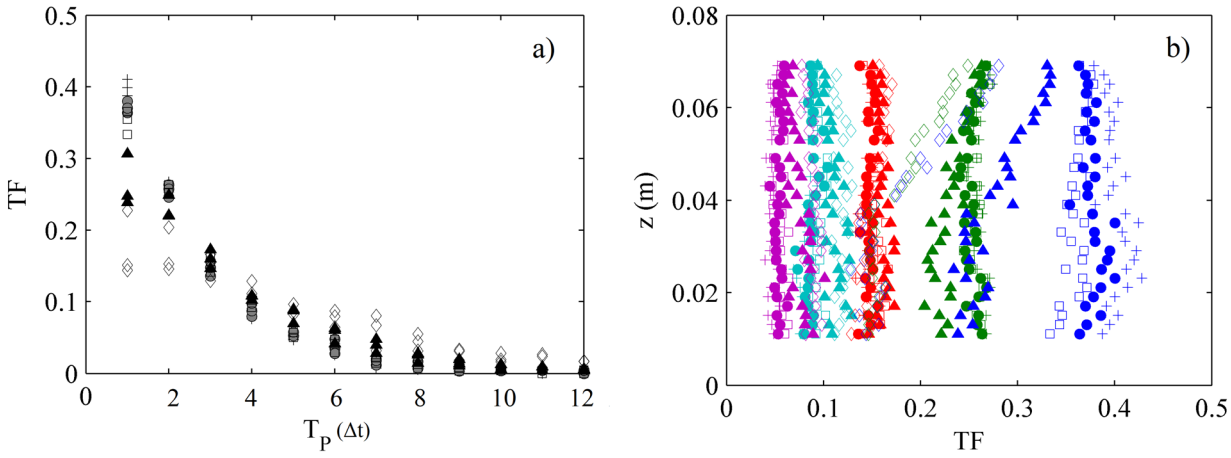

Figure A.19- (a) PDH of the point at height *z/d*=0.16, *z/d*=0.40 and *z/d*=0.64, and (b) Vertical distribution of the TF of the T_p, before and after filtering. Test RG3. Legend Markers*: + OS, ● Despiking filter, □ COR_{CR}=10, ▲ COR_{CR}=20, ◊ COR_{CR}=30. Legend colors (b)* ● T_p=1Δt, ● T_p=2Δt, ● T_p=3Δt, ● T_p=4Δt, ● T_p=5Δt.

Figure A.20 divides the PDH of Figure A.19-a by quadrants for all the filters and the OS, that is to say, the TF of each T_p is plotted only for the quadrant where they are placed, in this case only for the point (*z/d*=0.16) to avoid redundancy. The pulses from quadrants Q2 and Q4 are by far the most affected by the filters, increasing notably the TF of pulses longer than 2Δt (T_p >2Δt), reaching up above the TF of the shortest ones (T_p=1Δt). Although the PDHs of Q1 and Q3 are also affected, the most common pulses are still those of duration T_p=1Δt, even after the filter application.

It was seen that those modifications on the pattern distributions are more evidenced at points near the bed, as shown in Figure A.20, while for points above *z/d* >0.4, are much stable for the four quadrants, due to the less amount of data filtered. The Table A.2 quantifies these changes for three different points in the profile.

It is possible to represent the values from Table A.2 in a figure where all points along the depth profile are characterized just as in Figure A.19-b. Figure A.21 shows the vertical distribution of pulse durations from T_p=1Δt to T_p =5Δt, same as in Figure A.19-b but divided by quadrants. The figure demonstrates graphically that the pulses more affected by the application of filters are the pulses of duration 1Δt from the Q1 and Q3 whose have more probability by the way. However, in all quadrants this decrease is noticeable.

Pulse duration itself does not represent completely the effects of applying filters because also the mean and maximum velocity inside the pulse is changed. Figure A.22 represents on the quadrant map the pulses of duration over 6Δt (T_p >6Δt). In some cases, pulses longer than T_p>16Δt appear in the signal after the application of the filters (they were not before). These new long pulses have been represented in the figure by green points for the COR-SNR filter COR_{CR}=20, and red points in case of COR_{CR}=30. The more increases the COR_{CR}, the longer the pulses appear. Looking at the case of COR_{CR}=30, the pulses of T_p over 6Δt have increased, and the mean velocity of these pulses is lower than for the ones from the OS.

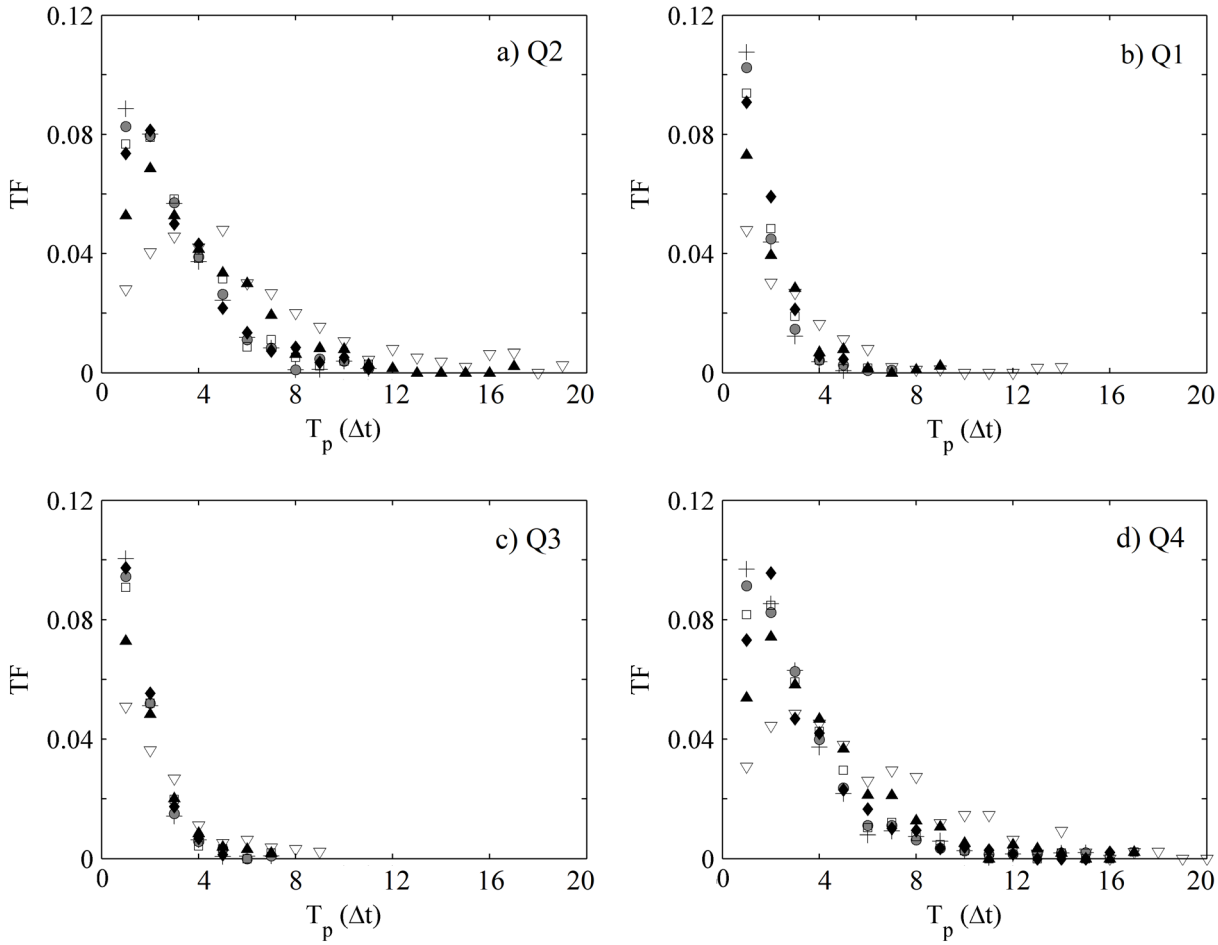

Figure A.20- PDH separated by quadrant (a) Q2, (b) Q1, (c) Q3 and (d) Q4, of a point *z/d*=0.16 of test RG3, before and after filtering. *Legend: + OS, ● Despiking filter, □ COR_{CR}=10, ▲ COR_{CR}=20, ◊ COR_{CR}=30.*

Table A.2- Differences between duration pulses by applying the filters.

Point (z/d)	Δt	OS	Despiking	COR_{CR}=10	COR_{CR}=20	COR_{CR}=30
	1	39,4	37,1	34,3	25,3	15,7
	2	26,1	25,9	26,4	23,1	15,1
0,14	**3**	14,7	14,9	15,6	16,0	14,8
	4	8,5	8,9	8,9	10,4	11,5
	5	4,7	5,6	6,6	8,2	10,2
	1	42,3	39,4	36,9	26,5	14,8
	2	25,7	24,7	24,7	21,6	15,1
0,40	**3**	14,3	14,7	15,7	17,3	15,0
	4	7,0	6,9	9,1	11,0	11,5
	5	4,6	5,1	5,8	7,9	9,5
	1	40,5	38,3	38,9	37,7	28,9
	2	27,5	26,5	27,6	26,3	24,0
0,70	**3**	14,7	15,0	14,9	16,3	18,0
	4	8,3	8,5	8,7	9,9	10,3
	5	4,1	4,6	4,0	5,1	7,1

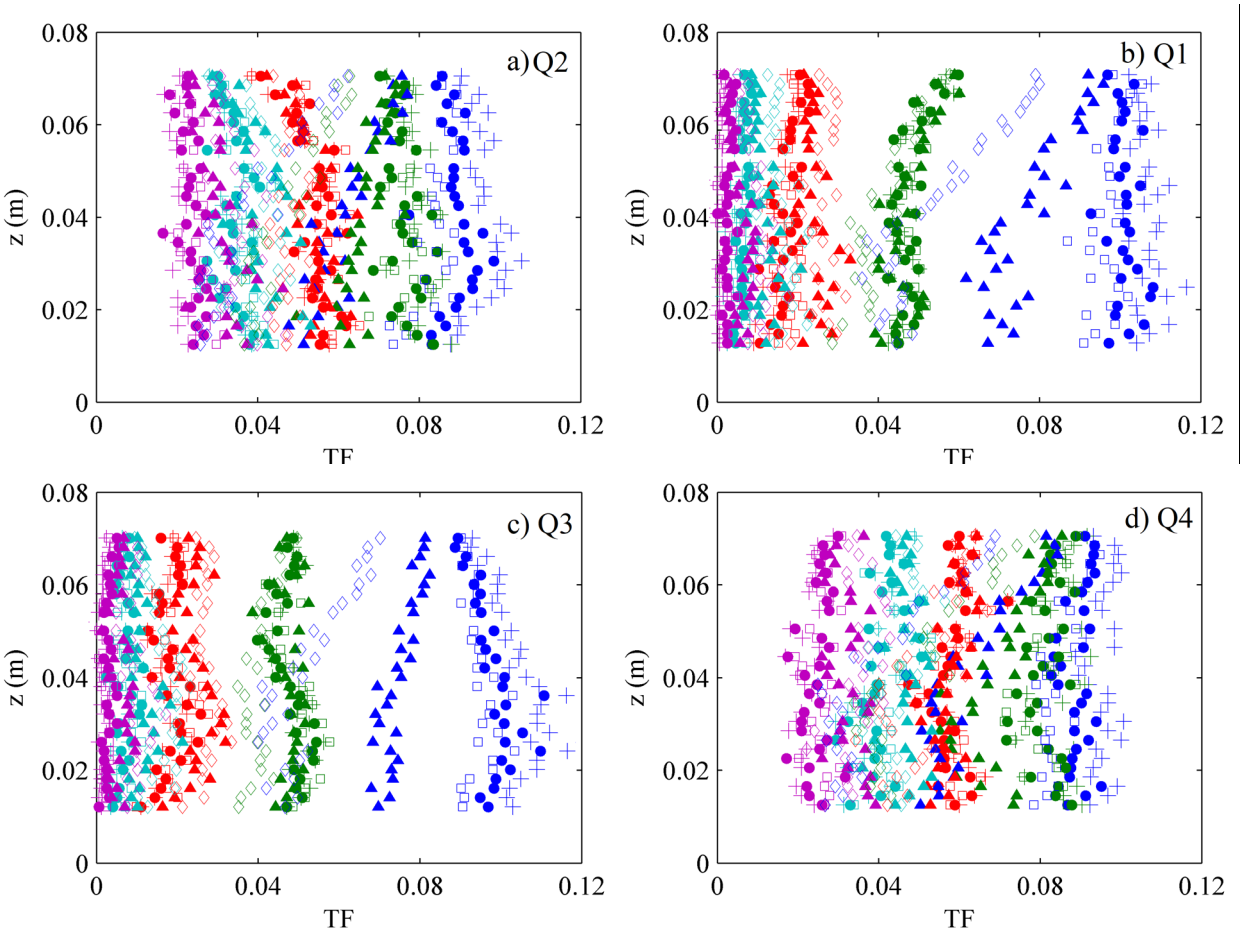

Figure A.21- Vertical distribution of the time fraction of the different pulse durations separated by quadrants (a) Q2, (b) Q1, (c) Q3 and (d) Q4. Test RG3. *Legend Markers, + OS, ● Despiking filter, □ COR_{CR}=10, ▲ COR_{CR}=20, ◊ COR_{CR}=30. Legend colors, ● T_p=1Δt, ● T_p=2Δt, ● T_p=3Δt, ● T_p=4Δt, ● T_p=5Δt.*

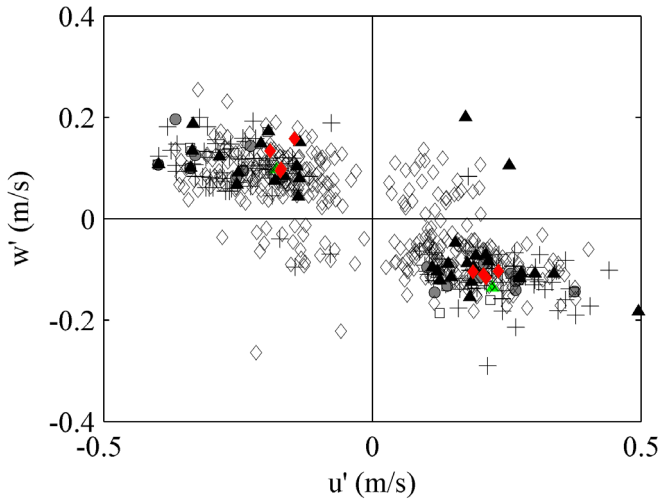

Figure A.22- Turbulent maps of the max (*u'w'*) value inside pulses of T_p=[6-16]Δt. Test RG3, z/d=0.16. *Legend, + OS, ● Despiking filter, □ COR_{CR}=10, ▲ COR_{CR}=20 (green if T_p >16Δt), ◊ COR_{CR}=30 (red if T_p >16Δt).*

A.5.2 Implications for the sediment entrainment

The pulse duration is an essential characteristic of a velocity time series, and it represents the time that $\overline{-\rho u'w'}$ is acting in the same direction. Recent studies have evidenced that not mean forces but the instantaneous values of forces are related to sediment transport. Moreover, the magnitude of the applied forces, i.e., Drag Force and Reynolds shear stress per unit area, is vital to the entrainment process, (Celik et al. (2010) and Celik et al. (2013) among others). Then, if the velocity signal changes time-wise, this forces also changes and its intervals of application (see chapter 7).

For example, if the Reynolds shear stress ($\overline{-\rho u'w'}$) are considered to be applied by blocks of time, when they are applied in one direction, the block has the duration of one pulse in one quadrant. The effect induced by the filters can affect severely the distribution of the T_p and, consequently, the impulse of the force. The concept of impulse is explained in chapter 7, and it will not be investigated in this part of the thesis. Nevertheless, effects on this physics are essential for understanding why the application of filters and bad data has been intensively studied throughout the present appendix.

The next figures represent the vertical distribution of the average impulse exerted by pulses (Reynolds Stress by packets) obtained from the OS and from the ones obtained after filtering. Figure A.23 represents the total impulse, counted by blocks of pulses. On the other hand, Figure A.24-a and Figure A.24-b represent the vertical distribution (before and after filtering) of the positive contribution to the impulse (pulses inside Q2 and Q4) and negative contribution (pulses inside Q1and Q3) respectively.

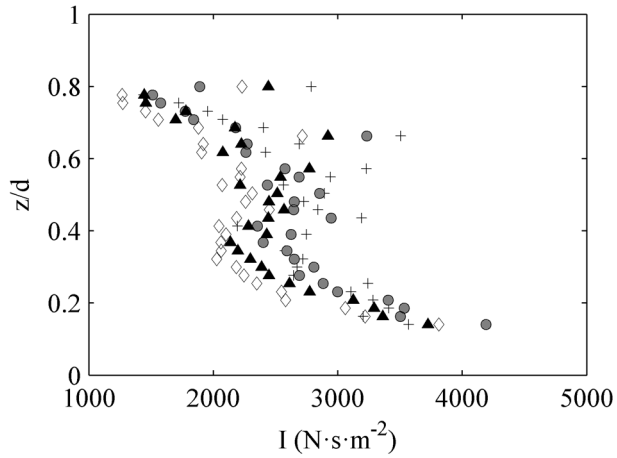

Figure A.23- Vertical distribution of the mean Impulse value before and after filtering, Test RG3. *Legend, + OS, ● Despiking filter, □ COR_{CR}=10, ▲ COR_{CR}=20, ◊ COR_{CR}=30.*

In the case of the total impulse (Figure A.23), the fact of removing the most energetic points by filtering the data, decrease the total impulse exerted by the flow. Although filters increase long pulses, the mean velocity is decreased, and all peak values are removed. For the positive (Figure A.24-a) and negative (Figure A.24-b) contributions, both of them are decreased in value, however, the negative contribution is more decreased and reduced until constant value, around -500-N·s/m^2 for COR_{CR}=30, disappearing the trend of a higher value in the near-bed region. In the case of the positive contribution, the value is reduced all along the depth profile. The reason is that the negative impulse is exerted by the Q1 and Q3 where the T_p=1Δt pulses, the most energetic ones, are more decreased than in the other two (Q2 and Q4).

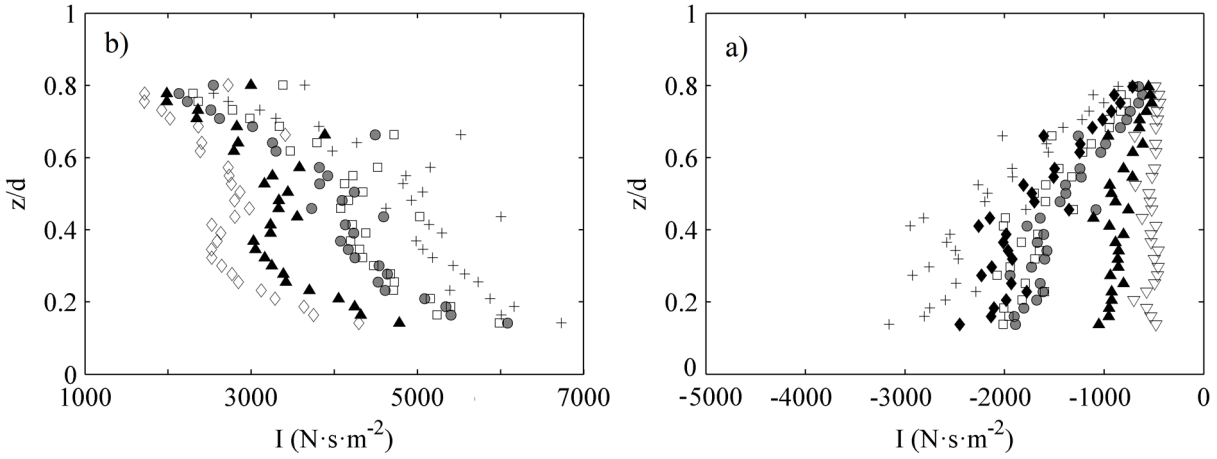

Figure A.24- Vertical distribution of the mean values of (a), Positive impulse and (b), negative impulse, before and after filtering. Test RG3. *Legend as for Figure A*.23.

A.6 Discussion

The high energy is erased and biased to the mean value. Turbulent properties such as Reynolds shear stress, turbulent intensities, TKE, energy dissipation rate, are intensely decreased by the use of filters. Conversely, the autocorrelation and therefore the Integral length scale, and both the Taylor and Kolmogorov scales are increased.

The quadrant analysis shows that events on quadrants Q2 and Q4, ejections and sweeps respectively, increase after filtering at the expense of the Q1 and Q3, which decrease. Nonetheless, despite Q2 and Q4 gained importance, the lessening of the peak velocities yields a decrease of the Reynolds shear stress. All filters produce changes of the QTF; these being more remarkable when increases the COR_{CR} value. The Despiking filter changes less the values than the other filters, which makes sense due to the low amount of removed data.

The trips with less probability of occurrence do not considerably change; conversely, the TF of trips Q2-Q2 and Q4-Q4 are more sensible to filtering. The effects on the PDH are also notable, with a decrease of the short pulses (T_p=1Δt), and an increase of pulses of duration T_p >3Δt. All these effects become more accentuated in the near-bed region, due to the percentage of data removed by the criterion of COR_{CR} being higher.

Changes in the pulse duration distribution have a repercussion on the sediment entrainment hypothesis made in this thesis (chapter 7). The value of the impulse exerted by pulses of Reynolds shear stress is lessened, owing to the removal of the most energetic velocities. This fact made us reconsider the use of the filters since the effects on the velocity signal affect deeply the data analysis carried out in this thesis. The arbitrary assumption of a subjective COR_{CR} value and the effects that have on the results show that the filter should not be used without prior study of its suitability.

The power spectrum obtained after the application of filters differs substantially from the OS spectrum, especially for frequencies over 1-Hz. Contrarily, the spectrums for frequencies f<1-Hz barely changes. The more increases the COR_{CR}, the more data is replaced, as a consequence the PSD fitted slope becomes steeper for frequencies over 1-Hz, enlarging the range where the theoretical -5/3 is reached by the spectrum. Therefore, less energy is contained in the highest frequencies.

The universal –5/3 slope is achieved in a broader range of frequencies when applying a COR_{CR}>20. However, it is important to emphasize that it is at expenses of the big amount of removed/filtered data (>50%) which can distort other results related to the history of the velocity signal. As a conclusion, the use of filters enlarge the range where the spectrum fits the theoretical proposed by Kolmogorov, but a significant amount of filtered data discredit the veracity of the velocity time series.

From this filter evaluation arise two questions, first; maybe the data detected by the filters cannot be considered wrong, and maybe the configuration of the device is affecting the results. From these deductions, Appendix B and Appendix C are dedicated to these questions.

APPENDIX B. LOW-QUALITY DATA EVALUATION

Table of Contents

Appendix B: Low-Quality Data Evaluation

B.1 Introduction

The filters have proven to eliminate valuable data and deviate all turbulent parameters towards a less energetic version of themselves, changing the turbulent nature of the flow. Therefore, a proper question is if the data detected by the filters is certainly wrong. Thus, the analysis questions the suitability of filtering data in highly turbulent flows.

The first part of this appendix has the purpose of shedding light on the low-COR values and spikes detected by the proposed filters, by means of the study of some turbulent properties. The second part intends to evaluate the method of replacement that better respects the nature of the flow, in the case of needing the application of filters.

B.2 Characteristics of the "bad" data

In the next paragraphs, the RG3 has been analyzed and specifically the point z/d=0.16. It has been distinguished between the spikes detected by the Despiking filter (4.48% of the OS), and the low-COR velocities (COR<30) (48.55% of the OS). The remaining 46.97% (after the removal of the spikes and COR<30 values) corresponds to "good" data.

B.2.1 Relationship of the spikes with the low-COR values

The characteristics of the spikes and the low-COR values are evaluated more deeply for the purpose of understanding their nature and relation between each other. Figure B.1 provides an interval of the longitudinal velocity series of the point z/d=0.16 (RG3), where the velocities detected as spikes are highlighted in red and the velocities with low-COR values (COR<30) are highlighted in green.

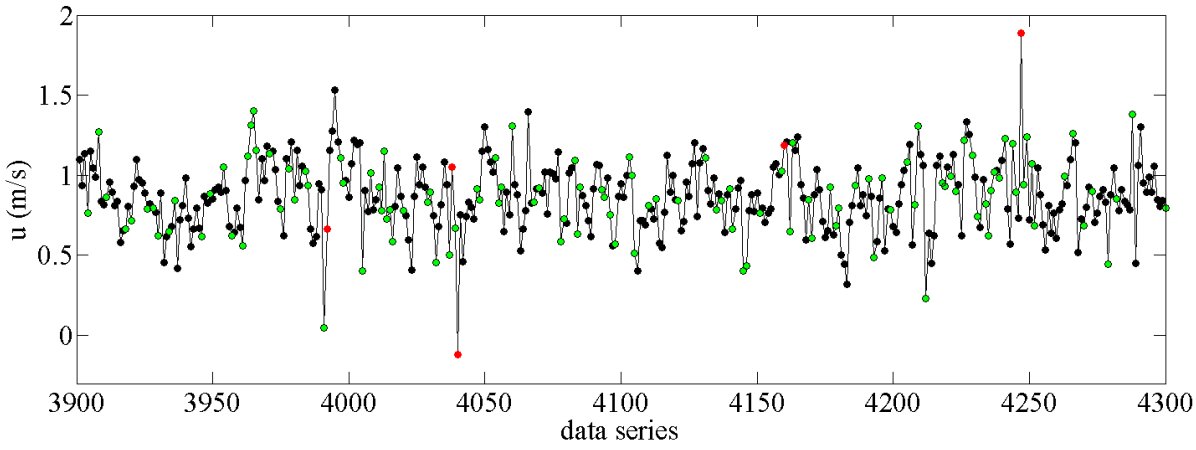

Figure B.1- Velocity series (z/d=0.16, RG3). *Legend,* ● *OS,* ● *Spikes,* ● *COR<30.*

At first sight, neither the spikes nor low-COR values show the behavior of the spikes presented by Goring & Nikora (2002), Figure B.2, where the spikes are biased from the mean value due to aliasing. Figure B.1 shows that only some of the spikes coincide with the low-COR values. Therefore, some spikes tend to have low-COR and SNR values, but not all of them.

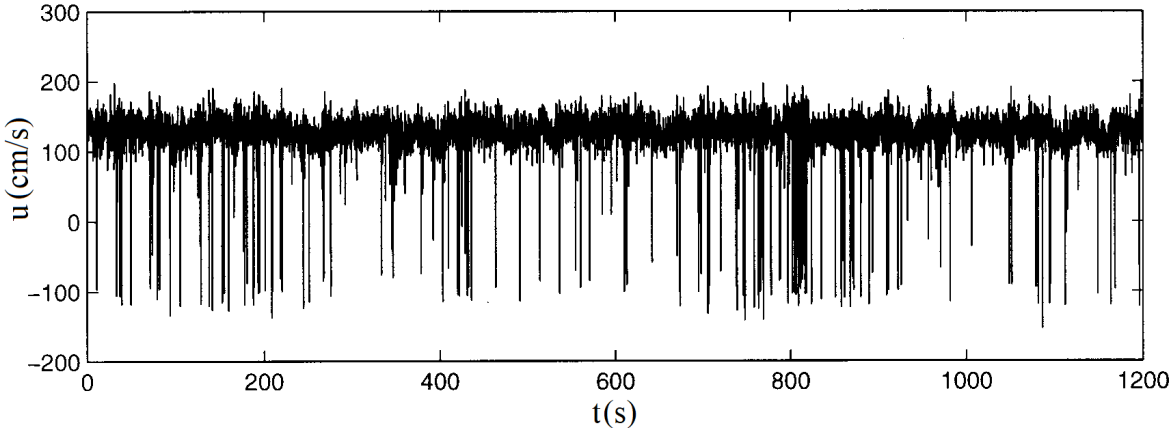

Figure B.2- Velocity data series contaminated with spikes. From Despiking Acoustic Doppler Velocimeter Data. Derek G. Goring & Vladimir I. Nikora (2002).

Figure B.3 shows the histogram of the COR values of three points (*z/d*=0.16, *z/d*=0.35 and *z/d*=0.7), test RG3. A positive skewness in the near-bed region that becomes negative at points far from the bottom is appreciable. In these histograms, the portion of spikes of each group overlaps, represented by the black bars. Although fewer spikes are removed from the lowest values of COR, the spikes detected by the Despiking filter tends to belong to the full range of COR values, demonstrating that spikes may not be linked with the lowest levels of COR. On the other hand, the spikes have high enough value of SNR, around 48-52 in most cases, higher than the minimum of 15 recommended by Wahl (2000), Figure B.4.

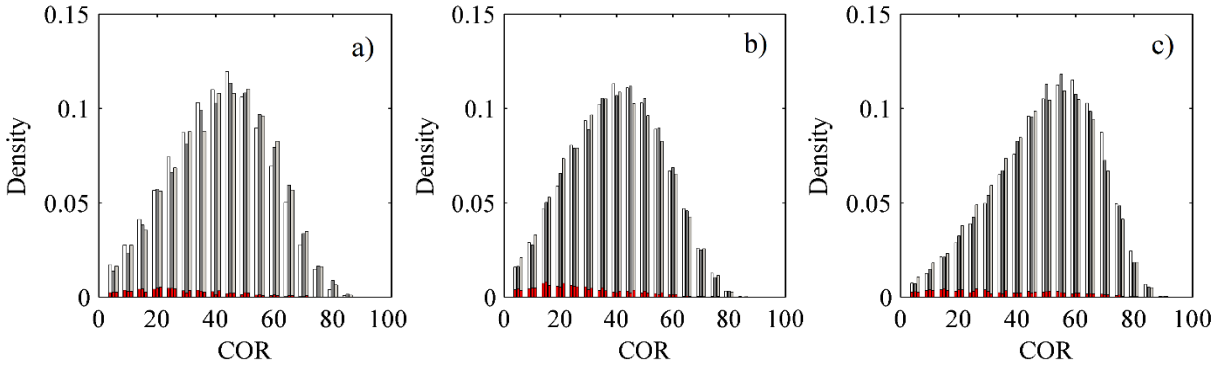

Figure B.3- COR histograms of the points (a) z/d=0.16, (b) z/d=0.35 and (c) z/d=0.7. Test RG3. *Legend,* COR_x, COR_y, COR_z, *Spikes.*

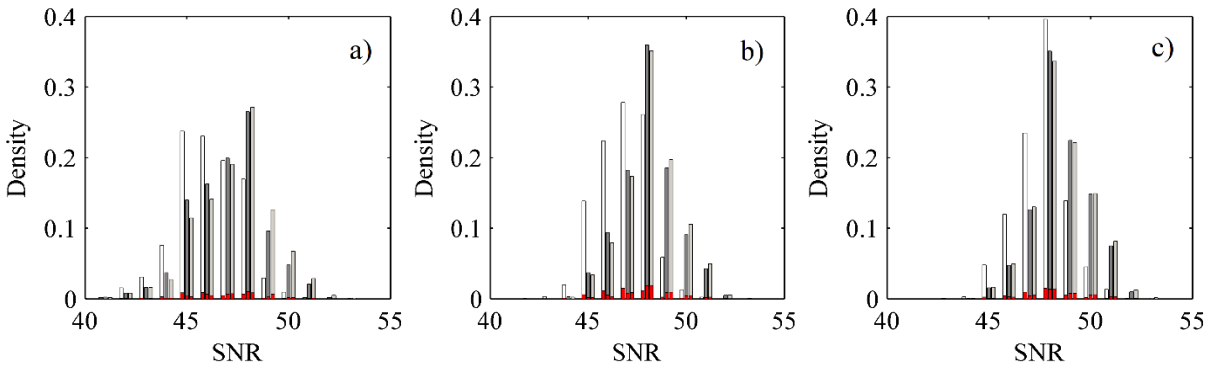

Figure B.4- SNR histograms of the points (a) z/d=0.16, (b) z/d=0.4 and (c) z/d=0.7. Test RG3. *Legend,* SNR_x, SNR_y, SNR_z, *Spikes.*

B.2.2 Quadrant Analysis

The time fraction (TF) that a pair of *u'w'* remains in each quadrant is very important and defines the type of flow. A significant difference in these time fractions between the "good" and the "bad" data, considering both spikes and low-COR values separately, gives substantial information about the behavior of the signal.

Figure B.5-a illustrates the histograms of quadrant time fraction QTF of each quadrant for the "good" and "bad data". The histograms belong to a point located at *z/d*=0.16 (RG3). The histograms show that the differences between the QTF are moderate for quadrants Q3 and Q4, inward interactions and sweeps respectively. However, spikes and low-COR values display a higher percentage of Outward interactions (Q1-TF) and a decrease of the ejections (Q2-TF), in comparison with the "good" data, being the differences more noticeable in the case of spikes.

It can be assumed that the low-COR values and the "good" data have almost the same pattern of QTF. Although the case of the spikes presents more differences than the low-COR values, it has to take into account that the percentage of spikes is always moderate in the sample, as in the studied point that represents 4.48 % of the data thus it does not have a significant impact on the results.

Figure B.5-b plots the turbulent maps (*u'w'*) of the points considered as "good" data, the spikes, and low-COR values (COR<30). The spikes tend to appear at high turbulent velocities, i.e., at the perimeter of the cloud, while the low-COR values are more spread in the map.

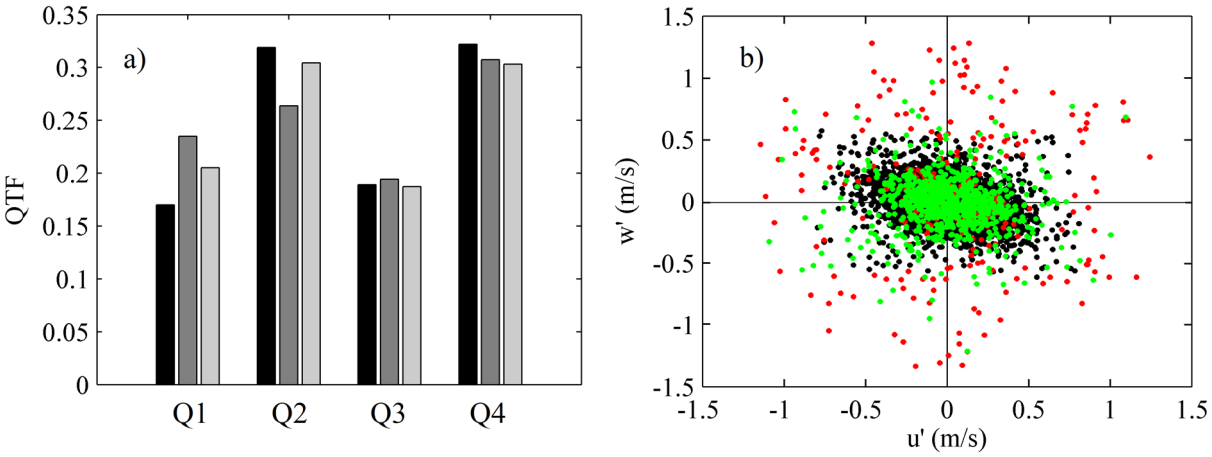

Figure B.5- (a), QTF histograms, and (b) Quadrant map superposition. *Legend (a),* ■ *"Good" data,* ■ *Spikes,* ■ *COR<30. Legend (b)* ● *"Good", data,* ● *Spikes,* ● *COR<30.*

Figure B.6 shows the quadrant time fraction (QTF) of each group of data as a function of the dimensionless depth (*z/d*). Spikes and COR<30 values have a higher percentage of Outward interactions (Q1) in the near-bed region and show a trend of decrease as they distance themselves from the bed, in contrast to the trend of the "good" data which increase in value from the bottom to the surface.

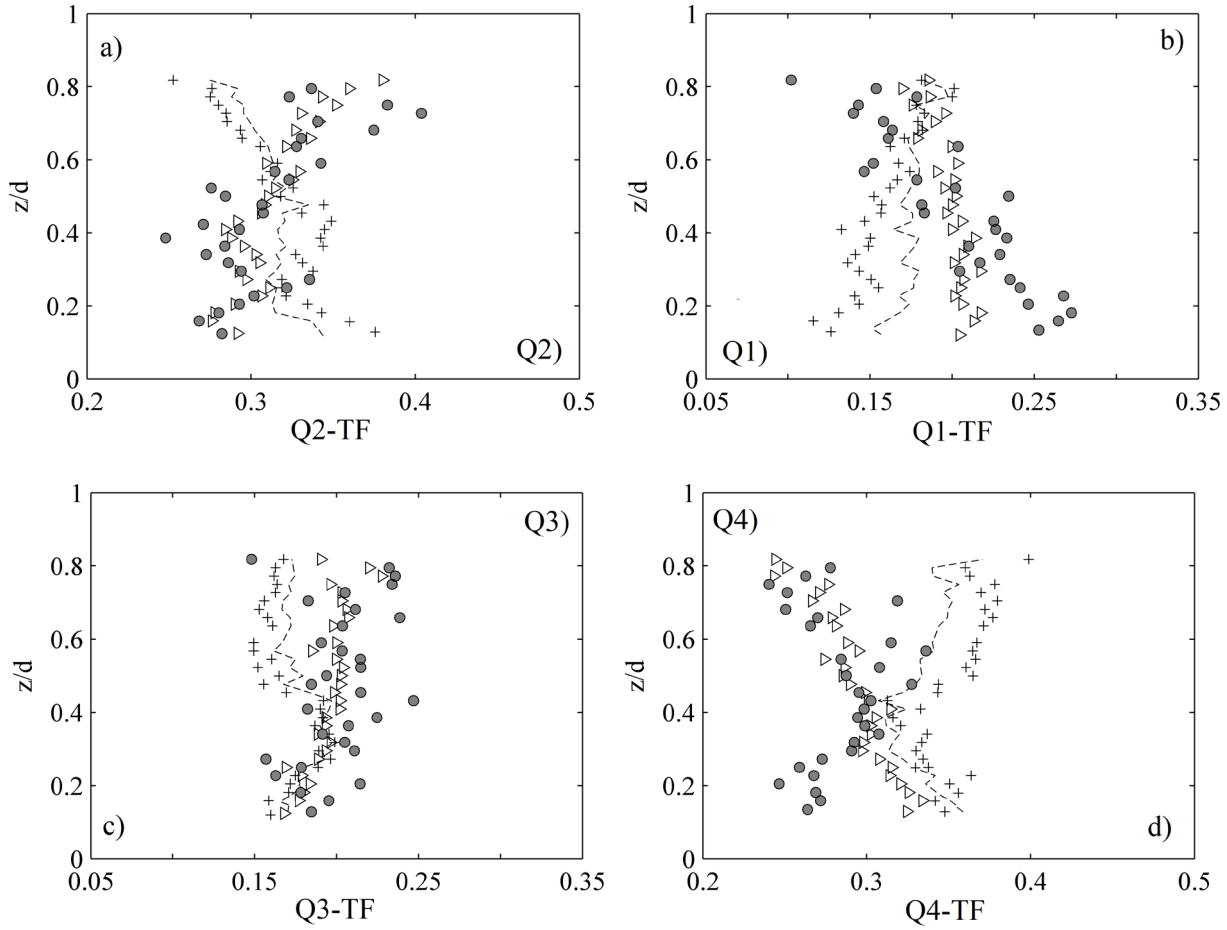

Figure B.6- Vertical distribution of the QTF of "good" and "bad" data fro, quadrant, (a) Q2, (b) Q1, (c) Q3 and (d) Q4. Test RG3. *Legend, ··· OS, + "Good" data, ● Spikes, ▹COR<30.*

The trend of the OS has a stable value along the profile, in the middle of the "good" and "bad" data. Opposite behavior have the ejections (Q2) which tend to decrease with the depth for the "good" data and increase in the case of spikes and COR<30. The Q3-TF (inward interactions) from all groups of data have similar values in the near-bed region, however, the trends start to separate as of z/d=0.4, decreasing the Q3-TF of the "good" data" while increasing that of the "bad" data. The same applies with the sweeps (Q4), the Q4-TF is similar near the bed z/d<0.4 for the "good" data and the COR<30, but from that height (z/d=0.4), Q4-TF increase for the "good" data and decrease for the COR<30. The spikes in the near-bed region are characterized by the similar Q1-TF and Q4-TF. Although the percentage of spikes is similar in the depth profile, at the region z/d<0.4 the spikes tend to belong to Q1, and beyond that height, to the Q2. The time fraction of the COR<30 is similar to the spikes with more moderate behavior.

B.2.3 Longitudinal velocity increments

In turbulence, the streamwise velocity increments (Δu), i.e. the variation of velocity occurs from one burst event to the next one, are very important since they define the structure functions defined by Kolmogorov to characterize the flow. The trend of the distribution of the Δu will show if the spikes and the low-COR values have the same nature than the data considered "good".

Figure B.7-a represents in the turbulent map the velocity fluctuations of longitudinal (*u'*) and vertical velocity (*w'*) axis from the "good" data, spikes and COR<30. "Good" data tend to be concentrated in the origin of coordinates. Both, spikes and COR<30 appear in the entire turbulent map, including the furthest areas on the map.

Figure B.7-b shows the probability of the distribution of the Δu of the "good" data, spikes and the COR<30 values obtained from the OS. In that figure, it has been distinguished between the OS (dashed black line), the "good" data, i.e. data series without the "bad" data (solid black line), the spikes (solid red line) and the low-COR values (solid green line). The distribution of the Δu of the "good" data, in comparison with that obtained from velocities with COR<30, shows a similar trend, however, the density becomes higher when close to zero, and lower for Δu>0.1 m/s. Therefore, velocities with COR<30 tend to have higher Δu and more density in the tails. On the other hand, the distribution of the Δu of the spikes (red line) has heavy tails, which makes sense since the methodology of spike detection is based on the phase-state maps. Although the spikes tend to have high Δu, the effects on the OS are negligible due to the low fraction of spikes (4.48%).

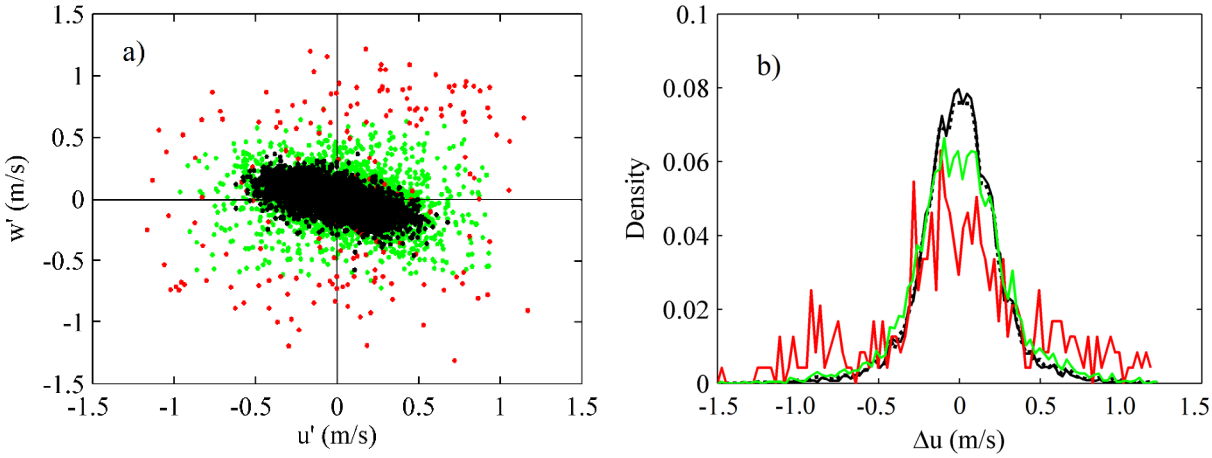

Figure B.7- Comparison between "good" and "bad" data. Figure (a), turbulent map. *Legend (a),* ● *Good data,* ● *Spikes,* ● *COR<30.* Figure (b), histograms of the longitudinal velocity increments. *Legend (b),* ···· *OS,* ▬ *Good data,* ▬ *Data COR<30,* ▬ *Spikes (Despiking).*

B.2.4 Pulse duration histogram

The pulse duration histogram (PDH) was introduced in Appendix A as the distribution of pulses as a function of their duration, considering a pulse as the uninterrupted time spent in one quadrant. This concept is further discussed in chapter 6, where the implications on the turbulent characterization are deeply studied. However, the concept is called in this section in order to validate the pulse concept with the current analysis. The target here was to detect whether the spikes and the low-COR values belong to a certain pulse duration (T_P).

In Figure B.8, the PDH obtained from the different groups of data (OS, Spikes, COR<5 and COR<30) are depicted for a point at height of z/d=0.16 of the test RG3. The vertical axis represents the number of pulses of a certain duration (N_P (T_P)) divided by the total number of pulses in the velocity series (N_{PT}).

The figure shows that both, spikes and data with COR<30, tend to have a higher percentage of the shortest pulses (T_P=1Δt). To be more precise, the spikes have a TF, defined as $N_P(T_P)/ N_{PT}$, of pulses of duration T_P=1Δt of 48.4%, the data of COR<5 have a TF of 49.6%, and data with COR<30 have 46.0%, in front of a TF of 36.9% of the "good" data.

The TF of short pulses (T_P=1Δt) from groups of data with different COR values, although not included in Figure B.8, were studied, and it was observed that the proportion of pulses of T_P=1Δt decreased proportionally as the COR value decreased, suggesting that low-COR values tend to be part of long pulses. This can be seen between COR<30 and COR<5), with 46% and 49.6% of pulses T_P=1Δt respectively. It is noticeable that the longest pulses found in the case of "good" data and COR<30 are pulses of T_P=12Δt, thus, the velocity remains in the same quadrant no more than 0.48 sec (12/25) Hz. Conversely, spikes are not present in pulses longer than 6Δt (T_P>6Δt).

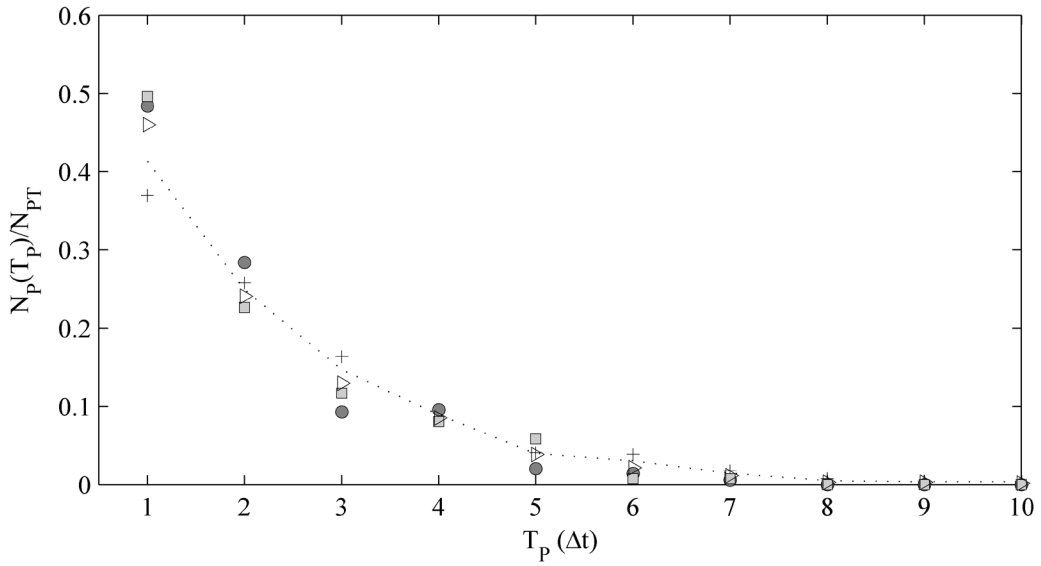

Figure B.8- Comparison between PDH from "good" and "bad" data. *Legend, ··· OS, + "Good" data, ● Spikes, □ COR<5, ▷ COR<30.*

The PDH of the burst events can be defined by each quadrant of occurrence, i.e., differentiating in which quadrant the pulse occurs. Figure B.9 depicts the PDH obtained from each quadrant of occurrence. In the figure, it is noticeable that distribution of pulses from the COR<30 data, is now close to the "good" data while the spikes have a particular behavior.

From the quadrant analysis it was noticed that spikes and low-COR values tend to appear in the Q1, above all in the near-bed region z/d<0.4, and the same can be deducted from the PDH of the quadrants. While the PDH of COR<30 is similar to the "good" data, although, with less amount of short pulses (T_P=1Δt), the spikes have a particular behavior. The spikes tend to appear in pulses of one and two periods of duration (T_P<2Δt). For example, the TF of the 1Δt pulses in the Q1 represents 14.55% of the total spikes, in front of 8.91% that represent the "good" data and 11.61% for COR<30 values (Figure B.9-b). In the remaining quadrants, spikes, COR<30 and "good" data show fewer differences.

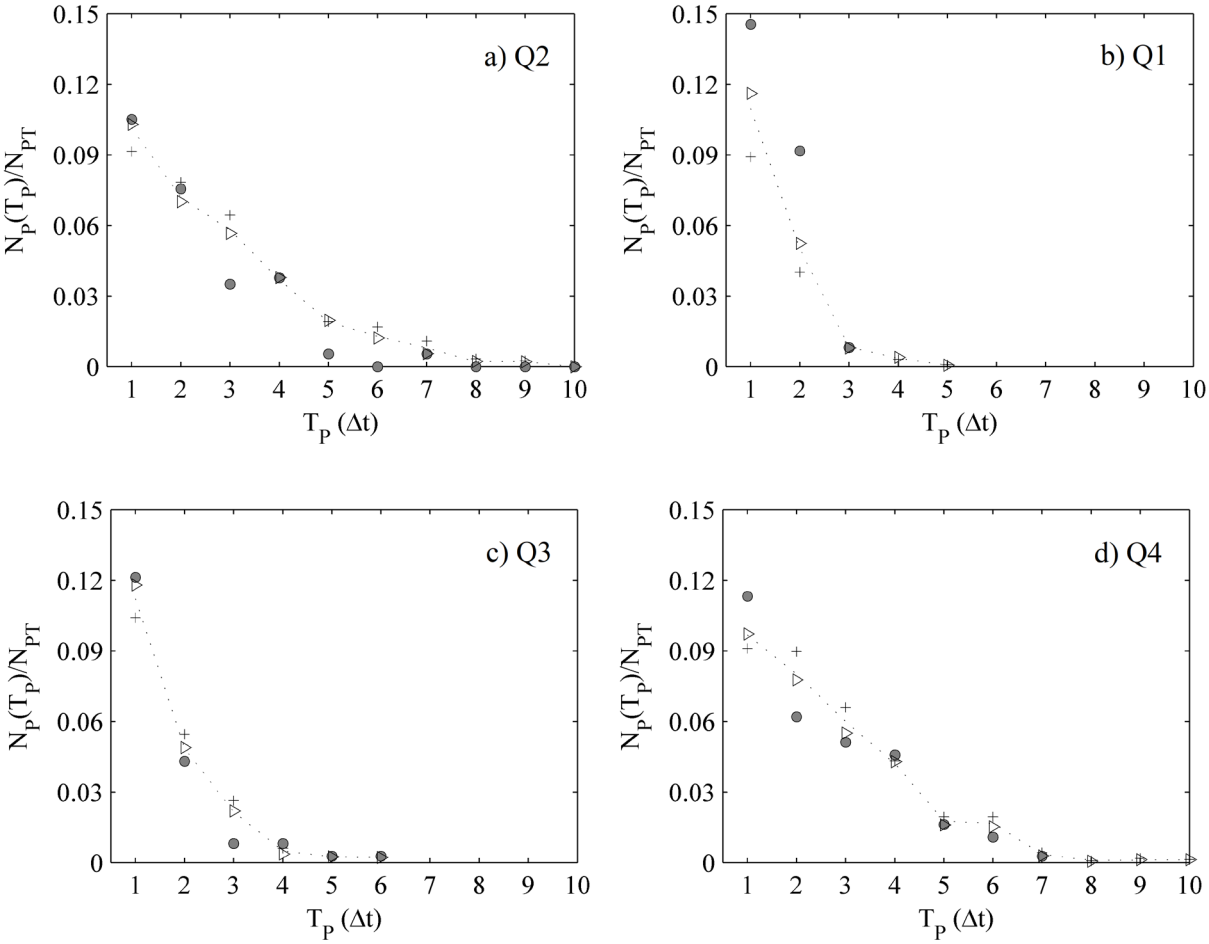

Figure B.9- Comparison between "good" and "bad" bad of the PDH separated by quadrants, (a) Q2, (b) Q1, (c) Q3 and (d) Q4. RG3, point z/d=0.16. *Legend, ····· OS, + "Good" data, ● Spikes, □ COR<5, ▷ COR<30.*

B.3 Methods of replacing "bad" data

The observed from the analysis of the effects of the filters gave rise to the two questions that are assessed in this appendix. The first question was the suspicion that the low-COR values should not be considered as "bad" data, examined in the last section. The second is the suitability of the replacement used in the first instance, the linear interpolation, which is assessed in this section.

The linear interpolation as replacement method used in appendix A has evidenced some uncertainties, taking away the highly turbulent nature of the flow and the high fluctuations of velocity. As a result, the interpolated value always falls around the mean velocity, and therefore all peaks of high intensity and energy are removed. Cea et al. (2007) suggested that the linear interpolation could be a good replacement method in highly turbulent flows, as long as the time integral scale is of the same order as the sampling time step. In the present Appendix, only the test RG3 is analyzed in detail. The time integral scale of tests RG3 is between 0.04 s and 0.06 s, similar to the sampling time step (1/25 Hz=0.04 s). Therefore the linear interpolation is in principle suitable for this experiment.

Goring & Nikora (2002) suggested using an interpolation by a third-order polynomial using 12 points on either side of the spike. They assumed that it was able to erase the peak velocity and preserve the behavior of the signal for sampling frequencies from 25 Hz to 100 Hz.

In order to evaluate the effects of the replacement process, three different interpolation methods have been evaluated, and a glimpse of the results are shown in this section. The replacement methods considered are; *a*) substitution by linear interpolation; and interpolation by a third-order polynomial considering, *b*) 12 points at each side of the value, Goring & Nikora (2002), or *c*) 2 points at each side.

In this part of the section, also the tests RG3 (point z/d=0.16) have been analyzed. The groups of velocity have been ordered as follows. It has been distinguished between the spikes (4.48% of the OS), detected by the Despiking filter, and the low COR velocities (COR<30) (48.55 % of the OS), both comprising the "bad" data group. The group of velocities from the OS not detected by the latter two filters is named "good" data (46.97% of the OS). On the other hand, the velocities obtained after the replacement by the three methods, or (53.03% of the OS), have been isolated, for the purpose of studying the characteristics of the new data in comparison with the original values.

Not all the characteristics evaluated during the research are revealed here, just some aspects considered relevant to understand how the replacement affects the results.

B.3.1 Evaluation of the replacement

In high turbulent flows, the use of an iterative Despiking filter could have some disadvantages when applied to a group of spikes since the replacement process could introduce new spikes. Therefore, it is more convenient to apply the replacement after the spikes have been detected, Cea et al. (2007), Islam & Zhu (2013). Despite this, some spikes can be introduced by the interpolation, and therefore the ability of the replacement process can be checked.

As a simple evaluation, the data was filtered by despiking, and the spikes were replaced by the different methods (*a*, *b* and *c*). The analyzed point in this section corresponds to a height of z/d=0.16, from the test RG3. The replacement of the spikes by the different methods may create some other spikes, and therefore the ability of the replacement process can be checked. The resulting data series was filtered again afterward to see if the spikes were sufficiently reduced in number. The proportion of spikes in the analyzed series was 4.48%, from this only 2.63 % has also COR<30. The percentage of spikes was reduced to 1.034% after the replacement by method *a*, until 1.08 % after the application of method *b*, and until 1.27% after method *c*. Therefore, the two first methods are more capable of erasing the spikes.

From the spikes (4.48%) only 2.63 % has also COR<30, meaning that 2.36% is the part that can be reduced by filtrating by COR_{CR}=30. The ability of the replacement methods to improve the low-COR values cannot be assessed since the replacement does not change the COR value. However, it can be assessed if this replacement introduces new spikes. The data series was filtered by the COR_{CR}=30 criteria and the "bad" data (48.55%) replaced by the different methods. After that, the Despiking filter was passed, and the number of detected spikes after the filtrating were 2.08 (method *a*), 1.91 (method *b*), and 3.07% (method *c*). Therefore, also the two first methods reduce more the number of spikes.

The COR value after filtration could not be evaluated since the value is given by the apparatus, from the measures made at 10 MHz, and the replacement does not change these. For a more in-depth understanding of the replacement methods, the substitution of "bad" data with COR<30 is used since the quantity of "bad" data is higher than the spikes, and the effects of the replacement can be better evaluated.

Figure B.10 shows an interval of the signal velocity and its modification by each replacement. The blue line represents method *a*; method *b* is represented by the green line, and finally method *c* by the red line. Method a, linear interpolation, takes away the high turbulent nature of the flow and the high fluctuations of the velocity. As a result, the interpolated value always falls around the mean velocity, therefore, all the high intensity and energy is removed, as it was seen in Appendix A.

It is appreciable that, although method *b* better respects the turbulent nature of the velocity series than method *a*, in which all turbulent pulsations are lost, it still obviates most of them, and consequently the characterization of the flow changes considerably.

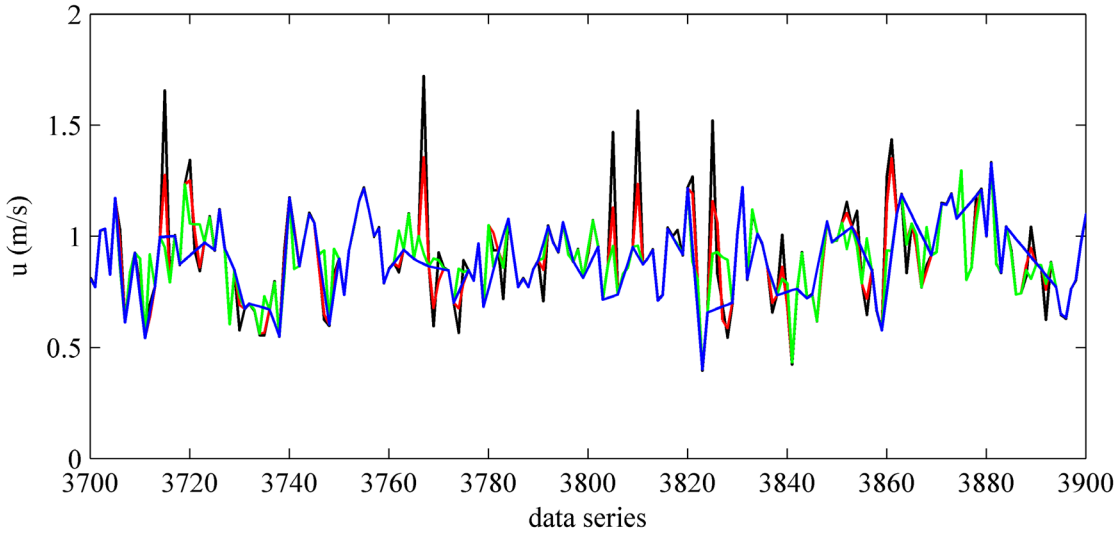

Figure B.10- Velocity data series before and after the different replacement methods. *Legend,* ___ *OS,* ___ *Linear replacement (a),* ___ *third-order Polynomial with 12 points each side, (b)* ___ *third-order Polynomial with 2 points each side (c).*

Figure B.10 displays that method *c*, third-order and 2 points, obtains turbulent maps (*u'w'*) and Poincare maps (*u', Δu*) more similar to the OS before filtering. The other two methods decrease all instantaneous velocities; therefore, the cloud of points in the turbulent maps becomes less spread out.

B.3.2 Longitudinal Velocity increments

Figure B.11-a represents in the turbulent map the streamwise velocity fluctuations (*u'*) in the horizontal axis and vertical velocity fluctuations (*w'*) in the vertical axis from the "good" data, "bad" data" and the replaced data from the three methods. The "good" data tend to be concentrated in the origin of coordinates, in contrast to the "bad" data that is more spread on the map. It is noticeable that the replacement method *c* includes higher fluctuations than the other two, which confines the filtered points close to the origin of coordinates.

Figure B.11-b shows the distribution of the *Δu* from the three series of filtered data, using the three mentioned methods. The replaced data (53.03% of the OS) corresponds to the sum of the spikes and COR<30. Method *a* is represented by the blue line, method *b* by the green line, and method *c* by the red line. The pink line represents the histogram of the "bad" data before replacement.

The *Δu* probability distribution of replacement method *c*, using a third-order polynomial with 2 points at each side of the data, respects the trend of the *Δu* from "bad" data (pink line) better than the other

two. Methods *a* and *b* obtain a high density of $\Delta u \sim 0$ m/s. It is very consistent that the last method achieves the same distribution that "good" data, or data with higher COR.

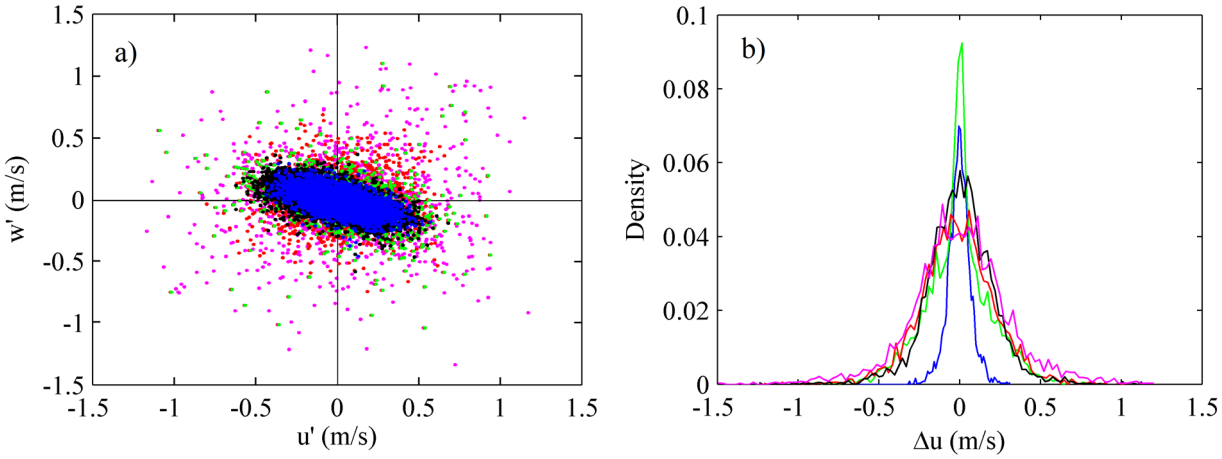

Figure B.11- Comparison between the "good" data and data after replacement. Test RG3, point z/d=0.16. Figure (a), turbulent map. *Legend (a),* ● *"Good data",* ● *"Bad" data,* ● *(method a),* ● *(method b),* ● *(method c)*. Figure (b), histograms of longitudinal velocity increments. *Legend (b),* ▬ *"Good data",* ▬ *"Bad" data,* ▬ *Linear replacement (a),* ▬ *third-order Polynomial with 12 points each side, (b)* ▬ *third-order Polynomial with 2 points each side (c).*

B.3.3 Pulse Duration Histogram

In Figure B.12 it is depicted the resulted PDH from the "good" and "bad" data, together with the obtained from the replaced data by the three methods. The "bad" data has a higher percentage of short pulses (T_P=1Δt) than the "good" data. It is noticeable that the longest pulses found in both series are pulses of T_P=13Δt. Thus, the velocity remains in the same quadrant no more than 0.48 seconds (13/25 Hz).

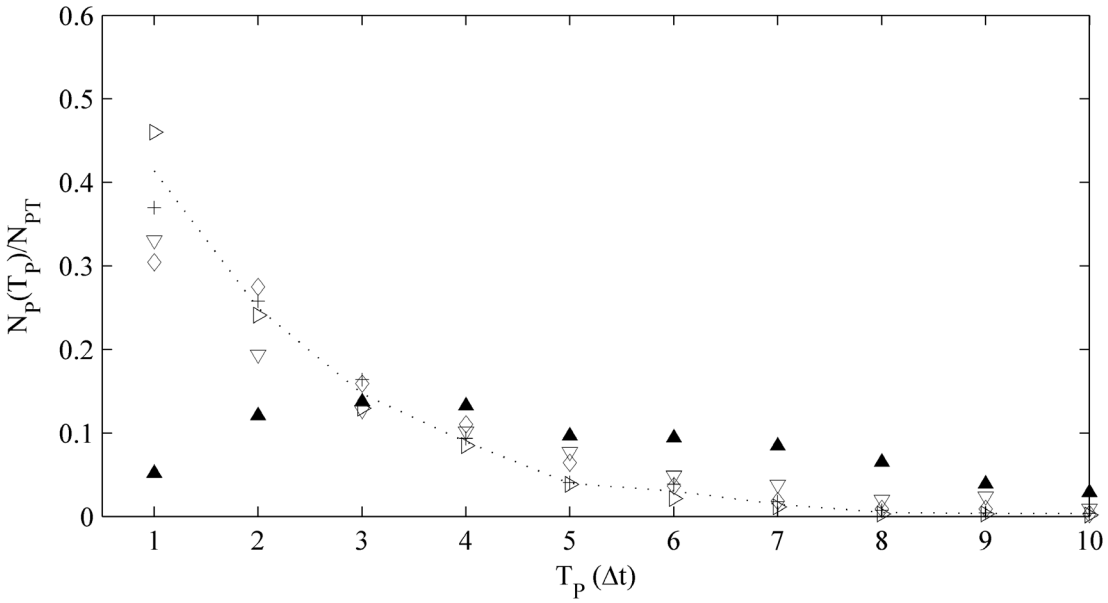

Figure B.12- PDH from the data before and after replacement. Test RG3, point *z/d*=0.16. *Legend,* ···*OS,* + *"good" data,* □ *"bad" data,* ▲*Method (a),* ▽ *Method (b), and* ◊ *Method (c).*

The method *a* changes the shape of the histogram (PDH) and pulses of duration below four time-intervals (T_P<4Δt) are intensely decreased in percentage, while those longer than that (T_P>Δt4) are increased, and even new pulse durations are created, with pulses of 25-Δt even appearing. Method *b* adjusts well to the "good" data trend, despite this, the percentage of pulses over 4Δt are increased, and pulses up to 2Δt are decreased. Finally, method *c* provides a "good" adjustment of all the duration pulses with the "good" data. Pulses of T_P=1Δt are a little decreased since they used to be of low-COR values, but the rest of durations have similar time fraction in the sample, and the longest pulse is T_P=13Δt as the "good" data.

B.3.4 Pulse sequences

In addition to the main turbulent characteristics, the concept of pulses it was seen that is very affected by the use of filters and the replacement of the "bad" data. For this reason, the last analysis shown in this section is the sequence of pulses, one of the most important ideas in the present thesis. It will be developed later that the sequence of the quadrant pulses plays a vital role in the turbulence description and it is in relation with some of the physics involved in sediment transport.

The sequences of quadrant pulses, as its name suggests, are the different combinations of quadrant pulses that can occur, for example, Q1-Q4-Q1. Only sequences of three pulse quadrants in a row are studied here since longer sequences do not show outstanding probability. In the sequences, no difference has been made between different pulse durations, but only the order of the occurrence quadrants.

Some sequences are more probable than others, showing that turbulence is not random but somewhat organized. The modification of this sequences, it has been evaluated here. Table B.1 shows some of the most likely sequences and how they change their time fraction in the data series after the replacement of the spikes (4.48% of the data) or the COR<30 data (48.55%). The time fraction that represents the sequences in the signal is written in the table and the mean error of each one in comparison with the original series (OS).

Table B.1- TF of the pulse-sequences.

Seq.			OS	After Despiking			After COR_{CR}=30		
				Linear (a)	third-12p (b)	third-2p (c)	Linear (a)	third-12p (b)	third-2p (c)
1	**4**	**1**	**3,86**	3,99	3,97	4,04	4,92	5,27	4,37
2	**1**	**4**	**3,4**	3,56	3,53	3,51	5,11	3,39	4,19
2	**3**	**2**	**5,56**	5,76	5,85	5,65	5,52	6,57	5,54
2	**3**	**4**	**2,8**	2,89	2,73	2,8	5,41	2,95	3,72
3	**2**	**3**	**4,19**	4,45	4,54	4,27	5,44	5,02	4,54
3	**2**	**4**	**4,13**	4,01	3,87	4,06	3,06	3,69	3,84
4	**1**	**2**	**2,95**	3,3	3,04	3,1	5,52	3,23	3,67
4	**1**	**4**	**5**	5,16	5,18	5,23	5,22	6,48	5,52
4	**2**	**4**	**3,61**	3,5	3,57	3,6	1,79	3,58	2,9
4	**3**	**2**	**3,61**	3,63	3,44	3,66	5,59	3,25	4,44
			error %	4,27%	4,15%	2,45%	42,42%	14,07%	16,25%

In the case of the replacements of the spikes, the differences are minimal; however, considering the low percentage of spikes, the differences become considerable. The sequences more affected are the Q3-Q2-Q3 and Q4-Q1-Q2. The mean error is decreasing in this order, linear interpolation (method *a*), third-order polynomial with 12 points (method b) and with 2 points (method *c*). In the case of the replacement of the low-COR values (COR<30), the differences are centered on the sequences Q2-Q3-Q2, Q4-Q1-Q2, and Q4-Q3-Q2, and now the mean error are more notable since the percentage of the replaced data is higher.

The lower mean error turns out to be the obtained from the third-order polynomial using just 2 points at each side of the replaced point (method *c*) being 2.45% in the case of the spikes and 16.25% for the low-COR values.

B.3.5 Power Spectrum Density

The last turbulent description analyzed here is the Power spectrum density (PSD), which explains how the turbulent energy is decomposed in all frequencies of the signal. The PSD is plotted in Figure B.13-a as a function of the frequency for the point, z/d=0.16 (RG3), obtained from the OS and from the series after the replacement of the "bad" data by each method considered here.

The OS (black line) just follow the -5/3 slope spectrum predicted by Kolmogorov for the developed turbulence in a very narrow range between 1 Hz and 3 Hz. Interpolation affected the spectra at frequencies higher than 2 Hz. After the replacement of the "bad" data, the slope is achieved by methods *a, b* and *c*, for higher frequencies.

Methods *b* and *c*, achieve the slope in a similar way, at the interval of [1-10]Hz, decreasing the energy for the lowest frequencies, while method *c* erases less energy from the small frequencies. On the other hand, the method *a* increases the spectral slope even above the theoretical -5/3. It seems that a better adjustment of the slope is achieved when the signal is filtered, yet, it must be considered that the filtering process removes more than 50% of the data, even for a COR_{CR}=30. Moreover, despite the fact that the method of replacement *c* better respects the shape of the signal, quadrants, longitudinal velocity increments and pulse-durations, it is noteworthy to remember that the "good" data do not show enough evidence of being wrong. Thus, it is possible that the OS is correct but just follow the theoretical slope until 3 Hz, from that point frequencies have more energy than the expected.

It is observed that in any case, the most important improvement on the spectral analysis, i.e., the Kolmogorov universal slope of -5/3 in the inertial subrange, is achieved when a linear interpolation is made to the considered as bad data. An example of that is the comparison between the spectral analysis of two series in the point z/d=0.16 of the experiment RG3, Figure B.13-b. The first one, filtered by the criterion of COR_{CR}=30, 48.55% of data replaced by method *b* (third-order polynomial with 12 points), and the second, filtered by using a threshold of COR_{CR}=20, 26.56% of data replaced by method *b* (linear).

Parsheh et al. (2010) stated that their despiking method improved the power spectra significantly. However, it has been seen in the present work that the power spectra improve as more extreme events

are replaced, as long as the linear interpolation is used, with the inconvenience of distorting the nature of the data even when the characteristics of the spikes are inside the turbulence normality.

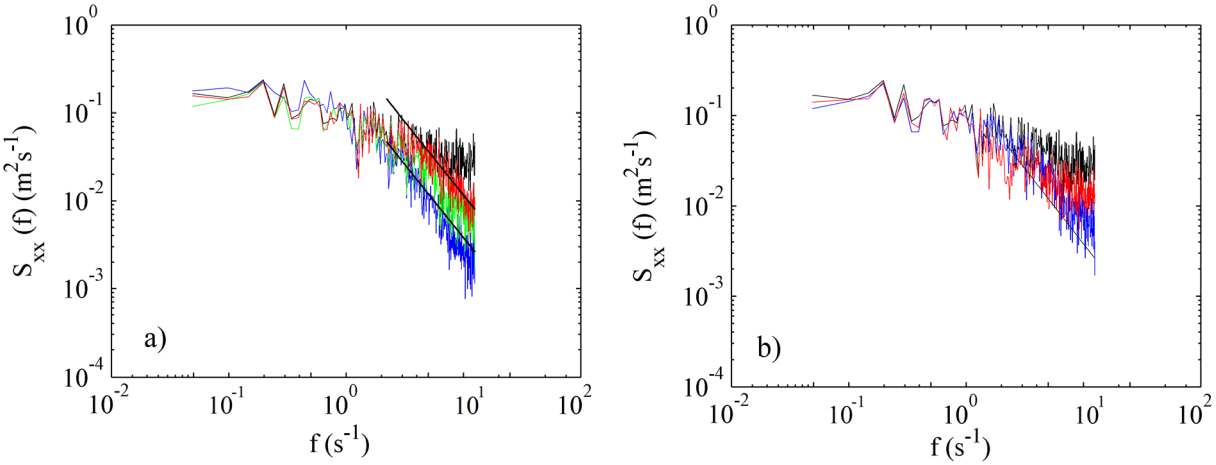

Figure B.13- PSD of the streamwise velocity component. Test RG3, z/d=0.16. *Legend (a),* ▬ *OS,* ▬ *method a,* ▬ *method b, and* ▬ *method c. Legend (b),* ▬ *"OS",* ▬ *filtrating by CORCR=20 and replacement by method a and* ▬ *filtrating by CORCR=30 and replacement by method c.*

B.4 Discussion

From the evaluation of the replaced data, or "bad" data, it follows that spikes are not related to the low-COR values since the former have a well-sorted distribution of COR values. Therefore, discarding data with a correlation below 30% removes a significant amount of useful data while retaining a portion of spikes and does not eliminate the necessity of applying the Despiking filter.

The low-COR values and spikes showed a more similar distribution of the longitudinal velocity increments (Δu) than those obtained from the different methods of replacement, which changed the pattern increasing the density of the histogram in Δu~zero. Although the time fraction of the quadrants obtained from "good" and "bad" data differ notably, these reflect the different mechanism of high and low turbulent events. Moreover, the method of replacement considered here does not manage to transform the trend towards "good" data entirely; the pattern tends to remain. In terms of PDH, spikes and low-COR values demonstrate that they tend to be short pulses ($1\Delta t$). It is interesting that pulses of T_P=$1\Delta t$ from the Q1 (outward interactions) are more susceptible to be considered as spikes than the other quadrants, and thus, the velocity fluctuation in this quadrant tend to be higher.

Despite the linear interpolation complies with Cea et al. (2007) recommendation in highly turbulent flows, the series after the replacement changes the PDH entirely. On the other hand, the interpolation by a third-order polynomial (methods *b* and *c*) better respects the natural trend of the series. Trying to detect which replacement method maintain more similar results to the non-filtered data does not make sense. Instead, it seems more natural to leave the data raw since the turbulent characteristics of the "bad" data are closer to the "good" data (non-filtered) than any of the interpolated data by the methods discussed here, an especially more so in the case of the distribution of velocity increments.

Regarding the spectral analysis, filtering affected the spectra at frequencies greater than 2 Hz. The more data is replaced, i.e., the more increases the COR_{CR}, the steeper the slope becomes for frequencies over 2 Hz, enlarging the range where the spectra reach the universal Kolmogorov slope -5/3. Therefore,

less energy is contained in the highest frequencies after filtering. Despite this, the large amount of replaced data (>50%) can distort other results related to the history of the velocity signal breaking the natural trend of highly turbulent events and making them look like velocities with a high COR value, removing the series from its real nature. As has been shown, the power spectrum improves from 2 Hz onwards whether or not the most extreme values are replaced by linear interpolation, however, misrepresenting the real turbulence of the flow.

The arbitrary operation of filtering methods and the effects that they have on the results show that the filter should not be applied without prior study of suitability. It is noteworthy that, in some cases, any filtering method has to be considered if the configuration of the device it is not enough to avoid aliasing.

APPENDIX C. ADV CONFIGURATION ANALYSIS

Table of Contents

Appendix C: ADV Configuration Analysis

C.1 Introduction

The configuration of the device plays an important role in data collection since one of the main sources of error normally encountered when analyzing ADV velocity time series apart from the Doppler noise is signal aliasing, as commented in chapter 3, section 3.2. These problems have been intensely studied by some users since ADV appeared (Garcia et al. 2005; Goring & Nikora 2002; Nikora & Goring 1998; Wahl 2000).

The present section was motivated by the necessity of further understanding about the effects of the ADV configuration on the turbulent properties of the flow. However, the device used for the primary experiments, the experiments from "the cube" channel (chapter 2), was unable to change the configuration parameters. For this reason, some other experiments were carried out in the FRITZ flume, explained below, using other ADV device. The frequency of Data Collection (FDC), the size of the Control Volume (CV) and the velocity range, were the target parameters of the device configuration of this study. The effects of the configuration on the turbulent parameters for the CUBE experiments were also analyzed using averaging window methods, by means of the performance curves included at the end of the present appendix.

C.2 Experimental set-up

C.2.1 Hydraulic channel

The tests were conducted at the hydraulic channel of the FRITZ laboratory (Lehigh University). The flume's dimensions are 20 m length, 1.2 m width, and 1 m depth straight rectangular Plexiglas channel. Figure C.1 shows the sketch of the experimental set-up.

The velocity data was taken using a vectrino (ADV) with four receivers, Figure C.3.-a, from the Nortek company. In this case, the device was introduced through the water surface (traditional way) until the target zone, with a side-looking physical arrangement, Figure C.3-b. Besides, the experimental set-up incorporates an automated elevator which allows the control of the ADV height through the computer (Figure C.2-b), and therefore ease the data acquisition. This device permits getting closer to the bed surface (without a hole), and the levels of turbulence (lower than the CUBE experiments) do not introduce bubbles in the sample even with the traditional placement of the device.

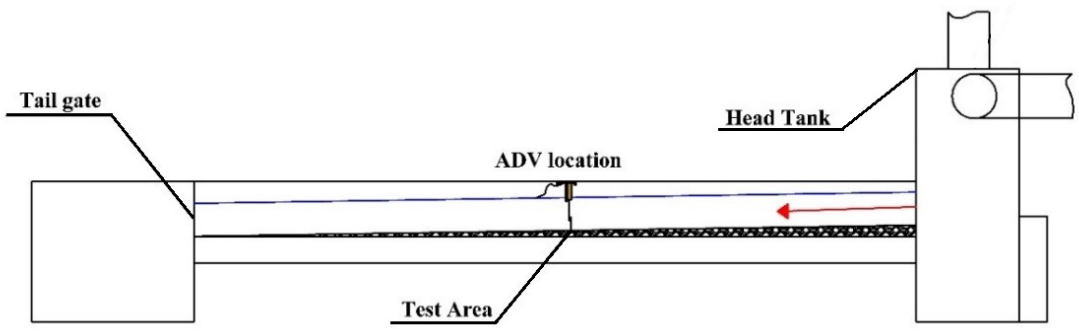

Figure C.1- Sketch of the Hydraulic flume. Fritz Laboratory. Lehigh University.

Figure C.2- Hydraulic flume. Fritz Laboratory. Lehigh University.

Figure C.3- ADV device positioning

C.2.2 Experimental campaign description

The bed was formed using silica sediment with a mean size of D_{50}=6 mm with a slope of 0.54%, and a flow rate of 0.06 m^2/s. There was particle seeding (~10-μm) during the experiments in order to reduce the noise of the received signal.

The flow stresses were kept below the critical values to assure no-motion conditions of the bed during the essays. The water depth (d) was constant with a value of 0.105 m. The mean velocity obtained is 0.58 m/s, with a Froude number of 0.57 and a Reynolds Number (Re) of $2{,}45 \cdot 10^5$. The zone of data acquisition was placed 7 meters downstream the source of water in the flume.

Five configurations were evaluated first by modifying the FDC, the height of the CV (h) and the nominal velocity range, indicated in Table C.1. Three different vertical points were measured, in order to avoid interferences of the CV with the boundary the first was located at z=5 mm from the bed, the second amid profile at z=36 mm, and the third at the height of z=62 mm from the bed.

Table C.1- ADV Configurations. Tests from T-1 to T-5.

Variables	**T-1**	**T-2**	**T-3**	**T-4**	**T-5**
Freq. Data Collection (Hz)	25	25	25	100	200
CV height (h) (mm)	7	7	2,5	7	7
Nominal vel. range (m/s)	2,5	1	2,5	2,5	2,5

As a first conclusion from these first experiments, the control volume's size (CV) and the frequency of data collection (FDC) were the most influential parameters on the velocity data series.

The second set of tests were conducted to evaluate the effects of these two parameters over the turbulent properties. Three different profiles of instantaneous velocities were obtained, with the same hydraulic conditions than the tests, but measuring the whole depth from 5 mm to 82 mm from the bed, obtaining 20 equally spaced points. The Table C.2 shows the device configurations studied over the profundity were values of FDC and CV were changed one to another, leaving a characteristic nominal velocity range at 2.5 m/s in all cases.

Table C.2- ADV Configuration Profiles. CF-1, CF-2 and CF-3.

Variables	**CF-1**	**CF-2**	**CF-3**
Freq. Data Collection (Hz)	100	100	25
Control Vol. 'd' (mm)	2,5	8,5	2,5
Nominal vel. range (m/s)	2,5	2,5	2,5

The capability of the device to characterize the flow, according to the different ADV configurations, is evaluated through the evaluation of data quality values and main turbulent properties of the flow such as Reynold stresses, turbulent intensities (TI) and Turbulent Kinetic Energy (TKE), etc. and Quadrant and pulse Analysis developed in this thesis. The next paragraphs evaluate these effects on the main turbulent parameters and data quality of the configurations.

The increase of the CV is represented from the CF-1 (h=2.5 mm) to CF-2 (h=8.5 mm), and the decrease of the FDC, represented from the CF-1 (100 Hz) to CF-3 (25 Hz).

C.3 ADV Data quality

The Despiking filter of Goring and Nikora (2002) was applied in these cases to eliminate the spikes and the contaminated data. The Despiking filter was used since the peak values of the velocity signals obtained from the FRITZ tests, unlike the CUBE experiments, showed similar appearance to the defined by Goring and Nikora (2002), Figure C.4. On the other hand, the COR and SNR values obtained from all trials achieved the minimum data quality requirements of Wahl (2000) because of the low level of turbulence of the flow, so it was not necessary the filtration of the COR values.

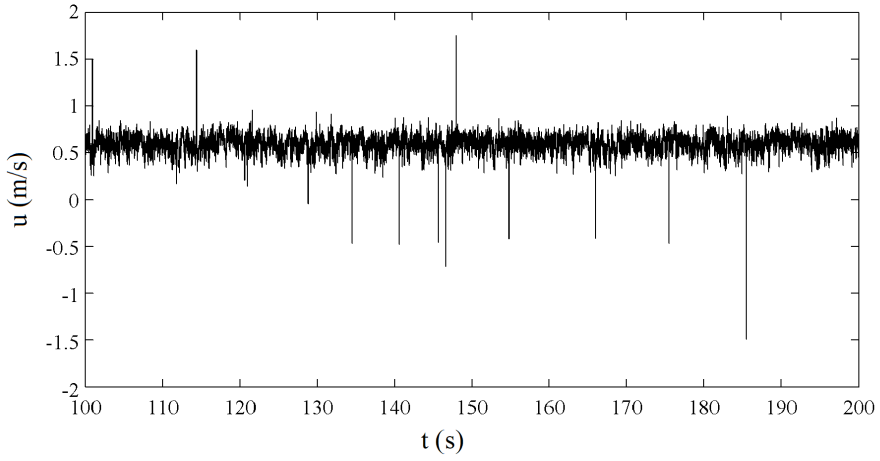

Figure C.4- Instantaneous velocity u, test CF- 1 (100 Hz)

Table C.3 presents the mean values of the data quality parameters COR and SNR. In this table, the tests T-1 and the CF-1 are taken as reference values to compare with the rest of the experiments, to see the effect of the modified parameters on the results. The outcomes from T-1 and CF-1 are displayed in the first rows in bold while the results of the rest are shown as the percentage difference from the reference experiments.

First, the nominal velocity range was evaluated between the tests T-1 and T-2 (variables of the tests in Table C.1). As a result, the mean COR and SNR were reduced, and their standard deviations (σ) were improved when the velocity interval was dropped until 1 m/s. This fact also resulted in a larger amount of spikes detected in the sample, due to the Aliasing effect. Concluding that for the studied flow, the nominal velocity range needs to be set at 2.5 m/s for all the following experiments. Figure C.5 shows the fraction of spikes detected by the Despiking filter, for the three configurations.

Table C.3- Data Quality. Averaged results in the profile

	COR_u		COR_v		COR_w		SNR_u		SNR_v		SNR_w	
	Mean	std	Mean	std	Mean	std	Mean	std	Mean	std	Mean	std
T-1	**84.66**	**7.03**	**83.26**	**7.23**	**81.48**	**7.28**	**64.45**	**3.05**	**65.47**	**3.21**	**67.32**	**3.17**
T-2	-2.45	1.60	-2.21	1.34	-7.40	2.21	-0.69	0.72	-2.13	1.20	0.34	0.11
T-3	0.84	1.07	1.26	0.77	0.72	1.47	-0.36	1.82	1.39	0.85	0.36	1.26
T-4	2.88	0.41	3.35	0.18	2.52	1.48	-0.22	1.83	-0.41	2.06	-0.07	1.94
T-5	3.05	1.12	3.29	1.09	2.66	2.79	-0.22	2.38	-0.59	2.88	0.16	2.46
CF-1	**87.55**	**10.69**	**86.97**	**11.08**	**82.73**	**14.47**	**66.23**	**6.42**	**66.41**	**8.80**	**70.10**	**5.82**
CF-2	-1.14	-2.92	-1.77	-2.96	-1.57	-4.45	-0.31	-2.52	0.73	-4.28	-0.21	-2.50
CF-3	-3.83	-2.02	-4.58	-1.88	-6.41	-3.85	-1.72	-1.59	-1.02	-2.43	-0.75	-2.05

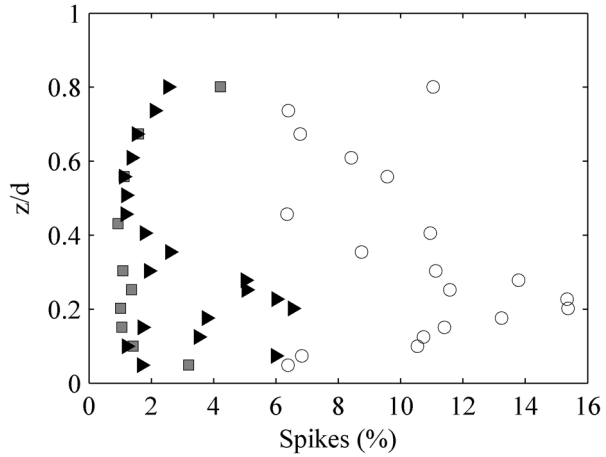

Figure C.5- Vertical distribution of the spikes (%) in the data series of CF-1, CF-2 and CF-3. *Legend, ○ CF-1 (100 Hz, h=2.5 mm, ■ CF-2(100 Hz, h=8.5 mm), and ▶ CF-3 (25 Hz, h=2.5 mm.*

In the next figures, mean COR values (Figure C.6-a), its standard deviation σ_{COR} (Figure C.6-b), mean SNR values (Figure C.6-c) and σ_{SNR} (Figure C.6-d), are plotted for the configurations CF-1, CF-2, and CF-3, along with the profile.

The figures show a general pattern of data quality values as they go up through the depth, for the three configurations. The mean values of COR and SNR tend to grow with the height (z/d) while their σ values show a trend of reduction. These facts are in concordance with the results observed in the primary experiments of the thesis, (from "The Cube" channel) presented in chapter 3, section 3.3.

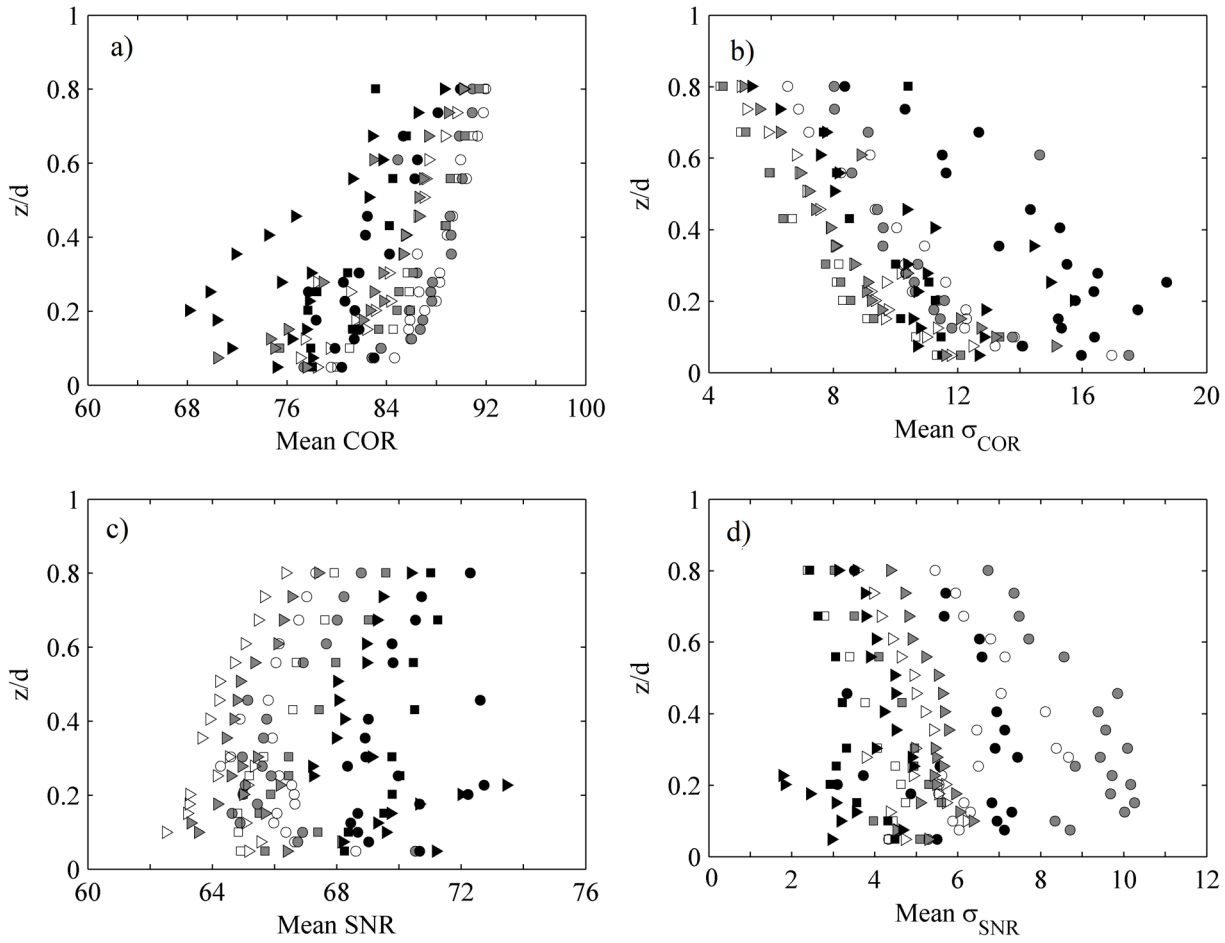

Figure C.6- Vertical distribution of the average values of (a) COR, (b) σ_{COR}, (c) SNR and (d) σ_{SNR}, of CF-1, CF-2, and CF-3. *Legend Markers, ○ CF-1 (100 Hz, h=2.5 mm), □ CF-2 (100 Hz, h=8.5 mm), and ▷ CF-3 (25 Hz, h=2.5 mm). Legend colors, ○COR_u, ● COR_v, and ● COR_w.*

C.3.1 Influence of the increased CV

In Figure C.6-a, the effects of the CV increase on the mean COR values are represented with the differences between the CF-1 (*h*=2.5 mm) and the CF-2 (*h*=8.5 mm), both with 100 Hz of FDC. The figure shows a proportional decline in the mean value of COR for the three axes when a larger CV is set. The mean reduction in the depth is 1.44%, 1.77% and 1.57% (Table C.3) for COR_X, COR_Y, and COR_Z respectively. However, Figure C.6-b shows that the standard deviation of COR (σ_{COR}) drops as well. The decrease of the mean σ_{COR} value in depth is 2.92%, 2.96% and 4.45% for σ_{CORX}, σ_{CORY}, and σ_{CORZ} respectively. Therefore, despite the mean value of COR decreases, it becomes more robust.

On the other hand, the enlargement of the *h* displays an improvement in the mean SNR values and their standard deviation (σ_{SNR}), Figure C.6-c and Figure C.6-d, increasing the first and decreasing the second over the whole profile. Then, in addition to increasing its value, it becomes more robust as well. The Table C.3 confirm that the improvement is moderate in the mean SNR values (less than 1%) but high for the σ_{SNR}, over 2.5% for the three axes.

The technique used by the device to enlarge the *h* suggests the reason for the general improvement of SNR values. The ADV rises the *h* by extending the length of the transmit signal, consequently making the signal stronger. The same effect is noticeable in Table C.3, where an elongation of the *h*, from T-

3 to T-1, have negative impacts on the mean COR (decrease) and improves the mean SNR, yet the changes are moderate. The effect of the CV increase on the number of spikes is beneficial over the whole depth (Figure C.5), where less than 3% of spikes are found in the CF-2 (h=8.5 mm) in front of the [6-16%] of spikes in CF-1 (h=2.5 mm).

C.3.2 Influence of the decreased FDC

The case of the reduction of the FDC is characterized from the CF-1 (100 Hz) to CF-3 (25 Hz). It is observed in Table C.3 that the mean COR value is significantly lessened in the three axes, above all for the vertical COR value which is reduced by a 6.41%. That reduction reaches its maximum at z/d=0.2, Figure C.6-a. However, as in the increased CV, the σ_{COR} is also reduced, and then the values become more constant and robust. This effect is similar than increasing the CV but presenting more erratic behavior above all at the near-bed region, up to z/d=0.3, mainly for the vertical axis.

The mean SNR remain very similar between the two configurations (CF-1 and CF-3), Figure C.6-c, owing to the strength of the signal which is equal for identical CV sizes. There is a moderate drop of the σ_{SNR} decreases but less than for the increased CV. Similar effects can be seen between tests T-1, T-4 and T-5, with different FDC but identical CV height (h), nonetheless, the diminishing of COR and SNR, due to the lessening of FDC, is noticeable especially between 100 Hz and 25 Hz.

Although the decrease of the FDC produces a reduction of the spikes over the depth, there are still some spikes [2-6%] at near-bed layer (z/d<0.3), Figure C.5.

C.3.3 Results discussion

For the three configurations (CF-1, CF-2, and CF-3), the evolution of the mean COR and SNR parameters along the profile, shows a trend of increase, Figure C.6-a, and Figure C.6-c. Moreover, there is an improvement of the robustness since the mean values of σ_{COR} and σ_{SNR} decrease with the depth, Figure C.6-b, and Figure C.6-d.

Steep velocity gradients and small coherent structures (SCS) are associated with near-bed flows, Finelli et al. 1999. According to this, both facts, the low COR values inside this region and the increase of them along the depth, put in evidence the inaccuracy of the configuration inside this region, due to an oversize of the CV or a too low FDC. Both facts, extending the CV or decreasing the FDC, evidence the non-suitability of the configurations in the presence of SCS. The low amount of captured SCS makes to drop off the mean value of COR, showing a significant variability in vortices scales where the SCS does not have enough presence as the reality. Nonetheless, the high value of σ_{COR} shows that they are there.

Setting a low FDC as CF-3 (25 Hz, h=2.5 mm), implies that each value of instantaneous velocity comes from a higher number of measures thus the COR value decreases if the level of turbulence is high and a significant amount of SCS cannot be caught by the device. However, the COR values among the instantaneous velocities are similar falling the σ_{COR}, due to the lack of presence of the SCS.

If a big CV is set as CF-2 (100 Hz, h=8.5 mm), the velocity registered become from more echoes reflected by the particles, and so it is closer to the mean value, the spikes are reduced and the variability of the COR and SNR are reduced from the CF-1 (100 Hz, h=2.5 mm), with smaller CV. When a small CV is set, CF-1 and CF-3, the SCS gather presence in the CV and the COR value increases, but its

standard deviation decreases. However, some instabilities appear along the depth, for all the quality parameters COR, σ_{COR}, SNR, σ_{SNR}, and spikes, especially in the near-bed region. The average SNR value is augmented by the increased CV due to the strength of the signal while is reduced by the decreased FDC. Therefore, this value does not represent well the lack of SCS, yet σ_{SNR} is declined all over the depth in both cases, more for the enlarged CV, showing scales size less than the CV.

C.4 Turbulent properties of the flow

Identical as in Table C.3, Table C.4 shows the main turbulent properties for all experiments in reference to the results obtained from T-1 and CF-1. Thus, the turbulent properties values obtained from these two experiments are shown while the values from the remaining trials are displayed in percent difference from reference experiments. The next figures show some of the turbulent properties, the integral length scale, turbulent intensities and Reynold stresses respectively.

Table C.4- Turbulent Properties results

	τ Re	$\bar{u}$	**TIX**	**TIY**	**TIZ**	**TKE**	ε	**% Spikes**	**Int. Scale**	**Kolm. Scale**	**Taylor Scale**
T-1	**13.5**	**0.642**	**0.112**	**$5.67\cdot10^{7}$**	**$2.1\cdot10^{10}$**	**1.0E-03**	**6.6E-04**	**1.415%**	**9.8E-02**	**4.3E-03**	**1.3E-02**
T-2	1.0%	1.0%	-2.2%	2.1%	400.0%	0.1%	-4.2%	7.3%	-3.2%	1.8%	1.5%
T-3	15.5%	0.3%	5.9%	-68.7%	-2.6%	6.7%	24.5%	206.6%	-29.0%	-26.4%	-3.6%
T-4	50.5%	50.5%	12.4%	128.2%	59.8%	546.7%	1537.4%	18.2%	-41.3%	-83.4%	-38.8%
T-5	64.9%	0.3%	20.3%	333.0%	128.6%	-41.5%	6882.3%	44.5%	-40.7%	-77.0%	-53.9%
CF-1	**26.9**	**0.592**	**0.174**	**$6.3\cdot10^{7}$**	**$2.4\cdot10^{10}$**	**1.6E-02**	**5.1E-02**	**10.2%**	**6.0E-02**	**5.6E-04**	**7.7E-03**
CF-2	-15.2%	0.28%	-12.5%	-48.1%	-5.1%	-56.6%	-54.6%	-83.4%	26.1%	41.3%	23.2%
CF-3	-35.4%	1.6%	-19.2%	3.1%	4.5%	-59.9%	-85.6%	-71.8%	30.4%	68.7%	40.6%

C.4.1 Influence of the increased CV

Extending the CV height (h), from CF-1 (h=2.5 mm) to CF-2 (h=8.5 mm), allows capturing more prominent structures. Consequently, all length scales, the integral scale L_X (Figure C.7-a), Taylor and Kolmogorov scales (Figure C.9-a), are enlarged. The autocorrelation values as a function of time are shown in Figure C.7-b, where is possible to see how the autocorrelation increases for all time lags when the h is enlarged, thus, obtaining larger L_X.

Mean turbulence properties such as TIs (Figure C.8-a), Reynold shear stresses (Figure C.8-b), Energy Dissipation Rate (ε) and TKE, are reduced in depth-averaged. If a big h is set, a lack of Reynolds stresses at near-bed region could be explained, where the amount of SCS is high. Nevertheless, all properties show a more stable behavior along the depth above all in the near-bed layer. In general, all mean values along the profile are decreased from CF-1 to CF-2.

On the other hand the dissipation rate (ε) has been obtained from each configuration in (Figure C.9-b), by means of the structure functions (see chapter 4, section 4.9). In the figure it is also depicted the theoretical value obtained though the power of the channel (hydrodynamic variables), also described in section 4.9 of chapter 4, with a value of ε=0.028. The increased CV from CF1 (100 Hz, h=2.5 mm) to CF2 (100 Hz, h=8.5 mm) show a decrease of the averaged ε of 54.6%.

C.4.2 Influence of the FDC

The lessening of the FDC, from CF-1(100 Hz) to CF-3 (25 Hz), produces a considerable growth of the length scales (Figure C.7-a), despite having a small CV, especially for the Kolmogorov length scale, while similar length scales of energy production (L_X), are found for the CF-2 and the CF-3. The elongation of the integral length scale is explained by the modification of the time interval by the FDC change. When the FDC decreases, the time interval increases, as can be seen in Figure C.8-b. As a result, the value of the Autocorrelation R_{xx} for the first time step (Δt) is increased, thus, the integral length scale increases as well. The elongation of η it must be due to the less representation of small scales, produced by the decrease of the FDC.

Mean turbulent properties are decreased, showing the same patterns of variation than for an increased CV. the reduction of the turbulent properties ($\overline{-\rho u'w'}$, ε, TKE, TI_X) is more noticeable for the CF-3, i.e., by reducing the FDC than by extending the CV. It has to be mentioned though that the TI_Z is less reduced, being event a little increased in the near-bed region z/d<0.3.

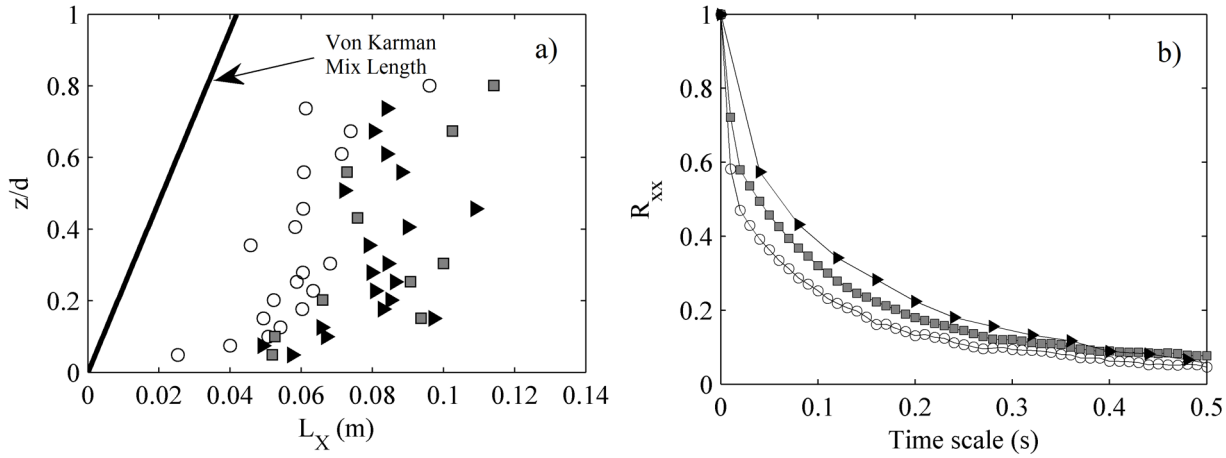

Figure C.7- (a) Vertical distribution of Lx and (b) Autocorrelation function at point z/d=0.14, of CF-1, CF-2, and CF-3. *Legend, ○ CF-1 (100 Hz, h=2.5 mm), ■ CF-2 (100 Hz, h=8.5 mm), ▶CF-3 (25 Hz, h=2.5 mm).*

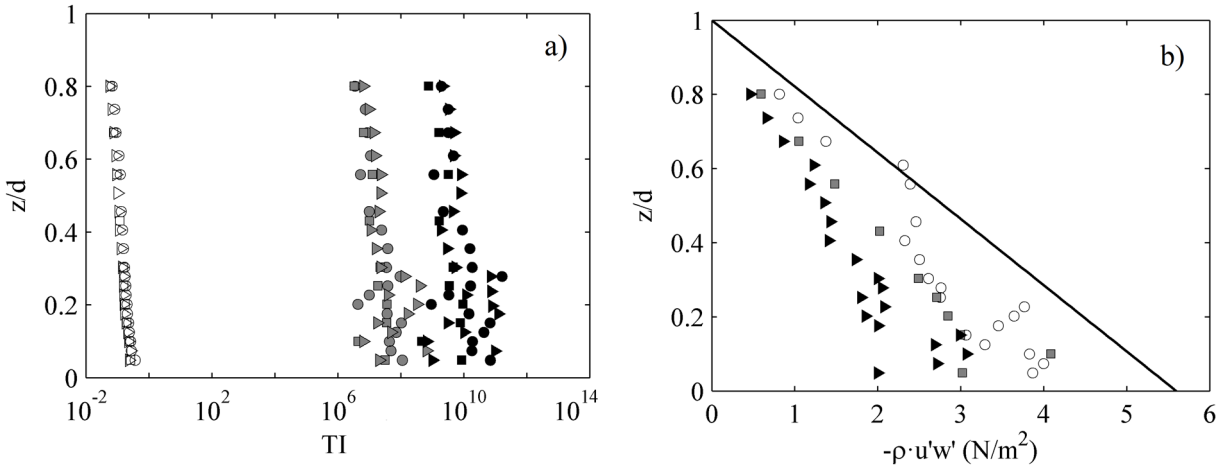

Figure C.8- Vertical distribution profiles of the mean values of (a) TIs and (b) Reynolds shear stresses for the configurations CF-1, CF-2 and CF-3. *Legend (a) as for Figure C.6. Legend (b) ○ CF-1, ■ CF-2, ▶CF-3.*

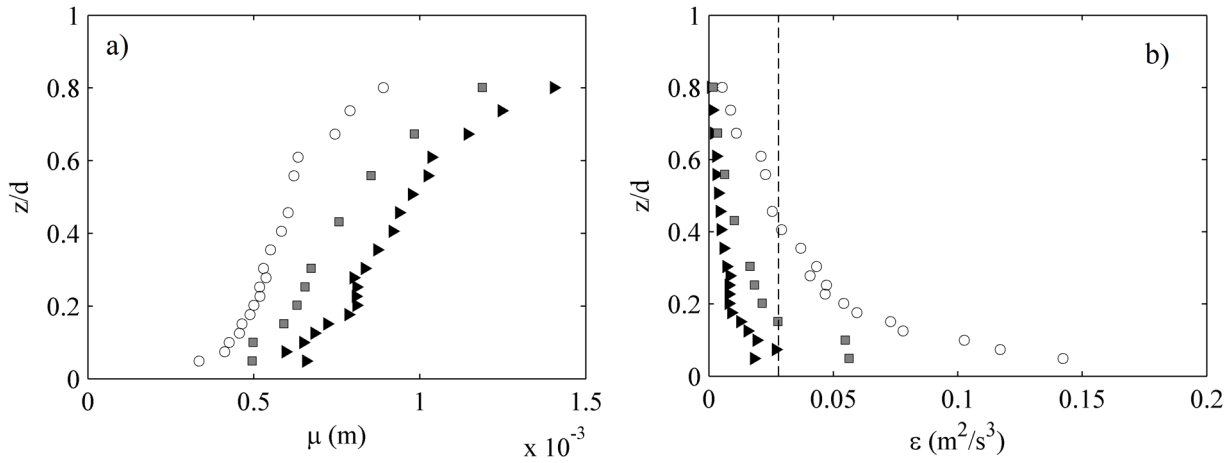

Figure C.9- Vertical distribution of (a) Kolmogorov length scales and (b) Dissipation rate. CF-1, CF-2 and CF-3. *Legend, ○ CF-1 (100 Hz, h=2.5 mm), ■ CF-2 (100 Hz, h=8.5 mm), ▶CF-3 (25 Hz, h=2.5 mm)*

C.4.3 Results discussion

The assumption that in the near-bed region the SCS is higher, Finelli et al. (1990), is appreciable over the turbulent properties as they decrease with the distance to the bed while the length scale rises. In the near-bed region, if a small CV is set, an unstable behavior of the Turbulence intensities is observed, even when a low FDC is established, while a long CV displays more stable behavior through the depth profile. A lack of the SCS representation in the profile is detected because of extending the CV, which is similar when decreasing the FDC.

Reynold stresses, TKE, and the dissipation rate (ε) are reduced significantly when the CV is increased from CF-1 to CF-2, being these reductions of 15.2%, 44.6% and 31.3% respectively, however, the reduction is even bigger if the FDC is reduced, even with the same size of CV, arriving to the reduction of the 95% of ε, Table C.4. The length scales, on the other hand, corroborate the lack of representation of SCS for the configurations CF-2 and CF-3. The increase of the length scales is remarkable in both cases but the increase produced by lowering the FDC in the CF-3 (25 Hz) is more notable, especially in the scales of Taylor and Kolmogorov where the rise is around of 60% in both lengths, Table C.4.

C.5 Power Spectrum Density

The Power spectrum density (PSD) decomposes the turbulent energy in all frequencies at the signal. Figure C.10 illustrates the value of the fitted slopes of the spectrum for frequencies over 1 Hz, as a function of the dimensionless depth, of the three configurations.

C.5.1 Influence of the increased CV

From Figure C.10 is observed that the CF-1(100 Hz, *h*=2.5 mm) obtains the flattest slope spectrum along the profile, being this value very changeable along the depth. The case of enlarging the CV but maintaining the same FDC is represented by the CF-2 (100 Hz, *h*=8.5 mm), and show a better adjustment of the Kolmogorov slope, with a slope value around -1.2 and -1.3. However, the value is still very changeable along the depth, but less than for the CF-1 though.

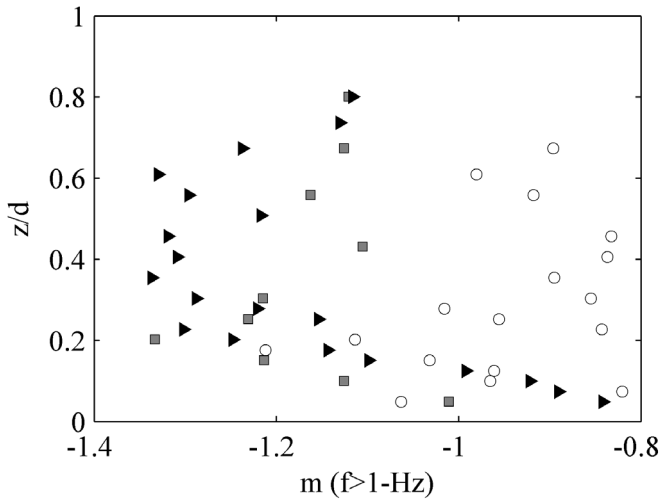

Figure C.10- Vertical distribution of the PSD slope for frequencies > 1 Hz. *Legend,* ○ *CF-1 (100 Hz, 2.5 mm),* ■ *CF-2 (100 Hz, 8.5 mm), and* ▶ *CF-3(25 Hz, 2.5 mm).*

The resulting PSD of a point close to bed (*z/d*) =0.2 is shown in Figure C.11. Figure C.11-a depicts the two mentioned experiments CF-1 (*h*=2.5 mm) and CF-2 (*h*=8.5 mm), which represent the increase of the CV for an FDC of 100 Hz. The figure shows how the slope of the PSD becomes steeper for the increased CV. The energy of the high frequencies decreases, probably because the little structures become less represented by the signal. However, the slope of both configurations is similar between the range of [1-8 Hz].

On the other hand, Figure C.11-b shows the same point but in this case for an FDC of 25 Hz, by the tests T-1(25 Hz, *h*=7 mm) and T-3 (25 Hz, *h*=2.5 mm), therefore, the increase of the CV is also represented from T-3 to T-1. In this case, the results are the same, the slope becomes steeper by the increase of the CV, decreasing the energy for the low frequencies, however, showing a similar slope for frequencies up to 7 Hz.

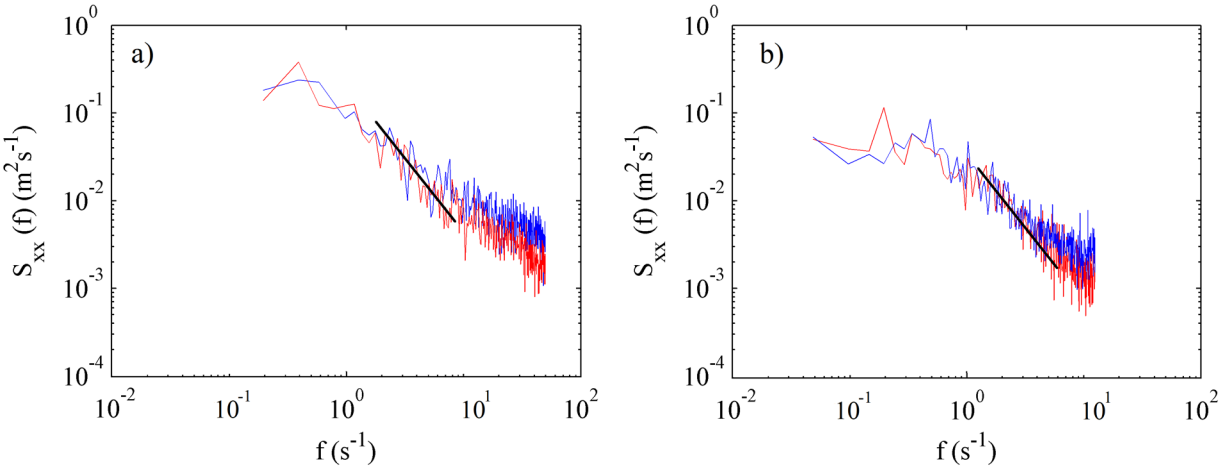

Figure C.11- PSD of the streamwise velocity component at *z/d*=0.2. Figure (a), *Legend:* ▁ *CF-1 (100 Hz, 2.5 mm),* ▁ *CF-2 (100 Hz, 8.5 mm),* ▁ *-5/3 slope.* Figure (b) *Legend:* ▁ *T-1 (25 Hz, 7 mm),* ▁ *T-3 (25 Hz, 2.5 mm),* ▁ *-5/3 slope.*

C.5.2 Influence of the FDC

When decreasing the FDC from the CF-1 (100 Hz, 2.5 mm) to the CF-3 (25 Hz, 2.5 mm), the slope of the spectrum becomes steeper, surrounding the value of -1.3 and thus closer to the theoretical -5/3 (-1.66) defined by Kolmogorov, Figure C.10. However, the CF-3 still has low values at depth under z/d<0.2. To see more detailed this effect the next figures show the effect of increasing the FDC on the spectra of a point close to the bed.

In Figure C.12-a, the effect is represented by the experiments CF-1 (100 Hz) and CF-3 (25 Hz), both with a CV of 2.5 mm. It shows that by increasing the FDC, the slope remains very similar in the range of [0.1-8] Hz. As of 10 Hz, the CF-1 shows a plainer slope, due to the signal noise.

Figure C.12-b shows the same effect but in this case using the tests T-1 (25 Hz), T-4 (100 Hz), and T-5 (200 Hz), all with a CV of 7 mm. The effects are very similar than for the previous figure, the three slopes up to the frequency of 8 Hz show similar behavior, however, in this case, the T-1 (25 Hz) achieves better the theoretical of -5/3 slope.

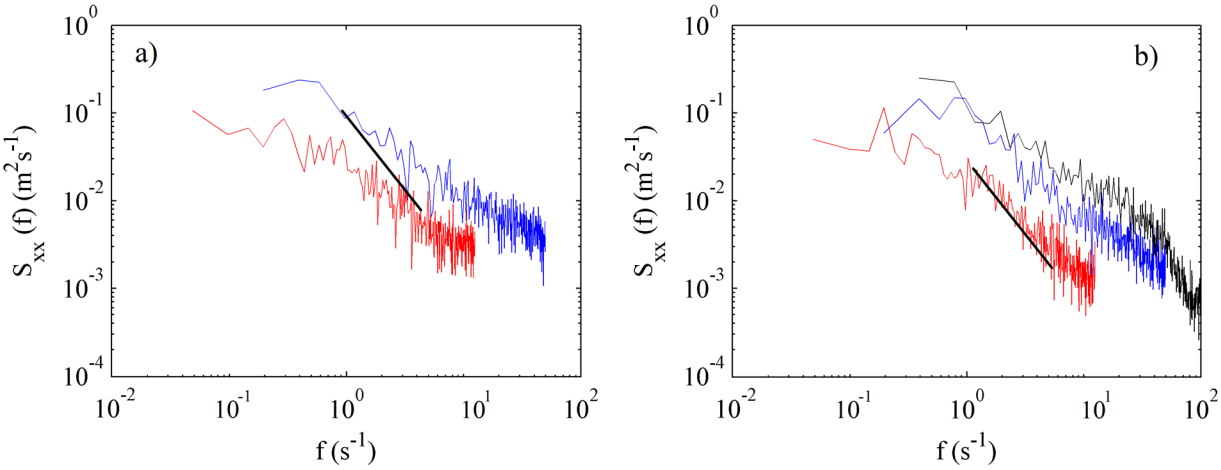

Figure C.12- PSD of the streamwise velocity component at z/d=0.16. Figure (a), *Legend: CF-1 (100 Hz, 2.5 mm), CF-3 (25 Hz, 2.5 mm), -5/3 slope.* Figure (b) *Legend: T-1 (25 Hz, 7 mm), T-4 (100 Hz, 7 mm), T-5 (200 Hz, 7 mm), -5/3 slope.*

C.5.3 Results discussion

From the results, it is obtained that the PSD slope is also affected by the configuration of the device. In fact, the best-fitted slope, closer to the -5/3 of Kolmogorov would be achieved by a configuration with an FDC of 25 Hz and a CV height of h=7 mm.

As the spectrum of the signal gives a level of energy to each frequency represented in the signal, it depends on the range of size vortex characterized by the data series. That is to say, providing that the large coherent structures be enough represented in the signal, the PSD achieves the theoretical slope.

However, for the studied case of 25 Hz the flow turbulence was not very high thus the range of the size vortex cascade is lower, and the configuration of 25 Hz and h=7 mm it is descriptive enough. In the case of higher turbulent flows, it may be necessary another configuration.

C.6 Quadrant Analysis

Quadrant analysis is a useful methodology to the study of turbulent structures through the called bursting events (chapter 5). The examination of the effect caused by the device configuration on the quadrant time fractions (QTF) and sequences of quadrants are analyzed in this section.

In Figure C.13-a, the velocity signal of a point from the near-bed region (z/d=0.04) are represented by the pairs u'w' in the Quadrant Map. It is remarkable that the cloud of points becomes smaller for both changes of the configuration, increasing the CV and decreasing the FDC, the points become more concentrated around the origin of coordinates. Additionally, in Figure C.13-b, the characteristic QTF of the data series is plotted along the profile for the three configurations. A common pattern is perceived, where the most common events are the sweeps (Q4) growing with the distance to the bed (z), the seconds are the ejections (Q2) with a decrease as z increases. The least common events are the Outward interactions (Q1) and Inward Interactions (Q3), showing similar percentages and without a clear pattern of evolution, remaining more constant over the depth profile.

C.6.1 Influence of the increased CV

The influence of the enlarged CV is represented by the differences between CF-1 (h=2.5 mm) and CF-2 (h=8.5 mm). Figure C.13-a show the turbulent map of the three configurations, see the legend in the figure description. The peak values are considerably reduced in the CF-2, above all in the Q1.

Figure C.13-b plots the QTF along the depth profile of the three configurations. The time fraction of the sweep events (Q4) is augmented, mainly at region near-bed, and ejections (Q2) are also raised but mainly beyond the near-bed region. The formers (Q4) have grown at expenses of the Outwards (Q1) in the near-bed region, with an overall increase of the negative vertical velocities. Beyond the near-bed region, the intensification of sweeps (Q4) and ejections (Q2) grows at expenses of the inward interactions (Q3). The most common events are sweeps (Q4) in both profiles, the percentages of Q2 and Q4 are similar for CF-1 at the region near the bed, while that for the CF-2 the differences between both percentages exists all over the profundity.

C.6.2 Influence of the decreased FDC

The CF-3 (25 Hz), despite having a similar effect on the Quadrant Map than CF-2 (100 Hz), Figure C.13-a, it achieves a greater contraction of the cloud, becoming more concentrated in the origin of coordinates, although some peak values are around this cloud.

On the other hand, the QTFs are less affected by the decreased FDC (CF-3, 25 Hz) than for the increased CV (CF-2, h=8.5 mm), Figure C.13-b. That is to say, the vertical distributions of the QTF from the CF-1 and CF-3 show a similar value and behavior, yet a lower FDC shows a slightly unsteady behavior along the depth. However, some differences are still appreciable especially at near-bed stratum when comparing the two configurations. By decreasing the FDC in CF-3 (25 Hz), sweeps events (Q4) augment in the near-bed layer; giving importance to big structures, and beyond this region, the quadrants remain similar to CF-1 (100 Hz).

A similar pattern is observed by increasing the CV than by decreasing the FDC, reducing the number of small structures collected by the device, especially in the near-bed region.

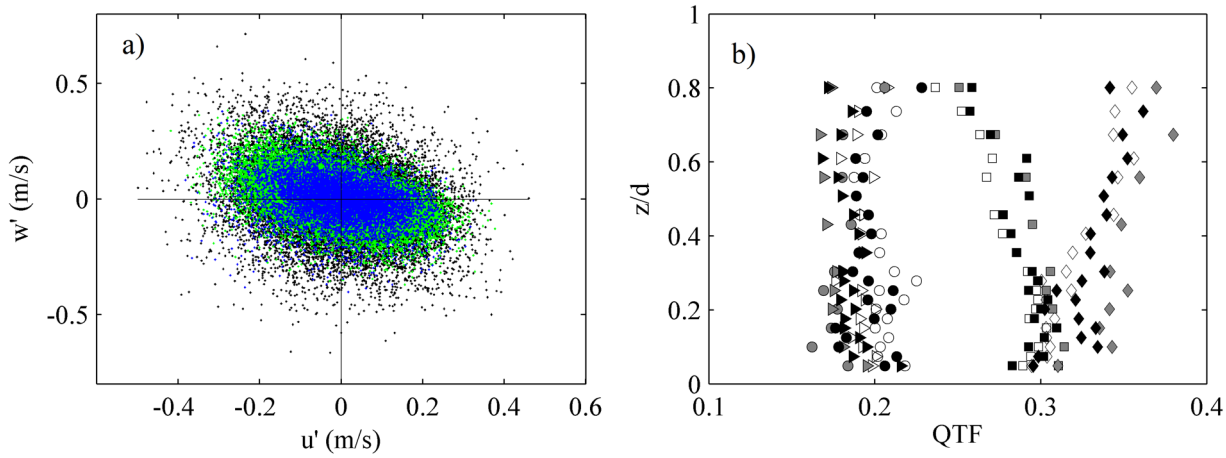

Figure C.13- (a) Quadrant Map of a point at height of z/d=0.04 and (b) vertical distribution of the QTF of the three configurations CF-1, CF-2 and CF-3. *Legend (a),* ● *CF-1,* ● *CF-2,* ● *CF-3. Legend colors (b),* ○ *CF-1,* ● *CF-2,* ● *CF-3. Legend markers (b),* ○ *Q-1,* □ *Q-2,* ▷ *Q-3,* ◇ Q4.

C.6.3 Results discussion

The percentage of sweep events (Q4) shows a pattern of up growth along the depth from the bed to the surface, similar to the average COR parameter and length scales. In contrast, the percentage of ejections (Q2) has a trend of reduction with the distance to the bed (z), like TI and σ_{COR} parameter. Therefore, it seems that large structures are characterized by a high percentage of sweeps (Q4), which are augmented with z at the expenses of the ejections (Q2).

The most affected quadrants by the configuration of the device are outward interactions (Q1) and sweeps (Q4), with a reduction of the first and increase in the second by increasing the CV and decreasing the FDC, supporting the relation between Q4 and large scales. The changes are noticeable particularly over the near-bed region and especially for CF-2 (h=8.5 mm), with the largest CV, due to the restriction of SCS in this region. Ejections (Q2) and the inward interactions (Q3) are less affected, with minor changes detected, being the firsts greater than before while the seconds are lessened. The three configurations show similar values of these quadrants on the near-bed zone (z/d=0.3).

The largest structures become better represented by the growth of Q4 events as z increases, which implies the reduction of Q2 events. Conversely, the smallest vortices seem to be represented by the highest values of Q2 time fraction and the lowest of Q4. In the near-bed layer, up to a height of about z/d=0.3, both quadrants have similar values for the CF-1 and CF-3 with a small CV, beyond this region, they start to separate. In opposition, the CF-2 presents the higher percentage of Q4 events from the bed.

The elongation of the CV in CF-2 (h=8.5 mm), and therefore the following opening of the monitoring window, allows detecting larger vortices all along the depth changing a little the patterns of quadrants of CF-1 (h=2.5 mm). Instead, a lower FDC, although permitting to see larger vortices, when the monitoring window is still small the size of maximum observable vortices is restricted, and variations start to be noticeable where the amount of SCS decreases, out of the near-bed region.

An unsuspected consequence is observed when setting a low FDC of 25 Hz (CF-3), obtaining similar QTFs than CF-1 with 100 Hz of FDC, despite changing the cloud of points more than an increased

CV. Values of the pair (u'w') are reduced while the trend is maintained. One velocity value from the CF-3 (25 Hz) can be decomposed in four velocity values of the CF-1 (100 Hz), and still the quadrant behavior is maintained, demonstrating a proportional statistics of events.

C.7 Trips between quadrants

Regarding the importance of the quadrant events and their sensitivity to the device configuration, the distribution over the time of these events has been studied along the depth profile. The most likely next event from each quadrant has been studied for all the configurations, and so the percentage of each trip (or time fraction), 16 trips in total, have been calculated, see more about trips in chapter 5, section 5.5.1.

The prevalent trips are plotted in Figure C.14. A general pattern was detected over the three profiles obtained regardless of the configuration. The trip with the highest time fraction (TF) is from Q4 to Q4 (Q4-Q4), increasing also with z, followed by Q2 to Q2 (Q2-Q2), in this case decreasing with z. Therefore, the Q2 and Q4 are not only the most likely quadrants but also contain more events that remain at least two time-intervals (Δt=1/FDC) inside them. The least frequent trips are from Q1 to Q3 (Q1-Q3) and Q3 to Q1 (Q3-Q1) and remaining constant through the depth.

C.7.1 Influence of the increased CV

For a large CV (CF-2, h=8.5 mm), as well as the QTF of Q2 and Q4, the trips between Q2-Q2 and Q4-Q4 were augmented, in comparison with the CF-1 (h=2.5 mm), while the rest of the trips decrease, particularly at the near-bed region, Figure C.14. In the same region, the Q4-Q4 trip becomes the most common, far ahead from Q2-Q2. Furthermore, as of z/d=0.3, the percentages of Q4-Q4 and Q2-Q2 start to separate as z increase for the CF-1, conversely, for CF-2 with a bigger CV the percentage of both trips are divergent from the bed.

The experimented acceleration between quadrants, i.e., the velocity increment from one burst to the next one divided by the time interval, is also reduced, when the CV is decreased, hence the assumption that SCS are related with peak events gains credibility.

C.7.2 Influence of the decreased FDC

The percentage of both trips, Q4-Q4 and Q2-Q2, are similar for same values of CV (h=2.5 mm) but different FDC (CF-1 with 100 Hz, and CF-3 with 25 Hz), Figure C.14. Furthermore, the similarity of these most common quadrants and trip TF, start at the channel bed and finish at a height of approximately z/d=0.3, beyond this region they start to separate. Nevertheless, despite showing similar patterns, by decreasing the FDC both trips are slightly diminished except for the trip Q4-Q4 in the near-bed region where percentages of the two profiles are coincident.

Although the FDC is changed, not just the QTF but also the trips TF, movements between quadrants, are preserved despite the accuracy of the signals, i.e., the size of the averaging window.

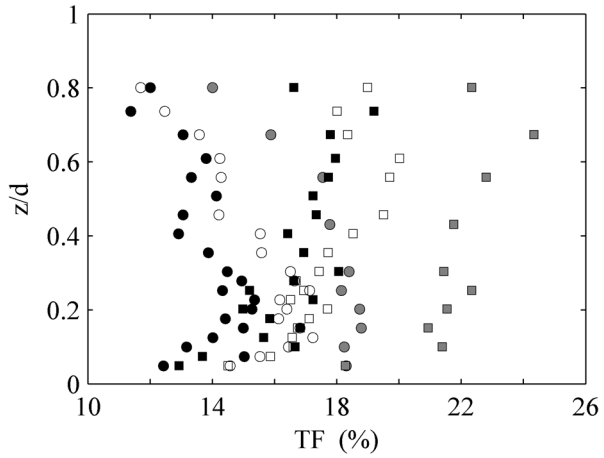

Figure C.14- Dimensionless profile of the time fraction of the trips Q2-Q2 and Q4-Q4. Configurations CF-1, CF-2, and CF-3. Legend Markers (b), ○ Q2-Q2, □ Q4-Q4. *Legend colors (b), ○ CF-1 (100 Hz, 2.5 mm), ● CF-2 (100 Hz, 8.5 mm), ● CF-3 (25 Hz, 2.5 mm).*

C.7.3 Results discussion

As it was seen in the previous section, it seems that big structures imply an increase of the Q4 events (ejections) and a reduction of the Q2 (sweeps), i.e., the big difference between these two quadrants shows the presence of large structures. Besides, both configurations CF-2 (100 Hz, h=8.5 mm) and CF-3 (25 Hz, h=2.5 mm), and therefore with low accuracy in SCS representation, obtain a similar trend of growth of both, Q2 and Q4 time fractions. However, variations in term of trips caused by the increased CV (CF-2) and decreased FDC (CF-3) do not follow the same trend. While effects of the CF-2 are the markedly rise of the trips Q2-Q2 and Q4-Q4, the effects of the CF-3 are the moderate reduction of both trips.

The variations are more noticeable for the enlarged CV (CF-2) than for the decreased FDC (CF-3), especially in the near-bed region, where the percentage of the two mentioned trips are separated from the bed. In addition, the evolution along the depth of the rest of trips have a steadier behavior. On the other hand, variations induced by the reduced FDC (CF-3) are low particularly in the near-bed region.

Low FDCs (CF-3) reduces trips inside a given quadrant, while trips between different quadrants are increased. To further development of this concept, the duration of a burst inside the same quadrant, called pulse, is evaluated in the next section.

Although the same behavior for different FDCs stated above for QTFs is also observed in trips, since changes between CF-1(100 Hz) and CF-3(25 Hz) are moderate, there is a lack of information when measuring with low FDC. Measurements with 25 Hz defines, by definition (1/FDC), longer events, in other words, each one contains four events of 100 Hz. Each 25 Hz trip contains seven 100 Hz trips; therefore, the averaging window in terms of trips works differently.

C.8 Pulse Analysis

From the analysis of the trips between quadrants arises the question about how long these events stay in the same quadrant. One pulse is defined in this thesis as the uninterrupted time that a burst event (u'w') remains in a particular quadrant before moving to another quadrant. The duration of a pulse

(T_P) is measured in time intervals, or periods (1Δt =1/FDC), since it is the minimum time spent in a quadrant without interruption.

The pulse duration histogram (PDH) reflects the time fraction (TF) that each pulse duration (1Δt, 2Δt, and 3Δt onwards) represents in the data series. The size of the turbulent structures is suspected to be related to pulse duration, and therefore, the PDH must change from samples with different ADV configurations.

However, as stated before, samples with different FDC have no same interval of the pulse since 1Δt =1/FDC. Therefore, a FDC of 100 Hz can record pulses as of 1Δt=0.01 sec, while a FDC of 25 Hz yields longer intervals of the pulses starting from 1Δt=0.04 sec, in consequence, the comparison between different FDC is made by steps or periods, although they do not have the same duration. For this reason, the size of the pulse is called now length (L_P) measured by (δ) instead of T_P (Δt). Notice that when the same FDC is used, both δ and Δt can be considered the same.

The pulse length histograms (PLH) of one point at the height of z/d=0.04, for each configuration, are overlapped in Figure C.15-a. The horizontal axis represents the L_P (δ) and the vertical axis the TF that pulses with a particular L_P represent in the signal. The point z/d=0.04 is used as an example since it was noticeable that in the near-bed region the pulses tend to be shorter, i.e., the percentage of L_P=1δ are higher, and they are more affected by the configuration of the device.

Additionally, in Figure C.15-b, the belonging quadrant of each pulse is considered, i.e., the PLH is divided into quadrants, and all configurations are overlapped for the same point as before. For the three configurations, the slope of the PLH of Q2 and Q4 are less steep, thus higher number of long pulses are found and are more affected by the configuration of the device. On the other hand, the slopes of Q1 and Q3 PLHs are steeper and remain more confined in a zone showing a similar pattern.

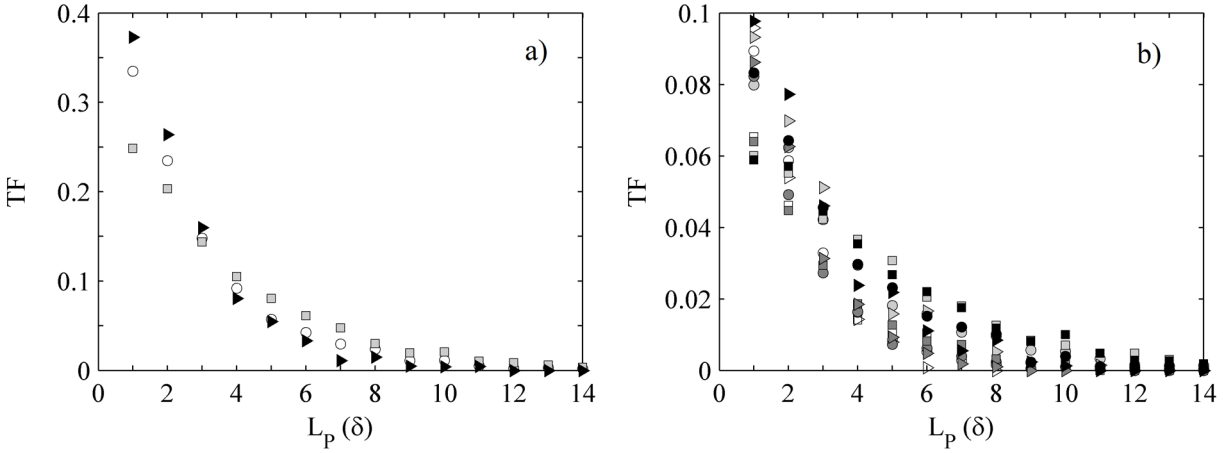

Figure C.15- PLH of the three configurations CF-1(100 Hz, 2.5 mm), CF-2 (100 Hz, 8.5 mm, and CF-3(25 Hz, 2.5 mm). (a) with no distinction between quadrants, and (b) separated by quadrants. *Legend (a), ○ CF-1, ■ CF-2, ▶ CF-3. Legend Markers (b), ○ CF-1, □ CF-2, ▷ CF-3. Legend colors (b), ○ Q-1, ● Q-2, ● Q-3, ● Q-4.*

Finally, in Figure C.16, three clouds (CF-1, CF-2, and CF-3) of pulses (*u'w'*) are plotted in the Quadrant Map for a point near the bed (z/d=0.04). The plotted points corresponding to the maximum velocity registered inside a pulse. The considered pulses drawn in the figure are pulses of a length as of 8δ onwards.

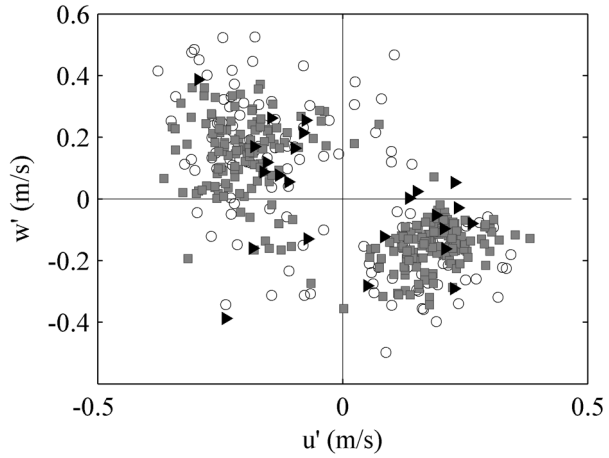

Figure C.16- Distribution of pulses L_P>8Δt on the quadrant map, of a point as *z/d*=0.04, for the three configurations. *Legend, ○ CF-1(100 Hz, 2.5 mm), ■ CF-2 (100 Hz, 8.5 mm), ▶ CF-3 (25 Hz, 2.5 mm).*

C.8.1 Influence of the increased CV

As it was seen formerly, the height (*h*) defines the size of structures that the device is able to capture; consequently, the PLH has to be also sensitive to it. When a bigger CV is set in the device, a lesser percentage of short pulses (L_P=1δ) is yielded, especially in the near-bed region dropping the value from 33% to 25 %, as is shown in Figure C.15-a by the comparison between the CF-1 (*h*=2.5 mm) vs. CF-2 (*h*=8.5 mm). In general, pulses of L_P=1δ and L_P=2δ decrease, while the pulses L_P=3δ show a similar percentage, and finally pulses longer or equal to 4δ are augmented.

In Figure C.15-b, where the PLH is separated by quadrants, it is perceived a reduction of the shortest pulses (1δ) from CF-1 to CF-2 in each quadrant. Nonetheless, while the slopes of the histograms remain similar for the Q1 and Q3, the slopes of the histograms of Q2 and Q4 become less steep, showing a significant drop of short pulses (1δ), by means of increasing the longers. On the other hand, Figure C.16 shows an intensification of long pulses (>8δ) mainly in the Q2 and Q4. Moreover, the peak velocity values inside the pulses reduce their value when the CV is increased (CF-2).

Large structures are present in the whole depth; therefore, all PSLs are very similar through the profundity, since a big CV (CF-2) gives them representation. On the other hand, the CF-1 with a small CV, with a better definition of the SCS mainly in the region near the bed, the PLH of a point close to the bed are more scarped than points far from the bed, obtaining a more extensive range the shortest pulses in the profile.

C.8.2 Influence of the decreased FDC

As in the case of the enlarged CV, the decreased FDC produces the same effect of narrowing the PLH into a thin zone for all points of the depth profile, due to the lack of SCS. However, the effects are not the same in terms of quantity. Contrarily to what was seen between CF-1 and CF-2, by decreasing the FDC (CF-3, 25 Hz), the percentage of these shortest pulses (1δ) increase from 26-34% (CF-1) to 33-37% (CF-3), Figure C.15-a. As of pulses of 4δ of length are diminished by the lower FDC (CF-3).

Figure 5.12-b plots the effects of the decreased FDC (CF-3, 25 Hz) on the pulse length in each quadrant. The consequences are the same as for the general PLH. Nonetheless, the pulses of length up

to 4δ contained in the quadrants Q2 and Q4 are augmented while long pulses as of 5δ are diminished. On the other hand, in the Q1 and Q3 only pulses of 1δ and 2δ of length are increased and pulses equal or over 3δ are reduced.

On the other hand, Figure C.16, Quadrant Map of maximum velocities of the pulses over 8δ, shows discrepancies between the CF-2 (100 Hz, h=8.5 mm) and CF-3 (25 Hz, h=2.5 mm), unlike what had been seen so far, where the effects in all respects were very similar. In both cases seem that the cloud of values *u'w'* becomes more confined; however, for the CF-3 much less long events (above 8δ) than in the other two cases appear in the signal.

C.8.3 Results discussion

When a large CV is set, the TF of pulses L_P <2δ are diminished, and longer pulses (L_P>4δ) become more likely. In contrast, when the FDC is decreased, the TF of pulses L_P<3δ is increased, while the TF of pulses L_P>4δ is reduced. It may seem a contradiction that having a low FDC, with the consequent reduction of the SCS representation, yields a higher amount of short pulses. However, it has to be pointed out that the length of the pulses has been considered in steps or periods (δ), thus the duration in seconds has not been considered.

Therefore, considering the pulse duration (T_P) in time (Δt), the duration of an isolated event from the CF-3 (25 Hz) is $1\Delta t_3$=0.04 s. This short pulse ($1\Delta t_3$) can be decomposed in four sub-pulses of $1\Delta t_1$=0.01 s, which is the duration of 1Δt in the CF-1 (100 Hz). Furthermore, $1\Delta t_3$=0.04s can be composed by different combinations of sub-pulses, i.e. ($1\Delta t_1$, $1\Delta t_1$, $1\Delta t_1$, $1\Delta t_1$); ($1\Delta t_1$, $1\Delta t_1$, $2\Delta t_1$); ($2\Delta t_1$ $2\Delta t_1$), ($1\Delta t_1$, $3\Delta t_1$); ($4\Delta t_1$). These sub-pulses (Δt_1) determine the pertaining quadrant of the pulse $1\Delta t_3$, but the information of the sub-pulse duration is not available. Consequently, the TF of T_P with different time interval ($1\Delta t_1$ and $1\Delta t_3$) cannot be compared quantitatively due to the lack of information precludes the correct interpretation of the pulses. As a conclusion, it is possible that pulses of $1\Delta t_3$=0.04 s contain a large quantity of $3\Delta t_1$=0.03 s and $4\Delta t_1$=0.04 s pulses. Therefore, an upsurge of the $1\Delta t_3$ can predict as well an upsurge of the $3\Delta t_1$ and $4\Delta t_1$ obtaining the same effect than when the CV is enlarged.

SCS seems to be represented by short pulses since the percentage of these are high in points near the bed, and the value is steadily reduced as going up through the depth, providing that a small CV is set so that SCS have representation in the samples. On the other hand, when a long CV or a low FDC is set, all PLH are confined in a region, showing the same trend, thus, just big structures are represented.

The patterns observed from the histograms are controlled by the Q2 and Q4 pulses since they present a wider range of trends. These pulse regulators from Q2 and Q4, are also more modified by the configurations. On the other hand, the Q1 and Q3 have a scarped slope and similar pattern of the pulse histograms no matter the height (z) at the profile, like a backbone of the flow that resists better the effects of the lack of SCS conditioned by the configurations or the distance to the bed.

Regarding the Turbulent map of pulses, points far from the origin of coordinates, i.e., high-velocity fluctuations, are likely to be part of a long pulse. If an event achieves to reach a point far from the coordinates, the most likely fact is that the next quadrant is the same, because it does not have time enough to change the sign of the velocity.

C.9 Performance curves of the ADV

The term of ADV performance curves was introduced by Garcia et al. (2005). They observed that the FDC has a great impact on the turbulent variables, so they evaluated these effects by means of the ADV performance curves. These curves define the optimal flow and sampling conditions for turbulence measurements or, in cases where necessary, can be used to make the appropriate corrections. Garcia et al. (2005) defined the curves using a dimensionless frequency (F) defined by Eq. C-1, where L is the energy containing eddy length scale (integral length scale), U_C the convective velocity (Eq. C-2), and h_R is the CV height set by the flow. They claim that the FDC effects.

$$F = L \cdot FDC / U_C = L/h_r \qquad \text{C-1}$$

$$U_c = \sqrt{\bar{u}^2 + 2\bar{v}^2 + 2\bar{w}^2 + u'^2 + 2v'^2 + 2w'^2} \qquad \text{C-2}$$

The curves ADV performance curves (Garcia et al. 2005) show the percentage of error of some turbulent properties, in comparison to the properties taken at the maximum FDC, as a function of F.

However, the maximum FDC could not be the best representation of a particular flow, due to the oversampling of the velocity signal and the value of L depends on the FDC. Moreover, it has been observed that the variations of the turbulent properties as a function of FDC depends also on the level of turbulence. That is to say, they have to be calibrated for each flow since the level of turbulence shows a different trend of evolution.

The experiments carried out in this thesis, both the CUBE and the FRITZ tests, do not show the necessary F (Figure C.17) for, according to Garcia et al. (2005) faithfully represent the turbulent properties. For all these reasons, the variation of each of the turbulent properties studied in the thesis has been assessed according to the FDC for different measurements with different levels of turbulence.

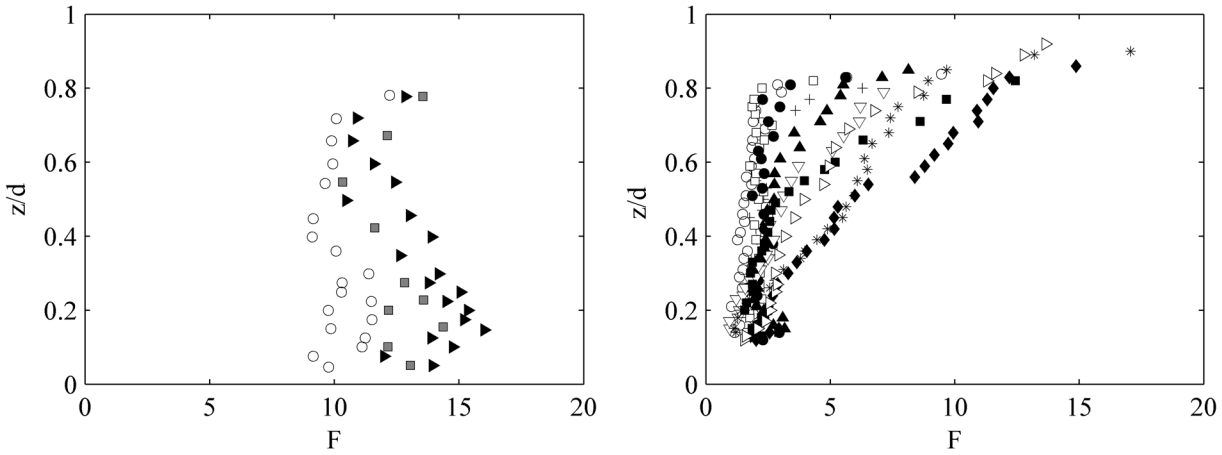

Figure C.17- Vertical distribution of F. for (a) the CUBE and (b) FRITS experiments. *Legend (a), ○ CF-1, ■ CF-2, ▶ CF-3. Legend (b), + RG1, ○ RG2, □ RG3, ● RG4, ▲ RG5, ▽ RG6, ✳ RG7, ♦ RG8, ■ RG9 and ▷ RG10.*

The next paragraphs represent the performance curves as a function of the FDC and the CV size for both channel experiments, the FRITZ, and the CUBE. Both kinds of experiments have different levels of turbulence.

C.9.1 The 'FRITZ' experiments

As already mentioned, the FDC defines the size of the time averaging window that the device uses to give information, and so some values are increased, and others are decreased by this fact. Nevertheless, it is crucial to remark that if the CV height set by the user (h) is bigger than the set by the flow h_R ($h > h_R$), the spatial averaging becomes more important than the time averaging occurred by using a low FDC. Then setting a long CV can yield similar effects on the turbulent parameters than setting a low FDC. That makes sense with what has been seen so far. Therefore, in the cases where $h > h_R$, the CV size set by the user (h) has to be included in the definition of the dimensionless Frequency (F) (Eq. C-1) instead of h_R, thus $F=L/h$, to take into account the spatial averaging.

However, in the FRITZ tests, the effect of the CV height (h) on the turbulent parameters are notable even when $h < h_R$. The latter can be demonstrated by focusing now on the first set of experiments (Tests) and specifically in the test T-1, with 25 Hz of FDC, h=7 mm of CV height and 2.5 m/s as velocity range, and the test T-3 with 25 Hz, h=2.5 mm, and 2.5-/s respectively.

The minimum velocity defines the smallest CV set by the flow (h_R), since h_R=U/FDC. Thus, if the velocity is low, it can occur $h > h_R$ causing that the effects of a big h set by the user start to have effects on the calculations. The minimum velocity for the mentioned tests was 0.41 m/s for a point located at z=5 mm from the bed with h_R=16.4 mm (0.41 ms^{-1}/25 s^{-1}). It is worthwhile to remember that all the FRITZ tests were conducted with the same flow conditions but changing the ADV configuration.

Even though $h < h_R$ in both experiments (T-1, 7 mm<16.4 mm and T-1, 2.5 mm<16.4 mm), some differences are detected between these two tests, as seen in Table C.4 of the previous section. In that table, the mean values of the profile were evaluated. The first row represents the results from the experiment T-1 and below this, the percentage of variation of the parameters for the rest of the tests. Differences from these two experiments are non-negligible, for example, an increase in Reynold stresses of the 15.5%, or a decrease of the integral length scale of the 29%, when the CV size is decreased from h=7 mm (T-1) to h=2.5 mm (T-3), in both cases $h < h_R$. For this reason, the spatial averaging has to be also considered even when the CV set by the user (h) is smaller than the set by the flow (*hr).*

In order to consider both effects of the ADV configuration (FDC and h), two performance curves have been obtained from each studied parameter. The Performance curves of the ADV for the FRITZ experiments are displayed below.

C.9.1.1 FDC Performance curves

The performance curves of the FDC have been created using the tests T-1, T-4, and T-5. All of them have same CV size h=7 mm and velocity range of 2.5 m/s but frequencies of 25, 100 and 200 Hz respectively, thus, just the effects of the frequency averaging are taken into account.

In the next figures some of the most important and relevant parameters for the present thesis, are presented as a function of the FDC. In the next figures, the three experiments are represented (by a different color) and the three points for each one (by different marker), see the legend in Figure C.18.

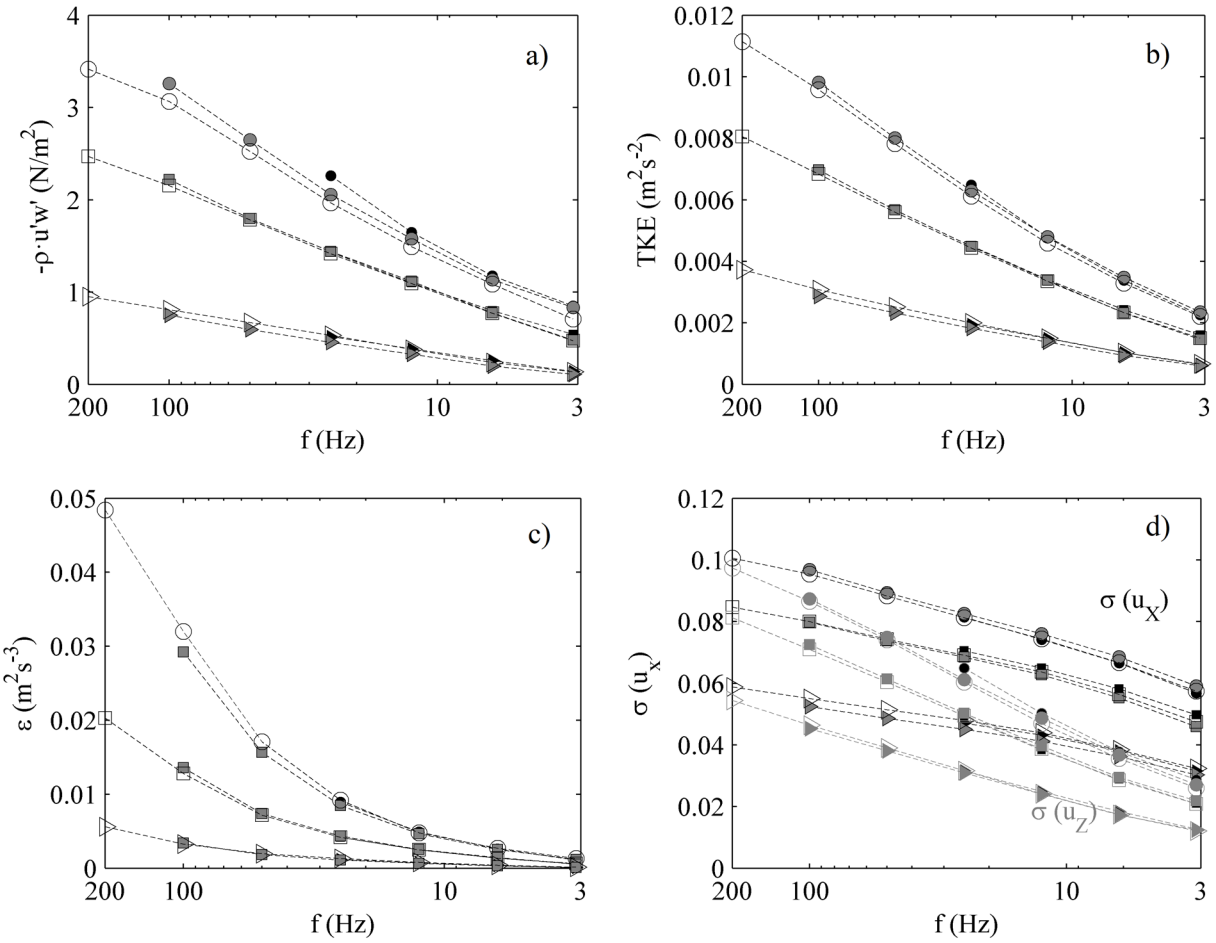

Figure C.18- FDC Performance curves of (a) Reynold stresses, (b) TKE, (c) Dissipation rate (ε) and (d) σ_u and σ_w. *Legend Marker, ○ z=5 mm, □ z=32 mm, ▷ z=62 mm. Legend Colors, Legend colors (b), ○ T-1, ● T-4, ● T-5.*

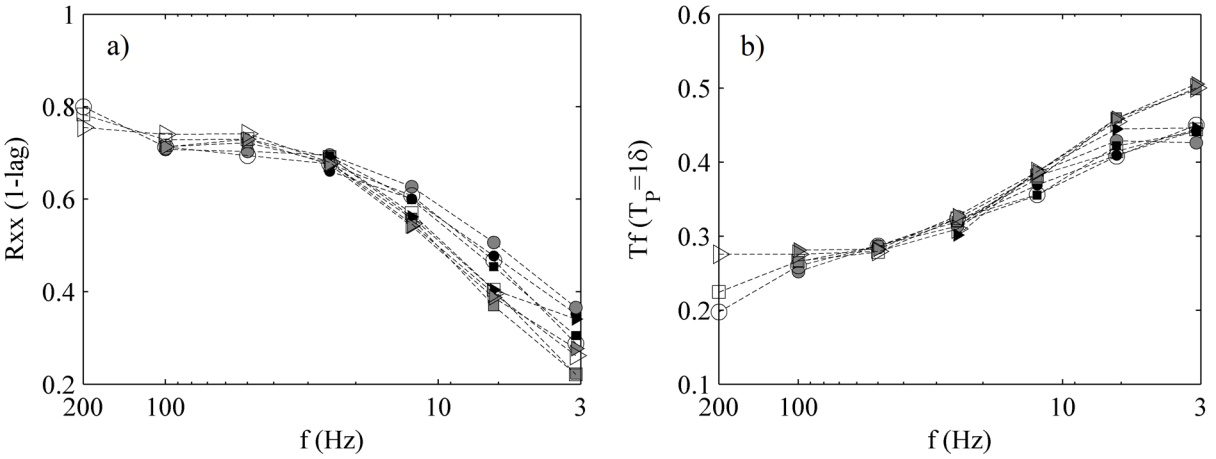

Figure C.19- FDC Performance curves of (a) Autocorrelation function values at lag-1, (b) TF of L_P=1δ. *Legend Marker, ○ z=5 mm, □ z=32 mm, ▷ z=62 mm. Legend Colors, Legend colors (b), ○ T-1, ● T-4, ● T-5.*

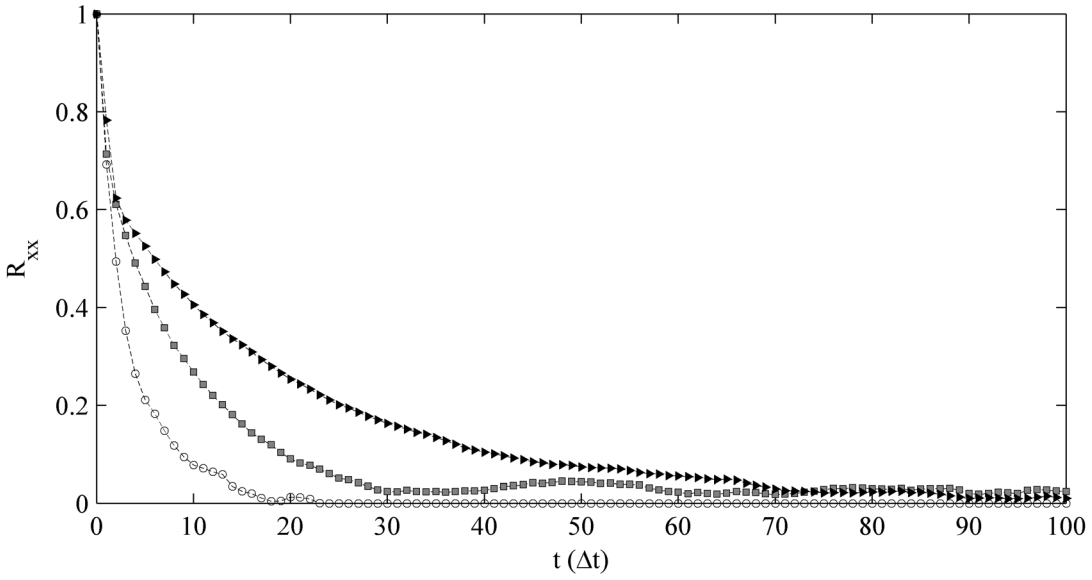

Figure C.20- Autocorrelation functions as a function of the time in Δt (periods). Legend, ○ T-1 (25 Hz) , ■ T-4 (100 Hz*) , and* ▶ *T-5 (200 Hz).*

The main difference from these curves and what was seen in the first part of the appendix is that for each studied point (z=5 mm, z=32 mm, and z=62 mm) and for each configuration (T-1, T-4 and T-5), a time averaging process has been made to reproduce the lessening of the FDC. In other words, the signals from the T-1 with 25 Hz, T-4 with 100 Hz and T-5 with 200 Hz are decreased until 3.125 Hz, using a time average window method, in the same way that the device does it.

It was corroborated first that the time averaging made afterward was the same made by the device by comparing different parameters. None of the comparisons have been included so that this section is not overloaded.

The turbulent parameters such as Reynold stresses, TKE, and dissipation rate (calculated by means of the structure functions of Kolmogorov), Figure C.18 (a, b and c respectively), show a decrease when the FDC is reduced. The latter is due to the lessening of the standard deviations of the longitudinal and vertical velocities (σ_u and σ_w) (Figure C.18-d), due to the attenuation of the peak velocities.

The value of the autocorrelation function at 1-lag show an increase when the FDC is augmented, Figure C.19-a, which makes sense since the time duration of the lag changes with the FDC, and therefore the 1-lag autocorrelation value becomes closer to one, as can be seen in Figure C.20. However, this result can not be considered in time, since different FDC have different time interval.

In the case of the time fraction of the short pulses (1δ), Figure C.19-b, the number of these pulses decrease when FDC is augmented. However, this was seen in the previous section to be a consequence of the accuracy of the information, and decomposing velocities. It has to be mentioned that pulses are measured in this section (FDC performance curves) by length (δ) instead of time (Δt) since the duration of each one is different due to the different FDC.

On the other hand, all length scales are decreased when the FDC augments, Figure C.21-a however, the Kolmogorov scale decreases more abruptly. The Kolmogorov scale represents the smallest whirls

present in the flow before the viscosity dissipates the energy. As said in the previous section, the FDC sets up the capture capacity of the small coherent structures.

Figure C.21-b shows the standard deviation obtained from the velocity increments produced in the longitudinal and vertical axis ($\sigma_{\Delta u}$ and $\sigma_{\Delta w}$). It is noteworthy that the $\sigma_{\Delta u}$ from different FDC do not show a clear tendency of decrease with the FDC as the $\sigma_{\Delta w}$ shows. This does not mean that the increments Δu au are not reduced with the increase of the FDC, however the variation with respect to the mean ($\overline{\Delta u} = 0$) is similar in all cases.

Figure C.22 shows the variation of the QTF. It is noticeable that from 25 Hz to 200 Hz, the variations are slight while as of 25 Hz the variation start to become more critical. The same effect is found in the sequences of pulses, Figure C.23, where the most common sequences of pulses are shown. They also remain stable up to 25 Hz and as of that FDC start to fall if the FDC decrease.

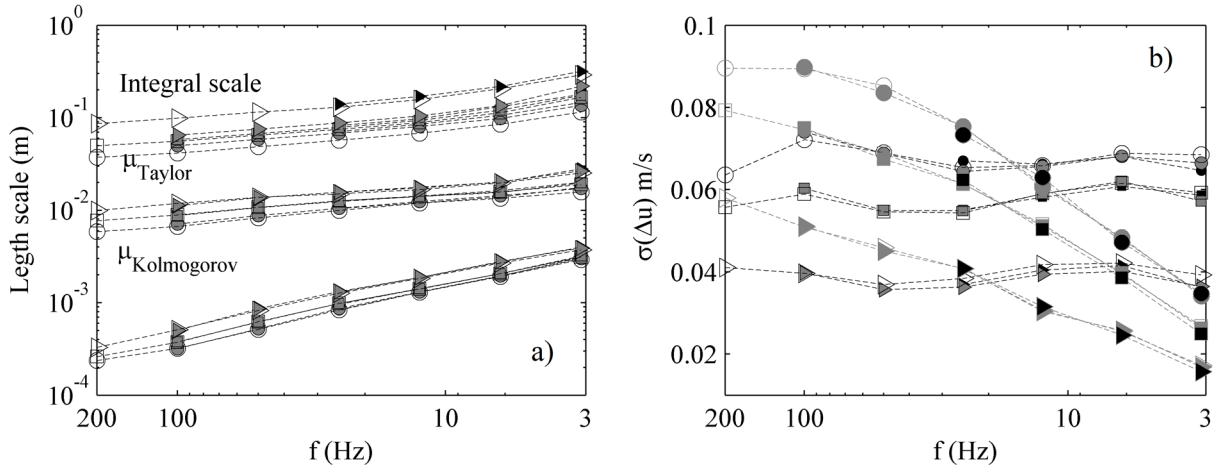

Figure C.21- Performance Curves of the FDC variation. Figure (a) Integral scale, Taylor scale and Kolmogorov scale and (b) Standard deviation of longitudinal (black) and vertical (grey) velocities. *Legend Marker, ○ z=5 mm, □ z=32 mm, ▷ z=62 mm. Legend Colors, Legend colors (b), ○ T-1, ● T-4, ● T-5.*

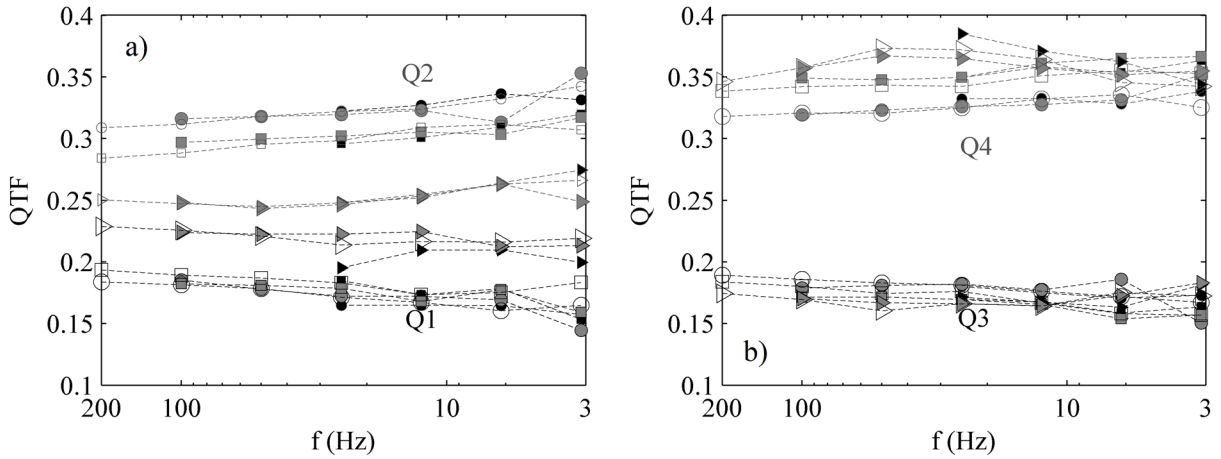

Figure C.22- Performance Curves of the FDC variation. Figure (a) Time fraction of the Q1 (black) and Q2 (dark gray), and (b) Time fraction of the Q3 (black) and Q4 (dark gray). *Legend Marker, ○ z=5 mm, □ z=32 mm, ▷ z=62 mm. Legend Colors, Legend colors (b), ○ T-1, ● T-4, ● T-5.*

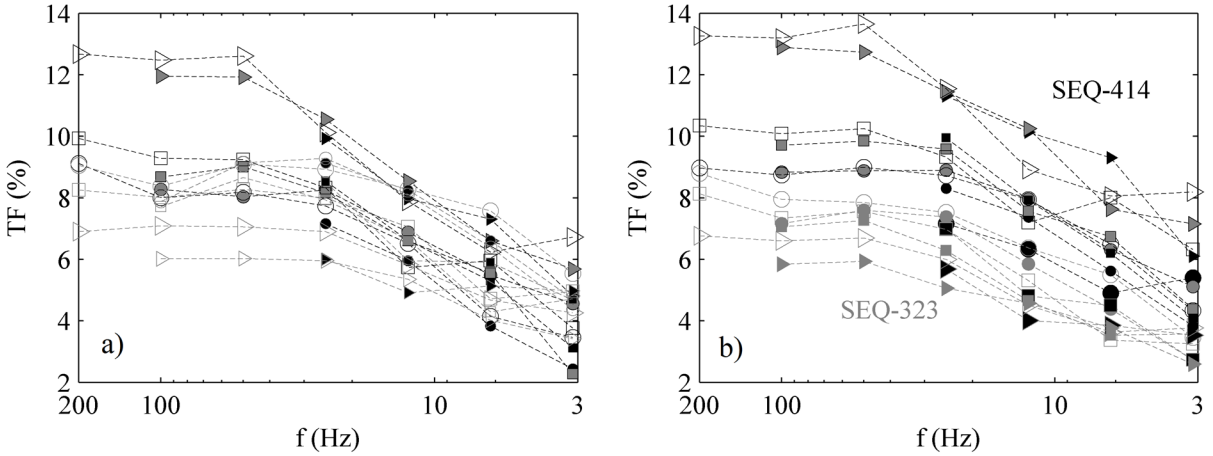

Figure C.23- Performance Curves of the FDC variation. Figure (a) Time fraction of the sequence pulse quadrants Q1-Q4-Q1 (black) and Q2-Q3-Q2 (dark gray), and (b) Time fraction of the sequence pulse quadrants Q4-Q1-Q4 (black) and Q3-Q2-Q1 (dark gray). *Legend as for* Figure C.22.

When the value of FDC value decreases, the information is reduced in terms of time, i.e., fewer velocities per second and less accurate, nonetheless, the QTF persist somewhat stable. It has been demonstrated that both the profile patterns of the QTFs and trips between quadrants were maintained. That is to say, that quadrant distribution is preserved despite the averaging window. This effect has been demonstrated again in the performance curves. All these facts evidence that the velocity signal obtained from a specific *h* shows the same patterns for different FDCs, despite the lack of information and different time intervals, showing that the sorting and statistics have the same behavior in the Quadrant Map.

Measurements at low FDCs yield more short events (1δ), Figure C.19-b, however, each of these can contain longer events at higher FDC. Therefore, the averaging window regarding pulses and sequences works differently. Nonetheless, the sequences maintain the same time fraction from 25 Hz until 200 Hz, therefore, if there is enough definition, its statistical behavior is proportional.

C.9.1.2 Control volume Performance curves

As said before, also the performance curves for the effects of the CV size have been evaluated. For this purpose, tests T-1 and T-3 have been evaluated since both of them have the same configuration (25 Hz and 2.5 m/s) but different CV sizes (*h*) of *h*=7 mm and *h*=2.5 mm, respectively. In this case, to reproduce the enlargement of the *h* and its spatial averaging effect, it has been used a moving average window. The moving average window obtains different series from the original by passing a window of averages, obtaining n-1 values (n=number of data in the original series) and therefore the frequency of the signal is not changed. The enlargement of this window reproduces the effect of the enlargement of the CV (*h*). The figures below (Figure C.24, Figure C.25, Figure C.26, Figure C.27 and Figure C.28), show the effects that the moving average window has on the tests T-1 and T-3, for the three points taken from the depth profile.

The Reynold stresses, the dissipation rate (ε) and the TKE diminish their value as the CV size increase and show the same pattern of decrease than for the FDC decreased (Figure C.24). This is due to the

decrease of the σ_u and σ_w, same as seen in the FDC performance curves, because of the attenuation of the peak velocities.

The values of the autocorrelation function at 1-lag (Figure C.25-a) and the time fraction of the 1Δt pulses (Figure C.25-b) behave differently than for the FDC. It was seen that when the reduction of the FDC the autocorrelation value decreases, which is considered normal because of the duration of the 1-lag increase and then becoming closer to time zero, where the value of the autocorrelation is one. However, in the case of the increase of the CV, with the same value of FDC and thus same duration of 1-lag, the autocorrelation value increases. That is to say, if a higher h is set the R_{xx} (autocorrelation function at 1-lag) increase, as a result, the integral length scale will be increased as well. This performance is in accordance with the results in the first part of the appendix.

The time fraction of the 1Δt pulses has now decreased with the increment of the CV (Figure C.25-b), in contrast with what happened with the decrease of the FDC. However, it should be recalled that now pulses are measured by duration (Δt) since all data series have the same FDC. As a consequence, the enlargement of the average window (or an increase of h) results in the decrease of the short pulses (1Δt) and longer pulses start to appear. That can be a consequence of a diminished representation of the SCS in the data series. As consequence of that all the length scales, Figure C.26-a, is increased. This behavior is in line with the results obtained in the first part of the appendix, meaning that the averaging window affects the duration pulses. On the other hand, the $\sigma_{\Delta u}$ and $\sigma_{\Delta w}$ (standard deviation of the velocity increments) decrease sharply with the increase of the CV (Figure C.26-b), different from the occurred with the decrease of the FDC where the values remained stable for $\sigma_{\Delta u}$.

The QTF behave in a similar way when the h is increased than when the FDC is decreased, Figure C.26. Therefore, the presence of each quadrant in the data series is a very robust value, no matter the CV or the FDC that has been set up. In the case of the pulse sequences (Figure C.27), the behavior changes in comparison with the FDC, now the time fraction of the most common sequences increases a little with the size of the CV. This performance is consistent with the enlargement of the pulses seen in Figure C.25-b.

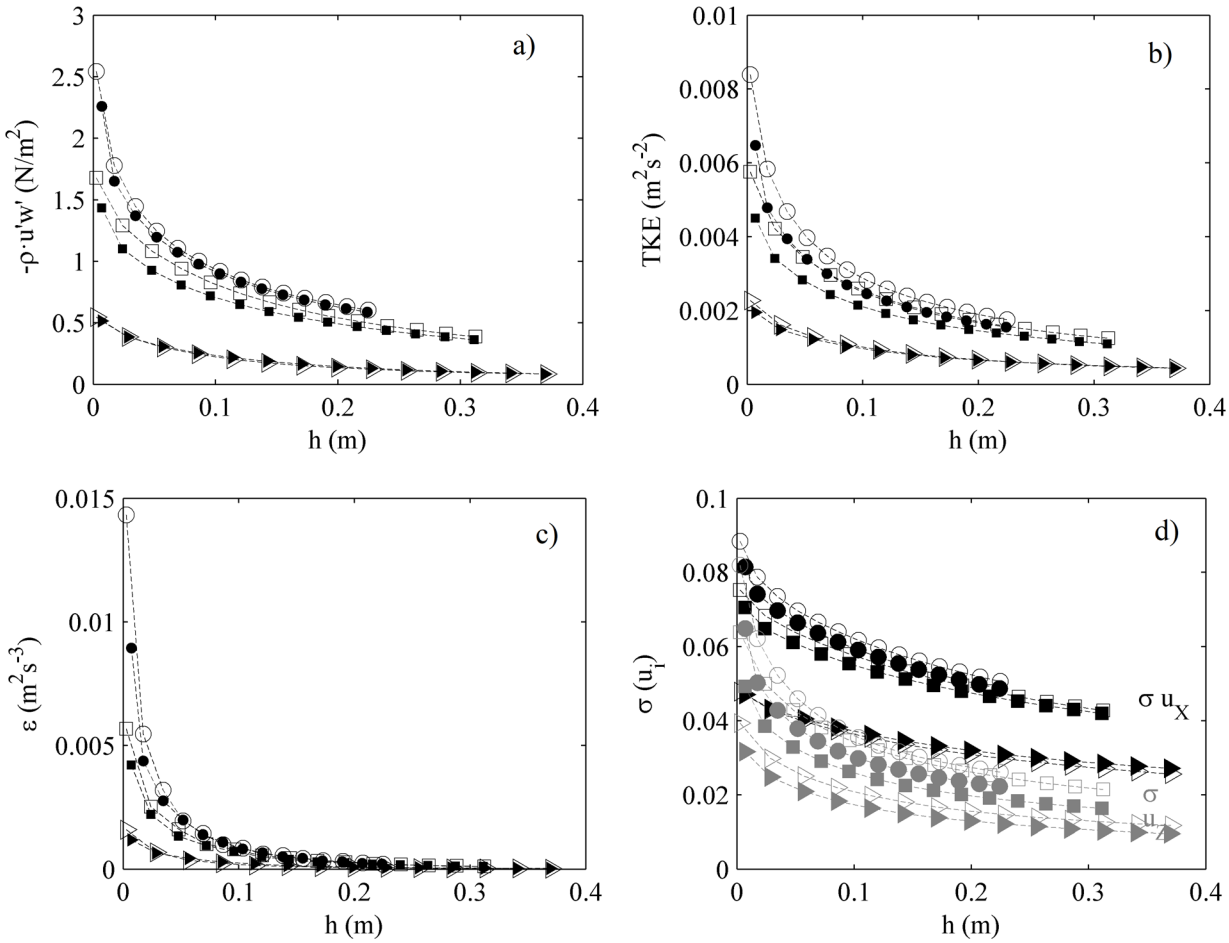

Figure C.24- CV height Performance curves of (a) Reynold stresses, (b) TKE, (c) Dissipation rate (ε) and (d) σ_u and σ_w. *Legend Marker, ○ z=5 mm, □ z=32 mm, ▷ z=62 mm. Legend Colors, Legend colors (b),○ T-1, ● T-3.*

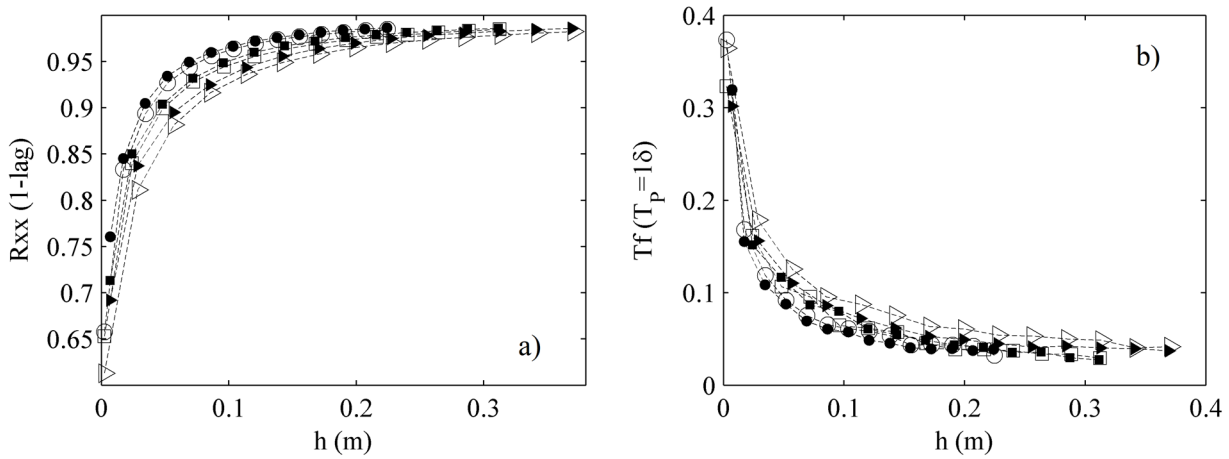

Figure C.25- CV height Performance curves of (a) Autocorrelation function values at lag-1, (b) Time fraction of 1δ pulses. *Legend Marker, ○ z=5 mm, □ z=32 mm, ▷ z=62 mm. Legend Colors, Legend colors (b),○ T-1, ● T-3.*

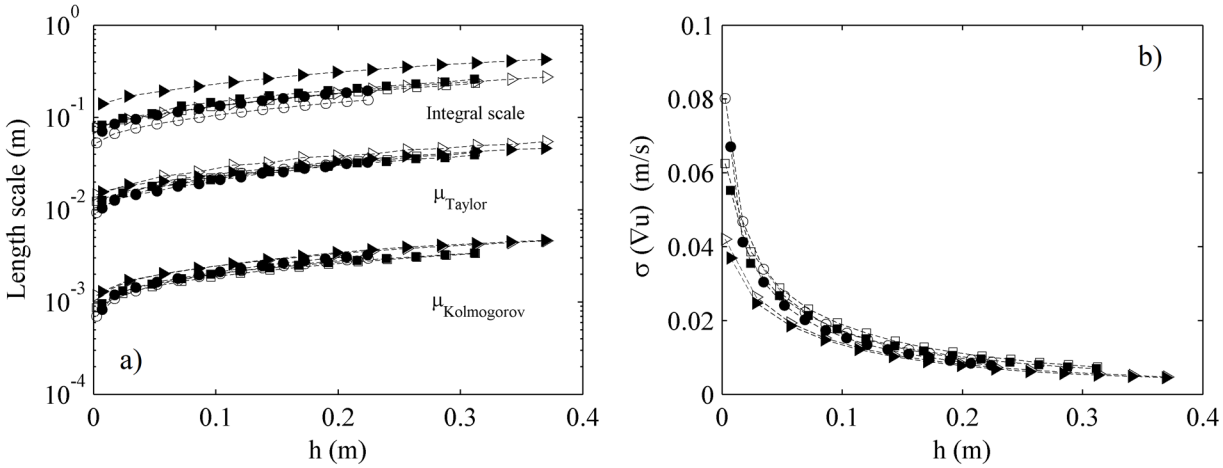

Figure C.26- Performance Curves of the CV size variation. Figure (a) Integral scale, Taylor scale and Kolmogorov scale and (b) Standard deviation of longitudinal (black) and vertical (gray) velocities. *Legend Marker, ○ z=5 mm, □ z=32 mm, ▷ z=62 mm. Legend Colors, Legend colors (b),○ T-1, ● T-3.*

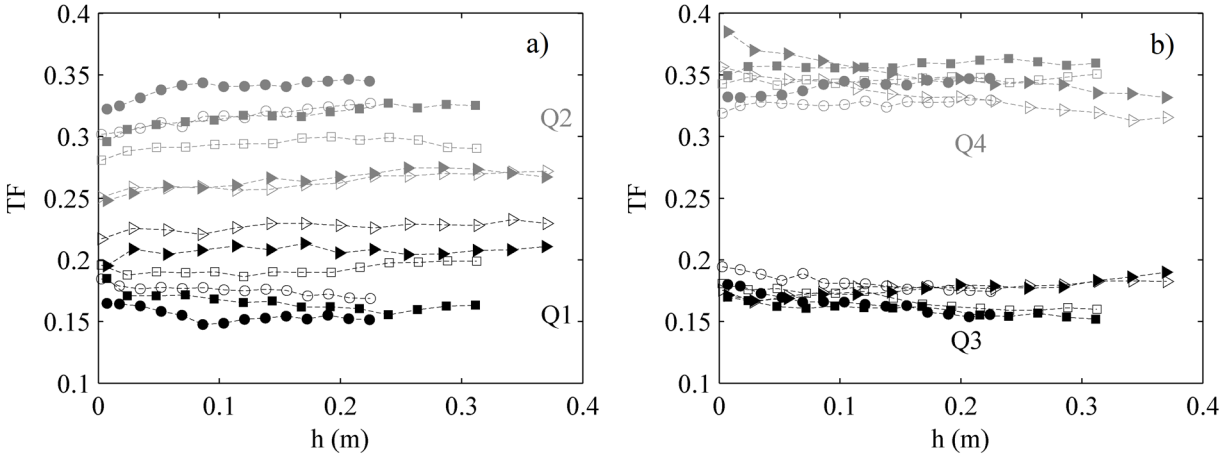

Figure C.27- Performance Curves of the CV height variation. Figure (a) Time fraction of the Q1 (black) and Q2 (dark gray), and (b) Time fraction of the Q3 (black) and Q4 (dark gray). *Legend as for Figure C.26.*

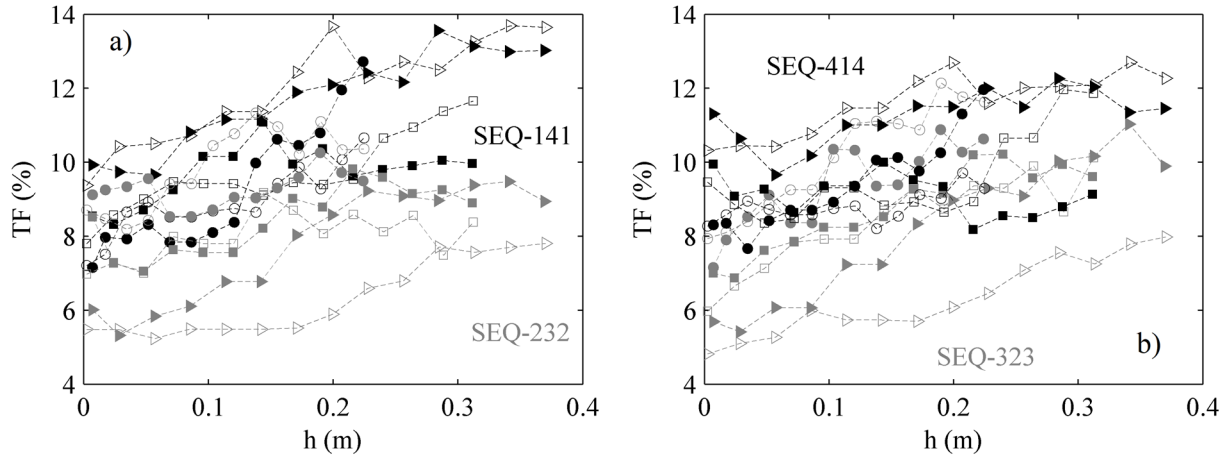

Figure C.28- Performance Curves of the CV height variation. Figure (a) Time fraction of the sequence pulse quadrants Q1-Q4-Q1 (black) and Q2-Q3-Q2 (dark gray), and (b) Time fraction of the sequence pulse quadrants Q4-Q1-Q4 (black) and Q3-Q2-Q1 (dark gray). *Legend as for Figure C.26.*

C.9.2 The 'CUBE' experiments

The next figures characterize the performance curves of the experiments carried out in "The Cube" channel. The black lines represent a point near the bed (z/d=0.16), and the gray lines represent a point at a height of z/d=0.4. The dashed lines describe the ten experiments from tests RG1 to RG10 with an ADV configuration of FDC=25 Hz and h=9 mm, so that an extensive range of turbulence level are covered, while the continuous lines represent the test T-1 (FDC=25 Hz and h=7 mm) from the tests carried out on the FRITZ channel. The purpose of overlapping both groups of experiments is to see how different flow conditions, although having almost the same configuration, can affect the results. The configuration of the RG experiments was FDC of 25 Hz, h=9 mm and 2.5 m/s as velocity range. The configuration of the test T-1 follows almost the same as the RG experiments, but CV size is 7 mm instead of 9 mm, in any case, very similar to each other.

All curves have characterized the parameter in the ordinate axis; the abscissa axis symbolizes the frequency and the CV height *(h*), the first being on a logarithmic scale. Both performance curves, FDC, and *h*, will be analyzed in parallel to see the differences between them.

The standard deviation of the longitudinal (σ_u) and vertical (σ_w) velocity can be thought as the turbulence intensities (TI). It is noticeable in Figure C.29 and Figure C.30 that both σ_u and σ_w decrease in a very similar way when the FDC decrease or the *h* or increase. As seen before, both configuration parameters determine the capacity of the device to capture the small structures (SCS) present in the flow. When the level of turbulence is high, i.e., experiments RG with a large flow rate, and especially at points near the bed, both σ_u and σ_w reduction seems to be a little more abrupt. In the case of the test T-1, both points z/d=0.16 (black) and z/d=0.4 (gray) the decline of σ_u and σ_w is low.

Figure C.31 shows the turbulent kinetic energy TKE evolution as a function of the *h* and *FDC*. The TKE include the σ of the three axes thus the reduction follows the same pattern. Both changes in the configuration parameters reduce notably the TKE value and the decrease are more remarkable if the initial TKE is high. In the case of the T-1 with low levels of turbulence, the decrease is lower, yet there is a reduction.

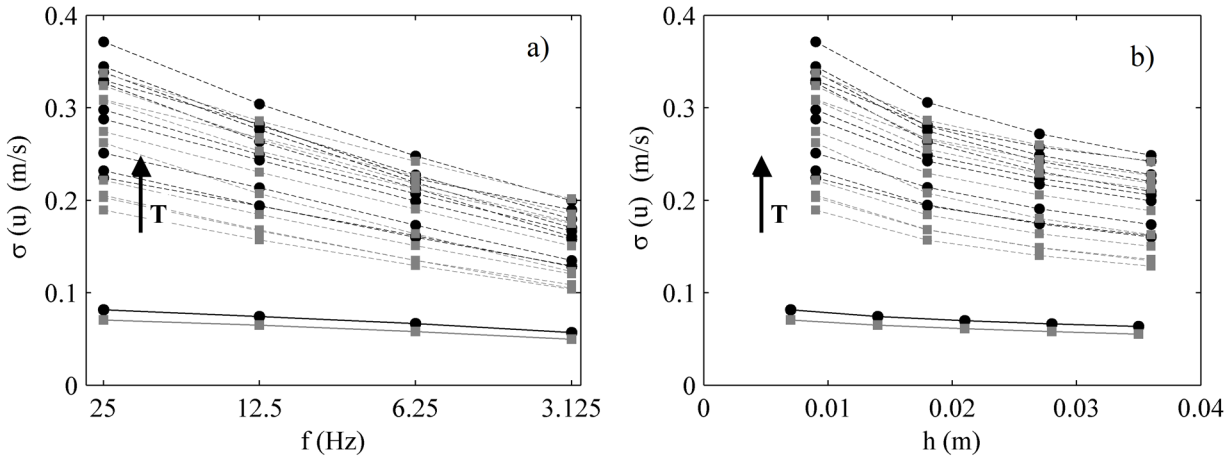

Figure C.29- Standard deviation of *u*, (a) as a function of the FDC, (b) as a function of *h*. *Legend colors,* ● *z/d=0.16,*■ *z/d=0.4. Legend Lines,* ▬ ▬ *RG Experiments,* ▬▬ *Test T-1.*

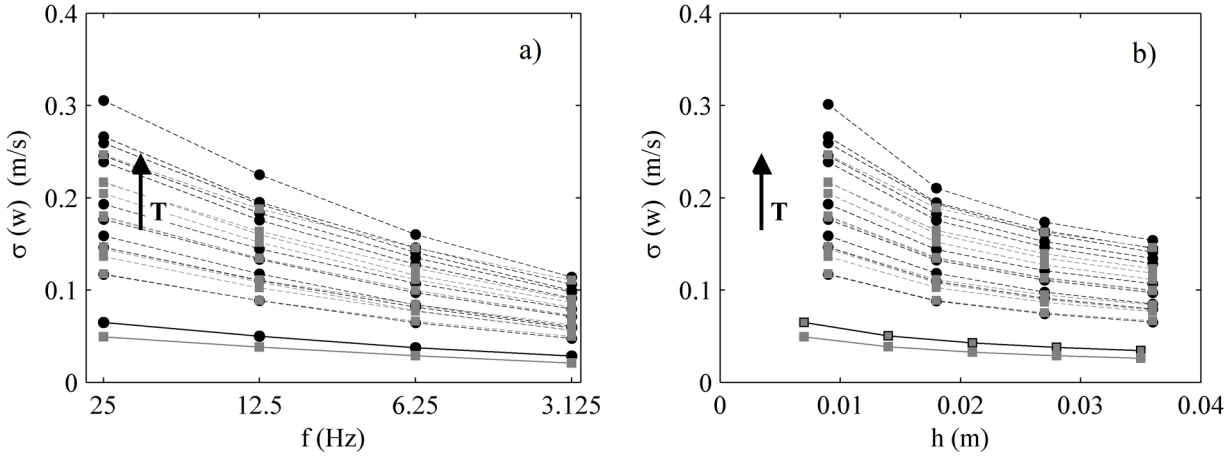

Figure C.30- Standard deviation of w, (a) as a function of the FDC, (b) as a function of the *h*. *Legend colors,* ● *z/d=0.16,* ■ *z/d=0.4. Legend Lines,* ▬ ▬ *RG Experiments,* ▬▬ *Test T-1.*

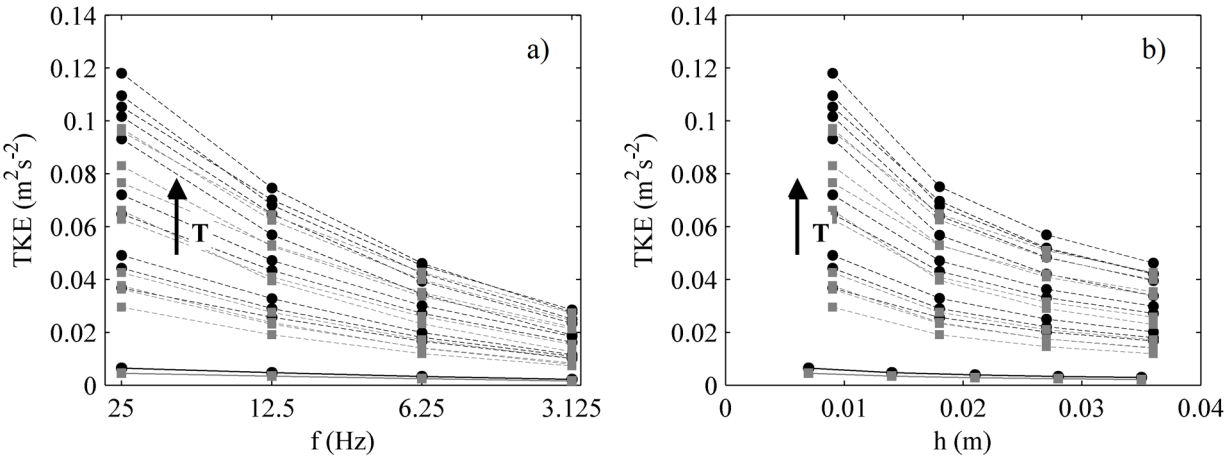

Figure C.31- Turbulent Kinetic Energy, figure (a) as a function of FDC, (b) as a function of the CV. *Legend colors,* ● *z/d=0.16,* ■ *z/d=0.4. Legend Lines,* ▬ ▬ *RG Experiments,* ▬▬ *Test T-1.*

Since the values from σ_u and σ_w multiplied by minus the density of water ($-\rho_w$) defines the values of the normal stresses τ_{xx} and τ_{zz}, it makes sense that they reduce their negative value with the FDC decrease. In the case of the Reynold stresses, Figure C.32-a and Figure C.32-b, the value is decreased intensely when the level of turbulence is high in both cases, the decreased FDC and the increased *h*. It is appreciable how for low turbulence from the point at *z/d*=0.4, the decrease is less steep, making very difficult to find a common trend of decrease for all cases.

The trend of the dissipation value (ε) as a function of FDC and *h* is shown in Figure C.33. Unlike the rest of the turbulent parameters, it shows the same rate of decrease for all experiments no matter the level of turbulence, showing a stable slope of decrease in all cases.

The same rate of increase is seen in all the RG cases for the length scales, Figure C.34-a when the FDC is reduced. The integral and Taylor scales reduce their value in the same manner when the level of turbulence is high enough; however, in the case of the Kolmogorov scales, the rate of increase is higher. The same effect, although more moderate, is shown by the test T-1, i.e., the increase of both points at different heights are parallel, and the Kolmogorov length shows a higher rate of increase. Figure C.34-b depicts the effects of the *h*, showing that the three length scales follow the same rate of increase.

Therefore it seems that the scale more affected by the configuration is the Kolmogorov scale and above all for the modification of the FDC.

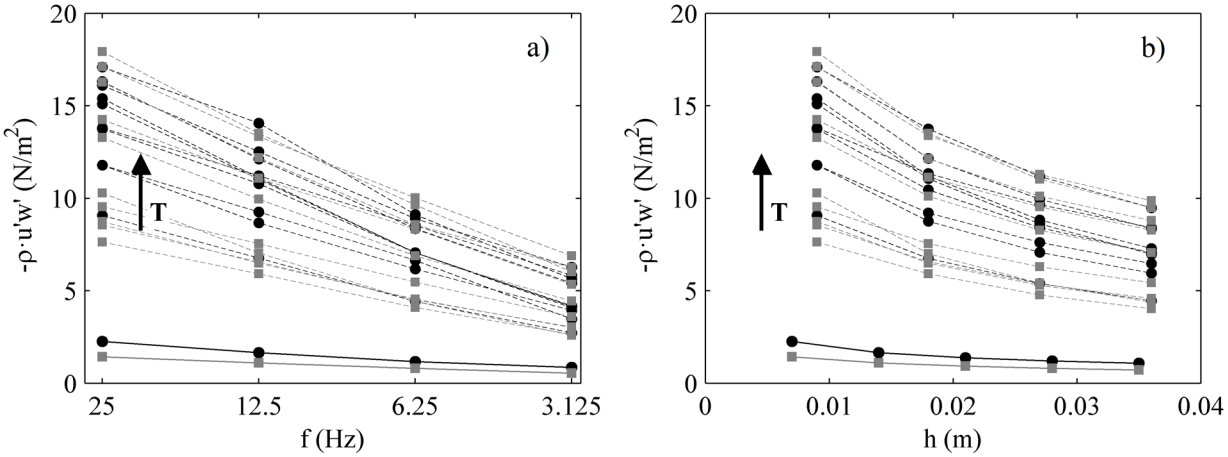

Figure C.32- Reynold Stresses, figure (a) as a function of FDC, (b) as a function of the CV. *Legend colors,* ● *z/d=0.16,* ■ *z/d=0.4. Legend Lines,* — — *RG Experiments,* ——— *Test T-1.*

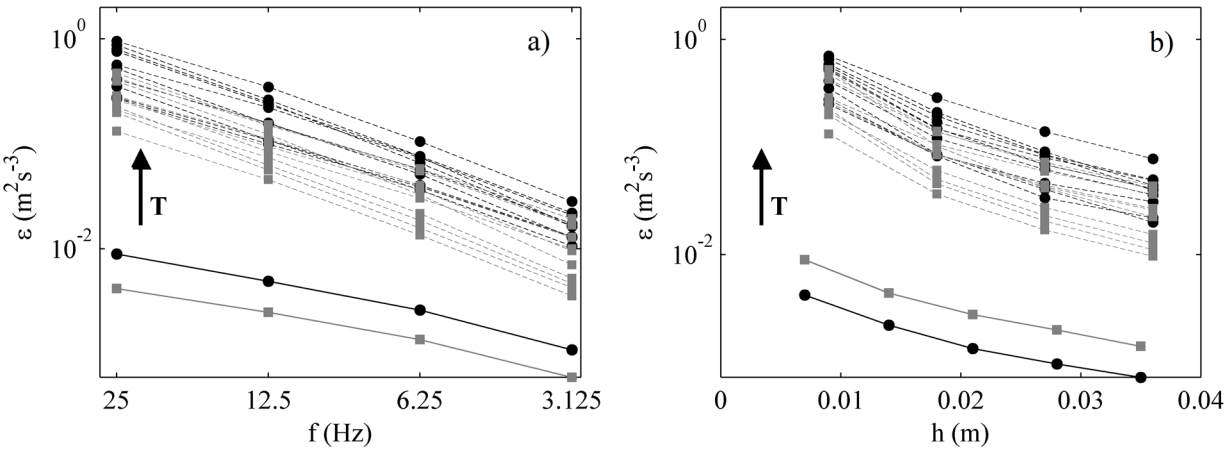

Figure C.33- Dissipation rate (ε), figure (a) as a function of FDC, (b) as a function of the CV. *Legend colors,* ● *z/d=0.16,* ■ *z/d=0.4. Legend Lines,* — — *RG Experiments,* ——— *Test T-1.*

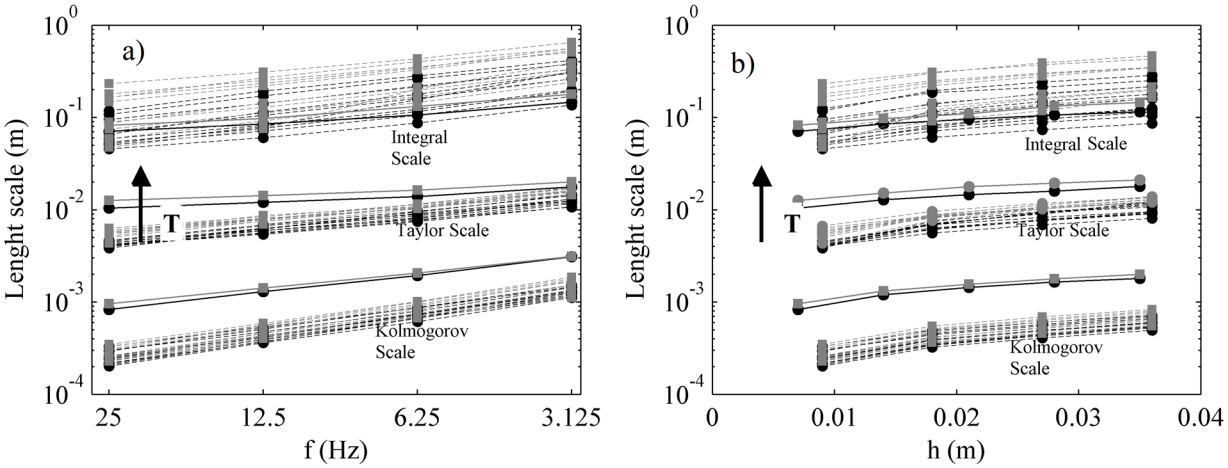

Figure C.34- Length Scales, figure (a) as a function of FDC, (b) as a function of CV. *Legend colors,* ● *z/d=0.16,* ■ *z/d=0.4. Legend Lines,* — — *RG Experiments,* ——— *Test T-1.*

Figure C.35 depicts the value of the autocorrelation function (R_{xx}). As mentioned before, the change in the FDC should not modify the function; however, the value obtained from the first lag belong to a different point of the abscissa axis, due to the change in the lag duration. Therefore, if the lag duration in time is increased, by decreasing the FDC, it makes sense that the R_{xx} (1-lag) increases its value since the abscissa point becomes further to zero, and therefore the ordinates point further to one. The integral length scale, Figure C.34, calculated from the integral of the R_{xx} function, increases as the FDC is decreased because the tail of the autocorrelation function is enlarged, showing correlation for higher time-lag values. However, increasing the *h* works different, the shape of the autocorrelation function is modified because the moving average window makes two consecutive velocities more similar between them. As a result, all the R_{xx} values, not just the (1-lag) are increased thus the length scales are increased in the same way.

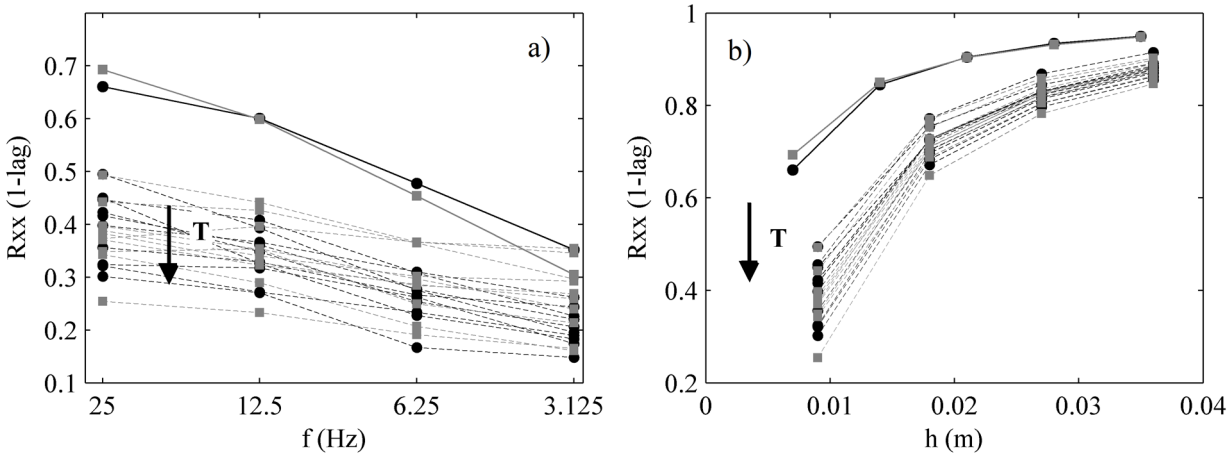

Figure C.35- Autocorrelation function value at 1-lag, figure (a) as a function of FDC, (b) as a function of the CV. *Legend colors,* ● *z/d=0.16,* ■ *z/d=0.4. Legend Lines,* — — *RG Experiments,* ——— *Test T-1.*

The standard deviation of the instantaneous longitudinal velocity increments ($\sigma_{\Delta u}$) as a function of the FDC or the *h* are depicted in Figure C.36. In the APCs of the 'FRITZ' tests, it was seen that the *h* affected more than the FDC, and the same can be seen in the RG experiments. However, the decrease caused by the FDC reduction is now more considerable due to the high level of turbulence, where there are more peak values of the instantaneous velocity.

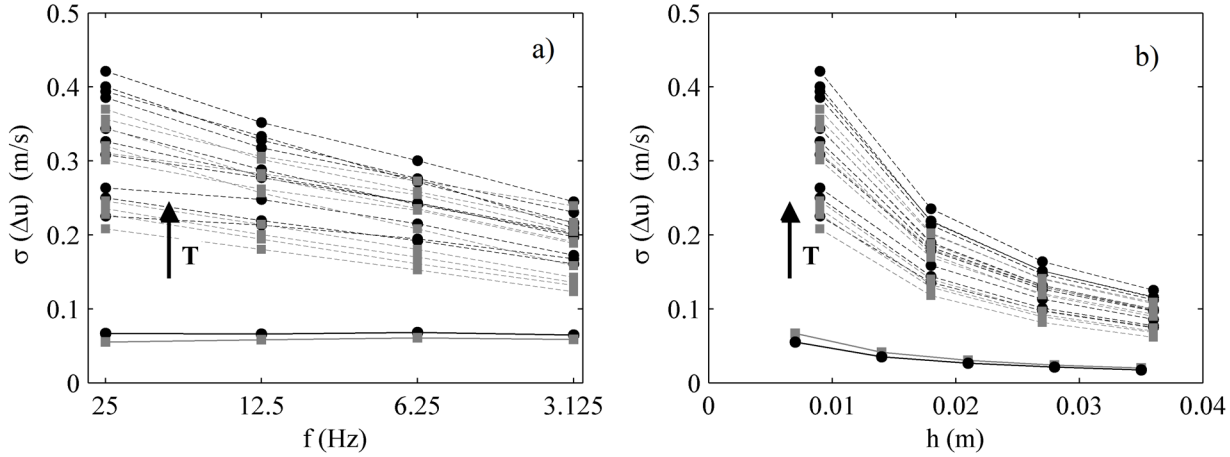

Figure C.36- Standard deviation of the velocity increments of u, (a) as a function of FDC, (b) as a function of the CV. *Legend colors,* ● *z/d=0.16,* ■ *z/d=0.4. Legend Lines,* — — *RG Experiments,* ——— *Test T-1.*

Regarding the QTFs, (Figure C.37 and Figure C.38) the trend of evolution is similar for the decreased FDC and the increased *h*. Moreover, differences between the experiments RG and the test T-1 are not remarkable. Despite the digital averaging and the moving average window, the value remains stable. That means that the QTF is a very robust characteristic of the flow regardless the configuration of the ADV, and level of turbulence.

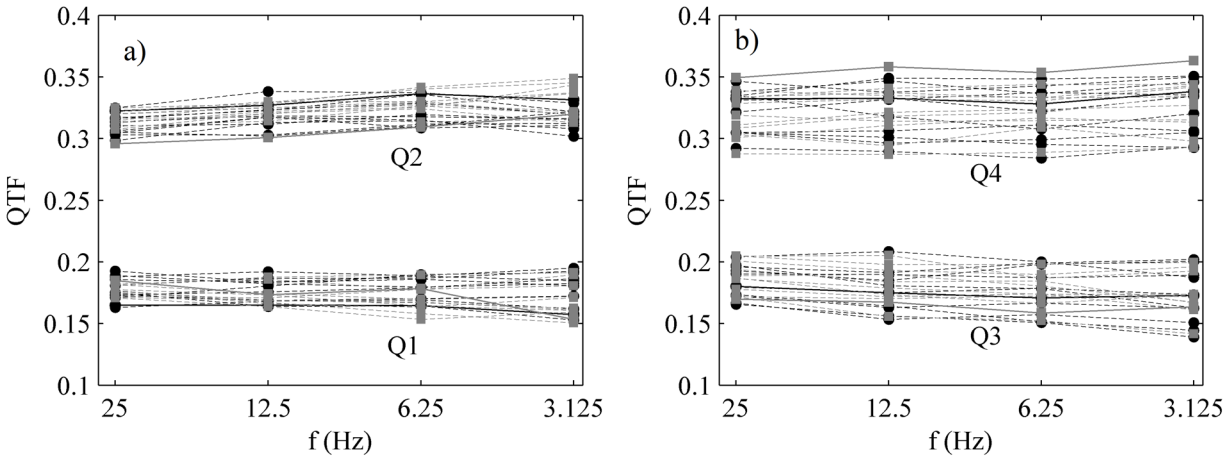

Figure C.37- Time fraction of the Quadrants as a function of the FDC, (a) Q1 and Q2, (b) Q3 and Q4. *Legend colors,* ● *z/d=0.16,* ■ *z/d=0.4. Legend Lines,* — — *RG Experiments,* ——— *Test T-1.*

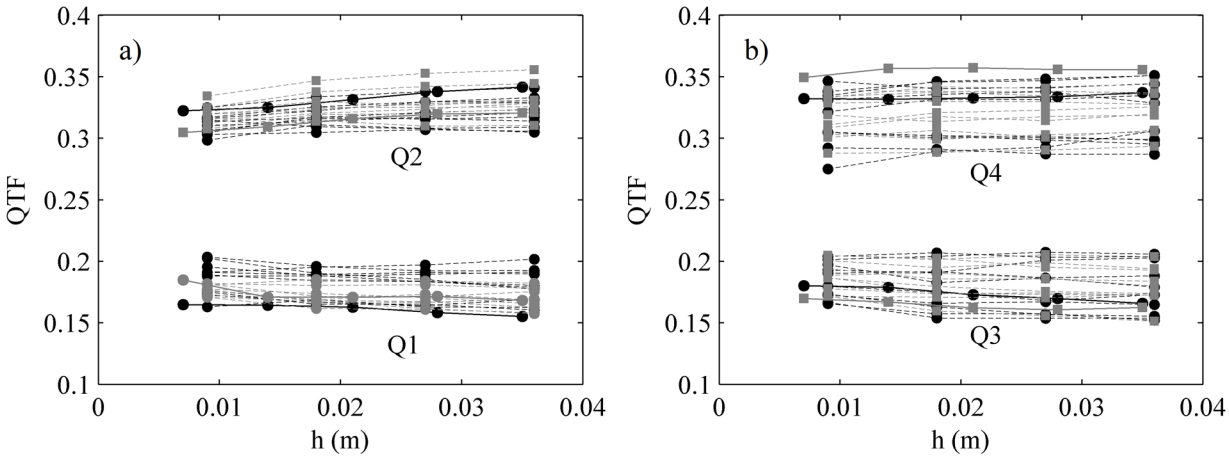

Figure C.38- Time fraction of the Quadrants as a function of the CV, (a) Q1 and Q2, (b) Q3 and Q4. *Legend colors,* ● *z/d=0.16,* ■ *z/d=0.4. Legend Lines,* — — *RG Experiments,* ——— *Test T-1.*

Regarding the trend of the time fraction of pulses of 1δ (as a function of FDC) and 1Δt (as a function of *h*), Figure C.39-a and Figure C.39-b respectively, evolves in the same way regardless the level of turbulence. That is, all them increase or decrease in a parallel way. Notwithstanding, the trend behaves differently whether the FDC decreases or the CV increases.

When the FDC is reduced the interval Δt from a pulse of length 1δ becomes longer in time, therefore, it could include shorter pulses inside that cannot be viewed. However, the time fraction of 1δ (even having different interval duration) remain rather steady in comparison with what happens when the *h* is increased. In the last case, the time fraction of the 1Δt pulses (now they can be assessed by time since they have the same FDC) declines considerably, although in the same way for all turbulence levels. As the moving average window is enlarged (*h* is increased), the velocities become more similar

between them and longer pulses, as of 2Δt, start to increase, inducing the reduction of the 1Δt pulses. The effect of the moving average window is similar to the effect that filtering when using linear interpolations to replace bad data.

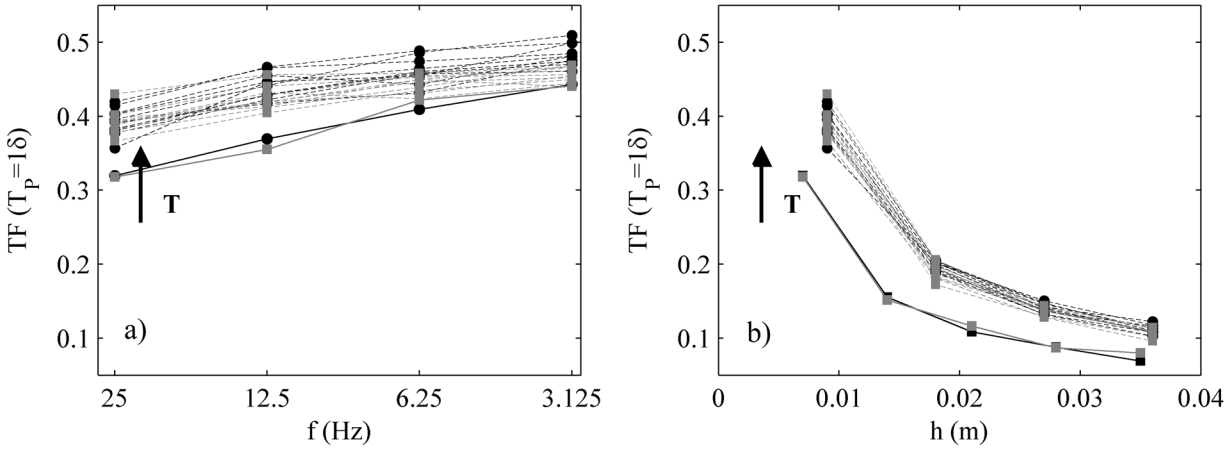

Figure C.39- Time fraction of the 1-Δt pulses, (a) as a function of FDC, (b) as a function of the CV. *Legend colors,* ● *z/d=0.16,* ■ *z/d=0.4. Legend Lines,* ▬ ▬ *RG Experiments,* ▬▬ *Test T-1.*

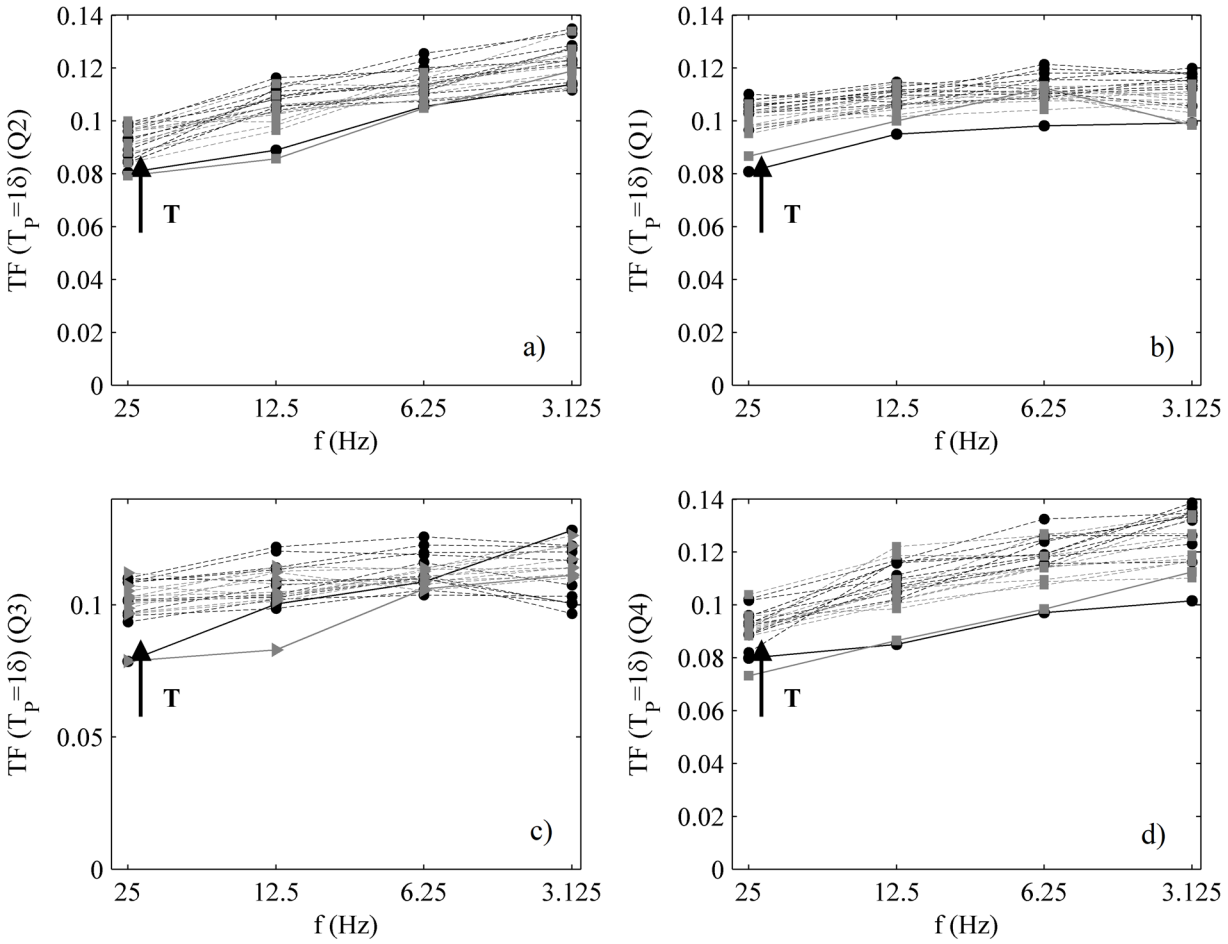

Figure C.40- Time fraction of the 1δ pulses separated by quadrants, as a function of the FDC, figure (a) Q2, (b) Q1, (c) Q3 and (d) Q4. *Legend colors,* ● *z/d=0.16,* ■ *z/d=0.4. Legend Lines,* ▬ ▬ *RG Experiments,* ▬▬ *Test T-1.*

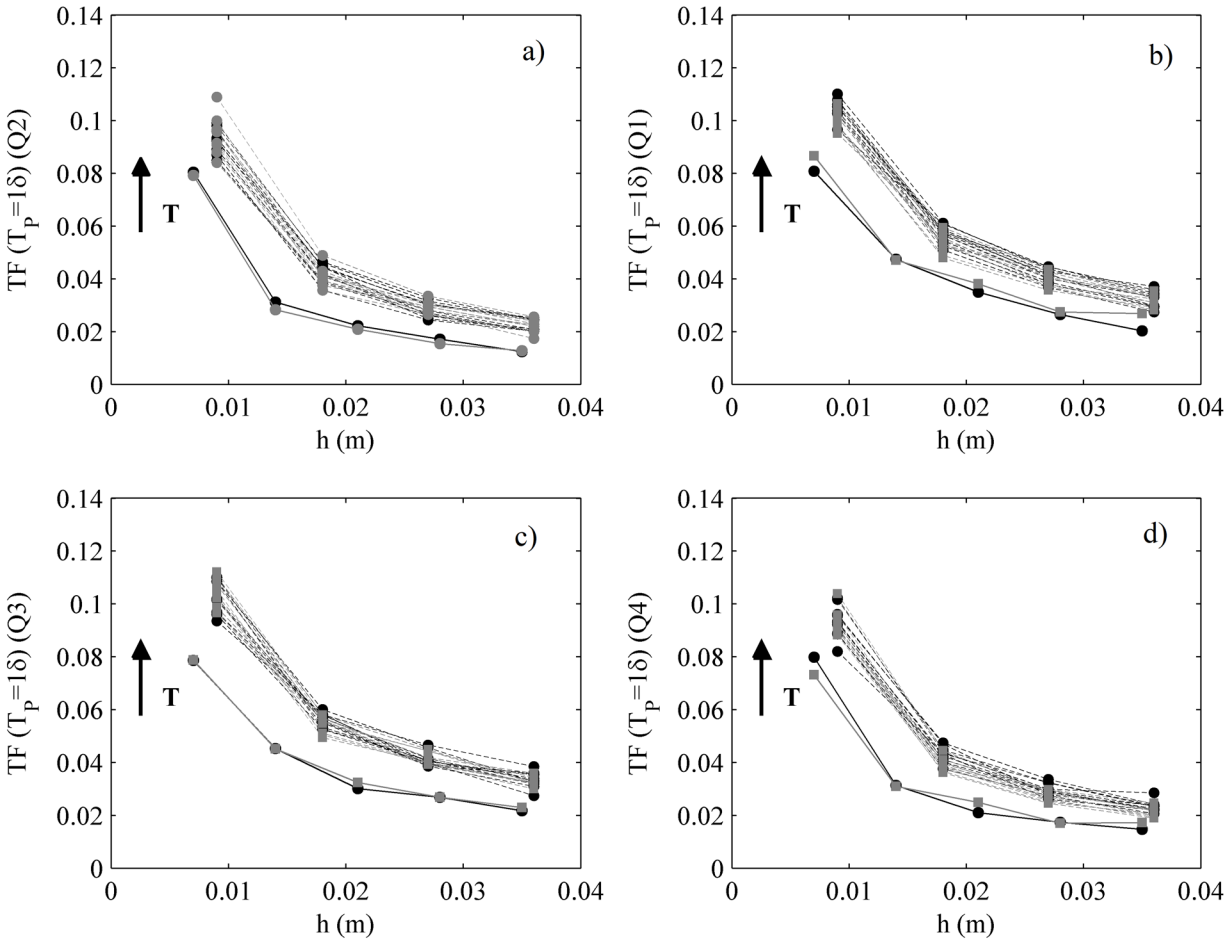

Figure C.41- Time fraction of the 1Δt pulses separated by quadrants, as a function of the *h*, figure (a) Q2, (b) Q1, (c) Q3 and (d) Q4. *Legend colors,* ● *z/d=0.16,* ■ *z/d=0.4. Legend Lines,* — — *RG Experiments,* —— *Test T-1.*

Figure C.40 and Figure C.41 show the performance curves of the TF of the short pulses (T_P=1δ) separated by quadrants. That is to say, the weight that the shortest pulses from each quadrant have on the different data series, by changing the FDC and *h*. Figure C.40 represents the evolution of the time fraction of the 1δ pulses for the four quadrants as a function of the FDC, and Figure C.41, the time fraction of 1Δt pulses as a function of the CV size. In all cases, each particular quadrant follows the same general trend of evolution than the shortest pulses without quadrant consideration, although certain nuances are distinguished.

The performance curves that characterize the decrease of the FDC (Figure C.40) show a stable trend of the 1δ pulses time fraction, especially for the quadrants Q1 and Q3, while the Q2 and Q4 seem to be more increased, controlling thus, the evolution of the general 1δ pulses.

Figure C.41 of the performance curves of the *h*, shows that the time fraction of the 1Δt pulses for the four quadrants decline their value as the CV is increased, as it was seen without the quadrant consideration in Figure C.39-b. The moving average window has the same effects on the pulses of the four quadrants.

When the interval duration of the pulses is changed, by the reduction of the FDC, it was seen that the short pulses (1δ) tend to increase a little (because they include longer pulses from the higher FDC). Figure C.42 shows the evolution of the time fraction from the most important sequences of pulses. A sequence of pulses is a three-component chain that corresponds to three different pulses (without considering the number of intervals) in three different quadrants, which have enough percentage of time fraction in the sample to be considered. Something that calls the attention of Figure C.42 is that the RG experiments (with high levels of turbulence) maintain more stable sequence time fraction along the changes in the FDCs than the test T-1. Sequences that involve quadrants Q1 and Q4 seem to have more constant values than those including quadrants Q2 and Q3. However, all turbulence levels and for the four considered sequences, although moderately, tend to decrease their presence in the sample. Therefore, the rest of sequences become more likely.

The case of Figure C.43, the performance curves of the pulse sequences as a function of the *h*, show a trend of increase for the four considered sequences, unlike the previous ones. Then, we saw that the short pulses of 1Δt decrease but the sequences increase. Therefore, the short pulses seem not to belong to these sequences.

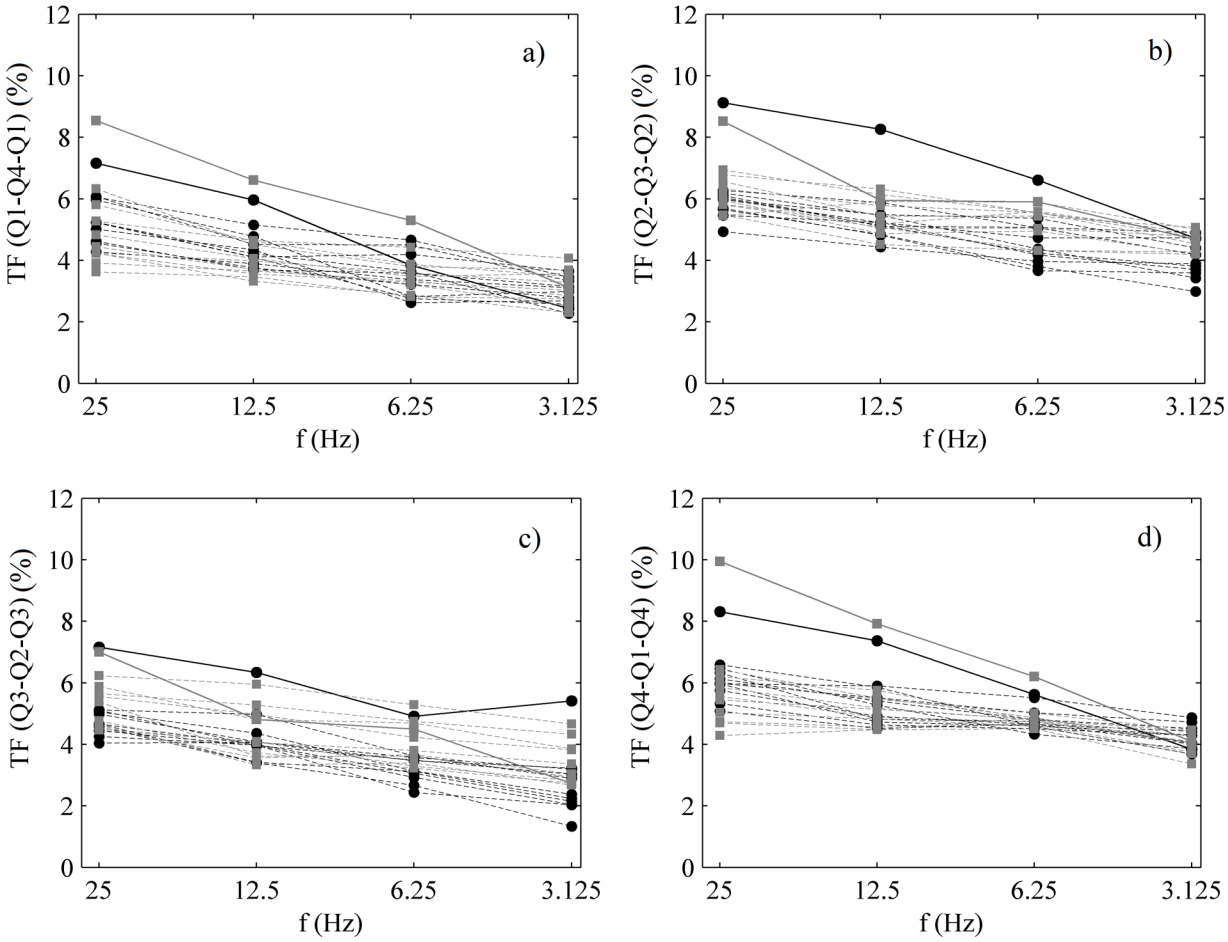

Figure C.42- Time fraction of most likely sequences as a function of the FDC, figure (a) Q1-Q4-Q1, (b) Q4-Q1-Q4, (c) Q2-Q3-Q2 and (d) Q3-Q2-Q3. *Legend colors,* ● *z/d=0.16,* ■ *z/d=0.4. Legend Lines,* ▬ ▬ *RG Experiments,* ▬▬ *Test T-1.*

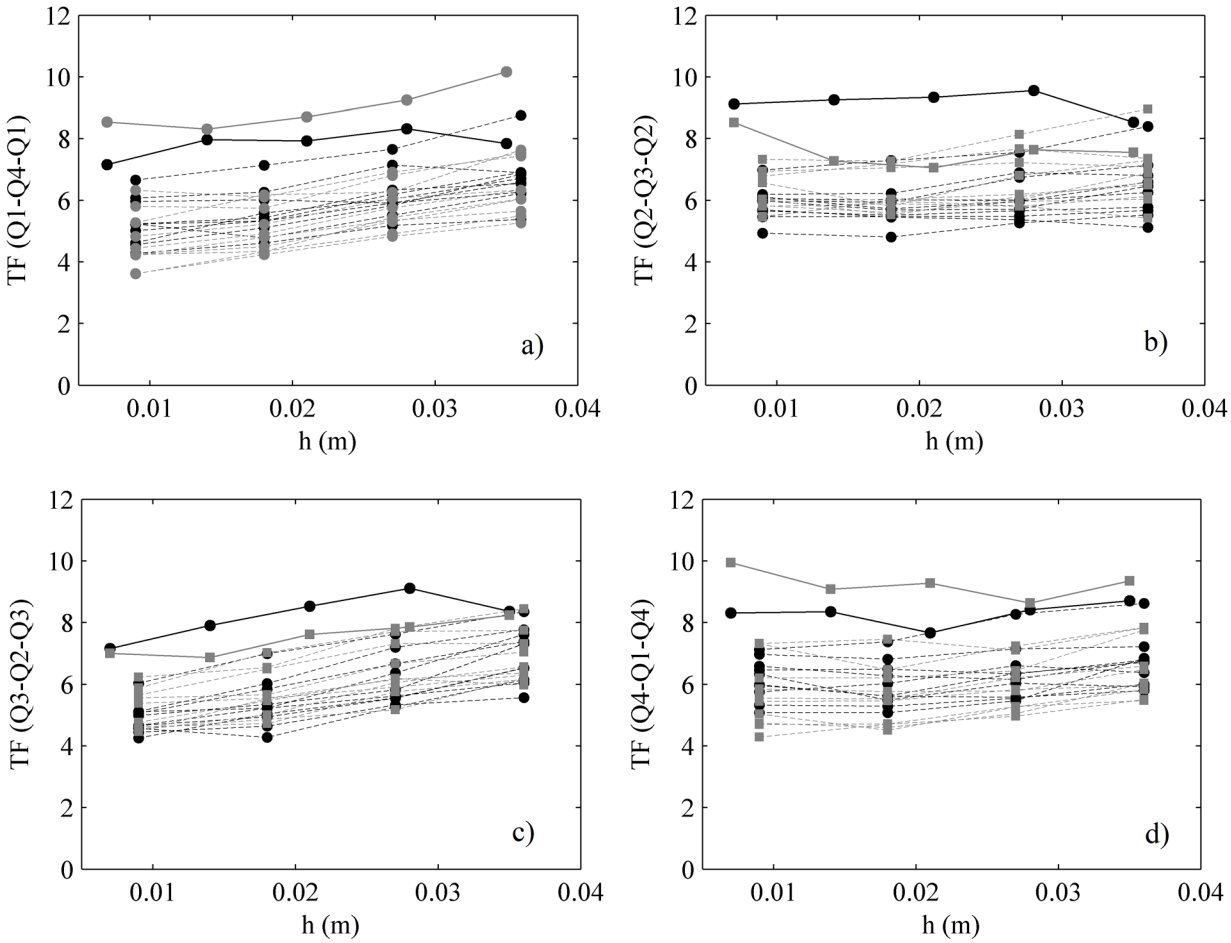

Figure C.43- Time fraction of most likely sequences as a function of the *h*, figure (a) Q1-Q4-Q1, (b) Q4-Q1-Q4, (c) Q2-Q3-Q2 and (d) Q3-Q2-Q3. *Legend colors, ● z/d=0.16, ■ z/d=0.4. Legend Lines, ▬ ▬ RG Experiments, ▬▬ Test T-1.*

Figure C.44 represents the evolution of the slope obtained from the PSD as a function of the *h* and the FDC. The slope is obtained by adjusting the values from the spectrum within the range of [1-10] Hz. As mentioned in appendix A and appendix B, the calculated values from the spectrum of the RG experiments do not follow the famous -5/3 of the Kolmogorov law, or better said, they just follow the theoretical slope in a little range of [1-3] Hz.

In order to interpret the figure correctly, it is necessary to represent the spectrum of some of the points from Figure C.44 since in the figure just the final values of the slope are included. Figure C.45 shows the complete PSD of a point situated at *z/d*=0.16 from the experiment RG-3, resulted from the decreased FDC and increased CV, by means of the averaging window methods described before. The resolution of the original series is 25 Hz and *h*=9 mm, therefore, it is only possible to increase the CV and diminish the FDC. In Figure C.45-a it is observed that the slope barely changes by decreasing the FDC, except within the range where the theoretical slope adjust that becomes shorter. Because of that, in Figure C.44-a, the obtained slope decreases with the FDC.

In the case of Figure C.45-b, where the PSD of the same point is plotted for different *h* values, it is noticeable that the shape of the spectrum changes completely due to the superposition of the velocities. As the moving average window enlarges, each time that a velocity is overlapped, the energy of some

frequencies are decreased abruptly, and the number of peaks is a function of the window size. For this reason, the obtained slope from the moving average window study cannot be discussed. As result of the latter, Figure C.44-b show an increase of the slope (of its negative value) as the CV is enlarged.

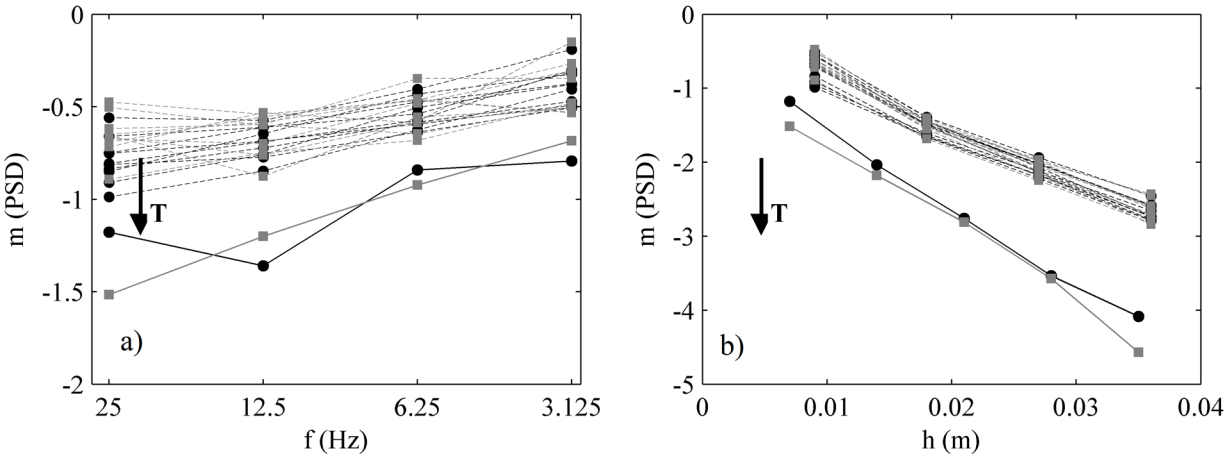

Figure C.44- Energy spectrum slopes. Figure (a) as a function of the FDC, and Figure (b) as a function of the CV. *Legend colors,* ● *z/d=0.16,* ■ *z/d=0.4. Legend Lines,* — — *RG Experiments,* —— *Test T-1.*

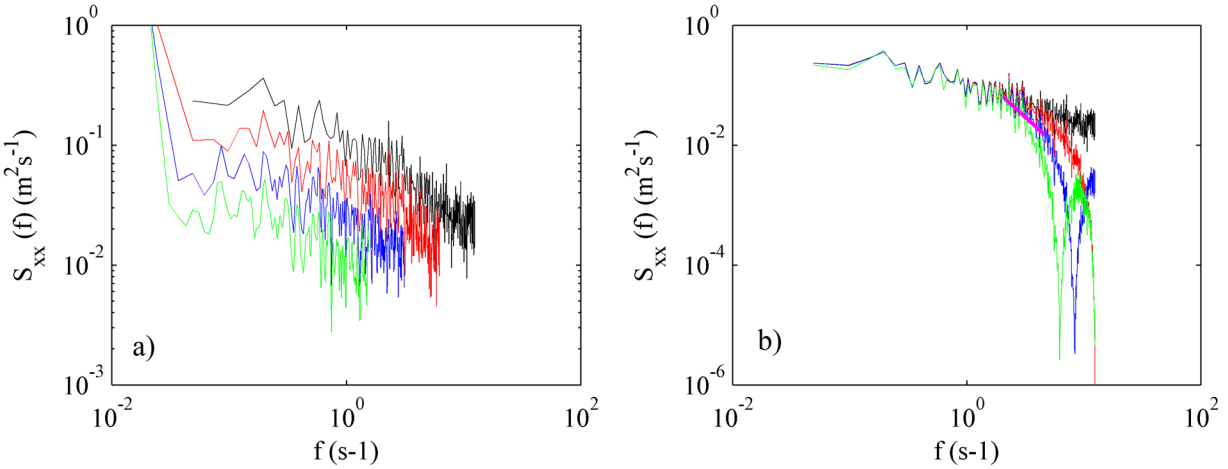

Figure C.45- PSD of the streamwise velocity component (*z/d*=0.16). Test RG-3. Figure (a) representing the FDC decrease. *Legend,* — *25 Hz,* — *12.5 Hz,* — *6.25 Hz,* — *3.125 Hz,* — *-5/3 slope.* Figure (b) representing the CV enlarge. *Legend,* — *9 mm,* — *18 mm,* — *27 mm,* — *36 mm,* — *-5/3 slope.*

C.10 Discussion

The present appendix has evaluated the ability of the ADV configuration to characterize the flow and its influence on the primary data quality parameters, turbulent properties, and Quadrant distribution through experimental work in a hydraulic flume. The results of the hydraulic characterization are summarized as follows.

The assumption of a thick layer above the boundary where the amount of SCS is higher than out of it has been corroborated by all the hypotheses assumed in the present work. Furthermore, for the specific flow conditions from the FRITZ experiments, this layer starts in the bed and ends at a height around *z/d*=0.3. In that region, called here near-bed, steep velocity gradients and small turbulence structures

(Finelli et al. 1999) yields elevated turbulence intensities and a significant amount of spikes, above all when a small CV is set in the device.

The low COR values inside this region and the increase of them along the depth, put in evidence the inaccuracy of the configuration inside this region, due to an oversize of the *h* or a too low FDC. The low amount of captured SCS makes to drop off the average COR value, showing a considerable variability in vortices scales where the SCS does not have enough presence, however, the COR value becomes more robust by decreasing σ_{COR}, which represents a low range of size structures. Nevertheless, a low FDC with a small *h* is still able to capture some SCS in the near-bed region while a long *h* obviates them all over the depth showing as consequence more constant values through the depth profile.

The time fraction of the sweeps events (Q4) shows a pattern of up-growth along the depth from the bed to the surface, similar to the average COR parameter and length scales, while the time fraction of the ejections (Q2) shows a trend of reduction, like TI and σ_{COR} parameter. The quadrants analysis suggests that the Q4 (sweeps) could evidence the existence of big structures, and this is noticeable in all patterns over the depth profile. The latter would imply that when the QTF of (Q4) and (Q2) are similar (z/d<0.3), show the existence of SCS, however, beyond the near-bed region they start to separate because the amount of SCS drops with the height (z/d).

In the case of the PLH, the time fraction of the shortest pulses (1δ) is always higher at a region near the bed, and they tend to be contained in the Q1 and Q3 quadrants, while longer pulses tend to appear in the Q2 and Q4. Therefore, it seems that long pulses in these quadrants and especially in the Q4 represent big structures, which is also the most affected by changes in the configurations. This effect is noticeable when the *h* is enlarged, by the augmentation of long pulses.

The observed patterns of all general histograms are controlled by the Q2 and Q4 PLH since they present a wider range of trends in a depth profile. These pulse regulators from Q2 and Q4, are also more modified by the configurations. On the other hand, the PLH from Q1 and Q3 have a scarped slope and similar pattern, no matter the distance to the bed, like a backbone of the flow turbulence that resists better the effects of the configuration or the height in depth.

Regarding the FDC reduction, it has been seen that even though the loss of information, i.e., less information per second and less accurate, the patterns over the depth of the QTFs and trips between quadrants are maintained. Moreover, the PLHs have similar shape despite having different time interval duration, as long as pulses are considered by length (δ) instead of time (Δt). All these facts evidence that the velocity signal obtained from a specific *h* shows the same patterns for different FDCs, showing a proportional behavior of a certain range of coherent structures, with respect to the Quadrant Map.

A small CV (*h*) yields many spikes, especially in the near-bed region, and the turbulent parameters become erratic along the depth profile. The larger is the *h*, the more echoes are received; consequently, less measurement error is obtained. On the other hand, aliasing is avoided by increasing the nominal velocity range.

Regarding the effects on the PSD, the closer fitted slope to the -5/3 of Kolmogorov was achieved by a configuration with an FDC of 25 Hz and a CV size of 7 mm. In both cases, enlarging the *h* and decreasing the FDC, show a better adjustment of the PSD to the Kolmogorov slope, becoming steeper from 8 Hz upward. That is, the energy of the high frequencies decreases, probably because the little structures become less represented in the sample (due to the configuration), showing a dependence on the size vortex range characterized by the data series. In other words, providing that the large coherent structures predominate over the smalls in the signal, the PSD spectrum comes closer to the theoretical slope.

However, the studied cases of 25 Hz (FRITZ experiments) in this appendix, have a low level of turbulence in comparison with the RG experiments, of "The Cube" channel. Consequently, the range of size vortex is shorter, and less energy is contained in the vortices. Thus, the configuration of 25 Hz and 7 mm of CV that achieves the -5/3 of slope could not be enough in the case of the RG experiments. Where the latter would need to emphasize the big ones over the smalls by decreasing more the FDC or increasing the CV, providing that the turbulence be well-developed, thus, the frequency range where the theoretical slope is achieved is short due to the not-suitable configuration of the device.

Performance Curves of the ADV

It has been demonstrated, by means of the performance curves, that the effects of the configuration also depend on the profundity of the measure because they have different turbulent conditions. Therefore not just the general flow conditions but also the particular along the profile have to be taken into account. For example, points near the bed are much more affected by the configuration than those closer to the surface. Nonetheless, the measured points show a similar pattern of change although having from different levels of turbulence.

In most of the cases has been assessed that the effect produced by the elongation of the *h* is similar to the reduction of the FDC, as is the case of the reduction of some turbulent parameters such as Reynold stresses, TKE or the dissipation rate. The length scales are also augmented in both cases. However, in cases where the time duration of the interval between velocities (Δt) is changed, because different FDCs, the comparison with the change in the *h* cannot be possible, as in the case of the autocorrelation function or the time fraction of the $1\Delta t$ pulses, since the level of definition is different.

In respect of the performance curves of the FDC, it is considered very interesting how some properties seem to be not dependent on the time interval of definition or to the accuracy of the signal time-wise. Measurements with low FDCs increase the time fraction of the short events (1δ); however, each of these can contain longer events in length ($>1\delta$) at higher FDC. The QTF and the most common sequences maintain the same percentage from 25 Hz until 200 Hz, therefore, if there is enough definition; the statistics on the quadrant map are reproduced repeatedly.

Moreover, the longitudinal velocity increments (Δu), although they are reduced by decreasing the FDC or increasing the *h*, its standard deviation ($\sigma_{\Delta u}$) remains very stable when decreasing the FDC, unlike what can be seen in the CV curves, where the value is reduced with the enlarging of the CV. The latter evidence the fact that a large *h* restricts more significantly the presence of SCS.

Regarding the CUBE Performance curves; The turbulent kinetic energy TKE, the Turbulence intensities, and Reynold stresses follow the same pattern of reduction, if the *h* is increased or the FDC reduced, as is what seen in the FRITZ experiments. However, this reduction is more remarkable if the initial values are high, i.e. with a high level of turbulence. It is appreciable how for low turbulence levels, points far to the bed, the decrease is less sharp, making very difficult to find a common trend of decrease that works for all cases.

Unlike the rest of the turbulence parameters, the dissipation rate (ε) it shows the same rate of decrease for all experiments no matter the level of turbulence, showing a stable slope of decrease in all cases. The same rate of increase of the three length scales is perceived in all the RG experiments when the FDC is reduced, or the *h* increased. In the case of the autocorrelation function (R_{xx}), the evolution of the value at the first time interval (R_{xx} at 1-lag) do not show the same trend for both ways to modify the configuration, because as explained before, the duration of the time interval changes with the FDC, thus the behavior of both modifications cannot be compared.

From the FRITZ experiments, it was observed that the CV height (*h*) affects more to the $\sigma_{\Delta u}$ than the FDC. However, higher modifications are seen now for the CUBE experiments than before, due to there are more extreme values of the instantaneous velocity.

Regarding the QTFs, the trend of evolution is similar to the changes in the FDC and the CV. That means that the QTF is a very robust characteristic of the flow regardless the configuration of the ADV. Therefore, despite the digital averaging and the moving average window, the value remains stable.

Something that calls the attention is that the RG experiments (with high levels of turbulence) maintain more stable the pulse sequences along the changes in the FDCs than the test T-1. This could be due to the level of turbulence is high enough to not lose its identity by decreasing the FDC, unlike the T-1. Sequences that involve quadrants Q1 and Q4 seem to have more constant values than those including quadrants Q2 and Q3.

In the first part of this appendix, it was seen that by increasing the *h* the adjusted slope from the PSD was also improved, i.e., the range where the theoretical -5/3 slope appears was increased. Moreover, from the study of the CUBE experiments and the moving average window, to simulate the *h* enlarging, it has been demonstrated that the slope fits better at the expense of reducing the energy abruptly from certain high frequencies.

APPENDIX D. INCIPIENT MOTION RESULTS

Table of Contents

Appendix D: Incipient Motion Results

D.1 Statistics of Impulse series

D.1.1 Test CG1

Table D.1- Impulse exerted by pulses. Test CG1

	Height	Number of pulses I>I_{cr}								
	z (m)	total	Q2	Q4	T_p=1Δt	T_p =2Δt	T_p =3Δt	T_p ≥4Δt	N_{PT}	*Imp. R.*
D_{50}	0,00	1	1	0	0	0	0	1	4574	0,022%
	0,012	1	0	1	0	1	0	0	4887	0,020%
D_{min}	0,003	22	12	10	3	2	6	11	4385	0,502%
	0,006	12	4	8	0	0	1	11	4574	0,262%
	0,008	49	23	26	5	5	7	32	4541	1,079%
	0,01	45	20	25	7	6	9	23	4792	0,939%
	0,012	62	29	33	7	5	4	46	4887	1,269%
	0,014	51	23	28	3	3	12	33	5059	1,008%
	0,016	57	25	32	7	10	11	29	4906	1,162%
	0,018	50	28	22	4	10	8	28	4875	1,026%
	0,02	36	26	10	3	5	4	24	4955	0,727%
	0,022	27	14	13	1	2	6	18	4559	0,592%
	0,024	15	8	7	0	0	1	14	4761	0,315%
	0,026	13	8	5	0	1	3	9	4511	0,288%
	0,028	16	5	11	0	2	0	14	4609	0,347%
	0,03	11	6	5	0	0	0	11	4760	0,231%

Table D.2- Impulse exerted by packets. Test CG1

	Height	Number of events I>Icr						
	z (m)	total	Q2Q4	Q4Q2	Q2-Q4-Q2	Q4-Q2-Q4	N_{ST}	*Imp. R.*
D_{max}	0,0245	1	1	0	0	0	2917	0,034%
D_{50}	0,006	1	0	1	0	0	3243	0,031%
	0,01	1	0	0	0	0	3204	0,031%
	0,014	2	0	1	0	0	3059	0,065%
D_{min}	0,003	32	8	10	6	8	2678	1,195%
	0,006	37	7	13	4	6	2790	1,326%
	0,008	33	7	11	1	6	2898	1,139%
	0,01	70	9	8	3	5	2877	2,433%
	0,012	89	9	12	3	4	3204	2,778%
	0,014	86	8	4	3	2	3393	2,535%
	0,016	92	13	15	2	7	3768	2,442%
	0,018	72	16	10	7	2	3059	2,354%
	0,02	84	11	14	6	7	3082	2,726%
	0,022	56	7	8	3	3	2943	1,903%
	0,024	43	8	4	1	3	3064	1,403%
	0,026	31	2	3	1	1	2899	1,069%
	0,028	34	7	5	3	3	2965	1,147%
	0,03	24	1	1	0	0	3122	0,769%

D.1.2 Test CG2

Table D.3- Impulse exerted by pulses. Test CG2

	Height	Number of pulses I>I_{cr}								
	z (m)	**total**	**Q2**	**Q4**	T_p **=1**Δt	T_p **=2**Δt	T_p **=3**Δt	T_p ≥4Δt	N_{PT}	***Imp. R.***
D_{50}	0,0165	1	0	1	0	1	0	0	4526	0,02%
	0,0245	1	1	0	0	0	1	0	4519	0,02%
D_{min}	0,0035	14	4	10	0	2	6	6	4834	0,290%
	0,0055	8	3	5	0	1	2	5	4521	0,177%
	0,0075	37	16	21	4	3	5	25	4402	0,841%
	0,0095	38	17	21	2	5	7	24	4633	0,820%
	0,0115	28	13	15	4	3	4	17	4773	0,587%
	0,0135	39	20	19	5	3	8	23	4526	0,862%
	0,0155	25	14	11	3	3	3	16	5267	0,475%
	0,0175	22	15	7	2	2	5	13	4749	0,463%
	0,0195	21	13	8	3	3	3	12	4566	0,460%
	0,0215	14	9	5	0	1	1	12	4519	0,310%
	0,0235	8	5	4	0	1	1	6	4796	0,167%
	0,0255	9	2	3	0	0	0	9	4767	0,189%
	0,0275	11	8	4	0	1	2	8	4617	0,238%
	0,03	6	4	2	0	0	2	4	4741	0,127%

Table D.4- Impulse exerted by packets. Test CG2

	Height	Number of events I>Icr						
	z (m)	**total**	**Q2Q4**	**Q4Q2**	**Q2-Q4-Q2**	**Q4-Q2-Q4**	N_{ST}	***Imp. R.***
D_{50}	0,0105	3	0	0	0	0	2898	0,10%
	0,0165	1	0	0	0	0	2923	0,03%
	0,0245	1	1	0	0	0	2917	0,03%
D_{min}	0,003	30	3	3	2	2	3012	0,996%
	0,006	20	2	2	3	0	2972	0,673%
	0,008	25	3	5	1	2	3243	0,771%
	0,0095	77	9	8	3	2	3120	2,468%
	0,0115	64	9	8	3	4	3077	2,080%
	0,0135	65	8	11	2	6	2923	2,224%
	0,0155	53	9	5	3	2	3388	1,564%
	0,0175	44	7	4	3	2	3099	1,420%
	0,0195	42	5	7	2	4	2891	1,453%
	0,0215	30	2	3	1	1	2917	1,028%
	0,0235	20	1	1	1	1	3143	0,636%
	0,0255	23	2	0	0	0	3056	0,753%
	0,0275	29	5	6	1	3	3020	0,960%
	0,03	14	4	3	2	2	2988	0,469%

D.1.2.1 Test CG3

Table D.5- Impulse exerted by pulses. Test CG3

	Height	Number of pulses I>I$_{cr}$								
	z (m)	**total**	**Q2**	**Q4**	T_p **=1**Δt	T_p **=2**Δt	T_p **=3**Δt	$T_p \geq$**4**Δt	N_{PT}	***Imp. R.***
D_{50}	0,006	4	2	0	0	1	1	2	4878	0,123%
	0,01	1	0	1	0	0	0	1	3734	0,027%
	0,038	1	1	0	0	0	1	0	4321	0,023%
D_{min}	0,003	32	18	14	10	8	4	10	4458	0,718%
	0,005	40	29	11	9	11	6	14	4878	0,820%
	0,007	29	12	17	3	6	7	13	4306	0,673%
	0,009	36	17	19	5	1	3	27	3734	0,964%
	0,011	22	9	13	2	4	6	10	4187	0,525%
	0,013	46	17	29	3	8	9	26	4639	0,992%
	0,015	18	7	11	2	4	5	7	4547	0,396%
	0,017	5	2	3	1	0	1	3	4454	0,112%
	0,019	8	3	5	1	2	2	3	4381	0,183%
	0,021	9	5	4	0	0	0	9	4307	0,209%
	0,023	12	5	7	1	2	3	6	4370	0,275%
	0,025	5	3	2	0	0	1	4	4433	0,113%
	0,027	6	2	4	1	1	2	2	4398	0,136%
	0,03	5	5	0	0	0	1	4	4362	0,115%

Table D.6- Impulse exerted by packets. Test CG3

	Height	Number of events I>Icr						
	z (m)	**total**	**Q2Q4**	**Q4Q2**	**Q2-Q4-Q2**	**Q4-Q2-Q4**	N_{ST}	***Imp. R.***
D_{max}	0,006	1	0	0	0	0	3137	0,032%
	0,014	1	0	0	0	0	2112	0,047%
D_{50}	0,006	5	3	1	0	0	3137	0,606%
	0,01	1	1	0	0	0	2965	0,034%
	0,014	3	3	1	2	0	2112	0,568%
	0,038	1	1	0	0	0	2918	0,034%
D_{min}	0,003	48	10	8	4	4	3002	1,60%
	0,005	41	4	4	1	1	3137	1,302%
	0,007	65	16	14	6	3	3051	2,114%
	0,009	45	4	6	2	1	2965	1,528%
	0,011	40	4	2	2	0	2539	1,576%
	0,013	52	6	4	3	2	2112	2,462%
	0,015	32	4	1	3	1	2498	1,281%
	0,017	21	4	1	1	1	2883	0,728%
	0,019	14	4	3	2	1	2866	0,488%
	0,021	21	5	6	2	1	2849	0,737%
	0,023	19	4	3	2	1	2908	0,653%
	0,025	11	3	2	1	1	2967	0,371%
	0,027	10	2	1	1	0	2956	0,338%
	0,03	17	5	4	2	0	2945	0,577%

D.1.2.2 Test CG4

Table D.7- Impulse exerted by pulses. Test CG4

	Height	Number of pulses $I>I_{cr}$								
	z (m)	**total**	**Q2**	**Q4**	T_p **=1**Δt	T_p **=2**Δt	T_p **=3**Δt	$T_p \geq 4\Delta$t	N_{PT}	***Imp. R.***
D_{50}	0,01	1	0	1	0	0	0	1	4545	0,022%
D_{min}	0,002	21	18	3	6	2	4	9	3966	0,530%
	0,004	14	6	8	3	3	4	4	4437	0,316%
	0,006	10	7	3	2	2	2	4	4908	0,204%
	0,008	24	10	14	5	5	6	8	4727	0,508%
	0,01	36	20	15	12	3	5	16	4545	0,792%
	0,012	15	6	9	4	3	4	4	4385	0,342%
	0,014	58	32	26	19	0	7	32	4224	1,373%
	0,016	12	5	7	1	2	3	6	4270	0,281%
	0,018	13	10	3	1	0	0	12	4315	0,301%
	0,02	10	4	6	1	2	3	4	4337	0,231%
	0,022	12	3	9	0	0	1	11	4359	0,275%
	0,024	3	1	2	0	1	1	1	4412	0,068%
	0,026	4	2	2	0	0	0	4	4378	0,091%
	0,03	5	1	4	0	0	0	5	4344	0,115%

Table D.8- Impulse exerted by packets. Test CG4

	Height	Number of events I>Icr						
	z (m)	**total**	**Q2Q4**	**Q4Q2**	**Q2-Q4-Q2**	**Q4-Q2-Q4**	N_{ST}	***Imp. R.***
D_{50}	0,002	1	0	1	0	0	2665	0,038%
	0,01	1	1	0	0	0	3067	0,033%
	0,014	3	0	0	0	0	2835	0,106%
D_{min}	0,002	27	4	3	3	1	2665	1,013%
	0,004	38	6	5	2	2	3000	1,267%
	0,006	45	6	4	1	0	3334	1,350%
	0,008	44	4	3	1	2	3201	1,369%
	0,01	46	5	4	1	1	3067	1,516%
	0,012	40	4	3	2	1	2951	1,356%
	0,014	44	5	6	1	2	2835	1,540%
	0,016	35	7	5	3	1	2830	1,237%
	0,018	30	7	5	3	1	2824	1,062%
	0,02	26	6	5	3	2	2822	0,922%
	0,022	22	4	1	3	0	2819	0,780%
	0,024	5	1	2	0	1	2905	0,172%
	0,026	9	2	3	0	1	2936	0,307%
	0,03	11	2	4	1	0	3362	0,327%

D.1.2.3 Test CG5

Table D.9- Impulse exerted by pulses. Test CG5

	Height	Number of pulses I>I_{cr}								
	z (m)	**total**	**Q2**	**Q4**	T_p **=1**Δt	T_p **=2**Δt	T_p **=3**Δt	$T_p \geq$4Δt	N_{PT}	***Imp. R.***
D_{min}	0,002	3	1	2	0	0	0	3	4229	0,071%
	0,004	2	1	1	0	0	1	1	4234	0,047%
	0,006	1	0	1	0	0	0	1	4239	0,024%
	0,008	3	1	2	0	1	1	1	4313	0,070%
	0,01	1	1	0	0	0	0	1	4386	0,023%
	0,012	1	0	1	0	0	0	0	4503	0,022%
	0,014	3	1	2	0	0	0	3	4619	0,065%
	0,016	1	0	1	0	0	0	0	5101	0,020%
	0,018	2	0	2	0	0	0	2	5582	0,036%
	0,02	3	1	2	0	1	1	1	5020	0,060%
	0,022	4	1	3	0	0	0	4	4458	0,090%
	0,024	2	1	1	0	0	1	1	4505	0,044%
	0,026	4	2	2	0	0	1	3	4552	0,088%
	0,028	2	1	1	0	0	0	1	4857	0,041%
	0,03	2	1	1	0	0	0	2	5161	0,039%

Table D.10- Impulse exerted by packets. Test CG5

	Height	Number of events I>Icr						
	z (m)	**total**	**Q2Q4**	**Q4Q2**	**Q2-Q4-Q2**	**Q4-Q2-Q4**	N_{ST}	***Imp. R.***
D_{min}	0,002	8	1	2	1	0	2896	0,276%
	0,004	4	0	1	0	1	2844	0,141%
	0,006	7	1	2	1	0	2791	0,251%
	0,008	5	2	1	2	0	2805	0,178%
	0,01	3	1	0	1	0	2819	0,106%
	0,012	7	0	1	0	0	2880	0,243%
	0,014	4	1	0	1	0	2940	0,136%
	0,016	3	0	1	0	0	3273	0,092%
	0,018	12	1	4	1	2	3606	0,333%
	0,02	5	1	2	0	1	3220	0,155%
	0,022	8	0	1	0	0	2833	0,282%
	0,024	4	0	0	0	0	2886	0,139%
	0,026	8	1	1	1	0	2939	0,272%
	0,028	5	1	0	0	0	3146	0,159%
	0,03	5	1	1	1	0	3353	0,149%

D.1.2.4 Test CG6

Table D.11- Impulse exerted by pulses. CG6

	Height	Number of pulses $I>I_{cr}$								
	z (m)	**total**	**Q2**	**Q4**	T_p **=1**Δt	T_p **=2**Δt	T_p **=3**Δt	$T_p \geq 4\Delta$t	N_{PT}	***Imp. R.***
D_{min}	0,002	2	1	1	0	1	0	1	4542	0,066%
	0,004	1	1	0	0	0	0	1	4753	0,021%
	0,006	2	1	1	0	0	1	1	4658	0,043%
	0,008	1	1	0	0	0	0	1	4753	0,021%
	0,01	2	1	1	0	0	0	1	4658	0,043%
	0,012	5	2	3	0	0	0	5	4562	0,110%
	0,014	1	0	1	0	0	0	0	4625	0,022%
	0,016	2	1	1	0	1	0	1	4687	0,043%
	0,018	1	0	1	0	0	0	0	4650	0,022%
	0,02	0	0	0	0	0	0	0	4612	0,000%
	0,022	3	1	2	0	1	1	1	4631	0,065%
	0,024	2	1	1	0	0	0	2	4650	0,043%
	0,026	2	1	1	0	0	0	1	4619	0,043%
	0,028	1	1	0	0	0	0	1	4588	0,022%
	0,03	1	0	1	0	0	0	0	4603	0,022%

Table D.12- Impulse exerted by packets. Test CG6

	Height	Number of events I>Icr						
	z (m)	**total**	**Q2Q4**	**Q4Q2**	**Q2-Q4-Q2**	**Q4-Q2-Q4**	N_{ST}	***Imp. R.***
D_{min}	0,002	4	1	1	0	1	3044	0,131%
	0,004	3	0	1	0	1	3195	0,094%
	0,006	5	1	1	0	0	3048	0,164%
	0,008	6	1	0	1	0	2900	0,207%
	0,01	4	1	0	0	0	2957	0,135%
	0,012	7	1	1	0	0	3014	0,232%
	0,014	4	1	2	0	1	2984	0,134%
	0,016	6	0	1	0	1	2954	0,203%
	0,018	5	0	0	0	0	2993	0,167%
	0,02	3	0	1	0	1	3031	0,099%
	0,022	3	0	0	0	0	2992	0,100%
	0,024	3	1	0	1	0	2952	0,102%
	0,026	2	0	1	0	1	2755	0,073%
	0,028	1	0	1	0	0	2879	0,035%
	0,03	2	0	1	0	1	2940	0,068%

D.2 Experimental evaluation of particle motions

D.2.1 Test CG1

Table D.13- Results from CG1

Flow R. (l/s)	d (m)	R (m)	S_f (m/m)	τ_o (N/m^2)	τ_o / τ_{cr} (%)	N_D (num.)	T_f (min)	*Motion I.* (%)	*Motion R.* (%/min)
32,68	0,055	0,051	0,031	15,22	0,91	10	11	0,56%	0,0505%
37,15	0,060	0,055	0,030	16,21	0,97	11	10	0,61%	0,0611%
43,27	0,066	0,060	0,030	17,24	1,03	12	9	0,67%	0,0741%
47,37	0,070	0,064	0,027	17,04	1,02	14	10	0,78%	0,0778%
51,97	0,072	0,065	0,030	19,32	1,15	15	10	0,83%	0,0833%
57,13	0,077	0,069	0,029	19,65	1,17	17	9	0,94%	0,1049%
61,91	0,081	0,072	0,029	20,38	1,22	25	12	1,39%	0,1157%
61,58	0,082	0,073	0,027	19,37	1,16	338	198	18,77%	0,0948%

Figure D.1- Photographs of the test CG1

D.2.2 Test CG2

Table D.14- Results from CG2

Flow R. (l/s)	d (m)	R (m)	S_f (m/m)	τ_o (N/m^2)	τ_o / τ_{cr} (%)	N_D (num.)	T_f (min)	*Motion I.* (%)	*Motion R.* (%/min)
32,72	0,057	0,053	0,029	14,70	0,88	6	10	0,33%	0,0333%
39,23	0,064	0,058	0,028	15,96	0,95	7	10	0,39%	0,0389%
43,01	0,067	0,061	0,028	16,51	0,99	10	10	0,56%	0,0555%
47,93	0,073	0,066	0,025	16,35	0,98	11	9	0,61%	0,0679%
52,03	0,074	0,067	0,028	18,50	1,10	15	10	0,83%	0,0833%
57,88	0,079	0,071	0,028	19,42	1,16	16	10	0,89%	0,0889%
65,97	0,085	0,076	0,028	20,75	1,24	23	11	1,28%	0,1161%
65,24	0,086	0,076	0,027	19,78	1,18	314	210	17,44%	0,0831%

Figure D.2- Photographs of the test CG2

D.2.3 Test CG3

Table D.15- Results from CG3

Flow R. (l/s)	d (m)	R (m)	S_f (m/m)	τ_o (N/m^2)	τ_o / τ_{cr} (%)	N_D (num.)	T_f (min)	*Motion I.* (%)	*Motion R.* (%/min)
33,13	0,058	0,053	0,031	15,83	0,56	1	10	1,43%	0,0143%
49,92	0,074	0,067	0,028	18,19	0,64	2	13	1,86%	0,0221%
63,23	0,084	0,075	0,029	20,94	0,74	3	12	1,72%	0,0359%
86,82	0,101	0,088	0,028	24,22	0,86	4	12	0,57%	0,0478%
105,27	0,114	0,098	0,027	25,61	0,91	5	10	0,72%	0,0717%
110,93	0,117	0,100	0,027	26,73	0,95	6	10	0,86%	0,0861%
114,34	0,118	0,101	0,028	27,33	0,97	6	11	0,86%	0,0782%
127,77	0,124	0,106	0,029	30,07	1,07	4	10	0,57%	0,0574%
130,76	0,128	0,109	0,027	28,76	1,02	6	10	0,86%	0,0861%
134,81	0,129	0,110	0,027	28,93	1,03	8	11	1,15%	0,1043%
137,79	0,130	0,110	0,028	30,28	1,07	12	12	1,72%	0,1434%
137,40	0,131	0,111	0,027	29,47	1,04	103	246	14,77%	0,0601%

Figure D.3- Photographs of the test CG3

D.2.4 Test CG4

Table D.16- Results from CG4

Flow R. (l/s)	d (m)	R (m)	S_f (m/m)	τ_o (N/m^2)	τ_o / τ_{cr} (%)	N_D (num.)	T_f (min)	*Motion I.* (%)	*Motion R.* (%/min)
33,23	0,053	0,049	0,031	14,55	0,52	1	5	0,72%	0,0287%
50,56	0,069	0,063	0,028	17,07	0,60	1	5	0,72%	0,0287%
63,03	0,079	0,071	0,029	19,74	0,70	2	8	0,29%	0,0359%
73,44	0,087	0,077	0,028	21,31	0,75	2	10	0,29%	0,0287%
82,29	0,093	0,082	0,028	22,54	0,80	2	10	0,29%	0,0287%
91,73	0,100	0,087	0,027	23,43	0,83	3	10	0,43%	0,0430%
99,35	0,105	0,091	0,027	24,21	0,86	2	10	0,29%	0,0287%
113,59	0,113	0,097	0,027	26,13	0,93	4	10	0,57%	0,0574%
128,06	0,119	0,102	0,029	29,00	1,03	3	10	0,43%	0,0430%
134,91	0,125	0,107	0,027	28,15	1,00	4	10	0,57%	0,0574%
137,48	0,126	0,108	0,027	28,49	1,01	6	10	0,86%	0,0861%
158,15	0,136	0,114	0,028	31,40	1,11	10	10	1,43%	0,1434%
157,84	0,136	0,114	0,028	31,40	1,11	92	245	13,20%	0,0539%

Figure D.4- Photographs of the test CG4

D.2.5 Test CG5

Table D.17- Results from CG5

Flow R. (l/s)	d (m)	R (m)	S_f (m/m)	τ_o (N/m^2)	τ_o / τ_{cr} (%)	N_D (num.)	T_f (min)	*Motion I.* (%)	*Motion R.* (%/min)
82,14	0,104	0,090	0,031	27,13	0,55	1	10	0,34%	0,0339%
89,21	0,109	0,095	0,030	27,71	0,57	1	10	0,34%	0,0339%
93,29	0,112	0,097	0,030	28,22	0,58	2	12	0,68%	0,0564%
101,76	0,117	0,101	0,030	29,17	0,60	1	10	0,34%	0,0339%
107,94	0,122	0,104	0,029	29,66	0,61	2	11	0,68%	0,0616%
117,14	0,125	0,107	0,030	31,75	0,65	3	12	1,02%	0,0847%
122,87	0,128	0,109	0,031	32,96	0,67	2	12	0,68%	0,0564%
128,76	0,130	0,111	0,032	34,35	0,70	3	13	1,02%	0,0781%
150,63	0,142	0,119	0,031	36,56	0,75	2	10	0,68%	0,0677%
164,04	0,151	0,126	0,029	36,24	0,74	3	10	1,02%	0,1016%
167,52	0,156	0,129	0,029	36,75	0,75	3	11	1,02%	0,0923%
200,38	0,171	0,140	0,030	41,15	0,84	4	11	1,35%	0,1231%
219,83	0,179	0,146	0,030	42,79	0,87	6	10	2,03%	0,2032%
231,64	0,180	0,146	0,030	42,85	0,88	8	11	2,71%	0,2463%
231,41	0,181	0,147	0,029	42,21	0,86	22	282	7,45%	0,0264%

Figure D.5- Photographs of the test CG5

D.2.6 Test CG6

Table D.18- Results from CG6

Flow R. (l/s)	d (m)	R (m)	S_f (m/m)	τ_o (N/m^2)	τ_o / τ_{cr} (%)	N_D (num.)	T_f (min)	*Motion I.* (%)	*Motion R.* (%/min)
81,76	0,103	0,090	0,031	26,85	0,55	1	11	0,34%	0,0308%
90,43	0,112	0,097	0,030	28,64	0,59	1	10	0,34%	0,0339%
102,11	0,118	0,101	0,030	29,70	0,61	1	10	0,34%	0,0339%
117,33	0,126	0,107	0,030	31,78	0,65	1	12	0,34%	0,0282%
128,26	0,131	0,111	0,031	33,97	0,69	1	11	0,34%	0,0308%
158,37	0,151	0,126	0,031	38,03	0,78	2	10	0,68%	0,0677%
164,04	0,155	0,129	0,030	37,58	0,77	1	14	0,34%	0,0242%
165,18	0,156	0,129	0,030	37,66	0,77	1	12	0,34%	0,0282%
167,49	0,157	0,130	0,030	37,91	0,77	3	10	1,02%	0,1016%
186,63	0,163	0,134	0,032	41,50	0,85	1	12	0,34%	0,0282%
201,78	0,173	0,141	0,029	40,73	0,83	2	10	0,68%	0,0677%
220,33	0,180	0,146	0,030	43,02	0,88	3	11	1,02%	0,0923%
238,42	0,188	0,152	0,030	44,05	0,90	4	10	1,35%	0,1354%
249,97	0,195	0,157	0,030	45,88	0,94	5	11	1,69%	0,1539%
261,84	0,201	0,161	0,030	47,48	0,97	7	12	2,37%	0,1975%
260,59	0,202	0,161	0,029	46,10	0,94	15	294	5,08%	0,0173%

Figure D.6- Photographs of the test CG6